Continuum Based Modeling and Analysis for the Mechanics of Fiber Reinforced Hyperelastic Composite Material: Plane, Out of Plane Response and Pseudo-elasticity

by

Suprabha Islam

A thesis submitted in partial fulfillment of the requirements for the degree of

Doctor of Philosophy

Department of Mechanical Engineering

University of Alberta

Abstract

In recent days, hyperelastic composites (i.e., elastomeric composites reinforced with fibers) have shown promising outcomes in various engineering applications involving tissue engineering, shape-morphing structures, microfluidics, wearable devices, biomechanics, and soft robotics. Typically, elastomeric materials can sustain a large range of strains e.g., Ecoflex can sustain up to 10 times its initial length. When the elastomeric materials are used in conjunction with systematically arranged continuous fibers such as fiber mesh and interpenetrating networks, they display a distinct strain-stiffening phenomenon, known as J-shaped stress-strain behavior. This unique characteristic makes elastomeric composite highly useful in tissue engineering, biomedical, and other engineering applications. Moreover, when elastomeric materials are filled with nanofibers, their mechanical, conductive, and dielectric properties can be improved greatly making them proper candidates for the design of flexible and wearable electronic devices. Due to the great potential of these materials, the modeling of hyperelastic composites has become a subject of intense study during the last few decades. The primary motivation behind this research study is to develop a generalized and complete hyperelastic model for the fiber-reinforced composite material. The presented generalized model may accommodate some unique features including, higher-order gradient continua, precise characterization of fiber reinforcement, pseudoelasticity, damage mechanics, and multi-scale capability that makes the model uniquely versatile in the modeling and design of hyperelastic composites. The existing hyperelastic models fail to attain this level of versatility.

We started by presenting a continuum model for hyperelastic material reinforced

with unidirectional fibers resistant to flexure and extension. Which is then refined to accommodate bi-directional fibers having different orientations (i.e., 45 and 90-degree orientations), different types of nonlinear extension potential (i.e., polynomial and exponential), and torsional resistance. The response of elastomeric matrix material is characterized by using the Moony-Rivlin strain energy potential. The kinematics of the embedded fibers are formulated via the first and second gradient of continuum deformations through which the stretch, bending, and torsional responses of fibers are modeled. By means of variational principles and a virtual work statement, the Euler equilibrium equation and the associated boundary conditions are derived. The system is then numerically solved via custom-built numerical procedures. The results from the generalized model demonstrate excellent correspondence to the experimental results in capturing the deformations and mechanical responses under different loading conditions including pure bending, uniaxial tension, and out-of-plane deformations. The model is then further refined by introducing damage parameters and damage functions inspired by Ogden Roxburgh's model and Weibull's fiber damage model. The obtained models can successfully predict the Mullins effects in biological soft tissues and damage mechanics due to fiber breakage. Furthermore, we have extended our model to accommodate the size, orientation effects, and volume fraction of the reinforcing fibers by introducing the shear-lag, Krenchel orientation, and energy fraction parameters, respectively. This extension allows the model to predict the responses of nanofiber-reinforced hyperelastic composites having different micromechanical characterizations. We also propose a non-uniform interface stiffness parameter to incorporate the damage mechanics of nanofiber-reinforced elastomeric composites due to interfacial debonding. The resulting model closely assimilates both the gradual and rapid debonding processes of a certain type of soft/stiff matrix-based nanocomposite. The practical utility of the presented generalized model may be expected in the design and analysis of elastomeric composites for different engineering applications.

Preface

The materials in this thesis are part of the research project under the supervision of Professor Chun Il Kim.

Chapter 2 of this work has been published as Kim, C. I. and Islam, S. (2020). Mechanics of third-gradient continua reinforced with fibers resistant to flexure in finite plane elastostatics. Continuum Mechanics and Thermodynamics, 32, 1595–1617. doi: 10.1007/s00161-020-00867-3

Chapter 3 of this work has been published with slight differences as Islam, S. and Zhalmuratova, D. and Chung, H. and Kim, C. I. (2020). A model for hyperelastic materials reinforced with fibers resistance to extension and flexure. International Journal of Solids and Structures, 193-194, 418-433. doi: 10.1016/j.ijsolstr.2020.02.036

Chapter 4 of this work has been published as Islam, S. and Bolouri, S. E. S. and Kim, C. I. (2021). Mechanics of hyperelastic composites reinforced with non-linear elastic fibrous materials in finite plane elastostatics. International Journal of Engineering Science, 165, 103491. doi: 10.1016/j.ijengsci.2021.103491

Chapter 5 of this work has been submitted to International Journal of Mechanical Sciences journal entitled "A three-dimensional continuum model for the mechanics of an elastic medium reinforced with fibrous materials in finite elastostatics", which is currently under review.

Chapter 6 is currently under preparation for submitting to a peer-reviewed journal.

Chapter 7 of this work has been accepted as Islam, S., Yang, S., Kim, C.I. (2023). A multiscale continuum model for the mechanics of hyperelastic composite reinforced with nanofibers. International Journal of Solids and Structures, 267, 112168. doi: 10.1016/j.ijsolstr.2023.112168

" To my dear wife, and my parents, **Refat Sharna**, **Dr Md Rafiqul Islam**, *and* **Syeda Jesmin Sultana***"*

For their love, endless support, encouragement ,and sacrifices

Lives are short, but knowledge is eternal.

– Rachel Caine

Acknowledgements

In the name of God, the Beneficent the Merciful, I thank him foremost for the innumerable blessings I have received throughout my life, and especially, for the potency and the understanding needed to complete this endeavor, for He is the All-Knowing and Lord of the Universe.

I would like to thank greatly Dr. Chun Il Kim for taking me into his research group, and for guiding me throughout my research path. Besides my PhD supervisor, I would also like to thank my thesis committee, Dr. Hyun-Joong Chung for giving me the opportunity to carry out the uniaxial tension experiment with his research group. Furthermore, I would like to thank to my thesis committee, Dr. Peter Schiavone for his kind advice and constructive suggestions during my PhD candidacy exam which helped me a lot in preparing this thesis work.

Finally, I must express my gratefulness to my parents and my wife for providing me with constant encouragement and support during my graduate studies.

Table of Contents

List of Tables

List of Figures

xix

Chapter 1

Introduction

We begin this chapter with a brief introduction to fiber-reinforced hyperelastic composite materials, presented in section 1.1. In section 1.2, some applications of the hyperelastic composite are presented in various engineering fields. Some background on the constitutive modeling of the hyperelastic material is discussed in section 1.3. In section 1.4, the goals and motivations of the present study are outlined. Lastly, in section 1.5, the structure of the thesis is discussed.

1.1 Hyperelastic composite material

Hyperelastic composites are a special class of materials that undergo large elastic deformations and return to their initial shape when the load is removed. These materials show both a nonlinear material behavior as well as large shape changes [1]. A hyperelastic composite is a complex multi-component system where an elastomer or other hyperelastic-type matrix material is reinforced with either continuous fibers or nanofiber materials. One of the prominent examples of hyperelastic composite material is elastomeric composite. The properties of these composites depend on the type of elastomer (or mixtures of elastomers) as well as the type of fillers or fibers used and their arrangements in the matrix [2]. Depending on the types of reinforcement used for the composite material, it can be broadly classified into two major categories: elastomeric matrix reinforced with long continuous fiber and elastomeric matrix reinforced with nanofillers or short fibers.

Typically, elastomeric materials can sustain a large range of strains e.g., Ecoflex can sustain up to 10 times its initial length. When the elastomeric materials are

1

used in conjunction with systematically arranged fibers such as fiber mesh and interpenetrating networks, they display a distinct strain-stiffening phenomenon, known as J-shaped stress-strain behavior [3]-[4]. These unique characteristics of elastomeric composites make them suitable for a large number of engineering applications. In particular, J-shaped stress-strain behavior is commonly observed in many soft biological tissues, such as arteries, veins, cardiac muscles, skin, and tendons [5]-[6]. A considerable number of studies have been devoted to the fabrication and analysis of synthetic composites that can sustain J-shape stiffening in order to imitate closely the response of such soft biological tissues [4], [7]. Another interesting application of these materials lies in the development of shape-morphing structures [8]. Shape-morphing structures can be very practical in considerable applications including aircraft wings, deployable structures, and soft robotics. On the other hand, elastomeric composites reinforced with nanofillers are also very practical in engineering applications including flexible sensors and wearable devices due to their improved mechanical, thermal, conductive, and dielectric properties. For example, nanocomposites of barium titanate-filled Ecoflex or polydimethylsiloxane (PDMS) are excellent candidates in wearable sensor applications due to their excellent flexibility and capacitive properties [9]. The nanocomposite of carbon nanotube (CNT) in silicone-vinyl-methyl-silicone (VMQ) elastomer is useful in silicone-based stretchable electronics [10].

Due to these promising applications of elastomeric composites in recent years, the modeling of hyperelastic composites has become a subject of intense study. The primary theme of this thesis is to present a generalized hyperelastic model for elastomeric composites that may help to understand better the deformation kinematics, mechanical response, and damage mechanics of these composites. Such a model would be highly beneficial in the precise modeling and design of engineering devices and structures made up of elastomeric composites.

1.2 Applications of hyperelastic composites

In recent days, hyperelastic composites, such as elastomeric composites reinforced with fiber or nanofillers have found numerous promising applications in various engineering fields involving biomedical applications, wearable devices, soft robotics, and

shape-morphing structures. In this section, the applications of hyperelastic composites are discussed in more detail.

1.2.1 Biomedical application

Elastomeric materials reinforced with fibers have consistently been the subject of intense study [11]–[16] for their practical importance in biomaterial science and engineering including in the areas of tissue engineering and biomechanics. When the elastomeric matrix materials are used in conjunction with systematically arranged fiber families they form highly elastic materials that display direction-dependent properties (orthotropic properties) and sustain rapid strain stiffening response at low strain levels (20%–50%), known as ' J-shaped' stress-strain behavior [4]. In fact, J-shaped and orthotropic stress-strain behaviors are the characteristics of the biological materials such as blood vessels, tendons, muscles, skin, ligaments, cartilage, and other tissues ([5], [7], and [17]). This, in turn, suggests that biological tissues may be mimicked via the systematic adjustment and/or optimization of the mechanical responses of elastomeric composites. For example, one such interesting case can be found in [7] (see, Fig. 1.1 (a)). In [7], authors tried to mimic the J-shaped stress-strain behavior using an elastomeric composite for producing the Windkessal effect, which ensures continuous flow of blood through the aorta. This new material made from elastomeric composite may be used to replace the non-compliant plastic tube found in the ex vivo heart perfusion device which is used to preserve the donor in a warm beating state during transfer between extraction and implantation surgeries [7]. Another interesting case can be found in [18], where a skin-inspired stretchable electronic circuit is developed made up of elastomeric composite with programmable mechanical properties (see, Fig. 1.1 (b)). Sudhanshu et. al in [19], developed a 3D printed mechanically representative aortic model made of gelatin fiber reinforced silicone (GFRS) composite, that may contribute to the improvement in the transcatheter aortic valve replacement (TAVR) treatment (see, Fig. 1.2). Some studies have also been carried out ([20], and [21]–[28]) to model the pseudoelastic nature of highly elastic biological soft tissues found in the flight muscles using anisotropic hyperelastic composites which might be beneficial in designing soft-bodied robots with multimodal locomotion.
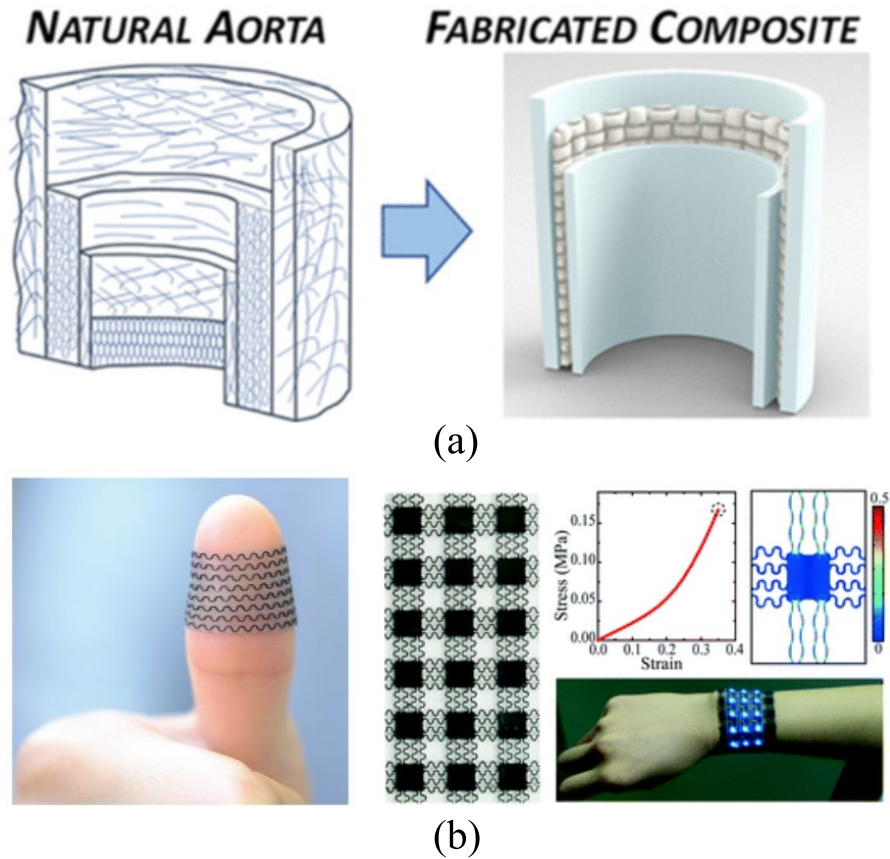
Figure 1.1: (a) An illustration of fabricated aorta from elastomeric composite [7]. (b) skin-inspired stretchable electronic circuit [18].

1.2.2 Wearable devices

Recently, hyperelastic nanocomposites reinforced with nanofillers have found numerous promising applications related to wearable and highly flexible sensors, as reported in multiple research studies ([29]–[32], and [33]-[34]). These ultra-stretchable sensors possess great potential in human motion monitoring (see, Fig. 1.3), medical rehabilitation, health monitoring, human-computer interaction, and soft robots ([29]–[32], and [34]). Authors in [29], developed an ultra-stretchable sensor made up of multi-walled carbon nanotubes (MWCNTs) and a highly stretchable elastomeric material (Ecoflex) which turns out to be as soft as the human skin. The sensor demonstrates high stretchability with outstanding linearity up to 200% strain which makes it suitable for various human motion detections (e.g., finger bending (Fig. 1.3 (d)), walking (Fig. 1.3 (g)) and speaking (Fig. 1.3 (c))). Gu et. al. presented a stretchable
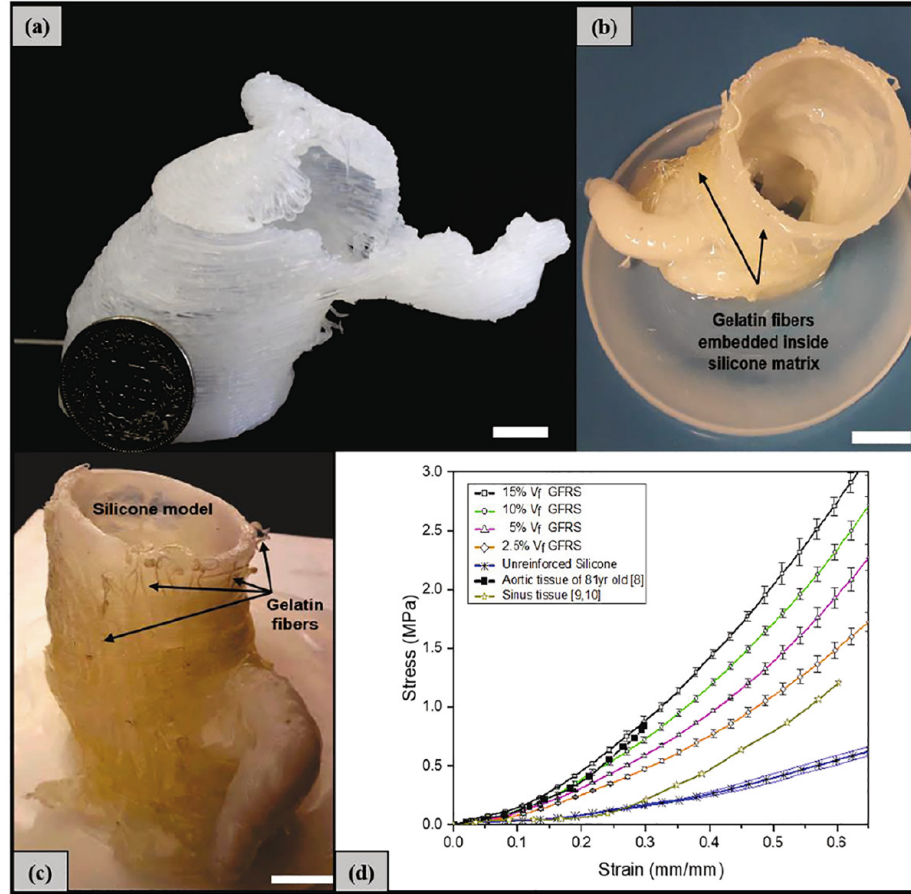
Figure 1.2: (a) 3D printed aortic model of silicone (scale bar = 10 mm), (b) GFRS aortic model after postprocessing (scale bar = 10 mm), (c) Printed silicon model reinforced with gelatin fibers (scale bar = 10 mm), (d) Tensile tests results of the materials [19].

strain sensor based on the modulation of optical transmittance of carbon nanotube (CNT)-embedded Ecoflex, which exhibits good stretchability ($\varepsilon \sim 400\%$), high linearity ($R2 > 0.98$), excellent stability, high sensitivity (gauge factor ~ 30), and small hysteresis ($\sim 1.8\%$) [30]. The sensor is further implemented to detect the bending motions of the fingers, neck movements (Fig. 1.3 (b)), and subtle human motions. In [35], a very high strain, up to 620% was able to measure using a flexible sensor made up of CNT and elastomeric matrix which is ~ 120 times greater than those of conventional metallic strain sensors. Zhang et. al. [33] reported a highly stretchable, flexible, and sensitive mono-filament tensile strain sensor, based on multi-walled carbon nanotubes/Ecoflex nanocomposites which provided good linearity (10.77%), low hysteresis (1.63%), good stability (6000 cycles under 100% strain), and ultra-high

5

strain range ($\varepsilon = 1300\%$). There are other applications of highly flexible capacitive sensors made from PDMS or Ecoflex matrix, filled with various dielectric nanofillers i.e., Barium titanate, CCTO, Ag-Nanowire, etc. [36]-[37].
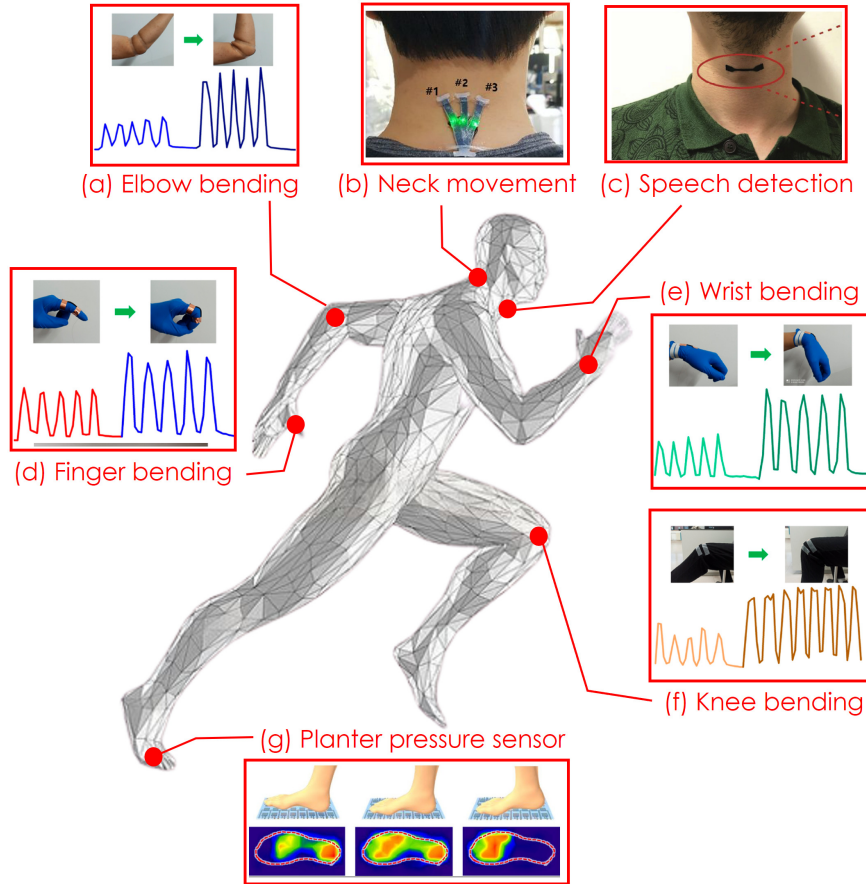
Figure 1.3: Illustration of different wearable sensors made from elastomeric nanocomposite for human motion detection in various locations.[29]–[32]

1.2.3 Soft robotics

The advantages of soft robots have rapidly been gaining the attention of the robotics community. Soft robotics can help us understand living creatures better as we can recreate them with more life-like movements and bodies. Furthermore, it provides increased flexibility and gentle manipulation of delicate objects [38]. Its flexible body allows it to fit through narrow openings in order to reach normally inaccessible locations [39]. Elastomeric composites reinforced with fibers are very promising materials in soft robotics applications. In [39], a fiber-reinforced soft elastomer is used to

6

build inflatable hemispherical and conical membranes inspired by the mantles found in nature [39] (see, Fig. 1.4). It has been demonstrated that the variable material properties afforded by the fiber reinforcement with intersecting fiber patterns help the structure to deform into a prescribed hemispherical geometry when inflated. It is also found that the geometry is constrained to a specified configuration even when the internal pressure and external load changes [39]. A practical application for the membrane was presented in [39], where the membrane is used to control the buoyancy of a bioinspired autonomous underwater robot. Cacucciolo et. al. [40] developed a soft bending fluidic actuator using fiber-reinforced hyperelastic material. Fiber-reinforced elastomeric composites are likewise used in the development of soft grippers [41] (see, Fig. 1.5).
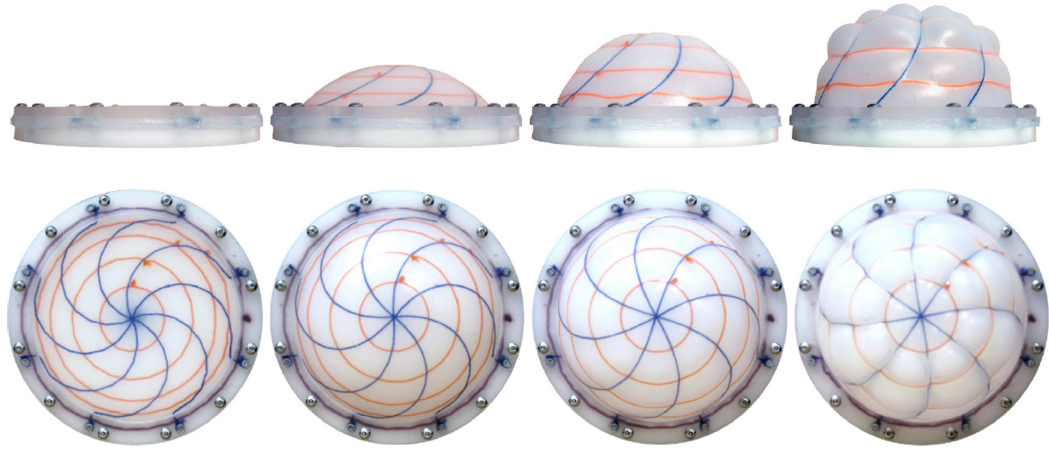
Figure 1.4: fiber-reinforced elastomeric membrane at various stages of the inflation test [39]
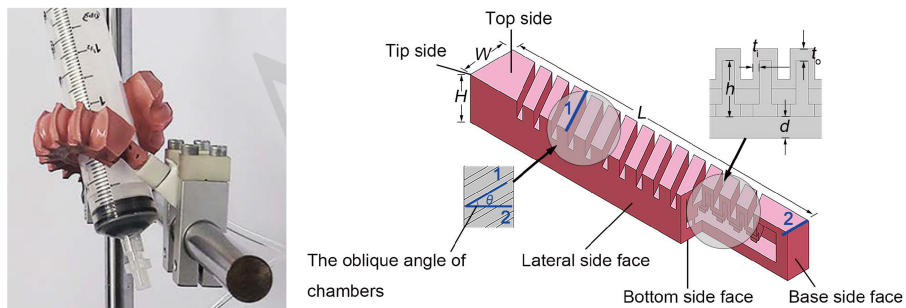
Figure 1.5: Pneumatic soft gripper [41].

1.2.4 Shape-morphing structures

The concept of shape-morphing structure is becoming exceedingly appealing nowadays, especially in the field of aerospace. The use of morphing technology can make aerospace structures aerodynamically more optimized [8]. Reinforced hyperelastic composites may be a very promising candidate for self-morphing technology due to their tailor-made mechanical properties, increased flexibility, and tear resistance. In engineering terms, the word morphing is referred to continuous shape change in a structure or object i.e., no discrete parts are moved relative to each other but one entity deforms upon actuation [8]. As an example, on an aircraft wing this could mean that a hinged aileron and/or flap would be replaced by a shape-morphing structure that can transform its surface area and camber (shape) without opening gaps in and between itself and the main wing, as a result, the aerodynamics efficiency could be improved a great deal [8], [42]. At the NASA Dryden Flight Research Center, a shape-morphing structure was experimented with in an aircraft where six wing leading edges (three on each wing) and two trailing edge segments (one on each wing) employed flexible, smooth upper surfaces made out of flexible composite material and actuated by hydraulic actuators which were used to vary the wing camber [8]. Lockheed Martin Skunk Works [8], [43] has been focusing on a folding wing concept i.e., out-of-plane morphing and targeting to achieve a $2 - 8$ times increase in wing surface area which can be applied to small UAV for US Air Force missions (see, Fig. 1.6 (a)). Hypercomp and NextGen Aeronautics [8], [44] derived a sliding wing concept, i.e., in-plane morphing, also called Batwing (see, Fig. 1.6 (b)). NextGen tested a 45kg remote-controlled model in 2006 that can change sweep from 15° to 35° and wing area by 40% in five to ten seconds. It has a silicone elastomeric composite skin with reinforcing fibers as an underlying ribbon structure to improve out-of-plane stiffness that can stretch up to 100% (see, Fig. 1.6 (b)). Kikuta [45] experimentally tested flexible composite material made up of Tecoflex 80 (a hyperelastic matrix reinforced with woven material like Spandura) to investigate the material's viability as morphing skins that could be useful in an aircraft wing. Based on the research findings of Kota et. al. [46] and Weiss [47], the FlexSys company designed and manufactured an aerofoil section made up from compliant structures, the Mission Adaptive Compliant

Wing (MACW) (see, Fig. 1.6 (c)) which can change the camber by morphing the trailing and leading edges. The compliant structures consist of flexible membranes acting as the primary aerodynamic structure and are reinforced by a network of fairly rigid longitudinal or radiating tubular hollow veins containing a fluid.
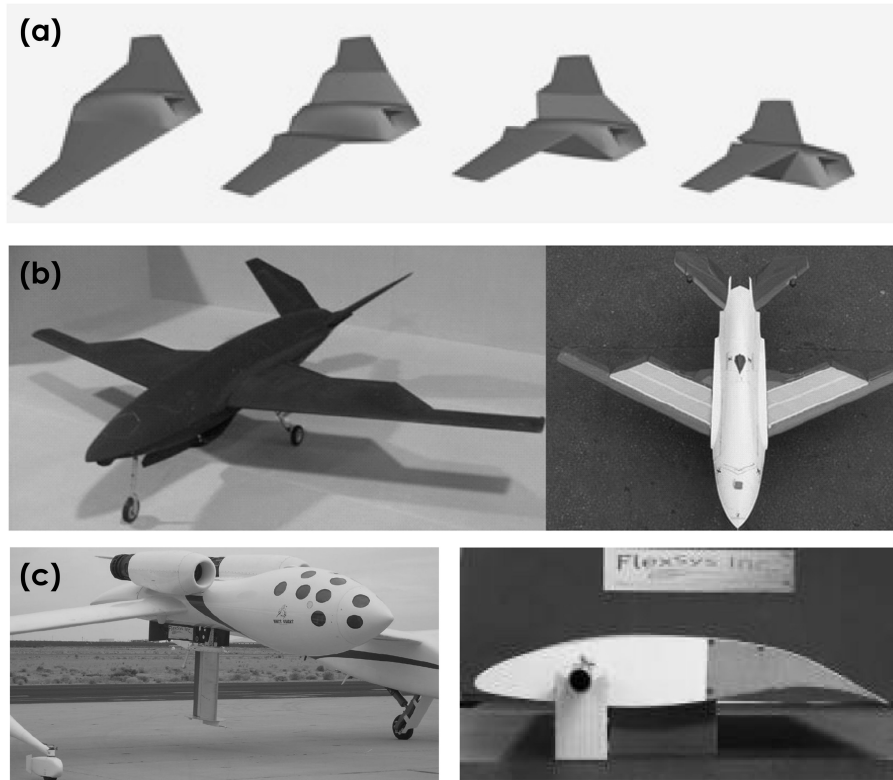
Figure 1.6: (a) Lockheed Martin's Z-wing morphing concept. (b) NextGen's Batwing morphing concept. (c) FlexSys MACW installed on White Knight for flight tests [48].

Another potential application of shape-morphing structures is in the development of flexible actuators made up of elastomeric composites. McKibben first developed such flexible actuators which are also called pneumatic artificial muscle (PAM) actuators that are made up of a tube-like membrane reinforced with a fiber mesh arranged in a double helical weave, called an inflatable inner bladder. The inner bladder can be pneumatically pressurized causing a lengthwise contraction and radial expansion. Typical materials used for the membrane are latex or silicone rubber while nylon is normally used for the reinforcing fibers [8]. Devereux and Tyler [49], later on, showed how PAMs could be used for morphing applications. The shape morphing can be achieved by embedding several braided composite tubes (PAMs) into an elastomeric

matrix making a multi-cellular FMC adaptive structure [8] (see, Fig. 1.7).
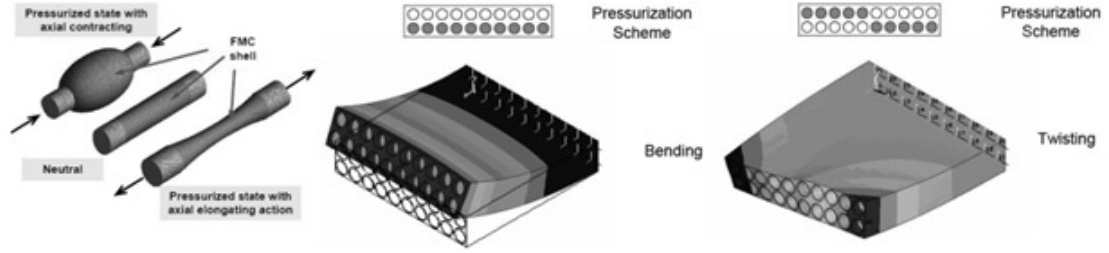
Figure 1.7: PAM actuators [50] and pressurisation scheme of actuators in an elastomer matrix [51].

1.3 Background on the constitutive modeling of hyperelastic materials

The study of the mechanical response of hyperelastic composite materials is getting intensive attention due to their promising applications. Elastomer composites exhibit large deformation, and the stress-strain response is typically non-linear. Due to the complexity, high-precision prediction of the mechanical behavior for this type of material cannot be achieved without dedicated and reliable hyperelastic constitutive models [52]. In this section, a brief classification of the hyperelastic constitutive models from the existing literature is presented.

Elastomeric composite can deform nonlinearly with large deformation, and it can almost completely recover its original configuration when the external force is removed [53]. Due to this nature, the constitutive models of such material are generally represented by an energy density function (W) rather than a direct stress-strain relation [53]. The hyperelastic constitutive models can be broadly classified into 3 categories: Phenomenological models, Micromechanical network models, and hybrid models [53].

1.3.1 Phenomenological models:

These models are based on fitting the experimental data of mechanical response via mathematical equations and in most cases, the material parameters do not have any physical meaning [53]-[54]. Phenomenological models [55]–[60] may be further divided into series function model, power law, exponential or logarithmic function model, and

limiting chain extensibility models [53]. These models can be expressed via stretch ratio [61], strain invariant or using the both [62]-[63]. Some of the most popular examples of Phenomenological models are presented below:

1.3.1.1 Fung:

Fung model can capture complex behaviors typically observed in living tissues and it serves as a starting point for many bioengineering modeling [64]. For isotropic material, the energy density function based on the Fung model can be expressed with respect to the principal stretches (λ_i) as follows:

$$W = \frac{1}{2}\left[a\left(\lambda_1^2 + \lambda_2^2 + \lambda_3^2 - 3\right) + b\left(e^{c\left(\lambda_1^2 + \lambda_2^2 + \lambda_3^2 - 3\right)} - 1\right)\right]. \tag{1.1}$$

1.3.1.2 Mooney-Rivlin:

In Mooney-Rivlin hyperelastic material model, the strain energy density function is expressed as a linear combination of the two invariants of the left Cauchy-Green deformation tensor. The model was proposed by Melvin Mooney in 1940 and expressed in terms of invariants by Ronald Rivlin in 1948 [65]. For an incompressible material, the strain energy density function based on the incompressible Mooney-Rivlin model can be expressed as follows:

$$W = C_1\left[(I_1 - 3) + C_2\left(I_1 - 3\right)\right], \tag{1.2}$$

where the 1st and 2nd invariants I_1 and I_2 can be expressed as:

$$\begin{aligned} I_1 &= \lambda_1^2 + \lambda_2^2 + \lambda_3^2, \\ I_2 &= \lambda_1^2\lambda_2^2 + \lambda_2^2\lambda_3^2 + \lambda_3^2\lambda_1^2. \end{aligned} \tag{1.3}$$

1.3.1.3 Ogden:

The Ogden model can describe the non-linear stress-strain behavior of complex materials such as rubbers, polymers, and biological tissue. The model was developed by Raymond Ogden in 1972 [66] and for incompressible material, the Ogden model can be expressed as follows:

$$W = \sum_{p=1}^{N} \frac{\mu_p}{\alpha_p}\left(\lambda_1^{\alpha_p} + \lambda_2^{\alpha_p} + \lambda_2^{-\alpha_p}\lambda_3^{-\alpha_p} - 3\right). \tag{1.4}$$

11

1.3.1.4 Polynomial:

The polynomial hyperelastic material model is a phenomenological model of rubber elasticity. In this model, the strain energy density function is in the form of a polynomial involving the two invariants I_1 and I_2 of the left Cauchy-Green deformation tensor [67]. Based on the incompressible Polynomial model, the strain energy density function can be expressed as follows:

$$W = \sum_{i,j=1}^{N} C_{ij} \left(I_1 - 3\right)^i \left(I_2 - 3\right)^j. \tag{1.5}$$

Other popular Phenomenological models include: Saint Venant-Kirchhoff, Yeoh, and Marlow [68].

1.3.2 Micromechanical network models:

Micromechanical network models are based on the physical and statistical methods of polymer chain networks and material microstructure [53]. The material parameters of micromechanical network models do have physical interpretations and can explain the relationship between microstructures and properties of the material [53]. According to the statistical characteristics of macromolecular chains, micromechanical network models can be further divided into three types [53]: Gaussian chain network models [69], non-Gaussian chain network models [70]-[71], and mixed micromechanical network models [72]–[75]. Some of the most popular examples of Micromechanical network models are presented below:

1.3.2.1 Arruda-Boyce model

The Arruda–Boyce model is a hyperelastic constitutive model that describes the mechanical behaviors of rubber and other polymeric substances. This model is based on the statistical mechanics of a material with a cubic representative volume element containing eight chains along the diagonal directions [76]. This model was published by Ellen Arruda and Mary Cunningham Boyce in 1993. The strain energy density function for the incompressible Arruda–Boyce model is given by

$$W = NK_B\theta\sqrt{n}\left[\beta\lambda_{chain} - \sqrt{n}\ln\left(\frac{\sinh\beta}{\beta}\right)\right], \tag{1.6}$$

12

where n is the number of chain segments, K_B is the Boltzmann constant, θ is the temperature in kelvins, N is the number of chains in the network of a cross-linked polymer, $\lambda_{chain} = \sqrt{\frac{I_1}{3}}, \beta = \Gamma^{-1}\left(\frac{\lambda_{chain}}{\sqrt{n}}\right)$. Where, I_1 is the first invarient of the Cauchy-Green deformation tensor and $\Gamma^{-1}(x)$ is the inverse Langevin function.

1.3.2.2 Neo-Hookean model

Neo-Hookean is a hyperelastic model similar to Hooke's law, that can be used for predicting the nonlinear stress-strain behavior of materials undergoing large deformations. The neo-Hookean model is based on the statistical thermodynamics of cross-linked polymer chains, which is usable for plastics and rubber-like substances [77]. The model was proposed by Ronald Rivlin in 1948. The strain energy density function based on the incompressible neo-Hookean model can be presented as follows

$$W = C_1(I_I - 3). \tag{1.7}$$

1.3.3 Hybrid models

There are also some hybrid models which are developed as a combination of the phenomenological and micromechanical network models. Some of the popular hybrid models are as follows:

1.3.3.1 Gent

The Gent hyperelastic material model is a hybrid type model of rubber elasticity that is based on the concept of limiting chain extensibility. In this model, the strain energy density function is designed such that it has a singularity when the first invariant (I_1) of the left Cauchy-Green deformation tensor reaches a limiting value (I_m) [78]. The strain energy density function based on the Gent model can be presented as follows

$$W = \frac{\mu J_m}{2} \ln\left(1 - \frac{I_1 - 3}{I_m - 3}\right), \tag{1.8}$$

where μ is the shear modulus.

1.3.3.2 Van der waals

The Van der Waals strain energy potential for a rubber material is analogous to the equations of state of a real gas [79]. The strain energy potential for Van der Waals

model for an incompressible material can be presented as follows

$$U = \mu\{-(\lambda_m^2 - 3)\left[\ln(1-\eta) + \eta\right] - \frac{2}{3}a\left(\frac{\tilde{I}-3}{2}\right)^{\frac{3}{2}}\},\qquad(1.9)$$

where $\tilde{I} = (1-\beta)I_1 + \beta I_2$, $\eta = \sqrt{\frac{\tilde{I}-3}{\lambda_m^2-3}}$, λ_m is the locking stretch, a is the global interaction parameter, and β is a linear mixing parameter.

1.3.4 Hyperelastic composite models

In the hyperelastic models for the composite material, an isotropic part of the energy density function (typically, Mooney-Rivlin or Neo-Hookean type) is combined with a fiber energy potential. The isotropic part resembles the response of the matrix material whereas the fiber energy potential part resembles the fiber's response. Some of the popular hyperelastic models for composites are briefly discussed as follows:

1.3.4.1 Holzapfel model

Holzapfel model consists of two parts in the energy density function, where the Neo-Hookean type isotropic part (W_{iso}) presents the non-collagenous tissues (matrix), and the anisotropic part (W_{ani}) describes the collagen fibers under an α angle typically with respect to the hoop direction of a hollow organ [80]. The energy density function based on the Holzapfel model can be presented as follows:

$$
\begin{aligned}
W &= W_{iso}(I_1) + W_{ani}(I_4, I_6) + u(J), & (1.10)\\
&= \frac{\mu}{2}(I_1 - 3) + \frac{k_{1H}}{2k_{2H}}\{\exp[k_{2H}(I_4-1)^2] - 1\} + \frac{k_{1H}}{2k_{2H}}\{\exp[k_{2H}(I_6-1)^2]\\
&\quad -1\}\} + \frac{1}{2}\left[\frac{2(1+\nu)}{3(1-2\nu)}\mu\right](J-1),
\end{aligned}
$$

where k_{iH} are the material parameters, I_1 is the 1st invariant of the Cauchy-Green tensor ($\mathbf{C}$), $I_4 = a_0 \cdot \mathbf{C}a_0$, and $I_6 = g_0 \cdot \mathbf{C}g_0$. Here, $a_0 = [0\cos\alpha\sin\alpha]^T$ and $g_0 = [0\cos\alpha - \sin\alpha]T$ are the unit direction vectors of two fiber families.

1.3.4.2 Modified Fung model

In [81]-[82], a modified Fung model is presented by combining a matrix portion (Neo-Hookean type) and a fiber portion of the energy density function. The energy density

function based on the modified Fung model can be presented as follows:

$$W = \frac{\mu}{2}(I_1 - 3) + C[\exp\{Q_{iso}(\mathbf{E})\} - 1], \tag{1.11}$$

where $Q_{iso}(\mathbf{E}) = c_1(E_1^2 + E_2^2 + E_3^2) + 2c_2(E_1E_2 + E_2E_3 + E_3E_1)$, C & c_i are the fiber parameters and E_i are the principal Green–Lagrange strains.

1.4 Goals and Motivations: A generalized higher-order gradient hyperelastic model for composites

The primary motivation behind this thesis work is to develop a generalized and complete hyperelastic model for the fiber-reinforced composite material. In the most generalized form, the energy density function based on the proposed higher-order gradient hyperelastic composite model may be expressed as follows:

$$\begin{aligned} W &= (1-\alpha)d_m W_{matrix}(\mathbf{F}) + \alpha[\eta_0 d_f W_{ext}(\varepsilon_1, \varepsilon_2, \varsigma) + \frac{1}{2}C_1\mathbf{g}_1 \cdot \mathbf{g}_1 \\ &+ \frac{1}{2}C_2\mathbf{g}_2 \cdot \mathbf{g}_2 + \frac{1}{2}T\mathbf{g}_1 \cdot \mathbf{g}_2], \end{aligned} \tag{1.12}$$

where W_{matrix} is the energy function for the hyperelastic matrix material. For Neo-Hookean type material, $W_{matrix} = \frac{\mu}{2}(I_1 - 3)$ and for Mooner-Rivlin type material, $W_{matrix} = \frac{\mu}{2}(I_1-3)+\frac{\lambda}{2}(I_2-3)$. The term $W_{ext}(\varepsilon_1, \varepsilon_2, \varsigma)$ is the fiber extension potential function. Based on the type of fiber being used, we can choose from the following different options (see, chapter 4 for more details),

$$\text{Quadratic function:} \quad W_{ext} = \frac{1}{2}E_1(\varsigma\varepsilon_1)^2 + \frac{1}{2}E_2(\varsigma\varepsilon_2)^2,$$

$$\text{3rd order polynomial function:} \quad W_{ext} = \frac{1}{2}E_{11}(\varsigma\varepsilon_1)^2 + \frac{1}{3}E_{12}(\varsigma\varepsilon_1)^3$$
$$+ \frac{1}{2}E_{21}(\varsigma\varepsilon_2)^2 + \frac{1}{3}E_{22}(\varsigma\varepsilon_2)^3,$$

$$\text{Exponential function:} \quad W_{ext} = E_{11}(E_{12}\varsigma\varepsilon_1 - 1)e^{E_{12}\varsigma\varepsilon_1}$$
$$+ E_{21}(E_{22}\varsigma\varepsilon_2 - 1)e^{E_{22}\varsigma\varepsilon_2}.$$

Here, the strain variables (i.e., ε_1 and ε_2) may be defined using the following two definitions:

Green-Lagrange strain: $\quad \varepsilon_1 = \dfrac{1}{2}\left(\mathbf{FD}\cdot\mathbf{FD}-1\right),\ \varepsilon_2 = \dfrac{1}{2}\left(\mathbf{FL}\cdot\mathbf{FL}-1\right),$

Euler-Almansi strain: $\quad \varepsilon_1 = \dfrac{1}{2}\left(1-\dfrac{1}{\mathbf{FD}\cdot\mathbf{FD}}\right),\ \varepsilon_2 = \dfrac{1}{2}\left(1-\dfrac{1}{\mathbf{FL}\cdot\mathbf{FL}}\right),$

where $\mathbf{D}$ and $\mathbf{L}$ are direction vectors of the fiber.

The higher order terms, $\frac{1}{2}C_1\mathbf{g}_1\cdot\mathbf{g}_1+\frac{1}{2}C_2\mathbf{g}_2\cdot\mathbf{g}_2$ and $\frac{1}{2}T\mathbf{g}_1\cdot\mathbf{g}_2$ represent the bending and torsional potentials of the fibers, respectively, where $\mathbf{g}_1 = \nabla[\mathbf{FD}]\mathbf{D}$ and $\mathbf{g}_2 = \nabla[\mathbf{FL}]\mathbf{L}$ are the Geodesic curvatures. Further, α is the energy density parameter, η_0 is the Krenchel orientation factor and ς is the shear-lag parameter. The latter two parameters can be expressed as follows (see, chapter 7 for more details):

$$\eta_0 = \frac{8}{15} + \frac{8}{21}\langle P_2\cos\theta\rangle + \frac{3}{35}\langle P_4\cos\theta\rangle,\ \text{and} \tag{1.13}$$

$$\varsigma = \left[\frac{1}{2L}\int_{-L}^{L}\left(1-\frac{\cosh\left(\beta x\right)}{\cosh\left(\beta L\right)}\right)dx\right], \tag{1.14}$$

where $\beta = \sqrt{\frac{K_{eff}}{E_g h}}$ and $K_{eff} = K_0 - fun(\hat{\varepsilon})e^{-6.7\left(\frac{x}{L}\right)^2}$ is the interface stiffness. Also, $fun(\hat{\varepsilon})$ is the damage characterizing function, pertaining to the reduction of interface stiffness induced by the debonding at the interface, which may be expressed as

$$fun(\hat{\varepsilon}) = a\Gamma\left(\hat{\varepsilon}-\hat{\varepsilon}_{cric}\right)\left(1+\hat{\varepsilon}_{cric}\right)^b. \tag{1.15}$$

In the above, $\Gamma\left(\hat{\varepsilon}-\hat{\varepsilon}_{cric}\right)$ is referred to as the damage activation function which is switched from inactive mode to active mode when the overall strain of the material $(\hat{\varepsilon})$ exceeds a critical value $(\hat{\varepsilon}_{cric})$. The activation of the interface damage function is governed by the condition:

$$\Gamma(x) = \begin{cases} x \leq 0; \Gamma(x) = 0\ \text{(inactive mode)} \\ x > 0; \Gamma(x) = x\ \text{(active mode)} \end{cases}. \tag{1.16}$$

Moreover, the parameters d_m and d_f are called the damage variables, which may be decided from the following two options (see, chapter 6 for more details):

Ogden-Roxburgh model $\quad:\quad d_m = d_f = 1-\dfrac{1}{r}\,\mathrm{erf}\left[\dfrac{1}{m+BW_m}\left(W_m-\tilde{W}(F)\right)\right],$

Weibull fiber damage model: $\quad d_f = 1 - e^{-\delta A\hat{\gamma}^m}, d_m = 1.$

The obtained generalized model is able to accommodate multiple features including, higher-order gradient continua, precise characterization of fiber reinforcement, pseudoelasticity, damage mechanics, and multi-scale modeling capabilities. These features make the proposed model very useful in assimilating the hyperelastic response of fiber-reinforced composite material under different applications. All the existing hyperelastic models that are discussed in the previous section fail to harbor this level of versatility. These unique features of the proposed model are discussed here in more detail.

1.4.1 Higher-order gradient continua

All of the existing hyperelastic models that are presented in the previous section are based on first-order continuum theory. Thus they may not be able to accurately predict the mechanical responses under different deformation modes [83]. That's because using first-order continuum theory it is not possible to incorporate complete kinematics of the fibers. In order to overcome such deficiency we have proposed a higher-order gradient-based continuum model. Refining the first-order theory by considering a higher gradient of deformation it is possible to incorporate the bending and torsional resistance of the fibers along with the extension into the modes of deformations, thus complete kinematics of fiber is captured [84] (see, Fig. 1.12). There are several advantages that can be obtained when higher gradient deformation is considered, which are discussed below in more detail.

Microstructural characterization:

Higher gradient theory allows more detailed characterization of the continua with distinct microstructures [84], thus it may produce a more accurate prediction of the microstructural changes within the composite. Higher gradient theory can accommodate the relative rotation or rate of changes in angles/lengths at material points of an elastic body [84]. On the other hand, the classical 1st gradient theory is only able to describe the overall changes in the lengths/angles but they fail to capture relative changes between each material point (see, Fig. 1.8). In Fig. 1.9, the effectiveness of the higher gradient model in assimilating the microstructural changes in a fiber mesh-reinforced elastomeric composite material is demonstrated (which is discussed

further in chapter 4).
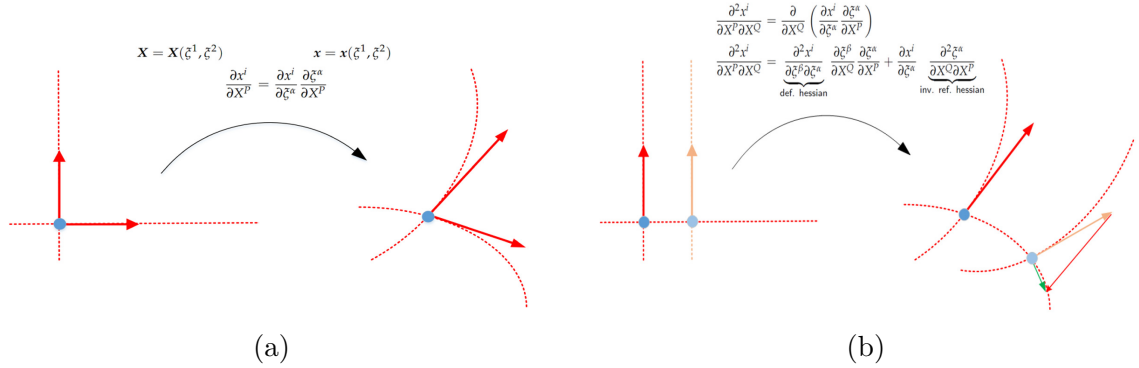
Figure 1.8: (a) Changes in lengths/angles from first gradient [84]. (b) Rate of changes in lengths/angles (relative changes) from second gradient [84].
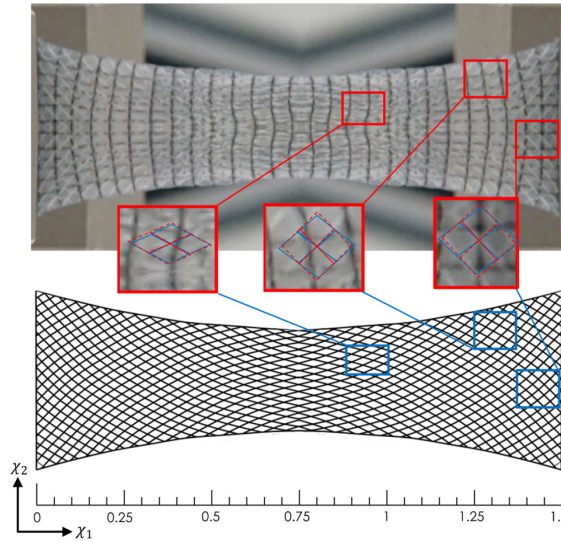
Figure 1.9: Local configurations of the fiber mesh at 50% elongation of PES3/Ecoflex-0050 composite.

Smooth transitions of shear strain fields:

Recent studies reveal that higher gradient theory can accurately predict the smooth transitions of shear strain fields (see, [85]–[88]). From Fig. 1.10 it can be noted, as we move from the classical 1st gradient model to the 3rd gradient model, it leads to smooth and dilatational shear angle distributions throughout the entire domain of interest. Other examples of smooth shear angle distributions obtained from a higher-order gradient model are discussed in chapter 4 in more detail.
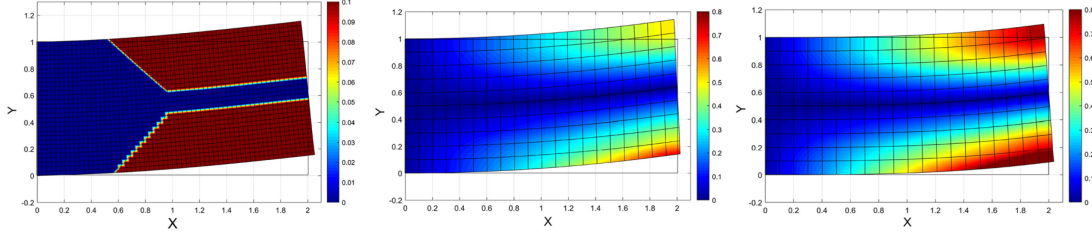
Figure 1.10: Shear angle contours: first gradient (left), second gradient (middle), third gradient (right).

Accurate prediction of large deformation:

It is found that the classical first-gradient theory is not accurate enough when talking about large deformation because it takes only up to the first (linear) order of deformations thus it may not be able to capture highly nonlinear and large deformation typically observed in hyperelastic composites [84], [89]. We have found that using a higher-order gradient model, it is possible to capture large extensions (i.e., up to 10 times the initial length) which is discussed in more detail in chapter 7.

Complete kinematic descriptions of the reinforcing fibers:

The classical first gradient theory can only accommodate the extension potential of fibers, which is described using the deformation gradient tensor ($\mathbf{F}$). Whereas bending and torsional potentials of fibers are described using geodesic curvatures (i.e., $\mathbf{g}_1$ and $\mathbf{g}_2$), which are second gradient terms, thus it is necessary to have a higher order model to accommodate these potentials (see, Fig. 1.11). Since higher-order theory can capture the complete kinematics of the reinforcing fibers by accommodating extension, bending, and torsional potentials, it can produce more accurate results in different deformation modes like tension, bending, twisting, out of plane deformations etc. [84], [90].
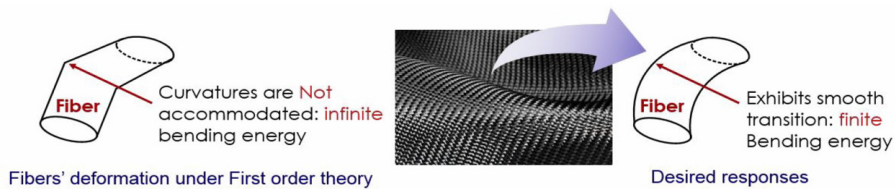
Figure 1.11: Comparison of classical and higher order theory [84].

Let's take an example to clarify the concept further. When a tensile load is applied to an elastic material reinforced with bidirectional fiber, different types of deformation (i.e., extension, bending, torsion) may occur simultaneously within the fiber mesh at different locations (see, Fig. 1.12). As it may be noted from the figure, the fiber colored in green is stretched and bent at the same time, thus it requires both extension and bending potential to fully describe the deformation. Further, the changes in the intersection of two fibers as indicated at point D requires the torsional potential term. This example illustrates the necessity to consider a generalized energy density function including extension, bending, and torsional potentials of the fiber mesh to describe the complete kinematics of the reinforcing fibers. Such a generalization can not be achieved using the classical model since it only allows to incorporate the extension potential of fibers.
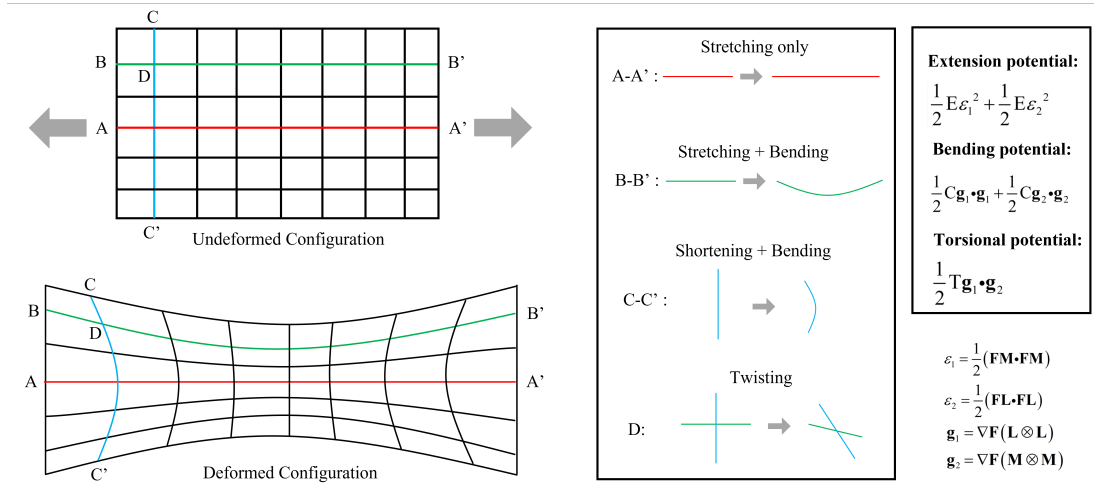
Figure 1.12: Differnet types of localized deformations in fiber mesh under uniaxial tension loading.

1.4.2 Precise characterization of fiber reinforcement

In the proposed model, we have incorporated direction vectors of fibers allowing precise characterization of fiber orientation within the composite material, i.e., uni-directional, bidirectional, fiber mesh at an angle, etc. (see, Fig. 1.13). Moreover, in the proposed model it is possible to easily modify the extension potential function of the fibers to address both linear and non-linear (i.e., polynomial, exponential, logarithmic, etc.) elastic response of fibers.
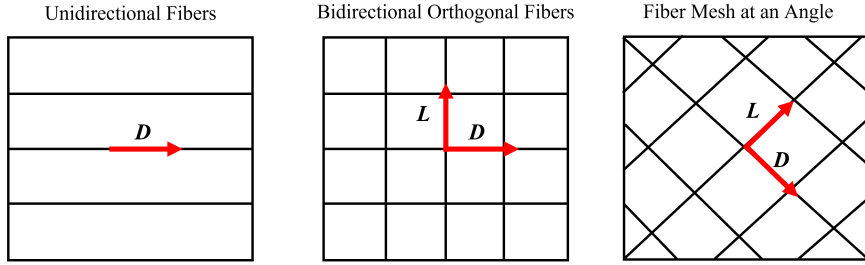
Figure 1.13: Fiber's direction vectors for different orientations of fibers.

1.4.3 Pseudoelasticity & damage mechanics

To assimilate the pseudoelastic response and damage mechanics of the hyperelastic composite, we have incorporated two types of damage variables into the proposed energy density function. One of the damage variables is inspired by the Ogden-Roxburgh model [91], which describes the Mullins effect of the hyperelastic composite. The Mullins effect is a kind of pseudoelastic phenomenon where the material undergoes an instantaneous and irreversible softening process, which is caused due to the internal structural changes in the matrix and fiber (see, Fig. 1.14 (left)). Whereas the other damage variable is inspired by the Weibull fiber damage model [92] which may accommodate the damage mechanics due to the breakage of individual load-carrying fibers (see, Fig. 1.14 (right)). More detailed discussions with corresponding results are presented in chapter 6.
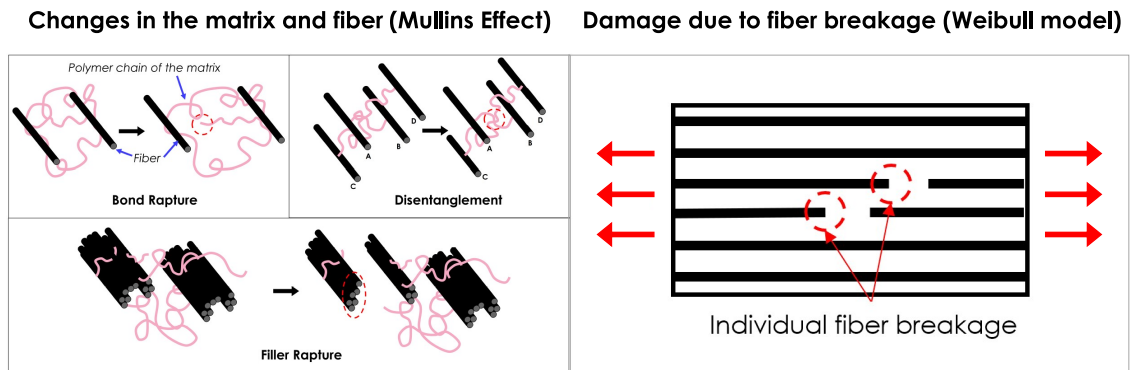
Figure 1.14: Psudoelastic behaviors of hyperelastic composite: Mullins effect caused by the internal structural changes (left); Damage mechanics due to individual fiber breakage (right).

1.4.4 Multi-scale modeling

Finally, we have incorporated the shear-lag parameter and Krenchel orientation parameters into the proposed energy density function which allows accommodating the size and orientation effects of the fibers, respectively. The shear-lag parameter relates the reinforcing capabilities of the fibers with their nano/microstructural characterization, i.e., length, thickness, aspect ratio, and interface stiffness. We have also augmented the interface stiffness parameter by integrating the interfacial debonding process that leads to the softening of the strain-strain response. Moreover, we have introduced the energy fraction parameter which is related to the volume fraction of fiber. These extensions of the strain energy density function allow the model to assimilate the response of nono/short fiber reinforced hyperelastic composite material, either with aligned or random orientations. With the help of these parameters, the proposed model attains multi-scale modeling capabilities. More details with corresponding results are presented in chapter 7.

1.5   Structure of Thesis

This thesis consists of six main chapters plus an introduction and conclusion. In the following section, the main topics for each chapter are briefly introduced.

In chapter 2, the effect of higher gradient terms in the deformation of a continuum is presented and some comparisons are made between the results of classical 1st gradient and higher gradient models. In this chapter, a third-gradient continuum model is developed for the deformation analysis of an elastic solid, reinforced with fibers resistant to flexure. The continuum model is framed in the second strain gradient elasticity theory within which the kinematics of fibers are formulated, and subsequently integrated into the models of deformations. It is found that the higher gradient model can produce smooth and dilatational shear angle distributions whereas the classical model fails to produce such a smooth shear angle distribution. Two case studies are also presented through the in-house experimental settings of crystalline nano-cellulose (CNC) fiber composites and Nylon-6 fiber Neoprene rubber composites, which illustrate that the obtained solutions successfully can predict the deformation profiles of both composites.

Chapter 3, presents a model for the mechanics of a soft hyperelastic material reinforced with unidirectional fibers, resistant to flexure and extension. In this chapter, the strain energy potential of the composite is refined by the Mooney Rivlin model to accommodate the hyperelastic behaviors of the matrix material. The elastic modulus of the four different types of fibers and material parameters of Ecoflex-0050 are obtained from the uniaxial tensions test experimental data. The results are compared against the experimental data demonstrating that the obtained model assimilates the responses of the Ecoflex-0050 elastomer-fiber composite subjected to uni-axial tension and successfully predicts the J-shaped stress-strain behavior and the deformation profiles.

Chapter 4, demonstrates the development of a series of continuum-based prediction models to accommodate the nonlinear responses of both the matrix material and the reinforcing fibers in a hyperelastic matrix material. The kinematics of the embedded fibers, including the torsional kinematics between two adjoining fibers, are formulated via the first and second gradient of continuum deformations. A set of in-house experiments are presented for the purpose of cross-examination and model implementation. The obtained models successfully predict the strain-stiffening responses of the elastomer–polyester fiber composites together with other key design considerations such as deformation profiles, shear strain distributions, and the deformed configurations of a local unit fiber mesh. The Euler–Almansi strain integrated model is also presented through which the strain-softening behaviors of a certain type of polyurethane fiber composites are predicted.

A three-dimensional model for the mechanics of elastic/hyperelastic materials reinforced with bidirectional fibers is presented in chapter 5. A dimension reduction process is applied to the resulting three-dimensional model through which a compatible two-dimensional model describing both the in-plane and out-of-plane deformations of thin elastic films reinforced with fiber mesh are obtained. It is demonstrated that the proposed model successfully predicts key design considerations of fiber mesh-reinforced composite films including stress-strain responses, deformation profiles, shear strain distributions, and local structure (a unit fiber mesh) deformations.

Chapter 6, presents a comprehensive analytical platform for modeling the pseudo-

elastic response of hyperelastic material reinforced with nonlinear fibers. In this chapter, two distinct pseudo-elastic behaviors generally observed in hyperelastic composites are accommodated within the proposed models which are the Mullins effect and damage mechanics due to fiber breakage. It is demonstrated that the obtained models successfully predict the Mullins effect of the human aorta in both longitudinal and circumferential directions. Also, the proposed model can assimilate the Mullins effect observed in soft biological tissue like Manduca Muscle. Moreover, by comparing against the in-house experiment results of elastomeric composite, is shown that the proposed model can closely simulate the damage mechanics, deformation profiles, and shear angles profiles of the elastomeric composite.

Chapter 7, discusses a multiscale continuum model for the mechanics of hyperelastic nanocomposites reinforced with randomly oriented fibers. The shear leg and Krenchel orientation parameters are incorporated into the model, through which the size and orientation effects of the short fibers are computed. Molecular dynamic simulations are also performed to obtain the microscopic responses of the graphene-reinforced composites with three distinct configurations of graphene sheets which are then incorporated into the proposed continuum model. The results are compared against the experimental data demonstrating that the obtained model can assimilate the hyperextension of nanocomposite and the continuum damage mechanics of two different nanocomposites induced by the interfacial debonding.

Throughout all chapters, we make use of a number of well-established symbols and conventions such as A^T, A^{-1}, A^* and $tr(A)$. These are the transpose, the inverse, the cofactor and the trace of a tensor A, respectively. The tensor product of vectors is indicated by interposing the symbol $\otimes$ and the Euclidian inner product of tensors A, B is defined by $A \cdot B = tr(AB^T)$; the associated norm $i\sqrt{A \cdot A}$. The symbol "$|\cdot|$" is used to denote the usual Euclidian norm of vectors. Latin and Greek indices take values in $\{1, 2\}$ and, when repeated, are summed over their ranges. Lastly, the notation F_A stands for the tensor-valued derivatives of a scalar-valued function $F(A)$.

Chapter 2

Mechanics of third-gradient continua reinforced with fibers resistance to flexure in finite plane elastostatics

In section 2.1, we develop kinematics and equilibrium equations. Moreover, we consider a case of a Neo-Hookian material reinforced with a single family of fibers in section 2.1.2. Through the method of virtual work and the computation of variational derivatives, the corresponding Euler equilibrium equation is derived, in the form of coupled Partial Differential Equations. In section 2.2, we present the derivation of the necessary boundary conditions. In section 2.3, a set of numerical solutions is obtained via a finite element analysis which is compared against the experimental data.

2.1 Kinematics

We introduce the vector field $\mathbf{D}$ representing the unit tangent to the fiber's trajectory in the reference configuration. The orientation of particular fibers is then given by,

$$\lambda = |\mathbf{d}| = \frac{ds}{dS} \text{ and } \boldsymbol{\tau} = \lambda^{-1}\mathbf{d}, \tag{2.1}$$

where

$$\mathbf{d} = \mathbf{F}\mathbf{D}. \tag{2.2}$$

In the above, $\mathbf{d}$ is the unit tangent to the fiber trajectory in the current configuration and $\mathbf{F}$ is the first gradient of the deformation function $(\chi(\mathbf{X}))$; i.e.

$$\mathbf{F} = \boldsymbol{\nabla}\chi(\mathbf{X}). \tag{2.3}$$

25

Eq. (2.2) can be derived by taking the derivative of $\mathbf{r}(S) = \boldsymbol{\chi}(\mathbf{X}(S))$, upon making the identifications $\mathbf{D} = \mathbf{X}'(S)$ and $\mathbf{d} = \mathbf{r}'(S)$. We denote that, unless otherwise specified, primes refer to derivatives with respect to arclength along a fiber (i.e. $(*)' = d(*)/dS$). Accordingly, from Eq. (2.2), the geodesic curvature of an arc $(\mathbf{r}(S))$ is expressed in terms of $\mathbf{F}$ and $\mathbf{d}$ as

$$\mathbf{g} = \mathbf{r}'' = \frac{d(\mathbf{r}'(S))}{dS} = \frac{\partial(\mathbf{FD})}{\partial\mathbf{X}}\frac{d\mathbf{X}}{dS} = \nabla[\mathbf{FD}]\mathbf{D}. \tag{2.4}$$

In a typical environment, most of the fibers are straight prior to deformations. Even slightly curved fibers can be regarded as 'fairly straight' fibers considering their length scales against the matrix materials. This further leads to the assumption of vanishing gradient fields of the unit tangent in the reference configuration (i.e. $\nabla\mathbf{D} = \mathbf{0}$). Hence, Eqs (2.4) reduce to

$$\mathbf{g} = \nabla\mathbf{F}(\mathbf{D} \otimes \mathbf{D}). \tag{2.5}$$

We now introduce the commonly used conventions of the second gradient of deformations:

$$\nabla\mathbf{F} \equiv \mathbf{G}, \tag{2.6}$$

where the compatibility condition of $\mathbf{G}$ can be seen as

$$G_{iAB} = F_{iA,B} = F_{iB,A} = G_{iBA}. \tag{2.7}$$

Accordingly, Eq. (2.5) becomes

$$\mathbf{g} = \mathbf{G}(\mathbf{D} \otimes \mathbf{D}) = \mathbf{g}(\mathbf{G}, \mathbf{D}). \tag{2.8}$$

Based on the above kinematical setting, authors in [93] propose the following energy density function in the continuum description of an elastic solid reinforced with fibers resistant to flexure:

$$W(\mathbf{F}, \mathbf{G}) = \widehat{W}(\mathbf{F}) + W(\mathbf{G}), \ W(\mathbf{G}) \equiv \frac{1}{2}C(\mathbf{F})|\mathbf{g}|^2, \tag{2.9}$$

where $C(\mathbf{F})$ refers to the material properties of the fibers and is, in general, independent of the deformation gradient; i.e.

$$C(\mathbf{F}) = C. \tag{2.10}$$

In this model (Eq. (2.9)), the fibers' bending energy is presumed to be dependent entirely on the second gradient of deformations, $\mathbf{G}$, which facilitates the development of the associated mathematical framework. The concept has been widely and successfully adopted in the relevant studies (see, for example, [90], [94]–[97]).

In the present study, we propose a more comprehensive model by introducing the third gradient of deformations into the model of deformations. For this purpose, we compute the rate of changes in curvature (the third gradient of deformations) at points on the fibers as

$$\begin{aligned}
\boldsymbol{\alpha} &= \mathbf{r}''' = \frac{d(\nabla[\mathbf{FD}]\mathbf{D})}{dS} = \frac{\partial(\nabla[\mathbf{FD}]\mathbf{D})}{\partial\mathbf{X}}\frac{d\mathbf{X}}{dS} = [\nabla\{\nabla[\mathbf{FD}]\mathbf{D}\}]\mathbf{D} \\
&= [\nabla\{\nabla[\mathbf{FD}]\}\mathbf{D} + \nabla[\mathbf{FD}](\nabla\mathbf{D})]\mathbf{D},
\end{aligned} \tag{2.11}$$

through which the interactions between the fibers and the surrounding matrix may be characterized. Further, we formulate the follow in the same sprit as Eqs. (2.5)-(2.8) that

$$\begin{aligned}
\boldsymbol{\alpha} &= \nabla(\nabla\mathbf{F})(\mathbf{D}\otimes\mathbf{D}\otimes\mathbf{D}), \\
\nabla(\nabla\mathbf{F}) &= \nabla(\mathbf{G}) \equiv \mathbf{H}, \text{ and} \\
\boldsymbol{\alpha} &= \mathbf{H}(\mathbf{D}\otimes\mathbf{D}\otimes\mathbf{D}) = \boldsymbol{\alpha}(\mathbf{H},\mathbf{D}).
\end{aligned} \tag{2.12}$$

Thus, the energy potential associated with the third gradient of deformations is incorporated and yields

$$W(\mathbf{F},\mathbf{G},\ \mathbf{H}) = \widehat{W}(\mathbf{F}) + W(\mathbf{G}) + W(\mathbf{H}),\ W(\mathbf{G}) \equiv \frac{1}{2}C(\mathbf{F})\,|\mathbf{g}|^2,\ W(\mathbf{H}) \equiv \frac{1}{2}A(\mathbf{F})\,|\boldsymbol{\alpha}|^2. \tag{2.13}$$

Here, the third gradient of deformations $\mathbf{H}$ is defined by

$$\nabla[\nabla\mathbf{G}] = \nabla\mathbf{G} \equiv \mathbf{H}, \tag{2.14}$$

which accounts for the rate of change in the fibers' curvature. The phenomenological implications vis a vis the third gradient of deformations (e.g. interactions between fibers and a matrix material), and the identification of the associated coefficient (here, denoted as A), are addressed in the literature [98]–[104]. Our emphasis here is on the development of a mathematical frame work, and the associated analyses, in order to provide the more general and comprehensive description of fiber composites with

27

fibers resistant to flexure. It is also noted that, in the forgoing analysis, the parameter A is assumed to be independent of the deformation gradient, similar to Eq. (2.10). That is

$$A(\mathbf{F}) = A. \qquad (2.15)$$

We adopt the variational principles in the derivations of the Euler equations and the associated boundary conditions. To obtain the desired expressions, we evaluated the induced energy variation of the response function with respect to $\mathbf{F}$, $\mathbf{G}$, and $\mathbf{H}$ as

$$\dot{W}(\mathbf{F},\ \mathbf{G},\ \mathbf{H}) = W_{\mathbf{F}} {\cdot} \dot{\mathbf{F}} + W_{\mathbf{G}} {\cdot} \dot{\mathbf{G}} + W_{\mathbf{H}} \cdot \dot{\mathbf{H}}, \qquad (2.16)$$

where the superposed dot refers to the derivatives with respect to a parameter ϵ at a fixed value (e.g. $\epsilon = 0$ at equilibrium) that labels a one-parameter family of deformations. Similarly, Eq. (2.13), yields

$$\dot{W}(\mathbf{G}) = C\mathbf{g} \cdot \dot{\mathbf{g}} \text{ and } \dot{W}(\mathbf{H}) = A\boldsymbol{\alpha} \cdot \dot{\boldsymbol{\alpha}}. \qquad (2.17)$$

Now, taking derivatives of Eqs. (2.5) and (2.12) with respect to ϵ (e.g. $\dot{\mathbf{g}} = \dot{\mathbf{G}}(\mathbf{D} \otimes \mathbf{D})$), and substituting them into Eq. (2.17), we obtain

$$
\begin{aligned}
\dot{W}(\mathbf{G}) &= C\mathbf{g}{\cdot}\dot{\mathbf{g}} = Cg_j\mathbf{e_j}{\cdot}\dot{G}_{iAB}D_AD_B\mathbf{e}_i = Cg_i\dot{G}_{iAB}D_AD_B, \text{ and} \\
\dot{W}(\mathbf{H}) &= A\boldsymbol{\alpha}{\cdot}\dot{\boldsymbol{\alpha}} = A\alpha_j\mathbf{e_j}{\cdot}\dot{H}_{iABC}D_AD_BD_C\mathbf{e}_i = A\alpha_i\dot{H}_{iABC}D_AD_BD_C. \quad (2.18)
\end{aligned}
$$

But, the above are also equivalent to

$$
\begin{aligned}
\dot{W}(\mathbf{G}) &= W_{\mathbf{G}} \cdot \dot{\mathbf{G}} = W_{G_{iAB}}(\mathbf{e}_i{\otimes}\mathbf{E}_A{\otimes}\mathbf{E}_B\otimes)\dot{G}_{jCD}(\mathbf{e}_j{\otimes}\mathbf{E}_C{\otimes}\mathbf{E}_D) = W_{G_{iAB}}\dot{G}_{iAB} \text{ and} \\
\dot{W}(\mathbf{H}) &= W_{\mathbf{H}} \cdot \dot{\mathbf{H}} = W_{H_{iABC}}(\mathbf{e}_i{\otimes}\mathbf{E}_A{\otimes}\mathbf{E}_B{\otimes}\mathbf{E}_C)\dot{H}_{jDEF}(\mathbf{e}_j{\otimes}\mathbf{E}_D{\otimes}\mathbf{E}_E{\otimes}\mathbf{E}_F) \quad (2.19) \\
&= W_{H_{iABC}}\dot{H}_{iABC}.
\end{aligned}
$$

Hence, we compare Eqs. (2.18)-(2.19) and obtain

$$\frac{\partial W}{\partial G_{iAB}} = Cg_iD_AD_B \text{ and } \frac{\partial W}{\partial H_{iABC}} = A\alpha_iD_AD_BD_C, \qquad (2.20)$$

or

$$W_{\mathbf{G}} = C\mathbf{g} \otimes \mathbf{D} \otimes \mathbf{D} \text{ and } W_{\mathbf{G}} = A\boldsymbol{\alpha} \otimes \mathbf{D} \otimes \mathbf{D} \otimes \mathbf{D}. \qquad (2.21)$$

In general, volumetric changes in the materials' deformations are energetically expensive processes (see, for example, [105]-[106]). Thus, for the desired application, the

energy density function, Eq. (2.13), is augmented by the condition of bulk incompressibility such that

$$U(\mathbf{F},\ \mathbf{G},\ \mathbf{H},\ p) = W(\mathbf{F}, \mathbf{G},\ \mathbf{H}) - p(J-1), \tag{2.22}$$

where J is determinant of $\mathbf{F}$ and p is a Lagrange-multiplied filed. We continue by using the identity $\dot{J} = J_{\mathbf{F}} \cdot \dot{\mathbf{F}} = \mathbf{F}^* \cdot \dot{\mathbf{F}}$, and obtain the variational derivative of the above as

$$\dot{U} = (W_{\mathbf{F}} - p\mathbf{F}^*) \cdot \dot{\mathbf{F}} + W_{\mathbf{G}} \cdot \dot{\mathbf{G}} + W_{\mathbf{H}} \cdot \dot{\mathbf{H}}, \tag{2.23}$$

or, equivalently,

$$\dot{U} = (W_{F_{iA}} - pF_{iA}^*)\dot{F}_{iA} + W_{G_{iAB}}\dot{G}_{iAB} + W_{H_{iABC}}\dot{H}_{iABC}. \tag{2.24}$$

Clearly, the obtained variational form (2.23) is dependent on both the second and the third gradient of deformations as intended; i.e. The rate of change in curvature is now incorporated into the model of deformations via the third gradient of deformations.

2.1.1 Equilibrium

The derivation of the Euler equation and boundary conditions arising in second-gradient elasticity are well documented in [101] and [107]-[108]. There authors formulate the weak form of the equilibrium equations by employing the principles of the virtual work statement:

$$\dot{E} = P, \tag{2.25}$$

where P is the virtual work of the applied load and the superposed dot refers to the variational and/or Gateâux derivative. In this section, we present a variational formulation which accounts for the third gradient of the continuum deformation by means of iterated integrations by parts (see, for example, [98]–[102]). To proceed, we express the strain energy of the system as

$$E = \int_{\Omega} U(\mathbf{F},\ \mathbf{G},\ \mathbf{H},\ p)dA, \tag{2.26}$$

where Ω is the domain occupied by a fiber-matrix material. Since the conservative loads are characterized by the existence of a potential L, such that $P = \dot{L}$, the problem

of determining equilibrium deformations is reduced to the problem of minimizing the potential energy $E - L$. Hence we find

$$\dot{E} = \int_\Omega \dot{U}(\mathbf{F},\ \mathbf{G},\ \mathbf{H},\ p)dA. \tag{2.27}$$

Also, from Eq. (2.19), the energy variations with respect to the second and third gradient of deformations (i.e. $\mathbf{G}$ and $\mathbf{H}$) can be expressed as

$$\frac{\partial W}{\partial G_{iAB}}\dot{G}_{iAB} = \frac{\partial W}{\partial G_{iAB}}u_{i,AB}\ \text{and}$$
$$\frac{\partial W}{\partial H_{iABC}}\dot{H}_{iABC} = \frac{\partial W}{\partial H_{iABC}}u_{i,ABC}, \tag{2.28}$$

where

$$u_i = \dot{\chi}_i \tag{2.29}$$

is the variation of the position field $\boldsymbol{\chi}(\mathbf{X})$. Applying integration by parts, Eq. (2.28) yields

$$\frac{\partial W}{\partial G_{iAB}}u_{i,AB} = \left(\frac{\partial W}{\partial G_{iAB}}u_{i,A}\right)_{,B} - \left(\frac{\partial W}{\partial G_{iAB}}\right)_{,B}u_{i,A}\ \text{and}$$
$$\frac{\partial W}{\partial H_{iABC}}u_{i,ABC} = \left(\frac{\partial W}{\partial H_{iABC}}u_{i,AB}\right)_{,C} - \left(\frac{\partial W}{\partial H_{iABC}}\right)_{,C}u_{i,AB}. \tag{2.30}$$

We now substitute Eqs. (2.24) and (2.30) into Eq. (2.27), and thereby obtain

$$\dot{E} = \int_\Omega \left[\left(\frac{\partial W}{\partial F_{iA}} - pF_{iA}^*\right)\cdot\dot{F}_{iA} + \left(\frac{\partial W}{\partial G_{iAB}}u_{i,A}\right)_{,B} - \left(\frac{\partial W}{\partial G_{iAB}}\right)_{,B}u_{i,A}\right.$$
$$\left. + \left(\frac{\partial W}{\partial H_{iABC}}u_{i,AB}\right)_{,C} - \left(\frac{\partial W}{\partial H_{iABC}}\right)_{,C}u_{i,AB}\right]dA. \tag{2.31}$$

Invoking Green-Stoke's theorem, the above further reduces to

$$\dot{E} = \int_\Omega\left[\frac{\partial W}{\partial F_{iA}} - pF_{iA}^* - \left(\frac{\partial W}{\partial G_{iAB}}\right)_{,B}\right]u_{i,A}dA - \int_\Omega\left(\frac{\partial W}{\partial H_{iABC}}\right)_{,C}u_{i,AB}dA$$
$$+ \int_{\partial\Omega}\left[\left(\frac{\partial W}{\partial G_{iAB}}u_{i,A}\right)N_B + \left(\frac{\partial W}{\partial H_{iABC}}u_{i,AB}\right)N_C\right]dS, \tag{2.32}$$

where $\mathbf{N}$ is the rightward unit normal to the boundary $\partial\Omega$. To obtain the expression of the Piola stresses, we again apply the integration by parts on $\left(\frac{\partial W}{\partial H_{iABC}}\right)_{,C}u_{i,AB}$; i.e.

$$\left(\frac{\partial W}{\partial H_{iABC}}\right)_{,C}u_{i,AB} = \left(\left(\frac{\partial W}{\partial H_{iABC}}\right)_{,C}u_{i,A}\right)_{,B} - \left(\frac{\partial W}{\partial H_{iABC}}\right)_{,CB}u_{i,A}, \tag{2.33}$$

30

and thus obtain from the second integral of the Eq. (2.32) that

$$\int_\Omega \left(\frac{\partial W}{\partial H_{iABC}}\right)_{,C} u_{i,AB} dA = \int_\Omega \left(\left(\frac{\partial W}{\partial H_{iABC}}\right)_{,C} u_{i,A}\right)_{,B} - \left(\frac{\partial W}{\partial H_{iABC}}\right)_{,CB} u_{i,A} dA. \quad (2.34)$$

But, Eq. (2.34) is equivalent to

$$\int_\Omega \left(\frac{\partial W}{\partial H_{iABC}}\right)_{,C} u_{i,AB} dA = \int_{\partial\Omega} \left(\left(\frac{\partial W}{\partial H_{iABC}}\right)_{,C} u_{i,A}\right) N_B dS - \int_\Omega \left(\frac{\partial W}{\partial H_{iABC}}\right)_{,CB} u_{i,A} dA,$$
$$(2.35)$$

in which we again applied the Green-Stokes theorem. We then substitute Eq. (2.35) into Eq. (2.32) and subsequently obtain

$$\begin{aligned}
\dot{E} &= \int_\Omega [\frac{\partial W}{\partial F_{iA}} - pF_{iA}^* - \left(\frac{\partial W}{\partial G_{iAB}}\right)_{,B}] u_{i,A} dA - [- \int_\Omega \left(\frac{\partial W}{\partial H_{iABC}}\right)_{,CB} u_{i,A} dA \\
&\quad + \int_{\partial\Omega} \left(\left(\frac{\partial W}{\partial H_{iABC}}\right)_{,C} u_{i,A}\right) N_B dS] + \int_{\partial\Omega} [\left(\frac{\partial W}{\partial G_{iAB}} u_{i,A}\right) N_B \\
&\quad + \left(\frac{\partial W}{\partial H_{iABC}} u_{i,AB}\right) N_C] dS.
\end{aligned} \quad (2.36)$$

Now, Eq. (2.36) may be recast as

$$\dot{E} = \int_\Omega P_{iA} \dot{F}_{iA} dA + \int_{\partial\Omega} [\{\frac{\partial W}{\partial G_{iAB}} - \left(\frac{\partial W}{\partial H_{iABC}}\right)_{,C}\} u_{i,A} N_B + \frac{\partial W}{\partial H_{iABC}} u_{i,AB} N_C] dS,$$
$$(2.37)$$

where

$$P_{iA} = \frac{\partial W}{\partial F_{iA}} - pF_{iA}^* - \left(\frac{\partial W}{\partial G_{iAB}}\right)_{,B} + \left(\frac{\partial W}{\partial H_{iABC}}\right)_{,CB} \quad (2.38)$$

is the expression of the Piola stress. It is evident from Eq. (2.38) that the resulting stress fields are dependent on both the second and third gradient of deformations. Also, it may be necessary to write the above equations in the tensorial form for the sake of clarity and completeness, especially for the terms which are obtained from the results of a multilinear transformations of higher-order tensors with mixed bases:

$$\dot{E} = \int_\Omega \mathbf{P} \cdot \dot{\mathbf{F}} dA + \int_{\partial\Omega} [W_{\mathbf{G}}^T \mathbf{F}^T \cdot \mathbf{N} + W_{\mathbf{H}}^T (\nabla \mathbf{F})^T \cdot \mathbf{N} - (Div(W_{\mathbf{H}}))^T \mathbf{F}^T \cdot \mathbf{N}] dS; \quad (2.39)$$

and

$$\mathbf{P} = W_{\mathbf{F}} - p\mathbf{F}^* - Div(W_{\mathbf{G}}) + Div(Div(W_{\mathbf{H}})). \quad (2.40)$$

In the case of initially straight fibers (i.e. $\nabla \mathbf{D} = \mathbf{0}$), we evaluate from Eqs. (2.20) that

$$\left(\frac{\partial W}{\partial G_{iAB}}\right)_{,B} = Cg_{i,B} D_A D_B \text{ and } \left(\frac{\partial W}{\partial H_{iABC}}\right)_{,CB} = A\alpha_{i,BC} D_A D_B D_C, \quad (2.41)$$

31

and thus reduce Eq. (2.38) to

$$P_{iA} = \frac{\partial W}{\partial F_{iA}} - pF_{iA}^* - Cg_{i,B}D_AD_B + A\alpha_{i,BC}D_AD_BD_C. \tag{2.42}$$

Finally, Eq. (2.42) satisfies

$$P_{iA,A} = 0 \text{ or } Div(\mathbf{P}) = 0, \tag{2.43}$$

which can be served as the Euler equilibrium equation for the reinforced solids occupying the domain of Ω.

2.1.2 Example: Neo-Hookean materials

In the case of Neo-Hookean materials, the energy density function is given by

$$W(I_1, I_3) = \frac{\mu}{2}(I_1 - 3) - \mu \log I_3 + \frac{\lambda}{2}(\log I_3)^2, \tag{2.44}$$

where μ and λ are the material constants, and I_1 and I_3 are respectively the first and third invariants of the deformation gradient tensor. By setting $I_3 = 1$, the incompressible model can be obtained as

$$W(I_1) = \frac{\mu}{2}(I_1 - 3) = \frac{\mu}{2}(\mathbf{F} \cdot \mathbf{F} - 3). \tag{2.45}$$

Now taking the derivative of the above with respect to $\mathbf{F}$ and subsequently substituting it into Eq. (2.42), we find

$$P_{iA} = \mu F_{iA} - pF_{iA}^* - Cg_{i,B}D_AD_B + A\alpha_{i,BC}D_AD_BD_C, \tag{2.46}$$

which is the expression of the Piola stress for the reinforced solid of Neo-Hookean type. Hence, the corresponding Euler equilibrium equation satisfies

$$P_{iA,A} = \mu F_{iA,A} - p_{,A}F_{iA}^* - Cg_{i,AB}D_AD_B + A\alpha_{i,ABC}D_AD_BD_C = 0, \tag{2.47}$$

where we use the Piola's identity (i.e. $F_{iA,A}^* = 0$).

For example, we consider the reinforced solid which consists of initially straight fibers such that

$$\mathbf{D} = \mathbf{E}_1 \text{ (i.e. } D_1 = 1 \text{ and } D_2 = 0), \tag{2.48}$$

32

and is subjected to finite plain deformaitons. Then, the equilibrium equation (2.47) reduces to

$$P_{iA,A} = \mu F_{iA,A} - p_{,A} F_{iA}^* - C g_{i,11} + A \alpha_{i,111} = 0.$$

Further, we evaluate from Eqs. (2.5) and (2.12) that

$$g_i = F_{i1,1}, \ \alpha_i = F_{i1,11}, \ F_{iA} = \chi_{i,A}, \ F_{iA}^* = \varepsilon_{ij} \varepsilon_{AB} F_{jB}, \tag{2.49}$$

where ε_{ij} is the 2-D permutation, $\varepsilon_{12} = -\varepsilon_{21} = 1$, $\varepsilon_{11} = \varepsilon_{22} = 0$. Consequently, invoking Eqs. (2.48)-(2.49), together with the constraint of the bulk incompressibility (i.e. $\det \mathbf{F} = 1$), we deliver the following system of PDEs,

$$P_{iA,A} \mathbf{e}_1 = (\mu \chi_{i,AA} - p_{,A} \varepsilon_{ij} \varepsilon_{AB} \chi_{j,B} - C \chi_{i,1111} + A \chi_{i,111111}) \mathbf{e}_1 = 0 \text{ and} \tag{2.50}$$

$$\chi_{1,1} \chi_{2,2} - \chi_{1,2} \chi_{2,1} = 1, \tag{2.51}$$

which solves for χ_1, χ_2 and p.

2.2 Boundary conditions

In this section, we present rigorous derivations vis a vis the admissible boundary conditions which arise in the third gradient of virtual displacement. Due to the presence of the high order terms, the corresponding formulation turns out to be mathematically quite involved. However the resulting expressions of boundary conditions are in relatively simple formats and thus, mathematically tractable. To proceed, we apply the decomposition $P_{iA} u_{i,A} = (P_{iA} u_i)_{,A} - P_{iA,A} u_i$ as in Eq. (2.30) and obtain from Eq. (2.37) that

$$
\begin{aligned}
\dot{E} &= \int_{\partial\Omega} P_{iA} u_i N_A dS - \int_{\Omega} P_{iA,A} u_i dA + \int_{\partial\Omega} [\{\frac{\partial W}{\partial G_{iAB}} - \left(\frac{\partial W}{\partial H_{iABC}}\right)_{,C}\} u_{i,A} N_B \\
&+ \frac{\partial W}{\partial H_{iABC}} u_{i,AB} N_C] dS.
\end{aligned}
\tag{2.52}
$$

Here, the Green-Stoke's theorem is applied in the first term of Eq. (2.52). Since the Euler equation, $P_{iA,A} = 0$, holds in Ω, the above reduces to

$$\dot{E} = \int_{\partial\Omega} P_{iA} u_i N_A dS + \int_{\partial\Omega} [\{\frac{\partial W}{\partial G_{iAB}} - \left(\frac{\partial W}{\partial H_{iABC}}\right)_{,C}\} u_{i,A} N_B + \frac{\partial W}{\partial H_{iABC}} u_{i,AB} N_C] dS. \tag{2.53}$$

Now, we project $\nabla \mathbf{u}$ onto the normal and tangential direction and thereby obtain

$$\nabla \mathbf{u} = \nabla \mathbf{u}(\mathbf{T} \otimes \mathbf{T}) + \nabla \mathbf{u}(\mathbf{N} \otimes \mathbf{N}) = \mathbf{u}' \otimes \mathbf{T} + \mathbf{u}_{,\mathbf{N}} \otimes \mathbf{N}, \tag{2.54}$$

such that $\mathbf{u}'$ and $\mathbf{u}_{,N}$ are respectively the tangential and normal derivatives of $\mathbf{u}$ on $\partial\Omega$; i.e.

$$u_i' = u_{i,A} T_A, \ \ u_{i,N} = u_{i,A} N_A, \tag{2.55}$$

where $\mathbf{T} = \mathbf{X}'(S) = \mathbf{k} \times \mathbf{N}$ defines the unit tangent to $\partial\Omega$, and $\mathbf{N}$ is the associated unit normal to the boundary. Thus, invoking Eqs. (2.54)-(2.55), $u_{i,A}$ can be decomposed into

$$u_{i,A} = \frac{du_i}{ds}\frac{ds}{dX_A} + \frac{du_i}{dN}\frac{dN}{dX_A} = u_i' T_A + u_{i,N} N_A, \tag{2.56}$$

and similarly for $u_{i,AB}$,

$$
\begin{aligned}
u_{i,AB} &= u_i'' T_A T_B + u_i'(T_A' T_B + T_{A,N} N_B) + u_{i,N}(N_A' T_B + N_{A,N} N_B) \\
&\quad + u_{i,N}'(N_A T_B + T_A N_B) + u_{i,NN} N_A N_B.
\end{aligned} \tag{2.57}
$$

Substituting the above results into Eq. (2.53) then yields

$$
\begin{aligned}
\dot{E} &= \int_{\partial\Omega} P_{iA} u_i N_A dS + \int_{\partial w} \left\{ \left(\frac{\partial W}{\partial G_{iAB}}\right) - \left(\frac{\partial W}{\partial H_{iABC}}\right)_{,C} \right\} \left(u_i' T_A N_B + u_{i,N} N_A N_B\right) dS \\
&\quad + \int_{\partial\Omega} \frac{\partial W}{\partial H_{iABC}}[u_i'' T_A T_B + u_i'(T_A' T_B + T_{A,N} N_B) + u_{i,N}(N_A' T_B + N_{A,N} N_B) \\
&\quad + u_{i,N}'(N_A T_B + T_A N_B) + u_{i,NN} N_A N_B] N_C dS.
\end{aligned} \tag{2.58}
$$

In order to extract the admissible boundary conditions from Eq. (2.58), we make use of iterated integrations by parts. For example,

$$\frac{\partial W}{\partial G_{iAB}} T_A N_B u_i' = \left(\frac{\partial W}{\partial G_{iAB}} T_A N_B u_i\right)' - \left(\frac{\partial W}{\partial G_{iAB}} T_A N_B\right)' u_i, \tag{2.59}$$

$$
\begin{aligned}
&\frac{\partial W}{\partial H_{iABC}}(N_A T_B N_C + T_A N_B N_C) u_{i,N}' \\
&= \left[\frac{\partial W}{\partial H_{iABC}}(N_A T_B N_C + T_A N_B N_C) u_{i,N}\right]' - \left[\frac{\partial W}{\partial H_{iABC}}(N_A T_B N_C \right. \\
&\quad \left. + T_A N_B N_C)\right]'' u_{i,N},
\end{aligned} \tag{2.60}
$$

34

$$\frac{\partial W}{\partial H_{iABC}} T_A T_B N_C u_i''$$

$$= \left(\frac{\partial W}{\partial H_{iABC}} T_A T_B N_C u_i \right)'' + \left(\frac{\partial W}{\partial H_{iABC}} T_A T_B N_C \right)'' u_i$$

$$- 2 \left[\left(\frac{\partial W}{\partial H_{iABC}} T_A T_B N_C \right)' u_i \right]', \tag{2.61}$$

and similarly for other terms in Eq. (2.58). Consequently, Eq. (2.58) becomes

$$\dot{E} = \int_{\partial\Omega} [P_{iA} N_A - \{ \frac{\partial W}{\partial G_{iAB}} T_A N_B - \left(\frac{\partial W}{\partial H_{iABC}} \right)_{,C} T_A N_B \}'] u_i dS$$

$$- \int_{\partial\Omega} [\{ \frac{\partial W}{\partial H_{iABC}} (T_A' T_B N_C + T_{A,N} N_B N_C) \}' + \left(\frac{\partial W}{\partial H_{iABC}} T_A T_B N_C \right)''] u_i dS$$

$$+ \int_{\partial\Omega} [\{ \frac{\partial W}{\partial G_{iAB}} T_A N_B - \left(\frac{\partial W}{\partial H_{iABC}} \right)_{,C} T_A N_B - 2 \left(\frac{\partial W}{\partial H_{iABC}} T_A T_B N_C \right)' \} u_i]' dS$$

$$+ \int_{\partial\Omega} [\frac{\partial W}{\partial H_{iABC}} (T_A' T_B N_C + T_{A,N} N_B N_C) u_i]' dS + \int_{\partial\Omega} [\frac{\partial W}{\partial H_{iABC}} (N_A T_B N_C$$

$$+ T_A N_B N_C) u_{i,N}]' dS + \int_{\partial\Omega} [\{ \left(\frac{\partial W}{\partial G_{iAB}} \right) - \left(\frac{\partial W}{\partial H_{iABC}} \right)_{,C} \} N_A N_B + \frac{\partial W}{\partial H_{iABC}} (N_A' T_B$$

$$+ N_{A,N} N_B) N_C] u_{i,N} dS - \int_{\partial\Omega} [\{ \frac{\partial W}{\partial H_{iABC}} (N_A T_B N_C + T_A N_B N_C) \}'] u_{i,N} dS$$

$$+ \int_{\partial\Omega} \left(\frac{\partial W}{\partial H_{iABC}} T_A T_B N_C u_i \right)'' dS + \int_{\partial\Omega} \frac{\partial W}{\partial H_{iABC}} u_{i,NN} N_A N_B N_C dS. \tag{2.62}$$

But, in view of Eqs. (2.20) and (2.41) (e.g., $\frac{\partial W}{\partial G_{iAB}} = Cg_i D_A D_B$, $\left(\frac{\partial W}{\partial G_{iAB}}\right)_{,B} = Cg_{i,B} D_A D_B$ etc...), the above may be recast as

$$
\begin{aligned}
\dot{E} = & \int_{\partial\Omega} [P_{iA} N_A - \{(Cg_i - A\alpha_{i,C} D_C) D_A T_A D_B N_B\}' - \{A\alpha_i D_C N_C (D_A T'_A D_B T_B \\
& + D_A T_{A,N} D_B N_B)\}'] u_i dS + \int_{\partial\Omega} [(A\alpha_i D_A T_A D_B T_B D_C N_C)''] u_i dS \\
& + \sum \left\| A\alpha_i (D_A T'_A D_B T_B D_C N_C + D_A T_{A,N} D_B N_B D_C N_C) u_i \right\| \\
& + \sum \left\| [(Cg_i - A\alpha_{i,C} D_C) D_A T_A D_B N_B - 2(A\alpha_i D_A T_A D_B T_B D_C N_C)'] u_i \right\| \\
& + \sum \| A\alpha_i (D_A N_A D_B T_B D_C N_C + D_A T_A D_B N_B D_C N_C) u_{i,N} \| \\
& + \sum \left\| \frac{d}{ds} (A\alpha_i D_A T_A D_B T_B N_C D_C u_i) \right\| + \int_{\partial\Omega} [(Cg_i - A\alpha_{i,C} D_C) D_A N_A D_B N_B \\
& + A\alpha_i D_C N_C (D_A N'_A D_B T_B + D_A N_{A,N} D_B N_B)] u_{i,N} dS \\
& - \int_{\partial\Omega} [\{A\alpha_i D_A D_B D_C (N_A T_B N_C + T_A N_B N_C)\}' u_{i,N}] dS \\
& + \int_{\partial\Omega} (A\alpha_i D_A N_A D_B N_B D_C N_C u_{i,NN}) dS, \tag{2.63}
\end{aligned}
$$

where the double bar symbol refers to the jump across the discontinuities on the boundary $\partial\Omega$ (i.e. $\|*\| = (*)^+ - (*)^-$) and the sum refers to the collection of all discontinuities. Since the virtual work statement $(\dot{E} = P)$ implies that the admissible mechanical powers are of the form

$$
P = \int_{\partial w_t} t_i u_i dS + \int_{\partial w} m_i u_{i,N} dS + \int_{\partial w} r_i u_{i,NN} dS + \sum f_i u_i + \sum h_i u_{i,N}, \tag{2.64}
$$

By comparing Eqs. (2.63) and (2.64), we find that

$$
\begin{aligned}
\mathbf{t} = & \; \mathbf{PN} + \frac{d^2}{ds^2} [A\boldsymbol{\alpha} (\mathbf{D} \cdot \mathbf{T})^2 (\mathbf{D} \cdot \mathbf{N})] \\
& - \frac{d}{ds} [(C\mathbf{g} - A(\nabla\boldsymbol{\alpha})\mathbf{D})(\mathbf{D} \cdot \mathbf{T})(\mathbf{D} \cdot \mathbf{N}) - A\boldsymbol{\alpha}(\mathbf{D} \cdot \mathbf{N})(\mathbf{D} \cdot \mathbf{T})(\mathbf{D} \cdot \mathbf{T}') \\
& + A\boldsymbol{\alpha}(\mathbf{D} \cdot \mathbf{N})^2 (\mathbf{D} \cdot \mathbf{T}_{,N})], \\
\mathbf{m} = & \; (C\mathbf{g} - A(\nabla\boldsymbol{\alpha})\mathbf{D})(\mathbf{D} \cdot \mathbf{N})^2 + A\boldsymbol{\alpha}(\mathbf{D} \cdot \mathbf{N})[(\mathbf{D} \cdot \mathbf{N}')(\mathbf{D} \cdot \mathbf{T}) \\
& + (\mathbf{D} \cdot \mathbf{N}_{,N})(\mathbf{D} \cdot \mathbf{N})] - \frac{d}{ds} [2A\boldsymbol{\alpha}(\mathbf{D} \cdot \mathbf{T})(\mathbf{D} \cdot \mathbf{N})^2],
\end{aligned}
$$

$$\mathbf{r} = A\boldsymbol{\alpha}(\mathbf{D}\cdot\mathbf{N})^3,$$

$$\mathbf{f} = (C\mathbf{g} - A(\nabla\boldsymbol{\alpha})\mathbf{D})(\mathbf{D}\cdot\mathbf{T})(\mathbf{D}\cdot\mathbf{N}) - \frac{d}{ds}[2A\boldsymbol{\alpha}(\mathbf{D}\cdot\mathbf{T})^2(\mathbf{D}\cdot\mathbf{N})]$$

$$+ A\boldsymbol{\alpha}[(\mathbf{D}\cdot\mathbf{T}')(\mathbf{D}\cdot\mathbf{T})(\mathbf{D}\cdot\mathbf{N}) + (\mathbf{D}\cdot\mathbf{T}_{,N})(\mathbf{D}\cdot\mathbf{N})^2],$$

$$\frac{d}{ds}[\mathbf{f}] = \frac{d}{ds}[A\boldsymbol{\alpha}(\mathbf{D}\cdot\mathbf{T})(\mathbf{D}\cdot\mathbf{N})],$$

$$\mathbf{h} = 2A\boldsymbol{\alpha}((\mathbf{D}\cdot\mathbf{T})(\mathbf{D}\cdot\mathbf{N})^2, \tag{2.65}$$

where $\mathbf{t}, \mathbf{m}$, and $\mathbf{f}$ are the expressions of edge tractions, edge moments and the corner forces, respectively. More importantly, unlike those from the second gradient models, additional boundary conditions (i.e. $\mathbf{r}$, $\frac{d}{ds}[\mathbf{f}]$ and $\mathbf{h}$) appeared as a result of the introduction of the third gradient of deformations. These boundary conditions are the set of admissible contact interactions that can be sustained by third gradient continua (see, also, [98], [100]-[101] and references therein). In fact, such interaction forces are in conjugation with the Piola-type triple stress and are necessary to capture the internal energy contributions to the contact interactions on edges and points of Cauchy cuts [100],[109]. In the present case, this would mean the effects of local interactions between the fiber and matrix on the adjoined deformation fields.

The proposed model has a close similarity to the theory of micropolar elasticity, which admits additional degrees of freedom associated with the rotation of a local point (microstructure) pertaining to couple stresses. Within the description of the proposed model, this is achieved via the computation of the third gradient of the continuum deformation; i.e. the rate of changes in curvature (local point rotations), which is determined by the imposition of the triple forces (e.g., $\mathbf{r}, \mathbf{h}$) on the desired boundaries. Therefore, the proposed model can be used as an alternative 2D Cosserat theory of non-linear elasticity.

In a typical environment where fibers are aligned along the directions of either normal and/or tangential to the boundary (e.g., rectangular boundaries), we compute

$$(\mathbf{D}\cdot\mathbf{T})(\mathbf{D}\cdot\mathbf{N}) = 0 \text{ and } \nabla\mathbf{T} = \boldsymbol{\nabla}\mathbf{N} = \mathbf{0}, \tag{2.66}$$

and thereby reduce Eq. (2.65) to

$$
\begin{aligned}
\mathbf{t} &= \mathbf{PN}, \\
\mathbf{m} &= [C\mathbf{g} - A(\nabla\boldsymbol{\alpha})\mathbf{D}](\mathbf{D} \cdot \mathbf{N})^2, \\
\mathbf{r} &= A\boldsymbol{\alpha}(\mathbf{D} \cdot \mathbf{N})^3, \\
\mathbf{f} &= 0, \\
\frac{d}{ds}[\mathbf{f}] &= 0, \\
\mathbf{h} &= 0,
\end{aligned}
\tag{2.67}
$$

where

$$
\begin{aligned}
P_{iA} &= \mu F_{iA} - p F_{iA}^* - C g_{i,B} D_A D_B + A\alpha_{i,BC} D_A D_B D_C, \\
g_i &= F_{iA,B} D_A D_B \text{ and } \alpha_i = F_{iA,BC} D_A D_B D_C.
\end{aligned}
\tag{2.68}
$$

Hence, in this case (Eq. (2.66)), $\mathbf{r}$ is the only meaningful boundary force associated with the third gradient of deformations (i.e. $\mathbf{f}$, $\mathbf{f}'$ and $\mathbf{h}$ are identically vanishes), which is required to obtain the unique solution. We note here that the clarification of such triple forces and associated boundary conditions (Eq. (2.65)) may be of particular mechanical interest to practitioners and theoreticians alike. In this regard, a number of cases are examined throughout the following section. However, the attempts are intrinsically limited due to the paucity of experimental resources which certainly deserve further researches.

Lastly, by imposing the admissible set of boundary conditions (Eq. (2.67)), the solution of the PDE system (Eqs. (2.50)-(2.51)) can be obtained via commercial packages (e.g. Matlab, COMSOL etc...).

2.3   Results and discussion

For the purpose of demonstration, we simulate a set of numerical solutions describing the deformations of a rectangular composite that is reinforced with fibers resistant to flexure and subjected to the double force $\mathbf{m}$ (bending moment) and triple force $\mathbf{r}$ (see, Fig. 2.1). More precisely, a half problem is considered in which the corresponding
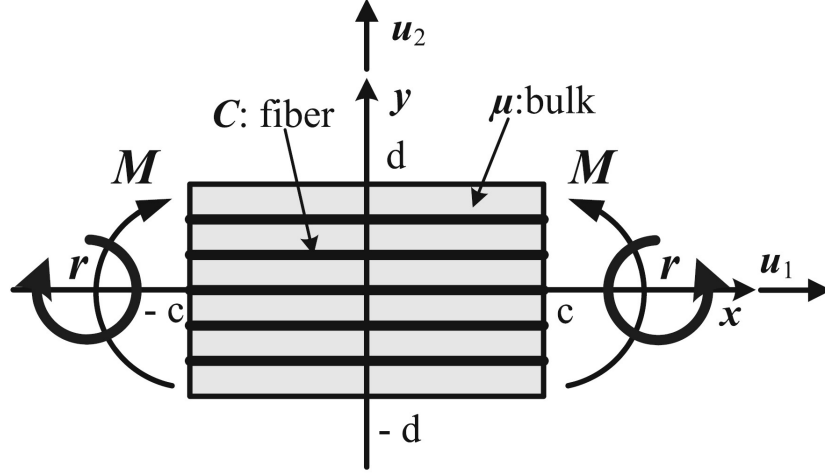
Figure 2.1: Schematic of problem

boundary conditions are prescribed as

$$
\begin{aligned}
m_1 &= C\chi_{1,11} - A\chi_{1,1111} = M/\mu, \ r_1 = A\chi_{1,111} = r/\mu, \\
m_2 &= C\chi_{2,11} - A\chi_{2,1111} = 0, \ r_2 = A\chi_{2,111} = 0, \\
\chi_1 &= 0, \ \chi_2 = 0, \ \text{at } x = c,
\end{aligned}
\tag{2.69}
$$

and symmetric boundary conditions are imposed at $x = 0$. It is noted that, unless otherwise specified, the corresponding data are obtained under the normalized setting (e.g. $\frac{C}{\mu} = 150$, $\frac{A}{\mu} = 50$ etc...). Also, here and henceforth, we conveniently refer to material constants associated with the Piola-type double stress and triple stress (i.e. C and A) as the 'double stress parameter' and 'triple stress parameter', respectively.

The obtained solutions in Fig. 2.2 illustrate gradual decreases in deformed configurations of the composite with increasing double stress parameter, C (bending stiffness of fibers), which also agrees with the results in [96] and [110]. Further, the corresponding deformation fields in Figs 2.3-2.4 demonstrate sensitivity to both the triple stress parameter, A, and the triple force, $\mathbf{r}$, as intended, and accommodate the solutions from the second gradient model [96] and [110] when the third gradient effects are removed (see, Fig. 2.5).

More importantly, we examine shear strain fields and the associated shear angle distributions over the domain of interest in order to have a more in-depth understanding of the influences of the third gradient of deformations. In the analysis, the shear
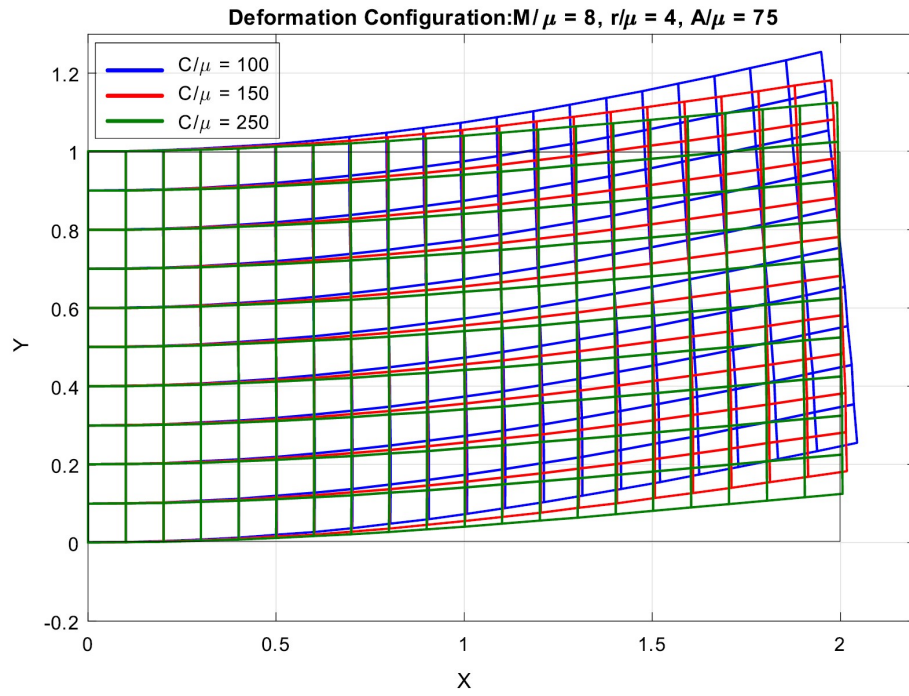
Figure 2.2: Deformed configurations with respect to C/μ.
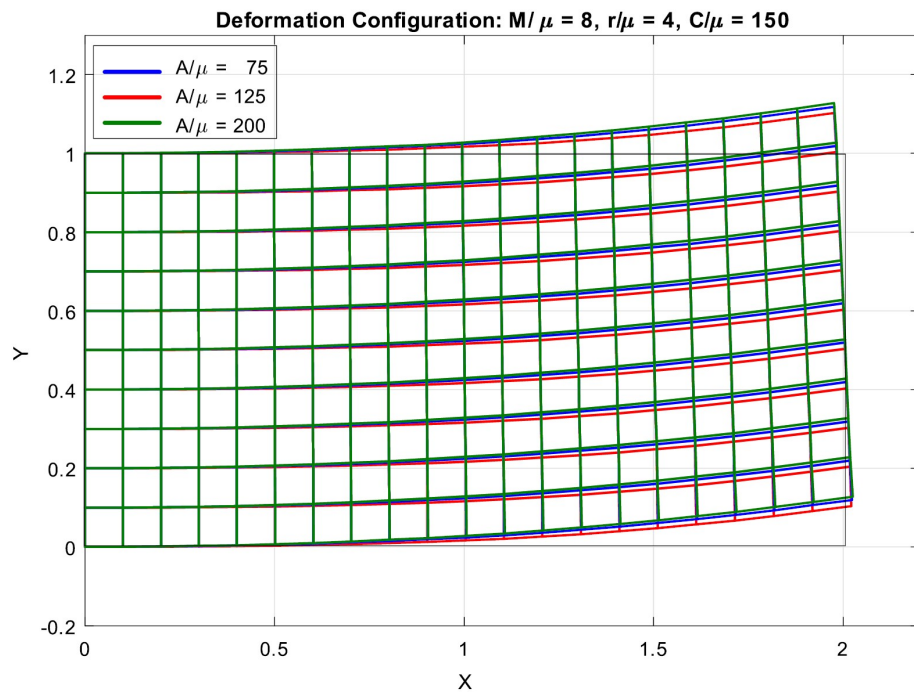
Figure 2.3: Deformed configurations with respect to A/μ.
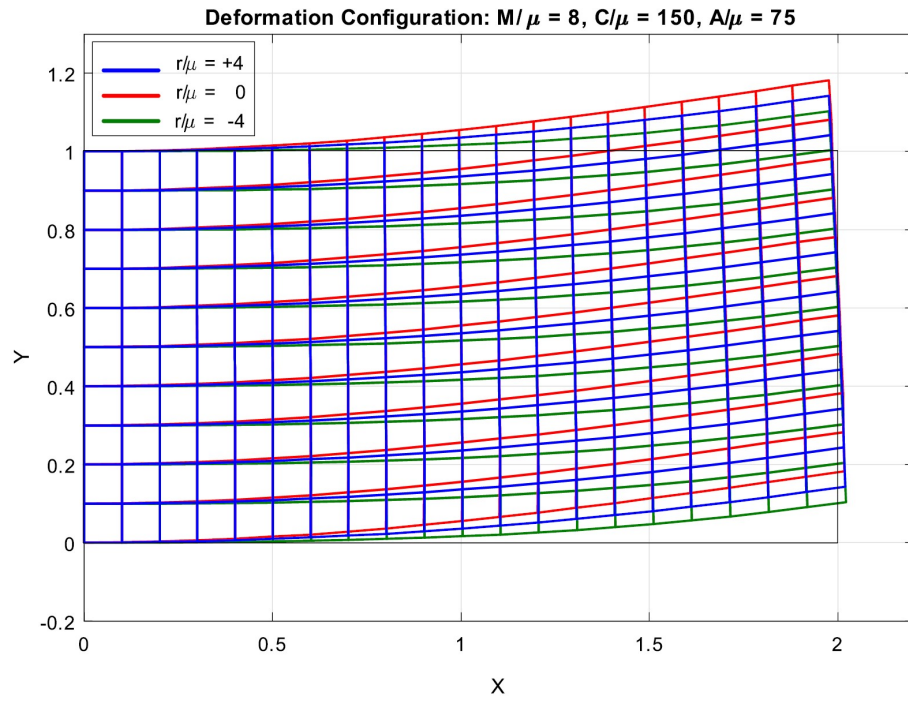
Figure 2.4: Deformed configurations with respect to r/μ.
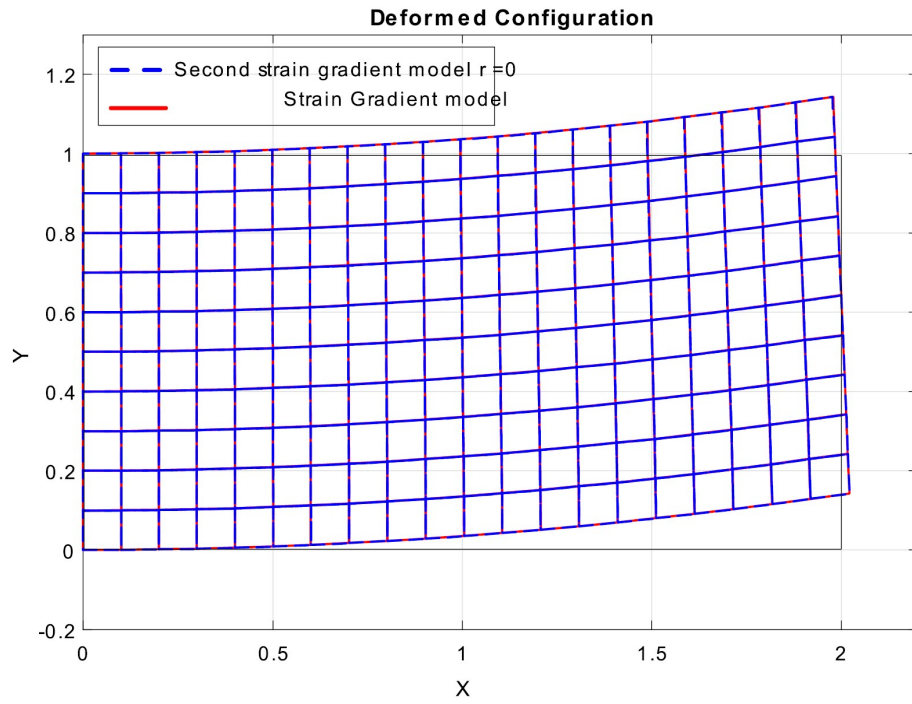
Figure 2.5: Comparison of the deformed configurations between the third gradient model and the second gradient model.

strain gradients and shear angles are computed using the following relations [111]:

$$\phi' = \frac{u_2''(1 + u_1') - u_2'u_1''}{u_2'^2 + (1 + u_1')^2}, \tag{2.70}$$

and

$$\phi = \tan^{-1}\left(\frac{\chi_{2,1} - \chi_{1,1}}{2 + \chi_{1,1} + \chi_{2,1}}\right). \tag{2.71}$$

It is shown in Fig. 2.6 that the magnitudes of shear strains either gradually increase or decrease with respect to the signs of applied triple force; i.e. the shear strain increases when $\mathbf{r} > 0$ and decreases with $\mathbf{r} < 0$. This further leads to the smooth and dilatational shear angle distributions throughout the entire domain of interest where the rate of dilatation is governed by the triple force $\mathbf{r}$. In other words, when the composite is subjected to the double force $\mathbf{m}$, the proposed model predicts multiple configurations of shear angle distributions, depending on the applied triple force $\mathbf{r}$, whereas only one configuration (smooth but non-dilatational distribution) is possible within the description of the strain gradient theory (see, for example, [85]-[86], and [112]). Indeed, the shear angle distribution from the result of the second gradient continuum model is the special case of those predicted by the obtained solution in the limit of the vanishing triple force (i.e. $\mathbf{r} = 0$, see, Fig. 2.8). This also can be seen directly from Eqs. (2.47), (2.67) and (2.68). For example, by setting $\mathbf{r} = 0$, we find from Eq. (2.67) that,

$$\mathbf{r} = A\boldsymbol{\alpha}(\mathbf{D} \cdot \mathbf{N})^3 = 0. \tag{2.72}$$

Accordingly, the boundary conditions in Eq.(2.67) and the expression of the Piola-type stress (Eq.(2.68)) reduce to

$$\mathbf{t} = \mathbf{PN}, \ \mathbf{m} = C\mathbf{g}(\mathbf{D} \cdot \mathbf{N})^2, \ \text{and} \tag{2.73}$$

$$P_{iA} = \mu F_{iA} - pF_{iA}^* - Cg_{i,B}D_AD_B. \tag{2.74}$$

Similarly, by invoking Eq. (2.72), the system of coupled PDEs (Eq. (2.47)) becomes

$$P_{iA,A} = \mu F_{iA,A} - p_{,A}F_{iA}^* - Cg_{i,AB}D_AD_B = 0. \tag{2.75}$$

The triple force $\mathbf{r}$ is meaningful only if its conjugate pair exists: the Piola-type triple stress. In the present case, the stress expression in Eq. (2.46) is a combination of the Piola-type stress (μF_{iA}), double stress ($Cg_{i,B}D_AD_B$), and triple stress
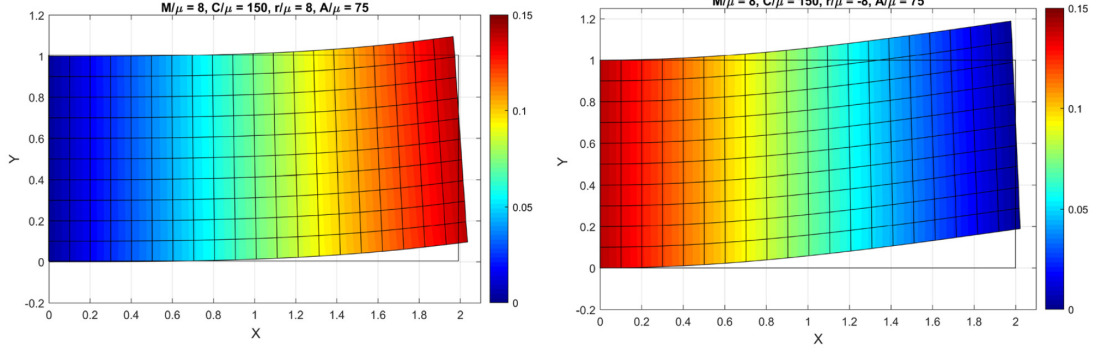
Figure 2.6: Shear strain gradients with respect to $\mathbf{r}$: $\mathbf{r} > 0$ (left) and $\mathbf{r} < 0$ (right).
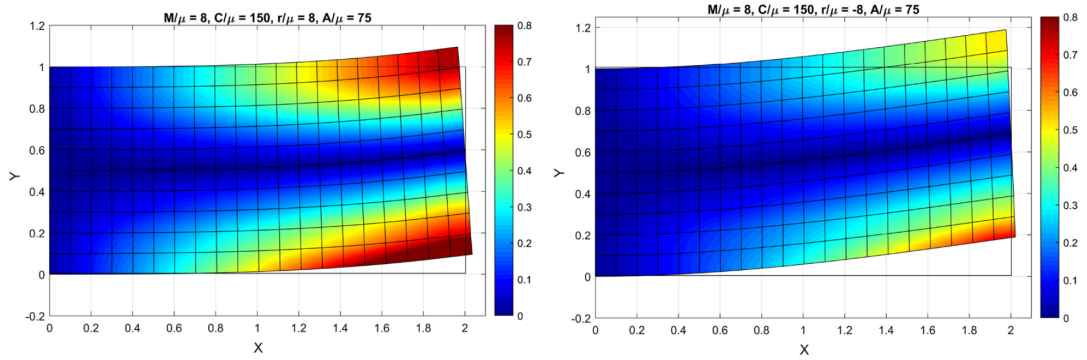
Figure 2.7: Shear angle contours with respect to $\mathbf{r}$: $\mathbf{r} > 0$ (left) and $\mathbf{r} < 0$ (right).

$(A\alpha_{i,BC}D_A D_B D_C)$ such that the third gradient of the deformation term in Eq. (2.46) (i.e., $A\alpha_{i,BC}D_A D_B D_C$) can be interpreted as the energy pair of the applied triple force $\mathbf{r}$. The same statement holds in cases of the second gradient continuum models. For example, the Piola-type double stress $(Cg_{i,B}D_A D_B)$ is the energy conjugate to the double force $\mathbf{m}$ (see, also, [99] and [109]).

Lastly, we summarize the associated field distributions predicted, respectively, by the first, second and third gradient continuum models for the purpose of comparison.
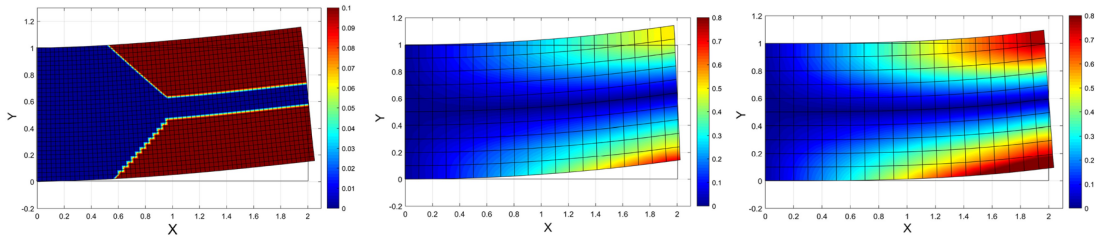
Figure 2.8: Shear angle contours: first gradient (left), second gradient (middle), third gradient (right).

In the summary, the second strain gradient, strain gradient, shear angle, deformation gradient and boundary conditions are denoted as SSG, SG, SA, DG and BCs, respectively. It is evident from Table. 1 that the Nth order continuum model predicts continuous (but not necessarily smooth) shear strain gradient fields up to (N-1)th order. For example, the second order continuum model predicts the first gradient of the shear strain fields (SG), see, case b) in Table. 2.1. Further, in order to uniquely determine such fields, the corresponding Nth order forces are required, which can be imposed on the desired boundaries only if there exists their energy couple, the Nth order gradient of the deformation map (see, DG and BCs in Table. 2.1).

Table 2.1: Field distributions predicted by the Nth-order gradient continuum model.

	(a) Classical model (first gradient)	**(b)** Second gradient model	**(c)** Third gradient model
SSG	No values (Zero)	No values (Zero)	Constant
SG	No values (Zero)	Constant	Gradual increase/decrease
SA	Non-smooth	Smooth and non-dilatational	Smooth and dilatatoinal
DG	$\mathbf{F}$	$\mathbf{F}$, $\nabla\mathbf{F}$	$\mathbf{F}$, $\nabla\mathbf{F}$, $\nabla[\nabla\mathbf{F}]$
BCs	Force ($\mathbf{P}$)	Force ($\mathbf{P}$) Double force ($\mathbf{m}$)	Force ($\mathbf{P}$) Double force ($\mathbf{m}$) Triple force ($\mathbf{r}$)
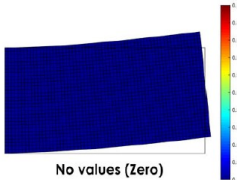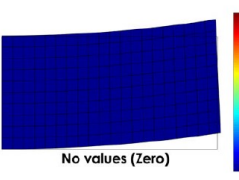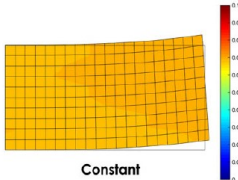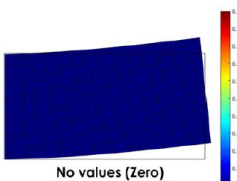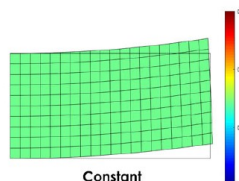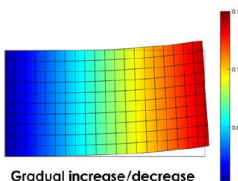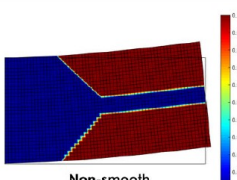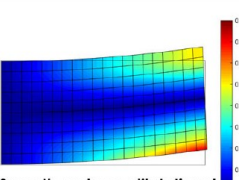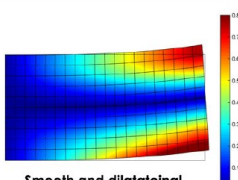
2.3.1 Characterization of the triple stress parameter

In the previous section, we observed that the responses of the composite, and the associated shear strain and shear angle distributions are sensitive to boundary forces

(i.e. double and triple forces) and, in particular, their energy couples via the Nth order stress parameters (i.e. C and A). The double stress parameter C represents the bending rigidity of a fiber such that each fiber family has their own unique C values, obtained from bending experiments. However, little has been devoted to the characterization of the parameter A mainly due to the complex nature of mechanical interactions on edges and points (see, also, [99]-[100], and [109]). Hence, in this section, we address this deficiency and investigate whether there exists a unique characteristic constant A associated with the Piola-Type triple stress. The accuracy and utility of the proposed model are also examined via comparison with the experimental results.

Two sets of experiments were designed for this purpose (see, Figs. 2.9-2.10): a three point bending test of a Crystalline Nanocellulose (CNC) fiber composite ($C = 150Gpa$, $\mu = 1Gpa$); and a bending test of a Nylon-6 Fiber Neoprene Rubber composite ($C = 2000Mpa$, $\mu = 1Mpa$), which is clamped on both ends. In both experiments, the out-of-plane direction (x_3) is aligned with either the loading cylinder or the guide clamps. This setting is a particular case of the proposed model when $c \gg d$. The resulting displacements are simultaneously recorded via the MTS load cell and high speed camera.
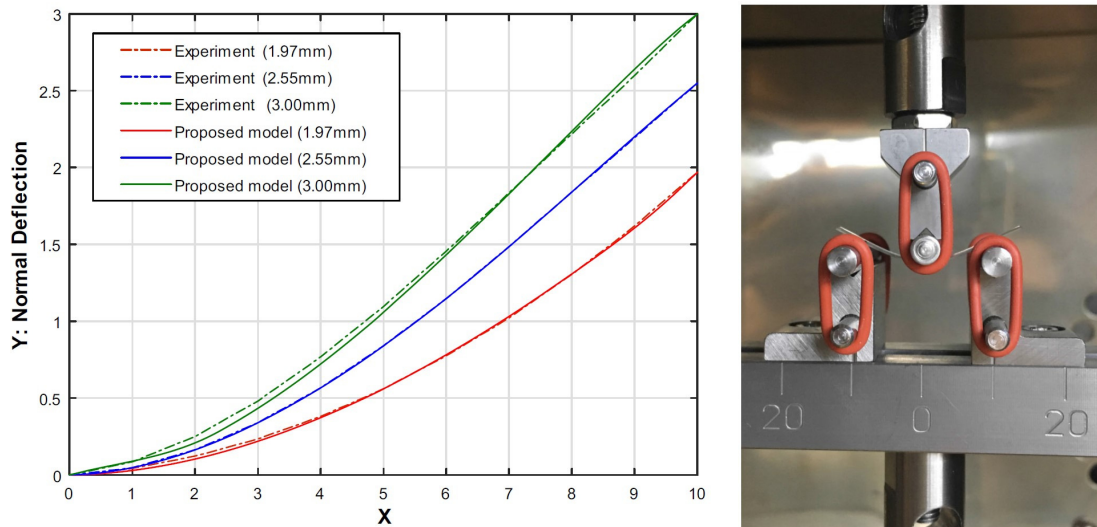
Figure 2.9: CNC fiber composites bending test: Experimental data and theoretical predictions.

Figs. 2.9 and 2.11 illustrate that the proposed model successfully predicts the
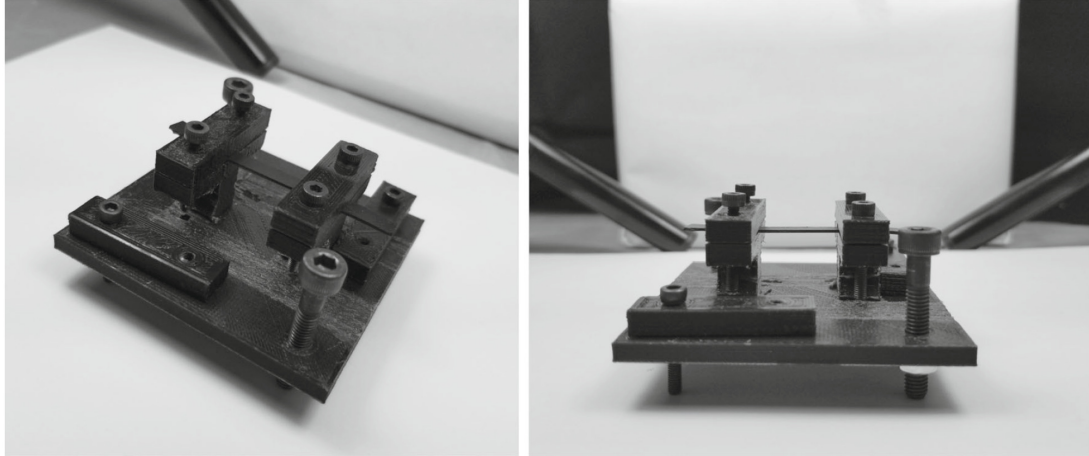
Figure 2.10: Nylon-6 fiber neoprene rubber composite experimental setup.

deformation profiles of both the CNC fiber composite and Nylon fiber composite with a maximum error of less then 2%. But more importantly, the results in Fig. 2.12 indicate that there exists a certain range of values for A which minimize the prediction errors. Further, we found that these characteristic numbers are unique for each composite and not affected by either the types of boundary conditions or the applied loadings (e.g., $\mathbf{r}, \mathbf{m}$, see, Fig. 2.12). Therefore, it is inferred that A is indeed an intrinsic property of the examined composites pertaining to the Piola-type triple stress, and can be uniquely determined for each case. For example, $A = 127$ for CNC fiber composite and $A = 0.825$ for Nylon rubber composite. Here, we may refer to A as the triple modulus of composites for use in analogous studies.

Lastly, we note that the obtained results can be further extended to encompass more practically important problems: determining the triple modulus of the composites subjected to different loading conditions (e.g., Bias extension); examining the existence of the triple modulus for an arbitrary composite; analyzing the effects of the residual Piola-type triple stresses on the mechanical responses of a composite. The researches on these subjects are currently underway and our intention is to report elsewhere when we collect enough case studies.
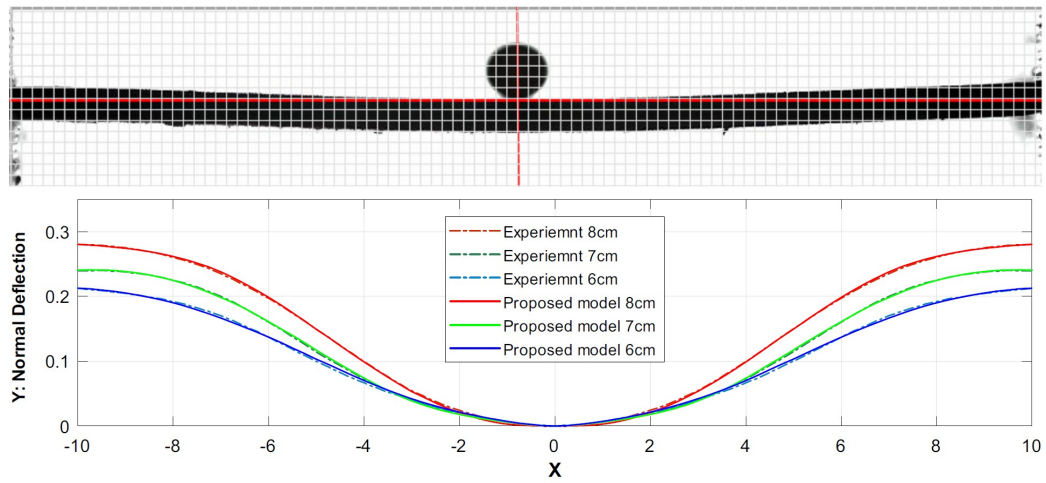
Figure 2.11: Nylon-6 fiber neoprene rubber composite: Experimental data and theoretical predictions.
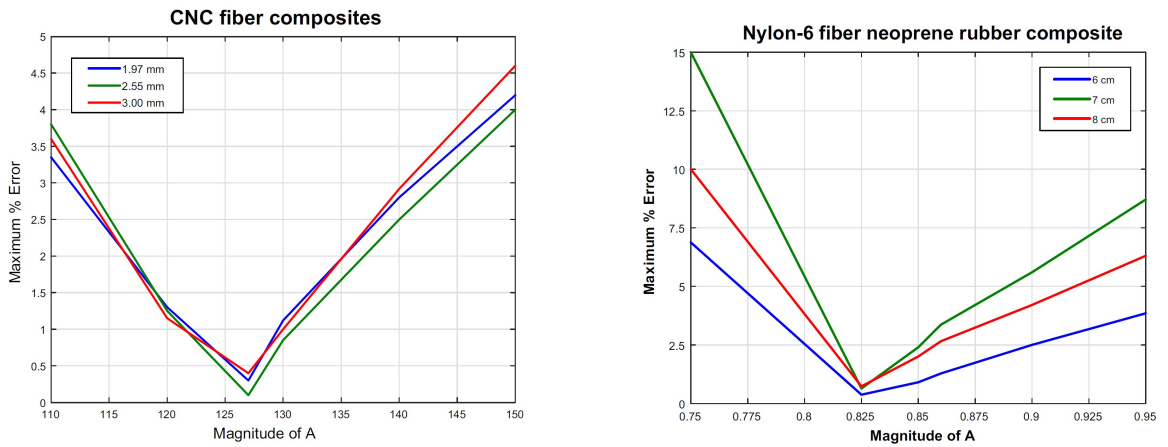
Figure 2.12: Maximum error with respect to A: CNC fiber composite (left), Neoprene rubber composite (right).

47

2.4 Finite element analysis of the 4th order coupled PDE

The resulting systems of PDEs (Eqs. (2.46)-(2.51)) is 6th order differential equations with coupled non-linear terms. The case of such less regular PDEs deserve delicate mathematical treatment as done similarly in [96] and [110] and is of particular practical interest. Therefore, it is not trivial to demonstrate numerical analysis procedures regarding FE analysis.

For preprocessing, Eqs. (2.50)-(2.51) may be recast as

$$
\begin{aligned}
\mu\left(Q + \chi_{1,22}\right) - A\chi_{2,2} + B\chi_{2,1} - CQ_{,11} + AS_{,11} &= 0, \\
\mu\left(R + \chi_{2,22}\right) + A\chi_{1,2} - B\chi_{1,1} - CR_{,11} + AT_{,11} &= 0, \\
Q - \chi_{1,11} &= 0, \\
R - \chi_{2,11} &= 0, \\
S - Q_{,11} &= 0, \\
T - R_{,11} &= 0, \\
A - \mu(Q + \chi_{1,22}) - CS &= 0, \\
B - \mu(R + \chi_{2,22}) - CT &= 0, \quad\quad (2.76)
\end{aligned}
$$

where $Q = \chi_{1,11}$, $R = \chi_{2,11}$, $S = Q_{,11}$ and $T = R_{,11}$. Thus, we reduced the order of deferential equations from three coupled equations of 6th order to eight coupled equations of 2nd order. In particular, the non-linear terms (e.g. $A\chi_{2,2}$, $B\chi_{2,1}$ etc...) in the above equations can be systematically treated via the Picard iterative procedure;

$$
\begin{aligned}
-A_{initial}\chi_{2,2}^{initial} + B_{initial}\chi_{2,1}^{initial} &\implies -A_0\chi_{2,2}^0 + B_0\chi_{2,1}^0, \\
A_{initial}\chi_{1,2}^{initial} - B_{initial}\chi_{1,1}^{initial} &\implies A_0\chi_{1,2}^0 - B_0\chi_{1,1}^0, \quad\quad (2.77)
\end{aligned}
$$

where the values of A and B continue to be updated based on their previous estimations (e.g. A_1 and B_1 are refreshed by their previous pair of A_0 and B_0) as iteration progresses. Hence, we generalize the above expression for N number of iterations as

$$
\begin{aligned}
-A_{N-1}\chi_{2,2}^{N-1} + B_{N-1}\chi_{2,1}^{N-1} &\implies -A_N\chi_{2,2}^N + B_N\chi_{2,1}^N, \\
A_{N-1}\chi_{1,2}^{N-1} - B_{N-1}\chi_{1,1}^{N-1} &\implies A_N\chi_{1,2}^N - B_N\chi_{1,1}^N, \quad\quad (2.78)
\end{aligned}
$$

in which the number of iteration can be determined by a convergence criteria.

In addition, the weighted forms of Eq. (2.76) is obtained by

$$0 = \int_{\Omega^e} w_1(\mu\left(Q + \chi_{1,22}\right) - A\chi_{2,2} + B\chi_{2,1} - CQ_{,11} + AS_{,11})d\Omega,$$

$$0 = \int_{\Omega^e} w_2(\mu\left(R + \chi_{2,22}\right) + A\chi_{1,2} - B\chi_{1,1} - CR_{,11} + AT_{,11})d\Omega,$$

$$0 = \int_{\Omega^e} w_3(Q - \chi_{1,11})d\Omega,$$

$$0 = \int_{\Omega^e} w_4(R - \chi_{2,11})d\Omega,$$

$$0 = \int_{\Omega^e} w_5(S - Q_{,11})d\Omega,$$

$$0 = \int_{\Omega^e} w_6(T - R_{,11})d\Omega,$$

$$0 = \int_{\Omega^e} w_7(A - \mu(Q + \chi_{1,22}) - CS)d\Omega,$$

$$0 = \int_{\Omega^e} w_8(B - \mu(R + \chi_{2,22}) - CT)d\Omega. \tag{2.79}$$

Applying integration by parts and Green-stokes theorem (e.g. $\mu\int_{\Omega^e} w_1\chi_{1,22}d\Omega = -\mu\int_{\Omega^e} w_{1,2}\chi_{1,2}d\Omega + \mu\int_{\Omega^e} w_1\chi_{1,2}Nd\Gamma$), we obtain from the above that

$$0 = \int_{\Omega^e} (\mu w_1 Q - \mu w_{1,2}\chi_{1,2} - w_1 A_0\chi_{2,2} + w_1 B_0\chi_{2,1} + Cw_{1,1}Q_{,1} - Aw_{1,1}S_{,1})d\Omega$$
$$+ \int_{\partial\Gamma^e} \mu w_1\chi_{1,2}Nd\Gamma - \int_{\partial\Gamma^e} Cw_1 Q_{,1}Nd\Gamma + \int_{\partial\Gamma^e} Aw_1 S_{,1}Nd\Gamma,$$

$$0 = \int_{\Omega^e} (\mu w_2 R - \mu w_{2,2}\chi_{2,2} + w_2 A_0\chi_{1,2} - w_2 B_0\chi_{1,1} + Cw_{2,1}R_{,1} - Aw_{2,1}T_{,1})d\Omega$$
$$+ \int_{\partial\Gamma^e} \mu w_2\chi_{2,2}Nd\Gamma - \int_{\partial\Gamma^e} Cw_2 R_{,1}Nd\Gamma + \int_{\partial\Gamma^e} Aw_2 T_{,1}Nd\Gamma,$$

$$0 = \int_{\Omega^e} (w_3 Q + w_{3,1}\chi_{1,1})d\Omega - \int_{\partial\Gamma^e} w_3\chi_{1,1}Nd\Gamma,$$

$$0 = \int_{\Omega^e} (w_4 R + w_{4,1}\chi_{2,1})d\Omega - \int_{\partial\Gamma^e} w_4\chi_{2,1}Nd\Gamma,$$

$$0 = \int_{\Omega^e} (w_5 S + w_{5,1}Q_{,1})d\Omega - \int_{\partial\Gamma^e} w_5 Q_{,1}Nd\Gamma,$$

$$0 = \int_{\Omega^e} (w_6 T + w_{6,1}R_{,1})d\Omega - \int_{\partial\Gamma^e} w_6 R_{,1}Nd\Gamma,$$

$$0 = \int_{\Omega^e} w_7(A_0 - \mu Q - CS - \mu w_{7,2}\chi_{1,2})d\Omega - \int_{\partial\Gamma^e} \mu w_7\chi_{1,2}Nd\Gamma$$

$$0 = \int_{\Omega^e} w_8(B_0 - \mu R - CT - \mu w_{8,2}\chi_{1,2})d\Omega - \int_{\partial\Gamma^e} \mu w_7\chi_{2,2}Nd\Gamma, \qquad (2.80)$$

where Ω, $\partial\Gamma$ and $\mathbf{N}$ are the domain of interest, the associated boundary, and the rightward unit normal to the boundary $\partial\Gamma$ in the sense of the Green-stoke's theorem, respectively. The unknowns, χ_1, χ_2, Q, R, S, T, A and B can be written in the form of Lagrangian polynomial as

$$(*) = \sum_{j=1}^{n=4} [(*)_j \Psi_j(x,\ y)]. \qquad (2.81)$$

Thus, the test function w is obtained by

$$w_m = \sum_{i=1}^{n=4} w_m^i \Psi_i(x,\ y) \text{ and } m = 1, 2, 3, ..., 8. \qquad (2.82)$$

Here, w_i is weight of the test function and $\Psi_i(x,y)$ are the shape functions for the 4-node rectangular elements such that

$$\Psi_1 = \frac{(x-c)(y-d)}{cd}, \Psi_2 = \frac{x(y-d)}{-cd},\ \Psi_3 = \frac{xy}{cd} \text{ and } \Psi_4 = \frac{y(x-c)}{-cd}. \qquad (2.83)$$

By means of Eq. (2.81), Eq. (2.80) can be rewritten in terms of Lagrangian polyno-

mial representation as

$$
\begin{aligned}
0 =& \sum_{i,j=1}^{n}\{\int_{\Omega^e}(\mu\Psi_i\Psi_j+C\Psi_{i,1}\Psi_{j,1})d\Omega\}Q_j-\sum_{i,j=1}^{n}\{\int_{\Omega^e}(\mu\Psi_{i,2}\Psi_{j,2})d\Omega\}\chi_{1j}\\
&-\sum_{i,j=1}^{n}\{\int_{\Omega^e}(\Psi_iA_0\Psi_{j,2}-\Psi_iB_0\Psi_{j,1})d\Omega\}\chi_{2j}-\sum_{i,j=1}^{n}\{\int_{\Omega^e}(A\Psi_{i,1}\Psi_{j,1})d\Omega\}S_j\\
&+\int_{\partial\Gamma^e}(\mu\Psi_i\chi_{1,2})Nd\Gamma-\int_{\partial\Gamma^e}(C\Psi_iQ_{,1})Nd\Gamma+\int_{\partial\Gamma^e}A\Psi_iS_{,1}Nd\Gamma,\\
0 =& \sum_{i,j=1}^{n}\{\int_{\Omega^e}(\mu\Psi_i\Psi_j+C\Psi_{i,1}\Psi_{j,1})d\Omega\}R_j-\sum_{i,j=1}^{n}\{\int_{\Omega^e}(\mu\Psi_{i,2}\Psi_{j,2})d\Omega\}\chi_{2j}\\
&+\sum_{i,j=1}^{n}\{\int_{\Omega^e}(\Psi_iA_0\Psi_{j,2}-\Psi_iB_0\Psi_{j,1})d\Omega\}\chi_{1j}-\sum_{i,j=1}^{n}\{\int_{\Omega^e}(A\Psi_{i,1}\Psi_{j,1})d\Omega\}T_j\\
&+\int_{\partial\Gamma^e}(\mu\Psi_i\chi_{2,2})Nd\Gamma-\int_{\partial\Gamma^e}(C\Psi_iR_{,1})Nd\Gamma+\int_{\partial\Gamma^e}A\Psi_iT_{,1}Nd\Gamma,\\
\\
0 =& \sum_{i,j=1}^{n}\{\int_{\Omega^e}(\Psi_i\Psi_j)d\Omega\}Q_j+\sum_{i,j=1}^{n}\{\int_{\Omega^e}\Psi_{i,1}\Psi_{j,1})d\Omega\}\chi_{1j}-\int_{\partial\Gamma^e}(\Psi_i\chi_{1,1})Nd\Gamma,\\
0 =& \sum_{i,j=1}^{n}\{\int_{\Omega^e}(\Psi_i\Psi_j)d\Omega\}R_j+\sum_{i,j=1}^{n}\{\int_{\Omega^e}\Psi_{i,1}\Psi_{j,1})d\Omega\}\chi_{2j}-\int_{\partial\Gamma^e}(\Psi_i\chi_{2,1})Nd\Gamma,\\
0 =& \sum_{i,j=1}^{n}\{\int_{\Omega^e}(\Psi_i\Psi_j)d\Omega\}S_j+\sum_{i,j=1}^{n}\{\int_{\Omega^e}\Psi_{i,1}\Psi_{j,1})d\Omega\}Q_j-\int_{\partial\Gamma^e}(\Psi_iQ_{,1})Nd\Gamma,\\
0 =& \sum_{i,j=1}^{n}\{\int_{\Omega^e}(\Psi_i\Psi_j)d\Omega\}T_j+\sum_{i,j=1}^{n}\{\int_{\Omega^e}\Psi_{i,1}\Psi_{j,1})d\Omega\}R_j-\int_{\partial\Gamma^e}(\Psi_iR_{,1})Nd\Gamma,\\
0 =& \sum_{i,j=1}^{n}\{\int_{\Omega^e}(\Psi_i\Psi_j)d\Omega\}A_j-\sum_{i,j=1}^{n}\{\int_{\Omega^e}(\mu\Psi_i\Psi_j)d\Omega\}Q_j-\sum_{i,j=1}^{n}\{\int_{\Omega^e}(C\Psi_i\Psi_j)d\Omega\}S_j\\
&-\sum_{i,j=1}^{n}\{\int_{\Omega^e}(\mu\Psi_{i,2}\Psi_{j,2})d\Omega\}\chi_{1j}+\int_{\partial\Gamma^e}(\mu\Psi_i\chi_{1,2})Nd\Gamma,\\
0 =& \sum_{i,j=1}^{n}\{\int_{\Omega^e}(\Psi_i\Psi_j)d\Omega\}B_j-\sum_{i,j=1}^{n}\{\int_{\Omega^e}(\mu\Psi_i\Psi_j)d\Omega\}R_j-\sum_{i,j=1}^{n}\{\int_{\Omega^e}(C\Psi_i\Psi_j)d\Omega\}T_j\\
&-\sum_{i,j=1}^{n}\{\int_{\Omega^e}(\mu\Psi_{i,2}\Psi_{j,2})d\Omega\}\chi_{2j}+\int_{\partial\Gamma^e}(\mu\Psi_i\chi_{2,2})Nd\Gamma.
\end{aligned}
\tag{2.84}
$$

Now, for the lolcal stiffness matrices and forcing vectors for each elements, we find

$$\begin{bmatrix} K_{11}^{11} & K_{12}^{11} & K_{13}^{11} & K_{14}^{11} \\ K_{21}^{11} & K_{22}^{11} & K_{23}^{11} & K_{24}^{11} \\ K_{31}^{11} & K_{32}^{11} & K_{33}^{11} & K_{34}^{11} \\ K_{41}^{11} & K_{42}^{11} & K_{43}^{11} & K_{44}^{11} \end{bmatrix}_{Local} \begin{bmatrix} \chi_1^1 \\ \chi_1^2 \\ \chi_1^3 \\ \chi_1^4 \end{bmatrix}_{Local} = \begin{bmatrix} F_1^1 \\ F_2^1 \\ F_3^1 \\ F_4^1 \end{bmatrix}_{Local} \quad , \tag{2.85}$$

or alternatively, in a compact form,

$$\left[K_{ij}^{11} \right] \left[\chi_1^i \right] = \left[F_i^1 \right] \text{ for } i, \ j = 1, 2, 3, 4, \tag{2.86}$$

where

$$\left[K_{ij}^{11} \right] = \int_{\Omega^e} (\mu \Psi_{i,2} \Psi_{j,2}) d\Omega, \tag{2.87}$$

and

$$\left[F_i^1 \right] = -\mu \int_{\partial \Gamma^e} \Psi_i \chi_{1,2} N d\Gamma + C \int_{\partial \Gamma^e} \Psi_i Q_{,1} N d\Gamma - \int_{\partial \Gamma^e} A \Psi_i S_{,1} N d\Gamma. \tag{2.88}$$

Accordingly, the unknowns (i.e. $Q, \ R, S, T, \ A$ and B) can be expressed as

$$Q_i = \{\chi_1^i\}_{,11}, \ R_i = \{\chi_2^i\}_{,11}, \ S_i = \{Q^i\}_{,11} \text{ etc...} \tag{2.89}$$

Finally, we repeat the same procedures for the rest of components (e.g. $\left[K_{ij}^{21} \right] \left[\chi_2^i \right] = \left[F_i^2 \right]$ etc...) and, thereby obtain the following systems of equations (in the Global form) for each individual elements.

$$\begin{bmatrix} [K^{11}] & [K^{12}] & . & . & . & . & [K^{17}] & [K^{18}] \\ [K^{21}] & [K^{22}] & . & . & . & . & [K^{27}] & [K^{28}] \\ [K^{31}] & [K^{32}] & . & . & . & . & [K^{37}] & [K^{38}] \\ [K^{41}] & [K^{42}] & . & . & . & . & [K^{47}] & [K^{48}] \\ [K^{51}] & [K^{52}] & . & . & . & . & [K^{57}] & [K^{58}] \\ [K^{61}] & [K^{62}] & . & . & . & . & [K^{67}] & [K^{68}] \\ [K^{71}] & [K^{72}] & . & . & . & . & [K^{77}] & [K^{78}] \\ [K^{81}] & [K^{82}] & . & . & . & . & [K^{87}] & [K^{88}] \end{bmatrix}_{Global} \begin{bmatrix} \{\chi_1^i\} \\ \{\chi_2^i\} \\ Q_i \\ R_i \\ A_i \\ B_i \\ S_i \\ T_i \end{bmatrix}_{Global} = \begin{bmatrix} \{F_i^1\} \\ \{F^2\} \\ \{F^3\} \\ \{F^4\} \\ \{F^5\} \\ \{F^6\} \\ \{F^7\} \\ \{F^8\} \end{bmatrix}_{Global}. \tag{2.90}$$

In the simulation, the following convergence criteria are used for both nonlinear terms;

$$|A_{n+1} - A_n| = e_1 \le \varepsilon, \ |B_{n+1} - B_n| = e_2 \le \varepsilon \text{ and } \varepsilon = \text{maximum error} = 10^{-4}, \tag{2.91}$$

which demonstrate fast convergence within 20 iterations (see, Table. 2.2)

Table 2.2: Maximum numerical errors with respect to the number of iterations.

Number of iteration	Mximum error
1	1.2e-01
5	5.7e-02
10	3.5e-03
17	9.2e-05
20	5.0e-05

2.5   Denouement

In this chapter, we present a second gradient-based continuum model for the mechanics of an elastic solid reinforced with extensible fibers and subjected to plane deformations. The fibers are presumed as continuously distributed spatial rods of Kirchhoff type, under which the kinematics of fibers has been formulated via the second and third gradient of continuum deformations. By means of the variational principles and the virtual work statement, the Euler equations and the associated necessary boundary conditions are obtained. The energy density function of Spencer and Soldatos type is augmented by the third gradient of deformations to accommodate the third gradient continua and the associated bulk incompressibility.

The presented model is solved using finite element analysis method. The proposed model predicts smooth and dilatational shear angle distributions, as opposed to those obtained from the first and second-gradient theory where the resulting shear zones are either non-dilatational or non-smooth. Case studies are also performed through the inhouse experimental settings of crystalline nanocellulose (CNC) fiber composites and Nylon-6 fiberNeoprene rubber composites, which illustrate that the obtained solutions successfully predict the deformation profiles of both composites.

Chapter 3

A model for hyperelastic materials reinforced with fibers resistance to extension and flexure

In sections 3.1 and 3.2, we develop the kinematics of the reinforcing fibers and equilibrium equations, respectively. The boundary conditions are presented in section 3.3. In section 3.4, a case of Mooner-Rvilin type hyperelastic material is considered as the matrix material which is reinforced with unidirectional fibers. Through the method of virtual work and the computation of variational derivatives, the corresponding Euler equilibrium equation is derived, forming a set of coupled Partial Differential Equations, which is solved using the finite element method. In section 3.5, the prediction performance of the presented model is compared against a set of in-house experimental data.

3.1   Kinematics

Our intention throughout this section is to establish the kinematical framework which will be used in the constitutive formulations of hyperelastic matrix-fiber composites. We note that, in the forgoing development, a unidirectional fiber-reinforced composites are considered for the sake of simplicity. The cases of bidirectional fibers can be readily implemented to the proposed model using the similar approaches as done in [86] and [113].

Let $\mathbf{r}(s)$ is the parametric curve which represents fibers' trajectory on the deformed configuration and let $\boldsymbol{\tau}$ be the unit tangent in the direction of increasing s. We also

define $\mathbf{X}(S)$ and S as the counter parts of $\mathbf{r}(s)$ and s in the reference configuration. The orientation of a particular fiber is then defined by

$$\lambda = |\mathbf{d}| \text{ and } \lambda\boldsymbol{\tau} = \mathbf{d}; \ \lambda \equiv \frac{ds}{dS} \text{ and } \boldsymbol{\tau} \equiv \frac{d\mathbf{r}(s)}{ds}, \tag{3.1}$$

where

$$\mathbf{d} = \mathbf{FD}, \ \mathbf{F} = \lambda\boldsymbol{\tau} \otimes \mathbf{D}, \tag{3.2}$$

and $\mathbf{F}$ is the gradient of the deformation function $(\boldsymbol{\chi}(\mathbf{X}))$. Eq. (3.2) are obtained by taking the derivative of $\mathbf{r}(s(S)) = \boldsymbol{\chi}(\mathbf{X}(S))$ with respect to arclength parameters S and ultimately s, upon making the identifications $\mathbf{D} = d\mathbf{X}/dS$. Here, $d(*)/dS$ and $d(*)/ds$ refer to the arclength derivatives of $(*)$ along fibers' directions in the reference and deformed configurations, respectively. Eq. (3.2) can be projected using the orthonormal bases of $\{\mathbf{E}_A : reference\}$ and $\{\mathbf{e}_i : current\}$ to yield

$$\lambda\tau_i = d_i = F_{iA}D_A \text{ for } \mathbf{D} = D_A\mathbf{E}_A \text{ and } \mathbf{d} = d\mathbf{e}_i. \tag{3.3}$$

which may also used in the later sections.

The expression for geodesic curvature of a parametric curve $(\mathbf{r}(s))$ is then obtained from Eqs. (3.2)-(3.3) that

$$\mathbf{g} \equiv \mathbf{r}'' = \frac{d(\frac{\mathbf{r}(S)}{dS})}{dS} = \frac{\partial(\mathbf{FD})}{\partial\mathbf{X}}\frac{\partial\mathbf{X}}{\partial S} = \nabla[\mathbf{FD}]\mathbf{D}. \tag{3.4}$$

In general, most of the fibers are straight prior to deformations. Even slightly curved fibers can be idealized as 'fairly straight' fibers, considering their length scales with respect to that of matrix materials. This indicates that the gradients of unit tangents in the reference configuration are vanishes identically (i.e. $\nabla\mathbf{D} = 0$). Hence, Eq. (3.4) reduces to

$$\mathbf{g} = \nabla\mathbf{F}(\mathbf{D} \otimes \mathbf{D}) = \mathbf{G}(\mathbf{D} \otimes \mathbf{D}), \tag{3.5}$$

where we employ the convention of the second gradient of deformations as

$$\nabla\mathbf{F} \equiv \mathbf{G}, \text{ and} \tag{3.6}$$

$$G_{iAB} = F_{iA,B} = F_{iB,A} = G_{iBA} \tag{3.7}$$

is the compatibility condition of $\mathbf{G}$. For the desired applications, we propose the following strain energy function:

$$W(\mathbf{F}, \mathbf{G}) = \widehat{W}(\mathbf{F}) + W(\mathbf{G}), \ \ W(\mathbf{G}) \equiv \frac{1}{2}C(\mathbf{F})|\mathbf{g}|^2, \tag{3.8}$$

55

where the response of the fiber materials are governed by both the first and second gradient of deformations. Further, $C(\mathbf{F})$ refers to the material property associated with the bending motions of fibers which, in general, independent of the deformation gradient (i.e. $C(\mathbf{F}) = C$). Eq. (3.8) is consistent with the model proposed by [93] that, in the case of a single family of fibers, the dependence of the strain energy on $\mathbf{G}$ occurs through $\mathbf{g}$ such that

$$W(\mathbf{G}) = W(\mathbf{g}(\mathbf{G})). \tag{3.9}$$

In particular, we introduce the strain energy function which addresses the fiber's resistance to extension as

$$W(\varepsilon) = \frac{1}{2}E\varepsilon^2, \text{and} \tag{3.10}$$

$$\varepsilon = \frac{1}{2}(\lambda^2 - 1), \tag{3.11}$$

where E is a modulus pertaining to the fiber's extension and the expression of λ^2 can be obtained from Eq. (3.3):

$$\lambda^2 = \mathbf{FD} \cdot \mathbf{FD} = \mathbf{F}^T\mathbf{FD} \cdot \mathbf{D} = (\mathbf{F^TF}) \cdot \mathbf{D} \otimes \mathbf{D}. \tag{3.12}$$

It is inferred from Eq. (3.12) that the fiber's extension is $\mathbf{F}$ dependent via ε (i.e. $\varepsilon = \varepsilon(\mathbf{F})$). Thus, the strain energy function Eq. (3.8) is now augmented by Eq. (3.10) to yields

$$W(\mathbf{F}, \varepsilon(\mathbf{F}), \mathbf{g}(\mathbf{G})) = W(\mathbf{F}) + \frac{1}{2}E\varepsilon^2 + \frac{1}{2}C\left|\mathbf{g}(\mathbf{G})\right|^2. \tag{3.13}$$

For uses in the derivation of Euler equations and the associated boundary conditions, we continue by evaluating the induced energy variation of the response function (Eq. (3.13)) with respect to $\mathbf{F}$, ε, and $\mathbf{g}$ as

$$\dot{W}(\mathbf{F}, \varepsilon, \mathbf{g}) = W_{\mathbf{F}}{\cdot}\dot{\mathbf{F}} + W_\varepsilon\dot{\varepsilon} + W_{\mathbf{g}}{\cdot}\dot{\mathbf{g}}. \tag{3.14}$$

Here, the superposed dot refers to derivatives with respect to a parameter ε at the particular configuration of the composite ($\varepsilon = 0$) that labels a one-parameter family of deformations.

The desired expressions for the variational derivatives can be obtained from Eqs. (3.10)-(3.13) that

$$\dot{\varepsilon} = \frac{1}{2}\dot{\overline{(\lambda^2 - 1)}} = \frac{1}{2}\dot{\overline{(\mathbf{FD} \cdot \mathbf{FD} - 1)}} = \mathbf{FD} \cdot \dot{\mathbf{F}}\mathbf{D} = \mathbf{FD} \otimes \mathbf{D} \cdot \dot{\mathbf{F}}, \tag{3.15}$$

56

$$W_\varepsilon = E\varepsilon, \text{ and } W_\mathbf{g} = C\mathbf{g}. \tag{3.16}$$

Hence, the above lead to

$$W_\varepsilon \dot{\varepsilon} = E\varepsilon\dot{\varepsilon} = E[\frac{1}{2}\{(\mathbf{F^T F}) \cdot \mathbf{D} \otimes \mathbf{D} - 1\}][\mathbf{FD} \otimes \mathbf{D}] \cdot \dot{\mathbf{F}} \tag{3.17}$$

$$W_\mathbf{g} \dot{\mathbf{g}} = C\mathbf{g} \cdot \dot{\mathbf{g}} = \mathbf{G}(\mathbf{D} \otimes \mathbf{D}) \cdot \dot{\mathbf{G}}(\mathbf{D} \otimes \mathbf{D}) = (C\mathbf{g} \otimes \mathbf{D} \otimes \mathbf{D}) \cdot \dot{\mathbf{G}}, \tag{3.18}$$

where, from Eq. (3.5), $\mathbf{g} = \mathbf{G}(\mathbf{D} \otimes \mathbf{D})$.

Finally, combining Eqs. (3.14)-(3.18), we find

$$\dot{W}(\mathbf{F}, \varepsilon, \mathbf{g}) = W_\mathbf{F} \cdot \dot{\mathbf{F}} + E[\frac{1}{2}\{(\mathbf{F^T F}) \cdot \mathbf{D} \otimes \mathbf{D} - 1\}][\mathbf{FD} \otimes \mathbf{D}] \cdot \dot{\mathbf{F}} + (C\mathbf{g} \otimes \mathbf{D} \otimes \mathbf{D}) \cdot \dot{\mathbf{G}}. \tag{3.19}$$

or equivalently

$$\dot{W}(\mathbf{F}, \varepsilon, \mathbf{g}) = W_{F_{iA}} \dot{F}_{iA} + \frac{E}{2}(F_{jC}F_{jD}D_C D_D - 1)(F_{iB}D_B D_A)\dot{F}_{iA} + Cg_i D_A D_B \dot{G}_{iAB}. \tag{3.20}$$

3.2 Equilibrium

The derivation of the Euler equation and boundary conditions arsing in second-gradient elasticity is well studied [98], [101], and [107]-[108]. We reformulate the results in the present context for the sake of clarity and completeness, and, in particular, for the purpose of establishing the connections between the applied loads and the deformations. The weak form of the equilibrium equations is given by the virtual-work statement

$$\dot{E} = P, \tag{3.21a}$$

where P is the virtual power of the applied loads and the superposed dot refers to the variational and/or Gateâux derivative;

$$E = \int_\Omega W(\mathbf{F}, \varepsilon, \mathbf{g}) \, dA \tag{3.22a}$$

is the strain energy. In general, volumetric changes in materials' deformations are energetically expensive processes and thus are typically constrained in the constitutive modeling of engineering materials (see, [105]-[106]). To accommodate the condition

of the bulk incompressibility, the strain energy potential is augmented by the weak form, $p(J-1)$; i.e.,

$$U = W - p(J-1) \text{ and } E = \int_\Omega U\left(\mathbf{F}, \varepsilon, \mathbf{g}\right) dA, \tag{3.23}$$

where J is determinant of $\mathbf{F}$ and p is a constitutively indeterminate scalar field. The associated variation is then given by

$$\dot{U} = \dot{W} - p\dot{J}, \text{ and } \dot{J} = J_{\mathbf{F}}\mathbf{F} \cdot \dot{\mathbf{F}} = \mathbf{F}^*\!\cdot\dot{\mathbf{F}}. \tag{3.24}$$

It is noted that conservative loads are characterized by the existence of a potential L such that $P = \dot{L}$. Thus the problem of determining equilibrium deformations is reduced to the problem of minimizing the potential energy, $E - L$. In the present case, this means

$$\dot{E} = \int_\Omega \dot{U}\left(\mathbf{F}, \varepsilon, \mathbf{g},p\right) dA. \tag{3.25}$$

We now substitute Eqs. (3.21a) and (3.24) into Eq. (3.25) and thereby obtain

$$\dot{E} = \int_\Omega [W_{F_{iA}} u_{i,A} + \frac{E}{2}(F_{jC}F_{jD}D_CD_D - 1)(F_{iB}D_BD_A)u_{i,A} + C(g_iD_AD_B)u_{i,AB}$$
$$-pF_{iA}^* u_{iA}]dA, \tag{3.26}$$

where $u_i = \dot{\chi}_i$ is the variation of the position field. Applying integration by part on $C(g_iD_AD_BG)u_{i,AB}$ we find

$$C(g_iD_AD_B)u_{i,AB} = C(g_iD_AD_Bu_{i,A})_{,B} - C(g_iD_AD_B)_{,B}u_{i,A}. \tag{3.27}$$

Thus from the above, Eq. (3.26) may be recast as

$$\dot{E} = \int_\Omega [\{W_{F_{iA}} + \frac{E}{2}(F_{jC}F_{jD}D_CD_D - 1)(F_{iB}D_BD_A) - pF_{iA}^* - C(g_iD_AD_B)_{,B}\}u_{i,A}$$
$$+C(g_iD_AD_Bu_{i,A})_{,B}]dA. \tag{3.28}$$

But Eq. (3.28) is equivalent to

$$\dot{E} = \int_\Omega [W_{F_{iA}} + \frac{E}{2}(F_{jC}F_{jD}D_CD_D - 1)(F_{iB}D_BD_A) - pF_{iA}^* - C(g_iD_AD_B)_{,B}]u_{i,A}dA$$
$$+\int_{\partial\Omega} C(g_iD_AD_Bu_{i,A})N_BdS, \tag{3.29}$$

where N_A is the rightward unit normal to $\partial\Omega$ in the sense of Green–Stokes theorem.

Consequently, we find

$$\dot{E} = \int_{\Omega} P_{iA}u_{i,A}dA + \int_{\partial\Omega} C(g_iD_AD_Bu_{i,A})N_BdS, \qquad (3.30)$$

where

$$P_{iA} = W_{F_{iA}} + \frac{E}{2}(F_{jC}F_{jD}D_CD_D - 1)(F_{iB}D_BD_A) - pF_{iA}^* - C(g_iD_AD_B)_{,B} \qquad (3.31)$$

is the expression of the Piola type stress. Also, for initially straight fiber (see, Eqs. (3.4)-(3.5)), the above further reduces to

$$P_{iA} = W_{F_{iA}} + \frac{E}{2}(F_{jC}F_{jD}D_CD_D - 1)(F_{iB}D_BD_A) - pF_{iA}^* - Cg_{i,B}D_AD_B. \qquad (3.32)$$

Thus the Euler equation is obtained by

$$P_{iA,A} = 0 \text{ or } Div(\mathbf{P}) = 0, \qquad (3.33)$$

which holds in Ω.

3.3 Boundary conditions

Applying integration by part on Eq. (3.30) (i.e. $P_{iA}u_{i,A} = (P_{iA}u_i)_{,A} - (P_{iA})_{,A}u_i$), we find

$$\dot{E} = \int_{\Omega} [(P_{iA}u_i)_{,A} - P_{iA,A}u_i]dA \int_{\partial\Omega} C(g_iD_AD_Bu_{i,A})N_BdS. \qquad (3.34)$$

The above may be recast as

$$\dot{E} = \int_{\partial\Omega} [P_{iA}u_iN_A + C(g_iD_AD_Bu_{i,A})N_B]dS - \int_{\Omega} P_{iA,A}u_idA. \qquad (3.35)$$

With the Euler equation ($P_{iA,A} = 0$) satisfied on Ω, Eq. (3.30) becomes

$$\dot{E} = \int_{\partial\Omega} P_{iA}u_iN_AdS + \int_{\partial\Omega} C(g_iD_AD_Bu_{i,A})N_BdS. \qquad (3.36)$$

Now, we project $\nabla\mathbf{u}$ onto the normal and tangent directions as;

$$\nabla\mathbf{u} = \nabla\mathbf{u}(\mathbf{T} \otimes \mathbf{T}) + \nabla\mathbf{u}(\mathbf{N} \otimes \mathbf{N}) = \mathbf{u}'\otimes\mathbf{T} + \mathbf{u}_{,\mathbf{N}}\otimes\mathbf{N} \qquad (3.37)$$

where $\mathbf{T} = \mathbf{X}'(s) = \mathbf{k} \times \mathbf{N}$ is the unit tangent to the boundary $\partial\Omega$; and $\mathbf{u}'$ and $\mathbf{u}_{,N}$ are the tangential and normal derivatives of $\mathbf{u}$ on $\partial\Omega$ (i.e. $u_i' = u_{i,A}T_A$, $u_{i,N} = u_{i,A}N_A$). Accordingly, Eq. (3.36) is then decomposed to

$$\dot{E} = \int_{\partial\Omega} P_{iA}u_iN_AdS + \int_{\partial\Omega} Cg_iD_AD_B\left(u_i'T_AN_B + u_{i,N}N_AN_B\right)dS. \qquad (3.38)$$

59

Since,

$$Cg_iD_AD_BT_AN_Bu_i' = (Cg_iD_AD_BT_AN_Bu_i)' - (Cg_iD_AD_BT_AN_B)' u_i, \qquad (3.39)$$

we obtain from Eq. (3.38) that

$$\dot{E} = \int_{\partial\Omega}[P_{iA}N_A - (Cg_iD_AD_BT_AN_B)']u_i dS + \int_{\partial\Omega}Cg_iD_AD_Bu_{i,N}N_AN_B dS$$
$$+ \int_{\partial\Omega}(Cg_iD_AD_BT_AN_Bu_i)' dS. \qquad (3.40)$$

The above can be rewritten as

$$\dot{E} = \int_{\partial\Omega}[P_{iA}N_A - (Cg_iD_AT_AD_BN_B)']u_i dS + \int_{\partial\Omega}Cg_iD_AN_AD_BN_Bu_{i,N} dS$$
$$- \sum\|Cg_iD_AT_AD_BN_Bu_i\|, \qquad (3.41)$$

where the double bar symbol refers to the jump across the discontinuities on the boundary $\partial\Omega$ (i.e. $\|*\| = (*)^+ - (*)^-$) and the sum refers to the collection of all discontinuities.

It follows from Eq. (3.21a) that admissible powers are of the form

$$P = \int_{\partial w_t} t_iu_i dS + \int_{\partial w} m_iu_{i,N} dS + \sum f_iu_i. \qquad (3.42)$$

Hence, by comparing Eqs. (3.41) and (3.42), we obtain

$$t_i = P_{iA}N_A - \frac{d}{dS}[Cg_iD_AT_AD_BN_B],$$
$$m_i = Cg_iD_AN_AD_BN_B,$$
$$f_i = Cg_iD_AT_AD_BN_Bu_i, \qquad (3.43)$$

which are the expressions of edge tractions, edge moments and the corner forces, respectively.

For instance, if the fiber's directions are either normal or tangential to the boundary (i.e. $(\mathbf{D}\cdot\mathbf{T})(\mathbf{D}\cdot\mathbf{N}) = 0$), Eq. (3.43) furnishes

$$t_i = P_{iA}N_A,$$
$$m_i = Cg_iD_AN_AD_BN_B,$$
$$f_i = 0, \qquad (3.44)$$

60

where

$$P_{iA} = W_{F_{iA}} + \frac{E}{2}(F_{jC}F_{jD}D_C D_D - 1)(F_{iB}D_B D_A) - pF_{iA}^* - Cg_{i,B}D_A D_B,$$

$$g_{i,B} = F_{iC,BD}D_C D_D \text{ (see, Eq. (3.5))}. \tag{3.45}$$

Thus, the solution of Eq. (3.33) can be uniquely determined by imposing the admissible set of boundary conditions in Eq. (3.43).

3.4 Hyperelastic matrix material – fiber composites

Based on the constitutive framework discussed in the previous sections, we develop a prediction model which describes the responses of hyperelastic matrix material – composites such as carbon fiber reinforced polymers and elastomeric composites. For this purpose, we employ the Mooney rivlin strain energy potential which is widely adopted in the large deformation analyses (see, also, [105]-[106]);

$$W(\mathbf{F}) = \frac{\mu}{2}(I_1 - 3) + \frac{\lambda}{2}(I_2 - 3), \tag{3.46}$$

where I_1 and I_2 are the principal invariants of the deformation gradient tensor defined respectively by

$$I_1 = tr(\mathbf{F}^T\mathbf{F}) \text{ and } I_2 = \frac{1}{2}[(tr(\mathbf{F}^T\mathbf{F}))^2 - tr((\mathbf{F}^T\mathbf{F})^2)]. \tag{3.47}$$

Since $(I_1)_{\mathbf{F}} = 2\mathbf{F}$ and $(I_2)_{\mathbf{F}} = 2\mathbf{F}(I_1\mathbf{I} - \mathbf{F}^T \cdot \mathbf{F})$ (see, [114]), the variational derivative of Eq. (3.46) can be evaluated as

$$W_{\mathbf{F}} \cdot \dot{\mathbf{F}} = [\frac{\mu}{2}(I_1)_{\mathbf{F}} + \frac{\lambda}{2}(I_2)_{\mathbf{F}}] \cdot \dot{\mathbf{F}} = [\mu\mathbf{F} + \lambda\mathbf{F}\{(\mathbf{F} \cdot \mathbf{F})\mathbf{I} - \mathbf{F}^T\mathbf{F}\}] \cdot \dot{\mathbf{F}}, \tag{3.48}$$

Therefore, we find from Eq. (3.32) that

$$\mathbf{P} = P_{iA}(\mathbf{e}_i \otimes \mathbf{E}_A)$$

$$= [\mu F_{iA} + \lambda F_{iB}(F_{jC}F_{jC}\delta_{AB} - F_{jA}F_{jB}) + \frac{1}{2}E(F_{iB}F_{jC}F_{jC})D_A D_B D_D D_D - \frac{1}{2}EF_{iB}D_A D_B$$

$$- Cg_{i,B}D_A D_B - pF_{iA}^*](\mathbf{e}_i \otimes \mathbf{E}_A), \tag{3.49}$$

which may be served as the expression of the Piola stress for soft composite materials. Further, the corresponding Euler equilibrium equation can be derived as

$$0 = Div(\mathbf{P}) = P_{iA,A}\mathbf{e}_i = [\mu F_{iA,A} + \lambda\{F_{iB}(F_{jC}F_{jC}\delta_{AB} - F_{jA}F_{jB})\}_{,A} - Cg_{i,AB}D_A D_B$$

$$- p_{,A}F_{iA}^* + \frac{1}{2}E(F_{iB}F_{jC}F_{jC})_{,A}D_A D_B D_D D_D - \frac{1}{2}EF_{iB,A}D_A D_B]\mathbf{e}_i, \tag{3.50}$$

61

which hold on Ω.

In the above, μ and λ are the material constants of a hyperelastic matrix material of Mooney rivlin type, and E and C are, respectively the extension and bending modulus of fibers. For example, if the soft composite material reinforced with a single family of fibers (i.e. $\mathbf{D} = \mathbf{E}_1$, $D_1 = 1$, $D_2 = 0$ with the modulus E and C), Eq. (3.50) furnishes

$$
\begin{aligned}
0 \;=\; & [\mu\chi_{i,AA} - p_{,A}\varepsilon_{ij}\varepsilon_{AB}\chi_{j,B} + \lambda(\chi_{i,AA}\chi_{j,C}\chi_{j,C} + \chi_{i,A}\chi_{j,CA}\chi_{j,C} + \chi_{i,A}\chi_{j,C}\chi_{j,CA} \\
& -\chi_{i,BA}\chi_{j,A}\chi_{j,B} - \chi_{i,B}\chi_{j,AA}\chi_{j,B} - \chi_{i,B}\chi_{j,A}\chi_{j,BA}) + \frac{1}{2}E(\chi_{i,11}\chi_{j,1}\chi_{j,1} \\
& +\chi_{i,1}\chi_{j,11}\chi_{j,1} + \chi_{i,1}\chi_{j,1}\chi_{j,11}) - \frac{1}{2}EF_{i1,1} - C\chi_{i,1111}]\mathbf{e}_i, \quad (3.51)
\end{aligned}
$$

where $F_{iA} = \chi_{i,A} = \frac{\partial\chi_i}{\partial X_A}$, $F_{iA}^* = \varepsilon_{ij}\varepsilon_{AB}F_{jB}$, and ε_{ij} is the 2-D permutation; $\varepsilon_{12} = -\varepsilon_{21} = 1, \varepsilon_{11} = -\varepsilon_{22} = 0$. Performing Einstein summation and some efforts, we arrive

$$
\begin{aligned}
0 \;=\; & \mu(\chi_{1,11} + \chi_{1,22}) - p_{,1}\chi_{2,2} + p_{,2}\chi_{2,1} + \lambda(\chi_{1,11}\chi_{2,2}\chi_{2,2} + \chi_{1,22}\chi_{2,1}\chi_{2,1} \\
& +2\chi_{1,1}\chi_{2,21}\chi_{2,2} + 2\chi_{1,2}\chi_{2,12}\chi_{2,1} - \chi_{1,21}\chi_{2,1}\chi_{2,2} - \chi_{1,12}\chi_{2,2}\chi_{2,1} \\
& -\chi_{1,2}\chi_{2,11}\chi_{2,2} - \chi_{1,1}\chi_{2,22}\chi_{2,1} - \chi_{1,2}\chi_{2,1}\chi_{2,21} - \chi_{1,1}\chi_{2,2}\chi_{2,12}) \\
& +\frac{1}{2}E(3\chi_{1,11}\chi_{1,1}\chi_{1,1} + \chi_{1,11}\chi_{2,1}\chi_{2,1} + 2\chi_{2,11}\chi_{1,1}\chi_{2,1}) - C\chi_{1,1111}, \quad (3.52)
\end{aligned}
$$

$$
\begin{aligned}
0 \;=\; & \mu(\chi_{2,11} + \chi_{2,22}) - p_{,2}\chi_{1,1} + p_{,1}\chi_{1,2} + \lambda(\chi_{2,11}\chi_{1,2}\chi_{1,2} + \chi_{2,22}\chi_{1,1}\chi_{1,1} \\
& +2\chi_{2,1}\chi_{1,21}\chi_{1,2} + 2\chi_{2,2}\chi_{1,12}\chi_{1,1} - \chi_{2,21}\chi_{1,1}\chi_{1,2} - \chi_{2,12}\chi_{1,2}\chi_{1,1} \\
& -\chi_{2,2}\chi_{1,11}\chi_{1,2} - \chi_{2,1}\chi_{1,22}\chi_{1,1} - \chi_{2,2}\chi_{1,1}\chi_{1,21} - \chi_{2,1}\chi_{1,2}\chi_{1,12}) \\
& +\frac{1}{2}E(3\chi_{2,11}\chi_{2,1}\chi_{2,1} + \chi_{2,11}\chi_{1,1}\chi_{1,1} + 2\chi_{1,11}\chi_{2,1}\chi_{1,1}) - C\chi_{2,1111}, \quad (3.53)
\end{aligned}
$$

which together with the constraint of the bulk incompressibility;

$$
\det \mathbf{F} = \chi_{1,1}\chi_{2,2} - \chi_{1,2}\chi_{2,1} = 1, \quad (3.54)
$$

solves the unknown potentials of χ_1, χ_2 and p. The solutions can be uniquely determined by imposing the admissible boundary conditions presented in Eq. (3.44). For the common rectangular samples where $\mathbf{D} \cdot \mathbf{T} = 0$ and $\mathbf{D} \cdot \mathbf{N} = 1$, Eq. (3.44) takes

the following form

$$
\begin{aligned}
t_1 &= P_{11}, \; t_2 = 0, \\
m_1 &= Cg_1, \; m_2 = 0, \\
f_1 &= f_2 = 0,
\end{aligned}
\tag{3.55}
$$

where from Eqs. (3.5) and (3.49), the expressions of P_{11} and g_1 can be obtained respectively as

$$
\begin{aligned}
P_{11} &= \mu\chi_{1,1}+\lambda(\chi_{1,1}\chi_{2,2}\chi_{2,2}-\chi_{1,2}\chi_{2,1}\chi_{2,2}) + \frac{1}{2}E\chi_{1,1}(\chi_{1,1}\chi_{1,1} + \chi_{2,1}\chi_{2,1} \\
&\quad +\chi_{1,2}\chi_{1,2} +_{2,1}\chi_{2,22,1}\chi_{2,2}) - \frac{1}{2}E\chi_{1,1}-C\chi_{1,111} - p\chi_{2,2}, \\
g_1 &= G_{111}D_1D_1 = \chi_{1,11}.
\end{aligned}
\tag{3.56}
$$

The numerical solution of the obtained PDE system (Eqs. (3.52)-(3.54)) can be accommodated via commercial packages (e.g. Matlab, COMSOL etc...).

3.4.1 Consideration of linear theory

Although the proposed model is intended for large deformation analyses, the development of the compatible linear model may be of practical interest especially when the induced deformations are determined to be '*small*'. In such cases, the linear theory may supply reasonable alternatives with reduced computational reassures. Our intention here is to investigate the possibility of the compatible linear model for the materials of the Mooney Rivlin type within the description of superposed incremental deformations.

We consider superposed '*small*' deformations defined by

$$
\boldsymbol{\chi} = \boldsymbol{\chi}_o + \epsilon\dot{\boldsymbol{\chi}} \; ; |\epsilon| \ll 1,
\tag{3.57}
$$

where $(\dot{*}) = \partial(*)/\partial\varepsilon$, $\dot{\boldsymbol{\chi}} = \mathbf{u}$ and $(*)_o$ denote configuration of $*$ evaluated at $\epsilon = 0$, $(\dot{*}) = \partial(*)/\partial\varepsilon$. Here caution needs to be taken that the present notation is not confused with the one used for the variational computation. Accordingly, the deformation gradient tensor can be expressed as

$$
\mathbf{F} = \mathbf{F}_o + \epsilon\nabla\mathbf{u}, \; \text{where } \dot{\mathbf{F}} = \nabla\mathbf{u}.
\tag{3.58}
$$

In a typical environment, the body is initially undeformed and stress free (i.e. at $\varepsilon = 0$, $\mathbf{F}_o = \mathbf{I}$ and $\mathbf{P}_o = \mathbf{0}$). This can be accommodated by imposing the initial conditions of

$$\mathbf{F}_o = \mathbf{I} \text{ and } \mathbf{P}_o = \mathbf{0}, \text{ at } \varepsilon = 0, \tag{3.59}$$

from which Eq. (3.58) reduces to

$$\mathbf{F} = \mathbf{I} + \varepsilon \nabla \mathbf{u}, \tag{3.60}$$

and successively yields

$$\mathbf{F}^{-1} = \mathbf{I} - \epsilon \nabla \mathbf{u} + o(\epsilon) \text{ and } J = \det \mathbf{F} = 1 + \epsilon \operatorname{div} \mathbf{u} + o(\epsilon). \tag{3.61a}$$

Also, in view of Eq. (3.57), we expand Eq. (3.33) as

$$Div(\mathbf{P}) = Div(\mathbf{P}_o) + \epsilon Div(\dot{\mathbf{P}}) + o(\epsilon) = \mathbf{0}. \tag{3.62}$$

Dividing the above by ϵ and letting $\epsilon \to 0$, we find the following linearized Euler equation.

$$Div(\dot{\mathbf{P}}) = 0 \text{ or } \dot{P}_{iA,A} = 0 \tag{3.63}$$

The expression of $\dot{P}_{iA}$ in the above Euler equation can be obtained from Eq. (3.45) that

$$\begin{aligned}
\dot{P}_{iA} &= (W_{F_{iA}}\dot{)} + E[\dot{F}_{jC}(F_{jD})_o D_C D_D][(F_{iB})_o D_B D_A)] - \dot{g}_{i,B} D_A D_B \\
&\quad + \frac{E}{2}[(F_{jC})_o(F_{jD})_o D_C D_D - 1](\dot{F}_{iB} D_B D_A) - \dot{p}(F_{iA}^*)_o - p\dot{F}_{iA}^*. \tag{3.64}
\end{aligned}$$

Since $(F_{jD})_o = \delta_{jD}$ and $(F_{iA}^*)_o = \delta_{iA}$ at $\epsilon = 0$, Eq. (3.64) further reduces to

$$\dot{P}_{iA} = (W_{F_{iA}}\dot{)} + Eu_{j,B} D_A D_B D_i D_j - \dot{p}\delta_{iA} - p\dot{F}_{iA}^* - u_{i,BCD} D_C D_D D_A D_B, \tag{3.65}$$

where $\delta_{jC}\delta_{jD} D_C D_D = D_C D_C = 1$ and $\dot{g}_{i,B} = \dot{F}_{iC,BD} D_C D_D$. We note that, in the above equation, the initial director field $\mathbf{D}$ is represented by the current basis (i.e. $D_i \mathbf{e}_i$) not by the reference frame (i.e. $D_A \mathbf{E}_A$). This is due to the collapse of two different bases which arises in small deformations superposed on large (i.e. $\mathbf{e}_i \equiv \mathbf{E}_A$; see, also, [105]-[106]). Hence, the associated tensor operations are possible without violating the bases mismatches.

Now, for the Mooney Rivlin strain energy, we find from Eqs. (3.48)-(3.49) that

$$
\begin{aligned}
(\dot{W_{F_{iA}}}) &= \mu\dot{F}_{iA} + \lambda\dot{F}_{iB}(\delta_{jC}\delta_{jC}\delta_{AB} - \delta_{jA}\delta_{jB}) + \lambda\delta_{iB}(2\dot{F}_{jC}\delta_{jC}\delta_{AB} - \dot{F}_{jA}\delta_{jB} - \delta_{jA}\dot{F}_{jB}) \\
&= \mu\dot{F}_{iA} + 2\lambda\dot{F}_{BB}\delta_{iA} - \lambda\dot{F}_{Ai}.
\end{aligned} \tag{3.66}
$$

The substitution of Eq. (3.66) into Eq. (3.64) then furnishes

$$
\dot{P}_{iA} = \mu u_{i,A} - \lambda u_{A,i} + E u_{j,B} D_A D_B D_i D_j - \dot{p}\delta_{iA} - p_o\dot{F}^*_{iA} - u_{i,BCD} D_C D_D D_A D_B, \tag{3.67}
$$

,where $p_o = \mu$ to recover the initial stress free state at $\epsilon = 0$ (i.e. $(\dot{P}_{iA})_{\epsilon=0} = 0$), and $\dot{F}_{BB} = u_{B,B}$ vanishes from the linearized condition of bulk incompressibility; i.e.,

$$
(\dot{J-1}) = (F^*_{iA})_o \dot{F}_{iA} = \delta_{iA}u_{i,A} = u_{A,A} = 0. \tag{3.68}
$$

Thus, using the identities of $\dot{F}^*_{iA,A} = 0$ (Piola's identity) and $(\dot{p}\delta_{iA})_{,A} = \dot{p}_{,A}\delta_{iA} = \dot{p}_{,i}$, the expression of $\dot{P}_{iA,A}$ can be subsequently formulated as

$$
\dot{P}_{iA,A} = \mu u_{i,AA} - \lambda u_{A,iA} + E u_{j,AB} D_A D_B D_i D_j - \dot{p}_{,i} - u_{i,ABCD} D_C D_D D_A D_B = 0. \tag{3.69}
$$

But, from the compatibility condition of $u_{A,iA}$ together with Eq. (3.69), it can be shown that

$$
u_{A,iA} = u_{A,Ai} = (u_{A,A})_i = 0. \tag{3.70}
$$

Consequently, Eq. (3.69) becomes

$$
\dot{P}_{iA,A} = \mu u_{i,AA} + E u_{j,AB} D_A D_B D_i D_j - \dot{p}_{,i} - u_{i,ABCD} D_C D_D D_A D_B = 0, \tag{3.71}
$$

which can be served as the compatible linear Euler equation for the materials of Mooney Rivlin type.

We remark that the linearized equations derived from the proposed model (Eq (3.71)) is the same as those obtained from the setting of the Neo Hookean model. This is mainly due to the fact that the influence of the higher-order invariant term I_2 in the Mooney Rivlin energy potential is gradually diminished as entering into the small deformation regime. Since the existence of the high-order invariant term I_2 is the primary distinction between the Mooney Rivlin and Neo Hookean models, the above would mean that the two models become essentially identical within the prescription of superposed incremental deformations. Therefore, the linear consideration of the Mooney Rivlin may not be necessary in the present cases. Thet corresponding solutions of Eqs. (3.68) and (3.71) and the necessary boundary conditions can be found in [86] and [115].

3.5 Model implementation and discussions

A comparison with experimental results is presented in this section to demonstrate the accuracy and utility of the proposed model. We designed the uniaxial tension test of four different types of elastomeric composites that are reinforced, respectively, by polyester fibers (PES-2, PES-3) and nylon/spandex fibers (NSP-8515, NSP-8020). *Ecoflex 0050* is used for the matrix materials for both cases, which is known to be one of the promising materials in biomechanical applications for its high tear resistance and large extensibility. The reinforced elastomeric composites were fabricated in three-layer configuration using layer by layer method. First, *Ecoflex 0050* elastomer was prepared by mixing two components (a base and curing agent) in 1 : 1 ratio and subsequent degassing in a vacuum chamber to remove entrapped bubbles. The second layer of long fibers was then placed flat on elastomer and allowed to wet at the interface. A small amount of elastomer was poured and rolled over the fibers to wet it again and to fill the gaps between pores and level the second layer. Lastly, a sufficient amount of elastomer was poured over the second layer and placed into the film applicator rod to yields uniform film. The dimensions of the fabricated elastomeric materials and composites were measured using a caliper and an aspect ratio of length-to-width was kept as 2 : 1 for all samples. Instron 5943 (Illinois Tool Works Inc., USA) was used to measure stress-strain responses the prepared composites (See, Fig. 3.1). The extension rate was set $10mm$ per minute to avoid/minimize viscous responses. The stress-strain curves and deformations on each material points were simultaneously recorded for the comparisons with the prediction results from the proposed model.

The material parameters of the matrix material (i.e. λ and μ) was determined from the experimental data of Ecoflex-0050 (see, Fig. 3.2) using the Mooney-Rivlin model. The elastic modulus of fibers (i.e. E and C) were obtained from the stress-strain curve of the two different fibers (Fig. 3.3(b)) in which we used the formula [116]

$$E = \frac{P}{a - \lambda(a)}(1 - \lambda^{'}(a)) \tag{3.72}$$

Here, P and a are respectively, stress and extension ratio of fibers while $\lambda(a)$ is the stretch ratio in the orthogonal direction from the stress-strain data of fibers (Fig.
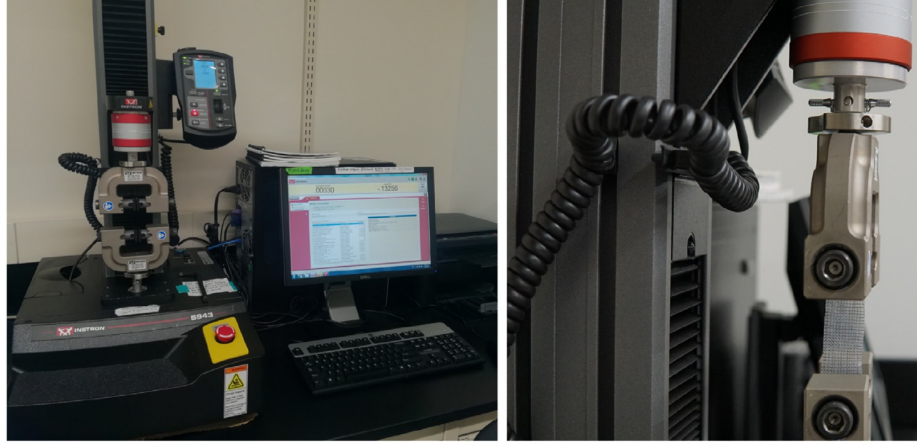
Figure 3.1: Experimental set up: Elastomeric composite sample ($50mm \times 25mm$) under uniaxial tension test.

3.3(b)). The obtained material properties are then used as the input parameters of the obtained PDEs (see, Eqs. (3.64) and (3.65)) which are numerically solved via the custom-built algorithm. In the assimilations, the applied load P_{11} is computed from Eq. (3.49) that

$$
\begin{aligned}
P_{11} &= \mu\chi_{1,1} + \lambda(\chi_{1,1}\chi_{2,2}\chi_{2,2} - \chi_{1,2}\chi_{2,1}\chi_{2,2}) + \frac{1}{2}E\chi_{1,1}(\chi_{1,1}\chi_{1,1} + \chi_{2,1}\chi_{2,1} \\
&\quad + \chi_{1,2}\chi_{1,2} +_{2,1}\chi_{2,22,1}\chi_{2,2}) - \frac{1}{2}E\chi_{1,1} - C\chi_{1,111} - p\chi_{2,2}
\end{aligned}
\tag{3.73}
$$

and the associated boundary conditions are prescribed as follows (see, Fig. 3.4)

$$
\begin{aligned}
t_1 &= P_{11}, \ t_2 = P_{12} = 0, \ \text{at } X_1 = a, -a \text{ and} \\
t_1 &= P_{21} = 0, \ t_2 = P_{22} = 0, \ \text{at } X_2 = b, -b
\end{aligned}
\tag{3.74}
$$

In addition, the following Holzapfel model [117] is also employed in the prediction of the experimental results and is subsequently compared with the proposed model:

$$
W = \frac{c}{2}(I_1 - 3) + \frac{k_1}{2k_2}\sum_{i=4,6}\{\exp[k_2(I_i - 1)^2] - 1\},
\tag{3.75}
$$

where c is the property of matrix and k_1 and k_2 are empirical fitting parameters pertaining to the composites. The Holzapfel model is widely adopted in biomaterials applications such as mimicking natural aorta, vein, and cartilage, aortic valve where the *J-shaped* strain-stiffening response ([5], [7], [17], and [118]) and significant
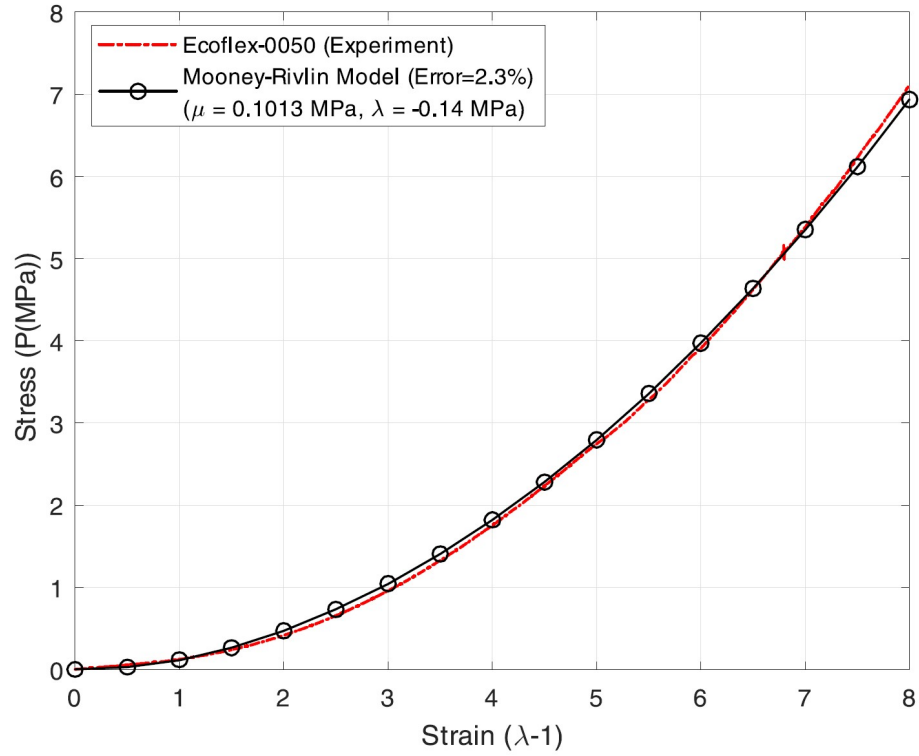
Figure 3.2: Stress-strain curves: Ecoflex-0050 and Mooney-Rivlin curve fitting.
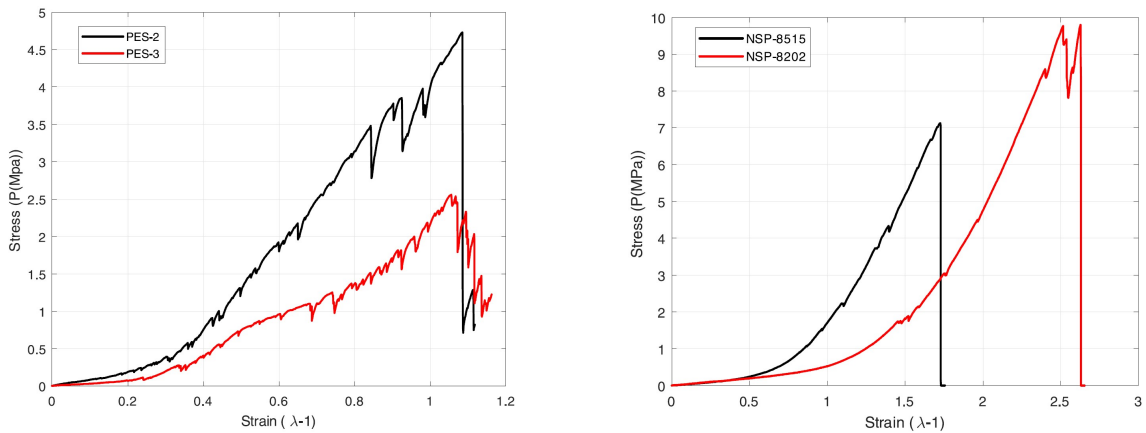
Figure 3.3: (a) Stress-strain: PES-2 and PES-3 fibers. (b) Stress-strain: NSP-8515 and NSP-8020 fibers.
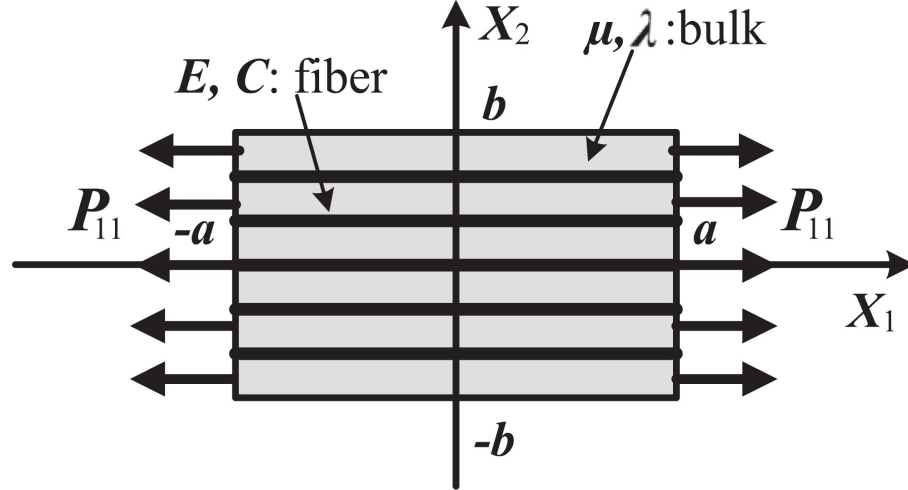
Figure 3.4: Schematic of the problem: $2a = 50mm$ and $2b = 25mm$.

anisotropy [6],[119] are the essential design considerations. Our intension here is to seek the potential applications of the proposed model in the design and analysis of such biocompatible materials that can be implanted to replace or repair damaged/missing tissue.

A comparison among the stress-strain curves obtained from the experimental data, the proposed model and the Holzapfel model are presented in Fig. 3.5 and 3.6. It is shown in Figs. 3.5 and 3.6 that the proposed model successfully predict the J-shaped stress-strain responses of the composites regardless of the different strain-stiffening rates. The Holzapfel model also produces reasonably accurate estimations of the stress-strain curves of the tested samples except the slight deviations in the transition (i.e., strain-stiffening) regimes of PES-3 and NSP-8515 composites where rapid strain-stiffening responses are observed at a low strain level. In other words, the Holzapfel model is less sensitive to the steep variations of the stress-strain curve than the proposed model. Such limited sensitivity may not compromise the overall prediction accuracy of the model. However, it may be potential disadvantage, especially when mimicking biological tissues, considering the fact that one of the primary requirements of the theoretical model is the ability to predict rapid strain-stiffening behaviors at a low level of strain, which is also known to be a characteristic of most biological tissues ([5],[17]).

More importantly, unlike the Holzapfel model in which the empirical constants
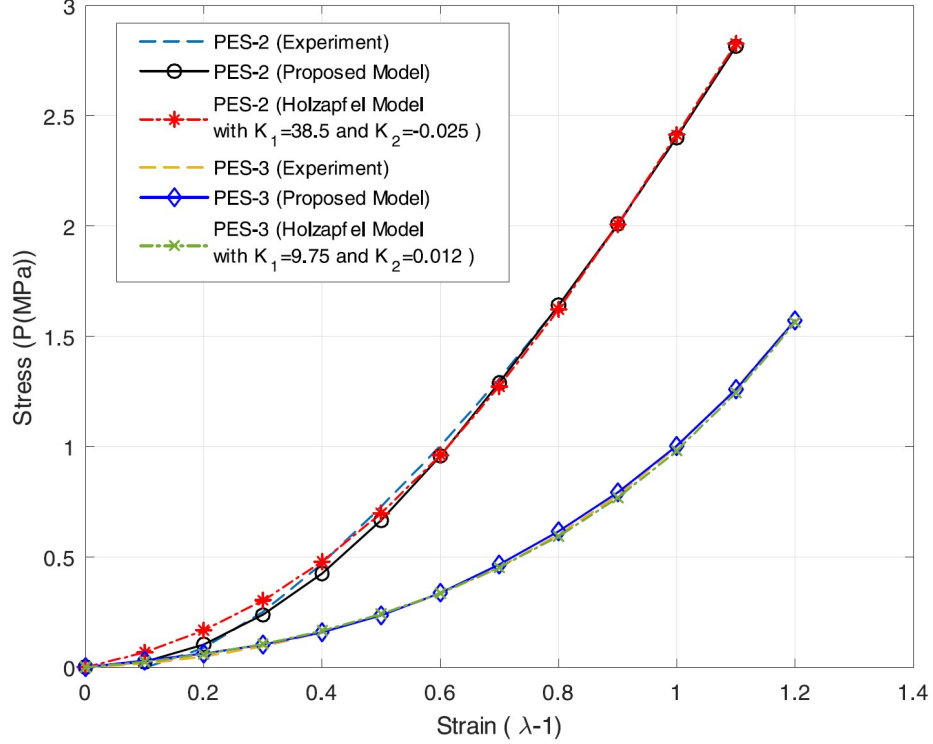
Figure 3.5: Stress-strain curves from different prediction models: PES-2 and PES-3.

k_1 and k_2 are obtained from the fabricated composites, the proposed model predicts the resultant properties of desired composites prior to the composition as long as the material parameters of matrix materials and fibers are provided (i.e. no empirical curve fitting of the composite is necessary). This may be of more practical interest, especially in the design stage of composites. Since the responses of the intended composites can be predetermined using the proposed model, through which the required resources in the sample productions may be minimized.

In addition to the abovementioned technical merits, the proposed model provides the quantitative predictions of other key design considerations such as deformation profiles and contours. Fig. 3.7 (a)–(d) illustrate the χ_1 and χ_2 deformation profiles of the polyester fiber-composites (PES-2, PES-3) at different strain levels. Despite the inevitable uncertainties (e.g., image processing and curve fitting), the deformation profiles from the experiment and the theoretical predictions demonstrate close agreement throughout the entire domain of interest. In the case of the nylon/spandex fiber-composites (NSP-8515, NSP-8020), the proposed model accurately predicts the χ_1 deformations (axial elongation) of both samples (see, Fig. 3.8 (a)–(c)), yet has
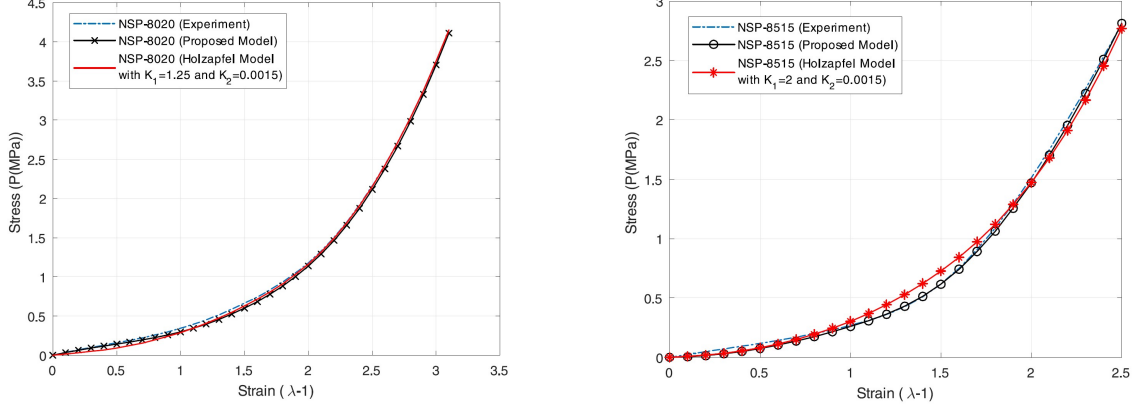
Figure 3.6: Stress-strain curves from different prediction models: NSP-8020 (left) and NSP-8515 (right)

limitations in the prediction of χ_2 deformations, especially those in the NSP-8515 composites at lower strain levels (Fig. 3.8 (d)). This may be due to the NSP-8515 fibers' resistance along the χ_2 direction within the composites, which hinders the χ_2 deformation. We speculate that the bidirectional fiber model may be suitable for the deformation analysis of NSP-8515 fiber-composites. Further research on these cases is, however, beyond the scope of the present study, yet is certainly of practical interest. The graphical comparisons between the theoretical prediction and experimental result for the cases of the PES-3 sample at 50% and 100% elongations, and the NSP-8020 sample at 167% and 235% elongations are presented in Figs. 3.9-3.10 for the purpose of cross-examination with the deformation data obtained in Figs. 3.7 and 3.8. The plotted deformation contours are the norms of displacement fields (i.e. $\sqrt{\chi_1^2 + \chi_2^2}$) and demonstrate reasonably close agreement with the deformed configurations of both composite samples. The same comparisons are made for the PES-2 and NSP-8515 cases, which again indicate close correspondence with experiments except NSP-8515 at 50% elongation (see, also, Fig. 3.8 (d)). However, these have been intentionally omitted for the sake of conciseness.

Further, the corresponding stress fields become "Piola type double stress" (see, for example, [99],[109], and [111]) due to the introduction of bending stiffness of fibers into the model of continuum deformation (second-gradient continuum). In other words, the resulting stress fields now depend both on the axial stiffness (E) and bending stiffness (C) of fibers (see, Eq. (3.73)). More detailed discussions regarding the

71
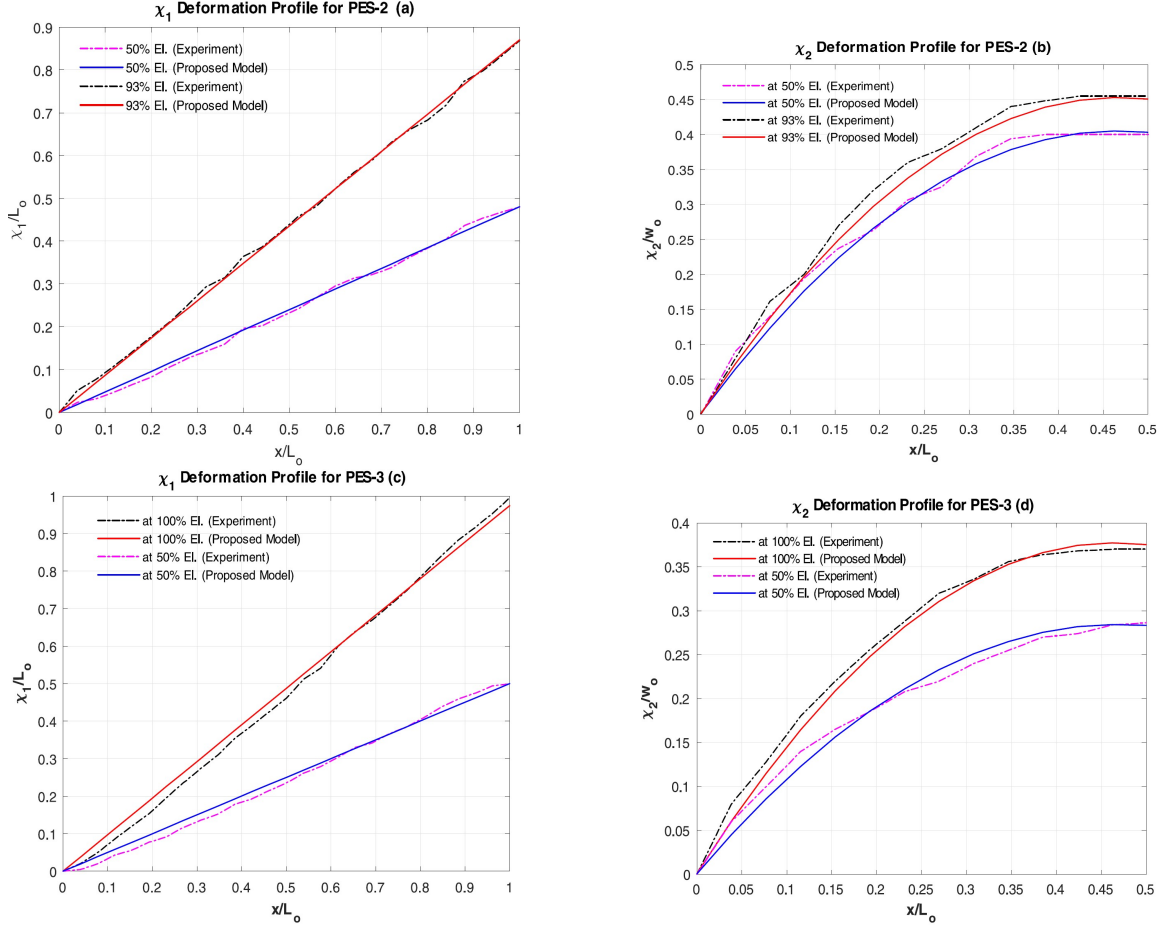
Figure 3.7: Deformation profiles: (a) χ_1 (PES-2); (b) χ_2 (PES-2); (c) χ_1 (PES-3); (d) χ_2 (PES-3).

qualitive sensitivity of the deformation, stress and strain fields with respect to the material parameters of fibers can be found in [86] and [115]. In the present case, the J-shaped stress-strain response of a certain composite tends to be stiffer with increasing bending modulus of fibers.

Overall, the proposed model successfully predicts the various important mechanical responses of the tested elastomeric composites and therefore may also serve as an alternative of the Holzapfel model in the design and analysis of biomimetic composites, especially those exhibiting significant strain-stiffening responses at a low level of strain.
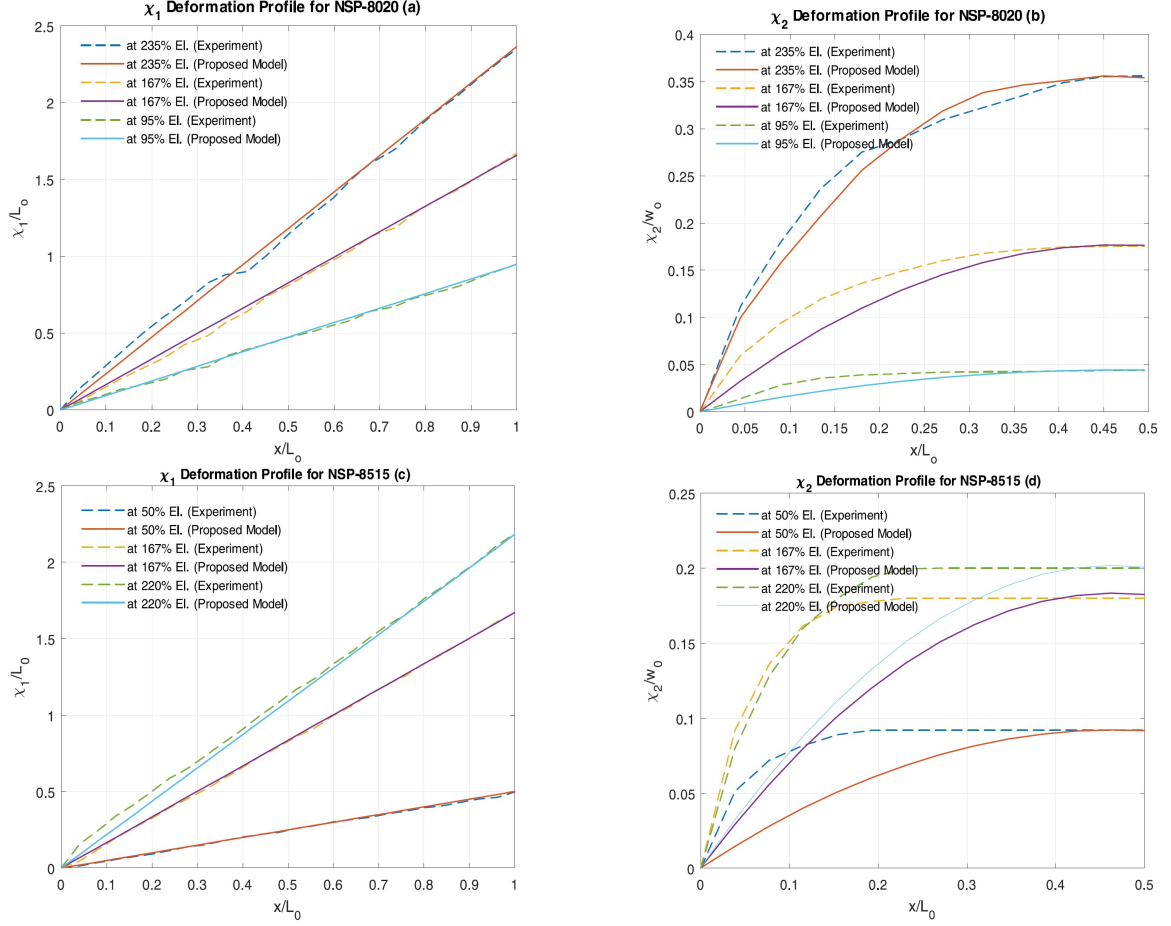
Figure 3.8: Deformation profiles: (a) χ_1 (NSP-8020); (b) χ_2 (NSP-8020); (c) χ_1 (NSP-8515); (d) χ_2 (NSP-8515).

3.6 Finite element analysis of the 4th order coupled PDE

The systems of PDEs in Eqs. (3.52)-(3.54) are 4th order differential equations with coupled non-linear terms. The case of such less regular PDEs deserve delicate mathematical treatment and is of particular practical interest. Hence, it is not trivial to demonstrate the associated numerical analysis procedures. For preprocessing, Eqs.
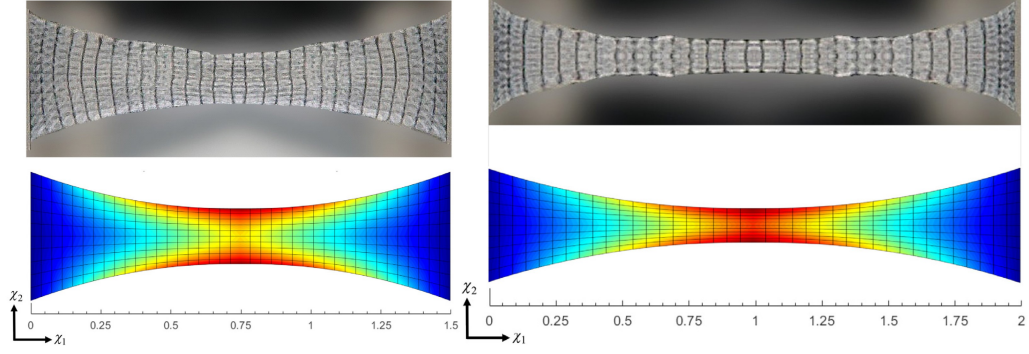
Figure 3.9: Comparisons of the overall deformations: PES-3 at 50% (left) and 100% (right) elongations.
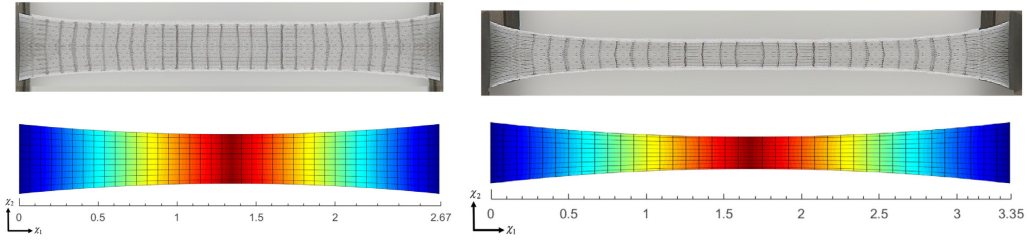
Figure 3.10: Comparisons of the overall deformations: NSP-8020 at 167% (left) and 235% (right) elongations.

(3.52)-(3.54) may be recast as

$$
\begin{aligned}
0 =\ & \mu(Q + \chi_{1,22}) - A\chi_{2,2} + B\chi_{2,1} - CQ_{,11} + \lambda(QFF + \chi_{1,22}DD + 2C\chi_{2,21}F \\
& + 2E\chi_{2,12}D - \chi_{1,21}DF - \chi_{1,12}FD - ERF - C\chi_{2,22}D - ED\chi_{2,21} - CF\chi_{2,12}) \\
& - \frac{1}{2}EQ + \frac{1}{2}E(3Q\chi_{1,1}\chi_{1,1} + Q\chi_{2,1}\chi_{2,1} + 2R\chi_{1,1}\chi_{2,1}) \\
0 =\ & \mu(\chi R + \chi_{2,22}) - B\chi_{1,1} + A\chi_{1,2} - CR_{,11} + \lambda(REE + \chi_{2,22}CC + 2D\chi_{1,21}E \\
& + 2F\chi_{1,12}C - \chi_{2,21}CE - \chi_{2,12}EC - FQE - D\chi_{1,22}C - FC\chi_{1,21} - DE\chi_{1,12}) \\
& - \frac{1}{2}ER + \frac{1}{2}E(3R\chi_{2,1}\chi_{2,1} + R\chi_{1,1}\chi_{1,1} + 2Q\chi_{2,1}\chi_{1,1})
\end{aligned}
$$

$$
\begin{aligned}
0 &= Q - \chi_{1,11}, \\
0 &= R - \chi_{2,11}, \\
0 &= C - \chi_{1,1}, \\
0 &= D - \chi_{2,1}, \\
0 &= E - \chi_{1,2}, \\
0 &= F - \chi_{2,2}, \\
0 &= A - \mu(Q + \chi_{1,22}) - CQ_{,11}, \\
0 &= B - \mu(R + \chi_{2,22}) - CR_{,11}, \qquad (3.76)
\end{aligned}
$$

where $Q = \chi_{1,11}$, $R = \chi_{2,11}$, $C = \chi_{1,1}$, $D = \chi_{2,1}, E = \chi_{1,2}, F = \chi_{2,2}$. Thus, the order of differential equations is reduced from the three coupled equations of 4th order to ten coupled equations of 2nd order. In particular, the non-linear terms in the above equations (e.g. $A\chi_{2,2}, B\chi_{2,1}$ etc...) can be systematically treated via the following Picard iterative procedure;

$$
\begin{aligned}
-A^{initial}\chi_{2,2}^{initial} + B^{initial}\chi_{2,1}^{initial} &\implies -A_0\chi_{2,2}^0 + B_0\chi_{2,1}^0 \\
A^{initial}\chi_{1,2}^{initial} - B^{initial}\chi_{1,1}^{initial} &\implies A_0\chi_{1,2}^0 - B_0\chi_{1,1}^0, \qquad (3.77)
\end{aligned}
$$

where the estimated values of A and B continue to be updated based on their previous estimations (e.g. A_1 and B_1 are refreshed by their previous pair of A_o and B_o) as iteration progresses and similarly for other non-linear terms.

Further, we find the weight forms of Eq. (3.76) as

$$0 = \int_\Omega w_1(\mu(Q + \chi_{1,22}) - A_0\chi_{2,2} + B_0\chi_{2,1} - CQ_{,11} + \lambda(QF_0F_0 + \chi_{1,22}D_0D_0$$
$$+ 2C_0\chi_{2,21}F_0 + 2E_0\chi_{2,12}D_0 - \chi_{1,21}D_0F_0 - \chi_{1,12}F_0D_0 - E_0RF_0 - C_0\chi_{2,22}D_0$$
$$- E_0D_0\chi_{2,21} - C_0F_0\chi_{2,12}) - \frac{1}{2}Ew_1Q + \frac{1}{2}Ew_1(3QC_0^2 + QD_0^2 + 2RC_0D_0))d\Omega$$

$$0 = \int_\Omega w_2(\mu(R + \chi_{2,22}) - B_0\chi_{1,1} + A_0\chi_{1,2} - CR_{,11} + \lambda(RE_0E_0 + \chi_{2,22}C_0C_0$$
$$+ 2D_0\chi_{1,21}E_0 + 2F_0\chi_{1,12}C_0 - \chi_{2,21}C_0E_0 - \chi_{2,12}E_0C_0 - F_0QE_0 - D_0\chi_{1,22}C_0$$
$$- F_0C_0\chi_{1,21} - D_0E_0\chi_{1,12}) - \frac{1}{2}Ew_2R + \frac{1}{2}w_2E(3RD_0^2 + RC_0^2 + 2QD_0C_0))d\Omega$$

$$0 = \int_\Omega w_3(Q - \chi_{1,11})d\Omega,$$

$$0 = \int_\Omega w_4(R - \chi_{2,11})d\Omega,$$

$$0 = \int_\Omega w_5(C - \chi_{1,1})d\Omega,$$

$$0 = \int_\Omega w_6(D - \chi_{2,1})d\Omega,$$

$$0 = \int_\Omega w_7(E - \chi_{1,2})d\Omega,$$

$$0 = \int_\Omega w_8(F - \chi_{2,2})d\Omega,$$

$$0 = \int_\Omega w_9(A_0 - \mu(Q + \chi_{1,22}) - CQ_{,11})d\Omega,$$

$$0 = \int_\Omega w_{10}(B_0 - \mu(R + \chi_{2,22}) - CR_{,11})d\Omega, \tag{3.78}$$

Hence, applying integration by part and Green-stokes theorem, (e.g. $\mu\int_{\Omega^e} w_1\chi_{1,22}d\Omega = -\mu\int_{\Omega^e} w_{1,2}\chi_{1,2}d\Omega + \mu\int_{\partial\Gamma} w_1\chi_{1,2}Nd\Gamma$) the final weak forms of Eq. (3.78) can be ob-

tained as follows

$$
\begin{aligned}
0 \; = \; & \int_\Omega (w_1\mu Q - \mu w_{1,2}\chi_{1,2} - w_1 A_0\chi_{2,2} + w_1 B_0\chi_{2,1} + Cw_{1,1}Q_{,1} + \lambda w_1 Q F_0 F_0 \\
& - \lambda w_{1,2}\chi_{1,2}D_0 D_0 - 2\lambda w_{1,1}C_0\chi_{2,2}F_0 - 2\lambda w_{1,2}E_0\chi_{2,1}D_0 + \lambda w_{1,1}\chi_{1,2}D_0 F_0 \\
& + \lambda w_{1,2}\chi_{1,1}F_0 D_0 - \lambda w_1 E_0 R F_0 + \lambda w_{1,2}C_0\chi_{2,2}D_0 + \lambda w_{1,1}E_0 D_0\chi_{2,2} \\
& + \lambda w_{1,2}C_0 F_0\chi_{2,1} + \frac{1}{2}Ew_1 Q + \frac{1}{2}Ew_1(3QC_0^2 + QD_0^2 + 2RC_0 D_0))d\Omega \\
& + \int_{\partial\Gamma}\mu w_1\chi_{1,2}Nd\Gamma - \int_{\partial\Gamma}Cw_1 Q_{,1}Nd\Gamma + \int_{\partial\Gamma}\lambda w_1\chi_{1,2}D_0 D_0 Nd\Gamma \\
& + 2\int_{\partial\Gamma}\lambda w_1 C_0\chi_{2,2}F_0 Nd\Gamma + 2\int_{\partial\Gamma}\lambda w_1 E_0\chi_{2,1}D_0 Nd\Gamma - \int_{\partial\Gamma}\lambda w_1\chi_{1,1}F_0 D_0 Nd\Gamma \\
& - \int_{\partial\Gamma}\lambda w_1\chi_{1,2}D_0 F_0 Nd\Gamma - \int_{\partial\Gamma}\lambda w_1 C_0\chi_{2,2}D_0 Nd\Gamma - \int_{\partial\Gamma}\lambda w_1 E_0 D_0\chi_{2,2}Nd\Gamma \\
& - \int_{\partial\Gamma}\lambda w_1 C_0 F_0\chi_{2,1}Nd\Gamma
\end{aligned}
$$

$$
\begin{aligned}
0 \; = \; & \int_\Omega (w_2\mu R - \mu w_{2,2}\chi_{2,2} - w_2 B_0\chi_{1,1} + w_2 A_0\chi_{1,2} + Cw_{2,1}R_{,1} + \lambda w_2 R E_0 E_0 \\
& - \lambda w_{2,2}\chi_{2,2}C_0 C_0 - 2\lambda w_{2,1}D_0\chi_{1,2}E_0 - 2\lambda w_{2,2}F_0\chi_{1,1}C_0 + \lambda w_{2,1}\chi_{2,2}C_0 E_0 \\
& + \lambda w_{2,2}\chi_{2,1}E_0 C_0 - \lambda w_2 F_0 Q E_0 + \lambda w_{2,2}D_0\chi_{1,2}C_0 + \lambda w_{2,1}F_0 C_0\chi_{1,2} \\
& + \lambda w_{2,2}D_0 E_0\chi_{1,1} - \frac{1}{2}Ew_2 R + \frac{1}{2}w_2 E(3RD_0^2 + RC_0^2 + 2QD_0 C_0))d\Omega \\
& + \int_{\partial\Gamma}\mu w_2\chi_{2,2}Nd\Gamma - \int_{\partial\Gamma}Cw_2 R_{,1}Nd\Gamma + \int_{\partial\Gamma}\lambda w_2\chi_{2,2}C_0 C_0 Nd\Gamma \\
& + 2\int_{\partial\Gamma}\lambda w_2 D_0\chi_{1,2}E_0 Nd\Gamma + 2\int_{\partial\Gamma}\lambda w_2 F_0 C_0\chi_{1,1}Nd\Gamma - \int_{\partial\Gamma}\lambda w_2 D_0\chi_{1,2}C_0 Nd\Gamma \\
& - \int_{\partial\Gamma}\lambda w_2\chi_{2,2}C_0 E_0 Nd\Gamma - \int_{\partial\Gamma}\lambda w_2 F_0 C_0\chi_{1,2}Nd\Gamma - \int_{\partial\Gamma}\lambda w_2\chi_{2,1}E_0 C_0 Nd\Gamma \\
& - \int_{\partial\Gamma}\lambda w_2 D_0 E_0\chi_{1,1}Nd\Gamma
\end{aligned}
$$

$$
\begin{aligned}
0 &= \int_\Omega (w_3 Q + w_{3,1}\chi_{1,1})d\Omega - \int_{\partial\Gamma} w_3 \chi_{1,1} N d\Gamma \\
0 &= \int_\Omega (w_4 R + w_{4,1}\chi_{2,1})d\Omega - \int_{\partial\Gamma} w_{4,1}\chi_{2,1} N d\Gamma \\
0 &= \int_\Omega (w_5 C - w_5 \chi_{1,1})d\Omega \\
0 &= \int_\Omega (w_6 D - w_6 \chi_{2,1})d\Omega, \\
0 &= \int_\Omega (w_7 E - w_7 \chi_{1,2})d\Omega, \\
0 &= \int_\Omega (w_8 F - w_8 \chi_{2,2})d\Omega, \\
0 &= \int_\Omega (w_9 A - \mu w_9 Q + \mu w_{9,2}\chi_{1,2} + C w_{9,1} Q_{,1})d\Omega - \int_{\partial\Gamma} \mu w_9 \chi_{1,2} N d\Gamma \\
&\quad - \int_{\partial\Gamma} C w_9 Q_{,1} N d\Gamma \\
0 &= \int_\Omega (w_{10} B - \mu w_{10} R + \mu w_{10,2}\chi_{2,2} + C w_{10,1} R_{,1})d\Omega - \int_{\partial\Gamma} \mu w_{10}\chi_{2,2} N d\Gamma \\
&\quad - \int_{\partial\Gamma} C w_{10} R_{,1} N d\Gamma
\end{aligned}
\tag{3.79}
$$

where Ω, $\partial\Gamma$ and N are, respectively the domain of interest, the associated boundary, and the rightward unit normal to the boundary $\partial\Gamma$ in the sense of the Green-stoke's theorem. The unknowns, χ_1, χ_2, Q, R, C, D, E, F, A and B can be written in the form of Lagrangian polynomial such that

$$
(*) = \sum_{j=1}^{n=4} [(*)_j \Psi_j(x, y)].
\tag{3.80}
$$

Thus, the test function w is found to be

$$
w = \sum_{i=1}^{n=4} w_i \Psi_i(x, y); \ \ i = 1, 2, 3, 4, \ \text{ and } j = 1, 2, 3, 4,
\tag{3.81}
$$

where w_i is weight of the test function and $\Psi_i(x, y)$ are the shape functions; $\Psi_1 = \frac{(x-2)(y-1)}{2}$, $\Psi_2 = \frac{x(y-1)}{-2}$, $\Psi_3 = \frac{xy}{2}$ and $\Psi_4 = \frac{y(x-2)}{-2}$. By means of Eq. (3.80), Eq. (3.79)

may be recast in terms of Lagrangian polynomial as

$$
\begin{aligned}
0 &= \sum\{\int_{\Omega^e}(\lambda\Psi_{i,1}\Psi_{j,2}D_0F_0 + \lambda\Psi_{i,2}\Psi_{j,1}F_0D_0 - \mu\Psi_{i,2}\Psi_{j,2} - \lambda\Psi_{i,2}\Psi_{j,2}D_0D_0)d\Omega\}\chi_{1j} \\
&+ \sum\{\int_{\Omega^e}(\Psi_i\Psi_{j,1}B_0 - \Psi_i\Psi_{j,2}A_0 - 2\lambda\Psi_{i,1}\Psi_{j,2}C_0F_0 - 2\lambda\Psi_{i,2}\Psi_{j,1}E_0D_0 \\
&+ \lambda\Psi_{i,2}\Psi_{j,2}C_0D_0 + \lambda\Psi_{i,1}\Psi_{j,2}E_0D_0 + \lambda\Psi_{i,2}\Psi_{j,1}C_0F_0)d\Omega\}\chi_{2j} + \sum\{\int_{\Omega^e}(\mu\Psi_i\Psi_j \\
&+ C\Psi_{i,1}\Psi_{j,1} + \lambda\Psi_i\Psi_jF_0F_0 + \frac{1}{2}E\Psi_i\Psi_j + \frac{3}{2}E\Psi_i\Psi_jC_0^2 + \frac{1}{2}E\Psi_i\Psi_jD_0^2)d\Omega\}Q_j \\
&+ \sum\{\int_{\Omega^e}(-\lambda\Psi_i\Psi_jE_0F_0 + E\Psi_i\Psi_jC_0D_0)d\Omega\}R_j + \int_{\partial\Gamma}(\mu\Psi_i\chi_{1,2})Nd\Gamma \\
&- \int_{\partial\Gamma}(C\Psi_iQ_{,1})Nd\Gamma + \int_{\partial\Gamma}(\lambda\Psi_i\chi_{1,2}D_0D_0)Nd\Gamma + \int_{\partial\Gamma}(2\lambda\Psi_iC_0\chi_{2,2}F_0)Nd\Gamma \\
&+ 2\int_{\partial\Gamma}(\lambda\Psi_iE_0D_0\chi_{2,1})Nd\Gamma - \int_{\partial\Gamma}(\lambda\Psi_i\chi_{1,2}D_0F_0)Nd\Gamma - \int_{\partial\Gamma}(\lambda\Psi_iC_0\chi_{2,2}D_0)Nd\Gamma \\
&- \int_{\partial\Gamma}(\lambda\Psi_iE_0D_0\chi_{2,2})Nd\Gamma - \int_{\partial\Gamma}(\lambda\Psi_iC_0F_0\chi_{2,1})Nd\Gamma - \int_{\partial\Gamma}(\lambda\Psi_i\chi_{1,1}F_0D_0)Nd\Gamma
\end{aligned}
$$

$$
\begin{aligned}
0 &= \sum\{\int_{\Omega^e}(-\Psi_i\Psi_{j,1}B_0 + \Psi_i\Psi_{j,2}A_0 - 2\lambda\Psi_{i,1}\Psi_{j,2}D_0E_0 + \lambda\Psi_{i,1}\Psi_{j,2}F_0C_0 \\
&- 2\lambda\Psi_{i,2}\Psi_{j,1}F_0C_0\lambda\Psi_{i,2}\Psi_{j,2}D_0C_0 + \lambda\Psi_{i,2}\Psi_{j,1}D_0E_0)d\Omega\}\chi_{1j} \\
&+ \sum\{\int_{\Omega^e}(-\mu\Psi_{i,2}\Psi_{j,2} - \lambda\Psi_{i,2}\Psi_{j,2}C_0C_0 + \lambda\Psi_{i,1}\Psi_{j,2}C_0E_0 \\
&+ \lambda\Psi_{i,2}\Psi_{j,1}E_0C_0)d\Omega\}\chi_{2j} + \sum\{\int_{\Omega^e}(-\lambda\Psi_i\Psi_jF_0E_0 + E\Psi_i\Psi_jC_0D_0)d\Omega\}Q_j \\
&+ \sum\{\int_{\Omega^e}(\mu\Psi_i\Psi_j + C\Psi_{i,1}\Psi_{j,1} + \lambda\Psi_i\Psi_jE_0E_0 + \frac{1}{2}E\Psi_i\Psi_j + \frac{3}{2}E\Psi_i\Psi_jD_0^2 \\
&+ \frac{1}{2}E\Psi_i\Psi_jC_0^2)d\Omega\}R_j + \int_{\partial\Gamma}(\mu\Psi_i\chi_{2,2})Nd\Gamma - \int_{\partial\Gamma}(C\Psi_iR_{,1})Nd\Gamma \\
&+ \int_{\partial\Gamma}(\lambda\Psi_i\chi_{2,2}C_0C_0)Nd\Gamma + 2\int_{\partial\Gamma}(\lambda\Psi_iD_0\chi_{1,2}E_0)Nd\Gamma + 2\int_{\partial\Gamma}(\lambda\Psi_iF_0C_0\chi_{1,1})Nd\Gamma \\
&- \int_{\partial\Gamma}(\lambda\Psi_i\chi_{2,2}C_0E_0)Nd\Gamma - \int_{\partial\Gamma}(\lambda\Psi_i\chi_{2,1}E_0C_0)Nd\Gamma - \int_{\partial\Gamma}(\lambda\Psi_iD_0\chi_{1,2}C_0)Nd\Gamma \\
&- \int_{\partial\Gamma}(\lambda\Psi_iD_0E_0\chi_{1,1})Nd\Gamma - \int_{\partial\Gamma}(\lambda\Psi_iF_0C_0\chi_{1,2})Nd\Gamma
\end{aligned}
$$

$$0 = \sum \{ \int_{\Omega^e} (\Psi_i \Psi_j) d\Omega \} Q_j + \sum \{ \int_{\Omega^e} \Psi_{i,1} \Psi_{j,1}) d\Omega \} \chi_{1j} - \int_{\partial\Gamma^e} (\Psi_i \chi_{1,1}) N d\Gamma,$$

$$0 = \sum \{ \int_{\Omega^e} (\Psi_i \Psi_j) d\Omega \} R_j + \sum \{ \int_{\Omega^e} \Psi_{i,1} \Psi_{j,1}) d\Omega \} \chi_{2j} - \int_{\partial\Gamma^e} (\Psi_i \chi_{2,1}) N d\Gamma,$$

$$0 = \sum \{ \int_{\Omega^e} (\Psi_i \Psi_j) d\Omega \} C_j - \sum \{ \int_{\Omega^e} (\Psi_i \Psi_{j,1}) d\Omega \} \chi_{1j}$$

$$0 = \sum \{ \int_{\Omega^e} (\Psi_i \Psi_j) d\Omega \} D_j - \sum \{ \int_{\Omega^e} (\Psi_i \Psi_{j,1}) d\Omega \} \chi_{2j}$$

$$0 = \sum \{ \int_{\Omega^e} (\Psi_i \Psi_j) d\Omega \} E_j - \sum \{ \int_{\Omega^e} (\Psi_i \Psi_{j,2}) d\Omega \} \chi_{1j}$$

$$0 = \sum \{ \int_{\Omega^e} (\Psi_i \Psi_j) d\Omega \} F_j - \sum \{ \int_{\Omega^e} (\Psi_i \Psi_{j,2}) d\Omega \} \chi_{2j}$$

$$0 = \sum \{ \int_{\Omega^e} (\Psi_i \Psi_j) d\Omega \} A_j + \sum \{ \int_{\Omega^e} (-\mu \Psi_i \Psi_j + C \Psi_{i,1} \Psi_{j,1}) d\Omega \} Q_j$$
$$+ \sum \{ \int_{\Omega^e} (\mu \Psi_{i,2} \Psi_{j,2}) d\Omega \} \chi_{1j} - \int_{\partial\Gamma^e} (\mu \Psi_i \chi_{1,2}) N d\Gamma - \int_{\partial\Gamma} (C \Psi_i Q_{,1}) N d\Gamma$$

$$0 = \sum \{ \int_{\Omega^e} (\Psi_i \Psi_j) d\Omega \} B_j + \sum \{ \int_{\Omega^e} (-\mu \Psi_i \Psi_j + C \Psi_{i,1} \Psi_{j,1}) d\Omega \} R_j$$
$$+ \sum \{ \int_{\Omega^e} (\mu \Psi_{i,2} \Psi_{j,2}) d\Omega \} \chi_{2j} - \int_{\partial\Gamma^e} (\mu \Psi_i \chi_{2,2}) N d\Gamma - \int_{\partial\Gamma} (C \Psi_i R_{,1}) N d\Gamma \quad (3.82)$$

Now, for the lolcal stiffness matrices and forcing vectors for each elements, we find

$$\begin{bmatrix} K_{11}^{11} & K_{12}^{11} & K_{13}^{11} & K_{14}^{11} \\ K_{21}^{11} & K_{22}^{11} & K_{23}^{11} & K_{24}^{11} \\ K_{31}^{11} & K_{32}^{11} & K_{33}^{11} & K_{34}^{11} \\ K_{41}^{11} & K_{42}^{11} & K_{43}^{11} & K_{44}^{11} \end{bmatrix}_{Local} \begin{bmatrix} \chi_1^1 \\ \chi_1^2 \\ \chi_1^3 \\ \chi_1^4 \end{bmatrix}_{Local} = \begin{bmatrix} F_1^1 \\ F_2^1 \\ F_3^1 \\ F_4^1 \end{bmatrix}_{Local}, \quad (3.83)$$

where

$$\left[K_{ij}^{11} \right] = \int_{\Omega} (\lambda \Psi_{i,1} \Psi_{j,2} D_0 F_0 + \lambda \Psi_{i,2} \Psi_{j,1} F_0 D_0 - \mu \Psi_{i,2} \Psi_{j,2} - \lambda \Psi_{i,2} \Psi_{j,2} D_0 D_0) d\Omega, \quad (3.84)$$

and

$$\{ F_i^1 \} = \int_{\partial\Gamma} \mu w_i \chi_{1,2} N d\Gamma - \int_{\partial\Gamma} C w_i Q_{,1} N d\Gamma + \int_{\partial\Gamma} \lambda w_i \chi_{1,2} D_0 D_0 N d\Gamma$$
$$+ 2 \int_{\partial\Gamma} \lambda w_i C_0 \chi_{2,2} F_0 N d\Gamma + 2 \int_{\partial\Gamma} \lambda w_i E_0 \chi_{2,1} D_0 N d\Gamma$$
$$- \int_{\partial\Gamma} \lambda w_i \chi_{1,2} D_0 F_0 N d\Gamma - \int_{\partial\Gamma} \lambda w_i C_0 \chi_{2,2} D_0 N d\Gamma$$
$$- \int_{\partial\Gamma} \lambda w_i E_0 D_0 \chi_{2,2} N d\Gamma - \int_{\partial\Gamma} \lambda w_i C_0 F_0 \chi_{2,1} N d\Gamma$$
$$- \int_{\partial\Gamma} \lambda w_i \chi_{1,1} F_0 D_0 N d\Gamma. \quad (3.85)$$

Thus, the unknowns (i.e. $\chi_1, \chi_2, Q, R, C, D, E, F, A$ and B) can be expressed as

$$Q_i = \{\chi_1^i\}_{,11}, \ R_i = \{\chi_2^i\}_{,11}, \ S_i = \{Q^i\}_{,11} \text{ etc...,} \tag{3.86}$$

and similarly for the rest of unknowns.

Consequently, we obtain the following systems of equations (in the Global form) for each individual elements as

$$\begin{bmatrix}
[K^{11}] & [K^{12}] & [K^{13}] & . & . & . & . & . & [K^{19}] & [K^{110}] \\
[K^{21}] & [K^{22}] & [K^{23}] & . & . & . & . & . & [K^{29}] & [K^{210}] \\
[K^{31}] & [K^{32}] & [K^{33}] & . & . & . & . & . & [K^{39}] & [K^{310}] \\
[K^{41}] & [K^{42}] & [K^{43}] & . & . & . & . & . & [K^{49}] & [K^{410}] \\
[K^{51}] & [K^{52}] & [K^{53}] & . & . & . & . & . & [K^{59}] & [K^{510}] \\
[K^{61}] & [K^{62}] & [K^{63}] & . & . & . & . & . & [K^{69}] & [K^{610}] \\
[K^{71}] & [K^{72}] & [K^{73}] & . & . & . & . & . & [K^{79}] & [K^{710}] \\
[K^{81}] & [K^{82}] & [K^{83}] & . & . & . & . & . & [K^{89}] & [K^{810}] \\
[K^{91}] & [K^{92}] & [K^{93}] & . & . & . & . & . & [K^{99}] & [K^{910}] \\
[K^{101}] & [K^{102}] & [K^{103}] & . & . & . & . & . & [K^{109}] & [K^{1010}]
\end{bmatrix}
\begin{bmatrix}
\chi_1^i \\ \chi_2^i \\ Q_i \\ R_i \\ A_i \\ B_i \\ C_i \\ D_i \\ E_i \\ F_i
\end{bmatrix}
=
\begin{bmatrix}
\{F_1\} \\ \{F_2\} \\ \{F_3\} \\ \{F_4\} \\ \{F_5\} \\ \{F_6\} \\ \{F_7\} \\ \{F_8\} \\ \{F_9\} \\ \{F_{10}\}
\end{bmatrix}
. \tag{3.87}$$

In the simulation, we set the following convergence criteria,

$$|A_{n+1} - A_n| = e_1 \leq \varepsilon, \ \ |B_{n+1} - B_n| = e_2 \leq \varepsilon \text{ and } \varepsilon = \text{maximum error} = 10^{-4}, \tag{3.88}$$

which demonstrate fast convergence within 20 iterations (see, Table. 3.1).

Table 3.1: Maximum numerical errors with respect to the number of iterations.

Number of iteration	Mximum error
1	1.2e-01
5	6.4e-02
10	3.4e-03
15	1.4e-04
20	4.1e-05

3.7 Denouement

In this chapter, a second-order continuum model is presented for the mechanics of a hyperelastic matrix material reinforced with unidirectional fibers in finite plane

elastostatics. The elastic resistance of fibers against stretch and flexure are integrated into the models of the continuum deformation via the first and second gradient of deformations, respectively. To accommodate the hyperelastic responses of the matrix material, the strain energy function of the composite is refined by the Mooney-Rivlin model. Within the framework of the second gradient theory, the Euler equation and necessary boundary conditions are also derived using the variational principles and the virtual work statement. These, in turn, furnish a highly nonlinear PDE from which a set of numerical solutions describing the hyperelastic responses of the composites are obtained via the custom-built numerical procedures.

It is also demonstrated that the presented model successfully predicts rapid strain-stiffening behavior of the Ecoflex/polyester fiber composite at a low strain level. Further, the deformation profiles of the composites are computed which demonstrate good agreement with the in-house experiment data.

Chapter 4

Mechanics of hyperelastic composites reinforced with nonlinear elastic fibrous materials

In section 4.1, the kinematics is presented for hyperelastic material reinforced with unidirectional fibers. The equilibrium and boundary conditions are presented in section 4.2. In section 4.3, the fiber potential function is refined to incorporate three distinct types of nonlinear response. The kinematics of bi-directional fiber mesh embedded in a hyperelastic matrix material is discussed in section 4.4. In section 4.5, the in-house experimental setup is discussed in detail. In section 4.6, the prediction performance of the presented models is compared against the in-house experimental data.

4.1   Kinematics of fibers embedded in a hyperelastic matrix material

In this section, we present the kinematics of fibers that will be used in the constitutive formulation of a hyperelastic matrix-fiber composite reinforced with nonlinear elastic and extensible fibers. Emphasis is placed on the derivations of compact kinematic descriptions for a unidirectional fiber family in terms of the first and second gradient of continuum deformations. The cases of bidirectional fiber meshes with a particular mesh orientation will be discussed separately in later sections.

Let $\mathbf{r}(s)$ is the parametric curve of fibers' trajectory on the deformed configuration and $\boldsymbol{\tau}$ be the unit tangent in the direction of increasing arclength parameter s. We also define $\mathbf{X}(S)$ and S as the counter parts of $\mathbf{r}(s)$ and s in the reference configuration.

The configuration of a particular fiber is then obtained by

$$\lambda = |\mathbf{d}| \text{ and } \lambda\boldsymbol{\tau} = \mathbf{d}; \ \lambda \equiv \frac{ds}{dS} \text{ and } \boldsymbol{\tau} \equiv \frac{d\mathbf{r}(s)}{ds}, \tag{4.1}$$

where

$$\mathbf{d} = \mathbf{FD}, \ \mathbf{F} = \lambda\boldsymbol{\tau} \otimes \mathbf{D}, \tag{4.2}$$

and $\mathbf{F}$ is the gradient of the deformation function $(\boldsymbol{\chi}(\mathbf{X}))$. Eq. (4.2) can be obtained via the successive differentiation of $\mathbf{r}(s(S)) = \boldsymbol{\chi}(\mathbf{X}(S))$ with respect to the referential position vector $\mathbf{X}(S)$ and the arclength parameter S using chain rule, upon making the identification of $\mathbf{D} = d\mathbf{X}/dS$. Here, $d(*)/dS$ and $d(*)/ds$ refer to the arclength derivatives of $(*)$ along fibers' directions, respectively in the reference and deformed configurations. Eq. (4.2) may be projected using the orthonormal bases of $\{\mathbf{E}_A :$ reference$\}$ and $\{\mathbf{e}_i :$ current$\}$ to yield

$$\lambda\tau_i = d_i = F_{iA}D_A \text{ for } \mathbf{D} = D_A\mathbf{E}_A, \ \mathbf{d} = d\mathbf{e}_i. \tag{4.3}$$

Further, using Eqs. (4.1)-(4.2), we find

$$\lambda^2 = \mathbf{FD} \cdot \mathbf{FD} = \mathbf{F}^T\mathbf{F} \cdot \mathbf{D} \otimes \mathbf{D}, \tag{4.4}$$

which will also be used in the later sections.

Now, the geodesic curvature of a parametric curve $(\mathbf{r}(s))$ is then formulated from Eqs. (4.2)-(4.3) that

$$\mathbf{g} \equiv \mathbf{r}'' = \frac{d(\frac{\mathbf{r}(S)}{dS})}{dS} = \frac{\partial(\mathbf{FD})}{\partial\mathbf{X}}\frac{\partial\mathbf{X}}{\partial S} = \nabla[\mathbf{FD}]\mathbf{D}. \tag{4.5}$$

In general, most of the fibers are straight prior to deformations. Even slightly curved fibers may be idealized as 'fairly straight' fibers, considering their length scales comparing with those of matrix materials. This further suggests that the gradient of the unit tangent in the reference configuration identically vanishes; i.e.,

$$\nabla\mathbf{D} = 0. \tag{4.6}$$

Thus, Eq. (4.5) deduces

$$\mathbf{g} = \nabla\mathbf{F}(\mathbf{D} \otimes \mathbf{D}) = \mathbf{G}(\mathbf{D} \otimes \mathbf{D}), \tag{4.7}$$

84

where we adopt the convention of the second gradient of deformations as

$$\nabla \mathbf{F} \equiv \mathbf{G}, \text{ and} \tag{4.8}$$

the associated compatibility condition of $\mathbf{G}$ is given by

$$G_{iAB} = F_{iA,B} = F_{iB,A} = G_{iBA}. \tag{4.9}$$

The forging developments purports that the responses of an elastic material reinforced with fibers may be characterized by the first and second gradient of continuum deformations such that

$$W(\mathbf{F}, \varepsilon, \mathbf{g}) = W(\mathbf{F}) + \frac{1}{2} C(\mathbf{F}) \mathbf{g}(\mathbf{G}) \cdot \mathbf{g}(\mathbf{G}), \tag{4.10}$$

where $W(\mathbf{F})$ refers the energy function of a matrix material. In particular, the second term in the above $(1/2[C(\mathbf{F})\mathbf{g}(\mathbf{G}) \cdot \mathbf{g}(\mathbf{G})])$ is the fiber's bending energy potential of Spencer and Soldatos type [93] which presumes that the bending responses of fibers are dependent entirely on the second gradient of continuum deformations via the geodesic curvature of fibers;

$$\mathbf{g} = \mathbf{g}(\mathbf{G}). \tag{4.11}$$

The associated modulus $C(\mathbf{F})$ is, in general, independent of the deformation gradient (i.e. $C(\mathbf{F}) = C$). The postulation of Spencer and Soldatos [93] has been widely and successfully adopted in the relevant subjects of studies (see, for example, [86], [95], [96], [110], [113], [115], and [120]). It is also noted that the invariance requirements (i.e. frame indefference) arising in the second gradient deformation remain valid for the finite elastic deformations of general continuum bodies [121]-[122] and for the cases of hyperelastic soft tissues [123], and hence, have been adopted in the present study without further proof.

To accommodate the cases of nonlinear extensible fibers exhibiting rapid strain-stiffening at low strain level (see, for example, Fig. 2 in [7] and Fig. 7 in [124]), we augment the potential of Eq. (4.10) as

$$W(\mathbf{F}, \varepsilon, \mathbf{g}) = W(\mathbf{F}) + W(\varepsilon) + \frac{1}{2} C \mathbf{g} \cdot \mathbf{g}, \tag{4.12}$$

where $W(\varepsilon)$ is the potential energy function characterizing the states of fiber's extensibility and ε is the corresponding strain measure.

Applications vis a vis particular types of energy functions of fibers ($W(\varepsilon)$) and the associated strain measures will be discussed, separately, in later sections. Further, in this study, we adopt the Mooney-Rivlin strain energy potential for the descriptions of hyperelastic matrix materials which has been widely adopted in the large deformation analyses (see, also, [105]-[106] and references therein):

$$W(\mathbf{F}) = \frac{\mu}{2}(I_1 - 3) + \frac{\kappa}{2}(I_2 - 3), \tag{4.13}$$

where I_1 and I_2 are the principal invariants of the deformation gradient tensor defined, respectively, by

$$I_1 = tr(\mathbf{F}^T\mathbf{F}) \text{ and } I_2 = \frac{1}{2}[(tr(\mathbf{F}^T\mathbf{F}))^2 - tr((\mathbf{F}^T\mathbf{F})^2)]. \tag{4.14}$$

Based on the obtained kinematic formulations for the fibers and matrix materials, we now evaluate the induced energy variation of the response function (Eq. (4.12)) as

$$\dot{W}(\mathbf{F}, \varepsilon, \mathbf{g}) = W(\mathbf{F})_{\mathbf{F}}\cdot\dot{\mathbf{F}} + W(\varepsilon)_\varepsilon\varepsilon_{\mathbf{F}}\cdot\dot{\mathbf{F}} + C\mathbf{g}\cdot\dot{\mathbf{g}}, \tag{4.15}$$

which will be used in the derivation of the Euler equations and the associated boundary conditions. Here, the superposed dot refers to the variational derivatives with respect to a parameter ϵ at the particular configuration of the composite (i.e. $\epsilon = 0$) that labels a one-parameter family of deformations.

Lastly, the expressions for the associated energy variations with respect to the first and second gradient of continuum deformations can be obtained, respectively, as

$$W_{\mathbf{F}}\cdot\dot{\mathbf{F}} = [\frac{\mu}{2}(I_1)_{\mathbf{F}} + \frac{\kappa}{2}(I_2)_{\mathbf{F}}]\cdot\dot{\mathbf{F}} = [\mu\mathbf{F} + \kappa\mathbf{F}\{(\mathbf{F}\cdot\mathbf{F})\mathbf{I} - \mathbf{F}^T\mathbf{F}\}]\cdot\dot{\mathbf{F}}, \tag{4.16}$$

where $(I_1)_{\mathbf{F}} = 2\mathbf{F}$, $(I_2)_{\mathbf{F}} = 2\mathbf{F}(I_1\mathbf{I} - \mathbf{F}^T\cdot\mathbf{F})$ (see, [114]), and

$$C\mathbf{g}\cdot\dot{\mathbf{g}} \overset{(4.6)=(4.7)}{=} C\mathbf{g}\cdot\dot{\mathbf{G}}(\mathbf{D}\otimes\mathbf{D}) = (C\mathbf{g}\otimes\mathbf{D}\otimes\mathbf{D})\cdot\dot{\mathbf{G}}. \tag{4.17}$$

4.2   Equilibrium & Boundary conditions

In the present study, the framework of the virtual work statement is adopted in the formulations of the Euler equilibrium equations and the associated boundary conditions. To initiate the derivation, we evaluate the potential energy of the system as

$$E = \int_\Omega W(\mathbf{F}, \varepsilon, \mathbf{g})\, dA. \tag{4.18}$$

86

Hence, the weak form of the equilibrium equation can be obtained by the virtual-work statement,

$$\dot{E} = P, \tag{4.19}$$

where P is the virtual power of the applied loads and the superposed dot denotes the variational and/or Gateâux derivative. Here, the conservative loads are characterized by the existence of a potential L such that $P = \dot{L}$. Accordingly, the problem of determining equilibrium deformations is reduced to the problem of minimizing the potential energy, $E - L$. In the present context, this would mean that

$$\dot{E} = \int_{\Omega} \dot{W}\left(\mathbf{F}, \varepsilon, \mathbf{g}\right) dA. \tag{4.20}$$

In general, volumetric changes in materials' deformations are energetically expensive processes and therefore are typically constrained in the constitutive modeling of engineering materials (see, also, [105]-[106]). This can be achieved by augmenting the condition of bulk incompressibility (i.e. $p(J-1)$) on the strain energy potential (Eq. (4.10)) such that

$$U(\mathbf{F}, \varepsilon, \mathbf{g}, p) = W(\mathbf{F}) + W(\varepsilon) + \frac{1}{2}C\mathbf{g} \cdot \mathbf{g} - p(J-1), \tag{4.21}$$

where J is determinant of $\mathbf{F}$ and p is a constitutively indeterminate Lagrange multiplier field. Therefore, Eq. (4.20) becomes

$$\dot{E} = \int_{\Omega} \dot{U}(\mathbf{F}, \varepsilon, \mathbf{g}, p) dA. \tag{4.22}$$

In view of Eqs. (4.15) and (4.21), the associated energy variation then furnishes

$$\dot{U} = W(\mathbf{F})_{\mathbf{F}} \cdot \dot{\mathbf{F}} + W(\varepsilon)_{\varepsilon} \varepsilon_{\mathbf{F}} \cdot \dot{\mathbf{F}} + C\mathbf{g} \cdot \dot{\mathbf{g}} - p\dot{J}, \text{ and } \dot{J} = J_{\mathbf{F}}\mathbf{F} \cdot \dot{\mathbf{F}} = \mathbf{F}^* \cdot \dot{\mathbf{F}}. \tag{4.23}$$

We continue by substituting Eqs. (4.16), (4.17) and (4.23) into Eq.(4.22) and thereby obtain

$$\dot{E} = \int_{\Omega} [\{\mu\mathbf{F} + \kappa\mathbf{F}\{(\mathbf{F} \cdot \mathbf{F})\mathbf{I} - \mathbf{F}^T\mathbf{F}\} + W_{\varepsilon}\varepsilon_{\mathbf{F}} - p\mathbf{F}^*\} \cdot \dot{\mathbf{F}} + (C\mathbf{g} \otimes \mathbf{D} \otimes \mathbf{D}) \cdot \dot{\mathbf{G}}] dA, \tag{4.24}$$

or, equivalently,

$$\dot{E} = \int_{\Omega} [(\mu F_{iA} + \kappa F_{iB}(F_{jC}F_{jC}\delta_{AB} - F_{jA}F_{jB}) + W_{\varepsilon}\varepsilon_{F_{iA}} - pF_{iA}^*)\dot{\chi}_{i,A} + C(g_i D_A D_B)\dot{\chi}_{i,AB}] dA, \tag{4.25}$$

87

where $\dot{F}_{iA} = \dot{\chi}_{i,A}$ and $\dot{G}_{iAB} = \dot{\chi}_{i,AB}$ are the variations of the first and second gradient of deformations.

The framework of variational principles arising in the second-gradient finite elasticity has been well established in the literature (see, for example, [98], [101], [107] and [108],). Here, we apply the results in the present context to formulate the Euler equation and the associated boundary conditions, and further to identify relations between the applied loads sustained by the second-gradient continua and their energy couple pertaining to the Piola-type double stresses. It is also noted that, in the forthcoming derivations, we use the component forms of vectors and tensors (e.g. Eq. (4.25)) for the sake of clarity and conciseness.

Now, applying integration by part on the last term of Eq. (4.25), we find

$$C(g_i D_A D_B)\dot{\chi}_{i,AB} = C(g_i D_A D_B \dot{\chi}_{i,A})_{,B} - C(g_i D_A D_B)_{,B}\dot{\chi}_{i,A}. \tag{4.26}$$

Substituting the above into Eq. (4.25) then yields

$$\begin{aligned}
\dot{E} &= \int_\Omega [(\mu F_{iA} + \kappa F_{iB}(F_{jC}F_{jC}\delta_{AB} - F_{jA}F_{jB}) + W_\varepsilon \varepsilon_{F_{iA}} - pF_{iA}^*)\dot{\chi}_{i,A} - C(g_i D_A D_B)_{,B}\dot{\chi}_{i,A} \\
&\quad + C(g_i D_A D_B \dot{\chi}_{i,A})_{,B}]dA.
\end{aligned} \tag{4.27}$$

Eq. (4.27) further reduces to

$$\begin{aligned}
\dot{E} &= \int_\Omega [\mu F_{iA} + \kappa F_{iB}(F_{jC}F_{jC}\delta_{AB} - F_{jA}F_{jB}) + W_\varepsilon \varepsilon_{F_{iA}} - pF_{iA}^* - C(g_i D_A D_B)_{,B}]\dot{\chi}_{i,A}dA \\
&\quad + \int_{\partial\Omega} C(g_i D_A D_B \dot{\chi}_{i,A})N_B dS,
\end{aligned} \tag{4.28}$$

where N_B is the rightward unit normal to $\partial\Omega$ in the sense of the Green–Stokes' theorem. To extract the desired expression, Eq. (4.28) may be recast as

$$\dot{E} = \int_\Omega P_{iA}\dot{\chi}_{i,A}dA + \int_{\partial\Omega} C(g_i D_A D_B \dot{\chi}_{i,A})N_B dS, \tag{4.29}$$

where

$$P_{iA} = \mu F_{iA} + \kappa F_{iB}(F_{jC}F_{jC}\delta_{AB} - F_{jA}F_{jB}) + W_\varepsilon \varepsilon_{F_{iA}} - pF_{iA}^* - C(g_i D_A D_B)_{,B} \tag{4.30}$$

is the formulation of the Piola type stress. In the case of initially straight fibers (see, Eq. (4.6)), the above can be simplified to

$$P_{iA} = \mu F_{iA} + \kappa F_{iB}(F_{jC}F_{jC}\delta_{AB} - F_{jA}F_{jB}) + W_\varepsilon \varepsilon_{F_{iA}} - pF_{iA}^* - Cg_{i,B}D_A D_B. \tag{4.31}$$

Hence, the Euler equilibrium equation satisfies

$$P_{iA,A} = 0 \text{ or } Div(\mathbf{P}) = 0, \qquad (4.32)$$

which holds in Ω.

To derive the expressions of the associated boundary conditions, we again apply integration by part on Eq. (4.29) (i.e. $P_{iA}\dot{\chi}_{i,A} = (P_{iA}\dot{\chi}_i)_{,A} - (P_{iA})_{,A}\dot{\chi}_i$) and obtain

$$\dot{E} = \int_{\partial\Omega} P_{iA}\dot{\chi}_i N_A dS + \int_{\partial\Omega} C(g_i D_A D_B \dot{\chi}_{i,A}) N_B dS - \int_{\Omega} P_{iA,A}\dot{\chi}_i dA, \qquad (4.33)$$

where the Green-Stokes' theorem is applied in the first term of the above, i.e.,

$$\int_{\Omega} (P_{iA}\dot{\chi}_i)_{,A} dA = \int_{\partial\Omega} P_{iA}\dot{\chi}_i N_A dS. \qquad (4.34)$$

Since the Euler equation ($P_{iA,A} = 0$) holds in Ω, Eq. (4.33) reduces to

$$\dot{E} = \int_{\partial\Omega} P_{iA}\dot{\chi}_i N_A dS + \int_{\partial\Omega} C(g_i D_A D_B \dot{\chi}_{i,A}) N_B dS. \qquad (4.35)$$

We now decompose $\dot{\chi}_{i,A}$ into

$$\dot{\chi}_{i,A} = \frac{\partial\dot{\chi}_i}{\partial S}\frac{\partial S}{\partial X_A} + \frac{\partial\dot{\chi}_i}{\partial N}\frac{\partial N}{\partial X_A} = \dot{\chi}_i' T_A + \dot{\chi}_{i,N} N_A, \qquad (4.36)$$

where $T_A = \partial S/\partial X_A$ and $N_A = \partial N/\partial X_A$ are respectively, the unit tangent and normal to the boundary $\partial\Omega$. Combining Eqs. (4.35)-(4.36) then furnishes

$$\dot{E} = \int_{\partial\Omega} P_{iA}\dot{\chi}_i N_A dS + \int_{\partial\Omega} C g_i D_A D_B \left(\dot{\chi}_i' T_A N_B + \dot{\chi}_{i,N} N_A N_B \right) dS. \qquad (4.37)$$

In addition, since

$$C g_i D_A D_B T_A N_B \dot{\chi}_i' = (C g_i D_A D_B T_A N_B \dot{\chi}_i)' - (C g_i D_A D_B T_A N_B)' \dot{\chi}_i, \qquad (4.38)$$

Eq. (4.37) becomes

$$\dot{E} = \int_{\partial\Omega} [P_{iA} N_A - (C g_i D_A D_B T_A N_B)']\dot{\chi}_i dS + \int_{\partial\Omega} C g_i D_A D_B \dot{\chi}_{i,N} N_A N_B dS$$
$$+ \int_{\partial\Omega} (C g_i D_A D_B T_A N_B \dot{\chi}_i)' dS. \qquad (4.39)$$

The above may be recast to yield the standard form:

$$\dot{E} = \int_{\partial\Omega} [P_{iA} N_A - (C g_i D_A T_A D_B N_B)']\dot{\chi}_i dS + \int_{\partial\Omega} C g_i D_A N_A D_B N_B \dot{\chi}_{i,N} dS$$
$$+ \sum \|C g_i D_A T_A D_B N_B \dot{\chi}_i\|, \qquad (4.40)$$

where the double bar symbol refers to the jump across the discontinuities on the boundary $\partial\Omega$ (i.e. $\|*\| = (*)^+ - (*)^-$) and the sum denotes the collection of all discontinuities.

Lastly, it follows from Eq. (4.19) that the admissible mechanical powers take the following form

$$P = \int_{\partial w_t} t_i \dot{\chi}_i dS + \int_{\partial w} m_i \dot{\chi}_{i,N} dS + \sum f_i \dot{\chi}_i. \tag{4.41}$$

Thus, by comparing Eqs. (4.39) and (4.40), we conclude that

$$
\begin{aligned}
t_i &= P_{iA}N_A - \frac{d}{dS}[Cg_i D_A T_A D_B N_B], \\
m_i &= Cg_i D_A N_A D_B N_B, \\
f_i &= Cg_i D_A T_A D_B N_B,
\end{aligned}
\tag{4.42}
$$

where t_i, m_i, and f_i are the expressions of edge tractions, edge moments and the corner forces, respectively. It should be pointed out here that the stress expression in Eq. (4.30) is a combination of the Piola-type stress ($\mu F_{iA} + \kappa F_{iB}(F_{jC}F_{jC}\delta_{AB} - F_{jA}F_{jB}) + W_\varepsilon \varepsilon_{F_{iA}} - p F_{iA}^*$) and double stress ($C(g_i D_A D_B)_{,B}$) such that the second gradient of the deformation term (i.e. $C(g_i D_A D_B)_{,B}$) can be interpreted as the energy conjugate to the admissible double force m_i when it is prescribed on the desired boundaries.

4.3 Modeling of hyperelastic composites

Of central importance in this work is the incorporation of nonlinear responses (e.g. strain-stiffening behaviors) of fibers into the models of continuum deformations. In this section, we propose two different types of energy potentials in the descriptions of fibers (based on the Green-Lagrange strain measure) which exhibit moderate strain-stiffening and rapid strain-stiffening responses. Emphasis is placed on the derivation of compact and viable mathematical models while maintaining the rigor and sufficient generality in the associated constitutive formulations.

In cases of one-dimensional structures (e.g. fibers and wires), the Green-Lagrange strain is defined by (see, also, [105]-[106])

$$\varepsilon = \frac{1}{2}\left(\lambda^2 - 1\right). \tag{4.43}$$

Hence, in view of Eq. (4.4), we find

$$\varepsilon = \frac{1}{2}\left(\mathbf{FD}\cdot\mathbf{FD}-1\right) = \frac{1}{2}\left(F_{iA}F_{iB}D_A D_B - 1\right). \tag{4.44}$$

Accordingly, the variational derivatives of ε can be evaluated as

$$\dot{\varepsilon} = \varepsilon_{\mathbf{F}}\cdot\dot{\mathbf{F}} = \frac{\partial(1/2)(\mathbf{FD}\cdot\mathbf{FD}-1)}{\partial\mathbf{F}}\cdot\dot{\mathbf{F}} = \mathbf{F}(\mathbf{D}\otimes\mathbf{D})\cdot\dot{\mathbf{F}}, \text{ or equivalently,}$$

$$\dot{\varepsilon} = \varepsilon_{F_{iA}}\dot{F}_{iA} = F_{iB}D_B D_A \dot{F}_{iA}, \tag{4.45}$$

which will be used in the forthcoming variational formulations.

4.3.1 Fibers with moderate strain-stiffening behavior: Polynomial potentials

The mechanical responses of the polyester (PES) fibers may be mimicked by using the following polynomial form of energy potential:

$$W(\varepsilon) = \frac{1}{3}E_1\varepsilon^3 + \frac{1}{2}E_2\varepsilon^2. \tag{4.46}$$

In the above, E_1 and E_2 are the material parameters, characterizing the moderate strain-stiffening behaviors of the PES fibers which can be determined by fitting the stress-strain curves of the PES fibers in the similar manner as in the Mooney-Rivlin model. We note here that the use of higher order polynomials (e.g. ε^5, ε^4 etc...) may provide better fittings and thus lead to more accurate predictions. At the same time, the efficiency of the resulting models may be substantially compromised. We found that, after extensive trials, the proposed cubic polynomial yields reasonably accurate prediction results without much loss of computational efficiency. In this respect, performance analysis via the cross-examination with the inhouse experimental results will also be discussed separately in later sections.

Now, from Eqs. (4.44)-(4.45), the variational derivative of Eq. (4.46) can be formulated as

$$
\begin{aligned}
\dot{W}(\varepsilon) &= W_\varepsilon \varepsilon_{F_{iA}}\dot{F}_{iA} = (E_1\varepsilon^2 + E_2\varepsilon)\varepsilon_{F_{iA}}\dot{F}_{iA} \\
&= [\frac{E_1}{4}\left(\mathbf{FD}\cdot\mathbf{FD}-1\right)^2 + \frac{E_2}{2}\left(\mathbf{FD}\cdot\mathbf{FD}-1\right)]\mathbf{F}(\mathbf{D}\otimes\mathbf{D})\cdot\dot{\mathbf{F}} \\
&= [\frac{E_1}{4}(F_{jC}F_{jD}D_C D_D)(F_{kE}F_{kF}D_E D_F) + \frac{(E_2 - E_1)}{2}F_{jC}F_{jD}D_C D_D \\
&\quad + \frac{(E_1 - 2E_2)}{4}]F_{iB}D_B D_A \dot{\chi}_{i,A}. \tag{4.47}
\end{aligned}
$$

91

Therefore, the expression of the Piola stress (Eq. (4.31)) becomes

$$
\begin{aligned}
P_{iA} &= \mu F_{iA} + \kappa F_{iB}(F_{jC}F_{jC}\delta_{AB} - F_{jA}F_{jB}) - pF_{iA}^* - Cg_{i,B}D_AD_B \\
&\quad + [\frac{E_1}{4}(F_{jC}F_{jD}D_CD_D)(F_{kE}F_{kF}D_ED_F) + \frac{(E_2-E_1)}{2}F_{jC}F_{jD}D_CD_D \\
&\quad + \frac{(E_1-2E_2)}{4}]F_{iB}D_BD_A.
\end{aligned}
\tag{4.48}
$$

For the desired applications (uniaxial and single family of fibers, i.e. $\mathbf{D} = D_1\mathbf{E}_1$), the above may be further reduced to

$$
\begin{aligned}
P_{iA} &= \mu F_{iA} + \kappa F_{iB}(F_{jC}F_{jC}\delta_{AB} - F_{jA}F_{jB}) - pF_{iA}^* - CF_{i1,11}D_A \\
&\quad + [\frac{E_1}{4}(F_{j1}F_{j1})(F_{k1}F_{k1}) + \frac{(E_2-E_1)}{2}F_{j1}F_{j1} + \frac{(E_1-2E_2)}{4}]F_{i1}D_A,
\end{aligned}
\tag{4.49}
$$

where, $g_{i,B} = F_{iC,BD}D_CD_D$ from Eqs. (4.6)-(4.8). Further, since the Euler equation ($P_{iA,A} = 0$) holds in Ω, the above satisfies

$$
\begin{aligned}
0 &= P_{iA,A} = \mu\chi_{i,AA} + \kappa(\chi_{i,AA}\chi_{j,C}\chi_{j,C} - \chi_{i,BA}\chi_{j,A}\chi_{j,B}) + \kappa\chi_{i,B}(2\chi_{j,CB}\chi_{j,C} \\
&\quad -\chi_{j,AA}\chi_{j,B} - \chi_{j,A}\chi_{j,BA}) - p_{,A}\varepsilon_{ij}\varepsilon_{AB}\chi_{j,B} + [\frac{E_1}{4}(2\chi_{j,11}\chi_{j,1}\chi_{k,1}\chi_{k,1} \\
&\quad + 2\chi_{j,1}\chi_{j,1}\chi_{k,11}\chi_{k,1}) + (E_2-E_1)\chi_{j,11}\chi_{j,1}]\chi_{i,1} - C\chi_{i,1111} \\
&\quad + [\frac{E_1}{4}(\chi_{j,1}\chi_{j,1})(\chi_{k,1}\chi_{k,1}) + \frac{(E_2-E_1)}{2}\chi_{j,1}\chi_{j,1} + \frac{(E_1-2E_2)}{4}]\chi_{i,11},
\end{aligned}
\tag{4.50}
$$

where $F_{iA} = \chi_{i,A} = \partial\chi_i/\partial X_A$, $F_{iA}^* = \varepsilon_{ij}\varepsilon_{AB}F_{jB}$, and ε_{ij} is the 2-D permutation; $\varepsilon_{12} = -\varepsilon_{21} = 1, \varepsilon_{11} = -\varepsilon_{22} = 0$. Eq. (4.50) together with the constraint of the bulk incompressibility,

$$
\det \mathbf{F} = \chi_{1,1}\chi_{2,2} - \chi_{1,2}\chi_{2,1} = 1,
\tag{4.51}
$$

solve the unknown potentials of χ_1, χ_2 and p which describe the mechanical responses of hyperelastic composites with moderate strain-stiffening behaviors.

Lastly, the admissible boundary conditions (Eq. (4.42)) in the case of rectangular shaped samples (i.e. $\mathbf{D} \cdot \mathbf{T} = \mathbf{0}$ & $\mathbf{D} \cdot \mathbf{N} = \mathbf{1}$ or $\mathbf{D} \cdot \mathbf{T} = \mathbf{1}$ & $\mathbf{D} \cdot \mathbf{N} = \mathbf{0}$ on the boundaries) furnish

$$
\begin{aligned}
t_1 &= P_{11}, \ t_2 = 0, \\
m_1 &= Cg_1, \ m_2 = 0, \\
f_1 &= f_2 = 0,
\end{aligned}
\tag{4.52}
$$

from which the corresponding deformation mappings can be uniquely determined. Further, in view of Eqs. (4.7) and (4.49), we obtain the expressions of P_{11} and g_1, respectively, as

$$
\begin{aligned}
P_{11} &= \mu\chi_{1,1}+\kappa\chi_{1,B}(\chi_{j,C}\chi_{j,C}\delta_{1B}-\chi_{j,1}\chi_{j,B})-C\chi_{1,111}-p\chi_{2,2} \\
&\quad+[\frac{E_1}{4}(\chi_{j,1}\chi_{j,1}\chi_{k,1}\chi_{k,1})+\frac{(E_2-E_1)}{2}\chi_{j,1}\chi_{j,1}+\frac{(E_1-2E_2)}{4}]\chi_{1,1}, \\
g_1 &= G_{111}D_1D_1 = \chi_{1,11}.
\end{aligned}
\tag{4.53}
$$

The numerical solution of the above system of PDEs (Eqs. (4.50)-(4.51)) can be accommodated via commercial packages (e.g. Matlab, COMSOL etc. . .).

4.3.2 Fibers with rapid strain-stiffening behavior: Exponential potentials

For fibers exhibiting rapid strain-stiffening responses at low strain level such as the Nylon/Spandex (NSP) fibers (see, also, [7] and [125]), the polynomial types of energy potentials may not be suitable to capture sharp changes in stress-strain responses of NSP fibers. In this case, the following exponential potential may be considered:

$$
W(\varepsilon) = E_1(E_2\varepsilon-1)e^{E_2\varepsilon} = E_1(E_2\varepsilon-1)e(\exp(E_2\varepsilon)),
\tag{4.54}
$$

where the material parameters E_1 and E_2 can be determined by fitting the stress-strain curves of NSP fibers.

In view of Eqs. (4.44)-(4.45), we find the variational derivatives of Eq. (4.54) as

$$
\begin{aligned}
\dot{W}(\varepsilon) &= W_\varepsilon\varepsilon_{F_{iA}}\dot{F}_{iA}=E_1E_2^2\varepsilon e(\exp(E_2\varepsilon))\varepsilon_{F_{iA}}\dot{F}_{iA} \\
&= \frac{E_1E_2^2}{2}(\mathbf{FD}\cdot\mathbf{FD}-1)\,e[\exp(\frac{E_2}{2}(\mathbf{FD}\cdot\mathbf{FD}-1))]\mathbf{F}(\mathbf{D}\otimes\mathbf{D})\cdot\dot{\mathbf{F}} \\
&= \frac{E_1E_2^2}{2}(F_{kE}F_{kF}D_ED_F-1)\,e[\exp(\frac{E_2}{2}(F_{jC}F_{jD}D_CD_D-1))]F_{iB}D_BD_A\dot{\chi}_{i,A}.
\end{aligned}
\tag{4.55}
$$

Hence, the expression of the Piola stress can be obtained by

$$
\begin{aligned}
P_{iA} &= \mu F_{iA}+\kappa F_{iB}(F_{jC}F_{jC}\delta_{AB}-F_{jA}F_{jB})-pF_{iA}^*-Cg_{i,B}D_AD_B \\
&\quad+\frac{E_1E_2^2}{2}(F_{kE}F_{kF}D_ED_F-1)\,e[\exp(\frac{E_2}{2}(F_{jC}F_{jD}D_CD_D-1))]F_{iB}D_BD_A.
\end{aligned}
\tag{4.56}
$$

Similarly as in the polynomial case, the above becomes, in the case of uniaxial and single family of fibers (i.e. $\mathbf{D} = D_1\mathbf{E}_1$), that

$$
\begin{aligned}
P_{iA} &= \mu F_{iA} + \kappa F_{iB}(F_{jC}F_{jC}\delta_{AB} - F_{jA}F_{jB}) - pF_{iA}^* - CF_{i1,11}D_A \\
&\quad + \frac{E_1 E_2^2}{2}(F_{k1}F_{k1}-1)\,e[\exp(\frac{E_2}{2}(F_{j1}F_{j1}-1))]F_{i1}D_A,
\end{aligned} \tag{4.57}
$$

from which, we derive the following Euler equilibrium equation:

$$
\begin{aligned}
0 &= P_{iA,A} = \mu\chi_{i,AA} + \kappa(\chi_{i,AA}\chi_{j,C}\chi_{j,C} - \chi_{i,BA}\chi_{j,A}\chi_{j,B}) + \kappa\chi_{i,B}(2\chi_{j,CB}\chi_{j,C} \\
&\quad - \chi_{j,AA}\chi_{j,B} - \chi_{j,A}\chi_{j,BA}) - p_{,A}\varepsilon_{ij}\varepsilon_{AB}\chi_{j,B} \\
&\quad - C\chi_{i,1111} + E_1 E_2^2\left(\chi_{k,11}\chi_{k,1}-1\right)e[\exp(\frac{E_2}{2}\left(\chi_{j,1}\chi_{j,1}-1\right))]\chi_{i,1} \\
&\quad + \frac{E_1 E_2^2}{2}\left(\chi_{k,1}\chi_{k,1}-1\right)e[\exp(\frac{E_2}{2}\left(\chi_{j,1}\chi_{j,1}-1\right))][E_2\chi_{j,11}\chi_{j,1}\chi_{i,1} - \chi_{i,11}], \tag{4.58}
\end{aligned}
$$

which holds in Ω. Since the NSP fiber composite specimens are fabricated and tested under the same inhouse experimental settings as those in the PES fiber-composite cases, the same boundary conditions (Eq. (4.52)) can be used without further modification except the expression of the Piola stress, P_{11}, which can be obtained from Eq. (4.57) that

$$
\begin{aligned}
P_{11} &= \mu\chi_{1,1} + \kappa\chi_{1,B}(\chi_{j,C}\chi_{j,C}\delta_{1B} - \chi_{j,1}\chi_{j,B}) - C\chi_{1,111} - p\chi_{2,2} \\
&\quad + \frac{E_1 E_2^2}{2}\left(\chi_{k,1}\chi_{k,1}-1\right)e[\exp(\frac{E_2}{2}\left(\chi_{j,1}\chi_{j,1}-1\right))]\chi_{1,1}. \tag{4.59}
\end{aligned}
$$

The numerical solutions of the resulting system of PDEs (i.e. Eq. (4.58) and Eq. (4.51)) can be uniquely determined by imposing the admissible boundary conditions (Eq. (4.52)) to yield the explicit deformation mappings of the NSP fiber-composites exhibiting rapid stress-strain behaviors. The corresponding simulation results and comparisons with the experimental data will be discussed separately in later sections.

4.3.3 Consideration of the Euler-Almansi finite strain measure

The proposed model may also be employed in the analysis of the strain-softening responses of fiber-composites such as polydimethylsiloxane (PDMS) composite and polyurethane (integrated with polydopamine (PU/D)) composite (see, for example,

[126]-[127]). For the desired application, we may consider the Euler-Almansi finite strain measure defined by

$$\varepsilon = \frac{1}{2}\left(1 - \frac{1}{\lambda^2}\right). \tag{4.60}$$

Also, in the forthcoming model derivation, the polynomial energy potential of fibers is considered for the sake of clear and concise demonstration. The cases of exponential potentials can be easily implemented via the similar approaches as done in this section.

Now, the substitution of Eq. (4.4) into Eq. (4.60) furnishes

$$\varepsilon = \frac{1}{2}\left(1 - \frac{1}{\mathbf{FD} \cdot \mathbf{FD}}\right) = \frac{1}{2}\left(1 - \frac{1}{F_{iA}F_{iB}D_A D_B}\right). \tag{4.61}$$

The variational derivatives of ε can then be evaluated as

$$\begin{aligned}
\dot{\varepsilon} &= \varepsilon_{\mathbf{F}} \cdot \dot{\mathbf{F}} = \frac{\partial(1/2)[1 - (\mathbf{FD} \cdot \mathbf{FD})^{-1}]}{\partial \mathbf{F}} \cdot \dot{\mathbf{F}} = \frac{1}{2}(\mathbf{FD} \cdot \mathbf{FD})^{-2} \frac{\partial \mathbf{FD} \cdot \mathbf{FD}}{\partial \mathbf{F}} \cdot \dot{\mathbf{F}} \\
&= \frac{\mathbf{F}(\mathbf{D} \otimes \mathbf{D}) \cdot \dot{\mathbf{F}}}{(\mathbf{FD} \cdot \mathbf{FD})^{-2}},
\end{aligned} \tag{4.62}$$

or, in the component form,

$$\dot{\varepsilon} = \varepsilon_{F_{iA}} \dot{F}_{iA} = \frac{F_{iB}D_B D_A \dot{F}_{iA}}{(F_{jC}F_{jD}D_C D_D)^2}. \tag{4.63}$$

Further, in view of (4.46)-(4.47), we compute the corresponding variational derivatives of $W(\varepsilon)$ as

$$\begin{aligned}
\dot{W}(\varepsilon) &= W_\varepsilon \varepsilon_{F_{iA}} \dot{F}_{iA} = (E_1 \varepsilon^2 + E_2 \varepsilon) \varepsilon_{F_{iA}} \dot{F}_{iA} \\
&= [\frac{E_1}{4}\left(1 - \frac{1}{\mathbf{FD} \cdot \mathbf{FD}}\right)^2 + \frac{E_2}{2}\left(1 - \frac{1}{\mathbf{FD} \cdot \mathbf{FD}}\right)] \frac{\mathbf{F}(\mathbf{D} \otimes \mathbf{D}) \cdot \dot{\mathbf{F}}}{(\mathbf{FD} \cdot \mathbf{FD})^{-2}} \\
&= [\frac{E_1}{4} \frac{1}{(F_{kE}F_{kF}D_E D_F)^2} - (\frac{E_1 + E_2}{2}) \frac{1}{F_{kE}F_{kF}D_E D_F} \\
&\quad + (\frac{E_1}{4} + \frac{E_2}{2})] \frac{F_{iB}D_B D_A}{(F_{jC}F_{jD}D_C D_D)^2} \dot{\chi}_{i,A}.
\end{aligned} \tag{4.64}$$

Hence, it is customary to show

$$\begin{aligned}
P_{iA} &= \mu F_{iA} + \kappa F_{iB}(F_{jC}F_{jC}\delta_{AB} - F_{jA}F_{jB}) - pF_{iA}^* - Cg_{i,B}D_A D_B \\
&\quad + [\frac{E_1}{4} \frac{1}{(F_{kE}F_{kF}D_E D_F)^2} - (\frac{E_1 + E_2}{2}) \frac{1}{F_{kE}F_{kF}D_E D_F} \\
&\quad + (\frac{E_1}{4} + \frac{E_2}{2})] \frac{F_{iB}D_B D_A}{(F_{jC}F_{jD}D_C D_D)^2}.
\end{aligned} \tag{4.65}$$

For uniaxial and single family of fibers (i.e. $\mathbf{D} = D_1 \mathbf{E}_1$), this reduces to

$$
\begin{aligned}
P_{iA} &= \mu F_{iA} + \kappa F_{iB}(F_{jC}F_{jC}\delta_{AB} - F_{jA}F_{jB}) - pF_{iA}^* - CF_{i1,11}D_A \\
&\quad + [\frac{E_1}{4}\frac{1}{(F_{k1}F_{k1})^2} - (\frac{E_1 + E_2}{2})\frac{1}{F_{k1}F_{k1}} \\
&\quad + (\frac{E_1}{4} + \frac{E_2}{2})]\frac{F_{i1}D_A}{(F_{j1}F_{j1})^2}.
\end{aligned}
\tag{4.66}
$$

Consequently, we obtain the following Euler equilibrium equation

$$
\begin{aligned}
0 &= P_{iA,A} = \mu\chi_{i,AA} + \kappa(\chi_{i,AA}\chi_{j,C}\chi_{j,C} - \chi_{i,BA}\chi_{j,A}\chi_{j,B}) + \kappa\chi_{i,B}(2\chi_{j,CB}\chi_{j,C} \\
&\quad - \chi_{j,AA}\chi_{j,B} - \chi_{j,A}\chi_{j,BA}) + [\frac{E_1}{4}\frac{1}{(\chi_{k,1}\chi_{k,1})^2} - (\frac{E_1 + E_2}{2})\frac{1}{\chi_{k,1}\chi_{k,1}} \\
&\quad + (\frac{E_1}{4} + \frac{E_2}{2})](\frac{\chi_{i,11}}{(\chi_{j,1}\chi_{j,1})^2} - \frac{4\chi_{i,1}\chi_{k,11}\chi_{k,1}}{(\chi_{j,1}\chi_{j,1})^3}) + [(E_1 + E_2)\frac{\chi_{j,11}\chi_{j,1}}{(\chi_{k,1}\chi_{k,1})^4} \\
&\quad - E_1\frac{\chi_{j,11}\chi_{j,1}}{(\chi_{k,1}\chi_{k,1})^5}]\chi_{i,1} - p_{,A}\varepsilon_{ij}\varepsilon_{AB}\chi_{j,B} - C\chi_{i,1111}.
\end{aligned}
\tag{4.67}
$$

The corresponding deformation map, describing strain-softening behavior of the composites, can then be completely determined from Eqs. (4.51), (4.52) and (4.67). It is noted here that, in the Euler- Almansi cases, we were unable to conduct inhouse experiment due to the ongoing pandemic crisis. Instead, comparisons with the existing results in the literature have been made which will be discussed together with the other proposed models in later sections.

4.4 Hyperelastic materials reinforced with bidirectional fibers

In this section, we develop a continuum model which describes the mechanical responses of hyperelastic materials reinforced with fiber mesh. The fiber mesh is embedded in the matrix material with 45 degrees orientation (see, Fig. 4.1) such that it forms a distinct pantographic sheet like structure within the matrix material. For the stated purpose, we define unit vectors $\mathbf{L}$ and $\mathbf{M}$ to identify the fibers' trajectories in reference configuration:

$$
\mathbf{L} = \frac{d\mathbf{X}(S,U)}{dS} \text{ and } \mathbf{M} = \frac{d\mathbf{X}(S,U)}{dU},
\tag{4.68}
$$

where S and U are, respectively, the arclength parameters in the directions of $\mathbf{L}$ and $\mathbf{M}$.

Here, we confine our attention to the case of initially uniform and orthogonal fiber mesh (i.e. $\mathbf{L} \cdot \mathbf{M} = \mathbf{0}$, see, also, Fig. 4.1) for the sake of simplicity and conciseness. The cases of non-orthogonal meshes with different orientation angles can be readily accommodated via the simple modification of fibers' director fields (e.g. $\mathbf{L} \cdot \mathbf{M} = \cos \alpha$ etc...), but the presumed orthogonality and the orientation of fiber mesh suffice to extract the important aspects of the intended model and, further, the desired applications.
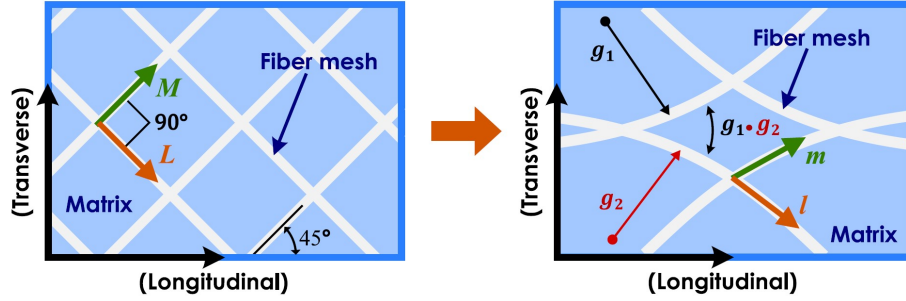
Figure 4.1: Schematics of fiber mesh prior and after deformations.

The stretch and orientation of a particular fiber after deformations are then defined by (see, also, Eqs. (4.1)-(4.2))

$$\lambda = |\boldsymbol{\eta}| = \frac{ds}{dS}, \ \gamma = |\boldsymbol{\tau}| = \frac{du}{dU} \text{ and } (\frac{d\mathbf{r}}{ds}) = \mathbf{l} = \lambda^{-1}\boldsymbol{\eta}, \ (\frac{d\mathbf{r}}{du}) = \mathbf{m} = \gamma^{-1}\boldsymbol{\tau}, \qquad (4.69)$$

where

$$\lambda\mathbf{l} = \mathbf{FL} \text{ and } \gamma\mathbf{m} = \mathbf{FM}, \qquad (4.70)$$

and $\mathbf{l}, \ \mathbf{m}, s$ and u are the counter parts of $\mathbf{L}, \ \mathbf{M}, S$, and U in the current configuration. Eq. (4.70) together with the presumed orthogonality (i.e. $\mathbf{L} \cdot \mathbf{M} = \mathbf{0}$) furnish a useful fiber decomposition of the deformation gradient tensor:

$$\mathbf{F} = \lambda\mathbf{l} \otimes \mathbf{L} + \gamma\mathbf{m} \otimes \mathbf{M}. \qquad (4.71)$$

which will also be used in the forthcoming model derivation. Hence, the geodesic curvatures of a parametric curve $(\mathbf{r}(s, u))$ can be formulated from Eqs. (4.69)-(4.70) that

$$\mathbf{g}_1 = \frac{d^2\mathbf{r}(S)}{dS^2} = \frac{d(\frac{\mathbf{r}(S)}{dS})}{dS} = \frac{\partial(\mathbf{FL})}{\partial\mathbf{X}}\frac{\partial\mathbf{X}}{\partial S} = \nabla[\mathbf{FL}]\mathbf{L}, \text{ and} \qquad (4.72)$$

$$\mathbf{g}_2 = \frac{d^2\mathbf{r}(U)}{dU^2} = \frac{d(\frac{\mathbf{r}(U)}{dU})}{dU} = \frac{\partial(\mathbf{FM})}{\partial\mathbf{X}}\frac{\partial\mathbf{X}}{\partial U} = \nabla[\mathbf{FM}]\mathbf{M}. \tag{4.73}$$

In the case of initially straight fibers (see, Eq. (4.6)), the above reduces to

$$\mathbf{g}_1 = \nabla\mathbf{F}(\mathbf{L}\otimes\mathbf{L}) = \mathbf{G}(\mathbf{L}\otimes\mathbf{L}) \text{ and } \mathbf{g}_2 = \nabla\mathbf{F}(\mathbf{M}\otimes\mathbf{M}) = \mathbf{G}(\mathbf{M}\otimes\mathbf{M}). \tag{4.74}$$

The forgoing developments suggest that the mechanical responses of the fiber mesh can be described by the following energy function:

$$W_{fiber} = W(\varepsilon_1, \varepsilon_2) + \frac{1}{2}C(\mathbf{g}_1 \cdot \mathbf{g}_1 + \mathbf{g}_2 \cdot \mathbf{g}_2) + \frac{1}{2}T\mathbf{g}_1 \cdot \mathbf{g}_2, \tag{4.75}$$

where terms with $\mathbf{g}_\alpha \cdot \mathbf{g}_\alpha$ and $\mathbf{g}_1 \cdot \mathbf{g}_2$ account for the bending and torsional kinematics of the fiber mesh, respectively (see, Fig. 4.1), and C and T are the associated moduli. In particular, the energy potential of $W(\varepsilon_1, \varepsilon_2)$ in Eq. (4.75) characterizes the responses of the fiber mesh against extensions, which may take the following compact quadratic form for the purpose of clear and concise demonstration.

$$W(\varepsilon_1, \varepsilon_2) = \frac{1}{2}E(\varepsilon_1^2 + \varepsilon_2^2). \tag{4.76}$$

Further, invoking Eqs. (4.43) and (4.70), the expressions for the associated strains can be found as

$$\varepsilon_1 = \frac{1}{2}\left(\lambda^2 - 1\right) = \frac{1}{2}\left(\mathbf{FL} \cdot \mathbf{FL} - 1\right) \text{ and } \varepsilon_2 = \frac{1}{2}\left(\gamma^2 - 1\right) = \frac{1}{2}\left(\mathbf{FM} \cdot \mathbf{FM} - 1\right). \tag{4.77}$$

It should also be noted that the refinement of $W(\varepsilon_1, \varepsilon_2)$ to accommodate the more general responses of the fiber mesh is straightforward using the results from the cases of the polynomial and exponential potentials, discussed in the previous sections.

Now, we use chain rule in the form

$$\dot{W}_{fiber} = W(\varepsilon_1, \varepsilon_2)_{\varepsilon_1}(\varepsilon_1)_{\mathbf{F}} \cdot \dot{\mathbf{F}} + W(\varepsilon_1, \varepsilon_2)_{\varepsilon_2}(\varepsilon_2)_{\mathbf{F}} \cdot \dot{\mathbf{F}} + C(\mathbf{g}_1 \cdot \dot{\mathbf{g}}_1 + \mathbf{g}_2 \cdot \dot{\mathbf{g}}_2)$$
$$+ \frac{T}{2}(\dot{\mathbf{g}}_1 \cdot \mathbf{g}_2 + \mathbf{g}_1 \cdot \dot{\mathbf{g}}_2), \tag{4.78}$$

and thereby obtain the variational derivative of W_{fiber} as

$$\dot{W}_{fiber} = \frac{E}{2}[(\mathbf{FL} \cdot \mathbf{FL} - 1)\mathbf{F}(\mathbf{L}\otimes\mathbf{L}) + (\mathbf{FM} \cdot \mathbf{FM} - 1)\mathbf{F}(\mathbf{M}\otimes\mathbf{M})] \cdot \dot{\mathbf{F}}$$
$$+ C(\mathbf{g}_1 \otimes \mathbf{L} \otimes \mathbf{L} + \mathbf{g}_2 \otimes \mathbf{M} \otimes \mathbf{M}) \cdot \dot{\mathbf{G}} + \frac{T}{2}(\mathbf{g}_2 \otimes \mathbf{L} \otimes \mathbf{L} + \mathbf{g}_1 \otimes \mathbf{M} \otimes \mathbf{M}) \cdot \dot{\mathbf{G}}$$
$$= \frac{E}{2}[(F_{jC}F_{jD}L_CL_D - 1)F_{iB}L_BL_A + (F_{jC}F_{jD}M_CM_D - 1)F_{iB}M_BM_A]\dot{\chi}_{i,A}$$
$$+ CG_{iCD}(L_AL_BL_CL_D + M_AM_BM_CM_D)\dot{\chi}_{i,AB} + \frac{T}{2}G_{iCD}(L_AL_BM_CM_D$$
$$+ M_AM_BL_CL_D)\dot{\chi}_{i,AB}. \tag{4.79}$$

Using the similar procedures as in Eqs. (4.24)-(4.28), it can be easily shown that

$$
\begin{aligned}
P_{iA} = {} & \mu F_{iA} + \kappa F_{iB}(F_{jC}F_{jC}\delta_{AB} - F_{jA}F_{jB}) - pF_{iA}^* \\
& + \frac{E}{2}[(F_{jC}F_{jD}L_CL_D - 1)F_{iB}L_AL_B + (F_{jC}F_{jD}M_CM_D - 1)F_{iB}M_AM_B] \\
& + CG_{iCD,B}(L_AL_BL_CL_D + M_AM_BM_CM_D) + \frac{T}{2}G_{iCD,B}(L_AL_BM_CM_D \\
& + M_AM_BL_CL_D).
\end{aligned}
\tag{4.80}
$$

Hence, the Euler equilibrium equation is obtained:

$$
\begin{aligned}
0 = {} & P_{iA,A} = \mu\chi_{i,AA} + \kappa(\chi_{i,AA}\chi_{j,C}\chi_{j,C} - \chi_{i,AB}\chi_{j,A}\chi_{j,B}) + \kappa\chi_{i,B}(2\chi_{j,BC}\chi_{j,C} \\
& - \chi_{j,AA}\chi_{j,B} - \chi_{j,A}\chi_{j,AB}) - p_{,A}\varepsilon_{ij}\varepsilon_{AB}\chi_{j,B} + \frac{E}{2}(\chi_{i,AB}\chi_{j,C}\chi_{j,D} \\
& + \chi_{i,B}\chi_{j,AC}\chi_{j,D} + \chi_{i,B}\chi_{j,C}\chi_{j,D,A})L_AL_BL_CL_D - \frac{E}{2}\chi_{i,AB}L_AL_B \\
& + \frac{E}{2}(\chi_{i,AB}\chi_{j,C}\chi_{j,D} + \chi_{i,B}\chi_{j,AC}\chi_{j,D} + \chi_{i,B}\chi_{j,C}\chi_{j,AD})M_AM_BM_CM_D \\
& - \frac{E}{2}\chi_{i,AB}M_AM_B + C\chi_{i,ABCD}(L_AL_BL_CL_D + M_AM_BM_CM_D) \\
& + \frac{T}{2}\chi_{i,ABCD}(L_AL_BM_CM_D + M_AM_BL_CL_D),
\end{aligned}
\tag{4.81}
$$

which holds in Ω. With this satisfied, the corresponding boundary condition can be formulated as

$$
\begin{aligned}
t_i &= P_{iA}N_A - \frac{d}{dS}[(C(g_1)_i + \frac{T}{2}(g_2)_i)L_AT_AL_BN_B + (C(g_2)_i + \frac{T}{2}(g_1)_i)M_AT_AM_BN_B], \\
m_i &= (C(g_1)_i + \frac{T}{2}(g_2)_i)L_AN_AL_BN_B + (C(g_2)_i + \frac{T}{2}(g_1)_i)M_AN_AM_BN_B, \\
f_i &= (C(g_1)_i + \frac{T}{2}(g_2)_i)L_AT_AL_BN_B + (C(g_2)_i + \frac{T}{2}(g_1)_i)M_AT_AM_BN_B,
\end{aligned}
\tag{4.82}
$$

by applying the same procedure as demonstrated in Eqs. (4.33)-(4.38). Lastly, since the fiber mesh is oriented at a 45 degree angle with respect to the reference coordinate frame (see, Fig. 4.1), we find

$$
\begin{aligned}
\mathbf{L} &= L_1\mathbf{E}_1 + L_2\mathbf{E}_2 = \cos(\pi/4)\mathbf{E}_1 - \sin(\pi/4)\mathbf{E}_2, \\
\mathbf{M} &= M_1\mathbf{E}_1 + M_2\mathbf{E}_2 = \cos(\pi/4)\mathbf{E}_1 + \sin(\pi/4)\mathbf{E}_2.
\end{aligned}
\tag{4.83}
$$

The implementation of the obtained model and comparisons with the experimental results will be discussed in the following sections.

4.5 Materials and methods

4.5.1 Materials

a) **Elastomer matrix:** Ecoflex 0050 used in the inhouse experiment was manufactured from Smooth-On, Inc. This is used as the matrix materials for all the fabricated fiber composite samples for the proposed experiment. Ecoflex 0050 is known to be one of the promising materials in biomechanical applications for its high tear resistance and large extensibility up to 1000% [128]–[130].

b) **Fibrous reinforcements:** In the experiment, four different types of fibers are considered. Two of them are fabrics composed of 85% nylon / 15% spandex (NSP-8515), and 80% nylon / 20% spandex (NSP-8020) blend which were obtained from the local store Marshall's Fabrics (Telio, Montreal, CA). Other two samples are surgical polyester knit which are referred to as PETKM2005 (PES-2) and PETKM2006 (PES-3), fabricated from the Surgical Mesh (Brookfield, CT, USA).

4.5.2 Sample preparation

a) **Elastomeric material preparation:** Ecoflex 0050 is a room-temperature-vulcanizing (RTV) silicone which was prepared by mixing two components (a base and curing agent) in 1:1 ratio and subsequent degassing in a vacuum to remove the entrapped bubbles.

b) **Fiber/fiber mesh – elastomer composite preparation:** For the experiments, we prepared four different types of fiber/fiber mesh – Ecoflex 0050 composite samples that are reinforced, respectively, with polyester fibers (PES-2, PES-3) and nylon/spandex fibers (NSP-8515, NSP-8020), forming unidirectional and/or bidirectional (pantographic) arrays within the matrix material (see, Fig. 4.2 (c) and Fig. 4.3). The dimension of fabricated composite samples is $50mm \times 25mm$, keeping an aspect ratio of 2:1 (length-to-with). The reinforced elastomer composites were fabricated in a three-layer configuration using a layer by layer method. The schematic diagram of the sample preparation and the local structures of the fabricated composite samples are shown in Figs. 4.2-4.3. To prepare the bottom elastomer layer, a sufficient amount of elastomer mixture was poured on a glass substrate and rolled using the film applicator rod to make a uniform film (see, Fig. 4.2 (a)). The second

layer of fiber/fiber mesh was then placed flat on elastomer and allowed to soak at the interface (Fig. 4.2 (b)). A small amount of elastomer was then poured and rolled over the fiber/fiber mesh to wet it again and to fill the gaps between pores and level the second layer. To make a third layer, a sufficient amount of elastomer was poured over the second layer and a uniform film was created using a film applicator rod. We note here that the thickness of the fiber/fiber mesh remains constant and is specific to each material used in the experiment. However, the thickness of the elastomer matrix layers on the top and bottom of the second layer (fiber/fiber mesh) may be varied, which nevertheless can be controlled by the amount of poured matrix substance and the area of rolling surface.
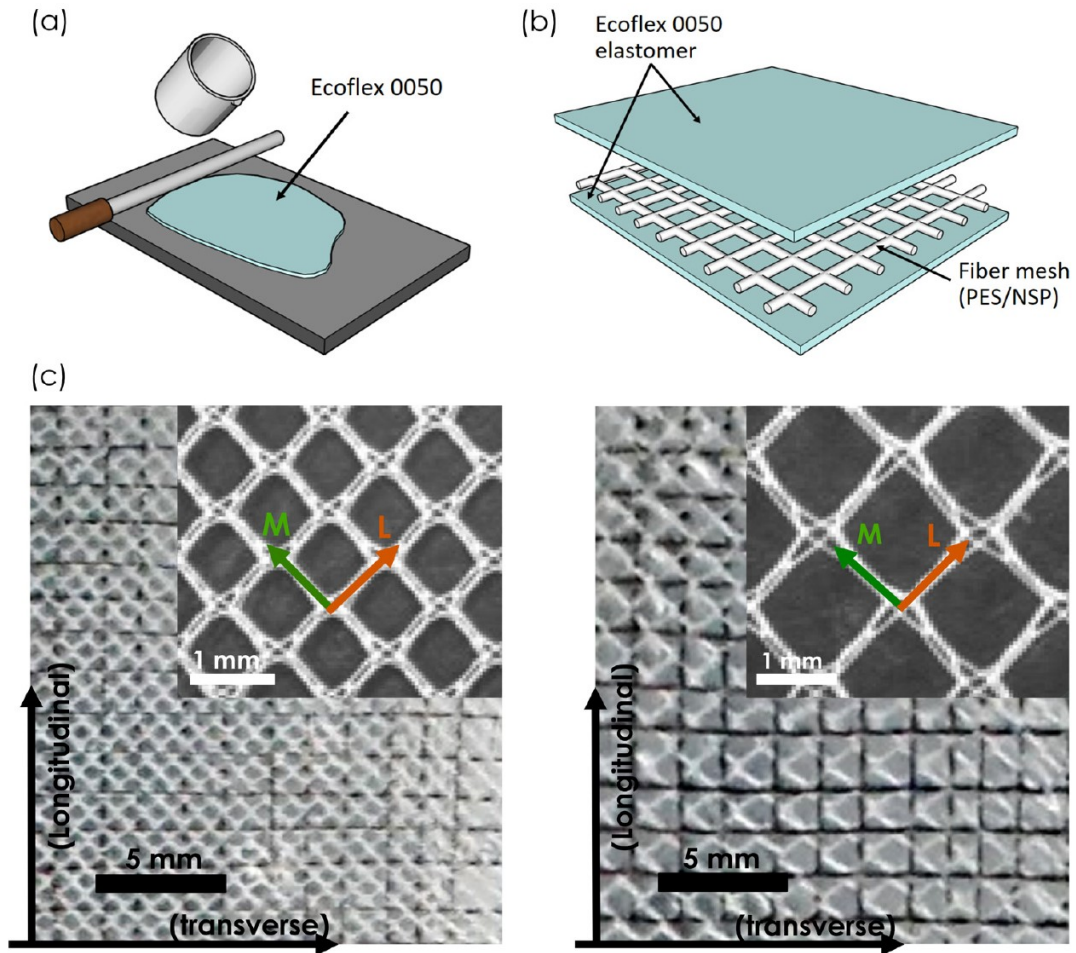
Figure 4.2: Sample preparation: (a) schematic diagram of composite sample preparation; (b) composite structure; (c) Local structure images of fabricated composite samples: PES-2 (left), PES-3 (right).

4.5.3 Uniaxial tensile test of the Ecoflex 0050 - fiber/fiber mesh composites

The width, length and thickness of the prepared Ecoflex 0050 matrix material and composite samples were measured using a caliper. An aspect ratio of length-to-width was maintained as 2:1 in all cases. Instron 5943 (Illinois Tool Works Inc., USA) was used to measure the stress-strain responses of the Ecoflex 0050 and the composites (see, Fig. 4.3). The test apparatus recorded the displacement and force as a function of time for each uniaxial tensile test. The extension rate was set to be 2.5mm/min for all cases to avoid/minimize the viscous responses.

4.5.4 Data Collection and Analysis

The uniaxial tensile test results were then used to determine the mechanical responses of the matrix, fibers, fiber meshes and composites. To compute strains, the displacement and gauge length were used. The corresponding stresses were calculated from the applied load and the cross-sectional area of the samples. For example, the principal strains and the engineering stresses were calculated using the relations of $\varepsilon = \Delta l / l_o$ and $\sigma = F/A_o = F/(w_o t_o)$, respectively, where l_o is the original sample length, w_o is the initial width, and t_o is the initial thickness which were measured using a caliper. The amount of extension, Δl, was then calculated as $\Delta l = l - l_o$ where l is the current length. To analyze the local microstructure deformations of the reinforced composites, mesh grids of $1.5mm \times 1.5mm$ were printed on the surfaces of each sample (see, Fig. 4.2 (c)). A Sony A6000 camera was used to capture the deformed images of the fiber meshes and the printed mesh grids which were then compared with the simulation results, predicted from the proposed model. The orientations of the fiber meshes prior to the deformation are shown in Fig. 4.2 (c) (PES-2 (left) and PES-3 (right)) where the fiber lines are orthogonal to each other and are tilted to form an angle of 45 degrees with respect to the longitudinal and transverse directions. The pore sizes of PES-2 and PES-3 fiber meshes are, respectively, $1mm \times 1mm$ and $1.5mm \times 1.5mm$ (see, Fig. 4.2 (c)).
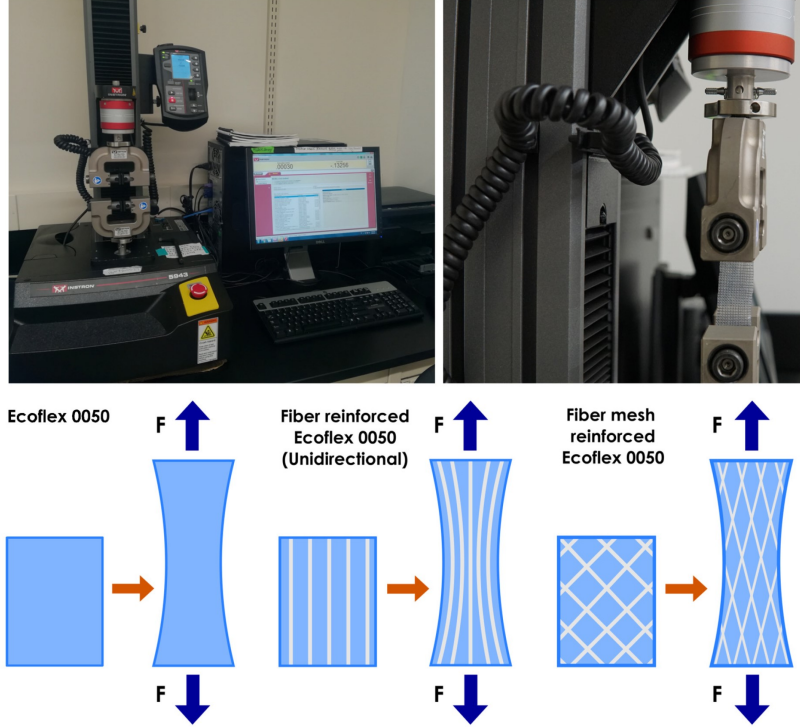
Figure 4.3: Experimental set up (top): uniaxial tensile test of elastomeric composite ($25mm \times 50mm$). Schematic illustration of the uniaxial strain of the unreinforced and reinforced elastomers (bottom).

4.6 Model implementation and discussions

A model implementation and comparison with experimental results are presented in this section to demonstrate the accuracy and utility of the proposed models. The response of Ecoflex 0050 (matrix material) is characterized by using the Mooney-Rivlin model (Eq. (4.13)) and the corresponding material parameters are found to be $\mu = 0.082\ MPa$ and $\kappa = 0.01\ Mpa$, respectively, with the fitting error less than 2% (see, Fig. 4.4). The obtained μ and κ values will then be used in the forthcoming analyses as the modulus of the matrix material. The schematic illustration of the model implementations is illustrated in Fig. 4.5, where E_1 and E_2 are the material parameters of the fibers, which will be determined using the proposed energy potentials (i.e. Eqs. (4.46) and (4.54)).
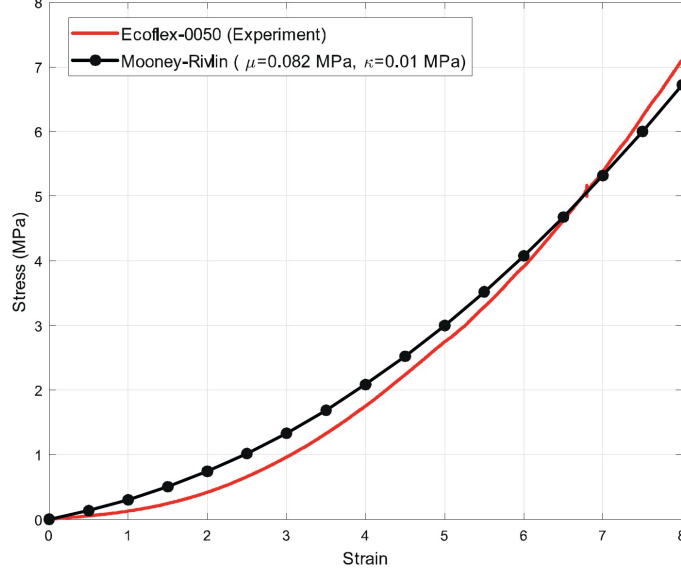
Figure 4.4: Stress-strain curves: Ecoflex-0050 and the Mooney Rivlin model.

4.6.1 Cases of the polynomial potential: PES-2 and PES-3 composites

The stress-strain curves of PES-2 and PES-3 fibers are shown in Fig. 4.6, where gradual stiffening phenomena are observed in both cases. Such moderate strain-stiffening responses of fibers may be accommodated by the proposed polynomial energy potential (Eq. (4.46)), from which the characterization parameters of fibers can be determined as $E_1 = 3.45\ MPa$ and $E_2 = 0.65\ MPa$ for PES-2, and $E_1 = 2.35\ MPa$ and $E_2 = -0.2\ MPa$ for PES-3 (see, Fig. 4.6).

Hence, the energy potential of the PES-2 composite can be obtained from Eqs. (4.13), (4.21), and (4.46) that

$$U(\mathbf{F}, \varepsilon, \mathbf{g}, p) = \frac{0.082}{2}(I_1 - 3) + \frac{0.01}{2}(I_2 - 3) + \frac{3.45}{3}\varepsilon^3 + \frac{0.65}{2}\varepsilon^2 + \frac{1}{2}\mathbf{g} \cdot \mathbf{g} - p(J - 1), \quad (4.84)$$

which, together with the Eq. (4.50), furnishes the following Euler equilibrium equation:

$$
\begin{aligned}
0 \ = \ & P_{iA,A} = 0.01(\chi_{i,AA}\chi_{j,C}\chi_{j,C} - \chi_{i,BA}\chi_{j,A}\chi_{j,B}) + 0.01\chi_{i,B}(2\chi_{j,CB}\chi_{j,C} \\
& -\chi_{j,AA}\chi_{j,B} - \chi_{j,A}\chi_{j,BA}) - p_{,A}\varepsilon_{ij}\varepsilon_{AB}\chi_{j,B} + [\frac{3.45}{4}(2\chi_{j,11}\chi_{j,1}\chi_{k,1}\chi_{k,1} \\
& +2\chi_{j,1}\chi_{j,1}\chi_{k,11}\chi_{k,1}) - 2.8\chi_{j,11}\chi_{j,1}]\chi_{i,1} + 0.082\chi_{i,AA} \\
& +[\frac{3.45}{4}(\chi_{j,1}\chi_{j,1})(\chi_{k,1}\chi_{k,1}) - \frac{2.8}{2}\chi_{j,1}\chi_{j,1} + \frac{2.15}{4}]\chi_{i,11} - \chi_{i,1111}. \quad (4.85)
\end{aligned}
$$
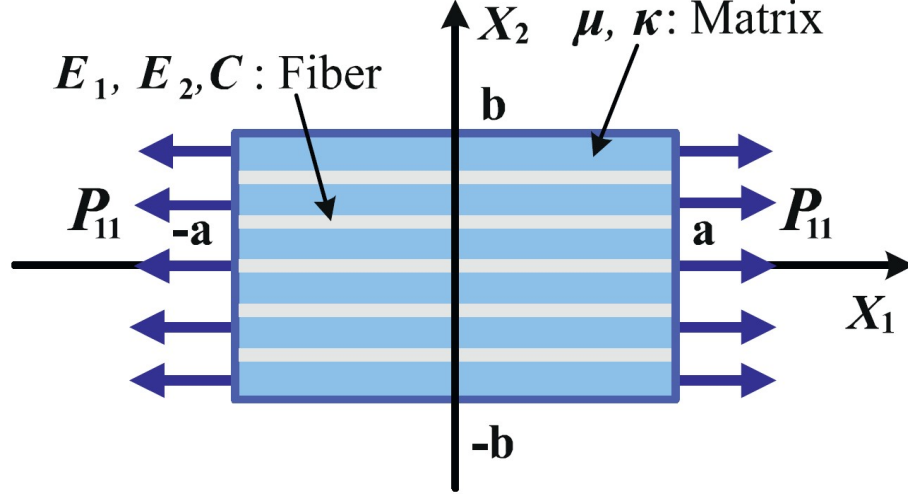
Figure 4.5: Schematic of the problem (unidirectional fiber composite): $2a = 50mm$ and $2b = 25mm$.

The solutions of the above system of PDEs can be uniquely determined by imposing the boundary conditions of (see, Fig. 4.5)

$$
\begin{aligned}
t_1 &= P_{11}, \ t_2 = P_{12} = 0 \text{ at } X_1 = a, \ -a \text{ and} \\
t_1 &= P_{21} = 0, \ t_2 = P_{22} = 0 \text{ at } X_2 = b, \ -b.
\end{aligned}
\tag{4.86}
$$

In the present study, we employ the Finite Element Method (FEM) to obtain the numerical solution of the PDEs system. Repeating the same process as illustrated in the above, the case of the PES-3 composite can also be simulated using the input parameters of $E_1 = 2.35 \ MPa$ and $E_2 = -0.2 \ MPa$.

It is shown in Fig. 4.7 that the proposed model successfully predicts the moderate strain-stiffening behaviors of the PES composites. More importantly, the proposed model directly estimates the resultant stress-strain curves of the intended composites, prior to the fabrication, by utilizing the predetermined material parameters of the matrix and fiber materials (i.e. no empirical back-fitting of the fabricated composites is required in the proposed model). This may be of more practical interest in the design of composite materials by reducing the fabrication cost of sample composites, since the responses of the intended composite can be instantly pre-estimated via the proposed model.

Lastly, considering the sharp variations in the fiber data readings (Fig. 4.6), repeated tests for fine tuning of the material parameters (E_1 and E_2) may be necessary
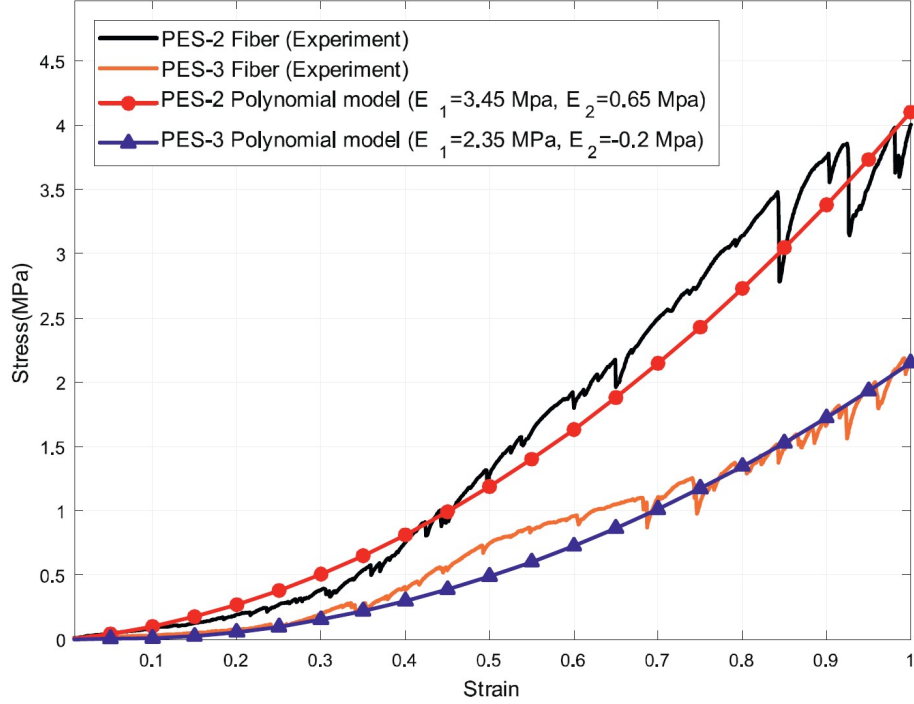
Figure 4.6: Stress-strain curves: PES-2 & PES-3 fibers and polynomial model of $W(\varepsilon) = \frac{1}{3}E_1\varepsilon^3 + \frac{1}{2}E_2\varepsilon^2$

which, however, were limited due to the shortage in fiber sample supplies during the current pandemic. At the same time, this may not necessarily restrict the practical utility of the proposed model, since the model provides reasonably accurate predictions in the general strain-stiffening responses of both the raw fiber materials and the resulting composites.

4.6.2 Cases of the exponential potential: NSP-8515 and NSP-8020 composites

Although, the polynomial energy potential demonstrated sufficient accuracy in the predictions of fiber composites with moderate strain-stiffening responses, it may not be ideal for the analyses of fibers and the resulting composites exhibiting rapid strain-stiffening behaviors, especially those arising at low strain levels (see, Fig. 4.8). In this case, an exponential form of energy potential (Eq. (4.54)) may be sought as a promising alternative through which the responses of NSP fibers can be characterized via the material parameters; $E_1 = 0.12 MPa$ and $E_2 = 1.25 MPa$ for NSP-8020,
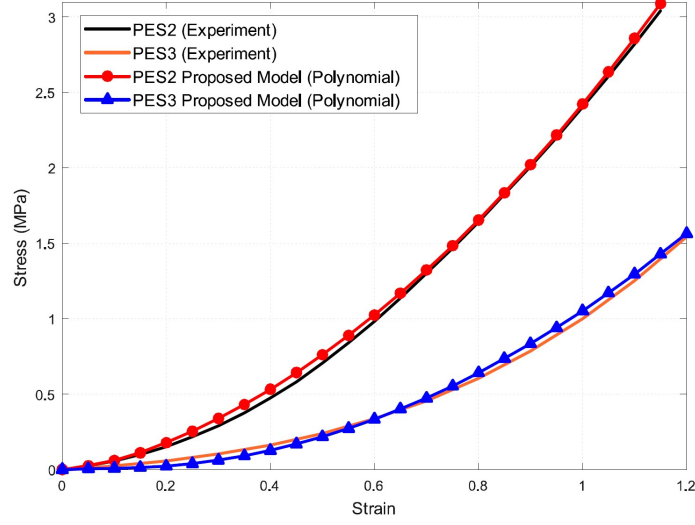
Figure 4.7: Stress-strain curves of PES composites predicted by the proposed polynomial model.

and $E_1 = 0.155MPa$ and $E_2 = 1.525MPa$ for NSP-8515, respectively. It is evident from Fig. 4.8 that the exponential energy potential provides sufficiently accurate descriptions of the stress-strain responses of NSP fibers unlike those estimated by the polynomial potential.
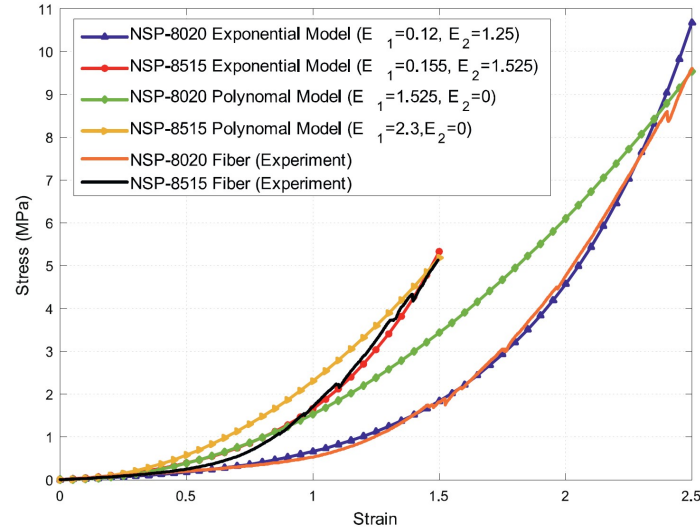
Figure 4.8: Stress-strain curves: NSP-8515 & NSP-8020 fibers and Exponential model of $W(\varepsilon) = E_1(E_2\varepsilon - 1)e^{E_2\varepsilon}$.

Therefore, combining the results in Eqs. (4.13), (4.21), and (4.54) the following

energy potential may be proposed for the constitutive description of the NSP-8020 composites

$$U(\mathbf{F}, \varepsilon, \mathbf{g}, p) = \frac{0.082}{2}(I_1 - 3) + \frac{0.01}{2}(I_2 - 3) + 0.12(1.25\varepsilon - 1)e(\exp(1.25\varepsilon))$$

$$+\frac{1}{2}\mathbf{g} \cdot \mathbf{g} - p(J - 1), \tag{4.87}$$

and thereby furnishes (see, Eqs. (4.57)-(4.58))

$$0 = P_{iA,A} = 0.01(\chi_{i,AA}\chi_{j,C}\chi_{j,C} - \chi_{i,BA}\chi_{j,A}\chi_{j,B})0.01\chi_{i,B}(2\chi_{j,CB}\chi_{j,C} \tag{4.88}$$

$$-\chi_{j,AA}\chi_{j,B} - \chi_{j,A}\chi_{j,BA}) - p_{,A}\varepsilon_{ij}\varepsilon_{AB}\chi_{j,B} - \chi_{i,1111}$$

$$+0.1875\left(\chi_{k,11}\chi_{k,1}-1\right)e[\exp(\frac{1.25}{2}\left(\chi_{j,1}\chi_{j,1}-1\right))]\chi_{i,1} + 0.082\chi_{i,AA}$$

$$+\frac{0.1875}{2}\left(\chi_{k,1}\chi_{k,1}-1\right)e[\exp(\frac{1.25}{2}\left(\chi_{j,1}\chi_{j,1}-1\right))][1.25\chi_{j,11}\chi_{j,1}\chi_{i,1} - \chi_{i,11}],$$

which serves as the associated Euler equilibrium equation. The solution of Eq. (4.88) is then obtained by imposing the admissible sets of boundary conditions as depicted in Eq. (4.86). The case of the NSP 8515 composite can also be simulated with the configuration parameters of $E_1 = 0.155MPa$ and $E_2 = 1.525MPa$, via the same procedure as demonstrated in the above and the corresponding results are summarized in Fig. 4.9. As illustrated in Fig. 4.9, the proposed exponential model accurately predicts the J-shaped stress-strain response of both the NSP-8020 and NSP-8515 composites for all strain levels. Similar to the polynomial case, only the pre-estimated material parameters of the matrix material and the NSP fibers are required in the predictions of the resultant properties of the intended composites and thus, no backfitting of the fabricated composite is necessary.

We remark that, in practice, the polynomial energy potential may be used for improved computational efficiency where strain-stiffening responses are insignificant. For composites exhibiting rapid strain-stiffening behaviors (J-shaped stress-strain responses), the exponential energy potential may better be considered to achieve greater prediction accuracy.

4.6.3   Cases of Euler-Almansi finite strain: PDMS and PU/D composites

The proposed model is sufficiently general to accommodate the strain-softening responses of fiber composites. In this section, we adopt the experimental results from
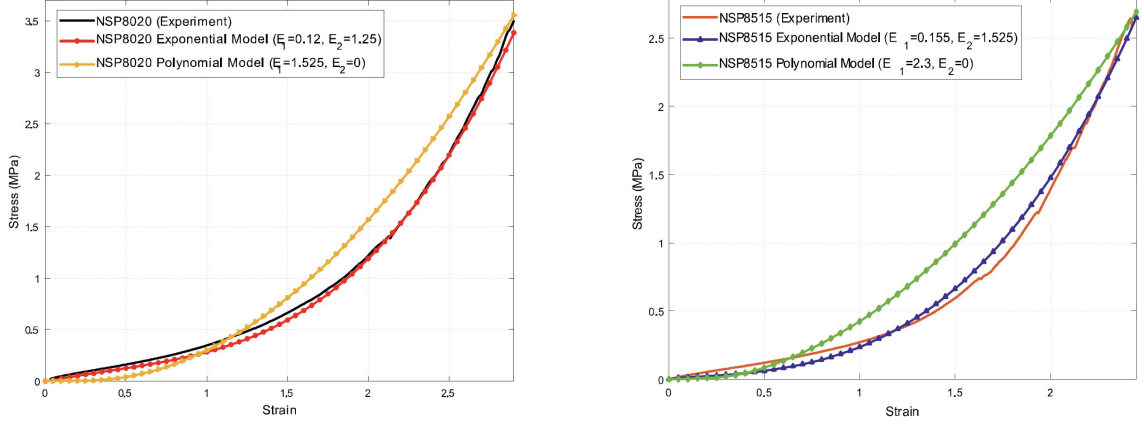
Figure 4.9: Stress-strain curves of the NSP composites predicted by the proposed exponential model.
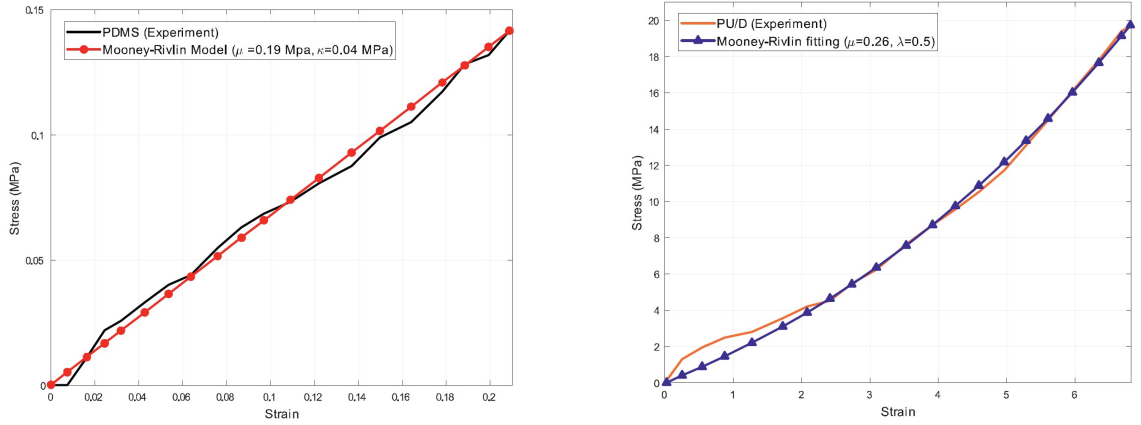
Figure 4.10: Stress-strain curves: PDMS and PU/D matrix materials.

the works of [126]-[127] and demonstrate the performance of the proposed Euler-Almansi strain integrated model. The tensile tests of two different types of composite materials are considered for this purpose. One is polydimethylsiloxane (PDMS) composites reinforced with graphite nanoplatelets (GNP) [126] and the other one is polyurethane (PU/D)- graphene nanocomposites [127].

Using Eq. (4.13) and the tensile test results in Fig. 4.10, the material parameters of PDMS and PU/D matrix materials are identified, respectively, as $\mu = 0.19 MPa$ and $\kappa = 0.04 MPa$, and $\mu = 0.26 MPa$ and $\kappa = 0.5 MPa$ which are then integrated into the energy potential of the polynomial type (Eq. (4.46)).

For example, in the case of the PDMS composite, we find

$$U(\mathbf{F}, \varepsilon, \mathbf{g}, p) = \frac{0.19}{2}(I_1 - 3) + \frac{0.04}{2}(I_2 - 3) - \frac{53}{3}\varepsilon^3 + \frac{12.7}{2}\varepsilon^2 + \frac{1}{2}\mathbf{g} \cdot \mathbf{g} - p(J - 1), \quad (4.89)$$

109

where the corresponding energy variation of the GNP fibers, within Euler-Almansi strain measure, can be evaluated as (see, also, Eqs. (4.60)-(4.62))

$$
\begin{aligned}
\dot{W}(\varepsilon) &= W_\varepsilon \varepsilon_{F_{iA}} \dot{F}_{iA} = (-53\varepsilon^2 + 12.7E_2\varepsilon)\varepsilon_{F_{iA}} \dot{F}_{iA} \\
&= [\frac{-53}{4(F_{kE}F_{kF}D_ED_F)^2} + \frac{40.3}{2F_{kE}F_{kF}D_ED_F} - 6.9]\frac{F_{iB}D_BD_A}{(F_{jC}F_{jD}D_CD_D)^2}\dot{\chi}_{i,1} \quad (4.90)
\end{aligned}
$$

Hence, we obtain the following Euler equilibrium equation (refer, Eqs. (4.66)-(4.67))

$$
\begin{aligned}
0 =\ & P_{iA,A} = 0.04(\chi_{i,AA}\chi_{j,C}\chi_{j,C} - \chi_{i,BA}\chi_{j,A}\chi_{j,B}) + 0.04\chi_{i,B}(2\chi_{j,CB}\chi_{j,C} \\
& -\chi_{j,AA}\chi_{j,B} - \chi_{j,A}\chi_{j,BA}) + [\frac{-53}{4(\chi_{k,1}\chi_{k,1})^2} + \frac{40.3}{2\chi_{k,1}\chi_{k,1}} - 6.9](\frac{\chi_{i,11}}{(\chi_{j,1}\chi_{j,1})^2} \\
& -\frac{4\chi_{i,1}\chi_{k,11}\chi_{k,1}}{(\chi_{j,1}\chi_{j,1})^3}) + 0.19\chi_{i,AA} + [-40.3\frac{\chi_{j,11}\chi_{j,1}}{(\chi_{k,1}\chi_{k,1})^4} + 53\frac{\chi_{j,11}\chi_{j,1}}{(\chi_{k,1}\chi_{k,1})^5}]\chi_{i,1} \\
& -p_{,A}\varepsilon_{ij}\varepsilon_{AB}\chi_{j,B} - \chi_{i,1111}, \quad (4.91)
\end{aligned}
$$

which solves the responses of the PDMS composites subjected to axial tension (imposed via Eq. (4.86)). The same procedure may be repeated with the configuration parameters of $\mu = 0.26MPa$, $\kappa = 0.5MPa$, $E_1 = -4.5MPa$ and $E_2 = 18.7MPa$ for the case of the PU/D graphene nanocomposites.

The results in Fig. 4.11 indicate that the obtained Euler-Almansi integrated model produces reasonably accurate estimations of the stress-strain curves of both the PDMS-GNP and the PU/D-graphene composites experiencing strain-softening. By integrating the previously obtained results of the higher order polynomial and/or exponential types of energy potentials, the proposed model can be further generalized to accommodate a wide range of composites exhibiting more aggressive strain-softening responses. However, due to the paucity of experimental resources (especially with the current pandemic), attempts for quantitative and qualitative analyses vis a vis the strain-softening behaviors of various types of composites are substantially limited which certainly deserve further attention.

4.6.4 Cases of bidirectional fiber composites: Ecoflex 0050 - PES fiber mesh

In this section, we demonstrate the implementation of the obtained bidirectional model in the deformation and local structure analyses of Ecoflex 0050 matrix material reinforced with PES fiber mesh. The problem description of the bidirectional fiber
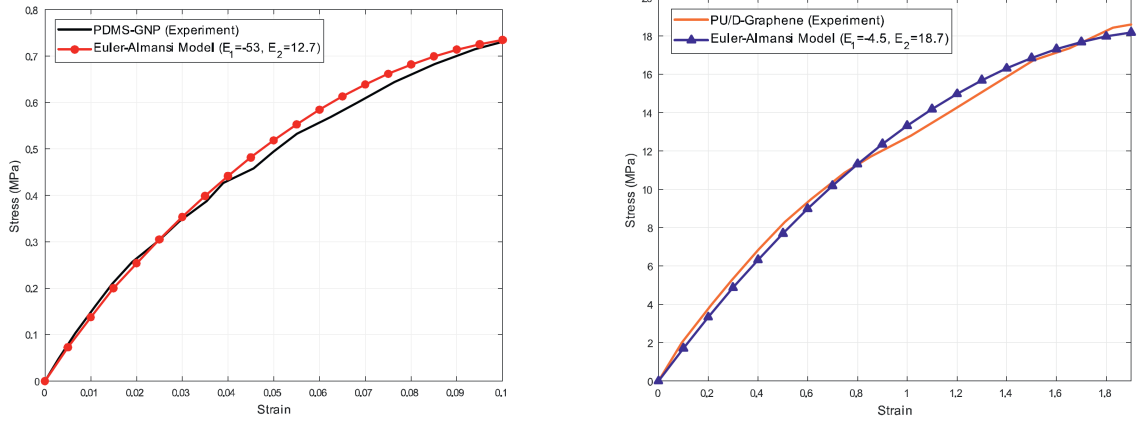
Figure 4.11: Stress-strain curves of PDMS & PU/D composites predicted by Euler-Almansi strain integrated model.

composite subjected to axial tension with 45 degrees orientation of PES fiber mesh is illustrated in Fig. 4.12. The corresponding material parameters of Ecoflex 0050 matrix material ($\mu = 0.1013MPa$, $\kappa = -0.14MPa$), PES-2 ($E = 3.21MPa, C = 1.962MPa, T = 2.2MPa$) and PES-3 ($E = 1.457MPa, C = 0.874MPa, T = 7MPa$) fiber meshes are obtained from the inhouse experiments. We note that the torsional parameter of PES fiber mesh (T) which is coupled with the deformation angles between the two fibers (i.e. $g_1 \cdot g_2$; see, also, Fig. 4.1) were indirectly measured using the deformed configuration of the composites (see, Fig. 4.17).
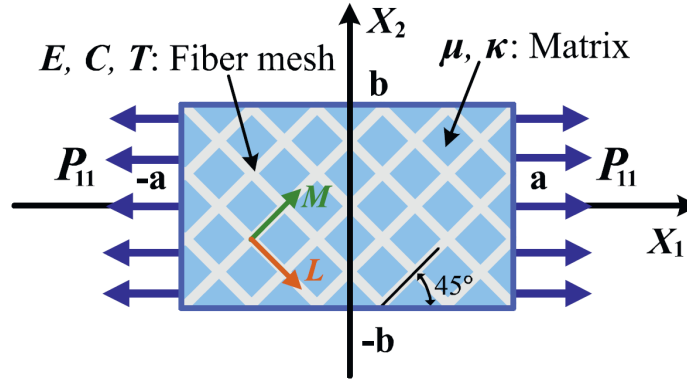
Figure 4.12: Schematic of the problem (bidirectional fiber composite): $2a = 50mm$ and $2b = 25mm$.

Thus, from Eqs. (4.13), (4.21), (4.51), and (4.75)-(4.76), we find in the case of

111

the PES-2 fiber mesh composite that

$$U(\mathbf{F},\varepsilon,\mathbf{g},p) = \frac{0.082}{2}(I_1 - 3) + \frac{0.01}{2}(I_2 - 3) + \frac{3.21}{2}(\varepsilon_1^2 + \varepsilon_2^2) + \frac{1.962}{2}(\mathbf{g}_1 \cdot \mathbf{g}_1 + \mathbf{g}_2 \cdot \mathbf{g}_2)$$
$$+ \frac{2.2}{2}\mathbf{g}_1 \cdot \mathbf{g}_2 - p(J - 1), \tag{4.92}$$

and thereby obtain the following Euler equilibrium equation (see, Eqs. (4.80)-(4.81))

$$0 = P_{iA,A} = 0.082\chi_{i,AA} + 0.01(\chi_{i,AB}\chi_{j,A}\chi_{j,B} - \chi_{i,AA}\chi_{j,C}\chi_{j,C}) + 0.01\chi_{i,B}(2\chi_{j,BC}\chi_{j,C}$$
$$-\chi_{j,AA}\chi_{j,B} - \chi_{j,A}\chi_{j,AB}) - p_{,A}\varepsilon_{ij}\varepsilon_{AB}\chi_{j,B} + \frac{3.21}{2}(\chi_{i,AB}\chi_{j,C}\chi_{j,D} + \chi_{i,B}\chi_{j,AC}\chi_{j,D}$$
$$+\chi_{i,B}\chi_{j,C}\chi_{j,D,A})L_A L_B L_C L_D - \frac{3.21}{2}\chi_{i,AB}L_A L_B + \frac{3.21}{2}(\chi_{i,AB}\chi_{j,C}\chi_{j,D} + \chi_{i,B}\chi_{j,AC}\chi_{j,D}$$
$$+\chi_{i,B}\chi_{j,C}\chi_{j,AD})M_A M_B M_C M_D - \frac{3.21}{2}\chi_{i,AB}M_A M_B + \frac{1.962}{2}\chi_{i,ABCD}(L_A L_B L_C L_D$$
$$+M_A M_B M_C M_D) + \frac{2.2}{2}\chi_{i,ABCD}(L_A L_B M_C M_D + M_A M_B L_C L_D), \tag{4.93}$$

which, together with Eqs. (4.82)-(4.83) and (4.86), solve unknown potentials of χ_1 and χ_2. The same procedure can be performed for the PES-3 fiber mesh composite with the parameters of $E = 1.457 MPa, C = 0.874 MPa$ and $T = 7 MPa$. The obtained solutions are then post-processed via the mapping:

$$\boldsymbol{\chi} = \chi_1(\mathbf{X})\mathbf{e}_1 + \chi_2(\mathbf{X})\mathbf{e}_2 \text{ (Deformed position)}, \text{ where } \mathbf{X} = X_1\mathbf{E}_1 + X_2\mathbf{E}_2 \text{ (Initial position)}, \tag{4.94}$$

to obtain the deformed configuration of the composites for further deformation analyses. Fig. 4.13 illustrates the averaged mesh angle distributions of the PES fiber mesh composites at 50% elongation. It is observed that the PES-2 fiber mesh composite experiences more drastic mesh angle changes than those of the PES-3 case, as approach the center zone where the maximum shear deformation arises. The rate of change in mesh angle configurations is primarily associated with the torsional rigidity of the two orthogonally aligned fibers. In the proposed model, this is accommodated by the torsional kinematics between two adjoining fibers via the parameter T (see, Eq. (4.75) and Fig. 4.1). For example, higher T value will result moderate/small angle changes and vice versa (see, also, the sensitivity analysis of T in Fig. 4.17). As a result, the proposed bidirectional model closely estimates the mesh angle distributions of both the PES-2 and the PES-3 fiber mesh composites throughout the entire
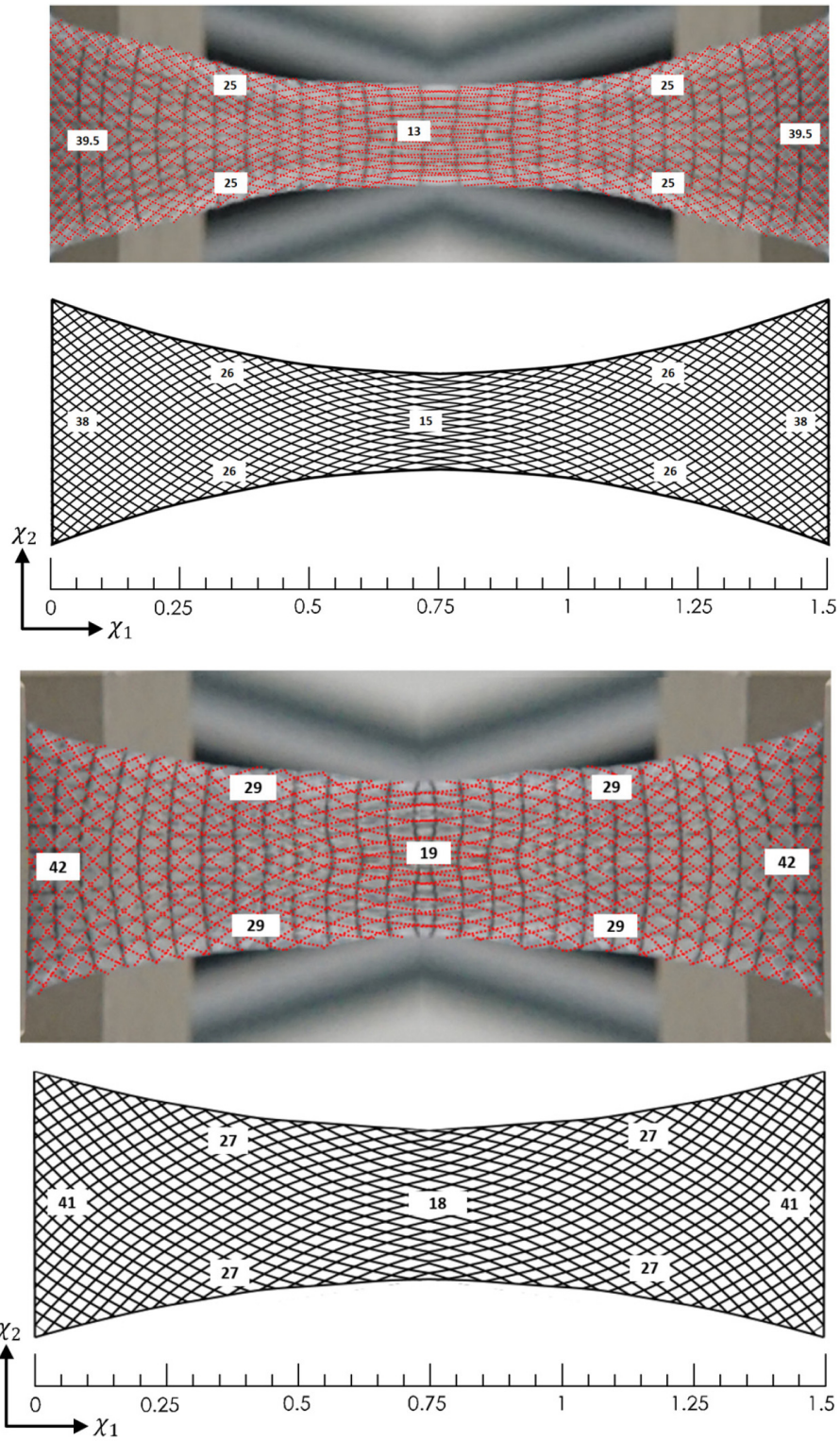
Figure 4.13: Mesh angle distributions at 50% elongation: PES-2 (top), PES-3 (bottom).

domain of interest (see, Fig. 4.13).

In particular, using the deformation map (Eq. (4.94)), we compute the deformation and orientation of the local structure of the composites (i.e. a unit cell structure of the PES fiber meshes). The results are then compared with those obtained from the experimental results to examine prediction accuracy of the proposed model. The magnified images in Fig. 4.14 clearly indicate that the deformation profiles simulated from the obtained bidirectional model demonstrate good agreement with the local configurations of the deformed fiber mesh in both PES-2 and PES-3 cases.

We also estimate the deformation profiles and the associated shear strain distributions of the PES composites to evaluate the utility and accuracy of the proposed model in macroscale deformation analyses. Using the individual cell structures of the PES fiber meshes and the mesh grid of $1.5mm \times 1.5mm$, printed on the surfaces of the PES composites, the material points of the deformed composites at the intersections of the mesh grids are post-processed via the Matlab image processing toolbox and are subsequently used to plot the shear strain distributions. For the purposes of cross-examination, the deformation maps of χ_1 and χ_2 are also computed directly from the proposed bidirectional model (i.e. Eqs. (4.92)-(4.93)) through which the corresponding shear strains are computed via the relation:

$$\gamma_{xy} = \alpha + \beta, \text{ where } \tan^{-1}(\frac{\chi_{2,1}}{1 + \chi_{1,1}}) = \alpha \text{ and } \tan^{-1}(\frac{\chi_{1,2}}{1 + \chi_{2,2}}) = \beta. \qquad (4.95)$$

It is apparent from the results in Fig. 4.15 that the proposed bidirectional model successfully assimilates the shear strain distributions of both the PES-2 and the PES-3 composites at 50% and 100% strain levels. More importantly, the proposed model predicts the smooth and continuous shear strain fields throughout the entire domain of interest as opposed to those obtained from the classical (first-order) continuum theory where significant discontinuities are observed (see, also, [85]–[88]). The phenomenologically compatible results, in the cases of pantographic structures (without matrix materials), can also be found in the work of [85], [112] (see, for example, Figs. 13, 14 and 18 in [112]).

Lastly, Fig. 4.16 (a)-(d) illustrate the χ_1 and χ_2 deformation profiles of the PES
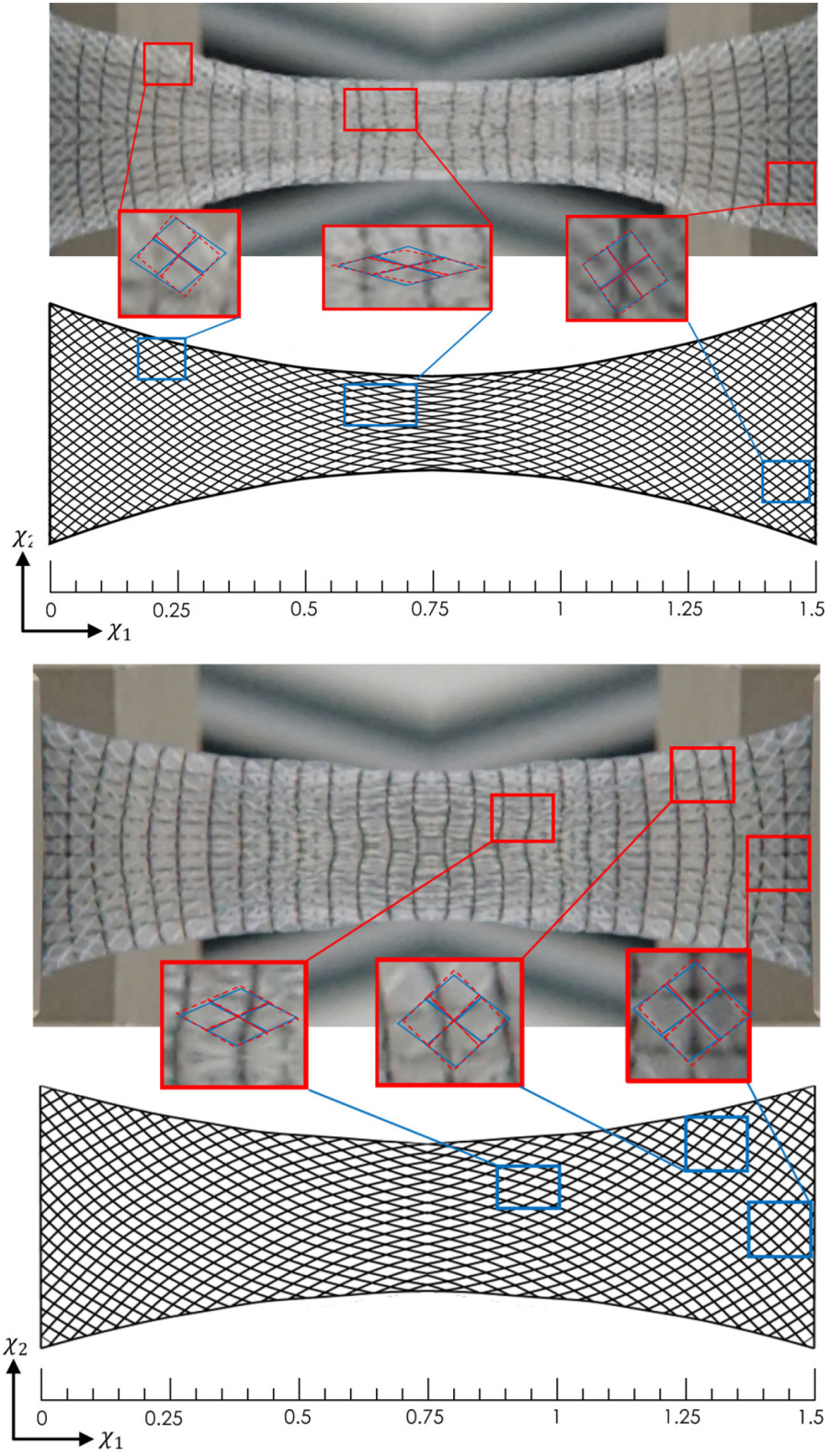
Figure 4.14: Local configurations of the fiber mesh at 50% elongation: PES-2 (top), PES-3 (bottom).

115
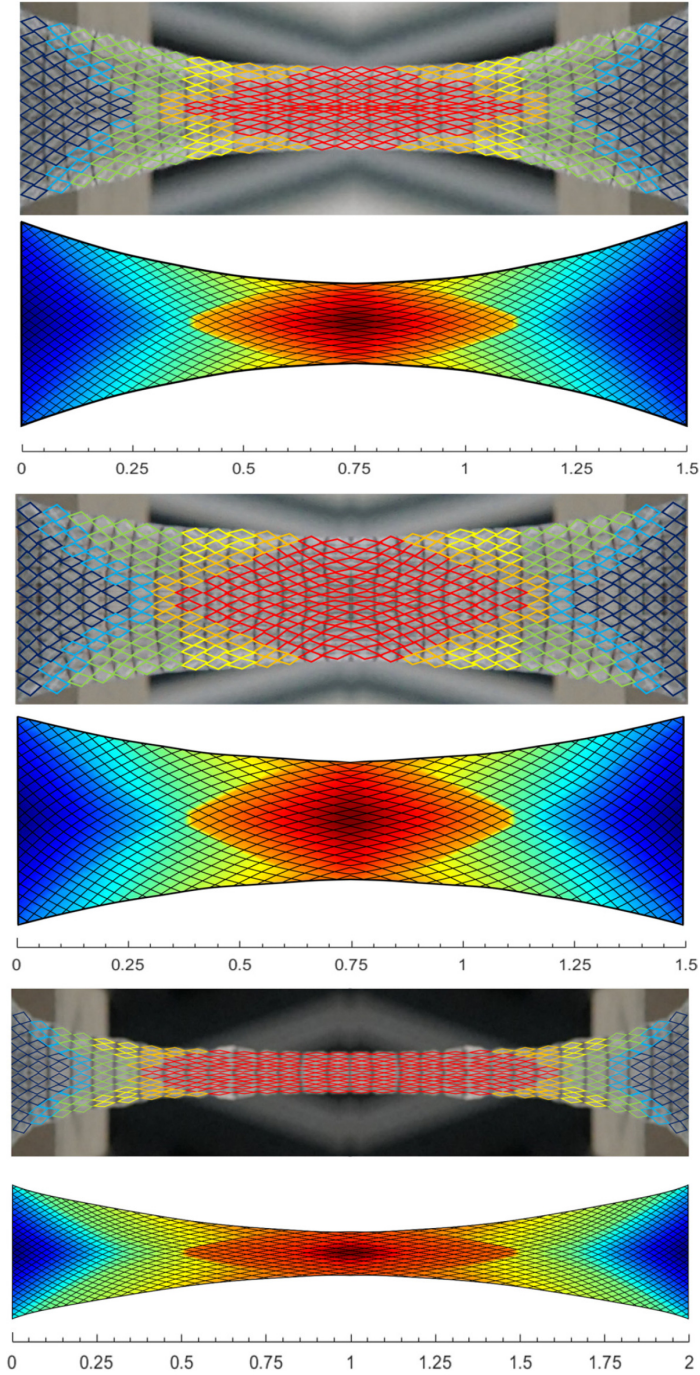
Figure 4.15: Shear strain distributions: PES-2 50% (top); PES-3 50% (middle); PES-2 100% (bottom).

composites at 50%, 93% and 100% elongations. In the plots, the corresponding deformation profiles are normalized by their initial length scales (i.e. L_o and W_o) for compact demonstrations. Despite the uncertainties arising in the Matlab image

processing and curve fittings, the proposed bidirectional model produces reasonably accurate predictions of the overall deformation profiles of the composites in all strain levels except the χ_2 profiles at 93% (PES-2) and 100% (PES-3) strain levels. This discrepancy may be attributable to the use of Mooney-Rivlin strain energy in the modeling of Ecoflex 0050 matrix material, knowing the fact that Mooney-Rivlin model is generally valid for strains less than 100% elongation (see, [105]-[106]). It is rational to believe that a more comprehensive type of energy potential such as Ogden model [106] may be suitable for these cases which is, however, beyond the scope of the present study, yet is certainly of more practical interest.
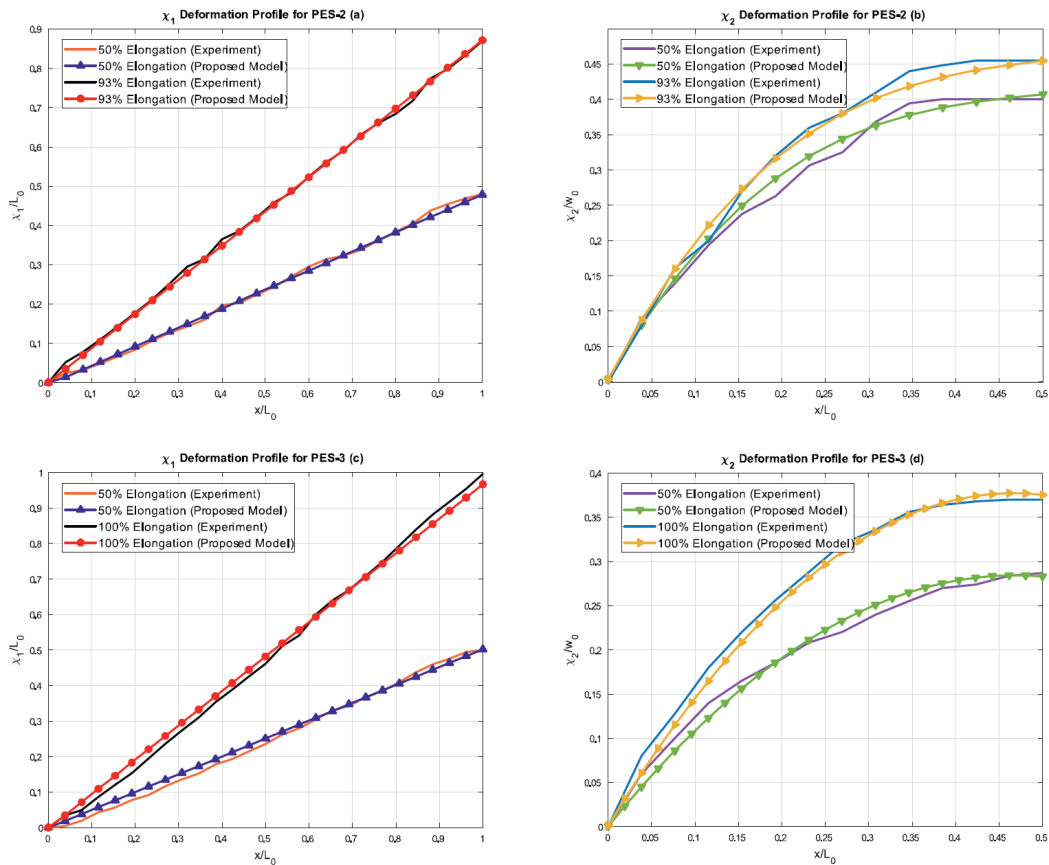
Figure 4.16: Deformation profiles: (a) χ_1 (PES-2); (b) χ_2 (PES-2); (c) χ_1 (PES-3); (a) χ_2 (PES-3).

4.7 Finite element analysis of the 4th order coupled PDE

To demonstrate the finite element analysis (FEA) procedures, we have chosen the system of PDEs obtained from the Euler – Almansi strain integrate model, which is the most general form of the PDEs system among all reported cases. The rest of the cases will follow the similar process.

The system of PDEs in Eqs. (4.51) and (4.91) are 4th order coupled differential equations. The case of such less regular PDEs system deserves delicate mathematical treatment and is of particular practical interest. Therefore, it may not be trivial to report the associated FEA procedure. For preprocessing, Eqs. (4.51) and (4.91) may be rearranged into the following form:

$$
\begin{aligned}
0 \;=\; & \mu(Q + \chi_{1,22}) + \kappa(Q + E_{,2})(CC + EE + DD + FF) \\
& -\kappa(Q + C_{,2} + E_{,1} + E_{,2})(CC + CE + EC + EE + DD \\
& +DF + FD + FF) + \kappa(C + E)(2QC + 2E_{,1}E + 2C_{,2}C \\
& +2E_{,2}E - QC - QE - E_{,2}C - E_{,2}E - CQ - CE_{,1} \\
& -EC_{,2} - EE_{,2} + 2RD + 2F_{,1}F + 2D_{,2}D + 2F_{,2}F - RD \\
& -RF - F_{,2}D - F_{,2}F - DR - DF_{,1} - FD_{,2} - FF_{,2}) \\
& +[\frac{E_1}{4}\frac{1}{(CC + DD)^2} - (\frac{E_1 + E_2}{2})\frac{1}{(CC + DD)} + (\frac{E_1}{4} + \frac{E_2}{2})] \\
& (\frac{Q}{(CC + DD)^2} - \frac{4C(QC + RD)}{(CC + DD)^3}) + [\frac{E_1 + E_2}{(CC + DD)^2} \\
& -\frac{E_1}{(CC + DD)^3}]\frac{(QC + RD)C}{(CC + DD)^2} - A_0\chi_{2,2} + B_0\chi_{2,1} - cQ_{,11},
\end{aligned}
$$

$$
\begin{aligned}
0 \;=\;& \mu(R + \chi_{2,22}) + \kappa(R + F_{,2})(CC + EE + DD + FF) \\
&- \kappa(R + D_{,2} + F_{,1} + F_{,2})(CC + CE + EC + EE + DD \\
&+ DF + FD + FF) + \kappa(D + F)(2QC + 2E_{,1}E + 2C_{,2}C \\
&+ 2E_{,2}E - QC - QE - E_{,2}C - E_{,2}E - CQ - CE_{,1} \\
&- EC_{,2} - EE_{,2} + 2RD + 2F_{,1}F + 2D_{,2}D + 2F_{,2}F - RD \\
&- RF - F_{,2}D - F_{,2}F - DR - DF_{,1} - FD_{,2} - FF_{,2}) \\
&+ [\frac{E_1}{4}\frac{1}{(CC + DD)^2} - (\frac{E_1 + E_2}{2})\frac{1}{(CC + DD)} + (\frac{E_1}{4} + \frac{E_2}{2})] \\
&(\frac{R}{(CC + DD)^2} - \frac{4D(QC + RD)}{(CC + DD)^3}) + [\frac{E_1 + E_2}{(CC + DD)^2} \\
&- \frac{E_1}{(CC + DD)^3}]\frac{(QC + RD)D}{(CC + DD)^2} + A_0\chi_{1,2} - B_0\chi_{1,1} - cR_{,11},
\end{aligned}
$$

$$
\begin{aligned}
0 \;=\;& Q - \chi_{1,11}, \; 0 = R - \chi_{2,11}, \; 0 = C - \chi_{1,1}, \; 0 = D - \chi_{2,1}, \\
0 \;=\;& E - \chi_{1,2}, \; 0 = F - \chi_{2,2}, \; 0 = A - \mu(Q + \chi_{1,22}) - cQ_{,11}, \\
0 \;=\;& B - \mu(R + \chi_{2,22}) - cR_{,11}, \tag{4.96}
\end{aligned}
$$

where $Q = \chi_{1,11}$, $R = \chi_{2,11}$, $C = \chi_{1,1}$, $D = \chi_{2,1}, E = \chi_{1,2}$, and $F = \chi_{2,2}$. Hence, the order of differential equations is reduced from the three coupled equations of the 4th order to ten coupled equations of the 2nd order. Especially, the non-linear terms in the above equations (e.g. $A\chi_{2,2}, B\chi_{2,1}$ etc...) can be systematically treated via the Picard iterative procedure and/or Newton method;

$$
\begin{aligned}
-A^{initial}\chi_{2,2}^{initial} + B^{initial}\chi_{2,1}^{initial} &\implies -A_0\chi_{2,2}^0 + B_0\chi_{2,1}^0 \\
A^{initial}\chi_{1,2}^{initial} - B^{initial}\chi_{1,1}^{initial} &\implies A_0\chi_{1,2}^0 - B_0\chi_{1,1}^0, \tag{4.97}
\end{aligned}
$$

where the estimated values of A, B continue to be updated based on their previous estimations (e.g. A_1 and B_1 are refreshed by their previous estimations of A_o and B_o) as iteration progresses and similarly for the rest of non-linear terms.

Also, the weight forms of Eq. (4.96) can be found as

$$
\begin{aligned}
0 \;=\; & \int_{\Omega} w_1\big(\mu(Q + \chi_{1,22}) + \kappa(Q + E_{,2})(CC + EE + DD + FF) \\
& -\kappa(Q + C_{,2} + E_{,1} + E_{,2})(CC + CE + EC + EE + DD \\
& +DF + FD + FF) + \kappa(C + E)(2QC + 2E_{,1}E + 2C_{,2}C \\
& +2E_{,2}E - QC - QE - E_{,2}C - E_{,2}E - CQ - CE_{,1} \\
& -EC_{,2} - EE_{,2} + 2RD + 2F_{,1}F + 2D_{,2}D + 2F_{,2}F - RD \\
& -RF - F_{,2}D - F_{,2}F - DR - DF_{,1} - FD_{,2} - FF_{,2}) \\
& +[\frac{E_1}{4}\frac{1}{(CC+DD)^2} - (\frac{E_1 + E_2}{2})\frac{1}{(CC+DD)} + (\frac{E_1}{4} + \frac{E_2}{2})] \\
& (\frac{Q}{(CC+DD)^2} - \frac{4C(QC+RD)}{(CC+DD)^3}) + [\frac{E_1 + E_2}{(CC+DD)^2} \\
& -\frac{E_1}{(CC+DD)^3}]\frac{(QC+RD)C}{(CC+DD)^2} - A_0\chi_{2,2} + B_0\chi_{2,1} - cQ_{,11})d\Omega,
\end{aligned}
$$

$$
\begin{aligned}
0 \;=\; & \int_{\Omega} w_2\big(\mu(R + \chi_{2,22}) + \kappa(R + F_{,2})(CC + EE + DD + FF) \\
& -\kappa(R + D_{,2} + F_{,1} + F_{,2})(CC + CE + EC + EE + DD \\
& +DF + FD + FF) + \kappa(D + F)(2QC + 2E_{,1}E + 2C_{,2}C \\
& +2E_{,2}E - QC - QE - E_{,2}C - E_{,2}E - CQ - CE_{,1} \\
& -EC_{,2} - EE_{,2} + 2RD + 2F_{,1}F + 2D_{,2}D + 2F_{,2}F - RD \\
& -RF - F_{,2}D - F_{,2}F - DR - DF_{,1} - FD_{,2} - FF_{,2}) \\
& +[\frac{E_1}{4}\frac{1}{(CC+DD)^2} - (\frac{E_1 + E_2}{2})\frac{1}{(CC+DD)} + (\frac{E_1}{4} + \frac{E_2}{2})] \\
& (\frac{R}{(CC+DD)^2} - \frac{4D(QC+RD)}{(CC+DD)^3}) + [\frac{E_1 + E_2}{(CC+DD)^2} \\
& -\frac{E_1}{(CC+DD)^3}]\frac{(QC+RD)D}{(CC+DD)^2} + A_0\chi_{1,2} - B_0\chi_{1,1} - cR_{,11})d\Omega,
\end{aligned}
$$

$$0 = \int_{\Omega} w_3(Q - \chi_{1,11})d\Omega, \ 0 = \int_{\Omega} w_4(R - \chi_{2,11})d\Omega,$$

$$0 = \int_{\Omega} w_5(C - \chi_{1,1})d\Omega, \ 0 = \int_{\Omega} w_6(D - \chi_{2,1})d\Omega,$$

$$0 = \int_{\Omega} w_7(E - \chi_{1,2})d\Omega, \ 0 = \int_{\Omega} w_8(F - \chi_{2,2})d\Omega,$$

$$0 = \int_{\Omega} w_9(A - \mu(Q + \chi_{1,22}) - cQ_{,11})d\Omega,$$

$$0 = \int_{\Omega} w_{10}(B - \mu(R + \chi_{2,22}) - cR_{,11})d\Omega. \tag{4.98}$$

Thus, we apply integration by part and the Green-Stokes' theorem, (e.g. $\mu \int_{\Omega^e} w_1 \chi_{1,22} d\Omega = -\mu \int_{\Omega^e} w_{1,2} \chi_{1,2} d\Omega + \mu \int_{\partial \Gamma} w_1 \chi_{1,2} N d\Gamma$) and thereby obtain the following weak forms of Eq. (4.98)

$$
\begin{aligned}
0 = \int_{\Omega} & (\mu w_1 Q - \mu w_{1,2} \chi_{1,2} + \kappa w_1(Q + E_{,2})(CC + EE + DD + FF) \\
& -\kappa w_1(Q + C_{,2} + E_{,1} + E_{,2})(CC + CE + EC + EE + DD \\
& +DF + FD + FF) + \kappa w_1(C + E)(2QC + 2E_{,1}E + 2C_{,2}C \\
& +2E_{,2}E - QC - QE - E_{,2}C - E_{,2}E - CQ - CE_{,1} \\
& -EC_{,2} - EE_{,2} + 2RD + 2F_{,1}F + 2D_{,2}D + 2F_{,2}F - RD \\
& -RF - F_{,2}D - F_{,2}F - DR - DF_{,1} - FD_{,2} - FF_{,2}) \\
& +[\frac{E_1}{4}\frac{1}{(CC+DD)^2} - (\frac{E_1 + E_2}{2})\frac{1}{(CC+DD)} + (\frac{E_1}{4} + \frac{E_2}{2})] \\
& (\frac{Q}{(CC+DD)^2} - \frac{4C(QC+RD)}{(CC+DD)^3}) + [\frac{E_1 + E_2}{(CC+DD)^2} \\
& -\frac{E_1}{(CC+DD)^3}]w_1\frac{(QC+RD)C}{(CC+DD)^2} - A_0 w_1 \chi_{2,2} + B_0 w_1 \chi_{2,1} + c w_{1,1} Q_{,1})d\Omega \\
& +\mu \int_{\partial \Gamma} w_1 \chi_{1,2} N d\Gamma - c \int_{\partial \Gamma} w_1 Q_{,1} N d\Gamma,
\end{aligned}
$$

$$
\begin{aligned}
0 \;=\; & \int_{\Omega}(w_2\mu R - w_{2,2}\mu\chi_{2,2} + \kappa w_2(R+F_{,2})(CC+EE+DD+FF) \\
& -\kappa w_2(R+D_{,2}+F_{,1}+F_{,2})(CC+CE+EC+EE+DD \\
& +DF+FD+FF) + \kappa w_2(D+F)(2QC+2E_{,1}E+2C_{,2}C \\
& +2E_{,2}E-QC-QE-E_{,2}C-E_{,2}E-CQ-CE_{,1} \\
& -EC_{,2}-EE_{,2}+2RD+2F_{,1}F+2D_{,2}D+2F_{,2}F-RD \\
& -RF-F_{,2}D-F_{,2}F-DR-DF_{,1}-FD_{,2}-FF_{,2}) \\
& +[\frac{E_1}{4}\frac{1}{(CC+DD)^2} - (\frac{E_1+E_2}{2})\frac{1}{(CC+DD)} + (\frac{E_1}{4}+\frac{E_2}{2})] \\
& (\frac{R}{(CC+DD)^2} - \frac{4D(QC+RD)}{(CC+DD)^3}) + [\frac{E_1+E_2}{(CC+DD)^2} \\
& -\frac{E_1}{(CC+DD)^3}]w_2\frac{(QC+RD)D}{(CC+DD)^2} + A_0w_2\chi_{1,2} - B_0w_2\chi_{1,1} + cw_{2,1}R_{,1})d\Omega \\
& +\mu\int_{\partial\Gamma}w_2\chi_{2,2}Nd\Gamma - c\int_{\partial\Gamma}w_2R_{,1}Nd\Gamma,
\end{aligned}
$$

$$
0 \;=\; \int_{\Omega}(w_3Q + w_{3,1}\chi_{1,1})d\Omega - \int_{\partial\Gamma}w_3\chi_{1,1}Nd\Gamma,
$$

$$
0 \;=\; \int_{\Omega}(w_4R + w_{4,1}\chi_{2,1})d\Omega - \int_{\partial\Gamma}w_{4,1}\chi_{2,1}Nd\Gamma,
$$

$$
0 \;=\; \int_{\Omega}(w_5C - w_5\chi_{1,1})d\Omega, \;\; 0 = \int_{\Omega}w_6(D - \chi_{2,1})d\Omega,
$$

$$
0 \;=\; \int_{\Omega}w_7(E - \chi_{1,2})d\Omega, \;\; 0 = \int_{\Omega}w_8(F - \chi_{2,2})d\Omega,
$$

$$
0 \;=\; \int_{\Omega}(w_9A - \mu w_9Q + \mu w_{9,2}\chi_{1,2} + cw_{9,1}Q_{,1})d\Omega - \int_{\partial\Gamma}\mu w_9\chi_{1,2}Nd\Gamma \\
- \int_{\partial\Gamma}cw_9Q_{,1}Nd\Gamma,
$$

$$
0 \;=\; \int_{\Omega}(w_{10}B - \mu w_{10}R + \mu w_{10,2}\chi_{2,2} + cw_{10,1}R_{,1})d\Omega - \int_{\partial\Gamma}\mu w_{10}\chi_{2,2}Nd\Gamma \\
- \int_{\partial\Gamma}cw_{10}R_{,1}Nd\Gamma, \tag{4.99}
$$

where Ω, $\partial\Gamma$ and N are, respectively the domain of interest, the associated boundary, and the rightward unit normal to the boundary $\partial\Gamma$ in the sense of the Green-Stokes' theorem. The unknown potentials of χ_1, χ_2, Q, R, C, D, E, F, A and B can be expressed in the form of Lagrangian polynomial that

$$
(*) = \sum_{j=1}^{n=4}[(*)_j\Psi_j(x,y)]. \tag{4.100}
$$

122

Accordingly, the test function w is found to be

$$w_m = \sum_{i=1}^{n=4} w_m^i \Psi_i(x,y); \ \ i = 1,2,3,4, \ \text{and} \ m = 1,2,3,4,...10 \tag{4.101}$$

where w_i is the weight of the test function and $\Psi_i(x,y)$ are the associated shape functions; $\Psi_1 = \frac{(x-2)(y-1)}{2}$, $\Psi_2 = \frac{x(y-1)}{-2}$, $\Psi_3 = \frac{xy}{2}$ and $\Psi_4 = \frac{y(x-2)}{-2}$. Invoking Eq. (4.100), (4.99) can be recast in terms of Lagrangian polynomial representation as

$$
\begin{aligned}
0 = &\sum_{i,j=1}^{n=4} \Big\{ \int_{\Omega^e} (\mu\Psi_i\Psi_j Q_j - \mu\Psi_{i,2}\Psi_{j,2}\chi_{1j} + \kappa(\Psi_i\Psi_j Q_j + \Psi_{i,2}\Psi_{j,2}E_j)(CC + EE \\
&+ DD + FF) - \kappa(\Psi_i\Psi_j Q_j + \Psi_i\Psi_{j,2}C_j + \Psi_i\Psi_{j,1}E_j + \Psi_i\Psi_{j,2}E_j)(CC + CE \\
&+ EC + EE + DD + DF + FD + FF) + \kappa(C+E)(2\Psi_i\Psi_j QC_j \\
&+ 2\Psi_i\Psi_{j,1}E_j E + 2\Psi_i\Psi_{j,2}C_j C + 2\Psi_i\Psi_{j,2}E_j E - \Psi_i\Psi_j QC - \Psi_i\Psi_j QE \\
&- \Psi_i\Psi_{j,2}E_j C - \Psi_i\Psi_{j,2}E_j E - \Psi_i\Psi_j CQ - \Psi_i\Psi_{j,1}CE_j - \Psi_i\Psi_{j,2}EC_j \\
&- \Psi_i\Psi_{j,2}EE_j + 2\Psi_i\Psi_j RD + 2\Psi_i\Psi_{j,1}F_j F + 2\Psi_i\Psi_{j,2}D_j D + 2\Psi_i\Psi_{j,2}F_j F \\
&- \Psi_i\Psi_j RD - \Psi_i\Psi_j RF - \Psi_i\Psi_{j,2}F_j D - \Psi_i\Psi_{j,2}F_j F - \Psi_i\Psi_j DR \\
&- \Psi_i\Psi_{j,1}DF_j - \Psi_i\Psi_{j,2}FD_j - \Psi_i\Psi_{j,2}FF_j) + [\frac{E_1}{4}\frac{1}{(CC+DD)^2} \\
&- (\frac{E_1+E_2}{2})\frac{1}{(CC+DD)} + (\frac{E_1}{4} + \frac{E_2}{2})](\frac{Q}{(CC+DD)^2} \\
&- \frac{4C(QC+RD)}{(CC+DD)^3}) + [\frac{E_1+E_2}{(CC+DD)^2} - \frac{E_1}{(CC+DD)^3}] \\
&\frac{(QC+RD)\Psi_i\Psi_j C_j}{(CC+DD)^2} - A_0\Psi_i\Psi_{j,2}\chi_{2j} + B_0\Psi_i\Psi_{j,1}\chi_{2j} \\
&+ c\Psi_{i,1}\Psi_{j,1}Q_j)d\Omega\Big\} + \sum_{i=1}^{n=4}\Big\{\mu\int_{\partial\Gamma^e}\Psi_i\chi_{1,2}Nd\Gamma - c\int_{\partial\Gamma^e}\Psi_i Q_{,1}Nd\Gamma\Big\},
\end{aligned}
$$

$$
\begin{aligned}
0 \;=\; \sum_{i,j=1}^{n=4} \Big\{ & \int_{\Omega^e} (\mu \Psi_i \Psi_j R_j - \mu \Psi_{i,2} \Psi_{j,2} \chi_{2j} + \kappa (\Psi_i \Psi_j R_j + \Psi_{i,2} \Psi_{j,2} F_j)(CC + EE \\
& + DD + FF) - \kappa (\Psi_i \Psi_j R + \Psi_i \Psi_{j,2} D_j + \Psi_i \Psi_{j,1} F_j + \Psi_i \Psi_{j,2} F_j)(CC + CE \\
& + EC + EE + DD + DF + FD + FF) + \kappa w_2 (D + F)(2\Psi_i \Psi_j QC_j \\
& + 2\Psi_i \Psi_{j,1} E_j E + 2\Psi_i \Psi_{j,2} C_j C + 2\Psi_i \Psi_{j,2} E_j E - \Psi_i \Psi_j QC - \Psi_i \Psi_j QE \\
& - \Psi_i \Psi_{j,2} E_j C - \Psi_i \Psi_{j,2} E_j E - \Psi_i \Psi_j CQ - \Psi_i \Psi_{j,1} CE_j - \Psi_i \Psi_{j,2} EC_j \\
& - \Psi_i \Psi_{j,2} EE_j + 2\Psi_i \Psi_j RD + 2\Psi_i \Psi_{j,1} F_j F + 2\Psi_i \Psi_{j,2} D_j D + 2\Psi_i \Psi_{j,2} F_j F \\
& - \Psi_i \Psi_j RD - \Psi_i \Psi_j RF - \Psi_i \Psi_{j,2} F_j D - \Psi_i \Psi_{j,2} F_j F - \Psi_i \Psi_j DR \\
& - \Psi_i \Psi_{j,1} DF_j - \Psi_i \Psi_{j,2} FD_j - \Psi_i \Psi_{j,2} FF_j) + [\frac{E_1}{4} \frac{1}{(CC + DD)^2} \\
& - (\frac{E_1 + E_2}{2}) \frac{1}{(CC + DD)} + (\frac{E_1}{4} + \frac{E_2}{2})] (\frac{R}{(CC + DD)^2} - \frac{4D(QC + RD)}{(CC + DD)^3}) \\
& + [\frac{E_1 + E_2}{(CC + DD)^2} - \frac{E_1}{(CC + DD)^3}] \frac{(QC + RD)\Psi_i \Psi_j D_j}{(CC + DD)^2} + A_0 \Psi_i \Psi_{j,2} \chi_{1j} \\
& - B_0 \Psi_i \Psi_{j,1} \chi_{1j} + c \Psi_{i,1} \Psi_{j,1} R_j) d\Omega \Big\} + \sum_{i=1}^{n=4} \Big\{ \mu \int_{\partial \Gamma^e} \Psi_i \chi_{2,2} N d\Gamma - c \int_{\partial \Gamma^e} \Psi_i R_{,1} N d\Gamma \Big\},
\end{aligned}
$$

124

$$0 = \sum_{i,j=1}^{n=4}\{\int_{\Omega^e}(\Psi_i\Psi_j)d\Omega\}Q_j + \sum_{i,j=1}^{n=4}\{\int_{\Omega^e}\Psi_{i,1}\Psi_{j,1})d\Omega\}\chi_{1j} - \sum_{i=1}^{n=4}\{\int_{\partial\Gamma^e}(\Psi_i\chi_{1,1})Nd\Gamma\},$$

$$0 = \sum_{i,j=1}^{n=4}\{\int_{\Omega^e}(\Psi_i\Psi_j)d\Omega\}R_j + \sum_{i,j=1}^{n=4}\{\int_{\Omega^e}\Psi_{i,1}\Psi_{j,1})d\Omega\}\chi_{2j} - \sum_{i=1}^{n=4}\{\int_{\partial\Gamma^e}(\Psi_i\chi_{2,1})Nd\Gamma\},$$

$$0 = \sum_{i,j=1}^{n=4}\{\int_{\Omega^e}(\Psi_i\Psi_j)d\Omega\}C_j - \sum_{i,j=1}^{n=4}\{\int_{\Omega^e}(\Psi_i\Psi_{j,1})d\Omega\}\chi_{1j},$$

$$0 = \sum_{i,j=1}^{n=4}\{\int_{\Omega^e}(\Psi_i\Psi_j)d\Omega\}D_j - \sum_{i,j=1}^{n=4}\{\int_{\Omega^e}(\Psi_i\Psi_{j,1})d\Omega\}\chi_{2j},$$

$$0 = \sum_{i,j=1}^{n=4}\{\int_{\Omega^e}(\Psi_i\Psi_j)d\Omega\}E_j - \sum_{i,j=1}^{n=4}\{\int_{\Omega^e}(\Psi_i\Psi_{j,2})d\Omega\}\chi_{1j},$$

$$0 = \sum_{i,j=1}^{n=4}\{\int_{\Omega^e}(\Psi_i\Psi_j)d\Omega\}F_j - \sum_{i,j=1}^{n=4}\{\int_{\Omega^e}(\Psi_i\Psi_{j,2})d\Omega\}\chi_{2j},$$

$$0 = \sum_{i,j=1}^{n=4}\{\int_{\Omega^e}(\Psi_i\Psi_j)d\Omega\}A_j + \sum_{i,j=1}^{n=4}\{\int_{\Omega^e}(-\mu\Psi_i\Psi_j + c\Psi_{i,1}\Psi_{j,1})d\Omega\}Q_j$$
$$+ \sum_{i,j=1}^{n=4}\{\int_{\Omega^e}(\mu\Psi_{i,2}\Psi_{j,2})d\Omega\}\chi_{1j} - \sum_{i=1}^{n=4}\{\int_{\partial\Gamma^e}(\mu\Psi_i\chi_{1,2})Nd\Gamma - \int_{\partial\Gamma^e}(c\Psi_iQ_{,1})Nd\Gamma\},$$

$$0 = \sum_{i,j=1}^{n=4}\{\int_{\Omega^e}(\Psi_i\Psi_j)d\Omega\}B_j + \sum_{i,j=1}^{n=4}\{\int_{\Omega^e}(-\mu\Psi_i\Psi_j + c\Psi_{i,1}\Psi_{j,1})d\Omega\}R_j$$
$$+ \sum_{i,j=1}^{n=4}\{\int_{\Omega^e}(\mu\Psi_{i,2}\Psi_{j,2})d\Omega\}\chi_{2j} - \sum_{i=1}^{n=4}\{\int_{\partial\Gamma^e}(\mu\Psi_i\chi_{2,2})Nd\Gamma$$
$$- \int_{\partial\Gamma^e}(c\Psi_iR_{,1})Nd\Gamma\}. \tag{4.102}$$

Now, for the local stiffness matrices and forcing vectors for each elements, we find

$$\begin{bmatrix} K_{11}^{11} & K_{12}^{11} & K_{13}^{11} & K_{14}^{11} \\ K_{21}^{11} & K_{22}^{11} & K_{23}^{11} & K_{24}^{11} \\ K_{31}^{11} & K_{32}^{11} & K_{33}^{11} & K_{34}^{11} \\ K_{41}^{11} & K_{42}^{11} & K_{43}^{11} & K_{44}^{11} \end{bmatrix}_{Local} \begin{bmatrix} \chi_1^1 \\ \chi_1^2 \\ \chi_1^3 \\ \chi_1^4 \end{bmatrix}_{Local} = \begin{bmatrix} F_1^1 \\ F_2^1 \\ F_3^1 \\ F_4^1 \end{bmatrix}_{Local}, \tag{4.103}$$

where

$$\left[K_{ij}^{11}\right] = \int_\Omega(-\mu\Psi_{i,2}\Psi_{j,2})d\Omega, \tag{4.104}$$

and

$$\{F_i^1\} = -\mu\int_{\partial\Gamma^e}w_i\chi_{1,2}Nd\Gamma + c\int_{\partial\Gamma^e}w_iQ_{,1}Nd\Gamma. \tag{4.105}$$

125

Thus, the unknown potentials (i.e. χ_1, χ_2, Q, R, C, D, E, F, A and B) can be expressed as

$$Q_i = \{\chi_1^i\}_{,11}, \ R_i = \{\chi_2^i\}_{,11}, \ S_i = \{Q^i\}_{,11} \text{ etc...,} \tag{4.106}$$

and similarly for the rest of unknowns.

Consequently, we obtain the following systems of equations (in the Global form) for each individual elements as

$$
\begin{bmatrix}
[K^{11}] & [K^{12}] & . & . & . & . & . & . & [K^{19}] & [K^{110}] \\
[K^{21}] & [K^{22}] & . & . & . & . & . & . & [K^{29}] & [K^{210}] \\
[K^{31}] & [K^{32}] & . & . & . & . & . & . & [K^{39}] & [K^{310}] \\
[K^{41}] & [K^{42}] & . & . & . & . & . & . & [K^{49}] & [K^{410}] \\
[K^{51}] & [K^{52}] & . & . & . & . & . & . & [K^{59}] & [K^{510}] \\
[K^{61}] & [K^{62}] & . & . & . & . & . & . & [K^{69}] & [K^{610}] \\
[K^{71}] & [K^{72}] & . & . & . & . & . & . & [K^{79}] & [K^{710}] \\
[K^{81}] & [K^{82}] & . & . & . & . & . & . & [K^{89}] & [K^{810}] \\
[K^{91}] & [K^{92}] & . & . & . & . & . & . & [K^{99}] & [K^{910}] \\
[K^{101}] & [K^{102}] & . & . & . & . & . & . & [K^{109}] & [K^{1010}]
\end{bmatrix}
\begin{bmatrix}
\chi_1^i \\ \chi_2^i \\ Q_i \\ R_i \\ A_i \\ B_i \\ C_i \\ D_i \\ E_i \\ F_i
\end{bmatrix}
=
\begin{bmatrix}
\{F_1\} \\ \{F_2\} \\ \{F_3\} \\ \{F_4\} \\ \{F_5\} \\ \{F_6\} \\ \{F_7\} \\ \{F_8\} \\ \{F_9\} \\ \{F_{10}\}
\end{bmatrix}. \tag{4.107}
$$

In the simulation, we employed the following convergence criteria

$$|A_{n+1} - A_n| = e_1 \leq \varepsilon, \ |B_{n+1} - B_n| = e_2 \leq \varepsilon, \text{ where } \varepsilon = \text{maximum error} = 10^{-10}, \tag{4.108}$$

which demonstrates fast convergence within 10 iterations using FEniCS nonlinear solver (see, Table. 4.1).

Table 4.1: Maximum numerical errors with respect to the number of iterations.

Number of iteration	Mximum error
1	5.392e-0
2	8.079e-01
3	6.588e-02
5	3.765e-10
7	1.25e-17

It should be also noted here that, in the case of the exponential energy potential, we expanded the corresponding exponential terms using the Taylor series up to the first 5 terms (e.g. $e^x = 1 + \frac{x}{1!} + \frac{x^2}{2!} + \frac{x^3}{3!} + \frac{x^4}{4!}$) to facilitate the numerical analysis of FE process.

4.8 Sensitivity test of parameters C and T

In order to figure out the parameters related to the higher gradient terms (i.e., C and T) we have performed the sensitivity test by analyzing how the deformation is affected as the numerical values of the parameters are changed. The deformation profiles with respect to torsional parameter T are illustrated in Fig. 4.17. It can be noted that the deformation angles of the PES fiber mesh composites decrease with increasing torsional rigidity (T). In Fig. 4.18-4.19, deformation profiles with respect to bending stiffness parameter C are illustrated.
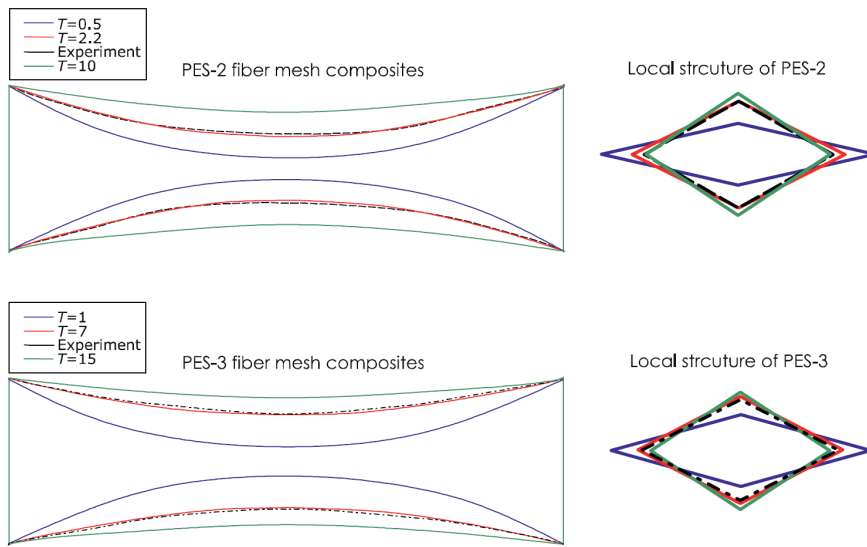
Figure 4.17: Deformation configurations with respect to T: PES-2 (up); PES-3 (bottom).

4.9 Denouement

In this chapter, a comprehensive analytical platform for the mechanics of a hyperelastic materials reinforced with fibrous materials is presented in finite plane elastostatics. The hyperelastic response of the elastomeric matrix material is accommodated by the Mooney-Rivlin model, while the nonlinear stress-strain behaviors of the reinforcing fibers are assimilated via the custom designed energy potentials of the polynomial/exponential types. The kinematics of reinforcing fibers are formulated by their position and direction fields and are subsequently integrated into the

127
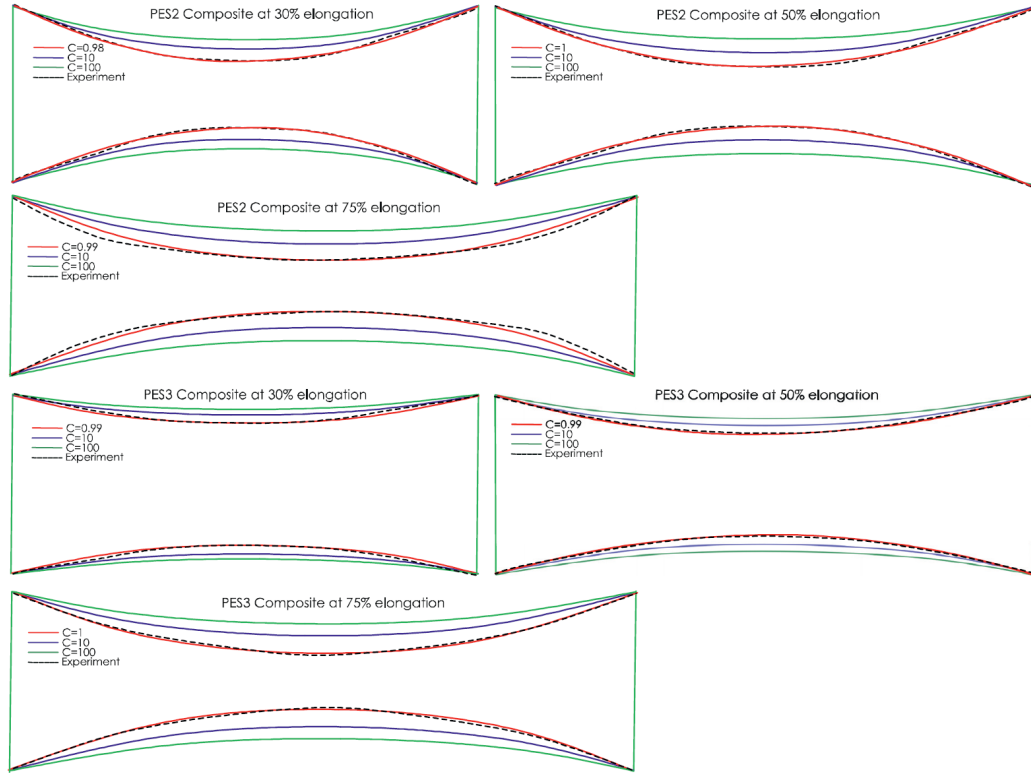
Figure 4.18: Deformation profiles of unidirectional PES composites with respect to C.

models of continuum deformation via the first and second gradient of deformations. In particular, we proposed three different types of strain energy functions based on the polynomial, exponential and Euler-Almansi strain which describe, respectively, the moderate strain-stiffening, rapid strain-stiffening and strain-softening responses of elastomeric composites. Within the framework of variational principles and virtual work statement, the Euler equilibrium equation and the necessary boundary conditions are derived. These, together with the constraint of the bulk incompressibility, furnish systems of coupled nonlinear PDEs from which a set of numerical solutions describing the hyperelastic responses of the elastomeric composites are obtained via the custom-built Finite Element Analysis (FEA) procedure. A series of inhouse experiments were also designed and performed for the purpose of model implementation and cross-validation.

We demonstrated that the presented models successfully predict the moderate strain-stiffening and rapid strain-stiffening behaviors (J-shaped stress-stress responses)

128
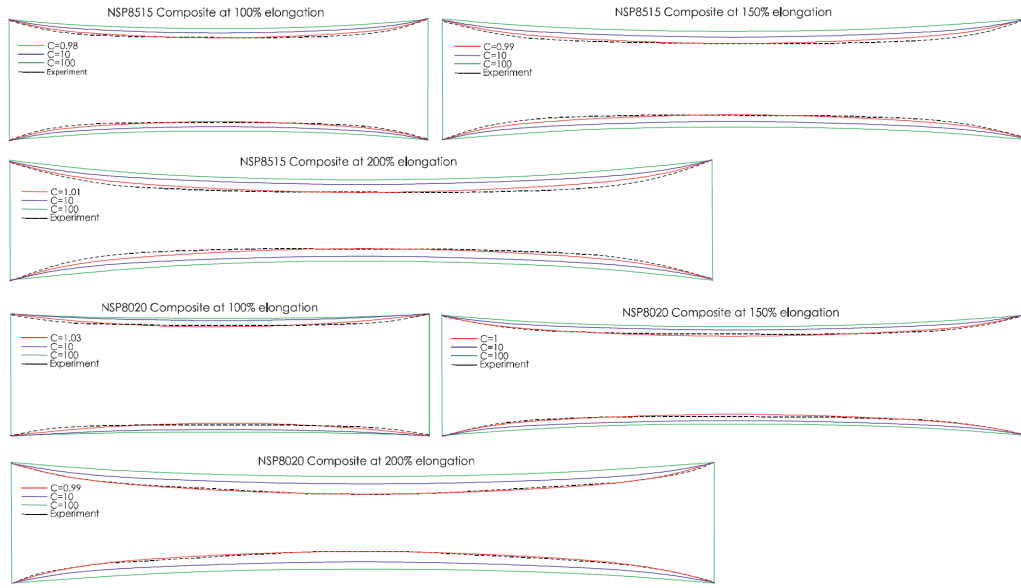
Figure 4.19: Deformation profiles of unidirectional NSP composites with respect to C.

of the elastomeric composites. The strain-softening responses of PDMS and PU/D composites are also predicted with reasonable accuracy by the Euler-Almansi strain integrated model. The case of an elastomeric matrix material reinforced with a polyester fiber mesh is also simulated using the presented bidirectional model from which complete deformation profiles and shear strain distributions are obtained, which demonstrate good agreement with the inhouse experimental results. Further, the solutions from the bidirectional model closely simulate the deformation angles between the two adjoining fibers and the deformed configurations of the local mesh structures.

Chapter 5

A three-dimensional continuum model for the mechanics of an elastic medium reinforced with fibrous materials

In section 5.1, the kinematics is presented for a thin hyperelastic film reinforced with bidirectional fibers in a three-dimensional setting. Within the framework of differential geometry and strain-gradient elasticity, the general kinematics of bidirectional fibers are formulated. The equilibrium and boundary conditions are presented in section 5.2. In section 5.3, the Mooney-Rivlin type energy model is integrated into the energy density function to accommodate the hyperelastic response of the matrix film. In section 5.5, different case studies related to the out-of-plane deformations of elastic films are presented to demonstrate the practical utilities of the presented model.

5.1 Kinematics

The kinematic framework of fibers that will be used in the constitutive formulations of matrix-fiber composite systems is presented in this section. Emphasis is placed on obtaining compact kinematic descriptions for a bidirectional fiber meshes while maintaining the rigor and sufficient generality in the corresponding derivations. It is also noted that the applications of differential geometry in the problems pertaining to elastic surfaces are well established in the literature (see, for example, and the references therein). Here, we reformulated the results into the present context for the

sake of clarity and completeness.

Let θ^i be the convected coordinate to label material points of the composite regarded as a three-dimensional continuum in $\mathbb{R}^3$, yet much like a plate structure with finite thickness (see, Fig. 5.1). We define the position fields $\mathbf{X}(\theta^i)$ and $\mathbf{r}(\theta^i)$ representing, respectively, a material point of a reference body $\mathbb{B}$ and a deformed body $\mathfrak{b}$. These parameterization furnish natural basis,

$$\mathbf{G}_i = \frac{\partial \mathbf{X}}{\partial \theta^i} = \frac{\partial X^A}{\partial \theta^i} \mathbf{E}_A \text{ and } \mathbf{g}_i = \frac{\partial \mathbf{r}}{\partial \theta^i} = \frac{\partial r^j}{\partial \theta^i} \mathbf{e}_j, \tag{5.1}$$

where $\{\mathbf{E}_A\}_{A=1}^3$ and $\{\mathbf{e}_j\}_{j=1}^3$ are Cartesian basis vectors in reference and deformed configurations, respectively. The $\mathbf{g}_i$ are linearly independent; i.e. $\mathbf{g}_i \cdot \mathbf{g}_j \times \mathbf{g}_k = \varepsilon_{ijk} = e_{ijk}\sqrt{g}$ and $g = \det(g_{ij})$, where e_{ijk} refers to the permutation tensor (e.g. $e_{123} = e_{231} = 1$, $e_{213} = e_{132} = -1$, $e_{112} = e_{223} = 0$ etc...). The matrix of the metric $g_{ij} = \mathbf{g}_i \cdot \mathbf{g}_j$ is positive-definite (i.e. $g > 0$) rendering the existence of dual metric $g^{ij} = (g_{ij})^{-1}$ from which the dual basis may be computed as $\mathbf{g}^i = g^{ij}\mathbf{g}_j$. Hence, it is straightforward to show

$$\mathbf{g}^i \cdot \mathbf{g}_j = \frac{\partial \theta^i}{\partial r^k} \mathbf{e}_k \cdot \frac{\partial r^l}{\partial \theta^j} \mathbf{e}_l = \delta^i_j \text{ and } g^{ij}g_{jk} = \delta^i_k, \tag{5.2}$$

where δ^i_k is the Kronecker delta. The same results can be obtained for the case of the natural basis in $\mathbb{B}$ as

$$G_{ij} = \mathbf{G}_i \cdot \mathbf{G}_j, \ G = \det(G_{ij}), \ \mathbf{G}^i = G^{ij}\mathbf{G}_j, \ \mathbf{G}^i \cdot \mathbf{G}_j = \delta^i_j \text{ and } G^{ij}G_{jk} = \delta^i_k, \tag{5.3}$$

which will also be used in the forgoing model derivation.

Of central importance in the proposed work is the incorporation of the second gradient effects of fibers (i.e. fiber bending and torsion between two adjoining fibers) into the models of continuum deformations. In the present context, this requires the second covariant derivative of the position field $\mathbf{r}(\theta^i)$;

$$\mathbf{r}_{;ij} = \mathbf{r}_{,ij} - \bar{\Gamma}^k_{ij}\mathbf{r}_{,k}; \text{ (evaluated with respect to the metric of } \mathbb{B}) \tag{5.4}$$

where

$$\bar{\Gamma}^k_{ij} = \mathbf{G}_{i,j} \cdot \mathbf{G}^k = -\mathbf{G}_i \cdot \mathbf{G}^k_{,j}, \tag{5.5}$$

is the Levi-Civita connection coefficient induced by the natural coordinates in $\mathbb{B}$. It should also note that the same holds true in a deformed body $\mathfrak{b}$ such that

$$\Gamma^k_{ij} = \mathbf{g}_{i,j} \cdot \mathbf{g}^k = -\mathbf{g}_i \cdot \mathbf{g}^k_{,j}. \tag{5.6}$$

131

Consider now an elastic continuum reinforced with two families of fibers that are continuously distributed throughout the matrix material. The fibers are presumed to be convected material curves with no relative slipping such that their kinematics and constitutive structures can be determined by their position and director fields [131]-[132] from which the main characteristics of the local macroscopic behaviors of the corresponding composites may be captured. The unit tangents to the fibers' trajectories in the referential body $\mathbb{B}$ are denoted by

$$\mathbf{L} = \frac{d\mathbf{X}(S,U)}{dS} \text{ and } \mathbf{M} = \frac{d\mathbf{X}(S,U)}{dU}, \tag{5.7}$$

where S and U are, respectively, the arclength parameters in the increasing directions of $\mathbf{L}$ and $\mathbf{M}$ (see, Fig. 5.1). In the present study, we limit our attention to the case of initially uniform and orthogonal fibers (i.e. $\mathbf{L} \cdot \mathbf{M} = \mathbf{0}$) for the sake of conciseness and clarity. Refinements of the model to accommodate initially non-orthogonal fibers are straightforward via the simple modification of fibers' director fields (e.g. $\mathbf{L} \cdot \mathbf{M} = \cos\alpha$). However, the presumed restriction suffices to extract the important aspects of the intended model and, further, the desired applications. The stretch and
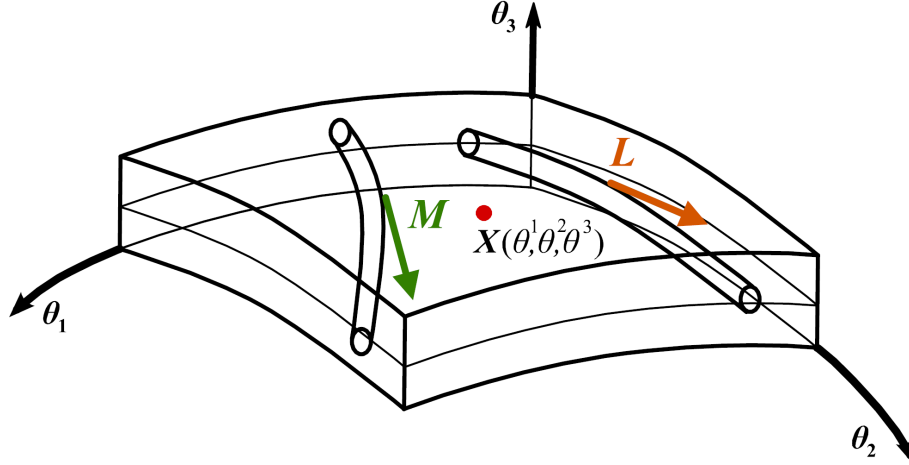
Figure 5.1: Schematic of the matrix-fiber composite system.

orientation of particular fibers are then computed as

$$\lambda = |\boldsymbol{\eta}| = \frac{ds}{dS}, \ \gamma = |\boldsymbol{\zeta}| = \frac{du}{dU} \text{ and } (\frac{d\mathbf{r}}{ds}) = \mathbf{l} = \lambda^{-1}\boldsymbol{\eta}, \ (\frac{d\mathbf{r}}{du}) = \mathbf{m} = \gamma^{-1}\boldsymbol{\zeta}, \tag{5.8}$$

where

$$\lambda\mathbf{l} = \mathbf{FL} \text{ and } \gamma\mathbf{m} = \mathbf{FM}, \tag{5.9}$$

132

and $\mathbf{F}$ is the gradient of the deformation function:

$$\mathbf{F} = \frac{d\boldsymbol{\chi}(\mathbf{X})}{d\mathbf{X}} = \mathbf{g}_i \otimes \mathbf{G}^i. \tag{5.10}$$

Eq. (5.9) can be obtained via the successive differentiation of $\mathbf{r}(s(S)) = \boldsymbol{\chi}(\mathbf{X}(S))$ with respect to the referential position vector $\mathbf{X}(S)$ and the arclength parameter S using chain rule, upon making the identification of $\mathbf{L} = d\mathbf{X}/dS$ and $\mathbf{l} = d\boldsymbol{\chi}/ds$ and similarly for $\mathbf{M}$ and $\mathbf{m}$ (i.e. $\mathbf{M} = d\mathbf{X}/dU$ and $\mathbf{m} = d\boldsymbol{\chi}/du$). Here, $d(*)/dS$ and $d(*)/ds$ refer to the arclength derivatives of $(*)$ along fibers' directions, respectively in the reference and deformed configurations. Eq. (5.9) together with the presumed orthogonality (i.e. $\mathbf{L} \cdot \mathbf{M} = \mathbf{0}$) furnish a useful fiber decomposition of the deformation gradient tensor:

$$\mathbf{F} = \lambda \mathbf{l} \otimes \mathbf{L} + \gamma \mathbf{m} \otimes \mathbf{M}, \tag{5.11}$$

or equivalently,

$$\mathbf{g}_i \overset{(5.3),(5.10)}{=} \mathbf{FG}_i \overset{(5.11)}{=} \lambda \mathbf{l} L_i + \gamma \mathbf{m} M_i. \tag{5.12}$$

Hence, for example, we write

$$\mathbf{L} = L^i \mathbf{G}_i, \ \ \mathbf{M} = M^i \mathbf{G}_i, \ \mathbf{l} = l^i \mathbf{g}_i \text{ and } \mathbf{m} = m^i \mathbf{g}_i, \tag{5.13}$$

and thereby obtain from Eqs. (5.9) and (5.12) that

$$\lambda l^i = L^i \text{ and } \gamma m^i = M^i, \tag{5.14}$$

which relate contravariant components of unit tangents of fibers. Similarly, invoking the decomposition of

$$\mathbf{g}_i = (\mathbf{g}_i \mathbf{l}) \cdot \mathbf{l} + (\mathbf{g}_i \mathbf{m}) \cdot \mathbf{m} = l_i \mathbf{l} + m_i \mathbf{m}, \tag{5.15}$$

the covariant components are related by (see, Eqs. (5.12) and (5.15))

$$\lambda l_i = L_i \text{ and } \gamma m_i = M_i. \tag{5.16}$$

Now, the expressions for the geodesic curvatures of a parametric curve $(\mathbf{r}(s, u))$ can be obtained from Eqs. (5.8)-(5.9) that

$$\mathbf{c}_1 = \frac{d^2 \mathbf{r}(S)}{dS^2} = \frac{d(\frac{\mathbf{r}(S)}{dS})}{dS} = \frac{\partial(\mathbf{FL})}{\partial \mathbf{X}} \frac{\partial \mathbf{X}}{\partial S} = \nabla[\mathbf{FL}]\mathbf{L}, \text{ and} \tag{5.17}$$

133

$$\mathbf{c}_2 \;=\; \frac{d^2\mathbf{r}(U)}{dU^2} \;=\; \frac{d(\frac{\mathbf{r}(U)}{dU})}{dU} \;=\; \frac{\partial(\mathbf{FM})}{\partial\mathbf{X}}\frac{\partial\mathbf{X}}{\partial U} \;=\; \nabla[\mathbf{FM}]\mathbf{M}. \tag{5.18}$$

In a typical environment, most of the fibers are straight prior to deformations. Even slightly curved fibers may be viewed as 'locally straight' fibers, considering their relatively high aspect ratios. Applying the idealization of initially straight fibers, Eqs (5.17)-(5.18) are then meaningfully simplified to

$$\mathbf{c}_1 \;=\; \nabla\mathbf{F}(\mathbf{L}\otimes\mathbf{L}) \text{ and } \mathbf{c}_2 \;=\; \nabla\mathbf{F}(\mathbf{M}\otimes\mathbf{M}); \; \because \nabla\mathbf{L}=\nabla\mathbf{M}=\mathbf{0}, \tag{5.19}$$

where $\nabla\mathbf{F}$ is the second gradient of deformation. Invoking chain rule on Eq. (5.10), this is found to be

$$\nabla\mathbf{F} = (\Gamma^i_{jk} - \bar{\Gamma}^i_{jk})\mathbf{g}_i\otimes\mathbf{G}^j\otimes\mathbf{G}^k. \tag{5.20}$$

The forgoing development suggests that the mechanical responses of a matrix-fiber systems may be characterized by the following energy function:

$$W(\mathbf{F}, \varepsilon, \mathbf{c}_1, \mathbf{c}_2) = W(\mathbf{F})_{matrix} + W(\varepsilon_1, \varepsilon_2)_{fiber} + \frac{1}{2}C_1\mathbf{c}_1\cdot\mathbf{c}_1 + \frac{1}{2}C_2\mathbf{c}_2\cdot\mathbf{c}_2 + \frac{1}{2}T\mathbf{c}_1\cdot\mathbf{c}_2, \tag{5.21}$$

where $\mathbf{c}_\alpha\cdot\mathbf{c}_\alpha$ and $\mathbf{c}_1\cdot\mathbf{c}_2$ are account for, respectively, the bending and torsional kinematics of the fibers (see, for example, Fig. 5.4 (c)), and C_α and T are the associated moduli which are, in general, independent of the deformation gradient (i.e. $C_\alpha(\mathbf{F}) = C_\alpha$ and $T(\mathbf{F}) = T$). The quadratic strain energy potentials of $\mathbf{c}_\alpha$ are based on the postulation of Spencer and Soldatos [93] which has been widely and successfully adopted in the relevant subjects of studies (see, for example, [90], [96], [115], and [120]). The energy function of $W(\mathbf{F})_{matrix}$ describes the responses of matrix materials. For example, in the case of an incompressible Neo-Hookean material, we find

$$W(\mathbf{F})_{matrix} = \mu(\mathbf{F}\cdot\mathbf{F} - 3). \tag{5.22}$$

Further, $W(\varepsilon_1, \varepsilon_2)_{fiber}$ characterizes the response of fibers against extension, which may take the following simple quadratic form of Green-Lagrange type for the purpose of a concise and compact demonstration

$$W(\varepsilon_1, \varepsilon_2)_{fiber} = \frac{1}{2}E_1\varepsilon_1^2 + \frac{1}{2}E_2\varepsilon_2^2, \tag{5.23}$$

where the expressions for the associated strains can be found as

$$\varepsilon_1 = \frac{1}{2}\left(\lambda^2 - 1\right) \overset{(5.9)}{=} \frac{1}{2}\left(\mathbf{FL}\cdot\mathbf{FL} - 1\right) \text{ and } \varepsilon_2 = \frac{1}{2}\left(\gamma^2 - 1\right) \overset{(5.9)}{=} \frac{1}{2}\left(\mathbf{FM}\cdot\mathbf{FM} - 1\right).$$
$$\tag{5.24}$$

It should be also noted here that one may choose different forms of energy potentials to accommodate particular types of materials. For example, the combination of the Mooney-Rivlin energy potential (for matrix materials) and cubic polynomial potentials (for fibers; e.g. $W(\varepsilon)_{fiber} = \frac{1}{3}E_1\varepsilon^3 + \frac{1}{2}E_2\varepsilon^2$) may be considered to assimilate hyperelastic responses of elastomeric composites which will be discussed further in later sections. Lastly, volumetric changes in materials' deformations are, in generally, energetically expensive process and thus are constrained in the constitutive modeling of most engineering materials (see, for example, [105]-[106]). In the present context, this can be accommodated by augmenting the proposed energy potential (Eq. (5.21)) using the constraint of bulk incompressibility (i.e. $p(J-1)$) from which we find

$$
\begin{aligned}
U(\mathbf{F}, \varepsilon, \mathbf{c_1}, \mathbf{c_2}, p) \;=\;\; & \mu(\mathbf{F} \cdot \mathbf{F} - 3) + \frac{1}{2}E_1\varepsilon_1^2 + \frac{1}{2}E_2\varepsilon_2^2 + \frac{1}{2}C_1\mathbf{c_1}\cdot\mathbf{c_1} + \frac{1}{2}C_2\mathbf{c_2}\cdot\mathbf{c_2} + \frac{1}{2}T\mathbf{c_1}\cdot\mathbf{c_2} \\
& -p(J-1)\;,
\end{aligned}
\tag{5.25}
$$

where J is determinant of $\mathbf{F}$ and p is a constitutively indeterminate Lagrange multiplier field.

5.2 Equilibrium and boundary conditions

In this section, the derivations of the Euler equilibrium equations and the associated boundary conditions are presented in light of the virtual work statement and variational principles. The relevant theoretical frameworks pertaining to the second-gradient elasticity are well established in the dedicated literature ([98], [101], [107], [108]). For the stated purpose, we evaluate the potential energy of the system as

$$
E = \int_{\mathbb{B}} U(\mathbf{F}, \varepsilon, \mathbf{c_1}, \mathbf{c_2}, p) dV.
\tag{5.26}
$$

The weak form of the Euler equilibrium equation may then be formulated by employing the virtual-work statement

$$
\dot{E} = P,
\tag{5.27}
$$

where P is the virtual power of the applied loads and the superposed dot denotes the variational and/or Gateâux derivative. Since the conservative loads are characterized by the existence of a potential L such that $P = \dot{L}$, the problem of determining equilibrium deformations is reduced to the problem of minimizing the potential energy,

$E - L$. In the present case, this would mean that

$$\dot{E} = \int_{\mathbb{B}} \dot{U}(\mathbf{F}, \varepsilon, \mathbf{c}_1, \mathbf{c_2}, p) dV. \tag{5.28}$$

5.2.1 Variational formulation

We continue by evaluating the induced energy variation of the response function (5.21) as

$$\dot{U}(\mathbf{F}, \varepsilon, \mathbf{c}_1, \mathbf{c_2}, p) = \dot{W}(\mathbf{F})_{matrix} + \dot{W}(\varepsilon_1, \varepsilon_2)_{fiber} + C_1 \mathbf{c}_1 \cdot \dot{\mathbf{c}}_1 + C_2 \mathbf{c}_2 \cdot \dot{\mathbf{c}}_2 + \frac{1}{2} T \dot{\mathbf{c}}_1 \cdot \mathbf{c}_2$$
$$+ \frac{1}{2} T \mathbf{c}_1 \cdot \dot{\mathbf{c}}_2 - [p(J-1)]. \tag{5.29}$$

In the above, the superposed dot refers to the variational derivatives with respect to ϵ at the particular configuration of the composite (i.e. $\epsilon = 0$) that labels a one-parameter family of deformations. To derive the desired expressions, we evaluate the variational derivative of Eq. (5.10):

$$\dot{\mathbf{F}} = \dot{\mathbf{g}}_i \otimes \mathbf{G}^i = \mathbf{u}_{,i} \otimes \mathbf{G}^i; \quad \because \dot{\mathbf{G}}^i = 0, \tag{5.30}$$

where $\mathbf{u} = \dot{\mathbf{r}}$ is the derivative of the deformation map, $\mathbf{r}$, with respect to ϵ.

Thus, from Eqs. (5.11), (5.14) and (5.22), we find

$$\dot{W}(\mathbf{F})_{matrix} = \mu \mathbf{F} \cdot \dot{\mathbf{F}} = \mu(\lambda \mathbf{l} \otimes \mathbf{L} + \gamma \mathbf{m} \otimes \mathbf{M}) \cdot (\mathbf{u}_{,i} \otimes \mathbf{G}^i)$$
$$= \mu(L^i L^j + M^i M^j) \mathbf{g}_i \cdot \mathbf{u}_{,j}, \tag{5.31}$$

or equivalently

$$\dot{W}(\mathbf{F})_{matrix} = \mu \mathbf{F} \cdot \dot{\mathbf{F}} = \mu(\mathbf{g}_i \otimes \mathbf{G}^i) \cdot (\mathbf{u}_{,j} \otimes \mathbf{G}^j) = \mu G^{ij} \mathbf{g}_i \cdot \mathbf{u}_{,j}, \tag{5.32}$$

from which it can be also seen that

$$G^{ij} = L^i L^j + M^i M^j. \tag{5.33}$$

Further, invoking the chain rule, we obtain from Eq. (5.23) that

$$\dot{W}(\varepsilon_1, \varepsilon_2)_{fiber} = E_1 \varepsilon_1 (\varepsilon_1)_{\mathbf{F}} \cdot \dot{\mathbf{F}} + E_2 \varepsilon_2 (\varepsilon_2)_{\mathbf{F}} \cdot \dot{\mathbf{F}}, \tag{5.34}$$

where the expression of $(\varepsilon_1)_{\mathbf{F}} \cdot \dot{\mathbf{F}}$ can be formulated (see, Eq. (5.24)) as

$$(\varepsilon_1)_{\mathbf{F}} \cdot \dot{\mathbf{F}} = \frac{\partial (1/2)(\mathbf{FL} \cdot \mathbf{FL} - 1)}{\partial \mathbf{F}} \cdot \dot{\mathbf{F}} = \mathbf{F}(\mathbf{L} \otimes \mathbf{L}) \cdot \dot{\mathbf{F}} = L^i L^j \mathbf{g}_i \cdot \mathbf{u}_{,j}, \tag{5.35}$$

136

and similarly for $(\varepsilon_2)_{\mathbf{F}} \cdot \dot{\mathbf{F}}$; i.e.,

$$(\varepsilon_2)_{\mathbf{F}} \cdot \dot{\mathbf{F}} = \mathbf{F}(\mathbf{M} \otimes \mathbf{M}) \cdot \dot{\mathbf{F}} = M^i M^j \mathbf{g}_i \cdot \mathbf{u}_{,j}. \tag{5.36}$$

Thus, for example, we evaluate

$$\varepsilon_1 (\varepsilon_1)_{\mathbf{F}} \cdot \dot{\mathbf{F}} = \frac{1}{2} \left(\mathbf{FL} \cdot \mathbf{FL} - 1 \right) L^i L^j \mathbf{g}_i \cdot \mathbf{u}_{,j} = \frac{1}{2} \left(g_{kl} L^k L^l - 1 \right) L^i L^j \mathbf{g}_i \cdot \mathbf{u}_{,j}, \tag{5.37}$$

and thereby obtain

$$\dot{W}(\varepsilon_1, \varepsilon_2)_{fiber} = [\frac{E_1}{2} \left(g_{kl} L^k L^l - 1 \right) L^i L^j + \frac{E_2}{2} \left(g_{kl} M^k M^l - 1 \right) M^i M^j] \mathbf{g}_i \cdot \mathbf{u}_{,j}. \tag{5.38}$$

We now consider the induced energy variations associated with the curvatures of fibers (i.e. $\mathbf{c}_\alpha \cdot \dot{\mathbf{c}}_\beta$). In view of Eqs. (5.19), we obtain

$$\dot{\mathbf{c}}_1 = (\nabla \dot{\mathbf{F}}) \, (\mathbf{L} \otimes \mathbf{L}) \text{ and } \dot{\mathbf{c}}_2 = (\nabla \dot{\mathbf{F}}) \, (\mathbf{M} \otimes \mathbf{M}). \tag{5.39}$$

The above requires the variational derivative of the second gradient of the deformation. Using Eq. (5.20), this is found to be

$$(\nabla \dot{\mathbf{F}}) = \dot{\Gamma}^i_{jk} \mathbf{g}_i \otimes \mathbf{G}^j \otimes \mathbf{G}^k + (\Gamma^i_{jk} - \bar{\Gamma}^i_{jk}) \mathbf{u}_{,i} \otimes \mathbf{G}^j \otimes \mathbf{G}^k. \tag{5.40}$$

To obtain the expressions of $\dot{\Gamma}^i_{jk}$, the differentiation of Eq. (5.6) yields

$$\dot{\Gamma}^i_{jk} = (\mathbf{g}_{j,k} \cdot \dot{\mathbf{g}^i}) = \mathbf{u}_{;jk} \cdot \mathbf{g}^i + \mathbf{g}_{j,k} \cdot \dot{\mathbf{g}}^i, \tag{5.41}$$

where $\mathbf{u}_{;jk} = \dot{\mathbf{g}}_{j,k}$ is the second covariant derivative of $\mathbf{u} = \dot{\mathbf{r}}$. We then use the identity of $\mathbf{g}^i = g^{il} \mathbf{g}_l$ and Eq. (5.2) to equate

$$\dot{\mathbf{g}}^i = \dot{g}^{il} \mathbf{g}_l + g^{il} \dot{\mathbf{g}}_l = -g^{im} g^{nl} \dot{g}_{mn} \mathbf{g}_l + g^{il} \dot{\mathbf{g}}_l; \quad \because (g^{im} g_{mn}) = (\dot{\delta}^i_n) = 0. \tag{5.42}$$

Since $\dot{g}_{mn} = (\mathbf{g}_m \cdot \dot{\mathbf{g}}_n)$, the above may be recast as

$$\dot{\mathbf{g}}^i = -(g^{im} \dot{\mathbf{g}}_m \cdot \mathbf{g}^l) \mathbf{g}_l - (\mathbf{g}^i \cdot \dot{\mathbf{g}}_n) \mathbf{g}^n + g^{il} \dot{\mathbf{g}}_l = -(\mathbf{g}^i \cdot \dot{\mathbf{g}}_n) \mathbf{g}^n, \tag{5.43}$$

where $(g^{im} \dot{\mathbf{g}}_m \cdot \mathbf{g}^l) \mathbf{g}_l$ is the projections of $g^{im} \dot{\mathbf{g}}_m$ onto $\mathbf{g}_l$ basis. The substitution of Eqs. (5.41) and (5.43) into Eq. (5.40) then furnishes

$$(\nabla \dot{\mathbf{F}}) = (\mathbf{g}^i \cdot \mathbf{u}_{;jk} - \Gamma^n_{jk} \mathbf{g}^i \cdot \mathbf{u}_{,n}) \mathbf{g}_i \otimes \mathbf{G}^j \otimes \mathbf{G}^k + (\Gamma^i_{jk} - \bar{\Gamma}^i_{jk}) \mathbf{u}_{,i} \otimes \mathbf{G}^j \otimes \mathbf{G}^k. \tag{5.44}$$

Hence, we find from Eqs. (5.39) and (5.44) that

$$\mathbf{c}_1 \cdot \dot{\mathbf{c}}_1 = c_1^l g_{il} L^j L^k \mathbf{g}^i \cdot \mathbf{u}_{;jk} - c_1^i \bar{\Gamma}_{lk}^j L^l L^k \mathbf{g}_i \cdot \mathbf{u}_{,j}, \tag{5.45}$$

where it can be readily shown that

$$-(\Gamma_{jk}^n \mathbf{g}^i \cdot \mathbf{u}_{,n}) \mathbf{c}_1 \cdot (\mathbf{g}_i \otimes \mathbf{G}^j \otimes \mathbf{G}^k)(\mathbf{L} \otimes \mathbf{L}) + \Gamma_{jk}^i \mathbf{c}_1 \cdot (\mathbf{u}_{,i} \otimes \mathbf{G}^j \otimes \mathbf{G}^k)(\mathbf{L} \otimes \mathbf{L}) = 0. \tag{5.46}$$

Similarly, we derive

$$\begin{aligned}
\mathbf{c}_2 \cdot \dot{\mathbf{c}}_2 &= c_2^l g_{il} M^j M^k \mathbf{g}^i \cdot \mathbf{u}_{;jk} - c_2^i \bar{\Gamma}_{lk}^j M^l M^k \mathbf{g}_i \cdot \mathbf{u}_{,j}, \\
\mathbf{c}_1 \cdot \dot{\mathbf{c}}_2 &= c_1^l g_{il} M^j M^k \mathbf{g}^i \cdot \mathbf{u}_{;jk} - c_1^i \bar{\Gamma}_{lk}^j M^l M^k \mathbf{g}_i \cdot \mathbf{u}_{,j}, \text{ and} \\
\mathbf{c}_2 \cdot \dot{\mathbf{c}}_1 &= c_2^l g_{il} L^j L^k \mathbf{g}^i \cdot \mathbf{u}_{;jk} - c_2^i \bar{\Gamma}_{lk}^j L^l L^k \mathbf{g}_i \cdot \mathbf{u}_{,j},
\end{aligned} \tag{5.47}$$

where

$$c_1^i \mathbf{g}_i = (\Gamma_{jk}^i - \bar{\Gamma}_{jk}^i) L^j L^k \mathbf{g}_i \text{ and } c_2^i \mathbf{g}_i = (\Gamma_{jk}^i - \bar{\Gamma}_{jk}^i) M^j M^k \mathbf{g}_i \tag{5.48}$$

(refer, Eqs. (5.19)-(5.20)).

To obtain the expression for the last term of Eq. (5.29), we evaluate

$$\dot{J} = J_{\mathbf{F}} \cdot \dot{\mathbf{F}} = \mathbf{F}^* \cdot \dot{\mathbf{F}} = J(\mathbf{g}^i \otimes \mathbf{G}_i) \cdot \dot{\mathbf{F}}, \tag{5.49}$$

and thus find

$$[p(J-1)]^{\cdot} = p\dot{J} = pJ \mathbf{g}^j \cdot \mathbf{u}_{,j}, \tag{5.50}$$

where

$$J = \sqrt{\frac{g}{G}}. \tag{5.51}$$

Lastly, we note here that the invariance requirements arising in the second gradient deformation remain valid for the cases of the finite elastic deformations of general continuum bodies [89],[121] and hyperelastic soft membranes [123], and therefore, have been adopted in the present study without further proof.

5.2.2 Euler equilibrium equation

The virtual-work statement (Eq. (5.27)) together with Eqs. (5.28)-(5.29) suggest that

$$\begin{aligned}
\dot{E} &= \int_{\mathbb{B}} [\dot{W}(\mathbf{F})_{matrix} + \dot{W}(\varepsilon_1, \varepsilon_2)_{fiber} + C_1 \mathbf{c}_1 \cdot \dot{\mathbf{c}}_1 + C_2 \mathbf{c}_2 \cdot \dot{\mathbf{c}}_2 + \frac{1}{2} T \dot{\mathbf{c}}_1 \cdot \mathbf{c}_2 \\
&\quad + \frac{1}{2} T \mathbf{c}_1 \cdot \dot{\mathbf{c}}_2 - \{p(J-1)\}^{\cdot}] dV.
\end{aligned} \tag{5.52}$$

To proceed, we substitute the previously obtained expressions (see, Eqs. (5.32), (5.38), (5.45), (5.47) and (5.50)) into Eq. (5.52) and rearrange them to a bilinear form in $\mathbf{u}_{;jk}$ and $\mathbf{u}_{,j}$;

$$
\begin{aligned}
\dot{E} = & \int_{\mathbb{B}} [\mu G^{ij} + \frac{E_1}{2} \left(g_{kl} L^k L^l - 1 \right) L^i L^j + \frac{E_2}{2} \left(g_{kl} M^k M^l - 1 \right) M^i M^j] \mathbf{g}_i \cdot \mathbf{u}_{,j} dV \\
& - \int_{\mathbb{B}} [C_1 c_1^i \bar{\Gamma}_{lk}^j L^l L^k + C_2 c_2^i \bar{\Gamma}_{lk}^j M^l M^k + \frac{T}{2} c_1^i \bar{\Gamma}_{lk}^j M^l M^k + \frac{T}{2} c_2^i \bar{\Gamma}_{lk}^j L^l L^k + pJg^{ji}] \mathbf{g}_i \cdot \mathbf{u}_{,j} dV \\
& + \int_{\mathbb{B}} (C_1 c_1^i L^j L^k + C_2 c_2^i M^j M^k + \frac{T}{2} c_1^i M^j M^k + \frac{T}{2} c_2^i L^j L^k) \mathbf{g}_i \cdot \mathbf{u}_{;jk} dV, \quad (5.53)
\end{aligned}
$$

where we use the identities of $g_{il}\mathbf{g}^i = \mathbf{g}_l$ on Eq. (5.47) and $\mathbf{g}^j = \mathbf{g}_i g^{ji}$ on Eq. (5.50). Further, the integration by part of the last term of Eq. (5.53) yields

$$
\begin{aligned}
& (C_1 c_1^i L^j L^k + C_2 c_2^i M^j M^k + \frac{T}{2} c_1^i M^j M^k + \frac{T}{2} c_2^i L^j L^k) \mathbf{g}_i \cdot \mathbf{u}_{;jk} \\
= & [(C_1 c_1^i L^j L^k + C_2 c_2^i M^j M^k + \frac{T}{2} c_1^i M^j M^k + \frac{T}{2} c_2^i L^j L^k) \mathbf{g}_i \cdot \mathbf{u}_{,j}]_{;k} \\
& - [(C_1 c_1^i L^j L^k + C_2 c_2^i M^j M^k + \frac{T}{2} c_1^i M^j M^k + \frac{T}{2} c_2^i L^j L^k) \mathbf{g}_i]_{;k} \cdot \mathbf{u}_{,j}. \quad (5.54)
\end{aligned}
$$

Substituting the above into Eq. (5.53), we then obtain

$$
\begin{aligned}
\dot{E} = & \int_{\mathbb{B}} [\{\mu G^{ij} + \frac{E_1}{2} \left(g_{kl} L^k L^l - 1 \right) L^i L^j + \frac{E_2}{2} \left(g_{kl} M^k M^l - 1 \right) M^i M^j - C_1 c_1^i \bar{\Gamma}_{lk}^j L^l L^k \\
& - C_2 c_2^i \bar{\Gamma}_{lk}^j M^l M^k - \frac{T}{2} c_1^i \bar{\Gamma}_{lk}^j M^l M^k - \frac{T}{2} c_2^i \bar{\Gamma}_{lk}^j L^l L^k - pJg^{ji}\} \mathbf{g}_i - \{(C_1 c_1^i L^j L^k \\
& + C_2 c_2^i M^j M^k + \frac{T}{2} c_1^i M^j M^k + \frac{T}{2} c_2^i L^j L^k) \mathbf{g}_i\}_{;k}] \cdot \mathbf{u}_{,j} dV + \int_{\mathbb{B}} [(C_1 c_1^i L^j L^k \\
& + C_2 c_2^i M^j M^k + \frac{T}{2} c_1^i M^j M^k + \frac{T}{2} c_2^i L^j L^k) \mathbf{g}_i \cdot \mathbf{u}_{,j}]_{;k} dV. \quad (5.55)
\end{aligned}
$$

Eq. (5.55) may be further reduces to

$$
\dot{E} = \int_{\mathbb{B}} [\varphi^{ij} \mathbf{g}_i - (\psi^{ijk} \mathbf{g}_i)_{;k}] \cdot \mathbf{u}_{,j} dV + \int_{\partial \mathbb{B}} \psi^{ijk} \nu_k \mathbf{g}_i \cdot \mathbf{u}_{,j} dA, \quad (5.56)
$$

where $\boldsymbol{\nu} = v_i \mathbf{G}^i$ is the rightward unit normal to $\partial\mathbb{B}$ in the sense of the Green-Stokes' theorem and

$$
\begin{aligned}
\varphi^{ij} = & \mu G^{ij} + \frac{E_1}{2} \left(g_{kl} L^k L^l - 1 \right) L^i L^j + \frac{E_2}{2} \left(g_{kl} M^k M^l - 1 \right) M^i M^j \\
& - \bar{\Gamma}_{lk}^j (C_1 c_1^i L^l L^k - C_2 c_2^i M^l M^k - \frac{T}{2} c_1^i M^l M^k - \frac{T}{2} c_2^i L^l L^k) - pJg^{ji}, \\
\psi^{ijk} = & C_1 c_1^i L^j L^k + C_2 c_2^i M^j M^k + \frac{T}{2} c_1^i M^j M^k + \frac{T}{2} c_2^i L^j L^k. \quad (5.57)
\end{aligned}
$$

In the absence of distributed loads, it follows from Eq. (5.27) that the Euler equilibrium equation, holding in $\mathbb{B}$, satisfies

$$[\varphi^{ij}\mathbf{g}_i - (\psi^{ijk}\mathbf{g}_i)_{;k}]_{;j} = 0, \tag{5.58}$$

where, from Eqs. (5.4) and (5.6), we find

$$\mathbf{g}_{i;k} = (\Gamma^j_{ik} - \bar{\Gamma}^j_{ik})\mathbf{g}_j. \tag{5.59}$$

5.2.3 Boundary conditions

To derive the expressions of the associated boundary conditions, we again apply integration by part on the first integral of Eq. (5.56) and thereby obtain,

$$\dot{E} = \int_{\mathbb{B}}[\{\varphi^{ij}\mathbf{g}_i - (\psi^{ijk}\mathbf{g}_i)_{;k}\}\cdot\mathbf{u}]_{;j}dV - \int_{\mathbb{B}}[\varphi^{ij}\mathbf{g}_i - (\psi^{ijk}\mathbf{g}_i)_{;k}]_{;j}\cdot\mathbf{u}_{,j}dV + \int_{\partial\mathbb{B}}\psi^{ijk}\nu_k\mathbf{g}_i\cdot\mathbf{u}_{,j}dA. \tag{5.60}$$

Since the Euler equilibrium equation satisfies in $\mathbb{B}$ (i.e. $[\varphi^{ij}\mathbf{g}_i - (\psi^{ijk}\mathbf{g}_i)_{;k}]_{;j} = 0$), Eq. (5.60) reduces to

$$\dot{E} = \int_{\partial\mathbb{B}}[\varphi^{ij}\mathbf{g}_i - (\psi^{ijk}\mathbf{g}_i)_{;k}]\nu_j\cdot\mathbf{u}dA + \int_{\partial\mathbb{B}}\psi^{ijk}\nu_k\mathbf{g}_i\cdot\mathbf{u}_{,j}dA, \tag{5.61}$$

where the Green-Stokes' theorem is applied on the first term of Eq. (5.61).

Now, we decompose $\mathbf{u}_{,j}$ to

$$\mathbf{u}_{,j} = \frac{\partial\mathbf{u}}{\partial s}\frac{\partial s}{\partial\theta^j} + \frac{\partial\mathbf{u}}{\partial\nu}\frac{\partial\nu}{\partial\theta^j} = \mathbf{u}'\tau_j + \mathbf{u}_{,\nu}\nu_j, \tag{5.62}$$

where $\boldsymbol{\tau} = \tau_i\mathbf{G}^i = \mathbf{N}\times\boldsymbol{\nu}$ is the unit tangent to the boundary $\partial\mathbb{B}$ and $\mathbf{u}'$ and $\mathbf{u}_{,\nu}$ are, respectively, the tangential and normal derivatives of $\mathbf{u}$ on $\partial\mathbb{B}$ (i.e. $\mathbf{u}' = \partial\mathbf{u}/\partial s$ and $\mathbf{u}_{,\nu} = \partial\mathbf{u}/\partial\nu$). The substitution of the above into the second integral of Eq. (5.61) furnishes

$$\dot{E} = \int_{\partial\mathbb{B}}[\varphi^{ij}\mathbf{g}_i - (\psi^{ijk}\mathbf{g}_i)_{;k}]\nu_j\cdot\mathbf{u}dA + \int_{\partial\mathbb{B}}\psi^{ijk}\tau_j\nu_k\mathbf{g}_i\cdot\mathbf{u}'dA + \int_{\partial\mathbb{B}}\psi^{ijk}\nu_j\nu_k\mathbf{g}_i\cdot\mathbf{u}_{,\nu}dA. \tag{5.63}$$

We continue by applying integration by part on the second integral of the above and thereby obtain

$$\begin{aligned}\dot{E} &= \int_{\partial\mathbb{B}}[\varphi^{ij}\nu_j\mathbf{g}_i - (\psi^{ijk}\mathbf{g}_i)_{;k}\nu_j - (\psi^{ijk}\tau_j\nu_k\mathbf{g}_i)']\cdot\mathbf{u}dA + \int_{\partial\mathbb{B}}[\psi^{ijk}\tau_j\nu_k\mathbf{g}_i\cdot\mathbf{u}]'dA \\ &+ \int_{\partial\mathbb{B}}\psi^{ijk}\nu_j\nu_k\mathbf{g}_i\cdot\mathbf{u}_{,\nu}dA. \end{aligned} \tag{5.64}$$

Eq. (5.64) may be recast into the following standard form:

$$\dot{E} = \int_{\partial\mathbb{B}} [\varphi^{ij}\nu_j\mathbf{g}_i - (\psi^{ijk}\mathbf{g}_i)_{;k}\nu_j - (\psi^{ijk}\tau_j\nu_k\mathbf{g}_i)']\cdot\mathbf{u}dA + \int_{\partial\mathbb{B}}\psi^{ijk}\nu_j\nu_k\mathbf{g}_i\cdot\mathbf{u}_{,\nu}dA$$

$$- \sum_{l=1}^{n}\left\|\psi^{ijk}\tau_j\nu_k\mathbf{g}_i\right\|_l\cdot\mathbf{u}_l, \tag{5.65}$$

where the double bar symbol refers to the forward jump as the discontinuities of the boundary $\partial\mathbb{B}$ is traversed (i.e. $\|*\| = (*)^+ - (*)^-$) and the sum denotes the collection of all discontinuities.

It follows from Eq. (5.65) that the admissible mechanical powers are of the form (see, also, [20], [101], and [133])

$$P = \int_{\partial\mathbb{B}_t}\mathbf{t}\cdot\mathbf{u}dA + \int_{\partial\mathbb{B}_m}\mathbf{m}\cdot\mathbf{u}_{,\nu}dA + \sum_{l=1}^{n}\mathbf{f}_l\cdot\mathbf{u}_l. \tag{5.66}$$

Therefore, by comparing Eqs. (5.65) and (5.66), we conclude that

$$\mathbf{t} = \varphi^{ij}\nu_j\mathbf{g}_i - (\psi^{ijk}\mathbf{g}_i)_{;k}\nu_j - (\psi^{ijk}\tau_j\nu_k\mathbf{g}_i)',$$

$$\mathbf{m} = \psi^{ijk}\nu_j\nu_k\mathbf{g}_i, \text{ and}$$

$$\mathbf{f}_l = -\psi^{ijk}\tau_j\nu_k\mathbf{g}_i, \tag{5.67}$$

where $\mathbf{t}$, $\mathbf{m}$ and $\mathbf{f}_l$ are, respectively, the edge traction and edge moment and the lth corner force.

Lastly, we remark that the edge moments (double force) in Eq. (5.67), $\psi^{ijk}\nu_j\nu_k\mathbf{g}_i$, is the result of the second gradient of deformations sustained by the second-grade continua and can be interpreted as the energy couple to the Piola-type double stress, when it is prescribed on the boundaries (see, also, [86] and [112]).

5.3 Consideration of hyperelastic composites

Contemporary composite materials often exhibit nonlinear hyperelastic behaviors as an intrinsic property. For example, when carbon-fibers and/or fibrous reinforcements are used together with elastomeric matrix materials, they display unique strain-stiffening responses, also referred to as 'J-shaped' stress-strain behaviors [3]-[4]. Such distinct nonlinear responses of hyperelastic composites can be readily accommodated by the proposed model via the refinement of the energy potentials of fibers,

$W(\varepsilon_1, \varepsilon_2)_{fiber}$, and matrix materials, $W(\mathbf{F})_{matrix}$. For the desired application, we replace the energy potential of $W(\mathbf{F})_{matrix}$ using the Mooney Rivlin strain energy;

$$W(\mathbf{F})_{matrix} = \frac{\mu}{2}(I_1 - 3) + \frac{\kappa}{2}(I_2 - 3), \qquad (5.68)$$

from which the non-linear stress-strain responses of matrix materials may be characterized via the two material parameters of μ and κ. In the above, I_1 and I_2 are the principal invariants of the deformation gradient tensor which are defined, respectively, by

$$I_1 = tr(\mathbf{F}^T\mathbf{F}) \text{ and } I_2 = \frac{1}{2}[(tr(\mathbf{F}^T\mathbf{F}))^2 - tr((\mathbf{F}^T\mathbf{F})^2)]. \qquad (5.69)$$

Since $(I_1)_\mathbf{F} = 2\mathbf{F}$ and $(I_2)_\mathbf{F} = 2\mathbf{F}(I_1\mathbf{I} - \mathbf{F}^T \cdot \mathbf{F})$ (see, also, [114]), the variational derivative of Eq. (5.68) can be evaluated as

$$\dot{W}(\mathbf{F})_{matrix} = [\frac{\mu}{2}(I_1)_\mathbf{F} + \frac{\kappa}{2}(I_2)_\mathbf{F}] \cdot \dot{\mathbf{F}} = [\mu\mathbf{F} + \kappa\mathbf{F}\{(\mathbf{F} \cdot \mathbf{F})\mathbf{I} - \mathbf{F}^T\mathbf{F}\}] \cdot \dot{\mathbf{F}}. \qquad (5.70)$$

The substitution of Eqs. (5.10) and (5.30) into the above then yields

$$\dot{W}(\mathbf{F})_{matrix} = [\mu G^{ij} + \kappa g_{kl}(G^{kl}G^{ij} - G^{ik}G^{lj})]\mathbf{g}_i \cdot \mathbf{u}_{,j}, \qquad (5.71)$$

where from Eqs. (5.15) and (5.33), we find

$$G^{ij} = L^iL^j + M^iM^j \text{ and } g_{ij} = l_il_j + m_im_j + \cos\gamma(l_im_j + l_jm_i); \ \mathbf{l} \cdot \mathbf{m} = \cos\gamma, \quad (5.72)$$

where γ is an angle between the two families of fibers (non-orthogonal in general) in the deformed configuration.

To accommodate the nonlinear stress-stain responses of fibers, we consider the following energy potential of the polynomial type

$$W(\varepsilon_1, \varepsilon_2) = \frac{1}{3}E_1^1\varepsilon_1^3 + \frac{1}{2}E_2^1\varepsilon_1^2 + \frac{1}{3}E_1^2\varepsilon_2^3 + \frac{1}{2}E_2^2\varepsilon_2^2, \qquad (5.73)$$

where ε_1 and ε_2 denote the strain measures of the two different fiber families and E_α^1 and E_α^2 are the associated material parameters. Using the chain rule, the variational derivative of Eq. (5.73) can be evaluated as

$$\dot{W}(\varepsilon_1, \varepsilon_2)_{fiber} = (E_1^1\varepsilon_1^2 + E_2^1\varepsilon_1)(\varepsilon_1)_\mathbf{F} \cdot \dot{\mathbf{F}} + (E_1^2\varepsilon_2^2 + E_2^2\varepsilon_2)(\varepsilon_2)_\mathbf{F} \cdot \dot{\mathbf{F}}. \qquad (5.74)$$

142

Further, invoking the results in Eqs. (5.10) and (5.24), it can be readily seen that

$$
\begin{aligned}
E_1^1 \varepsilon_1^2 + E_2^1 \varepsilon_1 &= \frac{E_1^1}{4} \left(\mathbf{FL} \cdot \mathbf{FL} - 1\right)^2 + \frac{E_2^1}{2} \left(\mathbf{FL} \cdot \mathbf{FL} - 1\right) \\
&= \frac{E_1^1}{4} g_{kl} g_{mn} L^k L^l L^m L^n + g_{kl} L^k L^l \frac{(E_2^1 - E_1^1)}{2} \\
&\quad + \frac{(E_1^1 - 2E_2^1)}{4},
\end{aligned}
\tag{5.75}
$$

and similarly for

$$
\begin{aligned}
E_1^2 \varepsilon_2^2 + E_2^2 \varepsilon_2 &= \frac{E_1^2}{4} g_{kl} g_{mn} M^k M^l M^m M^n + g_{kl} M^k M^l \frac{(E_2^2 - E_1^2)}{2} \\
&\quad + \frac{(E_1^2 - 2E_2^2)}{4}.
\end{aligned}
\tag{5.76}
$$

Now, we substitute Eqs. (5.35)-(5.36), and (5.75)-(5.76) into Eq. (5.74) and thereby obtain

$$
\begin{aligned}
\dot{W}(\varepsilon_1, \varepsilon_2)_{fiber} &= [\frac{E_1^1}{4} g_{kl} g_{mn} L^k L^l L^m L^n + g_{kl} L^k L^l \frac{(E_2^1 - E_1^1)}{2} + \frac{E_1^1 - 2E_2^1}{4}] L^i L^j \mathbf{g}_i \cdot \mathbf{u}_{,j} \\
&\quad + [\frac{E_1^2}{4} g_{kl} g_{mn} M^k M^l M^m M^n + g_{kl} M^k M^l \frac{(E_2^2 - E_1^2)}{2} \\
&\quad + \frac{E_1^2 - 2E_2^2}{4}] M^i M^j \mathbf{g}_i \cdot \mathbf{u}_{,j}.
\end{aligned}
\tag{5.77}
$$

Hence, in view of Eqs. (5.71) and (5.77), the virtual-work statement of the fiber-matrix system (Eq. (5.52)) then furnishes

$$
\begin{aligned}
\dot{E} &= \int_{\mathbb{B}} [\{\mu G^{ij} + \kappa g_{kl}(G^{kl}G^{ij} - G^{ik}G^{lj}) + (\frac{E_1^1}{4} g_{kl} g_{mn} L^k L^l L^m L^n + g_{kl} L^k L^l \frac{(E_2^1 - E_1^1)}{2} \\
&\quad + \frac{E_1^1 - 2E_2^1}{4}) L^i L^j + (\frac{E_1^2}{4} g_{kl} g_{mn} M^k M^l M^m M^n + g_{kl} M^k M^l \frac{(E_2^2 - E_1^2)}{2} \\
&\quad + \frac{E_1^2 - 2E_2^2}{4}) M^i M^j\} \mathbf{g}_i \cdot \mathbf{u}_{,j} + C_1 \mathbf{c}_1 \cdot \dot{\mathbf{c}}_1 + C_2 \mathbf{c}_2 \cdot \dot{\mathbf{c}}_2 + \frac{1}{2} T \dot{\mathbf{c}}_1 \cdot \mathbf{c}_2 \\
&\quad + \frac{1}{2} T \mathbf{c}_1 \cdot \dot{\mathbf{c}}_2 - \{p(J - 1)\}] dV.
\end{aligned}
\tag{5.78}
$$

Consequently, proceeding the same spirit as in Eqs. (5.53)-(5.56), we find that

$$
\begin{aligned}
\varphi^{ij} &= \mu G^{ij} + \kappa g_{kl}(G^{kl}G^{ij} - G^{ik}G^{lj}) + (\frac{E_1^1}{4} g_{kl} g_{mn} L^k L^l L^m L^n + g_{kl} L^k L^l \frac{(E_2^1 - E_1^1)}{2} \\
&\quad + \frac{E_1^1 - 2E_2^1}{4}) L^i L^j + (\frac{E_1^2}{4} g_{kl} g_{mn} M^k M^l M^m M^n + g_{kl} M^k M^l \frac{(E_2^2 - E_1^2)}{2} \\
&\quad + \frac{E_1^2 - 2E_2^2}{4}) M^i M^j - \bar{\Gamma}_{lk}^j (C_1 c_1^i L^l L^k - C_2 c_2^i M^l M^k - \frac{T}{2} c_1^i M^l M^k \\
&\quad - \frac{T}{2} c_2^i L^l L^k) - pJg^{ji}, \\
\psi^{ijk} &= C_1 c_1^i L^j L^k + C_2 c_2^i M^j M^k + \frac{T}{2} c_1^i M^j M^k + \frac{T}{2} c_2^i L^j L^k,
\end{aligned}
\tag{5.79}
$$

143

which satisfies the following equilibrium equation, holding in $\mathbb{B}$,

$$[\varphi^{ij}\mathbf{g}_i - (\psi^{ijk}\mathbf{g}_i)_{;k}]_{;j} = 0. \tag{5.80}$$

The associated boundary conditions can also be derived via the same procedures as done in Eqs. (5.60)-(5.66) which turn out to be the same form as in Eq. (5.67) except the expressions for φ^{ij} and ψ^{ijk} that are obtained in Eq. (5.79). Implementations of the obtained nonlinear model toward the particular types of hyperelastic composites will be discussed, separately, in later sections.

5.4   Model implementations

In this section, we present the implementation of the proposed model in the orthonormal Cartesian basis $(\theta = \theta^i \mathbf{e}_i)$ to examine its performance and practical utility. The associated results and comparisons with the experimental data sets will be discussed separately in the next section.

Let us consider an initially flat rectangular-shaped fiber composite with finite thickness (in X^3 direction) and its boundaries are aligned with the referential coordinate directions. Hence, it is assumed that the curvilinear coordinates, θ^i, are initially coincide with the referential Cartesian frame X^A (i.e. $\theta^i \equiv X^A$) and are orthogonal prior to deformations. Further, the fibers' trajectories are presumed to be initially straight and remain fairly straight within a finite local regime after deformations and thus their respective natural basis, $\mathbf{g}_i$, may be inferred to be locally a function of referential coordinate (i.e. $\mathbf{g}_i = \mathbf{g}_i(X^A)$). More general cases can be easily accommodated by using the appropriate curvilinear coordinates such as spherical, elliptical and polar coordinates. However, the presumed orthogonality framed in the orthonormal Cartesian coordinates suffices to extract the important aspect of the proposed model.

Within this prescription, we deduce

$$\begin{aligned}
\mathbf{G}_i &= \frac{\partial \mathbf{X}}{\partial \theta^i} = \frac{\partial \mathbf{X}}{\partial X^A} = \frac{\partial X^B \mathbf{E}_B}{\partial X^A} = \delta_{BA}\mathbf{E}_B = \mathbf{E}_A, \\
\mathbf{G}^i &= \frac{\partial \theta^i}{\partial \mathbf{X}} = \frac{\partial X^A}{\partial \mathbf{X}} = \frac{\partial X^A}{\partial X^B \mathbf{E}_B} = \mathbf{E}_A, \\
G_{ij} &= \mathbf{G}_i{\cdot}\mathbf{G}_j = \mathbf{E}_A{\cdot}\mathbf{E}_B \equiv G_{AB}, \ G^{ij} = \mathbf{E}_A{\cdot}\mathbf{E}_B \equiv G^{AB} \\
\text{and } \mathbf{G}^j &= \mathbf{G}_i G^{ij} = \mathbf{E}_A(\mathbf{E}_A{\cdot}\mathbf{E}_B) = \mathbf{E}_B.
\end{aligned} \tag{5.81}$$

Hence, the associated Levi-Civita connection coefficient identically vanishes; i.e.

$$\bar{\Gamma}^k_{ij} = \mathbf{G}_{i,j} \cdot \mathbf{G}^k = \mathbf{E}_{A,B} \cdot \mathbf{E}_C = 0; \ (\because \mathbf{E}_{A,B} = \frac{\partial \mathbf{E}_A}{\partial X^B} = 0). \tag{5.82}$$

It is noted that the above results do not necessarily mean that the natural curvilinear basis $(\mathbf{g}_i)$ induced by the deformed body, $\mathfrak{b}$, merges into the Lagrangian frame of reference $(\mathbf{e}_i)$. In fact, it can be seen that

$$\mathbf{g}_i = \frac{\partial \mathbf{r}}{\partial \theta^i} = \frac{\partial r^j \mathbf{e}_j}{\partial X^A} = F_{jA} \mathbf{e}_j \equiv \mathbf{g}_A, \tag{5.83}$$

where $F_{iA} = \partial r^i / \partial X^A$ are the components of the deformation gradient tensor and $\mathbf{e}_i = d\mathbf{r}/dx^i$ is the Lagrangian frame of reference. Further, using Eq. (5.83), we reduce $\mathbf{g}_{i,j}$ and $\mathbf{g}^i$ to

$$\begin{aligned}
\mathbf{g}_{i,j} &= \frac{\partial (F_{iA} \mathbf{e}_i)}{\partial \theta^j} = \frac{\partial (F_{iA} \mathbf{e}_i)}{\partial X^B} = F_{iA,B} \mathbf{e}_i \equiv \mathbf{g}_{A,B}, \\
\mathbf{g}^i &= \frac{\partial \theta^i}{\partial \mathbf{r}} = \frac{\partial X^A}{\partial \mathbf{r}} = \frac{\partial X^A}{\partial r^j \mathbf{e}_j} = (F_{jA})^{-1} \mathbf{e}_j \equiv \mathbf{g}^A,
\end{aligned} \tag{5.84}$$

and thereby obtain

$$\begin{aligned}
\Gamma^k_{ij} &= \mathbf{g}_{i,j} \cdot \mathbf{g}^k = \mathbf{g}_{A,B} \cdot \mathbf{g}^C = F_{iA,B} \mathbf{e}_i \cdot (F_{jC})^{-1} \mathbf{e}_j = F_{iA,B}(F_{iC})^{-1} \equiv \Gamma^C_{AB}, \\
g_{ij} &= \mathbf{g}_i \cdot \mathbf{g}_j = \mathbf{g}_A \cdot \mathbf{g}_B \overset{(5.83)}{=} F_{iA} F_{iB} \equiv g_{AB}, \\
\text{and } g^{ij} &= \mathbf{g}^i \cdot \mathbf{g}^j = \mathbf{g}^A \cdot \mathbf{g}^B \overset{(5.84)}{=} (F_{iA} F_{iB})^{-1} \equiv g^{AB},
\end{aligned} \tag{5.85}$$

which are, respectively, the Levi-Civita connection coefficients, the metric and the dual metric induced by the coordinates in $\mathfrak{b}$. Lastly, combining the results in Eqs. (5.82)-(5.85), the covariant derivative of $\mathbf{g}_i$ can be evaluated as

$$\mathbf{g}_{i;j} = (\Gamma^k_{ij} - \bar{\Gamma}^k_{ij}) \mathbf{g}_k \overset{(5.82)}{=} \Gamma^C_{AB} \mathbf{g}_C \overset{(5.83),(5.85)}{=} F_{iA,B}(F_{iC})^{-1} F_{jC} \mathbf{e}_j = F_{iA,B} \mathbf{e}_i \equiv \mathbf{g}_{A;B}, \tag{5.86}$$

where $(F_{iC})^{-1} F_{jC} = (\partial X^C / \partial r^i)(\partial r^j / \partial X_C) = \delta_{ij}$.

As a direct consequence of the results in Eqs. (5.81)-(5.85), the terms in Eqs.

(5.79)-(5.80)) now become, for example,

$$(\mu G^{ij}\mathbf{g}_i)_{;j} = (\mu G^{AB}\mathbf{g}_A)_{;B} = [\mu(\mathbf{E}_A\cdot\mathbf{E}_B)F_{iA}\mathbf{e}_i]_{;B} = (\mu\delta_{AB}F_{iA}\mathbf{e}_i)_{;B} = \mu F_{iB,B}\mathbf{e}_i,$$

$$(g_{kl}L^kL^lL^iL^j\mathbf{g}_i)_{;j} = (g_{CD}L^AL^BL^CL^D\mathbf{g}_A)_{;B} = (F_{iA}F_{jC}F_{jD}L^AL^BL^CL^D\mathbf{e}_i)_{;B}$$

$$= (F_{iA}F_{jC}F_{jD})_{,B}L^AL^BL^CL^D\mathbf{e}_i,$$

$$(pJg^{ji}\mathbf{g}_i)_{;j} = (pJg^{BA}\mathbf{g}_A)_{;B} = (pJ(F_{iA}F_{iB})^{-1}F_{jA}\mathbf{e}_j)_{;B} = (pF_{iB}^*\mathbf{e}_i)_{;B} = p_{,B}F_{iB}^*\mathbf{e}_i,$$

and $[c_1^i L^j L^k\mathbf{g}_i)_{;k}]_{;j} = [(\Gamma^i_{mn} - \bar{\Gamma}^i_{mn})L^mL^nL^jL^k\mathbf{g}_i)_{;k}]_{;j} = [\Gamma^A_{DE}L^DL^EL^BL^C\mathbf{g}_A)_{;C}]_{;B}$

$$= [(F_{jD,E}(F_{jA})^{-1}F_{iA}L^DL^EL^BL^C\mathbf{e}_i)_{;C}]_{;B}$$

$$= F_{iA,BCD}L^AL^BL^CL^D\mathbf{e}_i, \tag{5.87}$$

where we use the identities of $JF_{iA}^{-1} = F_{iA}^*$ and $F_{iA,A}^* = 0$ (the Piola identity). Thus, the equilibrium equation (Eqs. (5.79)-(5.80)) may be reformulated into the flowing form for the desired applications;

$$0 = [\mu F_{iA,A} - p_{,A}F_{iA}^* + \frac{E_1}{2}(F_{iB}F_{jC}F_{jD})_{,A}L^AL^BL^CL^D - \frac{E_1}{2}F_{iB,A}L^AL^B$$

$$+\frac{E_2}{2}(F_{iB}F_{jC}F_{jD})_{,A}M^AM^BM^CM^D - \frac{E_2}{2}F_{iB,A}M^AM^B + C_1F_{iB,ACD}L^AL^BL^CL^D$$

$$+C_2F_{iB,ACD}M^AM^BM^CM^D+\frac{T}{2}F_{iB,ACD}(L^AL^BM^CM^D+M^AM^BL^CL^D)]\mathbf{e}_i(5.88)$$

which hold in $\mathbb{B}$. In addition, we recast the associated boundary conditions (Eq. (5.67)) as

$$\mathbf{t} = \varphi^{AB}\mathbf{g}_A\nu_B - (\psi^{ABC}\mathbf{g}_A)_{;C}\nu_B - (\psi^{ABC}\tau_B\nu_C\mathbf{g}_A)',$$

$$\mathbf{m} = \psi^{ABC}\nu_B\nu_C\mathbf{g}_A, \text{ and } \mathbf{f} = -\psi^{ABC}\tau_B\nu_C\mathbf{g}_A, \tag{5.89}$$

where

$$\varphi^{AB}\mathbf{g}_A = [\mu F_{iB} + \frac{E_1}{2}[(F_{jC}F_{jD}L^CL^D - 1)F_{iA}L^AL^B + \frac{E_2}{2}[(F_{jC}F_{jD}M^CM^D$$

$$-1)F_{iA}M^AM^B - pF_{iB}^*]\mathbf{e}_i,$$

$$\psi^{ABC}\mathbf{g}_A = [F_{iA,D}L^AL^B(C_1L^CL^D + \frac{T}{2}M^CM^D) + F_{iA,D}M^AM^B(C_2M^CM^D$$

$$+\frac{T}{2}L^CL^D)]\mathbf{e}_i. \tag{5.90}$$

Lastly, invoking the results in Eq. (5.87) together with the evaluations of higher order

terms arising in the mapping of nonlinear stress-stain responses, we obtain

$$
\begin{aligned}
(\kappa g_{kl}G^{kl}G^{ij}\mathbf{g}_i)_{;j} &= (\kappa g_{CD}G^{CD}G^{AB}\mathbf{g}_A)_{;B} = (\kappa F_{jC}F_{jC}F_{iB}\mathbf{e}_i)_{;B} \\
&= \kappa(F_{jC}F_{jC}F_{iB})_{,B}\mathbf{e}_i, \\
(g_{kl}g_{mn}M^kM^lM^mM^n\mathbf{g}_i)_{;j} &= (g_{CD}g_{EF}M^CM^DM^EM^F\mathbf{g}_A)_{;B} \\
&= (F_{jC}F_{jD}F_{kE}F_{kF}M^CM^DM^EM^FF_{iA}\mathbf{e}_i)_{,B} \\
&= (F_{jC}F_{jD}F_{kE}F_{kF}F_{iA})_{,B}M^CM^DM^EM^F\mathbf{e}_i, \quad (5.91)
\end{aligned}
$$

and similarly for other higher order terms (e.g. $(g_{kl}g_{mn}L^kL^lL^mL^n\mathbf{g}_i)_{;j}$, $(\kappa g_{kl}G^{ik}G^{lj}\mathbf{g}_i)_{;j}$ etc...). Thus, the case of hyperelastic composites can be readily implemented as (see, Eqs. (5.77), and (5.79)-(5.80))

$$
\begin{aligned}
0 = [&\mu F_{iA,A} + \kappa(F_{jC}F_{jC}F_{iA} - F_{jA}F_{jB}F_{iB})_{,A} - p_{,A}F_{iA}^* \\
&+\frac{E_1^1}{4}(F_{jC}F_{jD}F_{kE}F_{kF}F_{iB})_{,A}L^AL^BL^CL^DL^EL^F \\
&+\frac{(E_2^1 - E_1^1)}{2}(F_{iB}F_{jC}F_{jD})_{,A}L^AL^BL^CL^D + \frac{E_1^1 - 2E_2^1}{4}F_{iB,A}L^AL^B \\
&+\frac{E_1^2}{4}(F_{jC}F_{jD}F_{kE}F_{kF}F_{iB})_{,A}M^AM^BM^CM^DM^EM^F \qquad (5.92)\\
&+\frac{(E_2^2 - E_1^2)}{2}(F_{iB}F_{jC}F_{jD})_{,A}M^AM^BM^CM^D + \frac{E_1^2 - 2E_2^2}{4}F_{iB,A}M^AM^B \\
&+F_{iB,ACD}(C_1 L^AL^BL^CL^D + C_2 M^AM^BM^CM^D + \frac{T}{2}L^AL^BM^CM^D + \frac{T}{2}M^AM^BL^CL^D)]\mathbf{e}_i.
\end{aligned}
$$

It is noted that the corresponding boundary conditions (Eqs. (5.89)-(5.90)) remain intact except the expression of $\varphi^{AB}\mathbf{g}_A$ which is found to be

$$
\begin{aligned}
\varphi^{AB}\mathbf{g}_A = [&\mu F_{iB} + \kappa F_{iA}(F_{jC}F_{jC}\delta_{AB} - F_{jA}F_{jB}) + \frac{E_1^1 - 2E_2^1}{2}(F_{iA}L^AL^B) \\
&+\frac{E_1^2 - 2E_2^2}{2}(F_{iA}M^AM^B) + F_{iA}F_{jC}F_{jD}F_{kE}F_{kF}(\frac{E_1^1}{4}L^AL^BL^CL^DL^EL^F \\
&+\frac{E_1^2}{4}M^AM^BM^CM^DM^EM^F) + F_{iA}F_{jC}F_{jD}(\frac{E_2^1 - E_1^1}{2}L^AL^BL^CL^D \\
&+\frac{E_2^2 - E_1^2}{2}M^AM^BM^CM^D) - pF_{iB}^*]\mathbf{e}_i. \qquad (5.93)
\end{aligned}
$$

5.5   Results and discussions

Comparisons with the inhouse experimental results and contemporary applications in the literature are presented in this section to demonstrate the performance and potential utility of the obtained model. For the stated purpose, we consider the uniaxial

tensile test of elastomeric composites, spherical indentation of Polyactic acid (PLA) composites and Deployable Composite Boom (DCB). Emphasis is placed on the characterization of the stress-strain responses and deformation analyses of intended composites while maintaining compactness and relative simplicity in the corresponding model implementation.

5.5.1 Uniaxial Tension of Hyperelastic Composite

The inhouse uniaxial tension test of elastomeric composites reinforced with polyester fibers (PES-2 and PES-3) are considered in this section. This is a special case of the proposed model where the elastomeric composite is subjected to finite plane deformation that the fiber's directors remain in a plane, with no out-of-plane components (i.e. $M_3 = L_3 = \chi_3 = 0$) and the corresponding deformations (i.e. χ_1 and χ_2) are independent of the out-of-plane coordinate (X_3). Ecoflex 0050 (Smooth-on Inc., USA) is used as the matrix material which is considered to be one of the promising materials in biomechanical applications for its high tear resistance and large extensibility [128]-[130]. The reinforced elastomer composite films were fabricated in a three-layer configuration using a layer by layer method (Fig. 5.2 (a)). The effective dimension of the samples is $50mm \times 25mm$; keeping an aspect ratio of $2:1$ and the actual size of fabricated composites is $78mm \times 25mm$ with the end allowance of $14mm$ to avoid end effects caused by the grips of the testing machine (see, Fig. 5.2 (c)). Instron 5943 (Illinois Tool Works Inc., USA) is used to measure the stress-strain responses of the Ecoflex 0050, PES fibers, and the composites (see, Fig. 5.2 (b)). The test apparatus records the displacement and force as a function of time for each uniaxial tensile test and the corresponding extension rate was set to be $2.5mm/min$ to avoid/minimize possible viscous responses (see, also, [134]–[136]). The response of Ecoflex 0050 (matrix material) is characterized by using the Mooney-Rivlin model and the corresponding material parameters are found to be $\mu = 0.1013~MPa$ and $\kappa = -0.14$ Mpa, respectively (see, Fig. 5.3 (left)). Further, the strain-stiffening responses of PES-2 and PES-3 fibers may be accommodated by the proposed polynomial energy potential (Eq. (5.73)) with the characterization parameters of $E_1^1 = E_1^2 = 3.45MPa$, $E_2^1 = E_2^2 = 0.65MPa$ for PES-2, and $E_1^1 = E_1^2 = 2.35MPa$, $E_2^1 = E_2^2 = -0.2MPa$ for PES-3 (Fig. 5.3 (right)). Hence, in view of Eqs. (5.21), (5.68) and (5.73), the
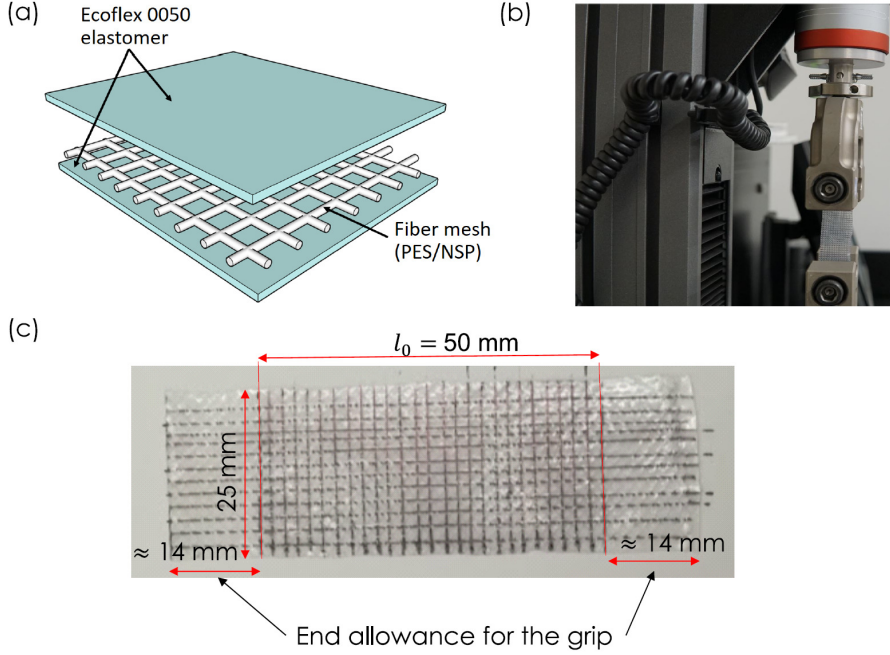
Figure 5.2: Sample preparation (a) and experimental set up for the uniaxial tension test (b)-(c).

following energy potential may be considered for the constitutive description of the PES-2 composite

$$
\begin{aligned}
U(\mathbf{F}, \varepsilon, \mathbf{g}, p) &= \frac{0.1013}{2}(I_1 - 3) - \frac{0.14}{2}(I_2 - 3) + \frac{3.45}{3}(\varepsilon_1^3 + \varepsilon_2^3) + \frac{0.65}{2}(\varepsilon_1^2 + \varepsilon_2^2) \\
&\quad + \frac{1}{2}(\mathbf{g}_1 \cdot \mathbf{g}_1 + \mathbf{g}_2 \cdot \mathbf{g}_2) + \frac{2.2}{2}\mathbf{g}_1 \cdot \mathbf{g}_2 - p(J - 1),
\end{aligned}
\tag{5.94}
$$

from which the corresponding Euler equilibrium equation can be obtained as (see, also, Eqs. (5.79)-(5.80) and (5.92))

$$
\begin{aligned}
0 =\ & [0.1013\chi_{i,AA} - 0.14(\chi_{j,C}\chi_{j,C}\chi_{i,A} - \chi_{j,A}\chi_{j,B}\chi_{iB}),_A - p,_A\chi_{i,A}^* \\
&+ \frac{3.45}{4}(\chi_{j,C}\chi_{j,D}\chi_{k,E}\chi_{k,F}\chi_{i,B}),_A L^A L^B L^C L^D L^E L^F + \frac{3.45 - 1.3}{4}\chi_{i,BA}M^A M^B \\
&+ \frac{(0.65 - 3.45)}{2}(\chi_{i,B}\chi_{j,C}\chi_{j,D}),_A L^A L^B L^C L^D + \frac{3.45 - 1.3}{4}\chi_{i,BA}L^A L^B \\
&+ \frac{3.45}{4}(\chi_{j,C}\chi_{j,D}\chi_{k,E}\chi_{k,F}\chi_{i,B}),_A M^A M^B M^C M^D M^E M^F \\
&+ \frac{(0.65 - 3.45)}{2}(\chi_{i,B}\chi_{j,C}\chi_{j,D}),_A M^A M^B M^C M^D \\
&+ \chi_{i,BACD}(0.5L^A L^B L^C L^D + 0.5M^A M^B M^C M^D + \frac{2.2}{2}L^A L^B M^C M^D + \frac{2.2}{2}M^A M^B L^C L^D)]\mathbf{e}_i.
\end{aligned}
\tag{5.95}
$$

149
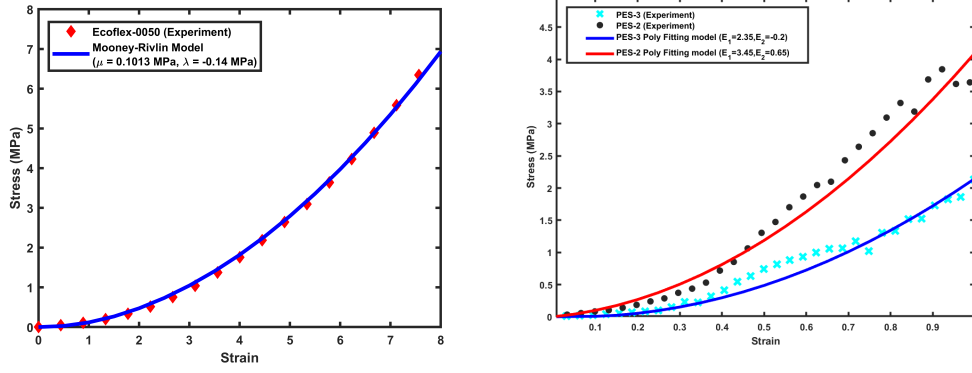
Figure 5.3: Stress-strain curves: Ecoflex-0050 and the Mooney Rivlin model (left); Stress-strain curves: PES-2 & PES-3 fibers and polynomial model ($W(\varepsilon) = \frac{1}{3}E_1\varepsilon^3 + \frac{1}{2}E_2\varepsilon^2$) (right).

In the above, ε_{ij} is the 2-D permutation; $\varepsilon_{12} = -\varepsilon_{21} = 1$, $\varepsilon_{11} = \varepsilon_{22} = 0$. Eq. (5.95) together with the condition of the bulk incompressibility,

$$\det F = \chi_{1,1}\chi_{2,2} - \chi_{1,2}\chi_{2,1} = 1, \tag{5.96}$$

determines the unknown potentials of χ_1, χ_2 and p which describes the nonlinear responses of the Ecoflex0050-PES composite.

Lastly, the admissible boundary conditions (Eqs. (5.89)-(5.90), and (5.93)) in the case of rectangular shaped samples (see, Fig. 5.4 (a)-(b)) furnish

$$
\begin{aligned}
t_1 &= \varphi^{A1}\chi_{1,A} - (\psi^{A1C}\chi_{1,A})_{;C} - (\psi^{A21}\chi_{1,A})', \ t_2 = 0 \text{ at } X_1 = a, \ -a, \text{ and} \\
t_1 &= 0, \ t_2 = 0 \text{ at } X_2 = b, \ -b,
\end{aligned}
\tag{5.97}
$$

where

$$
\begin{aligned}
\varphi^{AB}\chi_{i,A}\mathbf{e}_i &= [\mu\chi_{i,B} + \kappa\chi_{i,A}(\chi_{j,C}\chi_{j,C}\delta_{AB} - \chi_{j,A}\chi_{j,B}) + \frac{3.45 - 0.65}{2}(\chi_{i,A}L^A L^B) \\
&\quad + \frac{3.45 - 0.65}{2}(\chi_{i,A}M^A M^B) + \chi_{i,A}\chi_{j,C}\chi_{j,D}\chi_{k,E}\chi_{k,F}(\frac{3.45}{4}L^A L^B L^C L^D L^E L^F \\
&\quad + \frac{3.45}{4}M^A M^B M^C M^D M^E M^F) + \chi_{i,A}\chi_{j,C}\chi_{j,D}(\frac{0.65 - 3.45}{2}L^A L^B L^C L^D \\
&\quad + \frac{0.65 - 3.45}{2}M^A M^B M^C M^D) - p\chi_{i,B}^*]\mathbf{e}_i, \text{ and} \\
\psi^{ABC}\chi_{i,A}\mathbf{e}_i &= [\chi_{i,AD}L^A L^B(0.5L^C L^D + \frac{2.2}{2}M^C M^D) + \chi_{i,AD}M^A M^B(0.5M^C M^D \\
&\quad + \frac{2.2}{2}L^C L^D)]\mathbf{e}_i.
\end{aligned}
\tag{5.98}
$$

150

Eqs. (5.97)-(5.98) can be obtained by replacing $\mathbf{g}_A = F_{jA}\mathbf{e}_j$ on the left side of the Eq. (5.90)$_2$ and Eq. (5.93) while substituting the fibers' directors (i.e. $\mathbf{L} = L^1\mathbf{E}_1 + L^2\mathbf{E}_2 = \cos(\pi/4)\mathbf{E}_1 - \sin(\pi/4)\mathbf{E}_2$ and $\mathbf{M} = M^1\mathbf{E}_1 + M^2\mathbf{E}_2 = \cos(\pi/4)\mathbf{E}_1 + \sin(\pi/4)\mathbf{E}_2$) and the normal and tangential vectors of the designated boundary (i.e. $\boldsymbol{\nu} = \nu_1\mathbf{E}_1 + \nu_2\mathbf{E}_2 = \mathbf{E}_1$ and $\boldsymbol{\tau} = \tau_1\mathbf{E}_1 + \tau_2\mathbf{E}_2 = \mathbf{E}_2$, see, also, Fig. 5.4 (a)-(c)). Repeating the same procedure as demonstrated in Eqs. (5.94)-(5.98), the case of PES-3 composite can also be simulated with the configuration parameters of $E_1^1 = E_1^2 = 2.35MPa$ and $E_2^1 = E_2^2 = -0.2MPa$. Fig. 5.5 illustrates the stress-strain curves of the Ecoflex0050-
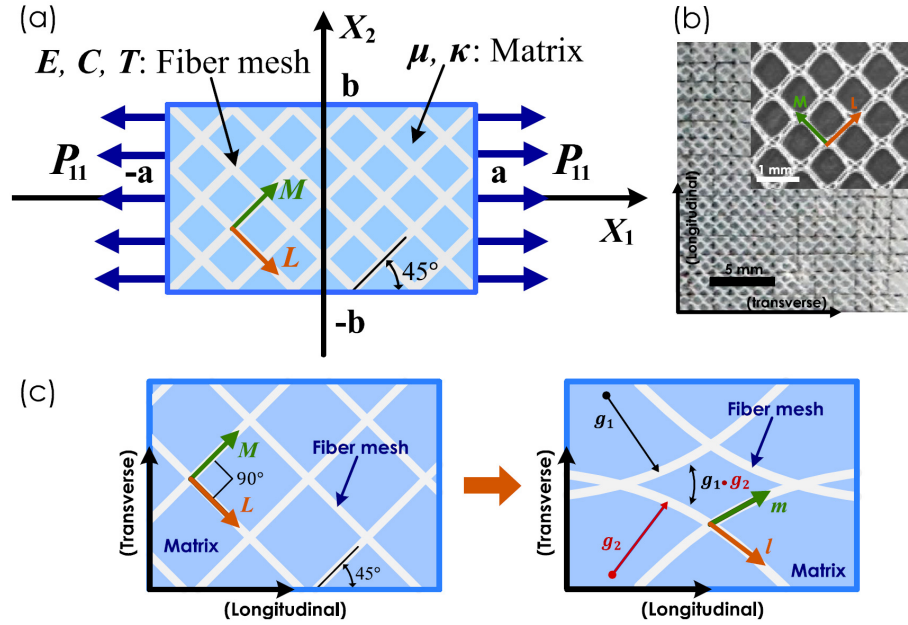
Figure 5.4: Schematic of the problem : $2a = 50mm$ and $2b = 25mm$ (a); Sample orientation(b); Kinematics of bidirectional fiber mesh under uniaxial tension (c).

PES composite reinforced, respectively, by the PES-2 and PES-3 fibers. It is evident that the proposed model successfully predicts the strain-stiffening responses of the composites by integrating the predetermined material parameters of the Ecoflex matrix material and the PES fibers. This may be of practical interest, especially in the design stage, since the mechanical responses of the intended composite can be instantly estimated using the proposed model. In addition, the general deformation profiles of the PES composite can be evaluated via the mapping:

$$\boldsymbol{\chi} = \chi_1(\mathbf{X})\mathbf{e}_2 + \chi_2(\mathbf{X})\mathbf{e}_2, \tag{5.99}$$

where $\mathbf{X} = X_1\mathbf{E}_1 + X_2\mathbf{E}_2$ is the initial position. The corresponding deformation profiles
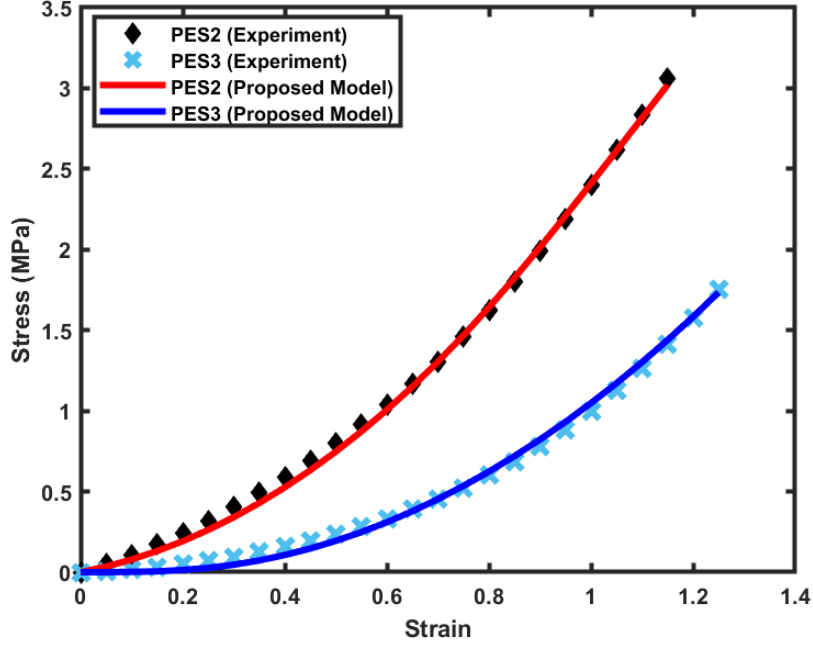
Figure 5.5: Stress-strain curves of PES composites predicted by the proposed model.

are then superposed on the experimental images of PES-2 and PES-3 composite samples at 50% elongation (see, Fig. 5.6). Despite the uncertainties arising in the image processing and fittings, the deformation profiles from the proposed bidirectional model and the uniaxial tension experiment demonstrate close agreement throughout the entire domain of interest for both the PES-2 and the PES-3 cases. Lastly, the shear strain distributions of the PES composites are computed to examine the utility and accuracy of the proposed model in the local microstructure deformation analysis of the reinforced composites. Using the mesh grids of $1.5mm \times 1.5mm$, printed on the surfaces of the PES composites, the material points of the deformed composite are recorded via the Matlab image processing toolbox from which the corresponding shear angle configurations are estimated. Also, the deformation maps of χ_1 and χ_2, obtained directly from the proposed bidirectional model, are post-processed using the relation:

$$\gamma_{xy} = \alpha + \beta \text{ where } \alpha = \tan^{-1}(\frac{\chi_{2,1}}{1+\chi_{1,1}}) \text{ and } \beta = \tan^{-1}(\frac{\chi_{1,2}}{1+\chi_{2,2}}) \qquad (5.100)$$

to evaluate the shear strain distributions of the resulting composites. The shear strain distribution results in Fig. 5.7 (bottom images of (a) and (b)) indicate that

152
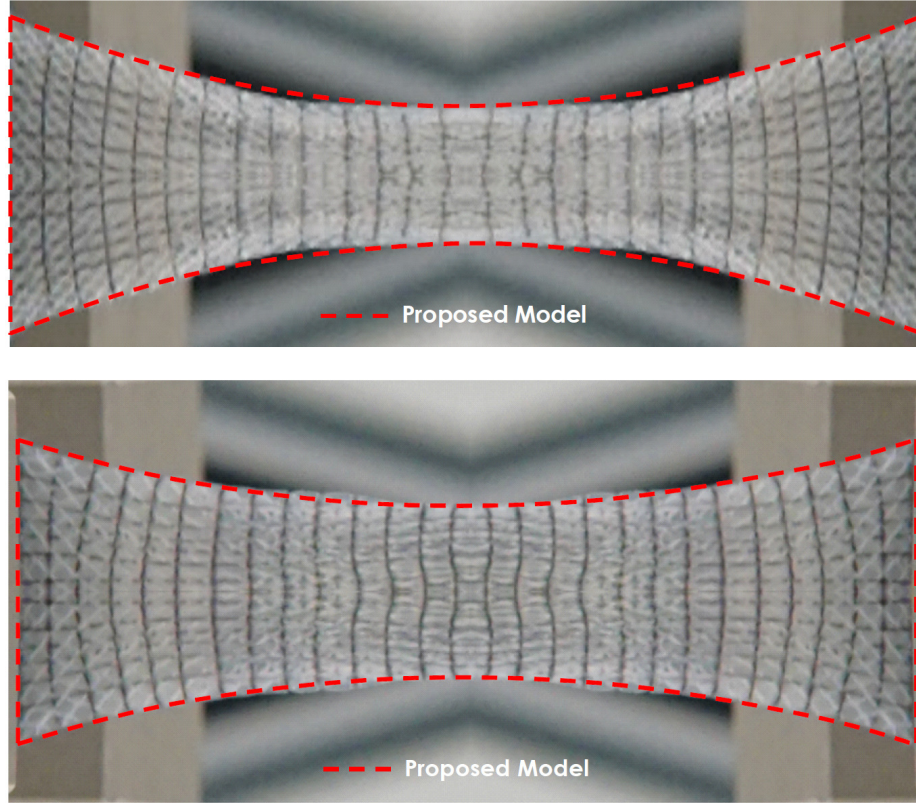
Figure 5.6: Deformation profiles at 50% elongation: PES-2 (top), PES-3 (bottom).

the proposed model successfully predicts the smooth and continuous shear strain fields throughout the entire domain of interest which also show good agreement with the in-house experiments (upper images of (a) and (b)) unlike those estimated by the traditional continuum theory (first-order) where substantial discontinuities are observed (see, also, [85], [87], [110]).

5.5.2 Draping of PLA- fabric Composites

Thermoplastic composites reinforced with fibrous materials have drawn increased amount of attention in recent years due to their enhanced properties in strength and toughness together with high service temperatures which make them a promising candidate in aerospace, engineering and biological applications [137]-[138]. The Polyether-Ketone-Ketone (PEKK), Polyether-Ether-Ketone (PEEK) and Polylactic Acid (PLA) are three common types of thermoplastic matrix materials. The applications of which, however, are somewhat limited in their raw form due to the low impact strength and brittleness [137], [139]–[142]. The properties of these thermo-
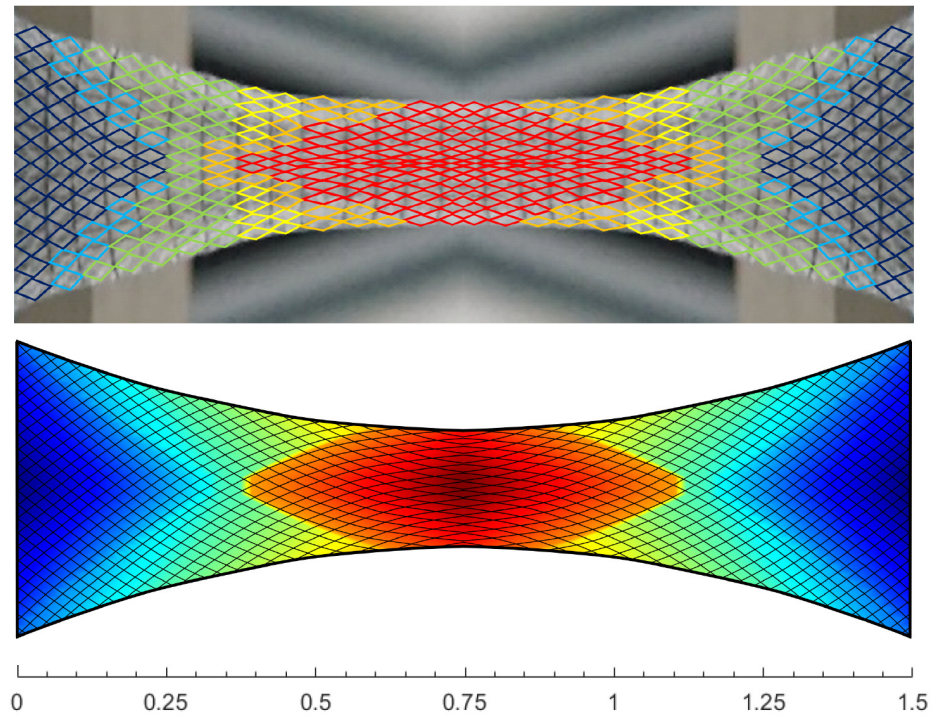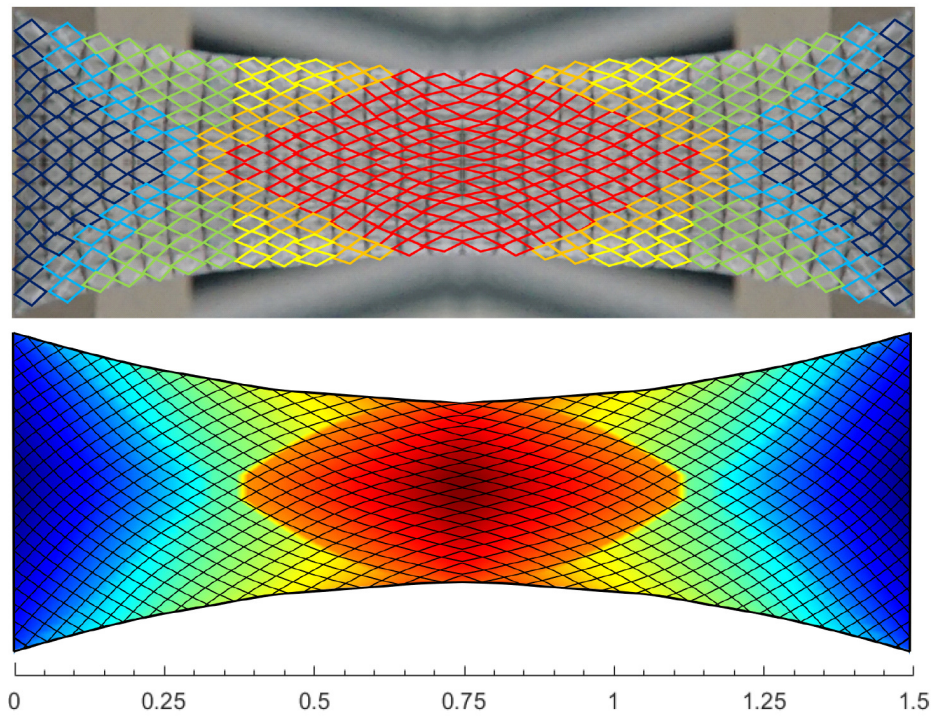
Figure 5.7: Shear strain distribution of PES2 at 50% elongation; experiement (top), simulation (bottom). (b) Shear strain distribution of PES3 at 50% elongation; experiement (top), simulation (bottom).

154

plastic materials can be effectively enhanced by using natural fiber reinforcements such as bamboo fibers [138] which has also drawn renewed attention for their easy accessibility, renewability, CO2 neutrality and non-toxicity [143]-[144]. In this section, we present the implementation of the proposed model in the characterization and deformation analysis of the PLA matrix material reinforced with natural bamboo fibers. For the stated purpose, we consider the PLA-bamboo fabric composite subjected to out-of-plane deformations in $\mathbf{E}_3$ direction such that the corresponding response functions, unlike those in the uniaxial tension case, no longer remain in a plane (i.e. $\boldsymbol{\chi} = \chi_1(\mathbf{X})\mathbf{e}_2 + \chi_2(\mathbf{X})\mathbf{e}_2 + \chi_3(\mathbf{X})\mathbf{e}_3$) and similarly for the rest of cases in the next section. The referred drape test in Fig. 5.8 is designed to evaluate the stretching deformation of a composite sheet under punching load (typically with a hemispherical punch) which is one of the common experimental settings for studying the formality of a thin composite sheet also known as Eichsen test [145]-[146]. The response of the PLA matrix material is characterize by using the Mooney-Rivlin
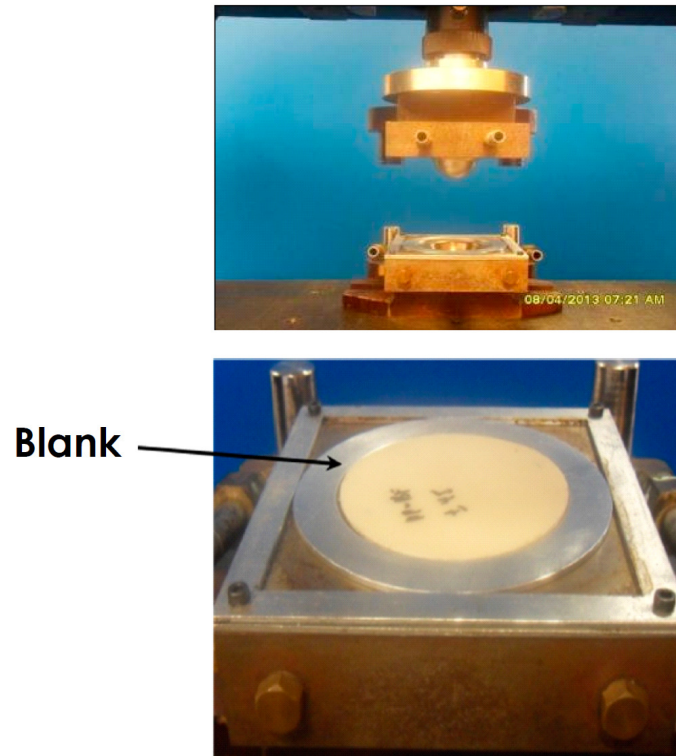
Figure 5.8: Experiment setup for the drape test of PLA-bamboo fabric composite [138].

model with the configuration parameters of $\mu = -10\ Gpa$ and $\kappa = 11\ GPa$ (see,

Fig. 5.9). The material parameters of a bidirectional bamboo fabrics are identified as $E_1 = E_2 = 45.45\ GPa$ and $C_1 = C_2 = 28\ GPa$, respectively, based on the work of [147]-[148]. Therefore, combining Eqs. (5.21), (5.23) and (5.68), we may propose
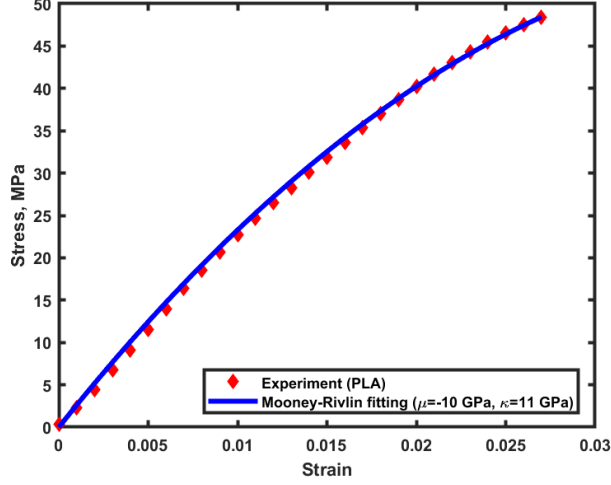
Figure 5.9: Stress-strain curves: PLA thermoplastic matrix material [149] and the Mooney-Rivlin model.

the following energy potential for the constitutive description of the PLA-bamboo composite

$$
\begin{aligned}
U(\mathbf{F}, \varepsilon, \mathbf{g}, p) \; = \;\; & \frac{-10}{2}(I_1 - 3) + \frac{11}{2}(I_2 - 3) + \frac{45.45}{2}(\varepsilon_1^2 + \varepsilon_2^2) + \frac{28}{2}(\mathbf{g}_1 \cdot \mathbf{g}_1 + \mathbf{g}_2 \cdot \mathbf{g}_2) \\
& + \frac{2.5}{2}\mathbf{g}_1 \cdot \mathbf{g}_2 - p(J - 1),
\end{aligned}
\tag{5.101}
$$

and thereby obtain the associated equilibrium equation as

$$
\begin{aligned}
0 \; = \;\; & P_{iA,A} = -10\chi_{i,AA} + 11(\chi_{i,AA}\chi_{j,C}\chi_{j,C} - \chi_{i,BA}\chi_{j,A}\chi_{j,B}) + 11\chi_{i,B}(2\chi_{j,CB}\chi_{j,C} \\
& - \chi_{j,AA}\chi_{j,B} - \chi_{j,A}\chi_{j,BA}) - p_{,A}F_{iA}^* + 45.45\chi_{j,11}\chi_{j,1}\chi_{i,1} \\
& + (\frac{45.45}{2}\chi_{j,1}\chi_{j,1} - \frac{45.45}{2})\chi_{i,11} + 45.45\chi_{j,22}\chi_{j,2}\chi_{i,2} + (\frac{45.45}{2}\chi_{j,2}\chi_{j,2} \\
& - \frac{45.45}{2})\chi_{i,22} + \frac{28}{2}(\chi_{i,1111} + \chi_{i,2222}) + \frac{2.5}{2}(\chi_{i,1122} + \chi_{i,2211}),
\end{aligned}
\tag{5.102}
$$

156

where $F_{iA}^* = \varepsilon_{mni}\varepsilon_{pqA}\chi_{p,m}\chi_{q,n}$. The solution of the above system of PDEs can be determined by imposing the boundary conditions of (see, Fig. 5.10)

$$\begin{aligned}
\chi_1 &= \chi_2 = \chi_3 = 0 \text{ at } X_1 = a, \ -a \text{ and} \\
\chi_1 &= \chi_2 = \chi_3 = 0 \text{ at } X_2 = b, \ -b. \\
\chi_3 &= f(X_1) = -0.66X_1^2 + 0.66 \text{ at the cross section } D - D' \\
\chi_3 &= f(X_2) = -0.66X_2^2 + 0.66 \text{ at the cross section } C - C', \quad (5.103)
\end{aligned}$$

where $f(X_1)$ and $f(X_2)$ are the shape profile functions describing the hemispherical punch head. As illustrated in Fig. 5.11, the proposed model closely assimilates the resultant stress-strain responses (Fig. 5.11 (left)) and the overall deformation contours (Fig. 5.11 (right)) of the PLA-bamboo composite.
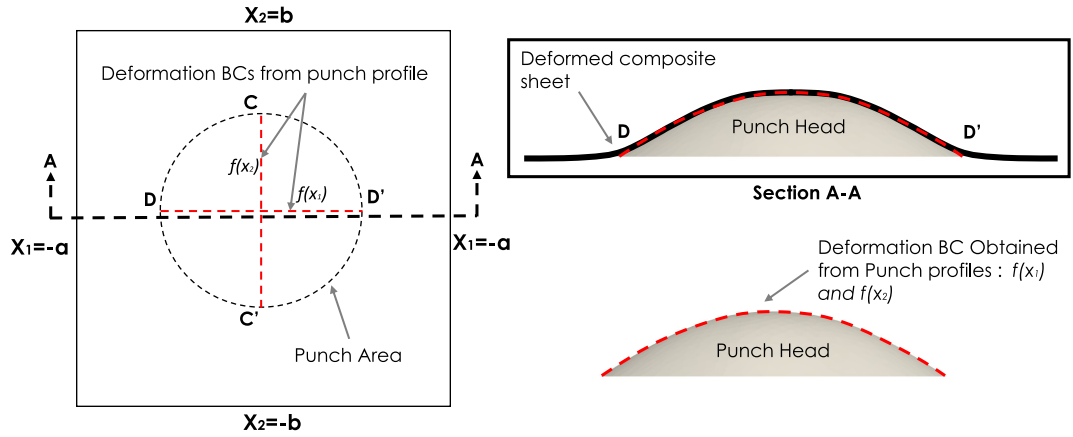
Figure 5.10: Boundary condition for draping over a hemisphere.

For the more in-depth analysis vis a vis the local deformations of the composite, we also perform the Grid Strain Analysis (GSA) which quantifies strain differences of grids prior and after the deformations [138]. The surface of a sheet marked with a series of square grids (see, #1(undeformed grids) and #2 (deformed grids) in Fig.5.12 (left)) is took from the work of [138] for the purpose of comparison. The grid map contour image in the right side of Fig. 5.12 (#3 (undeformed grid) and #4 (deformed grid)) is obtained by solving the resulting PDEs (Eq. (5.102)). It is evident that the proposed bidirectional model produces reasonably accurate prediction in the local deformation of PLA-fiber composite throughout the domain of interest (refer, the comparison images in Fig. 5.12 (mid)).
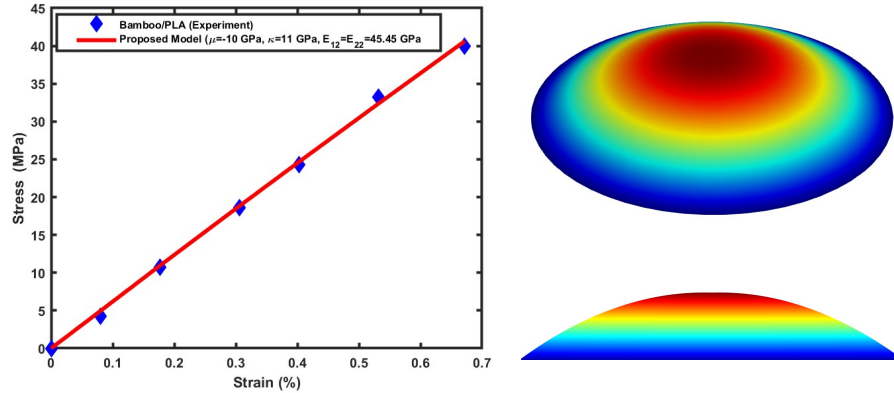
Figure 5.11: PLA-bamboo composite: stress-strain curve (left), deformation contour (right).

Lastly, we mention that the proposed model may be used in the design and characterization of thermoplastic composites reinforced with various types of natural fibers by interchanging energy potentials and material parameters for both fibers and matrix materials. Further studies in this regard are certainly of more practical interest which, however, were limited in the present study due to the paucity of the experimental resource.
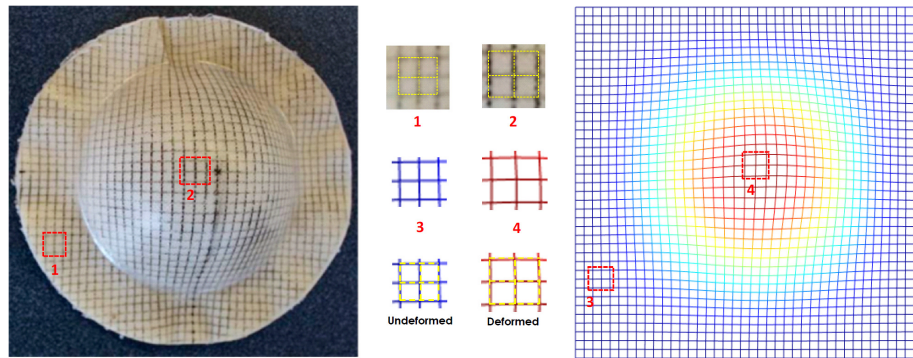
Figure 5.12: Deformed and undeformed configurations of unit grids obtained from the drape experiment of Bamboo fabrics / PLA Composite (left) [138] and proposed model (right).

5.5.3 Case studies in Self-Deployable Booms for Space Applications

Deployable structures such as solar sails and reflector antennas are widely studied for space applications due to the limited storage capacity in launch vehicles [150]–[153].

These deployable structures can be packaged into a small volume prior to launching and unfolded into large configurations during the operation state [150]. Among various types of deployable structures, thin-walled deployable composite structures made of high strain composites have drawn increasing attention in recent years for their superior stiffness, strength and ultralight weight characteristics [153]–[156]. In particular, a thin-walled deployable composite boom (DCB), which is folded elastically into smaller configurations can be self-recovered to its initial unfolded state by releasing the stored strain energy. During the coiling process, the boom undergoes compressive deformations to form a flattening state through which the strain energy can be effectively stored into the system [150] (see, highlighted deformation line (red) in Fig. 5.13). The stored strain energy is then used as a 'recovering' energy for self-deploy. Hence, it is important to study the compressive deformation responses for the design and operation of DCBs.
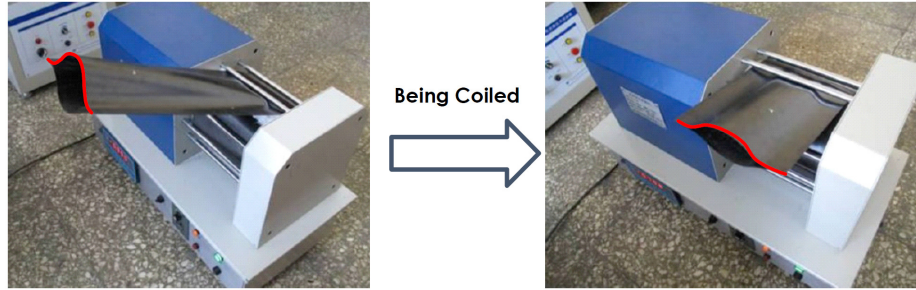
Figure 5.13: Compressive deformation of DCB during coiling process [150].

In this section, we employ the obtained model in the analysis of the coiling responses of a DCB which is made up of an epoxy resin laminate sheet reinforced with carbon fibers. The response of the epoxy resin matrix material is characterized by the Mooney-Rivlin model with the configuration parameters of $\mu = -10\ GPa$ and $\kappa = 11.09\ GPa$, respectively (see, Fig. 5.14). Further, the material parameters of bidirectional carbon fiber mesh are found to be $E_1 = E_2 = 228\ GPa$ and $C_1 = C_2 = 69\ GPa$. Together, the following energy potential may be proposed for the constitutive description of the DCB.

$$
\begin{aligned}
U(\mathbf{F}, \varepsilon, \mathbf{g}, p) \;=\; & \frac{-10}{2}(I_1 - 3) + \frac{11.09}{2}(I_2 - 3)\frac{228}{2}(\varepsilon_1^2 + \varepsilon_2^2) + \frac{69}{2}(\mathbf{g}_1 \cdot \mathbf{g}_1 + \mathbf{g}_2 \cdot \mathbf{g}_2) \\
& + \frac{50}{2}\mathbf{g}_1 \cdot \mathbf{g}_2 - p(J - 1).
\end{aligned}
\tag{5.104}
$$
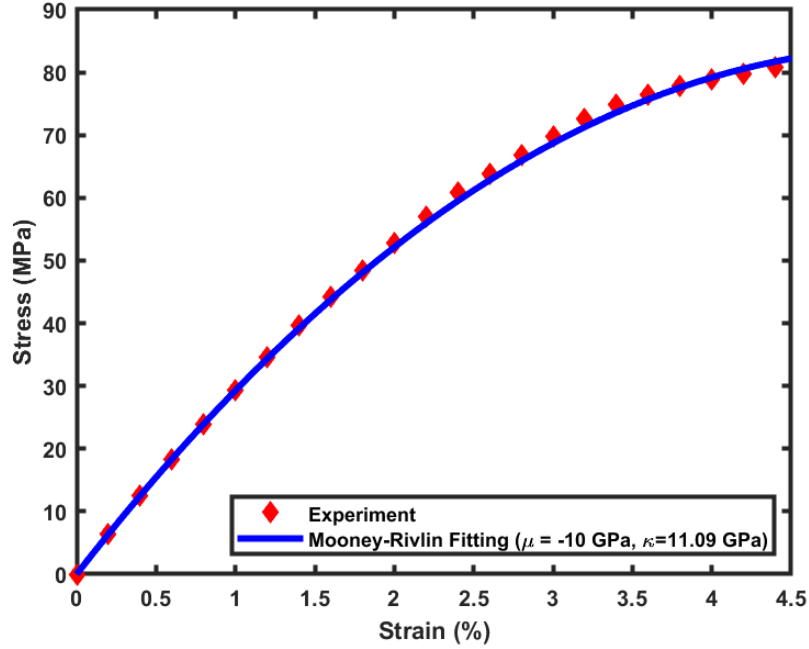
Figure 5.14: Stress-strain curves: epoxy resin matrix material [157] and the Mooney Rivlin-model.

Hence, the corresponding Euler equilibrium equation furnishes

$$
\begin{aligned}
0 \;=\; P_{iA,A} \;=\; &-10\chi_{i,AA} + 11.09(\chi_{i,AA}\chi_{j,C}\chi_{j,C} - \chi_{i,BA}\chi_{j,A}\chi_{j,B}) + 11.09\chi_{i,B}(2\chi_{j,CB}\chi_{j,C} \\
&-\chi_{j,AA}\chi_{j,B} - \chi_{j,A}\chi_{j,BA}) - p_{,A}\varepsilon_{ij}\varepsilon_{AB}\chi_{j,B} + 228\chi_{j,11}\chi_{j,1}\chi_{i,1} + (\frac{228}{2}\chi_{j,1}\chi_{j,1} \\
&-\frac{228}{2})\chi_{i,11} + 228\chi_{j,22}\chi_{j,2}\chi_{i,2} + (\frac{228}{2}\chi_{j,2}\chi_{j,2} - \frac{228}{2})\chi_{i,22} + \frac{69}{2}(\chi_{i,1111} \\
&+\chi_{i,2222}) + \frac{50}{2}(\chi_{i,1122} + \chi_{i,2211}).
\end{aligned}
\tag{5.105}
$$

The solutions of the above system of PDEs can be determined by imposing the boundary conditions as depicted in Fig. 5.15 and Eq. (5.106), where $f_s(X_2)$ is the shape function representing the initial shape profile of the boom and $f(P)$ is a function of P which becomes zero when $P = 0$.

$$
\begin{aligned}
\chi_1 \;&=\; 0 \text{ at } X_1 = a, \; -a \text{ and } \chi_3 = f_s(X_2)\{1 - f(P)\} \text{ at } X_1 = a, \text{ where} \\
f_s(X_2) \;&=\; 0.3386\{\frac{1}{1 + e^{-22(X_2-0.25)}} - \frac{1}{1 + e^{-22(X_2-0.75)}}\} \text{ and} \\
f(P) \;&=\; 0.0238P^3 - 0.2301P^2 + 0.7729P.
\end{aligned}
\tag{5.106}
$$
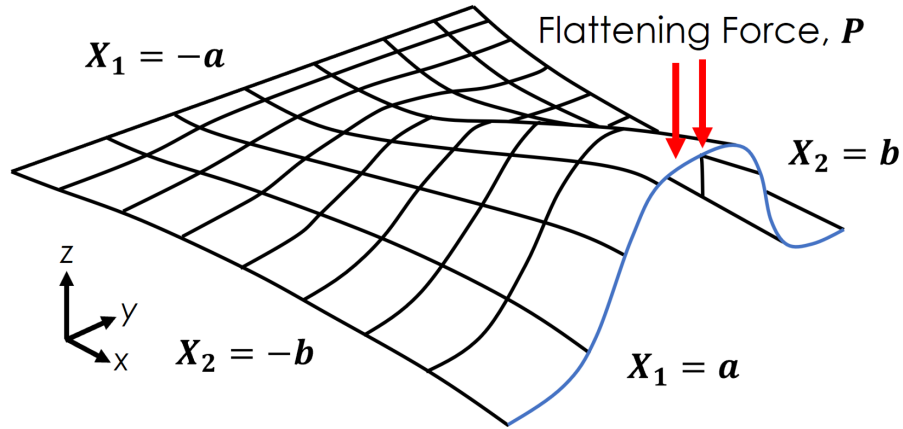
Figure 5.15: Schematic of the problem.

In the analysis, we consider two configurations of the boom which are the cross-sectional profiles (configuration "1") and the longitudinal deformation profiles (configuration "2") (see, also, Fig. 5.16 (a)-(b)). As illustrated in Figs. 5.16 (c)-5.17, the proposed bidirectional model successfully assimilate the general deformations of the boom. More precisely, it is observed that the magnitude of the cross-sectional profile of the boom (Config-1) is inversely proportional to the applied flattening force (refer, Fig. 5.17). Also, the longitudinal deformation profiles (Config-2) become 'straight' with the increasing bond parameter, T, at the intersection of the two orthogonally aligned fibers; i.e., the resulting longitudinal curvatures of the boom become less sensitive to the applied flattening force (see, Fig. 5.16(c)). The result suggests that the recovering energy may be further maximized (without considering higher strength materials for both matrix and reinforcing materials) by enhancing the fiber-to-fiber bond at the intersections.

Predictions from the proposed model are also cross-examined with the progressive flattening test results (compressions) of the DCB [154]. The experimental setup for the flattening test is illustrated in Fig. 5.18 (a), where the carbon-fiber reinforced epoxy composite samples of the half boom sections are loaded in the screw driven load frame. The incremental displacement is applied at the rate of $0.02mm/s$ via horizontal roller and the corresponding load-deformation readings are recorded using optical instruments (see, further details in [154]). It is seen from Fig. 5.18 (b) that the proposed model closely simulates the force-displacement responses of the DCB

161
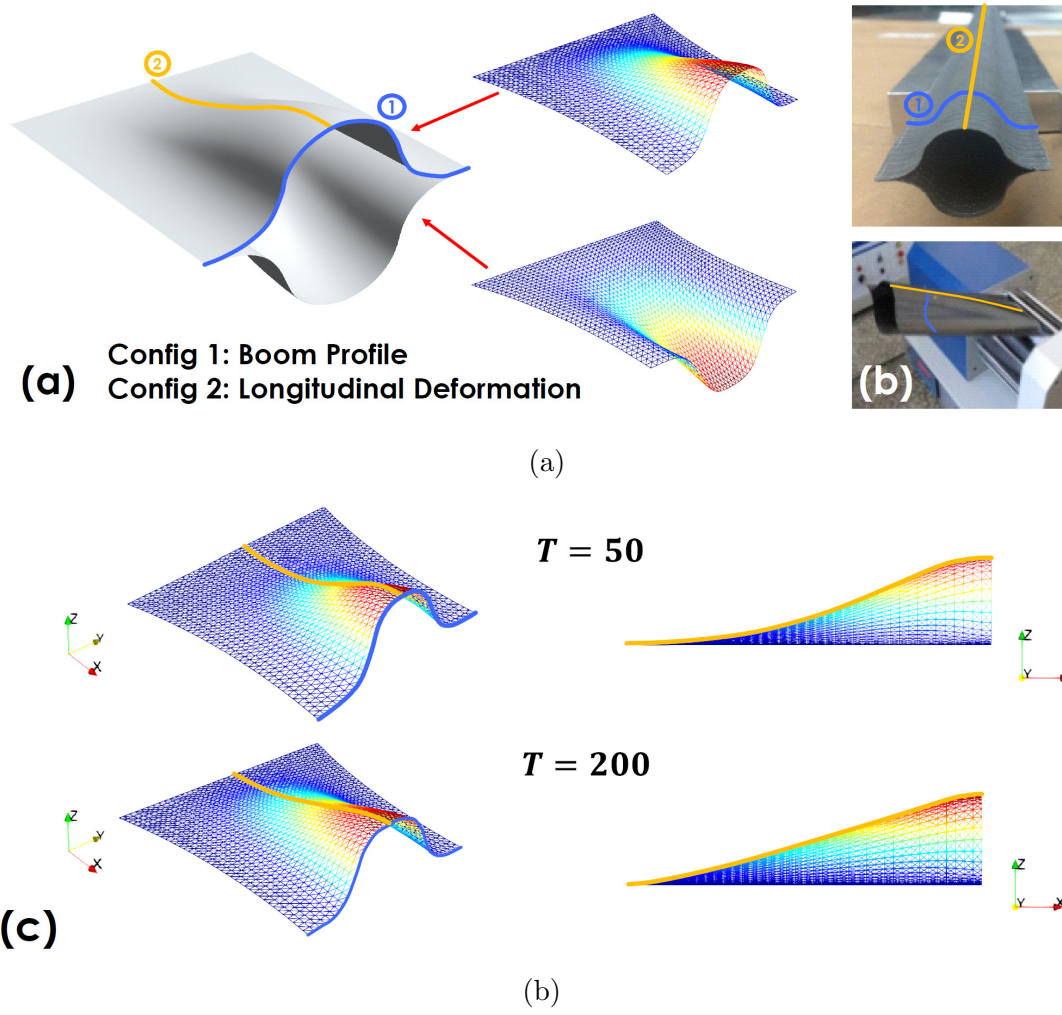
Figure 5.16: Cross-sectional profile (Config-1) and longitudinal deformation profile (Config-2) of the DCB. (b) Config-1 and Config-2 indicated on the actual DCB. (c) Longitudinal deformation profiles with respect to the torsional rigidity of fibers.

subjected to progressive flattening which arises during the coiling and/or folding processes. Lastly, we compute the shear strain distributions of the DCM with respect to the strain components of γ_{xy}, γ_{xz} and γ_{yz}. Unlike those estimated from the first gradient theory, where significant discontinuities are observed (see, [85], [87]), the proposed model predicts the smooth and continuous shear strain distributions throughout the entire domain of interest. More precisely, the maximum in-plane shear strain (γ_{xy}) is observed at the clamped end (Fig. 5.19 (top left)) whereas the out-of-plane shear strain components (γ_{xz}, γ_{yz}) gradually increase as they approach the line of contact where the flattening force is applied (Fig.5.19 (top right)-(bottom)) The results may
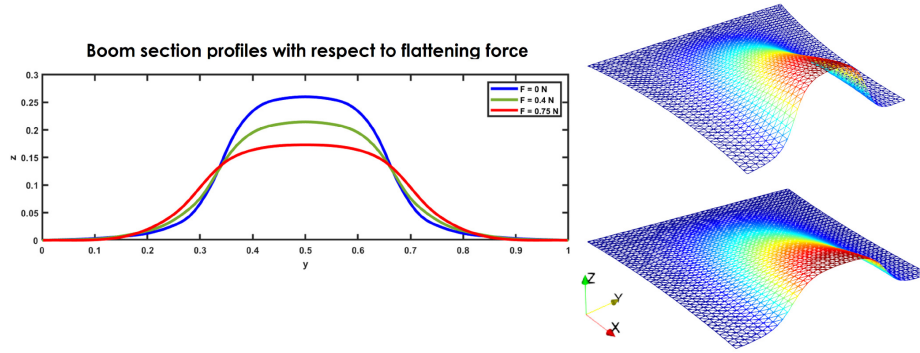
Figure 5.17: Cross-sectional profiles of the DCB with respect to the varying flattening force.
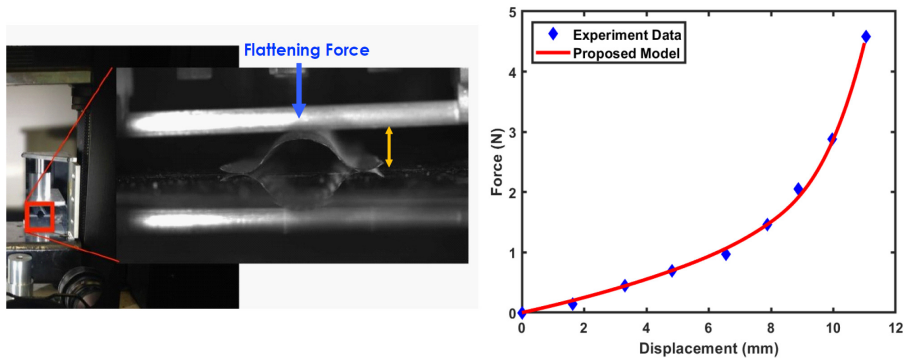
Figure 5.18: (a) Experimental setup for the flattening test. (b) Comparison of the load-deflection curve between the theoretical prediction and experimental data in [154].

be further employed to compute the amount of total strain energy stored into the boom structure during the packaging which can be converted to 'restoring' energy in the event of self-deployment. In addition to the aforementioned applications, the proposed model reproduces the equilibrium shapes of Hypar shell structures under arbitrary prescribed edge conditions [158]. In fact, the obtained model accommodates a more wide class of Hyper shell deformation structures via the generalized edge conditions of the form:

$$\boldsymbol{\chi}_3(X_1, X_2) = aX_1X_2 + bX_1^2 + cX_2^2 + dX_1 + eX_2 + f, \qquad (5.107)$$

where a, b, c, d, e and f are constant fields from which various types of edge conditions may be assimilated (see, Fig. 5.20).

The focal length variations of tunable elastomeric lens with respect to the vary-
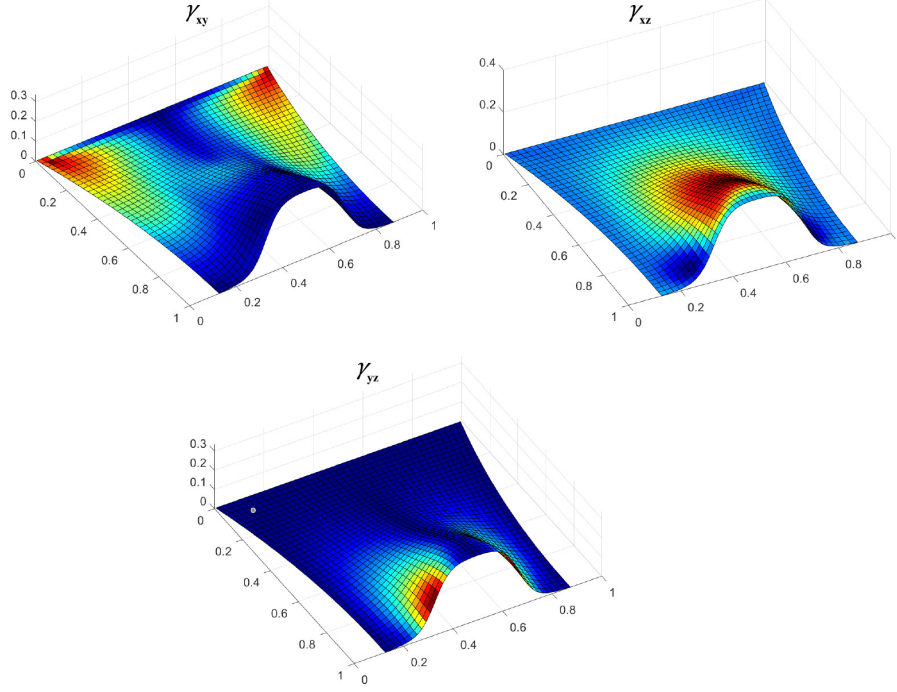
Figure 5.19: Shear strain distributions of the DCM: γ_{xy} (top left), γ_{xz} (top right) and γ_{yz} (bottom).

ing applied voltage [159] can also be predicted by employing the proposed model in the limit of vanishing fiber parameters. In the simulation, the changes in electrode voltages are applied using the following boundary conditions;

$$\frac{\partial \chi_3}{\partial X_1} + \frac{\partial \chi_3}{\partial X_2} = (aV^2 + bV + c)\{A(X_1 + X_2) + B\}, \qquad (5.108)$$

where a, b, c, A and B are the empirical constants which can be determined by fitting the applied voltage. It is evident from Fig. 5.21 that the proposed model produces reasonably accurate predictions in both the general deformation profiles (Fig. 5.21 (a)-(b)) and the focal length variations of the tunable elastomeric lens (see, Fig. 5.21 (right)). Further research in this regard is beyond the scope of the present study due to the paucity of available data, yet it is certainly of more practical interest.

5.6 Finite element analysis of the 4th order coupled PDE

The systems of PDEs in Eqs. (5.92)-(5.93) are 4th order differential equations with coupled

(a) $\chi_3 = 0.8X_1^2 - 0.8X_2^2 - 0.8X_1 + 0.8X_2$

(b) $\chi_3 = 0.4X_1^2 - 0.4X_2^2 - 0.4X_1 + 0.4X_2$

(c) $\chi_3 = 0.4X_1X_2 - 0.2X_1 - 0.2X_2 + 0.2$

(d) $\chi_3 = 0.25X_1X_2 + 0.25X_2^2 - 0.25X_1 - 0.25X_2 + 0.125$
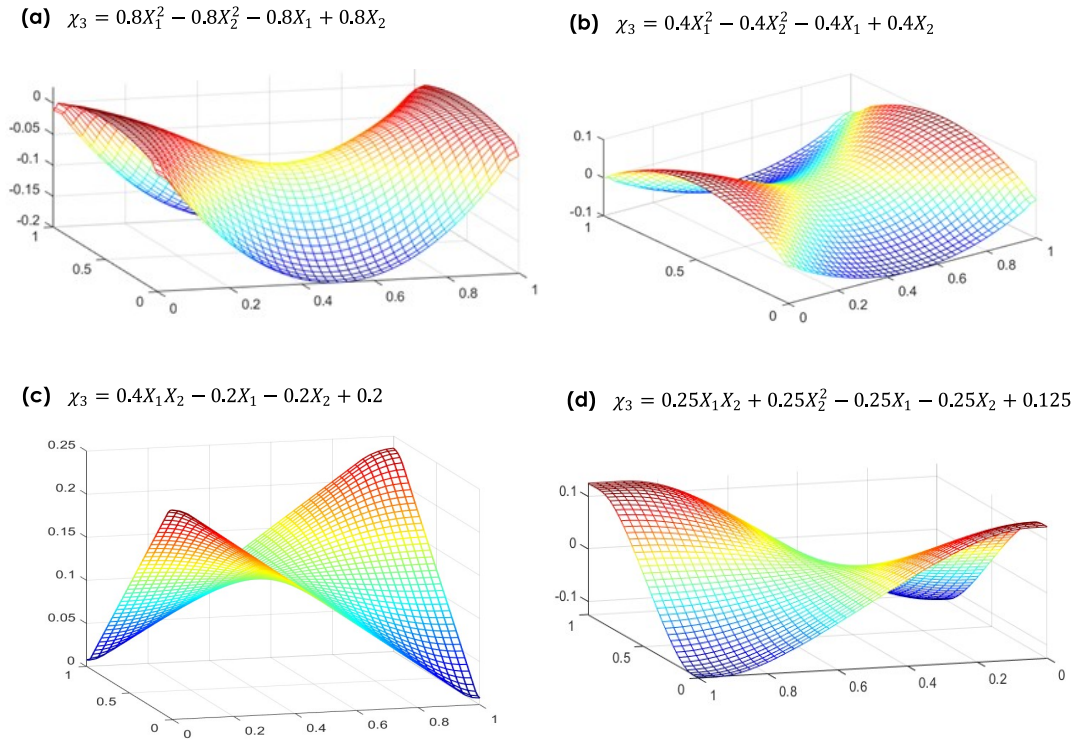
Figure 5.20: Deformed surfaces of Hypar shells: (a) Saddle-shape, (b)Saddle-shape (same magnitude with opposite curvatures), (c) Rotation and translation of straight lines, (d) Rotation and translation of curves.

non-linear terms. The case of such less regular PDEs deserve delicate mathematical treatment and is of particular practical interest. Hence, it is not trivial to demonstrate the associated numerical analysis procedures. For preprocessing, Eq. (5.92) may be recast as
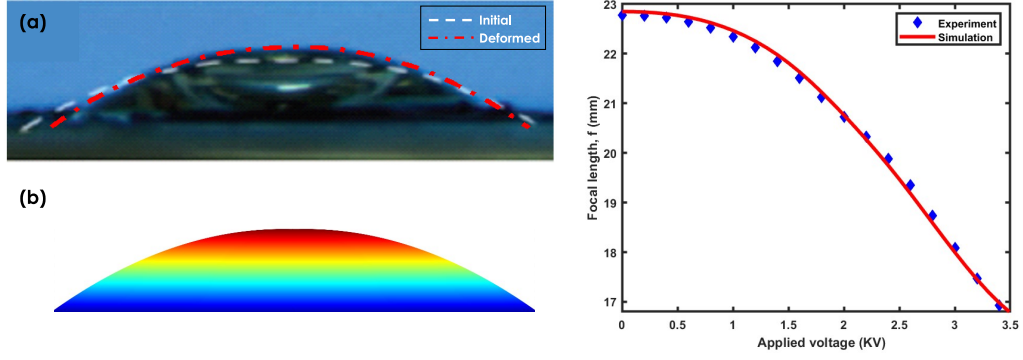
Figure 5.21: (a) Elastomeric lens profile from the experiment [159]. (the red dashed line corresponds to the prediction of the lens profile from proposed model), (b) Deformed lens profile from the proposed model, Focal length variations with respect to the applied voltage (right).

For $i = 1$:

$$
\begin{aligned}
0 =\ & \mu(Q + \chi_{1,22}) + \kappa(Q + E_{,2})(CC + EE + DD + FF + MM + NN) - \kappa(Q + C_{,2} \\
& + E_{,1} + E_{,2})(CC + CD + DD + DF + MM + MN + EC + EE + FD + FF \\
& + NM + NN) + \kappa(C + E)(2QC + 2E_{,1}E + 2C_{,2}C + 2UE - QC - QE - E_{,2}C \\
& + 2F_{,1}F + 2D_{,2}D + 2F_{,2}F - RD - RF - F_{,2}D - F_{,2}F + DR - DF_{,1} - FD_{,2} \\
& - FF_{,2} - E_{,2}E - CQ - CE_{,1} - EC_{,2} - EE_{,2} + 2N_{,1}N + 2M_{,2}M + 2N_{,2}N \\
& - M_{,1}M - M_{,1}N - N_{,2}M - N_{,2}N + MM_{,1} - MN_{,1} - NM_{,2} - MM_{,2}) \\
& + [\frac{E_{11}}{4}(2QCCC + 2QCDD + 2QCMM + 2RDCC + 2RDDD + 2RDMM \\
& + 2M_{,1}MCC + 2M_{,1}MDD + 2M_{,1}MMM + 2CCQC + 2CCRD + 2CCM_{,1}M \\
& + 2DDQC + 2DDRD + 2DDM_{,1}M + 2MMQC + 2MMD_{,1}D + 2MMM_{,1}M) \\
& + (E_{12} - E_{11})(QC + RD + M_{,1}M)]C + [\frac{E_{11}}{4}(CC + DD + MM)^2 \\
& + \frac{(E_{12} - E_{11})}{2}(CC + DD + MM) + \frac{(E_{11} - 2E_{12})}{4}]Q + [\frac{E_{21}}{4}(2E_{,2}DDD \\
& + 2E_{,2}DFF + 2E_{,2}ENN + 2F_{,2}FEE + 2F_{,2}FFF + 2F_{,2}FNN + 2SNEE \\
& + 2SNFF + 2SNNN + 2EEE_{,2}E + 2EEF_{,2}F + 2EESN + 2FFE_{,2}E \\
& + 2FFF_{,2}F + 2FFSN + 2NNE_{,2}E + 2NNF_{,2}F + 2NNSN)(E_{22} - E_{21})(E_{,2}E \\
& + F_{,2}F + SN)]E + [\frac{E_{21}}{4}(EE + FF + NN)^2 + \frac{(E_{22} - E_{21})}{2}(EE + FF + NN) \\
& + \frac{(E_{21} - 2E_{22})}{4}]Q - C_1Q_{,11} - C_2U_{,22} - \tau U_{,11} - \tau Q_{,22}
\end{aligned}
$$

166

For $i = 2$:

$$
\begin{aligned}
0 =\ & \mu(R + \chi_{2,22}) + \kappa(R + F_{,2})(CC + EE + DD + FF + MM + NN) - \kappa(R + D_{,2} \\
& + F_{,1} + F_{,2})(CC + CD + DD + DF + MM + MN + EC + EE + FD + FF \\
& + NM + NN) + \kappa(D + F)(2QC + 2E_{,1}E + 2C_{,2}C + 2UE - QC - QE \\
& + 2F_{,1}F + 2D_{,2}D + 2F_{,2}F - RD - RF - F_{,2}D - F_{,2}F + DR - DF_{,1} - FD_{,2} \\
& - FF_{,2} - E_{,2}C - E_{,2}E - CQ - CE_{,1} - EC_{,2} - EE_{,2} + 2N_{,1}N + 2M_{,2}M \\
& + 2N_{,2}N - M_{,1}M - M_{,1}N - N_{,2}M - N_{,2}N + MM_{,1} - MN_{,1} - NM_{,2} - MM_{,2}) \\
& + [\frac{E_{11}}{4}(2QCCC + 2QCDD + 2QCMM + 2RDCC + 2RDDD + 2RDMM \\
& + 2M_{,1}MCC + 2M_{,1}MDD + 2M_{,1}MMM + 2CCQC + 2CCRD + 2CCM_{,1}M \\
& + 2DDQC + 2DDRD + 2DDM_{,1}M + 2MMQC + 2MMD_{,1}D + 2MMM_{,1}M) \\
& + (E_{12} - E_{11})(QC + RD + M_{,1}M)]D + [\frac{E_{11}}{4}(CC + DD + MM)^2 \\
& + \frac{(E_{12} - E_{11})}{2}(CC + DD + MM) + \frac{(E_{11} - 2E_{12})}{4}]R + [\frac{E_{21}}{4}(2E_{,2}DDD \\
& + 2E_{,2}DFF + 2E_{,2}ENN + 2F_{,2}FEE + 2F_{,2}FFF + 2F_{,2}FNN + 2SNEE \\
& + 2SNFF + 2SNNN + 2EEE_{,2}E + 2EEF_{,2}F + 2EESN + 2FFE_{,2}E \\
& + 2FFF_{,2}F + 2FFSN + 2NNE_{,2}E + 2NNF_{,2}F + 2NNSN)(E_{22} - E_{21}) \\
& (E_{,2}E + F_{,2}F + SN)]F + [\frac{E_{21}}{4}(EE + FF + NN)^2 + \frac{(E_{22} - E_{21})}{2}(EE \\
& + FF + NN) + \frac{(E_{21} - 2E_{22})}{4}]R - C_1R_{,11} - C_2V_{,22} - \tau V_{,11} - \tau R_{,22}
\end{aligned}
$$

For $i = 3$:

$$\begin{aligned}
0 &= \mu(T + \chi_{3,22}) + \kappa(T + N_{,2})(CC + EE + DD + FF + MM + NN) - \kappa(T + M_{,2} \\
&\quad + N_{,1} + N_{,2})(CC + CD + DD + DF + MM + MN + EC + EE + FD + FF \\
&\quad + NM + NN) + \kappa(M + N)(2QC + 2E_{,1}E + 2C_{,2}C + 2UE - QC - QE - E_{,2}C \\
&\quad - E_{,2}E - CQ - CE_{,1} - EC_{,2} - EE_{,2} + 2F_{,1}F + 2D_{,2}D + 2F_{,2}F - RD \\
&\quad - RF - F_{,2}D - F_{,2}F + DR - DF_{,1} - FD_{,2} - FF_{,2} + 2N_{,1}N + 2M_{,2}M \\
&\quad + 2N_{,2}N - M_{,1}M - M_{,1}N - N_{,2}M - N_{,2}N + MM_{,1} - MN_{,1} - NM_{,2} - MM_{,2}) \\
&\quad + [\frac{E_{11}}{4}(2QCCC + 2QCDD + 2QCMM + 2RDCC + 2RDDD + 2RDMM \\
&\quad + 2M_{,1}MCC + 2M_{,1}MDD + 2M_{,1}MMM + 2CCQC + 2CCRD + 2CCM_{,1}M \\
&\quad + 2DDQC + 2DDRD + 2DDM_{,1}M + 2MMQC + 2MMD_{,1}D + 2MMM_{,1}M) \\
&\quad + (E_{12} - E_{11})(QC + RD + M_{,1}M)]M + [\frac{E_{11}}{4}(CC + DD + MM)^2 \\
&\quad + \frac{(E_{12} - E_{11})}{2}(CC + DD + MM) + \frac{(E_{11} - 2E_{12})}{4}]T + [\frac{E_{21}}{4}(2E_{,2}DDD \\
&\quad + 2E_{,2}DFF + 2E_{,2}ENN + 2F_{,2}FEE + 2F_{,2}FFF + 2F_{,2}FNN + 2SNEE \\
&\quad + 2SNFF + 2SNNN + 2EEE_{,2}E + 2EEF_{,2}F + 2EESN + 2FFE_{,2}E \\
&\quad + 2FFF_{,2}F + 2FFSN + 2NNE_{,2}E + 2NNF_{,2}F + 2NNSN)(E_{22} - E_{21}) \\
&\quad (E_{,2}E + F_{,2}F + SN)]N + [\frac{E_{21}}{4}(EE + FF + NN)^2 + \frac{(E_{22} - E_{21})}{2}(EE \\
&\quad + FF + NN) + \frac{(E_{21} - 2E_{22})}{4}]T - C_1T_{,11} - C_2S_{,22} - \tau S_{,11} - \tau T_{,22} \\
&\quad + \frac{1}{2}(A_0DN - A_0FM - B_0CN + B_0FM)
\end{aligned}$$

$$\begin{aligned}
0 &= Q - \chi_{1,11},\ 0 = R - \chi_{2,11},\ 0 = C - \chi_{1,1},\ 0 = D - \chi_{2,1}, \\
0 &= E - \chi_{1,2},\ 0 = F - \chi_{2,2},\ 0 = A - \mu(Q + \chi_{1,22}) - cQ_{,11}, \\
0 &= B - \mu(R + \chi_{2,22}) - cR_{,11}, 0 = M - \chi_{3,1}, 0 = N - \chi_{3,2}, \\
0 &= U - \chi_{1,22}, 0 = V - \chi_{2,22},\ 0 = T - \chi_{3,11},\ 0 = S - \chi_{3,22}. \qquad (5.109)
\end{aligned}$$

where $Q = \chi_{1,11}$, $R = \chi_{2,11}$, $T = \chi_{3,11}$, $C = \chi_{1,1}$, $D = \chi_{2,1}$, $M = \chi_{3,1}$, $E = \chi_{1,2}$, $F = \chi_{2,2}$, $N = \chi_{3,2}$, $U = \chi_{1,22}$, $V = \chi_{2,22}$ and $S = \chi_{3,22}$. Hence, the order of differential equations is reduced from the three coupled equations of the 4th order to seventeen coupled equations of the 2nd order. Especially, the non-linear terms in the

168

above equations (e.g. $A\chi_{2,2}, B\chi_{2,1}$ etc...) can be systematically treated via the Picard iterative procedure and/or Newton method;

$$-A^{initial}\chi_{2,2}^{initial} + B^{initial}\chi_{2,1}^{initial} \implies -A_0\chi_{2,2}^0 + B_0\chi_{2,1}^0$$
$$A^{initial}\chi_{1,2}^{initial} - B^{initial}\chi_{1,1}^{initial} \implies A_0\chi_{1,2}^0 - B_0\chi_{1,1}^0, \qquad (5.110)$$

where the estimated values of A, B continue to be updated based on their previous estimations (e.g. A_1 and B_1 are refreshed by their previous estimations of A_o and B_o) as iteration progresses and similarly for the rest of non-linear terms.

Also, the weight forms of Eq. (5.109) can be found as

$$
\begin{aligned}
0 = \int_\Omega & w_1\{\mu(Q + \chi_{1,22}) + \kappa(Q + E_{,2})(CC + EE + DD + FF + MM + NN) \\
& -\kappa(Q + C_{,2} + E_{,1} + E_{,2})(CC + CD + DD + DF + MM + MN + EC \\
& +EE + FD + FF + NM + NN) + \kappa(C + E)(2QC + 2E_{,1}E + 2C_{,2}C \\
& +2UE - QC - QE - E_{,2}C - E_{,2}E - CQ - CE_{,1} - EC_{,2} - EE_{,2} \\
& +2F_{,1}F + 2D_{,2}D + 2F_{,2}F - RD - RF - F_{,2}D - F_{,2}F + DR - DF_{,1} \\
& -FD_{,2} - FF_{,2} + 2N_{,1}N + 2M_{,2}M + 2N_{,2}N - M_{,1}M - M_{,1}N - N_{,2}M \\
& -N_{,2}N + MM_{,1} - MN_{,1} - NM_{,2} - MM_{,2}) + [\frac{E_{11}}{4}(2QCCC + 2QCDD \\
& +2QCMM + 2RDCC + 2RDDD + 2RDMM + 2M_{,1}MCC + 2M_{,1}MDD \\
& +2M_{,1}MMM + 2CCQC + 2CCRD + 2CCM_{,1}M + 2DDQC + 2DDRD \\
& +2DDM_{,1}M + 2MMQC + 2MMD_{,1}D + 2MMM_{,1}M) + (E_{12} - E_{11})(QC \\
& +RD + M_{,1}M)]C + [\frac{E_{11}}{4}(CC + DD + MM)^2 + \frac{(E_{12} - E_{11})}{2}(CC + DD \\
& +MM) + \frac{(E_{11} - 2E_{12})}{4}]Q + [\frac{E_{21}}{4}(2E_{,2}DDD + 2E_{,2}DFF + 2E_{,2}ENN \\
& +2F_{,2}FEE + 2F_{,2}FFF + 2F_{,2}FNN + 2SNEE + 2SNFF + 2SNNN \\
& +2EEE_{,2}E + 2EEF_{,2}F + 2EESN + 2FFE_{,2}E + 2FFF_{,2}F + 2FFSN \\
& +2NNE_{,2}E + 2NNF_{,2}F + 2NNSN)(E_{22} - E_{21})(E_{,2}E + F_{,2}F + SN)]E \\
& +[\frac{E_{21}}{4}(EE + FF + NN)^2 + \frac{(E_{22} - E_{21})}{2}(EE + FF + NN) \\
& +\frac{(E_{21} - 2E_{22})}{4}]Q - C_1Q_{,11} - C_2U_{,22} - \tau U_{,11} - \tau Q_{,22}\}d\Omega
\end{aligned}
$$

$$
\begin{aligned}
0 \;=\; & \int_\Omega w_2 \{ \mu(R + \chi_{2,22}) + \kappa(R + F_{,2})(CC + EE + DD + FF + MM + NN) \\
& - \kappa(R + D_{,2} + F_{,1} + F_{,2})(CC + CD + DD + DF + MM + MN + EC \\
& + EE + FD + FF + NM + NN) + \kappa(D + F)(2QC + 2E_{,1}E + 2C_{,2}C \\
& + 2UE - QC - QE - E_{,2}C - E_{,2}E - CQ - CE_{,1} - EC_{,2} - EE_{,2} \\
& + 2F_{,1}F + 2D_{,2}D + 2F_{,2}F - RD - RF - F_{,2}D - F_{,2}F + DR - DF_{,1} \\
& - FD_{,2} - FF_{,2} + 2N_{,1}N + 2M_{,2}M + 2N_{,2}N - M_{,1}M - M_{,1}N - N_{,2}M \\
& - N_{,2}N + MM_{,1} - MN_{,1} - NM_{,2} - MM_{,2}) + [\frac{E_{11}}{4}(2QCCC + 2QCDD \\
& + 2QCMM + 2RDCC + 2RDDD + 2RDMM + 2M_{,1}MCC + 2M_{,1}MDD \\
& + 2M_{,1}MMM + 2CCQC + 2CCRD + 2CCM_{,1}M + 2DDQC + 2DDRD \\
& + 2DDM_{,1}M + 2MMQC + 2MMD_{,1}D + 2MMM_{,1}M) + (E_{12} - E_{11})(QC \\
& + RD + M_{,1}M)]D + [\frac{E_{11}}{4}(CC + DD + MM)^2 + \frac{(E_{12} - E_{11})}{2}(CC + DD \\
& + MM) + \frac{(E_{11} - 2E_{12})}{4}]R + [\frac{E_{21}}{4}(2E_{,2}DDD + 2E_{,2}DFF + 2E_{,2}ENN \\
& + 2F_{,2}FEE + 2F_{,2}FFF + 2F_{,2}FNN + 2SNEE + 2SNFF + 2SNNN \\
& + 2EEE_{,2}E + 2EEF_{,2}F + 2EESN + 2FFE_{,2}E + 2FFF_{,2}F + 2FFSN \\
& + 2NNE_{,2}E + 2NNF_{,2}F + 2NNSN)(E_{22} - E_{21})(E_{,2}E + F_{,2}F + SN)]F \\
& + [\frac{E_{21}}{4}(EE + FF + NN)^2 + \frac{(E_{22} - E_{21})}{2}(EE + FF + NN) \\
& + \frac{(E_{21} - 2E_{22})}{4}]R - C_1 R_{,11} - C_2 V_{,22} - \tau V_{,11} - \tau R_{,22} \} d\Omega
\end{aligned}
$$

$$
\begin{aligned}
0 \;=\; & \int_\Omega w_3\{\mu(T+\chi_{3,22}) + \kappa(T+N_{,2})(CC+EE+DD+FF+MM+NN) - \kappa(T\\
& +M_{,2}+N_{,1}+N_{,2})(CC+CD+DD+DF+MM+MN+EC+EE+FD+FF\\
& +NM+NN) + \kappa(M+N)(2QC+2E_{,1}E+2C_{,2}C+2UE-QC-QE-E_{,2}C\\
& -E_{,2}E-CQ-CE_{,1}-EC_{,2}-EE_{,2}+2F_{,1}F+2D_{,2}D+2F_{,2}F-RD-RF\\
& -F_{,2}D-F_{,2}F+DR-DF_{,1}-FD_{,2}-FF_{,2}+2N_{,1}N+2M_{,2}M+2N_{,2}N-M_{,1}M\\
& -M_{,1}N-N_{,2}M-N_{,2}N+MM_{,1}-MN_{,1}-NM_{,2}-MM_{,2}) + [\tfrac{E_{11}}{4}(2QCCC\\
& +2QCDD+2QCMM+2RDCC+2RDDD+2RDMM+2M_{,1}MCC\\
& +2M_{,1}MDD+2M_{,1}MMM+2CCQC+2CCRD+2CCM_{,1}M+2DDQC\\
& +2DDRD+2DDM_{,1}M+2MMQC+2MMD_{,1}D+2MMM_{,1}M) + (E_{12}-E_{11})\\
& (QC+RD+M_{,1}M)]M + [\tfrac{E_{11}}{4}(CC+DD+MM)^2 + \tfrac{(E_{12}-E_{11})}{2}(CC+DD\\
& +MM) + \tfrac{(E_{11}-2E_{12})}{4}]T + [\tfrac{E_{21}}{4}(2E_{,2}DDD+2E_{,2}DFF+2E_{,2}ENN\\
& +2F_{,2}FEE+2F_{,2}FFF+2F_{,2}FNN+2SNEE+2SNFF+2SNNN+2EEE_{,2}E\\
& +2EEF_{,2}F+2EESN+2FFE_{,2}E+2FFF_{,2}F+2FFSN+2NNE_{,2}E+2NNF_{,2}F\\
& +2NNSN)(E_{22}-E_{21})(E_{,2}E+F_{,2}F+SN)]N + [\tfrac{E_{21}}{4}(EE+FF+NN)^2\\
& +\tfrac{(E_{22}-E_{21})}{2}(EE+FF+NN) + \tfrac{(E_{21}-2E_{22})}{4}]T - C_1T_{,11} - C_2S_{,22} - \tau S_{,11}\\
& -\tau T_{,22} + \tfrac{1}{2}(A_0DN - A_0FM - B_0CN + B_0FM)\}d\Omega
\end{aligned}
$$

$$
0 \;=\; \int_\Omega w_4(Q-\chi_{1,11})d\Omega, \;\; 0 = \int_\Omega w_5(R-\chi_{2,11})d\Omega, \;\; 0 = \int_\Omega w_6(T-\chi_{3,11})d\Omega,
$$

$$
0 \;=\; \int_\Omega w_7(C-\chi_{1,1})d\Omega, \;\; 0 = \int_\Omega w_8(D-\chi_{2,1})d\Omega, \;\; 0 = \int_\Omega w_9(M-\chi_{3,1})d\Omega,
$$

$$
0 \;=\; \int_\Omega w_{10}(E-\chi_{1,2})d\Omega, \;\; 0 = \int_\Omega w_{11}(F-\chi_{2,2})d\Omega, \;\; 0 = \int_\Omega w_{12}(N-\chi_{3,2})d\Omega,
$$

$$
0 \;=\; \int_\Omega w_{13}(U-\chi_{1,22})d\Omega, \;\; 0 = \int_\Omega w_{14}(V-\chi_{2,22})d\Omega, \;\; 0 = \int_\Omega w_{15}(S-\chi_{3,22})d\Omega,
$$

$$
0 \;=\; \int_\Omega w_{16}(A-\mu(Q+\chi_{1,22}) - C_1Q_{,11} - C_2U_{,22})d\Omega,
$$

$$
0 \;=\; \int_\Omega w_{17}(B-\mu(R+\chi_{2,22}) - C_1R_{,11} - C_2V_{,22})d\Omega. \tag{5.111}
$$

Thus, we apply integration by part and the Green-Stokes' theorem, (e.g. $\mu\int_{\Omega^e} w_1\chi_{1,22}d\Omega = -\mu\int_{\Omega^e} w_{1,2}\chi_{1,2}d\Omega + \mu\int_{\partial\Gamma} w_1\chi_{1,2}Nd\Gamma$) and thereby obtain the following weak forms of

171

Eq. (5.111)

$$
\begin{aligned}
0 = {} & \int_\Omega \{\mu w_1 Q - \mu w_{1,2}\chi_{1,2} + w_1\kappa(Q + E_{,2})(CC + EE + DD + FF + MM + NN) \\
& - w_1\kappa(Q + C_{,2} + E_{,1} + E_{,2})(CC + CD + DD + DF + MM + MN + EC \\
& + EE + FD + FF + NM + NN) + w_1\kappa(C + E)(2QC + 2E_{,1}E + 2C_{,2}C \\
& + 2UE - QC - QE - E_{,2}C - E_{,2}E - CQ - CE_{,1} - EC_{,2} - EE_{,2} \\
& + 2F_{,1}F + 2D_{,2}D + 2F_{,2}F - RD - RF - F_{,2}D - F_{,2}F + DR - DF_{,1} \\
& - FD_{,2} - FF_{,2} + 2N_{,1}N + 2M_{,2}M + 2N_{,2}N - M_{,1}M - M_{,1}N - N_{,2}M \\
& - N_{,2}N + MM_{,1} - MN_{,1} - NM_{,2} - MM_{,2}) + w_1[\frac{E_{11}}{4}(2QCCC \\
& + 2QCMM + 2RDCC + 2RDDD + 2RDMM + 2M_{,1}MCC + 2M_{,1}MDD \\
& + 2M_{,1}MMM + 2CCQC + 2CCRD + 2CCM_{,1}M + 2DDQC + 2DDRD \\
& + 2QCDD + 2DDM_{,1}M + 2MMQC + 2MMD_{,1}D + 2MMM_{,1}M) \\
& + (E_{12} - E_{11})(QC + RD + M_{,1}M)]C + w_1[\frac{E_{11}}{4}(CC + DD + MM)^2 \\
& + \frac{(E_{12} - E_{11})}{2}(CC + DD + MM) + \frac{(E_{11} - 2E_{12})}{4}]Q \\
& + w_1[\frac{E_{21}}{4}(2E_{,2}DDD + 2E_{,2}DFF + 2E_{,2}ENN + 2F_{,2}FEE + 2F_{,2}FFF \\
& + 2F_{,2}FNN + 2SNEE + 2SNFF + 2SNNN + 2EEE_{,2}E + 2EEF_{,2}F \\
& + 2EESN + 2FFE_{,2}E + 2FFF_{,2}F + 2FFSN + 2NNE_{,2}E + 2NNF_{,2}F \\
& + 2NNSN)(E_{22} - E_{21})(E_{,2}E + F_{,2}F + SN)]E + w_1[\frac{E_{21}}{4}(EE + FF \\
& + NN)^2 + \frac{(E_{22} - E_{21})}{2}(EE + FF + NN) + \frac{(E_{21} - 2E_{22})}{4}]Q \\
& + w_{1,1}C_1 Q_{,1} + w_{1,2}C_2 U_{,2} + w_{1,1}\tau U_{,1} + w_{1,2}\tau Q_{,2}\}d\Omega + \mu\int_{\partial\Gamma} w_1\chi_{1,2}N d\Gamma \\
& - C_1\int_{\partial\Gamma} w_1 Q_{,1}N d\Gamma - C_2\int_{\partial\Gamma} w_1 U_{,2}N d\Gamma - \tau\int_{\partial\Gamma} w_1 U_{,1}N d\Gamma \\
& - \tau\int_{\partial\Gamma} w_1 Q_{,2}N d\Gamma,
\end{aligned}
$$

$$\begin{aligned}
0 \;=\; & \int_\Omega \{\mu w_2 R - \mu w_{2,2}\chi_{2,2} + w_2\kappa(R + F_{,2})(CC + EE + DD + FF + MM + NN) \\
& -w_2\kappa(R + D_{,2} + F_{,1} + F_{,2})(CC + CD + DD + DF + MM + MN + EC \\
& +EE + FD + FF + NM + NN) + \kappa w_2(D + F)(2QC + 2E_{,1}E + 2C_{,2}C \\
& +2UE - QC - QE - E_{,2}C - E_{,2}E - CQ - CE_{,1} - EC_{,2} - EE_{,2} + 2F_{,1}F \\
& +2D_{,2}D + 2F_{,2}F - RD - RF - F_{,2}D - F_{,2}F + DR - DF_{,1} - FD_{,2} - FF_{,2} \\
& +2N_{,1}N + 2M_{,2}M + 2N_{,2}N - M_{,1}M - M_{,1}N - N_{,2}M - N_{,2}N + MM_{,1} \\
& -MN_{,1} - NM_{,2} - MM_{,2}) + w_2[\frac{E_{11}}{4}(2QCCC + 2QCDD + 2QCMM \\
& +2RDCC + 2RDDD + 2RDMM + 2M_{,1}MCC + 2M_{,1}MDD \\
& +2M_{,1}MMM + 2CCQC + 2CCRD + 2CCM_{,1}M + 2DDQC + 2DDRD \\
& +2DDM_{,1}M + 2MMQC + 2MMD_{,1}D + 2MMM_{,1}M) + (E_{12} - E_{11}) \\
& (QC + RD + M_{,1}M)]D + w_2[\frac{E_{11}}{4}(CC + DD + MM)^2 + \frac{(E_{12} - E_{11})}{2}(CC \\
& +DD + MM) + \frac{(E_{11} - 2E_{12})}{4}]R + w_2[\frac{E_{21}}{4}(2E_{,2}DDD + 2E_{,2}DFF \\
& +2E_{,2}ENN + 2F_{,2}FEE + 2F_{,2}FFF + 2F_{,2}FNN + 2SNEE + 2SNFF \\
& +2SNNN + 2EEE_{,2}E + 2EEF_{,2}F + 2EESN + 2FFE_{,2}E + 2FFF_{,2}F \\
& +2FFSN + 2NNE_{,2}E + 2NNF_{,2}F + 2NNSN)(E_{22} - E_{21})(E_{,2}E + F_{,2}F \\
& +SN)]F + w_2[\frac{E_{21}}{4}(EE + FF + NN)^2 + \frac{(E_{22} - E_{21})}{2}(EE + FF + NN) \\
& +\frac{(E_{21} - 2E_{22})}{4}]R + w_{2,1}C_1R_{,1} + w_{2,2}C_2V_{,2} + w_{2,1}\tau V_{,1} + w_{2,2}\tau R_{,2}\}d\Omega \\
& +\mu\int_{\partial\Gamma} w_2\chi_{2,2}Nd\Gamma - C_1\int_{\partial\Gamma} w_2R_{,1}Nd\Gamma - C_2\int_{\partial\Gamma} w_2V_{,2}Nd\Gamma \\
& -\tau\int_{\partial\Gamma} w_2V_{,1}Nd\Gamma - \tau\int_{\partial\Gamma} w_2R_{,2}Nd\Gamma,
\end{aligned}$$

$$
\begin{aligned}
0 \;=\; & \int_\Omega \{\mu w_3 T - \mu w_{3,2}\chi_{3,2} + w_3\kappa(T + N_{,2})(CC + EE + DD + FF + MM + NN) \\
& - w_3\kappa(T + M_{,2} + N_{,1} + N_{,2})(CC + CD + DD + DF + MM + MN + EC \\
& + EE + FD + FF + NM + NN) + w_3\kappa(M + N)(2QC + 2E_{,1}E + 2C_{,2}C \\
& + 2UE - QC - QE - E_{,2}C - E_{,2}E - CQ - CE_{,1} - EC_{,2} - EE_{,2} + 2F_{,1}F \\
& + 2D_{,2}D + 2F_{,2}F - RD - RF - F_{,2}D - F_{,2}F + DR - DF_{,1} - FD_{,2} \\
& - FF_{,2} + 2N_{,1}N + 2M_{,2}M + 2N_{,2}N - M_{,1}M - M_{,1}N - N_{,2}M - N_{,2}N \\
& + MM_{,1} - MN_{,1} - NM_{,2} - MM_{,2}) + w_3[\frac{E_{11}}{4}(2QCCC + 2QCDD \\
& + 2QCMM + 2RDCC + 2RDDD + 2RDMM + 2M_{,1}MCC + 2M_{,1}MDD \\
& + 2M_{,1}MMM + 2CCQC + 2CCRD + 2CCM_{,1}M + 2DDQC + 2DDRD \\
& + 2DDM_{,1}M + 2MMQC + 2MMD_{,1}D + 2MMM_{,1}M) + (E_{12} - E_{11})(QC \\
& + RD + M_{,1}M)]M + w_3[\frac{E_{11}}{4}(CC + DD + MM)^2 + \frac{(E_{12} - E_{11})}{2}(CC \\
& + DD + MM) + \frac{(E_{11} - 2E_{12})}{4}]T + w_3[\frac{E_{21}}{4}(2E_{,2}DDD + 2E_{,2}DFF \\
& + 2E_{,2}ENN + 2F_{,2}FEE + 2F_{,2}FFF + 2F_{,2}FNN + 2SNEE + 2SNFF \\
& + 2SNNN + 2EEE_{,2}E + 2EEF_{,2}F + 2EESN + 2FFE_{,2}E + 2FFF_{,2}F \\
& + 2FFSN + 2NNE_{,2}E + 2NNF_{,2}F + 2NNSN)(E_{22} - E_{21})(E_{,2}E + F_{,2}F \\
& + SN)]N + w_3[\frac{E_{21}}{4}(EE + FF + NN)^2 + \frac{(E_{22} - E_{21})}{2}(EE + FF + NN) \\
& + \frac{(E_{21} - 2E_{22})}{4}]T + w_{3,1}C_1 T_{,1} + w_{3,2}C_2 S_{,2} + w_{3,1}\tau S_{,1} + w_{3,2}\tau T_{,2} \\
& + \frac{1}{2}(w_3 A_0 DN - w_3 A_0 FM - w_3 B_0 CN + w_3 B_0 FM)\}d\Omega \\
& + \mu\int_{\partial\Gamma} w_3\chi_{3,2}N d\Gamma - C_1\int_{\partial\Gamma} w_3 T_{,1}N d\Gamma - C_2\int_{\partial\Gamma} w_3 S_{,2}N d\Gamma \\
& - \tau\int_{\partial\Gamma} w_3 S_{,1}N d\Gamma - \tau\int_{\partial\Gamma} w_3 T_{,2}N d\Gamma,
\end{aligned}
$$

$$0 = \int_\Omega (w_4 Q + w_{3,1}\chi_{1,1})d\Omega - \int_{\partial\Gamma} w_4\chi_{1,1}Nd\Gamma,$$

$$0 = \int_\Omega (w_5 R + w_{5,1}\chi_{2,1})d\Omega - \int_{\partial\Gamma} w_5\chi_{2,1}Nd\Gamma,$$

$$0 = \int_\Omega (w_6 T + w_{6,1}\chi_{3,1})d\Omega - \int_{\partial\Gamma} w_6\chi_{3,1}Nd\Gamma,$$

$$0 = \int_\Omega (w_7 C - w_7\chi_{1,1})d\Omega, \ \ 0 = \int_\Omega w_8(D - \chi_{2,1})d\Omega, \ \ 0 = \int_\Omega w_9(M - \chi_{3,1})d\Omega,$$

$$0 = \int_\Omega w_{10}(E - \chi_{1,2})d\Omega, \ \ 0 = \int_\Omega w_{11}(F - \chi_{2,2})d\Omega, \ \ 0 = \int_\Omega w_{12}(N - \chi_{3,2})d\Omega,$$

$$0 = \int_\Omega (w_{13}U + w_{13,2}\chi_{1,2})d\Omega - \int_{\partial\Gamma} w_{13}\chi_{1,2}Nd\Gamma,$$

$$0 = \int_\Omega (w_{14}V + w_{14,2}\chi_{2,2})d\Omega - \int_{\partial\Gamma} w_{14}\chi_{2,2}Nd\Gamma,$$

$$0 = \int_\Omega (w_{15}S + w_{15,2}\chi_{3,2})d\Omega - \int_{\partial\Gamma} w_{15}\chi_{3,2}Nd\Gamma,$$

$$0 = \int_\Omega (w_{16}A - \mu w_{16}Q + \mu w_{16,2}\chi_{1,2} + C_1 w_{16,1}Q_{,1} + C_2 w_{16,2}U_{,2})d\Omega$$

$$- \int_{\partial\Gamma} \mu w_{16}\chi_{1,2}Nd\Gamma - \int_{\partial\Gamma} C_1 w_{16}Q_{,1}Nd\Gamma - \int_{\partial\Gamma} C_2 w_{16}U_{,2}Nd\Gamma,$$

$$0 = \int_\Omega (w_{17}B - \mu w_{17}R + \mu w_{17,2}\chi_{2,2} + C_1 w_{17,1}R_{,1} + C_2 w_{17,2}V_{,2})d\Omega$$

$$- \int_{\partial\Gamma} \mu w_{17}\chi_{2,2}Nd\Gamma - \int_{\partial\Gamma} C_1 w_{17}R_{,1}Nd\Gamma - \int_{\partial\Gamma} C_2 w_{17}V_{,2}Nd\Gamma \tag{5.112}$$

where Ω, $\partial\Gamma$ and N are, respectively the domain of interest, the associated boundary, and the rightward unit normal to the boundary $\partial\Gamma$ in the sense of the Green-Stokes' theorem. The unknown potentials of $\chi_1, \chi_2, \chi_3, \ Q, \ R, C, D, E, F, T, S, U, V, M, N, \ A$ and B can be expressed in the form of Lagrangian polynomial that

$$(*) = \sum_{j=1}^{n=4} [(*)_j \Psi_j(x,y)]. \tag{5.113}$$

Accordingly, the test function w is found to be

$$w_m = \sum_{i=1}^{n=4} w_m^i \Psi_i(x,y); \ \ i = 1,2,3,4, \ \text{and} \ m = 1,2,3,4,...10 \tag{5.114}$$

where w_i is the weight of the test function and $\Psi_i(x,y)$ are the associated shape functions; $\Psi_1 = \frac{(x-2)(y-1)}{2}$, $\Psi_2 = \frac{x(y-1)}{-2}$, $\Psi_3 = \frac{xy}{2}$ and $\Psi_4 = \frac{y(x-2)}{-2}$. Invoking Eq.

(5.113), (5.112) can be recast in terms of Lagrangian polynomial representation as

$$
\begin{aligned}
0 =& \sum_{i,j=1}^{n=4} [\int_{\Omega^e} \{\mu\Psi_i\Psi_jQ_j - \mu\Psi_{i,2}\Psi_{j,2}\chi_{1j} + \kappa(\Psi_i\Psi_jQ + \Psi_i\Psi_{j,2}E_j)(CC + EE + DD \\
&+ FF + MM + NN) - \kappa(\Psi_i\Psi_jQ + \Psi_i\Psi_{j,2}C_j + \Psi_i\Psi_{j,1}E_j + \Psi_i\Psi_{j,2}E_j)(CC + CD \\
&+ DD + DF + MM + MN + EC + EE + FD + FF + NM + NN) + \kappa(\Psi_i\Psi_jC_j \\
&+ \Psi_i\Psi_jE_j)(2QC + 2E_{,1}E + 2C_{,2}C + 2UE - QC - QE - E_{,2}C - E_{,2}E - CQ \\
&- CE_{,1} - EC_{,2} - EE_{,2} + 2F_{,1}F + 2D_{,2}D + 2F_{,2}F - RD - RF - F_{,2}D - F_{,2}F \\
&+ DR - DF_{,1} - FD_{,2} - FF_{,2} + 2N_{,1}N + 2M_{,2}M + 2N_{,2}N - M_{,1}M - M_{,1}N \\
&- N_{,2}M - N_{,2}N + MM_{,1} - MN_{,1} - NM_{,2} - MM_{,2}) + [\frac{E_{11}}{4}(2QCCC + 2QCDD \\
&+ 2QCMM + 2RDCC + 2RDDD + 2RDMM + 2M_{,1}MCC + 2M_{,1}MDD \\
&+ 2M_{,1}MMM + 2CCQC + 2CCRD + 2CCM_{,1}M + 2DDQC + 2DDRD \\
&+ 2DDM_{,1}M + 2MMQC + 2MMD_{,1}D + 2MMM_{,1}M) + (E_{12} - E_{11})(QC \\
&+ RD + M_{,1}M)]\Psi_i\Psi_jC_j + [\frac{E_{11}}{4}(CC + DD + MM)^2 + \frac{(E_{12} - E_{11})}{2}(CC \\
&+ DD + MM) + \frac{(E_{11} - 2E_{12})}{4}]\Psi_i\Psi_jQ_j + [\frac{E_{21}}{4}(2E_{,2}DDD + 2E_{,2}DFF \\
&+ 2E_{,2}ENN + 2F_{,2}FEE + 2F_{,2}FFF + 2F_{,2}FNN + 2SNEE + 2SNFF \\
&+ 2SNNN + 2EEE_{,2}E + 2EEF_{,2}F + 2EESN + 2FFE_{,2}E + 2FFF_{,2}F \\
&+ 2FFSN + 2NNE_{,2}E + 2NNF_{,2}F + 2NNSN)(E_{22} - E_{21})(E_{,2}E + F_{,2}F \\
&+ SN)]\Psi_i\Psi_jE_j + [\frac{E_{21}}{4}(EE + FF + NN)^2 + \frac{(E_{22} - E_{21})}{2}(EE + FF \\
&+ NN) + \frac{(E_{21} - 2E_{22})}{4}]\Psi_i\Psi_jQ_j + \Psi_{i,1}\Psi_{j,1}C_1Q_j + \Psi_{i,2}\Psi_{j,2}C_2U_j \\
&+ \Psi_{i,1}\Psi_{j,1}\tau U_j + \Psi_{i,2}\Psi_{j,2}\tau Q_j\}d\Omega] + \sum_{i=1}^{n=4}\{\mu\int_{\partial\Gamma^e}\Psi_i\chi_{1,2}Nd\Gamma \\
&- C_1\int_{\partial\Gamma^e}\Psi_iQ_{,1}Nd\Gamma - C_2\int_{\partial\Gamma^e}\Psi_iU_{,2}Nd\Gamma - \tau\int_{\partial\Gamma^e}\Psi_iU_{,1}Nd\Gamma \\
&- \tau\int_{\partial\Gamma^e}\Psi_iQ_{,2}Nd\Gamma\},
\end{aligned}
$$

$$
\begin{aligned}
0 \;=\; & \sum_{i,j=1}^{n=4} \Big[\int_{\Omega^e} \{ \mu \Psi_i \Psi_j R_j - \mu \Psi_{i,2} \Psi_{j,2} \chi_{2j} + \kappa (\Psi_i \Psi_j R_j + \Psi_i \Psi_{j,2} F_j)(CC + EE + DD \\
& + FF + MM + NN) - \kappa(\Psi_i \Psi_j R_j + \Psi_i \Psi_{j,2} D_j + \Psi_i \Psi_{j,1} F_j + \Psi_i \Psi_{j,2} F_j)(CC + CD \\
& + DD + DF + MM + MN + EC + EE + FD + FF + NM + NN) + \kappa(\Psi_i \Psi_j D_j \\
& + \Psi_i \Psi_j F_j)(2QC + 2E_{,1}E + 2C_{,2}C + 2UE - QC - QE - E_{,2}C - E_{,2}E - CQ \\
& - CE_{,1} - EC_{,2} - EE_{,2} + 2F_{,1}F + 2D_{,2}D + 2F_{,2}F - RD - RF - F_{,2}D - F_{,2}F \\
& + DR - DF_{,1} - FD_{,2} - FF_{,2} + 2N_{,1}N + 2M_{,2}M + 2N_{,2}N - M_{,1}M - M_{,1}N \\
& - N_{,2}M - N_{,2}N + MM_{,1} - MN_{,1} - NM_{,2} - MM_{,2}) + [\frac{E_{11}}{4}(2QCCC + 2QCDD \\
& + 2QCMM + 2RDCC + 2RDDD + 2RDMM + 2M_{,1}MCC + 2M_{,1}MDD \\
& + 2M_{,1}MMM + 2CCQC + 2CCRD + 2CCM_{,1}M + 2DDQC + 2DDRD \\
& + 2DDM_{,1}M + 2MMQC + 2MMD_{,1}D + 2MMM_{,1}M) + (E_{12} - E_{11})(QC \\
& + RD + M_{,1}M)]\Psi_i \Psi_j D_j + [\frac{E_{11}}{4}(CC + DD + MM)^2 + \frac{(E_{12} - E_{11})}{2}(CC + DD \\
& + MM) + \frac{(E_{11} - 2E_{12})}{4}]\Psi_i \Psi_j R_j + [\frac{E_{21}}{4}(2E_{,2}DDD + 2E_{,2}DFF + 2E_{,2}ENN \\
& + 2F_{,2}FEE + 2F_{,2}FFF + 2F_{,2}FNN + 2SNEE + 2SNFF + 2SNNN + 2EEE_{,2}E \\
& + 2EEF_{,2}F + 2EESN + 2FFE_{,2}E + 2FFF_{,2}F + 2FFSN + 2NNE_{,2}E + 2NNF_{,2}F \\
& + 2NNSN)(E_{22} - E_{21})(E_{,2}E + F_{,2}F + SN)]\Psi_i \Psi_j F_j + [\frac{E_{21}}{4}(EE + FF + NN)^2 \\
& + \frac{(E_{22} - E_{21})}{2}(EE + FF + NN) + \frac{(E_{21} - 2E_{22})}{4}]\Psi_i \Psi_j R_j + \Psi_{i,1}\Psi_{j,1}C_1 R_j \\
& + \Psi_{i,2}\Psi_{j,2}C_2 V_j + \Psi_{i,1}\Psi_{j,1}\tau V_j + \Psi_{i,2}\Psi_{j,2}\tau R_j\}d\Omega] + \sum_{i=1}^{n=4}\{\mu \int_{\partial\Gamma^e} \Psi_i \chi_{2,2} N d\Gamma \\
& - C_1 \int_{\partial\Gamma^e} \Psi_i R_{,1} N d\Gamma - C_2 \int_{\partial\Gamma^e} \Psi_i V_{,2} N d\Gamma - \tau \int_{\partial\Gamma^e} \Psi_i V_{,1} N d\Gamma \\
& - \tau \int_{\partial\Gamma^e} \Psi_i R_{,2} N d\Gamma\},
\end{aligned}
$$

$$
\begin{aligned}
0 \;=\; &\sum_{i,j=1}^{n=4}\Big[\int_{\Omega^e}\{\mu\Psi_i\Psi_jT_j-\mu\Psi_{i,2}\Psi_{j,2}\chi_{3j}+\kappa(\Psi_i\Psi_jT_j+\Psi_i\Psi_{j,2}N_j)(CC+EE+DD\\
&+FF+MM+NN)-\kappa(\Psi_i\Psi_jT_j+\Psi_i\Psi_{j,2}M_j+\Psi_i\Psi_{j,1}N_j+\Psi_i\Psi_{j,2}N_j)(CC\\
&+CD+DD+DF+MM+MN+EC+EE+FD+FF+NM+NN)\\
&+\kappa(\Psi_i\Psi_jM_j+\Psi_i\Psi_jN_j)(2QC+2E_{,1}E+2C_{,2}C+2UE-QC\\
&-QE-E_{,2}C-E_{,2}E-CQ-CE_{,1}-EC_{,2}-EE_{,2}+2F_{,1}F+2D_{,2}D\\
&+2F_{,2}F-RD-RF-F_{,2}D-F_{,2}F+DR-DF_{,1}-FD_{,2}-FF_{,2}+2N_{,1}N\\
&+2M_{,2}M+2N_{,2}N-M_{,1}M-M_{,1}N-N_{,2}M-N_{,2}N+MM_{,1}-MN_{,1}-NM_{,2}\\
&-MM_{,2})+[\frac{E_{11}}{4}(2QCCC+2QCDD+2QCMM+2RDCC+2RDDD\\
&+2RDMM+2M_{,1}MCC+2M_{,1}MDD+2M_{,1}MMM+2CCQC+2CCRD\\
&+2CCM_{,1}M+2DDQC+2DDRD+2DDM_{,1}M+2MMQC+2MMD_{,1}D\\
&+2MMM_{,1}M)+(E_{12}-E_{11})(QC+RD+M_{,1}M)]\Psi_i\Psi_jM_j+[\frac{E_{11}}{4}(CC\\
&+DD+MM)^2+\frac{(E_{12}-E_{11})}{2}(CC+DD+MM)+\frac{(E_{11}-2E_{12})}{4}]\Psi_i\Psi_jT_j\\
&+[\frac{E_{21}}{4}(2E_{,2}DDD+2E_{,2}DFF+2E_{,2}ENN+2F_{,2}FEE+2F_{,2}FFF\\
&+2F_{,2}FNN+2SNEE+2SNFF+2SNNN+2EEE_{,2}E+2EEF_{,2}F\\
&+2EESN+2FFE_{,2}E+2FFF_{,2}F+2FFSN+2NNE_{,2}E+2NNF_{,2}F\\
&+2NNSN)(E_{22}-E_{21})(E_{,2}E+F_{,2}F+SN)]\Psi_i\Psi_jN_j+[\frac{E_{21}}{4}(EE+FF\\
&+NN)^2+\frac{(E_{22}-E_{21})}{2}(EE+FF+NN)+\frac{(E_{21}-2E_{22})}{4}]\Psi_i\Psi_jT_j\\
&+\Psi_{i,1}\Psi_{j,1}C_1T_j+\Psi_{i,2}\Psi_{j,2}C_2S_j+\Psi_{i,1}\Psi_{j,1}\tau S_j+\Psi_{i,2}\Psi_{j,2}\tau T_j+\frac{1}{2}(\Psi_i\Psi_jA_0DN_j\\
&-\Psi_i\Psi_jA_0FM_j-\Psi_i\Psi_jB_0CN_j+\Psi_i\Psi_jB_0FM_j)\}d\Omega]\\
&+\sum_{i=1}^{n=4}\{\mu\int_{\partial\Gamma^e}\Psi_i\chi_{3,2}Nd\Gamma-C_1\int_{\partial\Gamma^e}\Psi_iT_{,1}Nd\Gamma-C_2\int_{\partial\Gamma^e}\Psi_iS_{,2}Nd\Gamma\\
&-\tau\int_{\partial\Gamma^e}\Psi_iS_{,1}Nd\Gamma-\tau\int_{\partial\Gamma^e}\Psi_iT_{,2}Nd\Gamma\},
\end{aligned}
$$

$$0 = \sum_{i,j=1}^{n=4} (\Psi_i \Psi_j Q + \Psi_{i,1} \Psi_{j,1} \chi_{1j}) d\Omega - \sum_{i=1}^{n=4} \{ \int_{\partial \Gamma^e} \Psi_i \chi_{1,1} N d\Gamma \},$$

$$0 = \sum_{i,j=1}^{n=4} [(\Psi_i \Psi_j R_j + \Psi_i \Psi_{j,1} \chi_{2j}) d\Omega - \sum_{i=1}^{n=4} \{ \int_{\partial \Gamma^e} \Psi_i \chi_{2,1} N d\Gamma \},$$

$$0 = \sum_{i,j=1}^{n=4} [(\Psi_i \Psi_j T_j + \Psi_i \Psi_{j,1} \chi_{3j}) d\Omega - \sum_{i=1}^{n=4} \{ \int_{\partial \Gamma^e} \Psi_i \chi_{3,1} N d\Gamma \},$$

$$0 = \sum_{i,j=1}^{n=4} [(\Psi_i \Psi_j C_j - \Psi_i \Psi_{j,1} \chi_{1j}) d\Omega, \ 0 = \sum_{i,j=1}^{n=4} (\Psi_i \Psi_j D - \Psi_i \Psi_{j,1} \chi_{2j}) d\Omega,$$

$$0 = \sum_{i,j=1}^{n=4} (\Psi_i \Psi_j M_j - \Psi_i \Psi_{j,1} \chi_{3j}) d\Omega,$$

$$0 = \sum_{i,j=1}^{n=4} (\Psi_i \Psi_j E_j - \Psi_i \Psi_{j,2} \chi_{1j}) d\Omega, \ 0 = \sum_{i,j=1}^{n=4} (\Psi_i \Psi_j F_j - \Psi_i \Psi_{j,2} \chi_{2j}) d\Omega,$$

$$0 = \sum_{i,j=1}^{n=4} (\Psi_i \Psi_j N_j - \Psi_i \Psi_{j,2} \chi_{3j}) d\Omega,$$

$$0 = \sum_{i,j=1}^{n=4} [(\Psi_i \Psi_j U_j + \Psi_i \Psi_{j,2} \chi_{1j}) d\Omega - \sum_{i=1}^{n=4} \{ \int_{\partial \Gamma^e} \Psi_i \chi_{1,2} N d\Gamma \},$$

$$0 = \sum_{i,j=1}^{n=4} [(\Psi_i \Psi_j V_j + \Psi_i \Psi_{j,2} \chi_{2j}) d\Omega - \sum_{i=1}^{n=4} \{ \int_{\partial \Gamma^e} \Psi_i \chi_{2,2} N d\Gamma \},$$

$$0 = \sum_{i,j=1}^{n=4} [(\Psi_i \Psi_j S_j + \Psi_i \Psi_{j,2} \chi_{3j}) d\Omega - \sum_{i=1}^{n=4} \{ \int_{\partial \Gamma^e} \Psi_i \chi_{3,2} N d\Gamma \},$$

$$0 = \sum_{i,j=1}^{n=4} [(\Psi_i \Psi_j A_j - \mu \Psi_i \Psi_j Q_j + \mu \Psi_{i,2} \Psi_{j,2} \chi_{1j} + C_1 \Psi_{i,1} \Psi_{j,1} Q_j + C_2 \Psi_{i,2} \Psi_{j,2} U_j) d\Omega$$

$$- \sum_{i=1}^{n=4} \{ \int_{\partial \Gamma^e} \mu \Psi_i \chi_{1,2} N d\Gamma - \int_{\partial \Gamma^e} C_1 \Psi_i Q_{,1} N d\Gamma - \int_{\partial \Gamma^e} C_2 \Psi_i U_{,2} N d\Gamma \},$$

$$0 = \sum_{i,j=1}^{n=4} [(\Psi_i \Psi_j B_j - \mu \Psi_i \Psi_j R_j + \mu \Psi_{i,2} \Psi_{j,2} \chi_{2j} + C_1 \Psi_{i,1} \Psi_{j,1} R_j + C_2 \Psi_{i,2} \Psi_{j,2} V_j) d\Omega$$

$$- \sum_{i=1}^{n=4} \{ \int_{\partial \Gamma^e} \mu w_{17} \chi_{2,2} N d\Gamma - \int_{\partial \Gamma^e} C_1 w_{17} R_{,1} N d\Gamma - \int_{\partial \Gamma^e} C_2 \Psi_i V_{,2} N d\Gamma \}, \quad (5.115)$$

179

Now, for the local stiffness matrices and forcing vectors for each elements, we find

$$
\begin{bmatrix}
K_{11}^{11} & K_{12}^{11} & K_{13}^{11} & K_{14}^{11} \\
K_{21}^{11} & K_{22}^{11} & K_{23}^{11} & K_{24}^{11} \\
K_{31}^{11} & K_{32}^{11} & K_{33}^{11} & K_{34}^{11} \\
K_{41}^{11} & K_{42}^{11} & K_{43}^{11} & K_{44}^{11}
\end{bmatrix}_{Local}
\begin{bmatrix}
\chi_1^1 \\
\chi_1^2 \\
\chi_1^3 \\
\chi_1^4
\end{bmatrix}_{Local}
=
\begin{bmatrix}
F_1^1 \\
F_2^1 \\
F_3^1 \\
F_4^1
\end{bmatrix}_{Local}, \tag{5.116}
$$

where

$$
\left[K_{ij}^{11} \right] = \int_\Omega (-\mu \Psi_{i,2} \Psi_{j,2}) d\Omega, \tag{5.117}
$$

and

$$
\begin{aligned}
\{F_i^1\} &= \mu \int_{\partial \Gamma^e} \Psi_i \chi_{1,2} N d\Gamma - C_1 \int_{\partial \Gamma^e} \Psi_i Q_{,1} N d\Gamma - C_2 \int_{\partial \Gamma^e} \Psi_i U_{,2} N d\Gamma - \tau \int_{\partial \Gamma^e} \Psi_i U_{,1} N d\Gamma \\
&\quad - \tau \int_{\partial \Gamma^e} \Psi_i Q_{,2} N d\Gamma \tag{5.118}
\end{aligned}
$$

Thus, the unknown potentials (i.e. Q, $R, C, D, E, F, T, S, U, V, M, N$, A and B) can be expressed as

$$
Q_i = \{\chi_1^i\}_{,11}, \ R_i = \{\chi_2^i\}_{,11} \text{ etc...}, \tag{5.119}
$$

and similarly for the rest of unknowns.

In the simulation, we employed the following convergence criteria

$$
|A_{n+1} - A_n| = e_1 \le \varepsilon, \ \ |B_{n+1} - B_n| = e_2 \le \varepsilon, \text{ where } \varepsilon = \text{maximum error} = 10^{-10}, \tag{5.120}
$$

which demonstrates fast convergence within 12 iterations using FEniCS nonlinear solver (see, 5.1).

Table 5.1: Maximum numerical errors with respect to the number of iterations.

Number of iteration	Mximum error
1	8.384e-01
2	7.022e-02
3	9.674e-02
5	4.088e-01
7	3.599e+00
10	6.195e-03
11	5.0795e-07
12	6.703e-14

5.7   Denouement

In this chapter, a three-dimensional continuum model describing the elastic / hyperelastic responses of bidirectional fibrous composite materials is presented in finite elastostatics. The mechanics of matrix-fiber composite system is modeled via the Neo-Hookean strain energy potential and the Green-Lagrange strain measure in quadratic form which are then refined, respectively, by the Mooney Rivlin model and the high-order polynomial energy potential of fibers to accommodate the nonlinear hyperelastic responses of elastomeric composites. Emphasis is placed on the incorporation of both the in-plane and out-of-plane kinematics into the continuum model of the matrix-fiber system while maintaining the rigor and sufficient generality in the corresponding derivations. The three-dimensional bending and stretch of a fiber and the twist between the two adjoining fibers are formulated via the first and second gradient of continuum deformations. Within the framework of variational principles and virtual work statement, the Euler equilibrium equation and the associated boundary conditions are formulated. The solutions of the former are obtained via the custom-built FEA procedure which are subsequently cross-examined with the inhouse experimental data sets and existing results in the dedicated literature.

It is demonstrated that the presented model produces the complete deformation map of the PLA-bamboo composite together with the resultant stress-strain response when it is subjected to draping over a hemisphere. Deformation analysis pertaining to the local structures (a unit fiber mesh) is also performed via the GSA method illustrating that there is a good agreement in the grid map contour images obtained, respectively, from the proposed model and the experimental result in the dedicated literature. An analysis of the coiling responses of a thin-walled DCB reinforced with carbon fiber mesh is also presented. Solutions from the obtained two-dimensional model successfully predict the force-displacement response of the DCB subjected to progressive flattening which arises during the coiling process. In addition, the deformation profiles and the associated shear strain distributions predicted from the proposed model suggest that the recovering energy of the DCB may be further maximized, without considering higher strength materials for the matrix and reinforcing materials, by enhancing the fiber-to-fiber bond at the intersection. Lastly, imple-

mentations toward series of engineering problems such as the hyperelastic responses of elastomeric composites, the equilibrium shapes of Hypar shell structures and the focal length variations of tunable elastomeric lens have been considered implying the versatility of the proposed model in various engineering applications.

Chapter 6

A pseudo-elastic model for hyperelastic composites reinforced with nonlinear elastic fibrous materials

In section 6.1, the kinematics is presented for a hyperelastic material reinforced with bidirectional fibers. The 3rd order polynomial extension potential is used to accommodate the nonlinear response of the fiber and the Mooney-Rivlin model is used to address the hyperelastic response of the matrix material. The equilibrium and boundary conditions are presented in section 6.2. In section 6.3, two distinct kinds of pseudo-elastic behaviors are incorporated within the model. In section 6.4, the utilities of the models are demonstrated by comparing them against both in-house experiment data and experimental data from existing literature.

6.1   Kinematics of fibers embedded in a hyperelastic matrix material

In this section, we present a continuum model that describes the mechanical responses of biological soft tissues. For the stated purpose, a model of hyperelastic materials reinforced with nonlinear elastic and extensible fiber mesh is developed where the fibers are organized in a bidirectional arrangement.

Let the unit vectors $\mathbf{D}$ and $\mathbf{M}$ be the fibers' trajectories in reference configuration

are defined as follows:

$$\mathbf{D} = \frac{d\mathbf{X}(S,U)}{dS} \text{ and } \mathbf{M} = \frac{d\mathbf{X}(S,U)}{dU}, \tag{6.1}$$

where S and U are, respectively, the arclength parameters in the directions of $\mathbf{D}$ and $\mathbf{M}$. For the sake of mathematical tractability and conciseness, we confine our attention to the case of initially uniform and orthogonal fiber mesh (i.e. $\mathbf{D} \cdot \mathbf{M} = \mathbf{0}$, see, also, Fig. 6.1). The assumed orthogonality and uniformity of the fiber mesh is deemed sufficient to extract the important aspects of the intended model and, further, the desired applications. The cases of non-orthogonal fibers with different orientation angles can be readily accommodated via the simple modification of fibers' director fields (e.g. $\mathbf{D} \cdot \mathbf{M} = \cos\alpha$ etc...). Let's now define $r(u)$ and $r(s)$ to be the parametric
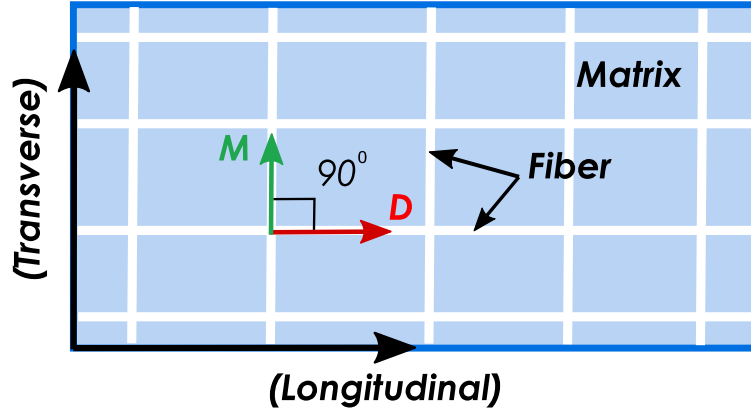
Figure 6.1: Schematics of bidirectional fibers (intial configuration).

curves of fibers' tragectories on the deformed (current) configuration. Also, $\mathbf{d}$, $\mathbf{m}$, s, and u are the counter parts of $\mathbf{D}$, $\mathbf{M}$, S, and U in the current configuration. Further, $\boldsymbol{\eta}$ and $\boldsymbol{\tau}$ are the unit tangents in the directions of increasing arclength parameters u and s, respectively. The stretch and orientation of a particular fiber after deformations are then defined by:

$$\lambda = |\boldsymbol{\eta}| = \frac{ds}{dS}, \ \gamma = |\boldsymbol{\tau}| = \frac{du}{dU} \text{ and } (\frac{d\mathbf{r}}{ds}) = \mathbf{d} = \lambda^{-1}\boldsymbol{\eta}, \ (\frac{d\mathbf{r}}{du}) = \mathbf{m} = \gamma^{-1}\boldsymbol{\tau}, \tag{6.2}$$

where

$$\lambda\mathbf{d} = \mathbf{FD} \text{ and } \gamma\mathbf{m} = \mathbf{FM}. \tag{6.3}$$

Here, $\mathbf{F}$ is the gradient of the deformation function ($\boldsymbol{\chi}(\mathbf{X})$). Eq. (6.3) together with the presumed orthogonality (i.e. $\mathbf{D} \cdot \mathbf{M} = \mathbf{0}$) furnish a useful fiber decomposition of

184

the deformation gradient tensor:

$$\mathbf{F} = \lambda \mathbf{d} \otimes \mathbf{D} + \gamma \mathbf{m} \otimes \mathbf{M}, \tag{6.4}$$

which will be used in the forthcoming model derivation. Hence, the geodesic curvatures of a parametric curve $(\mathbf{r}(s, u))$ can be formulated from Eqs. (6.2)-(6.3) as follows:

$$\mathbf{g}_1 = \frac{d^2\mathbf{r}(S)}{dS^2} = \frac{d(\frac{\mathbf{r}(S)}{dS})}{dS} = \frac{\partial(\mathbf{FD})}{\partial \mathbf{X}}\frac{\partial \mathbf{X}}{\partial S} = \nabla[\mathbf{FD}]\mathbf{D}, \text{ and} \tag{6.5}$$

$$\mathbf{g}_2 = \frac{d^2\mathbf{r}(U)}{dU^2} = \frac{d(\frac{\mathbf{r}(U)}{dU})}{dU} = \frac{\partial(\mathbf{FM})}{\partial \mathbf{X}}\frac{\partial \mathbf{X}}{\partial U} = \nabla[\mathbf{FM}]\mathbf{M}. \tag{6.6}$$

In the case of initially straight fibers, the above reduces to

$$\mathbf{g}_1 = \nabla\mathbf{F}(\mathbf{D} \otimes \mathbf{D}) = \mathbf{G}(\mathbf{D} \otimes \mathbf{D}) \text{ and } \mathbf{g}_2 = \nabla\mathbf{F}(\mathbf{M} \otimes \mathbf{M}) = \mathbf{G}(\mathbf{M} \otimes \mathbf{M}). \tag{6.7}$$

The forgoing developments suggest that the mechanical responses of the fiber mesh can be described by the following energy function:

$$W_{fiber} = W(\varepsilon_1, \varepsilon_2) + \frac{1}{2}C(\mathbf{g}_1 \cdot \mathbf{g}_1 + \mathbf{g}_2 \cdot \mathbf{g}_2) + \frac{1}{2}T\mathbf{g}_1 \cdot \mathbf{g}_2. \tag{6.8}$$

Here, the second term in the above ($\frac{1}{2}C(\mathbf{g}_1 \cdot \mathbf{g}_1 + \mathbf{g}_2 \cdot \mathbf{g}_2)$) is the fiber's bending energy potential of Spencer and Soldatos type [93] which presumes that the bending responses of fibers are dependent entirely on the second gradient of continuum deformations via the geodesic curvature of fibers. Also, the term $\frac{1}{2}T\mathbf{g}_1 \cdot \mathbf{g}_2$ accounts for the torsional kinematics of the fiber mesh. Here, C and T are the associated moduli of the reinforcing fiber mesh. In particular, the energy potential of $W(\varepsilon_1, \varepsilon_2)$ in Eq. (6.8) characterizes the responses of the fiber mesh against extensions, which will be discussed next in more details.

6.1.1 Modeling the nonlinear response of fibers

Soft biological tissues are complex fiber-reinforced composite structures. Mechanical behaviors of these materials are strongly influenced by the concentrations and structural arrangements of constituents such as collagen and elastin [160]. Flexible collagen fibers are one of the most abundant structural proteins, constituting about $30 - 40\%$ of all body proteins in most mammals [161]. This collagen fiber is the main

load-carrying element in a wide variety of soft tissues like tendons, ligaments, blood vessels, skins, articular cartilages, etc. [160]. Biomaterials reinforced with collagen fibers typically exhibit nonlinear stress-strain response which may be described as follows. The mechanics of soft tissues follow two distinct deformation regimes [162]-[163]. Initially, the collagen is oriented in a random pattern. Once a load is applied, these randomly oriented collagen fibers readily start to reorient along the direction of the applied load. During this deformation regime, the material demonstrates low stiffness because the response is largely determined by the elastin matrix rather than the collagen fibers [163]-[164]. As more stretch is applied to the material, the collagen fibers straighten even more and realign parallel to one another. At this phase, more load is required to induce further elongation because the collagen is now started to take most of the load [162]–[164]. This process may continue until the fibers are mostly aligned in the direction of the applied load [163]. Furthermore, due to the complex orientation pattern of the collagen fibers, soft tissues behave anisotropically showing different stiffnesses in the orthogonal directions [160]. To accommodate such anisotropic non-linear response of collagen fiber reinforced biomaterials, we have introduced polynomial type nonlinear energy potential, $W(\varepsilon_1, \varepsilon_2)$ for the fibers' extension as follows,

$$W(\varepsilon_1, \varepsilon_2) = \frac{1}{3}E_{11}\varepsilon_1^3 + \frac{1}{2}E_{12}\varepsilon_1^2 + \frac{1}{3}E_{21}\varepsilon_2^3 + \frac{1}{2}E_{22}\varepsilon_2^2. \tag{6.9}$$

Here, E_{1j} and E_{2j} representing the fiber tensile parameters in longitudinal and transverse directions, respectively. Now, the expressions for the associated strains can be found as follows:

$$\varepsilon_1 = \frac{1}{2}\left(\lambda^2 - 1\right) = \frac{1}{2}\left(\mathbf{FD} \cdot \mathbf{FD} - 1\right) \text{ and } \varepsilon_2 = \frac{1}{2}\left(\gamma^2 - 1\right) = \frac{1}{2}\left(\mathbf{FM} \cdot \mathbf{FM} - 1\right). \tag{6.10}$$

In variational form we can write,

$$
\begin{aligned}
\dot{\varepsilon}_1 &= \varepsilon_{1\mathbf{F}}\dot{\mathbf{F}} = \lambda\dot{\lambda} = \mathbf{FD} \cdot \dot{\mathbf{F}}\mathbf{D} = tr(\mathbf{FD} \otimes \dot{\mathbf{F}}\mathbf{D}) = tr((\mathbf{FD} \otimes \mathbf{D})\dot{\mathbf{F}}^T) \\
&= \mathbf{F}(\mathbf{D} \otimes \mathbf{D}) \cdot \dot{\mathbf{F}}, \tag{6.11} \\
\dot{\varepsilon}_2 &= \varepsilon_{2\mathbf{F}}\dot{\mathbf{F}} = \gamma\dot{\gamma} = \mathbf{FM} \cdot \dot{\mathbf{F}}\mathbf{M} = tr(\mathbf{FM} \otimes \dot{\mathbf{F}}\mathbf{M}) = tr((\mathbf{FM} \otimes \mathbf{M})\dot{\mathbf{F}}^T) \\
&= \mathbf{F}(\mathbf{M} \otimes \mathbf{M}) \cdot \dot{\mathbf{F}}. \tag{6.12}
\end{aligned}
$$

In components notation we can write:

$$\mathbf{F}(\mathbf{D}\otimes\mathbf{D})\cdot\dot{\mathbf{F}} = F_{jB}(\mathbf{e}_j\otimes\mathbf{E}_B)D_C D_D(\mathbf{E_C}\otimes\mathbf{E}_D)\cdot\dot{F}_{iA}(\mathbf{e}_i\otimes\mathbf{E}_A)$$

$$= F_{jB}D_C D_D\delta_{BC}(\mathbf{e}_j\otimes\mathbf{E}_D)\cdot\dot{F}_{iA}(\mathbf{e}_i\otimes\mathbf{E}_A)$$

$$= F_{jB}D_B D_D\dot{F}_{iA}\delta_{ij}\delta_{DA}$$

$$= F_{iB}D_B D_A\dot{F}_{iA}. \tag{6.13}$$

Let, $\dot{F}_{iA} = u_{i,A}$. Then we can write:

$$\mathbf{F}(\mathbf{D}\otimes\mathbf{D})\cdot\dot{\mathbf{F}} = F_{iB}D_B D_A u_{i,A}, \tag{6.14}$$

$$\mathbf{F}(\mathbf{M}\otimes\mathbf{M})\cdot\dot{\mathbf{F}} = F_{iB}M_B M_A u_{i,A}. \tag{6.15}$$

Similarly,

$$\mathbf{FD.FD} = F_{jC}F_{jD}D_C D_D, \tag{6.16}$$

$$\mathbf{FM.FM} = F_{jC}F_{jD}M_C M_D. \tag{6.17}$$

Further, we can also obtain,

$$(\mathbf{FD}\cdot\mathbf{FD}-1)^2 = (\mathbf{FD}\cdot\mathbf{FD})(\mathbf{FD}\cdot\mathbf{FD})-2(\mathbf{FD}\cdot\mathbf{FD})+1 \tag{6.18}$$

$$= (F_{jC}F_{jD}D_C D_D)(F_{kE}F_{kF}D_E D_F) - 2F_{jC}F_{jD}D_C D_D + 1,$$

$$(\mathbf{FM}\cdot\mathbf{FM}-1)^2 = (\mathbf{FM}\cdot\mathbf{FM})(\mathbf{FM}\cdot\mathbf{FM})-2(\mathbf{FM}\cdot\mathbf{FM})+1 \tag{6.19}$$

$$= (F_{jC}F_{jD}M_C M_D)(F_{kE}F_{kF}M_E M_F) - 2F_{jC}F_{jD}M_C M_D + 1,$$

$$(\mathbf{FD}\cdot\mathbf{FD}-1)^3 = (\mathbf{FD}\cdot\mathbf{FD})(\mathbf{FD}\cdot\mathbf{FD})(\mathbf{FD}\cdot\mathbf{FD})-3(\mathbf{FD}\cdot\mathbf{FD})(\mathbf{FD}\cdot\mathbf{FD})$$

$$+3(\mathbf{FD}\cdot\mathbf{FD})-1$$

$$= (F_{jC}F_{jD}D_C D_D - 1)^3 \tag{6.20}$$

$$= (F_{jC}F_{jD}D_C D_D)(F_{kE}F_{kF}D_E D_F)(F_{lM}F_{lN}D_M D_N)$$

$$-3(F_{jC}F_{jD}M_C M_D)(F_{kE}F_{kF}D_E D_F) + 3(F_{jC}F_{jD}D_C D_D) - 1,$$

$$(\mathbf{FM}\cdot\mathbf{FM}-1)^3 = (\mathbf{FM}\cdot\mathbf{FM})(\mathbf{FM}\cdot\mathbf{FM})(\mathbf{FM}\cdot\mathbf{FM})-3(\mathbf{FM}\cdot\mathbf{FM})(\mathbf{FM}\cdot\mathbf{FM})$$

$$+3(\mathbf{FM}\cdot\mathbf{FM})-1$$

$$= (F_{jC}F_{jD}M_C M_D - 1)^3 \tag{6.21}$$

$$= (F_{jC}F_{jD}M_C M_D)(F_{kE}F_{kF}M_E M_F)(F_{lM}F_{lN}M_M M_N)$$

$$-3(F_{jC}F_{jD}M_C M_D)(F_{kE}F_{kF}M_E M_F) + 3(F_{jC}F_{jD}M_C M_D) - 1.$$

These expressions in component notation would be directly used in the later derivation. We then express Eq. (6.8) in variational form using the chain rule as

$$
\begin{aligned}
\dot{W}_{fiber} \;=\;& W(\varepsilon_1,\varepsilon_2)_{\varepsilon_1}(\varepsilon_1)_{\mathbf{F}}\cdot\dot{\mathbf{F}} + W(\varepsilon_1,\varepsilon_2)_{\varepsilon_2}(\varepsilon_2)_{\mathbf{F}}\cdot\dot{\mathbf{F}} + C(\mathbf{g}_1\cdot\dot{\mathbf{g}}_1 + \mathbf{g}_2\cdot\dot{\mathbf{g}}_2)\\
&+\frac{T}{2}(\dot{\mathbf{g}}_1\cdot\mathbf{g}_2 + \mathbf{g}_1\cdot\dot{\mathbf{g}}_2),
\end{aligned}
\tag{6.22}
$$

where, $W(\varepsilon_1,\varepsilon_2)_{\varepsilon_1} = E_{11}\varepsilon_1^2 + E_{12}\varepsilon_1$ and $W(\varepsilon_1,\varepsilon_2)_{\varepsilon_2} = E_{21}\varepsilon_2^2 + E_{22}\varepsilon_2$. Thereby we obtain the variational derivative of W_{fiber} as

$$
\begin{aligned}
\dot{W}_{fiber}(\mathbf{F},\varepsilon_1,\varepsilon_2,\mathbf{g}) \;=\;& [\{\frac{1}{4}E_{11}(\mathbf{FD}\cdot\mathbf{FD}-1)^2 + \frac{1}{2}E_{12}(\mathbf{FD}\cdot\mathbf{FD}-1)\}\varepsilon_{1\mathbf{F}}\\
&+\{\frac{1}{4}E_{21}(\mathbf{FM}\cdot\mathbf{FM}-1)^2 + \frac{1}{2}E_{22}(\mathbf{FM}\cdot\mathbf{FM}-1)\}\varepsilon_{2\mathbf{F}}]\cdot\dot{\mathbf{F}}\\
&+C(\mathbf{g}_1\cdot\dot{\mathbf{g}}_1 + \mathbf{g}_2\cdot\dot{\mathbf{g}}_2) + T(\mathbf{g}_1\cdot\dot{\mathbf{g}}_2 + \mathbf{g}_1\cdot\dot{\mathbf{g}}_2).
\end{aligned}
\tag{6.23}
$$

Here, the superposed dot refers to the variational derivatives with respect to a parameter ϵ at the particular configuration of the composite (i.e., $\epsilon = 0$) that labels a one-parameter family of deformations.

6.1.2 Modeling the hyperelastic matrix material

Bio-fibers like collagen are generally embedded in extracellular matrix protein (e.g., elastin). These matrix proteins are usually described as hyperelastic materials [165]. In this study, we adopt the Mooney-Rivlin energy potential for the descriptions of hyperelastic matrix materials which has been widely adopted in the large deformation analyses (see, also, [105]-[106] and references therein):

$$
W(\mathbf{F}) = \frac{\mu}{2}(I_1 - 3) + \frac{\kappa}{2}(I_2 - 3),
\tag{6.24}
$$

where I_1 and I_2 are the principal invariants of the deformation gradient tensor defined, respectively, by

$$
I_1 = tr(\mathbf{F}^T\mathbf{F}) \text{ and } I_2 = \frac{1}{2}[(tr(\mathbf{F}^T\mathbf{F}))^2 - tr((\mathbf{F}^T\mathbf{F})^2)],
\tag{6.25}
$$

based on the obtained kinematic formulations for the fibers and matrix materials. The expressions for the associated energy variations can be obtained as

$$
W_{\mathbf{F}}\cdot\dot{\mathbf{F}} = [\frac{\mu}{2}(I_1)_{\mathbf{F}} + \frac{\kappa}{2}(I_2)_{\mathbf{F}}]\cdot\dot{\mathbf{F}} = [\mu\mathbf{F} + \kappa\mathbf{F}\{(\mathbf{F}\cdot\mathbf{F})\mathbf{I} - \mathbf{F}^T\mathbf{F}\}]\cdot\dot{\mathbf{F}},
\tag{6.26}
$$

where $(I_1)_\mathbf{F} = 2\mathbf{F}$ and $(I_2)_\mathbf{F} = 2\mathbf{F}(I_1\mathbf{I} - \mathbf{F}^T \cdot \mathbf{F})$. By combining the terms from Eq. (6.24) with the energy potential of the fiber mesh in Eq. (6.8), we get the energy function of the hyperelastic composite as follows:

$$
\begin{aligned}
W(\mathbf{F}, \varepsilon, \mathbf{g}) \;=\; & \frac{\mu}{2}(I_1 - 3) + \frac{\kappa}{2}(I_2 - 3) + \frac{1}{3}E_{11}\varepsilon_1^3 + \frac{1}{2}E_{12}\varepsilon_1^2 + \frac{1}{3}E_{21}\varepsilon_2^3 \\
& + \frac{1}{2}E_{22}\varepsilon_2^2 + \frac{1}{2}C(\mathbf{g}_1\cdot\mathbf{g}_1 + \mathbf{g}_2\cdot\mathbf{g}_2) + \frac{1}{2}T\mathbf{g}_1\cdot\mathbf{g}_2.
\end{aligned}
\tag{6.27}
$$

Lastly, we evaluate the induced energy variation of the response function for the hyperelastic composite in Eq. (6.27) as follows

$$
\begin{aligned}
\dot{W}(\mathbf{F}, \varepsilon, \mathbf{g}) \;=\; & W(\mathbf{F})_\mathbf{F}\cdot\dot{\mathbf{F}} + \dot{W}_{fiber} \\
\;=\; & W(\mathbf{F})_\mathbf{F}\cdot\dot{\mathbf{F}} + W(\varepsilon_1, \varepsilon_2)_{\varepsilon_1}(\varepsilon_1)_\mathbf{F}\cdot\dot{\mathbf{F}} + W(\varepsilon_1, \varepsilon_2)_{\varepsilon_2}(\varepsilon_2)_\mathbf{F}\cdot\dot{\mathbf{F}} + C(\mathbf{g}_1\cdot\dot{\mathbf{g}}_1 + \mathbf{g}_2\cdot\dot{\mathbf{g}}_2) \\
& + \frac{T}{2}(\dot{\mathbf{g}}_1\cdot\mathbf{g}_2 + \mathbf{g}_1\cdot\dot{\mathbf{g}}_2).
\end{aligned}
\tag{6.28}
$$

This will be used in the derivations of the Euler equations and the associated boundary conditions, as presented in the next section.

6.2   Equilibrium & Boundary conditions

In the present study, the framework of the virtual work statement is adopted in the formulations of the Euler equilibrium equations and the associated boundary conditions. To begin the derivation, we evaluate the potential energy of the system as

$$
E = \int_\Omega W(\mathbf{F}, \varepsilon_1, \varepsilon_2, \mathbf{g}_1, \mathbf{g}_2) \, dA.
\tag{6.29}
$$

Hence, the weak form of the equilibrium equation can be obtained by the virtual-work statement,

$$
\dot{E} = P,
\tag{6.30}
$$

where P is the virtual power of the applied loads and the superposed dot denotes the variational and/or Gateâux derivative. Here, the conservative loads are characterized by the existence of a potential L such that $P = \dot{L}$. Accordingly, the problem of determining equilibrium deformations is reduced to the problem of minimizing the potential energy, $E - L$. In the present context, this would mean that

$$
\dot{E} = \int_\Omega \dot{W}(\mathbf{F}, \varepsilon_1, \varepsilon_2, \mathbf{g}_1, \mathbf{g}_2) \, dA.
\tag{6.31}
$$

In general, volumetric changes in materials' deformations are energetically expensive processes and therefore are typically constrained in the constitutive modeling of engineering materials (see, also, [105]-[106]). This can be achieved by augmenting the condition of bulk incompressibility (i.e., $p(J-1)$) on the strain energy potential such that

$$U(\mathbf{F},\varepsilon,\mathbf{g},p) = W(\mathbf{F}) + W(\varepsilon_1,\varepsilon_2) + \frac{1}{2}C(\mathbf{g}_1{\cdot}\mathbf{g}_1 + \mathbf{g}_2{\cdot}\mathbf{g}_2) + \frac{1}{2}T\mathbf{g}_1{\cdot}\mathbf{g}_2 - p(J-1) , \quad (6.32)$$

where, J is determinant of $\mathbf{F}$ and p is a constitutively indeterminate Lagrange multiplier field. Therefore, Eq. (6.31) becomes

$$\dot{E} = \int_\Omega \dot{U}(\mathbf{F},\varepsilon_1,\varepsilon_2,\mathbf{g}_1,\mathbf{g}_2,p)dA. \quad (6.33)$$

In view of Eqs. (6.23), (6.28), and (6.32), the associated energy variation then furnishes

$$
\begin{aligned}
\dot{U} =~& [\{\mu\mathbf{F}{+}\kappa\mathbf{F}\{(\mathbf{F}\cdot\mathbf{F})\mathbf{I} - \mathbf{F}^T\mathbf{F}\} + \{\tfrac{1}{4}E_{11}\left(\mathbf{FD}\cdot\mathbf{FD}{-}1\right)^2 + \tfrac{1}{2}E_{12}\left(\mathbf{FD}\cdot\mathbf{FD}{-}1\right)\}\varepsilon_{1\mathbf{F}} \\
&+\{\tfrac{1}{4}E_{21}\left(\mathbf{FM}\cdot\mathbf{FM}{-}1\right)^2 + \tfrac{1}{2}E_{22}\left(\mathbf{FM}\cdot\mathbf{FM}{-}1\right)\}\varepsilon_{2\mathbf{F}}]{\cdot}\dot{\mathbf{F}} \\
&+C(\mathbf{g}_1{\cdot}\dot{\mathbf{g}}_1 + \mathbf{g}_2{\cdot}\dot{\mathbf{g}}_2) + T(\mathbf{g}_1{\cdot}\dot{\mathbf{g}}_2 + \mathbf{g}_2{\cdot}\dot{\mathbf{g}}_1) - p\dot{J},
\end{aligned}
\quad (6.34)
$$

$$\text{and } \dot{J} = J_{\mathbf{F}}\mathbf{F}\cdot\dot{\mathbf{F}} = \mathbf{F}^*{\cdot}\dot{\mathbf{F}}.$$

Now, using Eq. (6.7) we thereby obtain:

$$
\begin{aligned}
\dot{U} =~& \int_\Omega [\{\mu\mathbf{F}{+}\kappa\mathbf{F}\{(\mathbf{F}\cdot\mathbf{F})\mathbf{I} - \mathbf{F}^T\mathbf{F}\} + W(\varepsilon_1,\varepsilon_2)_{\varepsilon_1}(\varepsilon_1)_{\mathbf{F}} + W(\varepsilon_1,\varepsilon_2)_{\varepsilon_2}(\varepsilon_2)_{\mathbf{F}} \\
&-p\mathbf{F}^*\}{\cdot}\dot{\mathbf{F}} + \{C\mathbf{g}_1\otimes\mathbf{D}\otimes\mathbf{D}{+}C\mathbf{g}_2\otimes\mathbf{M}\otimes\mathbf{M} + T\mathbf{g}_1\otimes\mathbf{M}\otimes\mathbf{M} \\
&+T\mathbf{g}_2\otimes\mathbf{D}\otimes\mathbf{D}\}\cdot\dot{\mathbf{G}}]dA,
\end{aligned}
\quad (6.35)
$$

or, equivalently using index notation,

$$
\begin{aligned}
\dot{E} =~& \int_\Omega [\{\mu F_{iA}{+}\kappa F_{iB}(F_{jC}F_{jC}\delta_{AB}{-}F_{jA}F_{jB}) + W(\varepsilon_1,\varepsilon_2)_{\varepsilon_1}(\varepsilon_1)_{F_{iA}} + W(\varepsilon_1,\varepsilon_2)_{\varepsilon_2}(\varepsilon_2)_{F_{iA}} \\
&-pF_{iA}^*\}\dot{\chi}_{i,A}+\{C(g_1D_AD_B) + C(g_2M_AM_B) + T(g_1M_AM_B) \\
&+T(g_2D_AD_B)\}\dot{\chi}_{i,AB}]dA,
\end{aligned}
\quad (6.36)
$$

where $\dot{F}_{iA} = \dot{\chi}_{i,A}$ and $\dot{G}_{iAB} = \dot{\chi}_{i,AB}$ are the variations of the first and second gradient of deformations. It is also noted that, in the forthcoming derivations, we use the

190

component forms of vectors and tensors (e.g. Eq. (6.36)) for the sake of clarity and conciseness.

Now, applying integration by part on the last 4 higher-gradient terms of Eq. (6.36), we find

$$
\begin{aligned}
C(G_{iCD}D_C D_D D_A D_B)\dot{\chi}_{i,AB} &= C(G_{iCD}D_C D_D D_A D_B\dot{\chi}_{i,A})_{,B} \\
&\quad -C(G_{iCD}D_C D_D D_A D_B)_{,B}\dot{\chi}_{i,A}.
\end{aligned}
\tag{6.37}
$$

$$
\begin{aligned}
T(G_{iCD}D_C D_D M_A M_B)\dot{\chi}_{i,AB} &= T(G_{iCD}D_C D_D M_A M_B\dot{\chi}_{i,A})_{,B} \\
&\quad -T(G_{iCD}D_C D_D M_A M_B)_{,B}\dot{\chi}_{i,A}.
\end{aligned}
\tag{6.38}
$$

Similarly, we can do the same for the rest of the higher-gradient terms. Substituting these into Eq. (6.36) then yields

$$
\begin{aligned}
\dot{E} &= \int_\Omega [\{\mu F_{iA}+\kappa F_{iB}(F_{jC}F_{jC}\delta_{AB}-F_{jA}F_{jB}) + W(\varepsilon_1,\varepsilon_2)_{\varepsilon_1}(\varepsilon_1)_{F_{iA}} \\
&\quad +W(\varepsilon_1,\varepsilon_2)_{\varepsilon_2}(\varepsilon_2)_{F_{iA}} - pF_{iA}^*\}\dot{\chi}_{i,A} - \{C(g_1 D_A D_B)_{,B} \\
&\quad +C(g_2 M_A M_B)_{,B} + T(g_1 M_A M_B)_{,B} + T(g_2 D_A D_B)_{,B}\}\dot{\chi}_{i,A} \\
&\quad +C(g_1 D_A D_B\dot{\chi}_{i,A})_{,B} + C(g_2 M_A M_B\dot{\chi}_{i,A})_{,B} + C(g_1 M_A M_B\dot{\chi}_{i,A})_{,B} \\
&\quad +C(g_2 D_A D_B\dot{\chi}_{i,A})_{,B}]dA.
\end{aligned}
\tag{6.39}
$$

Applying the Green–Stokes' theorem, Eq. (6.39) further reduces to

$$
\begin{aligned}
\dot{E} &= \int_\Omega [\mu F_{iA}+\kappa F_{iB}(F_{jC}F_{jC}\delta_{AB}-F_{jA}F_{jB}) + W(\varepsilon_1,\varepsilon_2)_{\varepsilon_1}(\varepsilon_1)_{F_{iA}} + W(\varepsilon_1,\varepsilon_2)_{\varepsilon_2}(\varepsilon_2)_{F_{iA}} \\
&\quad -pF_{iA}^*\dot{\chi}_{i,A} - C(g_1 D_A D_B)_{,B} - C(g_2 M_A M_B)_{,B} - T(g_1 M_A M_B)_{,B} \\
&\quad -T(g_2 D_A D_B)_{,B}]\dot{\chi}_{i,A} + \int_{\partial\Omega} [C(g_1 D_A D_B\dot{\chi}_{i,A}) + C(g_2 M_A M_B\dot{\chi}_{i,A}) \\
&\quad +T(g_1 M_A M_B\dot{\chi}_{i,A}) + T(g_2 D_A D_B\dot{\chi}_{i,A})]N_B dS,
\end{aligned}
\tag{6.40}
$$

where N_B is the rightward unit normal to $\partial\Omega$ in the sense of the Green–Stokes' theorem. To extract the desired expression, Eq. (6.40) may be recast as

$$
\begin{aligned}
\dot{E} &= \int_\Omega P_{iA}\dot{\chi}_{i,A}dA + \int_{\partial\Omega} [C(g_1 D_A D_B\dot{\chi}_{i,A}) + C(g_2 M_A M_B\dot{\chi}_{i,A}) + T(g_1 M_A M_B\dot{\chi}_{i,A}) \\
&\quad +T(g_2 D_A D_B\dot{\chi}_{i,A})]N_B dS,
\end{aligned}
\tag{6.41}
$$

where

$$
\begin{aligned}
P_{iA} &= \mu F_{iA} + \kappa F_{iB}(F_{jC}F_{jC}\delta_{AB} - F_{jA}F_{jB}) + [\frac{E_1}{4}(F_{jC}F_{jD}D_CD_D)(F_{kE}F_{kF}D_ED_F) \\
&\quad + \frac{(E_2 - E_1)}{2}F_{jC}F_{jD}D_CD_D + \frac{(E_1 - 2E_2)}{4}]F_{iB}D_BD_A + [\frac{E_{21}}{4}(F_{jC}F_{jD}M_CM_D) \\
&\quad (F_{kE}F_{kF}M_EM_F) + \frac{(E_{22} - E_{21})}{2}F_{jC}F_{jD}M_CM_D + \frac{(E_{21} - 2E_{22})}{4}]F_{iB}M_BM_A \\
&\quad - pF_{iA}^* - CF_{iC,DB}(D_AD_BD_CD_D + M_AM_BM_CM_D) \\
&\quad - TF_{iC,DB}(D_AD_BM_CM_D + D_AD_BM_CM_D),
\end{aligned}
\tag{6.42}
$$

is the formulation of the Piola type stress. Now considering the orthogonal orientation of fibers (see, Fig. 6.1), we find

$$
\begin{aligned}
\mathbf{D} &= D_1\mathbf{E}_1 + D_2\mathbf{E}_2 = (1)\cos(0)\mathbf{E}_1 + (1)\sin(0)\mathbf{E}_2 = \mathbf{E}_1, \\
\mathbf{M} &= M_1\mathbf{E}_1 + M_2\mathbf{E}_2 = (1)\cos(\pi/2)\mathbf{E}_1 + (1)\sin(\pi/2)\mathbf{E}_2 = \mathbf{E}_2.
\end{aligned}
\tag{6.43}
$$

The Euler equilibrium equation satisfies

$$
P_{iA,A} = 0 \text{ or } Div(\mathbf{P}) = 0,
\tag{6.44}
$$

which holds in Ω. Hence, using $F_{jA} = \chi_{i,A}$ the Euler equilibrium equation is obtained as follows:

$$
\begin{aligned}
0 &= P_{iA,A} = \mu\chi_{i,AA} + \kappa(\chi_{i,AA}\chi_{j,C}\chi_{j,C} - \chi_{i,BA}\chi_{j,A}\chi_{j,B}) + \kappa\chi_{i,B}(2\chi_{j,CB}\chi_{j,C} \\
&\quad - \chi_{j,AA}\chi_{j,B} - \chi_{j,A}\chi_{j,BA}) - p_{,A}\varepsilon_{ij}\varepsilon_{AB}\chi_{j,B} + [\frac{E_{11}}{4}(2\chi_{j,11}\chi_{j,1}\chi_{k,1}\chi_{k,1} \\
&\quad + 2\chi_{j,1}\chi_{j,1}\chi_{k,11}\chi_{k,1}) + (E_{12} - E_{11})\chi_{j,11}\chi_{j,1}]\chi_{i,1} + [\frac{E_{11}}{4}(\chi_{j,1}\chi_{j,1})(\chi_{k,1}\chi_{k,1}) \\
&\quad + \frac{(E_{12} - E_{11})}{2}\chi_{j,1}\chi_{j,1} + \frac{(E_{11} - 2E_{12})}{4}]\chi_{i,11} + [\frac{E_{21}}{4}(2\chi_{j,22}\chi_{j,2}\chi_{k,2}\chi_{k,2} \\
&\quad + 2\chi_{j,2}\chi_{j,2}\chi_{k,22}\chi_{k,2}) + (E_{22} - E_{21})\chi_{j,22}\chi_{j,2}]\chi_{i,2} + [\frac{E_{21}}{4}(\chi_{j,2}\chi_{j,2})(\chi_{k,2}\chi_{k,2}) \\
&\quad + \frac{(E_{22} - E_{21})}{2}\chi_{j,2}\chi_{j,2} + \frac{(E_{21} - 2E_{22})}{4}]\chi_{i,22} - C(\chi_{i,1111} + \chi_{i,2222}) \\
&\quad - T(\chi_{i,1122} + \chi_{i,2211}).
\end{aligned}
\tag{6.45}
$$

To derive the expressions of the associated boundary conditions, we again apply integration by part on Eq. (6.41) (i.e. $P_{iA}\dot{\chi}_{i,A} = (P_{iA}\dot{\chi}_i)_{,A} - (P_{iA})_{,A}\dot{\chi}_i$) and obtain

$$
\begin{aligned}
\dot{E} &= \int_{\partial\Omega} P_{iA}\dot{\chi}_i N_A dS + \int_{\partial\Omega}\{C(g_1D_AD_B\dot{\chi}_{i,A}) + C(g_2M_AM_B\dot{\chi}_{i,A}) + T(g_1M_AM_B\dot{\chi}_{i,A}) \\
&\quad + T(g_2D_AD_B\dot{\chi}_{i,A})\}N_B dS, - \int_\Omega P_{iA,A}\dot{\chi}_i dA,
\end{aligned}
\tag{6.46}
$$

where the Green-Stokes' theorem is applied in the first term of the above, i.e.,

$$\int_{\Omega} (P_{iA}\dot{\chi}_i)_{,A} dA = \int_{\partial\Omega} P_{iA}\dot{\chi}_i N_A dS. \tag{6.47}$$

Since the Euler equation ($P_{iA,A} = 0$) holds in Ω, Eq. (6.46) reduces to

$$\dot{E} = \int_{\partial\Omega} P_{iA}\dot{\chi}_i N_A dS + + \int_{\partial\Omega} \{C(g_1 D_A D_B \dot{\chi}_{i,A}) + C(g_{2i} M_A M_B \dot{\chi}_{i,A}) + T(g_{1i} M_A M_B \dot{\chi}_{i,A})$$
$$+ T(g_{2i} D_A D_B \dot{\chi}_{i,A})\} N_B dS. \tag{6.48}$$

We now decompose $\dot{\chi}_{i,A}$ into

$$\dot{\chi}_{i,A} = \frac{\partial \dot{\chi}_i}{\partial S}\frac{\partial S}{\partial X_A} + \frac{\partial \dot{\chi}_i}{\partial N}\frac{\partial N}{\partial X_A} = \dot{\chi}_i' T_A + \dot{\chi}_{i,N} N_A, \tag{6.49}$$

where $T_A = \partial S/\partial X_A$ and $N_A = \partial N/\partial X_A$ are respectively, the unit tangent and normal to the boundary $\partial\Omega$. Combining Eqs. (6.48) and (6.49) then furnishes:

$$\dot{E} = \int_{\partial\Omega} P_{iA}\dot{\chi}_i N_A dS + \int_{\partial\Omega} Cg_1 D_A D_B \left(\dot{\chi}_i' T_A N_B + \dot{\chi}_{i,N} N_A N_B\right) dS + \int_{\partial\Omega} Cg_2 M_A M_B$$
$$\left(\dot{\chi}_i' T_A N_B + \dot{\chi}_{i,N} N_A N_B\right) dS + \int_{\partial\Omega} Tg_1 M_A M_B \left(\dot{\chi}_i' T_A N_B + \dot{\chi}_{i,N} N_A N_B\right) dS$$
$$+ \int_{\partial\Omega} Tg_2 D_A D_B \left(\dot{\chi}_i' T_A N_B + \dot{\chi}_{i,N} N_A N_B\right) dS. \tag{6.50}$$

In addition, since

$$Cg_1 D_A D_B T_A N_B \dot{\chi}_i' = (Cg_1 D_A D_B T_A N_B \dot{\chi}_i)' - (Cg_1 D_A D_B T_A N_B)' \dot{\chi}_i, \tag{6.51}$$

Eq. (6.50) becomes

$$\dot{E} = \int_{\partial\Omega} [P_{iA}N_A - (Cg_1 D_A D_B T_A N_B)' - (Cg_2 M_A M_B T_A N_B)'$$
$$- (Tg_1 M_A M_B T_A N_B)' - (Tg_2 D_A D_B T_A N_B)']\dot{\chi}_i dS$$
$$+ \int_{\partial\Omega} Cg_1 D_A D_B \dot{\chi}_{i,N} N_A N_B dS + \int_{\partial\Omega} (Cg_1 D_A D_B T_A N_B \dot{\chi}_i)' dS$$
$$+ \int_{\partial\Omega} Cg_2 M_A M_B \dot{\chi}_{i,N} N_A N_B dS + \int_{\partial\Omega} (Cg_2 M_A M_B T_A N_B \dot{\chi}_i)' dS$$
$$+ \int_{\partial\Omega} Tg_1 M_A M_B \dot{\chi}_{i,N} N_A N_B dS + \int_{\partial\Omega} (Tg_1 M_A M_B T_A N_B \dot{\chi}_i)' dS$$
$$+ \int_{\partial\Omega} Tg_2 D_A D_B \dot{\chi}_{i,N} N_A N_B dS + \int_{\partial\Omega} (Tg_2 D_A D_B T_A N_B \dot{\chi}_i)' dS. \tag{6.52}$$

193

The above may be recast to yield the standard form:

$$\begin{aligned}
\dot{E} &= \int_{\partial\Omega} [P_{iA}N_A - (Cg_1 D_A T_A D_B N_B)' - (Cg_2 M_A T_A M_B N_B)' \\
&\quad -(Tg_1 M_A T_A M_B N_B)' - (Tg_2 D_A T_A D_B N_B)']\dot{\chi}_i dS \\
&\quad + \int_{\partial\Omega} Cg_1 D_A N_A D_B N_B \dot{\chi}_{i,N} dS + \sum \|Cg_1 D_A T_A D_B N_B \dot{\chi}_i\| dS \\
&\quad + \int_{\partial\Omega} Cg_2 M_A M_B \dot{\chi}_{i,N} N_A N_B dS + \sum \|Cg_2 M_A T_A M_B N_B \dot{\chi}_i\| dS \\
&\quad + \int_{\partial\Omega} Tg_1 M_A M_B \dot{\chi}_{i,N} N_A N_B dS + \sum \|Tg_1 M_A T_A M_B N_B \dot{\chi}_i\| dS \\
&\quad + \int_{\partial\Omega} Tg_2 D_A D_B \dot{\chi}_{i,N} N_A N_B dS + \sum \|Tg_2 D_A T_A D_B N_B \dot{\chi}_i\| dS, \quad (6.53)
\end{aligned}$$

where the double bar symbol refers to the jump across the discontinuities on the boundary $\partial\Omega$ (i.e. $\|*\| = (*)^+ - (*)^-$) and the sum denotes the collection of all discontinuities.

Lastly, it follows that the admissible mechanical powers take the following form

$$P = \int_{\partial w_t} t_i \dot{\chi}_i dS + \int_{\partial w} m_i \dot{\chi}_{i,N} dS + \sum f_i \dot{\chi}_i. \quad (6.54)$$

Thus, by comparing Eqs. (6.53) and (6.54), we conclude that

$$\begin{aligned}
t_i &= P_{iA}N_A - \frac{d}{dS}[(CG_{iCD}D_C D_D + TG_{iCD}M_C M_D)D_A T_A D_B N_B \\
&\quad +(CG_{iCD}M_C M_D + TG_{iCD}D_C D_D)M_A T_A M_B N_B], \\
m_i &= (CG_{iCD}D_C D_D + TG_{iCD}M_C M_D)D_A N_A D_B N_B + (CG_{iCD}M_C M_D \\
&\quad +TG_{iCD}D_C D_D)M_A N_A M_B N_B, \\
f_i &= (CG_{iCD}D_C D_D + TG_{iCD}M_C M_D)D_A T_A D_B N_B + (CG_{iCD}M_C M_D \\
&\quad +TG_{iCD}D_C D_D)M_A T_A M_B N_B, \quad (6.55)
\end{aligned}$$

where t_i, m_i, and f_i are the expressions of edge tractions, edge moments, and the corner forces, respectively. It should be pointed out here that the stress expression is a combination of the Piola-type stress P_{iA} and double stress (i.e., $C(g_1 D_A D_B)_{,B} + C(g_2 M_A M_B)_{,B} + T(g_1 M_A M_B)_{,B} + T(g_2 D_A D_B)_{,B}$) such that the second gradient of the deformation term (i.e., $C(g_1 D_A D_B)_{,B} + C(g_2 M_A M_B)_{,B} + T(g_1 M_A M_B)_{,B} + T(g_2 D_A D_B)_{,B}$) can be interpreted as the energy conjugate to the admissible double force m_i when it
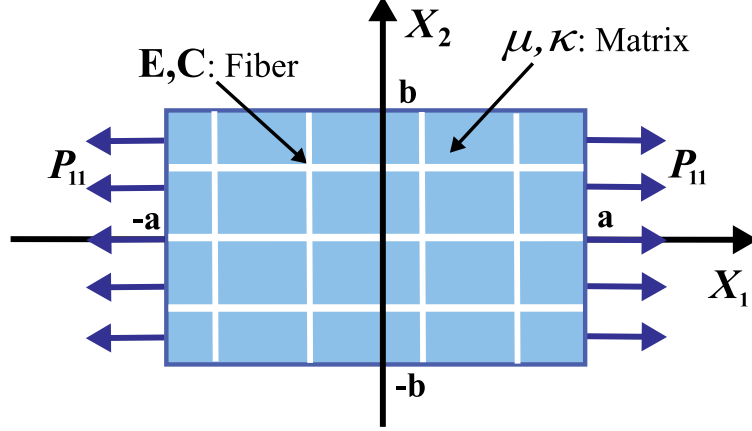
Figure 6.2: Schematic of the problem.

is prescribed on the desired boundaries. The solutions of the above system of PDEs may be determined by imposing the following boundary conditions (see, Fig. 6.2) and the corresponding results are discussed in the model implementation and discussion section.

$$
\begin{aligned}
t_1 &= P_{11}, \ t_2 = P_{12} = 0 \text{ at } X_1 = a, -a \text{ and} \\
t_1 &= P_{21} = 0, \ t_2 = P_{22} = 0 \text{ at } X_2 = b, -b.
\end{aligned}
\tag{6.56}
$$

6.3 Model for Pseudoelastic Behaviour of hyperelastic composite

In this section, we present two distinct models for assimilating the pseudoelastic behaviours of hyperelastic composite reinforced with bidirectional fibers. We first present a model describing the Mullins effect of the hyperelastic composite where the material undergoes an instantaneous and irreversible softening process. Next, the Weibull fiber damage model is presented which can accommodate the damage mechanics due to fiber breakage.

6.3.1 Model for Mullins effect

It has been observed that in many hyperelastic materials an instantaneous and irreversible softening of the stress-strain response takes place, which is described as the Mullins effect [91]. Mullins effect can be observed in biological soft tissues like,

aortic tissue, skin, muscles, etc. [166]. The Mullins effect can be caused by multiple phenomena related to changes in the internal structure which progress continuously as the material is stretched. These include (see, fig. 6.3): physical disentanglement of polymer chains in the elastin-rich matrix (fig. 6.3 (b)), decrease in the interactions between polymer molecules and filler surfaces at the interface (fig. 6.3 (a)), filler network breakdown (fig. 6.3 (c)), and chain scission of polymer molecules in the matrix [167].
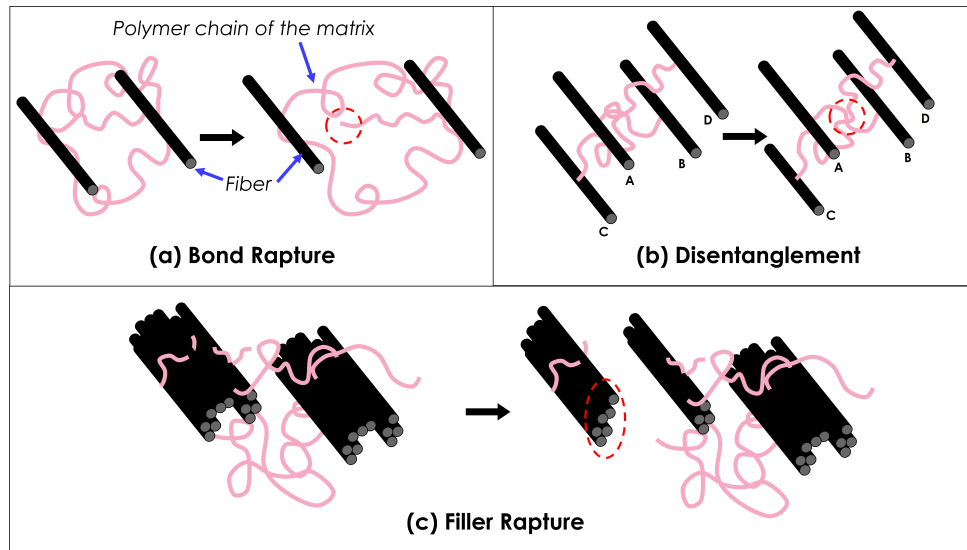
Figure 6.3: Schematics of the internal structural changes leading to the Mullins effect [167].

In an idealized form, the Mullins effect can be described in the following way. When previously non-loaded (also called the virgin state) material is loaded to a certain amount of strain, the obtained stress-strain curve is called the primary loading curve. From any point on this primary loading curve if we start to unload (submaximal unloading), the unloading stress-strain curve does not coincide with the primary loading curve and a stress softening is attained. Now if we start loading again (submaximal loading), the obtained loading curve coincides with the submaximal unloading curve. Thus, in this subsequent loading-unloading curve (submaximal loading/unloading) the material behaves like an elastic material. When the stress value returns to the previous stress maximum (which was just prior to the start of unloading), the primary loading curve continues [166]. While operating on the pri-

mary loading curve, the damage can be regarded as taking place continuously [91]. That is the reason the stress softening phenomena is evident on unloading from any point on the primary loading path, and damage increases with the magnitude of the strain on that path [91].

To model the Mullins effect of hyperelastic composite reinforced by nonlinear fiber, we incorporate the damage parameter η and damage function $\phi(\eta)$ inspired by Ogden-Roxburgh Model [91] into the proposed energy function in Eq. (6.27) as follows:

$$
\begin{aligned}
W(\mathbf{F}, \varepsilon_1, \varepsilon_2, \mathbf{g}) &= \eta\{W(\mathbf{F}) + W(\varepsilon_1, \varepsilon_2)\} + \phi(\eta) + W(g_1, g_2) \\
&= \eta\{\frac{\mu}{2}(I_1 - 3) + \frac{\kappa}{2}(I_2 - 3) + \frac{1}{3}E_{11}\varepsilon_1^3 + \frac{1}{2}E_{12}\varepsilon_1^2 + \frac{1}{3}E_{21}\varepsilon_2^3 + \frac{1}{2}E_{22}\varepsilon_2^2\} \\
&\quad + \phi(\eta) + \frac{1}{2}C(\mathbf{g}_1 \cdot \mathbf{g}_1 + \mathbf{g}_2 \cdot \mathbf{g}_2) + \frac{T}{2}(\mathbf{g}_1 \cdot \mathbf{g}_2 + \mathbf{g}_2 \cdot \mathbf{g}_1), \quad (6.57)
\end{aligned}
$$

The role of the parameter η can be interpreted from Ogden-Roxburgh Model as follows. During a deformation process, η may be either in active or inactive mode. When it is inactive, the material does not have any internal damage and correspondingly, $\eta = 1$ [91]. In this case, the stress-strain response of the material follows the primary loading curve. However, from any point on this primary loading curve if we start to unload, η becomes activated. When η is in active mode, it is determined by the following equation [91],[168]:

$$
\begin{aligned}
\eta &= 1 - \frac{1}{r}\operatorname{erf}\left[\frac{1}{m + \beta W_m}\left(W_m - \tilde{W}(F)\right)\right] \\
&= 1 - \frac{1}{r}\operatorname{erf}[\frac{1}{m + \beta W_m}(W_m - \frac{\mu}{2}(I_1 - 3) - \frac{\kappa}{2}(I_2 - 3) - \frac{1}{3}E_{11}\varepsilon^3 - \frac{1}{2}E_{12}\varepsilon^2 \\
&\quad - \frac{1}{3}E_{21}\varepsilon_2^3 - \frac{1}{2}E_{22}\varepsilon_2^2)], \quad (6.58)
\end{aligned}
$$

where W_m is the maximum potential energy that the material has experienced just prior to the start of unloading. We can treat W_m as a constant which does not change during submaximal loading and unloading. The parameters r and β are dimensionless, while the parameter m has the dimensions of energy. These parameters are subject to the restrictions $r \geqslant 1, \beta \geqslant 0$, and $m \geqslant 0$ (also, the parameters β and m cannot both be zero). The parameter m controls the degree of damage occurs at low strain levels. If $m = 0$, there is a significant amount of damage at low strain levels. On the

other hand, a nonzero m leads to little or no damage at low strain levels. Whereas the parameter r controls the amount of damage, as r increases, the damage decreases. This behavior follows from the fact that the larger the value of r, lesser the damage variable η can deviate from unity thus producing less damage. The term $\tilde{W}(F)$ is the potential energy function containing the potential of the hyperelastic matrix and extension potential of the fiber mesh. In Fig. 6.4, a flowchart is presented for the current model which demonstrates the operation of Mullins effect of hyperelastic composite.
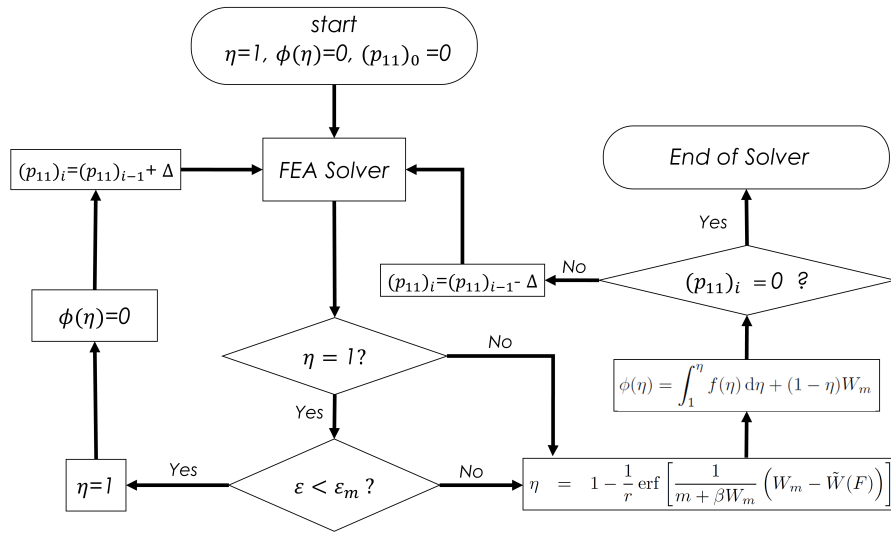
Figure 6.4: Flowchart of the model for Mullins effect of hyperelastic composite (where, ε_m is the strain level at which unloading is started).

Now, we can wrtie the Eq. (6.57) in variational form as

$$
\begin{aligned}
\dot{W}(\mathbf{F}, \varepsilon_1, \varepsilon_2, \mathbf{g}) &= \eta_{F_{iA}} W \dot{F}_{iA} + \eta W_\varepsilon \varepsilon_{F_{iA}} \dot{F}_{iA} \\
&= \eta_{\mathbf{F}} \{ W(\mathbf{F}) + W(\varepsilon_1, \varepsilon_2) \} \cdot \dot{\mathbf{F}} + \eta \{ W(\mathbf{F})_{\mathbf{F}} + W(\varepsilon_1, \varepsilon_2)_{\varepsilon_1} \varepsilon_{1\mathbf{F}} \cdot \dot{\mathbf{F}} \\
&\quad + W(\varepsilon_1, \varepsilon_2)_{\varepsilon_2} \varepsilon_{2\mathbf{F}} \} \cdot \dot{\mathbf{F}} + C(\mathbf{g}_1 \cdot \dot{\mathbf{g}}_1 + \mathbf{g}_2 \cdot \dot{\mathbf{g}}_2) + T(\mathbf{g}_1 \cdot \dot{\mathbf{g}}_2 \\
&\quad + \mathbf{g}_1 \cdot \dot{\mathbf{g}}_2). \quad\quad\quad (6.59)
\end{aligned}
$$

Using Eq. (6.23) we can rewrite Eq. (6.59) as,

$$
\begin{aligned}
\dot{W}(\mathbf{F}, \varepsilon_1, \varepsilon_2, \mathbf{g}) \;=\;\; & \eta_{\mathbf{F}}\{W(\mathbf{F}) + \frac{1}{24}E_{11}\,(\mathbf{FD}\cdot\mathbf{FD}{-}1)^3 + \frac{1}{8}E_{12}\,(\mathbf{FD}\cdot\mathbf{FD}{-}1)^2 \\
& + \frac{1}{24}E_{21}\,(\mathbf{FD}\cdot\mathbf{FD}{-}1)^3 + \frac{1}{8}E_{22}\,(\mathbf{FD}\cdot\mathbf{FD}{-}1)^2\}\cdot\dot{\mathbf{F}} \\
& + \eta[W(\mathbf{F})_{\mathbf{F}} + \{\frac{1}{4}E_{11}\,(\mathbf{FD}\cdot\mathbf{FD}{-}1)^2 + \frac{1}{2}E_{12}\,(\mathbf{FD}\cdot\mathbf{FD}{-}1)\}\varepsilon_{1\mathbf{F}} \\
& + \{\frac{1}{4}E_{21}\,(\mathbf{FM}\cdot\mathbf{FM}{-}1)^2 + \frac{1}{2}E_{22}\,(\mathbf{FM}\cdot\mathbf{FM}{-}1)\}\varepsilon_{2\mathbf{F}}]\cdot\dot{\mathbf{F}} \\
& + C(\mathbf{g}_1\cdot\dot{\mathbf{g}}_1 + \mathbf{g}_2\cdot\dot{\mathbf{g}}_2) + T(\mathbf{g}_1\cdot\dot{\mathbf{g}}_2 + \mathbf{g}_1\cdot\dot{\mathbf{g}}_2).
\end{aligned}
\tag{6.60}
$$

Again, $\phi(\eta)$ referred to as the damage function, which is a smooth function of its argument, η and, for consistency, when $\eta = 1$, $\phi(\eta)$ becomes 0. The function $\phi(\eta)$ depends, through W_m, on the point at which unloading starts, which can be expressed as follows (see, [91])

$$
\phi(\eta) = \int\limits_0^1 f(\eta)d\eta + (1-\eta)W_m.
\tag{6.61}
$$

The function f is defined such a way that, $f(1) = 1$ and $f(\eta_m) = W_m$. Here, η_m is the minimum value of η which is atttained when the material is fully unloaded from a submaximal loading state. From [91], we can write $\phi(\eta)$ in variational form as follows:

$$
\dot{\phi}(\eta) = \frac{\partial\phi(\eta)}{\partial\eta}\dot{\eta} = [-m\,\mathrm{erf}^{-1}(r(\eta - 1)) - W_m]\eta_F\dot{F}.
\tag{6.62}
$$

Also to note that, at η_m, $\phi(\eta_m)$ can be interpreted as the residual (non-recoverable) energy, which is a measure of the energy required to cause the damage in the material [91]. In a uniaxial test such as simple tension, $\phi(\eta_m)$ is the area between the primary loading curve and the relevant unloading curve. In the above, $\mathrm{erf}^{-1}(*)$ is the inverse of error function, which has properties particularly well suited to this purpose as described by [91]. Now using the expressions derived through Eqs. (6.10)-(6.21), we

can write the Eq. (6.60) in component form as,

$$
\begin{aligned}
\dot{W}(\mathbf{F}, \varepsilon_1, \varepsilon_2, \mathbf{g}) = \ & [W(F) + W(\varepsilon_1, \varepsilon_2)]\eta_{\mathbf{F}}\dot{F}_{iA} + \eta[\mu F_{iA} + \kappa F_{iB}(F_{jC}F_{jC}\delta_{AB} \\
& - F_{jA}F_{jB}) + \{\frac{E_{11}}{4}(F_{jC}F_{jD}D_C D_D)(F_{kE}F_{kF}D_E D_F) \\
& + \frac{(E_{12} - E_{11})}{2}F_{jC}F_{jD}D_C D_D + \frac{(E_{11} - 2E_{12})}{4}\}F_{iB}D_B D_A \\
& + \frac{E_{21}}{4}\{(F_{jC}F_{jD}M_C M_D)(F_{kE}F_{kF}M_E M_F) \\
& + \frac{(E_{22} - E_{21})}{2}F_{jC}F_{jD}M_C M_D + \frac{(E_{21} - 2E_{22})}{4}\}F_{iB}M_B M_A]\dot{F}_{iA} \\
& - pF_{iA}^* - CF_{iC,D}(D_A D_B D_C D_D + M_A M_B M_C M_D)\dot{F}_{iA,B} \\
& - TF_{iC,D}(D_A D_B M_C M_D + D_A D_B M_C M_D)\dot{F}_{iA,B} \\
& + \frac{\partial\phi(\eta)}{\partial\eta}\eta_{\mathbf{F}}\dot{F}_{iA},
\end{aligned}
\tag{6.63}
$$

where the variational form of η can be obtained as,

$$
\begin{aligned}
\dot{\eta} = \ & \eta_{\mathbf{F}}\cdot\dot{\mathbf{F}} = \frac{1}{r(m + \beta W_m)}\frac{2}{\sqrt{\pi}}\exp[-\left(\frac{1}{m + \beta W_m}\{W_m - \tilde{W}(F)\}\right)^2]W(\mathbf{F})_{\mathbf{F}}\cdot\dot{\mathbf{F}} \\
\dot{\eta} = \ & \varrho[\mu F_{iA} + \kappa F_{iB}(F_{jC}F_{jC}\delta_{AB} - F_{jA}F_{jB}) + \{\frac{E_{11}}{4}(F_{jC}F_{jD}D_C D_D)(F_{kE}F_{kF}D_E D_F) \\
& + \frac{(E_{12} - E_{11})}{2}F_{jC}F_{jD}D_C D_D + \frac{(E_{11} - 2E_{12})}{4}\}F_{iB}D_B D_A \\
& + \{\frac{E_{21}}{4}(F_{jC}F_{jD}M_C M_D)(F_{kE}F_{kF}M_E M_F) + \frac{(E_{22} - E_{21})}{2}F_{jC}F_{jD}M_C M_D \\
& + \frac{(E_{21} - 2E_{22})}{4}\}F_{iB}M_B M_A]\dot{F}_{iA}.
\end{aligned}
\tag{6.64}
$$

In the above,

$$
\varrho = \frac{1}{r(m + \beta W_m)}\frac{2}{\sqrt{\pi}}\exp[-\left(\frac{1}{m + \beta W_m}\{W_m - \tilde{W}(F)\}\right)^2].
\tag{6.65}
$$

Now, following the same process as described through Eqs. (6.29)-(6.42), we can obtain the following expression of the Piola type stress.

$$
\begin{aligned}
P_{iA} = \ & \eta[\mu F_{iA} + \kappa F_{iB}(F_{jC}F_{jC}\delta_{AB} - F_{jA}F_{jB}) \\
& + \{\frac{E_{11}}{4}(F_{j1}F_{j1})(F_{k1}F_{k1}) + \frac{(E_{12} - E_{11})}{2}F_{j1}F_{j1} + \frac{(E_{11} - 2E_{12})}{4}\}F_{i1}D_A \\
& + \{\frac{E_{21}}{4}(F_{j2}F_{j2})(F_{k2}F_{k2}) + \frac{(E_{22} - E_{21})}{2}F_{j2}F_{j2} + \frac{(E_{21} - 2E_{22})}{4}\}F_{i2}M_A] \\
& + [W(F) + W(\varepsilon_1, \varepsilon_2)]\eta_{\mathbf{F}} - pF_{iA}^* - CF_{iC,DB}(D_A D_B D_C D_D + M_A M_B M_C M_D) \\
& - TF_{iC,DB}(D_A D_B M_C M_D + D_A D_B M_C M_D) + \left(\frac{\partial\phi(\eta)}{\partial\eta}\eta_{\mathbf{F}}\right)_{iA}.
\end{aligned}
\tag{6.66}
$$

Taking divergent of P_{iA} we then obtain the following equilibrium equations:

$$
\begin{aligned}
P_{iA,A} &= \eta_{,A}[\mu F_{iA} + \kappa F_{iB}(F_{jC}F_{jC}\delta_{AB} - F_{jA}F_{jB}) \\
&\quad + \{\frac{E_{11}}{4}(F_{j1}F_{j1})(F_{k1}F_{k1}) + \frac{(E_{12} - E_{11})}{2}F_{j1}F_{j1} + \frac{(E_{11} - 2E_{12})}{4}\}F_{i1}D_1D_A \\
&\quad + \{\frac{E_{21}}{4}(F_{j2}F_{j2})(F_{k2}F_{k2}) + \frac{(E_{22} - E_{21})}{2}F_{j2}F_{j2} + \frac{(E_{21} - 2E_{22})}{4}\}F_{i2}M_2M_A] \\
&\quad + \eta[\mu F_{iA,A} + \kappa F_{iB,A}(F_{jC}F_{jC}\delta_{AB} - F_{jA}F_{jB}) + \kappa F_{iB}(2F_{jC,A}F_{jC}\delta_{AB} - F_{jA,A}F_{jB} \\
&\quad - F_{jA}F_{jB,A}) + \{\frac{E_{11}}{4}(2F_{j1,A}F_{j1}F_{k1}F_{k1} + 2F_{j1}F_{j1}F_{k1,A}F_{k1}) + (E_{12} \\
&\quad - E_{11})F_{j1,A}F_{j1}\}F_{i1,A}D_A + \{\frac{E_{21}}{4}(2F_{j2,A}F_{j2}F_{k2}F_{k2} + 2F_{j2}F_{j2}F_{k2,A}F_{k2}) \\
&\quad + (E_{22} - E_{21})F_{j2,A}F_{j2}\}F_{i2,A}M_A] + [W(F) + W(\varepsilon_1, \varepsilon_2)]_{,A}\eta_{\mathbf{F}} + [W(F) \\
&\quad + W(\varepsilon_1, \varepsilon_2)]\{\eta_{\mathbf{F}}\}_{,A} - p_{,A}F^*_{iA,A} - C(F_{i1,111} + F_{i2,222}) - T(F_{i1,122} + F_{i2,211}) \\
&\quad + \left[\left(\frac{\partial\phi(\eta)}{\partial\eta}\eta_{\mathbf{F}}\right)_{iA}\right]_{,A}.
\end{aligned} \tag{6.67}
$$

In the above,

$$
\begin{aligned}
\{\eta_{\mathbf{F}}\}_{,A} &= \left(\frac{1}{r(m + \beta W_m)}\frac{2}{\sqrt{\pi}}\exp[-\left(\frac{1}{m + \beta W_m}\{W_m - \tilde{W}(F)\}\right)^2]\right)_{,A} W(\mathbf{F})_{\mathbf{F}} \\
&\quad + \varrho\{W(\mathbf{F})_{\mathbf{F}}\}_{,A} \\
&= \frac{1}{r(m + \beta W_m)}\frac{2}{\sqrt{\pi}}\varrho\,[W(\mathbf{F})_{\mathbf{F}}]^2\{W(\mathbf{F})_{\mathbf{F}}\}_{,A} + \varrho\{W(\mathbf{F})_{\mathbf{F}}\}_{,A} \\
&= \{W(\mathbf{F})_{\mathbf{F}}\}_{,A}\left(\frac{1}{r(m + \beta W_m)}\frac{2}{\sqrt{\pi}}\varrho\,[W(\mathbf{F})_{\mathbf{F}}]^2 + \varrho\right) \\
&= [\mu F_{iA} + \kappa F_{iB}(F_{jC}F_{jC}\delta_{AB} - F_{jA}F_{jB}) + \{\frac{E_{11}}{4}(F_{jC}F_{jD}D_CD_D)(F_{kE}F_{kF}D_ED_F) \\
&\quad + \frac{(E_{12} - E_{11})}{2}F_{jC}F_{jD}D_CD_D + \frac{(E_{11} - 2E_{12})}{4}\}F_{iB}D_BD_A \\
&\quad + \{\frac{E_{21}}{4}(F_{jC}F_{jD}M_CM_D)(F_{kE}F_{kF}M_EM_F) + \frac{(E_{22} - E_{21})}{2}F_{jC}F_{jD}M_CM_D \\
&\quad + \frac{(E_{21} - 2E_{22})}{4}\}F_{iB}M_BM_A]_{,A}\left(\frac{1}{r(m + \beta W_m)}\frac{2}{\sqrt{\pi}}\varrho\,[W(\mathbf{F})_{\mathbf{F}}]^2 + \varrho\right), \tag{6.68}
\end{aligned}
$$

$$\eta_{,A} = (\eta_F)_{iC}\, F_{iC,A} = \varrho W(\mathbf{F})_{\mathbf{F}} F_{iC,A}$$

$$= \varrho[\mu F_{iC} + \kappa(F_{iB}F_{jD}F_{jD}\delta_{CB} - F_{iB}F_{jC}F_{jB}) + \{\frac{E_{11}}{4}(F_{jR}F_{jD}D_R D_D)$$

$$(F_{kT}F_{kL}D_T D_L) + \frac{(E_{12} - E_{11})}{2}F_{jE}F_{jD}D_E D_D + \frac{(E_{11} - 2E_{12})}{4}\}F_{iB}D_B D_C$$

$$+\{\frac{E_{21}}{4}(F_{jC}F_{jD}M_C M_D)(F_{kE}F_{kF}M_E M_F) + \frac{(E_{22} - E_{21})}{2}F_{jC}F_{jD}M_C M_D$$

$$+\frac{(E_{21} - 2E_{22})}{4}\}F_{iB}M_B M_C]F_{iC,A}, \tag{6.69}$$

and also,

$$\dot{\phi}(\eta) = \frac{\partial \phi(\eta)}{\partial \eta}\dot{\eta} = \frac{\partial \phi(\eta)}{\partial \eta}\eta_F \dot{F} \tag{6.70}$$

$$= [-(m + \beta W_m)\,\mathrm{erf}^{-1}(r(\eta - 1)) - W_m]\eta_F \dot{F}$$

$$= [-(m + \beta W_m)\,\mathrm{erf}^{-1}(r(\eta - 1)) - W_m]\varrho[\mu F_{iA} + \kappa F_{iB}(F_{jC}F_{jC}\delta_{AB} - F_{jA}F_{jB})$$

$$+\{\frac{E_{11}}{4}(F_{j1}F_{j1})(F_{k1}F_{k1}) + \frac{(E_{12} - E_{11})}{2}F_{j1}F_{j1} + \frac{(E_{11} - 2E_{12})}{4}\}F_{i1}D_A$$

$$+\{\frac{E_{21}}{4}(F_{j2}F_{j2})(F_{k2}F_{k2}) + \frac{(E_{22} - E_{21})}{2}F_{j2}F_{j2} + \frac{(E_{21} - 2E_{22})}{4}\}F_{i2}M_A]\dot{F},$$

$$\left\{\left(\frac{\partial \phi(\eta)}{\partial \eta}\eta_{\mathbf{F}}\right)_{iA}\right\}_{,A} = \left(\left[\frac{\partial \phi(\eta)}{\partial \eta}\right]_{,A}\eta_{\mathbf{F}} + \frac{\partial \phi(\eta)}{\partial \eta}\{\eta_{\mathbf{F}}\}_{,A}\right) \tag{6.71}$$

$$= [-(m + \beta W_m)\,\mathrm{erf}^{-1}(r(\eta - 1)) - W_m]_{,A}\,\eta_{\mathbf{F}}$$

$$+[-(m + \beta W_m)\,\mathrm{erf}^{-1}(r(\eta - 1)) - W_m]\{\eta_{\mathbf{F}}\}_{,A}$$

$$= -r(m + \beta W_m)\frac{\sqrt{\pi}}{2}\exp[\mathrm{erf}^{-1}\{r(\eta - 1)\}]^2\eta_{,A}\eta_{\mathbf{F}}$$

$$+[-(m + \beta W_m)\,\mathrm{erf}^{-1}(r(\eta - 1)) - W_m]\{\eta_{\mathbf{F}}\}_{,A}.$$

6.3.2 Weibull fiber damage model

Let's consider a hyperelastic composite is subjected to tensile stress in the fibers' direction. In such a case, the matrix carries only a small portion of the applied load, thus no damage is likely to occur in the matrix during such loading. Then, the ultimate tensile strength of the composite can be accurately predicted by computing the strength of a bundle of fibers [169]. Fibers' strength can be expressed as a function of the effective length, δ which determines how much of the fiber strength is actually used in a composite. Starting at a fiber's breaking point, the effective length is the length over which a fiber recovers a large percentage of its load [169]. As tensile load

is slowly applied to a bundle of fibers within a composite, the weaker fibers (i.e., with large flaw sizes) begin to fail and the stress on the remaining unbroken fibers increases accordingly [169]. Weibull expression is used to describe the cumulative probability that a fiber of length δ will fail at or below an effective stretch, $\hat{\gamma}$ (also termed as damage threshold). This cumulative probability represents the damage characterizing term, d as follows [92]:

$$d = 1 - e^{-\delta\alpha\hat{\gamma}^m},\tag{6.72}$$

where, δ is the effective fiber length, m is the dispersion of fiber strength, and α is defined by the follwoing expression:

$$\alpha = \frac{1}{\tilde{\sigma}_0^m L_0} = \left[\frac{\Gamma(1 + \frac{1}{m})}{\tilde{\sigma}_{av}}\right]^m \frac{1}{L_0}.\tag{6.73}$$

In the above, Γ is the gamma function, $\tilde{\sigma}_{av}$ is the average strength of the fiber bundle for a gauge length L_0. In practice it is often reported as a product $\delta\alpha$, where $\delta\alpha = \frac{(\sigma_{cr})^{-m}}{me}$ and σ_{cr} is the maximum (or critical) bundle strength. Lastly, the updated damage threshold, $\hat{\gamma}$ can be given by the highest value of stretch experienced by the material.

$$\hat{\gamma} = \max(\lambda_m, \lambda_D).\tag{6.74}$$

Here, λ_m is the current stretch and λ_D is the highest stretch in the history of the material. The damage threshold is always updated by the largest of these two values. At the very begining, it is necessary to provide an initial damage threshold as an input, which is the amount of stretch where damage starts to develop in the material. For any stretch below this initial damage threshold, the damage variable remains inactive and correspondingly, $d = 1$. This indicates no damage present in the material. Whenever the stretch reaches the initial damage threshold, the damage variable, d becomes activated and it is calculated using Eq. (6.72). From this point, d becomes non-zero which indicates the presence of damage within the material. When the stretch exceeds the initial damage threshold, the corresponding stretch value is recorded as λ_D and $\hat{\gamma}$ gets updated from Eqn. (6.74). From this updated vlaue of $\hat{\gamma}$, the damage variable d is calculated again from Eqn. (6.72). A flowchart of the Weibull damage model is presented in Fig. 6.5.

Now, introducing the damage variable, d (see, Eq. 6.72) in Eq. (6.42) we can

Figure 6.5: Flowchart of Weibull fiber damage model for hyperelastic composite.

rewrite the Piola stress expression as follows:

$$
\begin{aligned}
P_{iA} &= \mu F_{iA} + \kappa F_{iB}(F_{jC}F_{jC}\delta_{AB} - F_{jA}F_{jB}) + (1 - e^{-\delta\alpha\hat{\gamma}^m})[\frac{E_1}{4}(F_{jC}F_{jD}D_CD_D) \\
&\quad (F_{kE}F_{kF}D_ED_F) + \frac{(E_{12} - E_{11})}{2}F_{jC}F_{jD}D_CD_D + \frac{(E_{11} - 2E_{12})}{4}]F_{iB}D_BD_A \\
&\quad +(1 - e^{-\delta\alpha\hat{\gamma}^m})[\frac{E_{21}}{4}(F_{jC}F_{jD}M_CM_D)(F_{kE}F_{kF}M_EM_F) \\
&\quad +\frac{(E_{22} - E_{21})}{2}F_{jC}F_{jD}M_CM_D + \frac{(E_{21} - 2E_{22})}{4}]F_{iB}M_BM_A - pF_{iA}^* \\
&\quad -CF_{iC,DB}(D_AD_BD_CD_D + M_AM_BM_CM_D) - TF_{iC,DB}(D_AD_BM_CM_D \\
&\quad +D_AD_BM_CM_D).
\end{aligned}
\tag{6.75}
$$

Replacing $F_{iA} = \chi_{i,A}$ on Eqn. (6.75) and taking divergence, we then write the equi-

libirum equations as follows:

$$
\begin{aligned}
0 = P_{iA,A} &= \mu\chi_{i,AA} + \kappa(\chi_{i,AA}\chi_{j,C}\chi_{j,C} - \chi_{i,BA}\chi_{j,A}\chi_{j,B}) + \kappa\chi_{i,B}(2\chi_{j,CB}\chi_{j,C} \\
&\quad -\chi_{j,AA}\chi_{j,B} - \chi_{j,A}\chi_{j,BA}) - p_{,A}\varepsilon_{ij}\varepsilon_{AB}\chi_{j,B} + (1 - e^{-\delta\alpha\hat{\gamma}^m})[\frac{E_{11}}{4}(2\chi_{j,11}\chi_{j,1}\chi_{k,1}\chi_{k,1} \\
&\quad +2\chi_{j,1}\chi_{j,1}\chi_{k,11}\chi_{k,1}) + (E_{12} - E_{11})\chi_{j,11}\chi_{j,1}]\chi_{i,1} + (1 - e^{-\delta\alpha\hat{\gamma}^m})[\frac{(E_{11} - 2E_{12})}{4} \\
&\quad +\frac{(E_{12} - E_{11})}{2}\chi_{j,1}\chi_{j,1} + \frac{E_{11}}{4}(\chi_{j,1}\chi_{j,1})(\chi_{k,1}\chi_{k,1})]\chi_{i,11} + (1 - e^{-\delta\alpha\hat{\gamma}^m}) \\
&\quad [\frac{E_{21}}{4}(2\chi_{j,22}\chi_{j,2}\chi_{k,2}\chi_{k,2} + 2\chi_{j,2}\chi_{j,2}\chi_{k,22}\chi_{k,2}) + (E_{22} - E_{21})\chi_{j,22}\chi_{j,2}]\chi_{i,2} \\
&\quad +(1 - e^{-\delta\alpha\hat{\gamma}^m})[\frac{E_{21}}{4}(\chi_{j,2}\chi_{j,2})(\chi_{k,2}\chi_{k,2}) + \frac{(E_{22} - E_{21})}{2}\chi_{j,2}\chi_{j,2} \\
&\quad +\frac{(E_{21} - 2E_{22})}{4}]\chi_{i,22} - C(\chi_{i,1111} + \chi_{i,2222}) - T(\chi_{i,1122} + \chi_{i,2211}). \quad\quad (6.76)
\end{aligned}
$$

6.4 Model implementation and discussions

6.4.1 Mullins effect in biological soft tissues

In this present section, we implement the proposed model in assimilating the Mullins effect in biological soft tissues. First, we present the Mullins effect in human aortic tissue. Then we discuss the Mullins effect in Manduca muscle.

Human aorta

The main conduit for blood delivery called the aorta, is an elastic artery that consists of three distinct layers: the *tunica intima*, the *tunica media*, and the *tunica adventitia* [170]. The media is separated from the intima by an internal elastic lamina. The intima which is primarily involved in metabolic processes provides a negligible mechanical contribution to the wall resistance in young and healthy individuals [170]-[171]. Whereas media has the primary mechanical contribution, which supports the aortic wall against the physiological blood pressure [170]. The media is composed of as many as 70 fenestrated medial lamellar units, consisting of two adjacent elastic lamellae (involving elastin), which are interspersed with a layer of collagen fibers [170]. This structural arrangement of the medial lamellar unit can be thought of as analogous to the 3-layer configuration of an elastomeric composite reinforced with bi-directional fibers (as shown in Fig. 6.6). Where the matrix layer of elastin lamella

is a rubber-like protein with a modulus ranging from 0.6 to 1 MPa [7]. This layer is someway similar to the elastomeric matrix material, like Ecoflex. The collagen fiber layer at the middle of two adjacent elastin lamellae, which is stiff and relatively inextensible with a modulus of around 1 GPa [7], can be represented by a bidirectional fiber mesh layer with nonlinear properties. Further, the anisotropic nature of the aorta may be accommodated by considering different tensile properties for the fibers in each direction of the bidirectional fiber mesh layer.
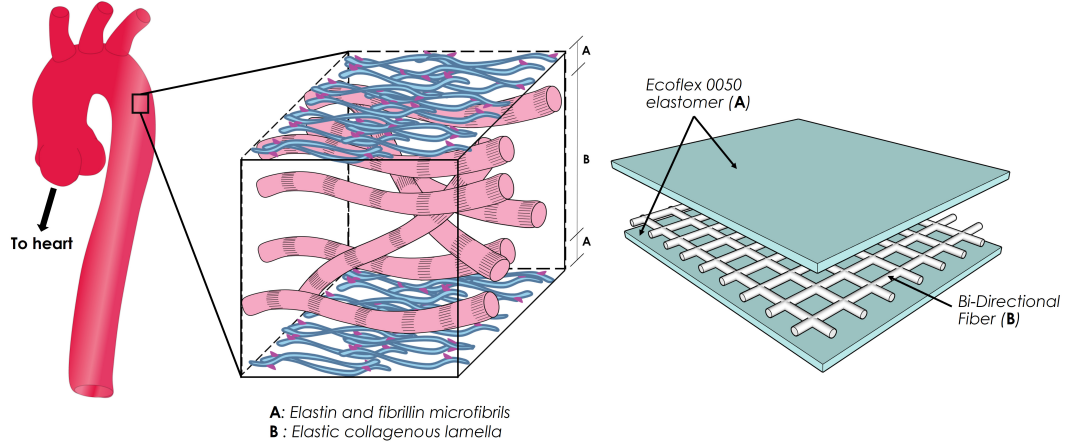
Figure 6.6: Structural analogy of medial lamellar unit (left) with 3-layer configuration of Ecoflex-0050 composite reinforced with bidirectional fiber mesh [170].

Elastomeric material, like Ecoflex-0050, is a very suitable biomedical material because of its biocompatibility, nearly instantaneous response to stresses, and fully reversible deformation. The stiffness of rubber-like elastin lamella in the medial lamellar unit varies between 0.6 to 1 MPa [7]. This range is closely related to the stiffness of Ecoflex-0050, where we have calculated the slope of the stress-strain curve of Ecoflex-0050 varies between 0.15 MPa to 0.9 MPa. Due to this close correspondence of properties between Ecoflex and elastin lamella, Ecoflex-0050 has been used to imitate the elastin lamella of the human aorta (for example, see, [7]). For this same reason, we also used Ecoflex-0050 for modeling the matrix material of the biocomposite in the present study. Ecoflex-0050 is characterized using the Mooney-Rivlin model and we obtain the fitting parameters, $\mu = 0.082$ MPa and $\kappa = 0.01$ MPa (see, Fig. 6.7).

The proposed model is compared against the experimental data from [166], where cyclic uniaxial tension tests were performed on the samples of human thoracic aorta
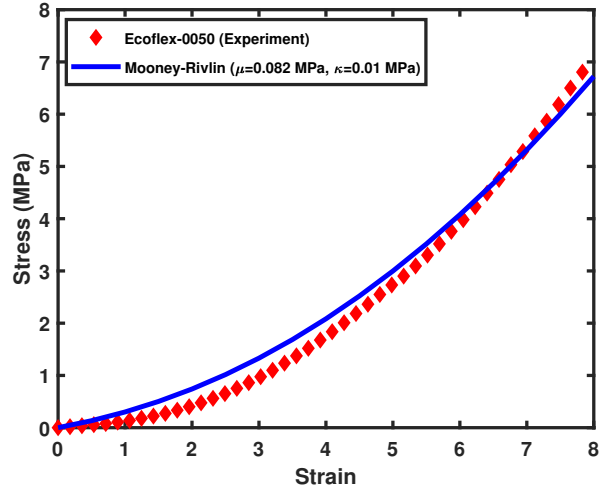
Figure 6.7: Mooney-Rivlin characterization of experimental stress strain data for Ecoflex-0050 matrix.

using the MTS Mini Bionix testing machine. In order to illustrate the Mullins effect in human aorta, two samples of human thoracic aorta were selected from cadaveric donors. The samples were resected in the circumferential and longitudinal directions with respect to the natural configuration of an artery (as shown in Fig. 6.8). The arteries were stored in a physiological solution at a temperature of about 5°C till the beginning of the experiment. All experiments were performed within 48 hours after the death. The temperature during the test was 23°C. The extensions and loading forces were measured by the MTS testing machine. Using the proposed model, we characterize the primary stress-strain response of both the longitudinal and circumferential samples and the tension parameters of the fiber in each direction i.e., E_{11}, E_{21}, E_{21}, and E_{22} are obtained. The obtained results with fiber orientations in the model are illustrated in Figs. 6.8 - 6.9 . The bending modulus (C) and torsion modulus (T) are chosen to be $0.55 MPa$.

Once the fiber and matrix parameters are obtained, we compare the results from our model with the cyclic loading-unloading experimental data, representing Mullins effect from [166]. For comparing the Mullins effect, two sets of submaximal unloading data from the experiment were taken into consideration with unloadings starting from 10% and 20% strain, respectively from the primary loading curve. It has been observed that the proposed model can simulate the Mullins effect for both the lon-
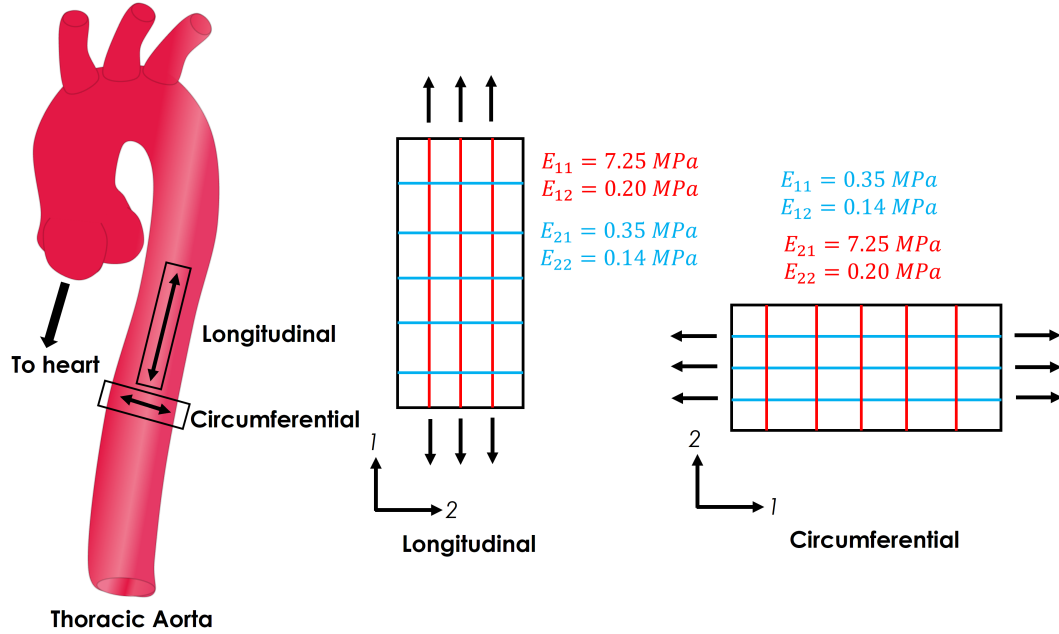
Figure 6.8: Fiber orientation with tensile modulus for longitudinal and circumferential samples of aorta.

gitudinal and circumferential samples of the human aorta with good accuracy. For both of these cases, unloading is initiated using the proposed model from 3 different positions along the primary loading curve which are at $10\%, 15\%$, and 20% strain. Thus we obtain three submaximal unloading curves along with the primary loading curve from the porposed model, through which we were able to precisely identify the three parameters associated with the Mullins effect i.e., m, r, and β. For the longitudinal case, the obtained parameters are $m = 0.0034, r = 1.65$, and $\beta = 0.397$, whereas for the circumferential case $m = 0.0012, r = 1.015$, and $\beta = 0.096$. The comparisons for the longitudinal and circumferential cases are presented in Figs. 6.10 and 6.11, respectively.

Manduca muscle

Studying the cyclic responses of larval muscles, e.g., the muscles from the larva of Manduca sexta, may be beneficial in the constructions and numerical simulations of soft-bodied robots with multimodal locomotion [20]. Furthermore, the flight muscle of Manduca sexta is reported to be an emerging model system for biophysical studies of muscle contraction [172]. These larval muscles are synchronous muscles [21]-[22],
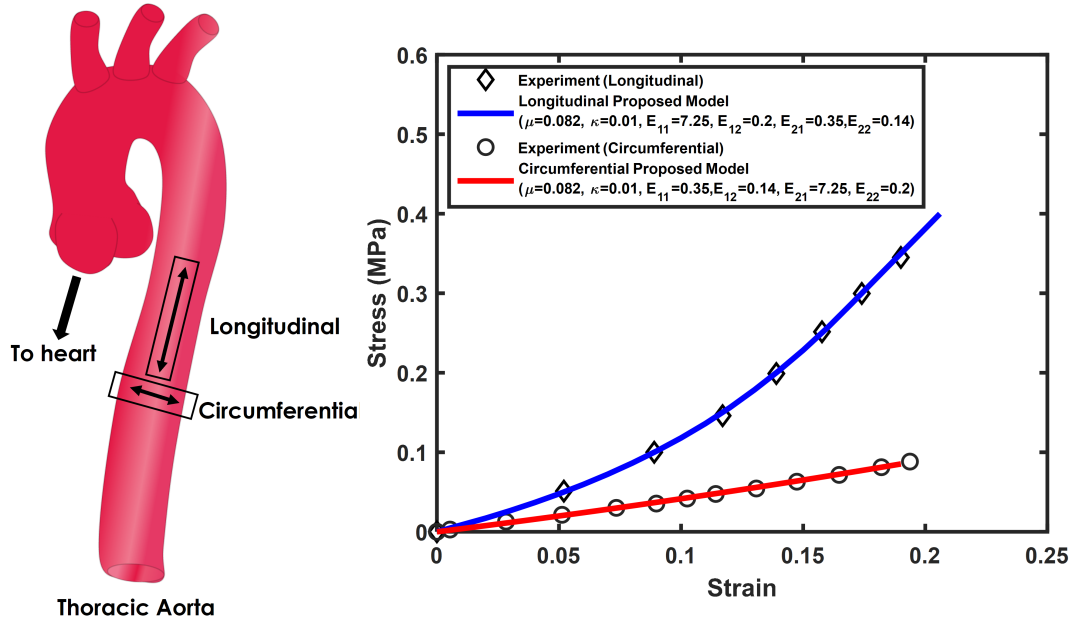
Figure 6.9: Comparison of stress-strain results from the model and experiment for longitudinal and circumferential samples [166].

where each contraction is coupled with neural stimulation. It has been also proposed that the flight muscle of Manduca sexta can be used as a comparative model system to possibly elucidate some aspects of mammalian cardiac muscle due to their similar physiological properties, for example, both cardiac and flight muscle of Manduca have large amplitudes of cyclical strain during contraction [23],[172]. The cyclic responses of these larval muscles exhibit pseudoelastic behavior described by the Mullins effect. During the last decades, some studies have been carried out to characterize the pseudoelastic nature of larval muscles, specifically from the larva of Manduca sexta [20]–[28]. These larval muscles are complex composites with profound anisotropy, which is very distinct from either amorphous or crystalline materials [20]. Each muscle fiber contains aligned actin and myosin filaments within an amorphous matrix material composed of proteins, lipids, and polysaccharides [20]. In addition, these muscles also contain molecularly massive elastic proteins such as titin which are being investigated extensively in several studies [173]–[177]. This giant elastic protein titin with folded domains results in interesting characteristics like asymmetric properties, time-dependent stretching, and shortening during load cycling [20].

The stress-strain response of the Manduca muscle is found to be nonlinear and
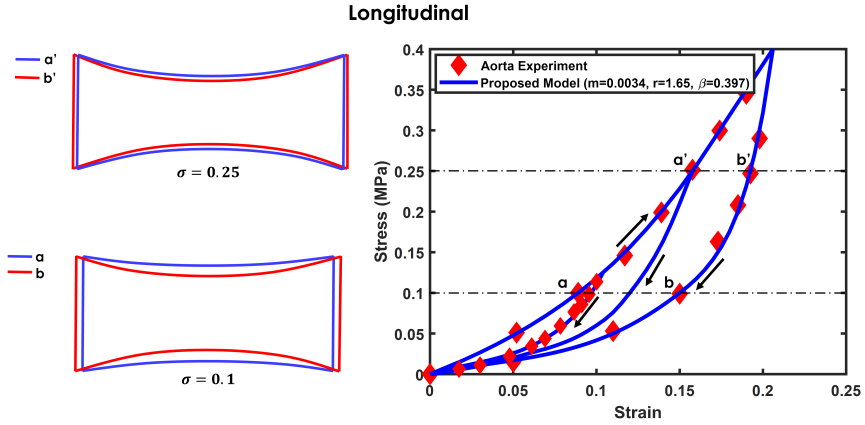
Figure 6.10: Comparison of Mullins effect between the results form the proposed model and experiment data for longitudinal sample of aorta [166].
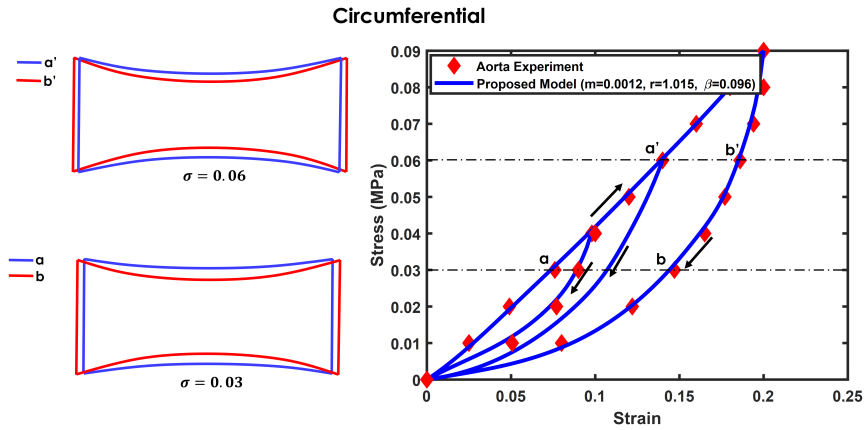
Figure 6.11: Comparison of Mullins effect between the results form the proposed model and experiment data for circumferential sample of aorta [166].

capable of large deformations [20]. Moreover, Manduca muscles were found to be elastomeric and dissipate work with each strain cycle (pseudoelasticity), undergoing stress softening on repeated cycling (the Mullins effect) [20]. Manduca larval muscles are attached directly to apodemes, infoldings of the cuticle wall due to the absence of a stiff skeleton. The muscles are organized in repeated segments corresponding to the body segments, in layers [20]. For demonstrating the utility of the proposed model in assimilating the pseudoelastic properties of the Manduca larval muscles, we adopted the experiment from [20]. Test data were gathered for the ventral interior lateral (VIL) muscle of the third abdominal segment (A3) (see, Fig. 6.12). A3 VIL is one of the largest larval muscles, comprising 14 fibers [28]. A3 VIL was
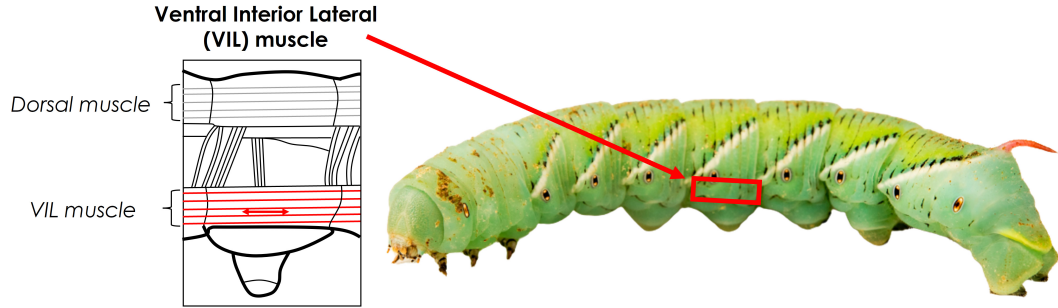
Figure 6.12: The location of the ventral interior lateral (VIL) muscle within the Manduca sexta caterpillar is illustrated . [178]-[179].

chosen because during crawling, VIL reaches its highest stress during the lengthening portion of its strain cycle, suggesting that its passive properties play an important role in its biological function [20]. The muscle was dissected out in physiological saline along with a small portion of the attached cuticle at each end. The preparation was transferred to a horizontal saline bath, with one end pinned to an elastomer platform in the bath and the other secured by a hook to an Aurora 300B-LR lever arm ergometer that administered strain cycling while measuring force [20]. The periodic loading, unloading, and reloading tests were performed using constant strain rates representative of those encountered in nature [20]. The initial distance of the pinned connections at each end of the muscle was used to determine the longitudinal strain. The reference length of the muscle was found to be 5.5 mm [20]. The nominal stress was determined as the ratio of the axial force to the cross-sectional area, measured in the reference configuration [20]. The magnitude of the cross-sectional area of the muscle tested and used to determine the nominal stress was 0.4 mm^2 [20]. The sample was stretched up to 1.18 and then unloaded to its undeformed state. Using our proposed model, we have assimilated the stress-strain cycle response of the Manduca muscle sample. The best result is obtained with the following parameters in our model, $E_{11} = E_{21} = 1.85 MPa$, $E_{12} = E_{22} = 0.06 MPa, C = T = 0.21 MPa$, $r = 1.025$, $m = 0.0035$, and $\beta = 1.075$. For the matrix material, we have used similar properties ($\mu = 0.082$ MPa and $\kappa = 0.01$ MPa) of Ecoflex-0050 elastomer. The result is compared against the experimental data in Fig 6.13. The figure shows that the proposed model can effectively assimilate the Mullins effect type pseudoelastic

behavior of the muscle.
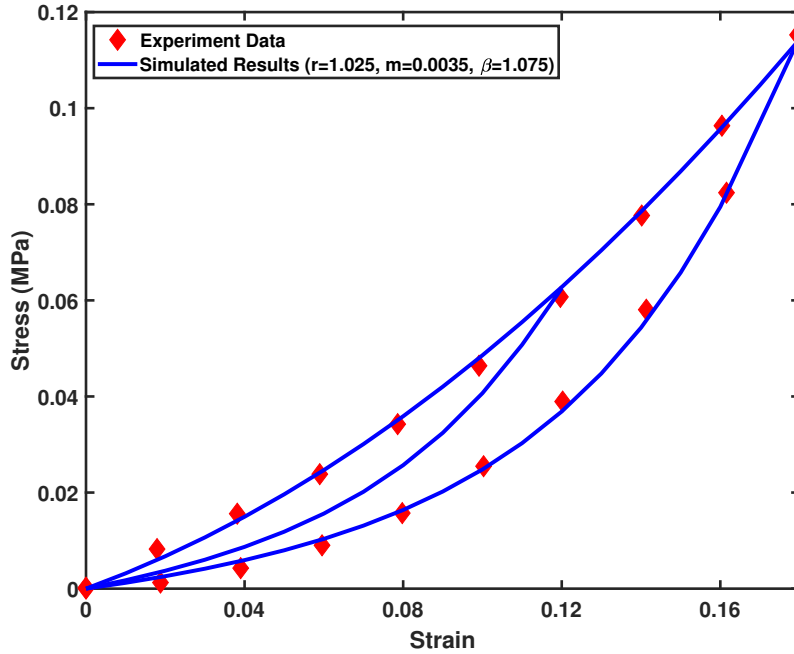
Figure 6.13: Comparison of Mullins effect between the results form the proposed model and experiment data for Manduca muscle [20].

6.4.2 Weibull fiber damage of Ecoflex/PES composite

In this section, we implement the proposed Weibull damage model (as presented in Eqn. (6.76)) to demonstrate the utility of the model in assimilating the damage mechanics of an elastomeric composite induced by fiber breakage. The results are compared against our in-house experimental data. For the experiments, we have selected Ecoflex-0050 as the elastomeric matrix material, which was manufactured by Smooth-On, Inc. Ecoflex-0050 is known to be one of the promising materials in biomechanical applications for its high tear resistance and large extensibility up to 1000% [128]-[130]. Ecoflex-0050 is a room-temperature-vulcanizing (RTV) silicone that was prepared by mixing two components (a base and curing agent) in 1:1 ratio and subsequently degassing in a vacuum to remove the entrapped bubbles. For the reinforcing fiber, we have selected a surgical polyester knitted mesh which is referred to as PETKM2006 (PES-3), fabricated by the Surgical Mesh (Brookfield, CT, USA). The effective dimension of fabricated composite samples is $50mm \times 25mm$, keeping

an aspect ratio of 2:1 (length-to-with). The actual size of fabricated composites was $78mm \times 25mm$ with an end allowance of $14mm$ at each side of the sample. The reinforced elastomer composites were fabricated in a three-layer configuration using a layer-by-layer method. The schematic diagram of the sample preparation and 3-layer configuration of the composite are shown in Figs. 6.14 (b) - 6.14 (c). To prepare the bottom elastomer layer, a sufficient amount of elastomer mixture was poured on a glass substrate and rolled using the film applicator rod to make a uniform film (see, Fig. 6.14 (b)). The second layer of fiber mesh was then placed flat on the elastomer and allowed to soak at the interface. A small amount of elastomer was then poured and rolled over the fiber mesh to wet it again and to fill the gaps between pores and level the second layer. To make the third layer, a sufficient amount of elastomer was poured over the second layer and a uniform film was created using a film applicator rod. The width, length, and thickness of the prepared Ecoflex-0050 matrix material, raw fiber, and composite samples were measured using a caliper. An aspect ratio of length-to-width was maintained as 2:1. Instron 5943 (Illinois Tool Works Inc., USA) was used to measure the stress-strain responses of the Ecoflex-0050, the raw fiber PES3, and the composite (see, Fig. 6.14 (a)). The test apparatus recorded the displacement and force as a function of time for each uniaxial tensile test. The extension rate was set to be $2.5mm/min$ for all cases to avoid/minimize the viscous responses [134]–[136].

The uniaxial tensile test results were then used to determine the mechanical responses of the matrix, fibers, and composites. To compute strains, the displacement and gauge length were used. The corresponding stresses were calculated from the applied load and the cross-sectional area of the samples. For example, the principal strains and the engineering stresses were calculated using the relations of $\varepsilon = \Delta l / l_o$ and $\sigma = F/A_o = F/(w_o t_o)$, respectively, where l_o is the original sample length, w_o is the initial width, and t_o is the initial thickness which were measured using a caliper. The amount of extension, Δl, was then calculated as $\Delta l = l - l_o$ where l is the current length. To analyze the local microstructure deformations of the reinforced composites, mesh grids of $1.5mm \times 1.5mm$ were printed on the surfaces of each sample. A Sony A6000 camera was used to capture the deformed images of the fiber meshes and the printed mesh grids which were then compared with the simulation results,
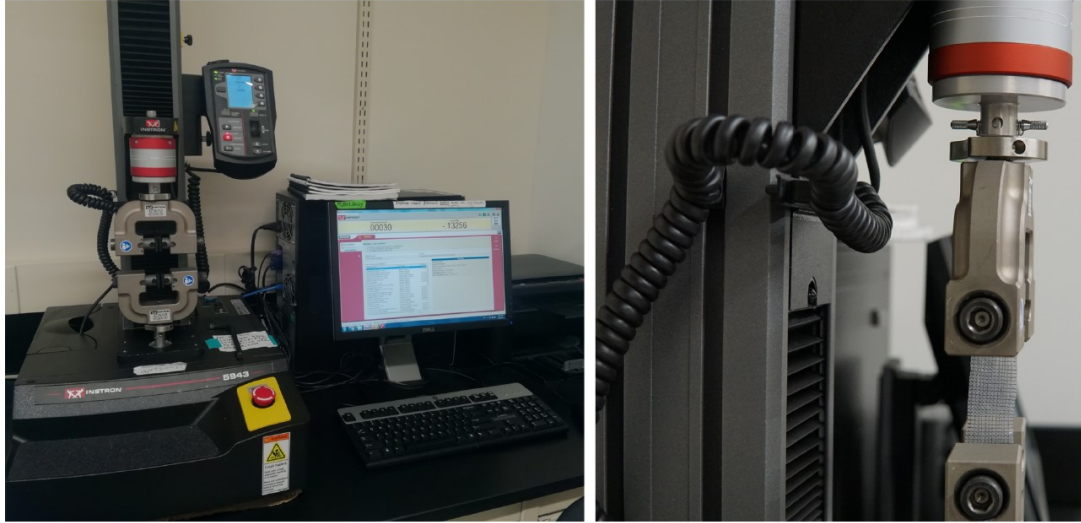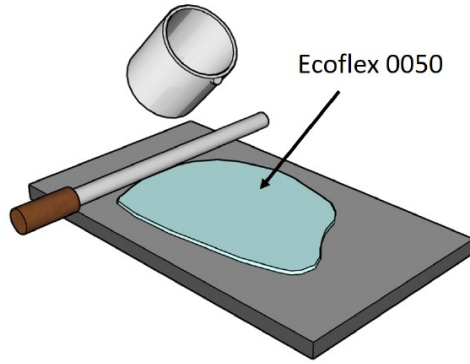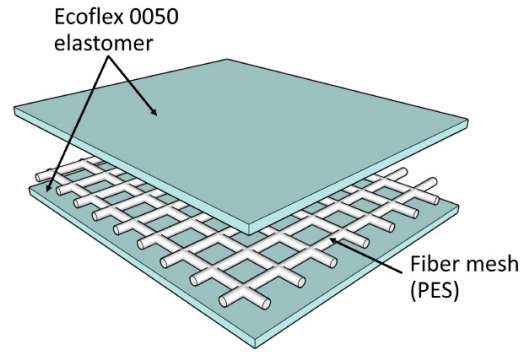
Figure 6.14: (a) Experimental setup for the uniaxial test. (b) Fabrication of the composite laminate. (c) 3-layer configuration of the Ecoflex-0050 / PES3 composite.

predicted from the proposed model.

In Fig. 6.15 (a) the stress-strain response of the PES-3 fiber is characterized using the polynomial model and we obtain the tension parameters of the PES3 fiber as, $E_{11} = E_{21} = 2.35MPa$ and $E_{12} = E_{22} = -0.2MPa$. The bending modulus (C) and torsion modulus (T) are chosen to be $1MPa$ and $7MPa$, respectively. For the Ecoflex 0050 matrix material, we have used Mooney-Rivlin model to characterize the experimental stress-strain response with the following matrix parameters $\mu = 0.082$ MPa and $\kappa = 0.01\ MPa$, this result is shown in Fig. 6.15 (b).

These obtained parameters are used in the proposed model which is then solved
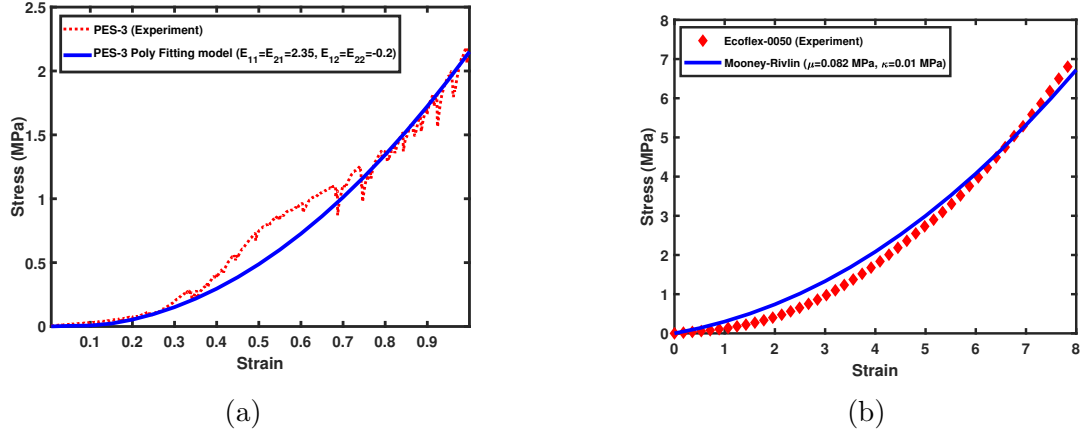
Figure 6.15: (a) Polynomial characterization of experimental stress-strain data for raw PES-3 fiber sample. (b) Mooney-Rivlin characterization of experimental stress-strain data for Ecoflex-0050 matrix.

using the FEA method and we obtained the response of the composite material. In Fig. 6.16 (a) and (b) the χ_1 and χ_2 deformation profiles are compared against the experimental data at 50% and 100% elongations, respectively. From the figure, good agreement between the experimental data and simulated results from the proposed model may be observed.
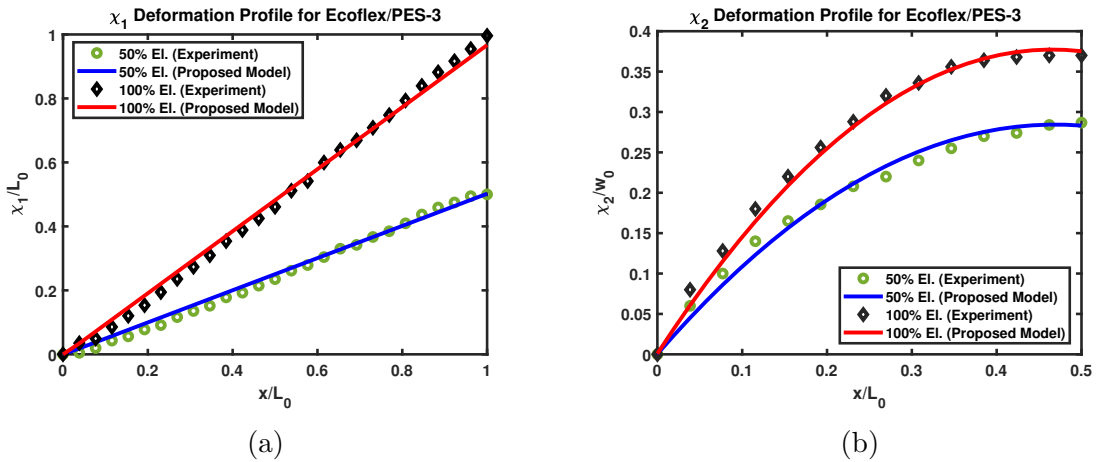
Figure 6.16: Comparison of deformation profiles between experiement data and proposed model for Ecoflex 0050/PES3 composite of (a) χ_1 deformation; (b) χ_2 deformation.

We have also compared the shear angle distribution within the composite against the experiment for 50% and 100% elongations of the composite, which also shows good agreement with the experimental finding. This comparison results for 50% and

215

100% elongation are presented in Fig. 6.17 (a) and (b), respectively. Also, it can be noted that the proposed model is able to generate smooth and continuous shear angle distribution, which is not possible using the classical first gradient theory (see, [87]).
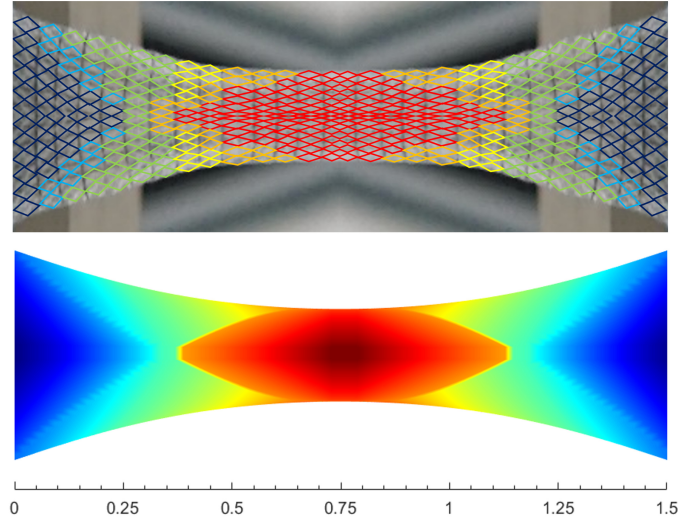
(a)
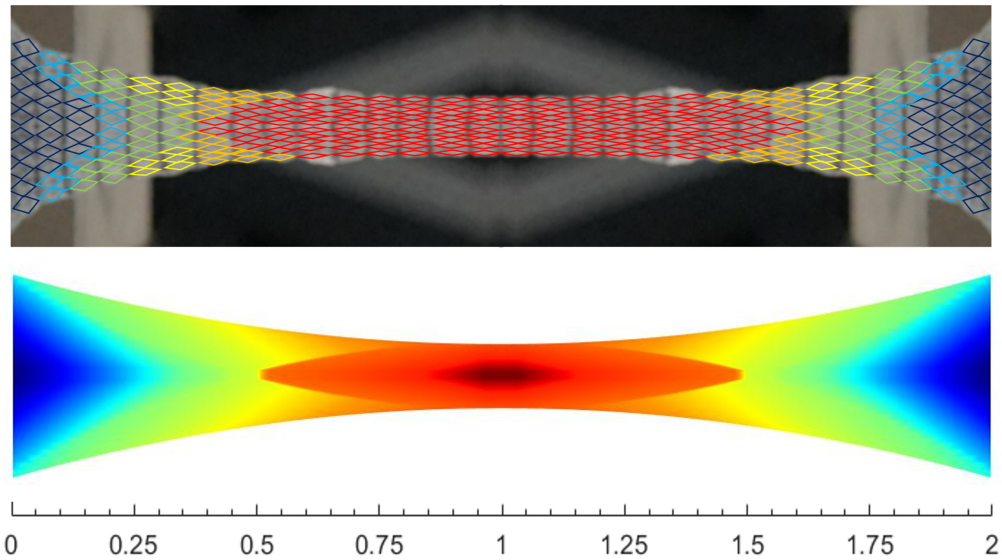
(b)

Figure 6.17: Comparison of shear angle distribution between experiement (top) and proposed model (bottom) for (a) 50% elongation; (b) 100% elongation.

Lastly, we compare the stress-strain results of the Ecoflex-0050/PES3 composite from the proposed model against the experiment data, which is presented in Fig. 6.18. It may be observed from the figure that the proposed model is able to predict the non-

linear stress-strain response and also the damage mechanics of the composite with good accuracy. In Fig. 6.18, the no-damage and damage regions are illustrated. The no-damage region is defined within the strain range where, either there is no-damage (applicable only for initial loading case) or damage does not grow. While in the damage region, damage continues to grow. During the no-damage region (see, curve OA in Fig. 6.18), our model behaves like a fully elastic material with damage variable (see, Eq. (6.72)), $d = 1$. For this specific case, strain at 1.17 is set as the initial damage threshold, which is obtained from the experiment data. When the strain from our simulation crosses the initial damage threshold, the material enters into the damage region (see, curve AB in Fig. 6.18). At the same time, the pseudoelastic model becomes activated and the value of d changes with the increase of strain following the relation described in Eq. (6.72). Simultaneously, the damage threshold is updated with this new strain value. Now, at any point in the damage region, if we start to unload, the material again follows an elastic nonlinear response but with a reduced stiffness (see, curve BO in Fig. 6.18), where the E_1 and E_2 are multiplied with d. During this unloading phase, the value of d remains unchanged and no additional damage grows. The process repeats this way. In the proposed model, we use the parameters $\delta\alpha = 0.0005$ and $m = 20$.
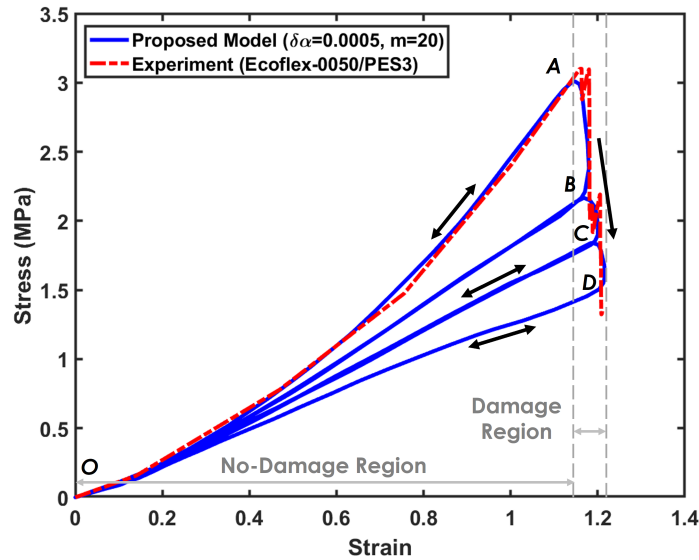
Figure 6.18: Comparison of stress-strain results between experiment and proposed model for Ecoflex-0050/PES3 composite.

From the cyclic stress-strain graph obtained from repeated loading and unloading, it is also possible to estimate the dissipated energy density and recovered energy density of the composite material. The dissipated and recovered energy is illustrated in Fig. 6.19. The area between any successive loading and unloading curves represents the dissipated energy for that cycle and the area under the unloading curve represents the recovered energy. From the assimilated cyclic stress-strain graph of Ecoflex-
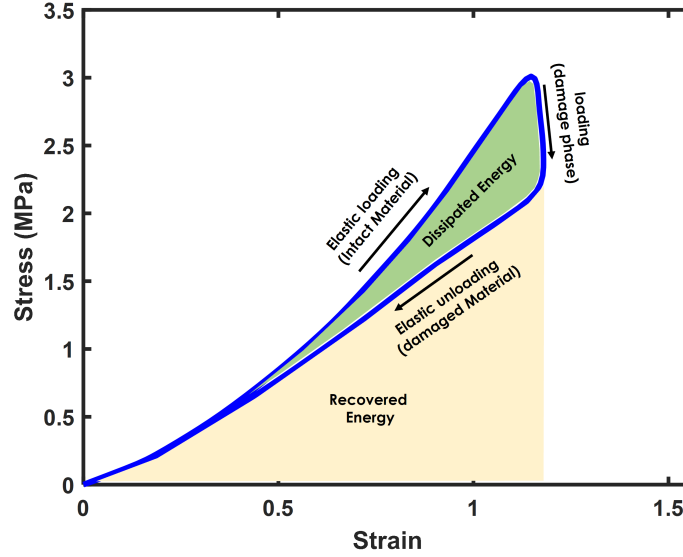
Figure 6.19: Illustration of dissipated energy and recovered energy in cyclic stress-strain graph.

0050/PES3 composite, we are able to estimate the dissipated and recovered energy density, which is illustrated in Fig. 6.20. The energy density is calculated via the area integration using the Trapezoidal rule method. For the first loading-unloading cycle, we have obtained the dissipated energy density $246\frac{MJ}{m^3}$, for the 2nd and 3rd cycles we have obtained $127\frac{MJ}{m^3}$ and $180\frac{MJ}{m^3}$, respectively. The final recovered energy density is found to be $904\frac{MJ}{m^3}$.

6.5 Finite element analysis of the 4th order coupled PDE

To demonstrate the finite element analysis (FEA) procedures, we have chosen the system of PDEs obtained from the Weibull fiber damage model. The rest of the cases will follow the similar process.
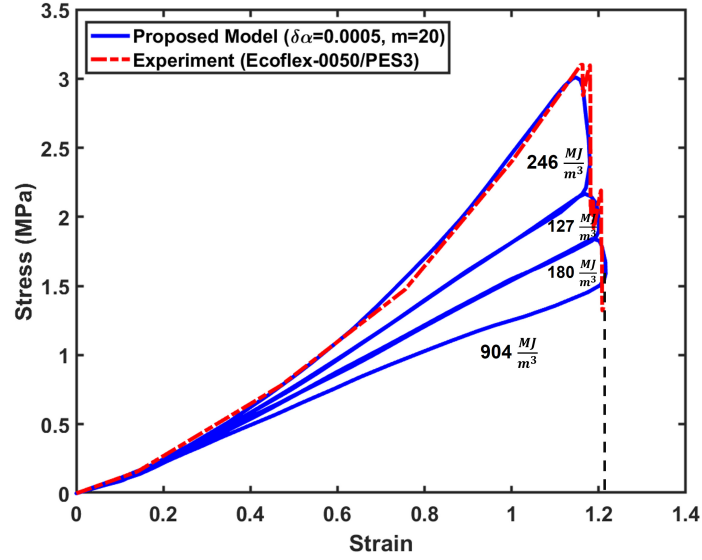
Figure 6.20: Estimation of dissipated and recovered energy from the cyclic stress-strain results of Ecoflex / PES3 composite.

The system of PDEs in Eqs. (6.76) represent systems of 4th order coupled differential equations. The case of such less regular PDEs system deserves delicate mathematical treatment and is of particular practical interest. Therefore, it may not be trivial to report the associated FEA procedure. For preprocessing, Eqs. (6.76) may be rearranged into the following form:

$$
\begin{aligned}
0 \;=\;& \mu(Q + \chi_{1,22}) + \kappa(Q + E_{,2})(CC + EE + DD + FF) \\
& -\kappa(Q + C_{,2} + E_{,1} + E_{,2})(CC + CE + EC + EE + DD \\
& +DF + FD + FF) + \kappa(C + E)(2QC + 2E_{,1}E + 2C_{,2}C \\
& +2E_{,2}E - QC - QE - E_{,2}C - E_{,2}E - CQ - CE_{,1} \\
& -EC_{,2} - EE_{,2} + 2RD + 2F_{,1}F + 2D_{,2}D + 2F_{,2}F - RD \\
& -RF - F_{,2}D - F_{,2}F - DR - DF_{,1} - FD_{,2} - FF_{,2}) \\
& -A_0\chi_{2,2} + B_0\chi_{2,1} + (1 - e^{-\delta\alpha\hat{\gamma}^m})[\frac{E_{11}}{4}\{2(QC + RD)(CC + DD) \\
& +2(CC + DD)(QC + RD)\} + (E_{12} - E_{11})(QC + RD)]C \\
& +(1 - e^{-\delta\alpha\hat{\gamma}^m})[\frac{E_{11}}{4}(CC + DD)(CC + DD) \\
& +\frac{(E_{12} - E_{11})}{2}(CC + DD) + \frac{(E_{11} - 2E_{12})}{4}]Q \\
& +(1 - e^{-\delta\alpha\hat{\gamma}^m})[\frac{E_{21}}{4}\{2(SD + NF)(EE + FF) \\
& +2(EE + FF)(SE + NF)\} + (E_{22} - E_{21})(SE + NF)]E \\
& +(1 - e^{-\delta\alpha\hat{\gamma}^m})[\frac{E_{21}}{4}(EE + FF)(EE + FF) \\
& +\frac{(E_{22} - E_{21})}{2}(EE + FF) + \frac{(E_{21} - 2E_{22})}{4}]S \\
& -C(Q_{,11} + S_{,22}) - T(Q_{,22} + S_{,11}),
\end{aligned}
$$

$$
\begin{aligned}
0 \;=\; & \mu(R + \chi_{2,22}) + \kappa(R + F_{,2})(CC + EE + DD + FF)\\
& -\kappa(R + D_{,2} + F_{,1} + F_{,2})(CC + CE + EC + EE + DD\\
& +DF + FD + FF) + \kappa(D + F)(2QC + 2E_{,1}E + 2C_{,2}C\\
& +2E_{,2}E - QC - QE - E_{,2}C - E_{,2}E - CQ - CE_{,1}\\
& -EC_{,2} - EE_{,2} + 2RD + 2F_{,1}F + 2D_{,2}D + 2F_{,2}F - RD\\
& -RF - F_{,2}D - F_{,2}F - DR - DF_{,1} - FD_{,2} - FF_{,2})\\
& -A_0\chi_{2,2} + B_0\chi_{2,1} + (1 - e^{-\delta\alpha\hat\gamma^m})[\frac{E_{11}}{4}\{2(QC + RD)(CC + DD)\\
& +2(CC + DD)(QC + RD)\} + (E_{12} - E_{11})(QC + RD)]D\\
& +(1 - e^{-\delta\alpha\hat\gamma^m})[\frac{E_{11}}{4}(CC + DD)(CC + DD)\\
& +\frac{(E_{12} - E_{11})}{2}(CC + DD) + \frac{(E_{11} - 2E_{12})}{4}]R\\
& +(1 - e^{-\delta\alpha\hat\gamma^m})[\frac{E_{21}}{4}\{2(SD + NF)(EE + FF)\\
& +2(EE + FF)(SE + NF)\} + (E_{22} - E_{21})(SE + NF)]F\\
& +(1 - e^{-\delta\alpha\hat\gamma^m})[\frac{E_{21}}{4}(EE + FF)(EE + FF)\\
& +\frac{(E_{22} - E_{21})}{2}(EE + FF) + \frac{(E_{21} - 2E_{22})}{4}]N\\
& -C(R_{,11} + N_{,22}) - T(R_{,22} + N_{,11}),
\end{aligned}
$$

$$
\begin{aligned}
0 \;=\; & Q - \chi_{1,11},\ 0 = R - \chi_{2,11},\ 0 = C - \chi_{1,1},\ 0 = D - \chi_{2,1},\\
0 \;=\; & E - \chi_{1,2},\ 0 = F - \chi_{2,2},\ 0 = A - \mu(Q + \chi_{1,22}) - cQ_{,11},\\
0 \;=\; & B - \mu(R + \chi_{2,22}) - cR_{,11}, 0 = S - \chi_{1,22}, 0 = N - \chi_{2,22} \qquad (6.77)
\end{aligned}
$$

where $Q = \chi_{1,11}$, $R = \chi_{2,11}$, $C = \chi_{1,1}$, $D = \chi_{2,1}, E = \chi_{1,2}$, $F = \chi_{2,2}$, $S = \chi_{1,22}$ and $N = \chi_{2,22}$. Hence, the order of differential equations is reduced from the three coupled equations of the 4th order to 12 coupled equations of the 2nd order. Especially, the non-linear terms in the above equations (e.g. $A\chi_{2,2}$, $B\chi_{2,1}$ etc...) can be systematically treated via the Picard iterative procedure and/or Newton method;

$$
\begin{aligned}
-A^{initial}\chi_{2,2}^{initial} + B^{initial}\chi_{2,1}^{initial} &\implies -A_0\chi_{2,2}^0 + B_0\chi_{2,1}^0\\
A^{initial}\chi_{1,2}^{initial} - B^{initial}\chi_{1,1}^{initial} &\implies A_0\chi_{1,2}^0 - B_0\chi_{1,1}^0, \qquad (6.78)
\end{aligned}
$$

where the estimated values of A, B continue to be updated based on their previous estimations (e.g. A_1 and B_1 are refreshed by their previous estimations of A_o and

B_o) as iteration progresses and similarly for the rest of non-linear terms. Also, the weight forms of Eq. (6.77) can be found as

$$
\begin{aligned}
0 \;=\; & \int_\Omega w_1\{\mu(Q+\chi_{1,22})+\kappa(Q+E_{,2})(CC+EE+DD+FF)\\
& -\kappa(Q+C_{,2}+E_{,1}+E_{,2})(CC+CE+EC+EE+DD\\
& +DF+FD+FF)+\kappa(C+E)(2QC+2E_{,1}E+2C_{,2}C\\
& +2E_{,2}E-QC-QE-E_{,2}C-E_{,2}E-CQ-CE_{,1}\\
& -EC_{,2}-EE_{,2}+2RD+2F_{,1}F+2D_{,2}D+2F_{,2}F-RD\\
& -RF-F_{,2}D-F_{,2}F-DR-DF_{,1}-FD_{,2}-FF_{,2})\\
& -A_0\chi_{2,2}+B_0\chi_{2,1}+(1-e^{-\delta\alpha\hat\gamma^m})[\frac{E_{11}}{4}\{2(QC+RD)(CC+DD)\\
& +2(CC+DD)(QC+RD)\}+(E_{12}-E_{11})(QC+RD)]C\\
& +(1-e^{-\delta\alpha\hat\gamma^m})[\frac{E_{11}}{4}(CC+DD)(CC+DD)\\
& +\frac{(E_{12}-E_{11})}{2}(CC+DD)+\frac{(E_{11}-2E_{12})}{4}]Q\\
& +(1-e^{-\delta\alpha\hat\gamma^m})[\frac{E_{21}}{4}\{2(SD+NF)(EE+FF)\\
& +2(EE+FF)(SE+NF)\}+(E_{22}-E_{21})(SE+NF)]E\\
& +(1-e^{-\delta\alpha\hat\gamma^m})[\frac{E_{21}}{4}(EE+FF)(EE+FF)\\
& +\frac{(E_{22}-E_{21})}{2}(EE+FF)+\frac{(E_{21}-2E_{22})}{4}]S\\
& -c(Q_{,11}+S_{,22})-T(Q_{,22}+S_{,11})\}d\Omega,
\end{aligned}
$$

$$0 = \int_\Omega w_2 \{ \mu(R + \chi_{2,22}) + \kappa(R + F_{,2})(CC + EE + DD + FF)$$
$$-\kappa(R + D_{,2} + F_{,1} + F_{,2})(CC + CE + EC + EE + DD$$
$$+DF + FD + FF) + \kappa(D + F)(2QC + 2E_{,1}E + 2C_{,2}C$$
$$+2E_{,2}E - QC - QE - E_{,2}C - E_{,2}E - CQ - CE_{,1}$$
$$-EC_{,2} - EE_{,2} + 2RD + 2F_{,1}F + 2D_{,2}D + 2F_{,2}F - RD$$
$$-RF - F_{,2}D - F_{,2}F - DR - DF_{,1} - FD_{,2} - FF_{,2})$$
$$-A_0\chi_{2,2} + B_0\chi_{2,1} + (1 - e^{-\delta\alpha\hat{\gamma}^m})[\frac{E_{11}}{4}\{2(QC + RD)(CC + DD)$$
$$+2(CC + DD)(QC + RD)\} + (E_{12} - E_{11})(QC + RD)]D$$
$$+(1 - e^{-\delta\alpha\hat{\gamma}^m})[\frac{E_{11}}{4}(CC + DD)(CC + DD)$$
$$+\frac{(E_{12} - E_{11})}{2}(CC + DD) + \frac{(E_{11} - 2E_{12})}{4}]R$$
$$+(1 - e^{-\delta\alpha\hat{\gamma}^m})[\frac{E_{21}}{4}\{2(SD + NF)(EE + FF)$$
$$+2(EE + FF)(SE + NF)\} + (E_{22} - E_{21})(SE + NF)]F$$
$$+(1 - e^{-\delta\alpha\hat{\gamma}^m})[\frac{E_{21}}{4}(EE + FF)(EE + FF)$$
$$+\frac{(E_{22} - E_{21})}{2}(EE + FF) + \frac{(E_{21} - 2E_{22})}{4}]N$$
$$-c(R_{,11} + N_{,22}) - T(R_{,22} + N_{,11})\}d\Omega,$$

$$0 = \int_\Omega w_3(Q - \chi_{1,11})d\Omega, \ 0 = \int_\Omega w_4(R - \chi_{2,11})d\Omega,$$
$$0 = \int_\Omega w_5(C - \chi_{1,1})d\Omega, \ 0 = \int_\Omega w_6(D - \chi_{2,1})d\Omega,$$
$$0 = \int_\Omega w_7(E - \chi_{1,2})d\Omega, \ 0 = \int_\Omega w_8(F - \chi_{2,2})d\Omega,$$
$$0 = \int_\Omega w_9(S - \chi_{1,22})d\Omega, \ 0 = \int_\Omega w_{10}(N - \chi_{2,22})d\Omega,$$
$$0 = \int_\Omega w_{11}(A - \mu(Q + \chi_{1,22}) - cQ_{,11})d\Omega,$$
$$0 = \int_\Omega w_{12}(B - \mu(R + \chi_{2,22}) - cR_{,11})d\Omega. \tag{6.79}$$

Thus, we apply integration by part and the Green-Stokes' theorem, (e.g. $\mu\int_{\Omega^e} w_1\chi_{1,22}d\Omega = -\mu\int_{\Omega^e} w_{1,2}\chi_{1,2}d\Omega + \mu\int_{\partial\Gamma} w_1\chi_{1,2}Nd\Gamma$) and thereby obtain the following weak forms of Eq. (6.79)

$$
\begin{aligned}
0 \;=\; & \int_\Omega \{\mu w_1 Q - \mu w_{1,2}\chi_{1,2} + \kappa w_1(Q+E_{,2})(CC+EE+DD+FF) \\
& -\kappa w_1(Q+C_{,2}+E_{,1}+E_{,2})(CC+CE+EC+EE+DD \\
& +DF+FD+FF) + \kappa w_1(C+E)(2QC+2E_{,1}E+2C_{,2}C \\
& +2E_{,2}E-QC-QE-E_{,2}C-E_{,2}E-CQ-CE_{,1} \\
& -EC_{,2}-EE_{,2}+2RD+2F_{,1}F+2D_{,2}D+2F_{,2}F-RD \\
& -RF-F_{,2}D-F_{,2}F-DR-DF_{,1}-FD_{,2}-FF_{,2}) \\
& +(1-e^{-\delta\alpha\hat\gamma^m})w_1[\frac{E_{11}}{4}(2(QC+RD)(CC+DD) \\
& +2(CC+DD)(QC+RD)) + (E_{12}-E_{11})(QC+RD)]C \\
& +(1-e^{-\delta\alpha\hat\gamma^m})w_1[\frac{E_{11}}{4}(CC+DD)(CC+DD) \\
& +\frac{(E_{12}-E_{11})}{2}(CC+DD) + \frac{(E_{11}-2E_{12})}{4}]Q \\
& +(1-e^{-\delta\alpha\hat\gamma^m})w_1[\frac{E_{21}}{4}(2(SD+NF)(EE+FF) \\
& +2(EE+FF)(SE+NF)) + (E_{22}-E_{21})(SE+NF)]E \\
& +(1-e^{-\delta\alpha\hat\gamma^m})w_1[\frac{E_{21}}{4}(EE+FF)(EE+FF) \\
& +\frac{(E_{22}-E_{21})}{2}(EE+FF) + \frac{(E_{21}-2E_{22})}{4}]S \\
& +c(w_{1,1}Q_{,1}+w_{1,2}S_{,2})+T(w_{1,2}Q_{,2}+w_{1,1}S_{,1}) \\
& -A_0 w_1\chi_{2,2}+B_0 w_1\chi_{2,1}\}d\Omega + \mu\int_{\partial\Gamma} w_1\chi_{1,2}Nd\Gamma \\
& -c\int_{\partial\Gamma} w_1 Q_{,1}Nd\Gamma - c\int_{\partial\Gamma} w_1 S_{,2}Nd\Gamma - T\int_{\partial\Gamma} w_1 Q_{,2}Nd\Gamma \\
& -T\int_{\partial\Gamma} w_1 S_{,1}Nd\Gamma,
\end{aligned}
$$

$$
\begin{aligned}
0 \;=\; & \int_{\Omega}\{w_2\mu R - w_{2,2}\mu\chi_{2,2} + \kappa w_2(R + F_{,2})(CC + EE + DD + FF) \\
& -\kappa w_2(R + D_{,2} + F_{,1} + F_{,2})(CC + CE + EC + EE + DD \\
& +DF + FD + FF) + \kappa w_2(D + F)(2QC + 2E_{,1}E + 2C_{,2}C \\
& +2E_{,2}E - QC - QE - E_{,2}C - E_{,2}E - CQ - CE_{,1} \\
& -EC_{,2} - EE_{,2} + 2RD + 2F_{,1}F + 2D_{,2}D + 2F_{,2}F - RD \\
& -RF - F_{,2}D - F_{,2}F - DR - DF_{,1} - FD_{,2} - FF_{,2}) \\
& +(1 - e^{-\delta\alpha\hat{\gamma}^m})w_2[\frac{E_{11}}{4}(2(QC + RD)(CC + DD) \\
& +2(CC + DD)(QC + RD)) + (E_{12} - E_{11})(QC + RD)]D \\
& +(1 - e^{-\delta\alpha\hat{\gamma}^m})w_2[\frac{E_{11}}{4}(CC + DD)(CC + DD) \\
& +\frac{(E_{12} - E_{11})}{2}(CC + DD) + \frac{(E_{11} - 2E_{12})}{4}]R \\
& +(1 - e^{-\delta\alpha\hat{\gamma}^m})w_2[\frac{E_{21}}{4}(2(SD + NF)(EE + FF) \\
& +2(EE + FF)(SE + NF)) + (E_{22} - E_{21})(SE + NF)]F \\
& +(1 - e^{-\delta\alpha\hat{\gamma}^m})w_2[\frac{E_{21}}{4}(EE + FF)(EE + FF) \\
& +\frac{(E_{22} - E_{21})}{2}(EE + FF) + \frac{(E_{21} - 2E_{22})}{4}]N \\
& +c(w_{2,1}R_{,1} + w_{2,2}N_{,2}) + T(w_{2,2}R_{,2} + w_{2,1}N_{,1}) \\
& +A_0 w_2\chi_{1,2} - B_0 w_2\chi_{1,1}\}d\Omega + \mu\int_{\partial\Gamma} w_2\chi_{2,2}Nd\Gamma \\
& -c\int_{\partial\Gamma} w_2 R_{,1}Nd\Gamma - c\int_{\partial\Gamma} w_2 N_{,2}Nd\Gamma - T\int_{\partial\Gamma} w_2 R_{,2}Nd\Gamma \\
& -T\int_{\partial\Gamma} w_2 N_{,1}Nd\Gamma,
\end{aligned}
$$

$$0 = \int_\Omega (w_3 Q + w_{3,1}\chi_{1,1})d\Omega - \int_{\partial\Gamma} w_3\chi_{1,1}Nd\Gamma,$$

$$0 = \int_\Omega (w_4 R + w_{4,1}\chi_{2,1})d\Omega - \int_{\partial\Gamma} w_{4,1}\chi_{2,1}Nd\Gamma,$$

$$0 = \int_\Omega (w_5 C - w_5\chi_{1,1})d\Omega, \ 0 = \int_\Omega w_6(D - \chi_{2,1})d\Omega,$$

$$0 = \int_\Omega w_7(E - \chi_{1,2})d\Omega, \ 0 = \int_\Omega w_8(F - \chi_{2,2})d\Omega,$$

$$0 = \int_\Omega (w_{9,2}S + w_{9,2}\chi_{1,2})d\Omega - \int_{\partial\Gamma} w_9\chi_{1,2}Nd\Gamma,$$

$$0 = \int_\Omega (w_{10,2}N + w_{10,2}\chi_{2,2})d\Omega - \int_{\partial\Gamma} w_{10}\chi_{2,2}Nd\Gamma,$$

$$0 = \int_\Omega (w_{11}A - \mu w_1 Q + \mu w_{11,2}\chi_{1,2} + cw_{11,1}Q_{,1})d\Omega - \int_{\partial\Gamma} \mu w_{11}\chi_{1,2}Nd\Gamma$$
$$- \int_{\partial\Gamma} cw_{11}Q_{,1}Nd\Gamma,$$

$$0 = \int_\Omega (w_{12}B - \mu w_{12}R + \mu w_{12,2}\chi_{2,2} + cw_{12,1}R_{,1})d\Omega - \int_{\partial\Gamma} \mu w_{12}\chi_{2,2}Nd\Gamma$$
$$- \int_{\partial\Gamma} cw_{12}R_{,1}Nd\Gamma, \tag{6.80}$$

where Ω, $\partial\Gamma$ and N are, respectively the domain of interest, the associated boundary, and the rightward unit normal to the boundary $\partial\Gamma$ in the sense of the Green-Stokes' theorem. The unknown potentials of χ_1, χ_2, Q, R, C, D, E, F, S, N, A and B can be expressed in the form of Lagrangian polynomial that

$$(*) = \sum_{j=1}^{n=4} [(*)_j \Psi_j(x,y)]. \tag{6.81}$$

Accordingly, the test function w is found to be

$$w_m = \sum_{i=1}^{n=4} w_m^i \Psi_i(x,y); \ i = 1,2,3,4, \ \text{and} \ m = 1,2,3,4,...10 \tag{6.82}$$

where w_i is the weight of the test function and $\Psi_i(x,y)$ are the associated shape functions; $\Psi_1 = \frac{(x-2)(y-1)}{2}$, $\Psi_2 = \frac{x(y-1)}{-2}$, $\Psi_3 = \frac{xy}{2}$ and $\Psi_4 = \frac{y(x-2)}{-2}$. Invoking Eq. (6.81), (6.80) can be recast in terms of Lagrangian polynomial representation as

$$
\begin{aligned}
0 \;=\; & \sum_{i,j=1}^{n=4}\Big\{\int_{\Omega^e}(\mu\Psi_i\Psi_j Q_j - \mu\Psi_{i,2}\Psi_{j,2}\chi_{1j} + \kappa(\Psi_i\Psi_j Q_j + \Psi_{i,2}\Psi_{j,2}E_j)(CC+EE \\
& +DD+FF) - \kappa(\Psi_i\Psi_j Q_j + \Psi_i\Psi_{j,2}C_j + \Psi_i\Psi_{j,1}E_j + \Psi_i\Psi_{j,2}E_j)(CC+CE \\
& +EC+EE+DD+DF+FD+FF) + \kappa(C+E)(2\Psi_i\Psi_j QC_j + 2\Psi_i\Psi_{j,1}E_j E \\
& +2\Psi_i\Psi_{j,2}C_j C + 2\Psi_i\Psi_{j,2}E_j E - \Psi_i\Psi_j QC - \Psi_i\Psi_j QE - \Psi_i\Psi_{j,2}E_j C \\
& -\Psi_i\Psi_{j,2}E_j E - \Psi_i\Psi_j CQ - \Psi_i\Psi_{j,1}CE_j - \Psi_i\Psi_{j,2}EC_j - \Psi_i\Psi_{j,2}EE_j + 2\Psi_i\Psi_j RD \\
& +2\Psi_i\Psi_{j,1}F_j F + 2\Psi_i\Psi_{j,2}D_j D + 2\Psi_i\Psi_{j,2}F_j F - \Psi_i\Psi_j RD - \Psi_i\Psi_j RF - \Psi_i\Psi_{j,2}F_j D \\
& -\Psi_i\Psi_{j,2}F_j F - \Psi_i\Psi_j DR - \Psi_i\Psi_{j,1}DF_j - \Psi_i\Psi_{j,2}FD_j - \Psi_i\Psi_{j,2}FF_j) \\
& +(1-e^{-\delta\alpha\hat\gamma^m})\Psi_i[\frac{E_{11}}{4}(2(QC+RD)(CC+DD) + 2(CC+DD)(QC+RD)) \\
& +(E_{12}-E_{11})(QC+RD)]\Psi_j C_j + (1-e^{-\delta\alpha\hat\gamma^m})\Psi_i[\frac{E_{11}}{4}(CC+DD)(CC+DD) \\
& +\frac{(E_{12}-E_{11})}{2}(CC+DD) + \frac{(E_{11}-2E_{12})}{4}]\Psi_j Q_j + (1-e^{-\delta\alpha\hat\gamma^m})\Psi_i[\frac{E_{21}}{4}(2(SD \\
& +NF)(EE+FF) + 2(EE+FF)(SE+NF)) + (E_{22}-E_{21})(SE+NF)]\Psi_j E_j \\
& +(1-e^{-\delta\alpha\hat\gamma^m})\Psi_i[\frac{E_{21}}{4}(EE+FF)(EE+FF) + \frac{(E_{22}-E_{21})}{2}(EE+FF) \\
& +\frac{(E_{21}-2E_{22})}{4}]\Psi_j S_j + c(\Psi_{i,1}\Psi_{j,1}Q_j + \Psi_{i,2}\Psi_{j,2}S_j) + T(\Psi_{i,1}\Psi_{j,2}Q_j + \Psi_{i,1}\Psi_{j,1}S_j) \\
& -A_0\Psi_i\Psi_{j,2}\chi_{2j} + B_0\Psi_i\Psi_{j,1}\chi_{2j})d\Omega\Big\} + \sum_{i=1}^{n=4}\Big\{\mu\int_{\partial\Gamma^e}\Psi_i\chi_{1,2}Nd\Gamma - c\int_{\partial\Gamma^e}\Psi_i Q_{,1}Nd\Gamma \\
& -c\int_{\partial\Gamma}\Psi_i S_{,2}Nd\Gamma - T\int_{\partial\Gamma}\Psi_i Q_{,2}Nd\Gamma - T\int_{\partial\Gamma}\Psi_i S_{,1}Nd\Gamma\Big\},
\end{aligned}
$$

$$
\begin{aligned}
0 \;=\; & \sum_{i,j=1}^{n=4}\Big\{\int_{\Omega^e}(\mu\Psi_i\Psi_j R_j - \mu\Psi_{i,2}\Psi_{j,2}\chi_{2j} + \kappa(\Psi_i\Psi_j R_j + \Psi_{i,2}\Psi_{j,2}F_j)(CC + EE \\
& + DD + FF) - \kappa(\Psi_i\Psi_j R + \Psi_i\Psi_{j,2}D_j + \Psi_i\Psi_{j,1}F_j + \Psi_i\Psi_{j,2}F_j)(CC + CE \\
& + EC + EE + DD + DF + FD + FF) + \kappa w_2(D + F)(2\Psi_i\Psi_j QC_j \\
& + 2\Psi_i\Psi_{j,1}E_j E + 2\Psi_i\Psi_{j,2}C_j C + 2\Psi_i\Psi_{j,2}E_j E - \Psi_i\Psi_j QC - \Psi_i\Psi_j QE \\
& - \Psi_i\Psi_{j,2}E_j C - \Psi_i\Psi_{j,2}E_j E - \Psi_i\Psi_j CQ - \Psi_i\Psi_{j,1}CE_j - \Psi_i\Psi_{j,2}EC_j \\
& - \Psi_i\Psi_{j,2}EE_j + 2\Psi_i\Psi_j RD + 2\Psi_i\Psi_{j,1}F_j F + 2\Psi_i\Psi_{j,2}D_j D + 2\Psi_i\Psi_{j,2}F_j F \\
& - \Psi_i\Psi_j RD - \Psi_i\Psi_j RF - \Psi_i\Psi_{j,2}F_j D - \Psi_i\Psi_{j,2}F_j F - \Psi_i\Psi_j DR - \Psi_i\Psi_{j,1}DF_j \\
& - \Psi_i\Psi_{j,2}FD_j - \Psi_i\Psi_{j,2}FF_j) + (1 - e^{-\delta\alpha\hat{\gamma}^m})\Psi_i[\tfrac{E_{11}}{4}(2(QC + RD)(CC + DD) \\
& + 2(CC + DD)(QC + RD)) + (E_{12} - E_{11})(QC + RD)]\Psi_j D_j(1 - e^{-\delta\alpha\hat{\gamma}^m}) \\
& \Psi_i[\tfrac{E_{11}}{4}(CC + DD)(CC + DD) + \tfrac{(E_{12} - E_{11})}{2}(CC + DD) \\
& + \tfrac{(E_{11} - 2E_{12})}{4}]\Psi_j R_j + (1 - e^{-\delta\alpha\hat{\gamma}^m})\Psi_i[\tfrac{E_{21}}{4}(2(SD + NF)(EE + FF) \\
& + 2(EE + FF)(SE + NF)) + (E_{22} - E_{21})(SE + NF)]\Psi_j F_j + (1 - e^{-\delta\alpha\hat{\gamma}^m}) \\
& \Psi_i[\tfrac{E_{21}}{4}(EE + FF)(EE + FF) + \tfrac{(E_{22} - E_{21})}{2}(EE + FF) \\
& + \tfrac{(E_{21} - 2E_{22})}{4}]\Psi_j N_j + c(\Psi_{i,1}\Psi_{j,1}R_j + \Psi_{i,2}\Psi_{j,2}N_j) + T(\Psi_{i,2}\Psi_{j,2}R_j \\
& + \Psi_{i,1}\Psi_{j,1}N_j) + A_0\Psi_i\Psi_{j,2}\chi_{1j} - B_0\Psi_i\Psi_{j,1}\chi_{1j} + c\Psi_{i,1}\Psi_{j,1}R_j)d\Omega\Big\} \\
& + \sum_{i=1}^{n=4}\Big\{\mu\int_{\partial\Gamma^e}\Psi_i\chi_{2,2}Nd\Gamma - c\int_{\partial\Gamma^e}\Psi_i R_{,1}Nd\Gamma - c\int_{\partial\Gamma}\Psi_i N_{,2}Nd\Gamma \\
& - T\int_{\partial\Gamma}\Psi_i R_{,2}Nd\Gamma - T\int_{\partial\Gamma}\Psi_i N_{,1}Nd\Gamma\Big\},
\end{aligned}
$$

$$
\begin{aligned}
0 &= \sum_{i,j=1}^{n=4}\{\int_{\Omega^e}\Psi_i\Psi_j Q_j d\Omega\} + \sum_{i,j=1}^{n=4}\{\int_{\Omega^e}\Psi_{i,1}\Psi_{j,1}\chi_{1j}d\Omega\} - \sum_{i=1}^{n=4}\{\int_{\partial\Gamma^e}\Psi_i\chi_{1,1}Nd\Gamma\}, \\
0 &= \sum_{i,j=1}^{n=4}\{\int_{\Omega^e}\Psi_i\Psi_j R_j d\Omega\} + \sum_{i,j=1}^{n=4}\{\int_{\Omega^e}\Psi_{i,1}\Psi_{j,1}\chi_{2j}d\Omega\} - \sum_{i=1}^{n=4}\{\int_{\partial\Gamma^e}\Psi_i\chi_{2,1}Nd\Gamma\}, \\
0 &= \sum_{i,j=1}^{n=4}\{\int_{\Omega^e}\Psi_i\Psi_j C_j d\Omega\} - \sum_{i,j=1}^{n=4}\{\int_{\Omega^e}\Psi_i\Psi_{j,1}\chi_{1j}d\Omega\}, \\
0 &= \sum_{i,j=1}^{n=4}\{\int_{\Omega^e}\Psi_i\Psi_j D_j d\Omega\} - \sum_{i,j=1}^{n=4}\{\int_{\Omega^e}\Psi_i\Psi_{j,1}\chi_{2j}d\Omega\}, \\
0 &= \sum_{i,j=1}^{n=4}\{\int_{\Omega^e}\Psi_i\Psi_j E_j d\Omega\} - \sum_{i,j=1}^{n=4}\{\int_{\Omega^e}\Psi_i\Psi_{j,2}\chi_{1j}d\Omega\}, \\
0 &= \sum_{i,j=1}^{n=4}\{\int_{\Omega^e}\Psi_i\Psi_j F_j d\Omega\} - \sum_{i,j=1}^{n=4}\{\int_{\Omega^e}\Psi_i\Psi_{j,2}\chi_{2j}d\Omega\}, \\
0 &= \sum_{i,j=1}^{n=4}\{\int_{\Omega}(\Psi_{i,2}\Psi_j S_j + \Psi_{i,2}\Psi_{j,2}\chi_{1j})d\Omega\} - \int_{\partial\Gamma}\Psi_i\chi_{1,2}Nd\Gamma, \\
0 &= \sum_{i,j=1}^{n=4}\{\int_{\Omega}(\Psi_{i,2}\Psi_j N_j + \Psi_{i,2}\Psi_{j,2}\chi_{2j})d\Omega\} - \int_{\partial\Gamma}\Psi_i\chi_{2,2}Nd\Gamma, \\
0 &= \sum_{i,j=1}^{n=4}\{\int_{\Omega^e}\Psi_i\Psi_j d\Omega\}A_j + \sum_{i,j=1}^{n=4}\{\int_{\Omega^e}(-\mu\Psi_i\Psi_j + c\Psi_{i,1}\Psi_{j,1})d\Omega\}Q_j \\
&\quad + \sum_{i,j=1}^{n=4}\{\int_{\Omega^e}\mu\Psi_{i,2}\Psi_{j,2}\chi_{1j}d\Omega\} - \sum_{i=1}^{n=4}\{\int_{\partial\Gamma^e}\mu\Psi_i\chi_{1,2}Nd\Gamma - \int_{\partial\Gamma^e}c\Psi_i Q_{,1}Nd\Gamma\}, \\
0 &= \sum_{i,j=1}^{n=4}\{\int_{\Omega^e}\Psi_i\Psi_j B_j d\Omega\} + \sum_{i,j=1}^{n=4}\{\int_{\Omega^e}(-\mu\Psi_i\Psi_j + c\Psi_{i,1}\Psi_{j,1}R_j)d\Omega\} \\
&\quad + \sum_{i,j=1}^{n=4}\{\int_{\Omega^e}\mu\Psi_{i,2}\Psi_{j,2}\chi_{2j}d\Omega\} - \sum_{i=1}^{n=4}\{\int_{\partial\Gamma^e}\mu\Psi_i\chi_{2,2}Nd\Gamma \\
&\quad - \int_{\partial\Gamma^e}c\Psi_i R_{,1}Nd\Gamma\}. \quad (6.83)
\end{aligned}
$$

Now, for the local stiffness matrices and forcing vectors for each elements, we find

$$
\begin{bmatrix}
K_{11}^{11} & K_{12}^{11} & K_{13}^{11} & K_{14}^{11} \\
K_{21}^{11} & K_{22}^{11} & K_{23}^{11} & K_{24}^{11} \\
K_{31}^{11} & K_{32}^{11} & K_{33}^{11} & K_{34}^{11} \\
K_{41}^{11} & K_{42}^{11} & K_{43}^{11} & K_{44}^{11}
\end{bmatrix}_{Local}
\begin{bmatrix}
\chi_1^1 \\
\chi_1^2 \\
\chi_1^3 \\
\chi_1^4
\end{bmatrix}_{Local}
=
\begin{bmatrix}
F_1^1 \\
F_2^1 \\
F_3^1 \\
F_4^1
\end{bmatrix}_{Local}, \quad (6.84)
$$

where

$$\left[K_{ij}^{11}\right] = \int_{\Omega}(-\mu\Psi_{i,2}\Psi_{j,2})d\Omega, \tag{6.85}$$

and

$$\{F_i^1\} = -\mu\int_{\partial\Gamma^e} w_i\chi_{1,2}Nd\Gamma + c\int_{\partial\Gamma^e} w_iQ_{,1}Nd\Gamma. \tag{6.86}$$

Thus, the unknown potentials (i.e. χ_1, χ_2, Q, R,C,D,E,F, A and B) can be expressed as

$$Q_i = \{\chi_1^i\}_{,11}, \ R_i = \{\chi_2^i\}_{,11}, \ S_i = \{Q^i\}_{,11} \text{ etc...,} \tag{6.87}$$

and similarly for the rest of unknowns.

Consequently, we obtain the following systems of equations (in the Global form) for each individual elements as

$$\begin{bmatrix} \left[K_{ij}^{0101}\right] & \left[K_{ij}^{0102}\right] & . & . & . & . & . & . & . & \left[K_{ij}^{0111}\right] & \left[K_{ij}^{0112}\right] \\ \left[K_{ij}^{0201}\right] & \left[K_{ij}^{0202}\right] & . & . & . & . & . & . & . & \left[K_{ij}^{0211}\right] & \left[K_{ij}^{0212}\right] \\ \left[K_{ij}^{0301}\right] & \left[K_{ij}^{0302}\right] & . & . & . & . & . & . & . & \left[K_{ij}^{0311}\right] & \left[K_{ij}^{0312}\right] \\ \left[K_{ij}^{0401}\right] & \left[K_{ij}^{0402}\right] & . & . & . & . & . & . & . & \left[K_{ij}^{0411}\right] & \left[K_{ij}^{0412}\right] \\ \left[K_{ij}^{0501}\right] & \left[K_{ij}^{0502}\right] & . & . & . & . & . & . & . & \left[K_{ij}^{0511}\right] & \left[K_{ij}^{0512}\right] \\ \left[K_{ij}^{0601}\right] & \left[K_{ij}^{0602}\right] & . & . & . & . & . & . & . & \left[K_{ij}^{0611}\right] & \left[K_{ij}^{0612}\right] \\ \left[K_{ij}^{0701}\right] & \left[K_{ij}^{0702}\right] & . & . & . & . & . & . & . & \left[K_{ij}^{0711}\right] & \left[K_{ij}^{0712}\right] \\ \left[K_{ij}^{0801}\right] & \left[K_{ij}^{0802}\right] & . & . & . & . & . & . & . & \left[K_{ij}^{0811}\right] & \left[K_{ij}^{0812}\right] \\ \left[K_{ij}^{0901}\right] & \left[K_{ij}^{0902}\right] & . & . & . & . & . & . & . & \left[K_{ij}^{0911}\right] & \left[K_{ij}^{0912}\right] \\ \left[K_{ij}^{1001}\right] & \left[K_{ij}^{1002}\right] & . & . & . & . & . & . & . & \left[K_{ij}^{1011}\right] & \left[K_{ij}^{1012}\right] \\ \left[K_{ij}^{1101}\right] & \left[K_{ij}^{1102}\right] & . & . & . & . & . & . & . & \left[K_{ij}^{1111}\right] & \left[K_{ij}^{1112}\right] \\ \left[K_{ij}^{1201}\right] & \left[K_{ij}^{1202}\right] & . & . & . & . & . & . & . & \left[K_{ij}^{1211}\right] & \left[K_{ij}^{1212}\right] \end{bmatrix} \begin{bmatrix} \chi_1^i \\ \chi_2^i \\ Q_i \\ R_i \\ C_i \\ D_i \\ E_i \\ F_i \\ S_i \\ N_i \\ A_i \\ B_i \end{bmatrix} = \begin{bmatrix} \{F_1\} \\ \{F_2\} \\ \{F_3\} \\ \{F_4\} \\ \{F_5\} \\ \{F_6\} \\ \{F_7\} \\ \{F_8\} \\ \{F_9\} \\ \{F_{10}\} \\ \{F_{11}\} \\ \{F_{12}\} \end{bmatrix}.$$

$$\tag{6.88}$$

In the simulation, we employed the following convergence criteria

$$|A_{n+1} - A_n| = e_1 \le \varepsilon, \ \ |B_{n+1} - B_n| = e_2 \le \varepsilon, \text{ where } \varepsilon = \text{maximum error} = 10^{-10},$$

which demonstrates fast (quadratic) convergence within just 5 iterations using FEn-iCS nonlinear solver (see, 6.1).

6.6   Denouement

In this chapter, continuum model for the mechanics of a hyperelastic materials reinforced with fibrous materials is presented in finite plane elastostatics. The hyperelastic response of the elastomeric matrix material is accommodated by the Mooney-Rivlin

Table 6.1: Maximum numerical errors with respect to the number of iterations.

Number of iteration	Mximum error
1	1.000e-00
2	2.934e-00
3	1.132e-02
4	2.976e-07
5	7.416e-14

model, while the nonlinear stress-strain behaviors of the reinforcing fibers are assimilated via the custom designed energy potentials of the polynomial types. The kinematics of reinforcing fibers are formulated by their position and direction fields and are subsequently integrated into the models of continuum deformation via the first and second gradient of deformations. We have implemented two different types of pseudo-elastic behaviors of the soft composite. To accommodate the Mullin's effect observed in the soft biological tissues, we have incorporated the damage parameter and damage function with the proposed model inspired from the Ogden and Roxburgh's model. Moreover, to capture the softening phenomena as a result of the bond rupture and fiber damage we have included the Weibull damage variable in our model. Within the framework of variational principles and virtual work statement, the Euler equilibrium equation and the necessary boundary conditions are derived. These, together with the constraint of the bulk incompressibility, furnish systems of coupled nonlinear PDEs from which a set of numerical solutions describing the pseudo-elastic responses of the soft composites are obtained via the custom-built Finite Element Analysis (FEA) procedure. Finally, the utilities of the presented models are justified by comparing them with the data from multiple experiments.

We demonstrated that the model successfully predict the Mullins effect of human aorta in both longitudinal and circumferential direction. Also the proposed model can simulate the Mullins effect observed in soft biological tissue like Manduca Muscle. To test the utility of the proposed model in capturing the softening due to fiber damage, the model was compared against the in house experiment results of polyester fiber reinforced ecoflex elastomeric composite. Where it can be observed that the model can closely simulate the fiber damage phenomena, deformation profiles and shear angles profiles of the elastomeric composite.

Chapter 7

A multiscale continuum model for the mechanics of hyperelastic composite reinforced with nanofibers

In section 7.1, we present two distinct stages pertaining to the modeling of randomly oriented nanofiber-reinforced hyperelastic composite. In section 7.1.1, the kinematics is presented for unidirectional fibers embedded in a hyperelastic matrix material. In section 7.1.2, the obtained unidirectional fiber system is transformed into a randomly oriented short fiber-matrix system by employing the concepts of shear lag and Krenchel orientation parameters. The equilibrium and boundary conditions are derived in section 7.2. In section 7.3, the interfacial debonding-induced damage mechanics is presented for the hyperelastic nanocomposite material. In section 7.4, the utility of the presented model is demonstrated by comparing it against MD simulation results and experimental results from the existing literature.

7.1 Kinematics of fibers embedded in a hyperelastic matrix material

In this section, we present three distinct stages pertaining to the modeling of fiber-reinforced composites, where randomly oriented nanofibers are embedded in a hyperelastic matrix material (see, Fig. 7.1). We begin with the derivation of compact kinematic descriptions for a unidirectional fiber family in terms of the first and sec-

ond gradient of continuum deformations (Fig. 7.1 (a)). This offers a more general mapping of fiber kinematics including stretch and bending responses resulting in phenomenologically relevant predictions such as smooth and continuous shear strain distributions (see, for example, [87],[125], and [180]). We then reformulate the obtained unidirectional model into an aligned short fiber-matrix system by employing the concept of shear lag parameter (Fig. 7.1 (b)). The continuum shear lag theory accounts for the effects of fiber's characteristic dimension toward the mechanical responses of composites [181]-[182]. For example, the reinforcing performance of fibers becomes intensified with increasing fiber aspect ratios as the tensile stress in the fibers may build up to the maximum load-carrying capacity and vice versa [181]. The shear lag parameter integrated model is expected to capture the responses of composites with respect to the size of fibers. Lastly, we adopt the Krenchel orientation factor through which the configurations of aligned fibers may be transformed into randomly oriented nanofibers (Fig. 7.1 (c)). As also reported in [183], one could achieve a more comprehensive and accurate prediction of the mechanical responses of fiber composites by implementing the Krenchel orientation and shear lag parameter.
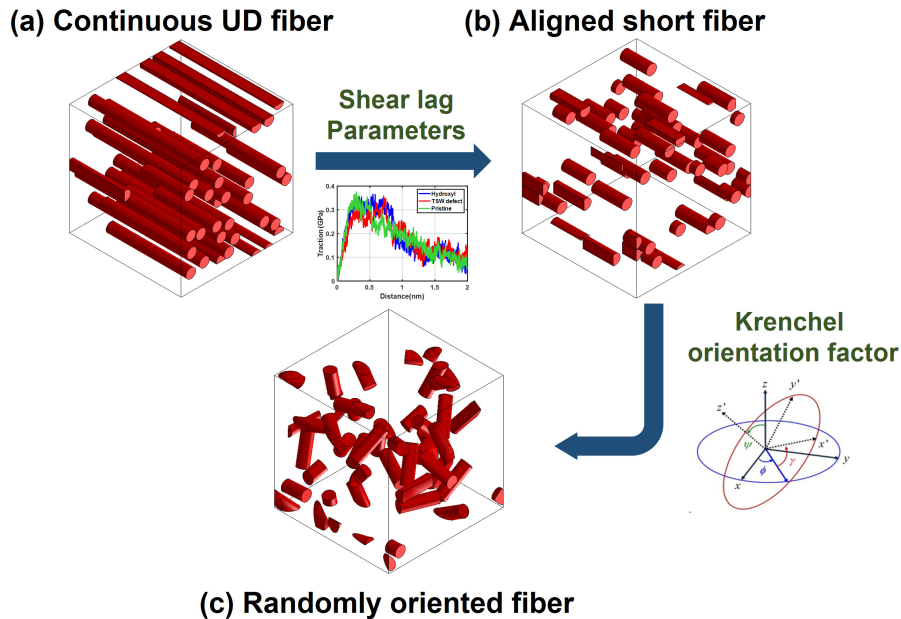
Figure 7.1: Illustration of the development of nanofiber composite model.

7.1.1 Development of the unidirectional fiber-matrix system

Let $\mathbf{r}(s)$ be the parametric curve of fibers' trajectory on the deformed configuration and $\boldsymbol{\tau}$ be the unit tangent in the direction of increasing arclength parameter s. We also define $\mathbf{X}(S)$ and S as the counterparts of $\mathbf{r}(s)$ and s in the reference configuration. The configuration of a particular fiber is then obtained by

$$\lambda = |\mathbf{d}| \text{ and } \lambda\boldsymbol{\tau} = \mathbf{d}; \ \lambda \equiv \frac{ds}{dS} \text{ and } \boldsymbol{\tau} \equiv \frac{d\mathbf{r}(s)}{ds}, \tag{7.1}$$

where

$$\mathbf{d} = \mathbf{FD}, \ \mathbf{F} = \lambda\boldsymbol{\tau} \otimes \mathbf{D}, \tag{7.2}$$

and $\mathbf{F}$ is the gradient of the deformation function $(\boldsymbol{\chi}(\mathbf{X}))$. Eq. (7.2) can be obtained via the successive differentiation of $\mathbf{r}(s(S)) = \boldsymbol{\chi}(\mathbf{X}(S))$ with respect to the referential position vector $\mathbf{X}(S)$ and the arclength parameter S using chain rule, upon making the identification of $\mathbf{D} = d\mathbf{X}/dS$. Here, $d(*)/dS$ and $d(*)/ds$ refer to the arclength derivatives of $(*)$ along fibers' directions, respectively, in the reference and deformed configurations. Eq. (7.2) may be projected using the orthonormal bases of $\{\mathbf{E}_A :$ reference$\}$ and $\{\mathbf{e}_i :$ current$\}$ to yield

$$\lambda\tau_i = d_i = F_{iA}D_A \text{ for } \mathbf{D} = D_A\mathbf{E}_A, \ \mathbf{d} = d\mathbf{e}_i. \tag{7.3}$$

Further, using Eqs. (7.1)-(7.2), we find

$$\lambda^2 = \mathbf{FD} \cdot \mathbf{FD} = \mathbf{F}^T\mathbf{F} \cdot \mathbf{D} \otimes \mathbf{D}, \tag{7.4}$$

which will also be used in the later sections.

Now, the Green-Lagrange strain is defined by (see, also, [105] and [106])

$$\varepsilon = \frac{1}{2}\left(\lambda^2 - 1\right). \tag{7.5}$$

Hence, in view of Eq. (7.4), we find

$$\varepsilon = \frac{1}{2}\left(\mathbf{FD} \cdot \mathbf{FD} - 1\right) = \frac{1}{2}\left(F_{iA}F_{iB}D_AD_B - 1\right). \tag{7.6}$$

Accordingly, the variational derivatives of ε can be evaluated as

$$\dot{\varepsilon} = \varepsilon_{\mathbf{F}} \cdot \dot{\mathbf{F}} = \frac{\partial(1/2)(\mathbf{FD} \cdot \mathbf{FD} - 1)}{\partial\mathbf{F}} \cdot \dot{\mathbf{F}} = \mathbf{F}(\mathbf{D} \otimes \mathbf{D}) \cdot \dot{\mathbf{F}}, \text{ or equivalently,}$$

$$\dot{\varepsilon} = \varepsilon_{F_{iA}}\dot{F}_{iA} = F_{iB}D_BD_A\dot{F}_{iA}, \tag{7.7}$$

where the superposed dot ($\dot{\ast}$) refers to the variational derivatives with respect to a parameter ϵ at the particular configuration of the composite (i.e., $\epsilon = 0$) that labels a one-parameter family of deformations. The tensile responses of the unidirectional continuous fibers may be represented by a simple quadratic form of the energy potential as follows:

$$W(\varepsilon) = \frac{1}{2} E \varepsilon^2. \tag{7.8}$$

In the above, E is the material parameter, characterizing the tensile or elastic modulus of the fibers. From Eqs. (7.6)-(7.7), the variational derivative of Eq. (7.8) can be formulated as

$$
\begin{aligned}
\dot{W}(\varepsilon) &= W_\varepsilon \varepsilon_{F_{iA}} \dot{F}_{iA} = (E\varepsilon) \varepsilon_{F_{iA}} \dot{F}_{iA} \\
&= [\frac{E}{2}(\mathbf{FD} \cdot \mathbf{FD} - 1)]\mathbf{F}(\mathbf{D} \otimes \mathbf{D}) \cdot \dot{\mathbf{F}} \\
&= [\frac{E}{2} F_{jC} F_{jD} D_C D_D - 1] F_{iB} D_B D_A \dot{F}_{iA}.
\end{aligned}
\tag{7.9}
$$

The geodesic curvature of a parametric curve ($\mathbf{r}(s)$) is then formulated from Eqs. (7.2)-(7.3) that

$$\mathbf{g} \equiv \mathbf{r}'' = \frac{d(\frac{d\mathbf{r}(S)}{dS})}{dS} = \frac{\partial(\mathbf{FD})}{\partial \mathbf{X}} \frac{\partial \mathbf{X}}{\partial S} = \nabla[\mathbf{FD}]\mathbf{D}. \tag{7.10}$$

In general, most of the fibers are straight prior to deformations. Even slightly curved fibers may be idealized as 'fairly straight' fibers, considering their length scales with respect to the characteristic dimension of matrix materials. This further suggests that the gradient of the unit tangent in the reference configuration vanishes; i.e.,

$$\nabla \mathbf{D} = 0. \tag{7.11}$$

Thus, Eq. (7.10) deduces

$$\mathbf{g} = \nabla \mathbf{F}(\mathbf{D} \otimes \mathbf{D}) = \mathbf{G}(\mathbf{D} \otimes \mathbf{D}), \tag{7.12}$$

where we adopt the convention of the second gradient of deformations as

$$\nabla \mathbf{F} \equiv \mathbf{G}, \text{ and} \tag{7.13}$$

the associated compatibility condition of $\mathbf{G}$ is given by

$$G_{iAB} = F_{iA,B} = F_{iB,A} = G_{iBA}. \tag{7.14}$$

235

The bending response of the fiber can be represented as follows:

$$W(\mathbf{g}) = \frac{1}{2}C\mathbf{g} \cdot \mathbf{g}.$$

Here, $\frac{1}{2}C\mathbf{g} \cdot \mathbf{g}$ is the fiber's bending energy potential of Spencer and Soldatos type [93] which presumes that the bending responses of fibers are dependent entirely on the second gradient of continuum deformations via the geodesic curvature of fibers;

$$\mathbf{g} = \mathbf{g}(\mathbf{G}). \tag{7.15}$$

The associated modulus C is the bending modulus of the fiber. The postulation of Spencer and Soldatos has been widely and successfully adopted in the relevant subjects of studies (see, for example, [85], [111]–[113], [115], and [120]). The associated variational derivative can be computed as

$$\dot{W}(\mathbf{g}) = C\mathbf{g} \cdot \dot{\mathbf{g}} \overset{(7.11)=(7.12)}{=} C\mathbf{g} \cdot \dot{\mathbf{G}}(\mathbf{D} \otimes \mathbf{D}) = (C\mathbf{g} \otimes \mathbf{D} \otimes \mathbf{D}) \cdot \dot{\mathbf{G}}. \tag{7.16}$$

The forging developments suggest that the responses of an elastic material reinforced with fibers may be expressed by the first and second gradient of continuum deformations that

$$W(\mathbf{F}, \varepsilon, \mathbf{g}) = W(\mathbf{F}) + \frac{1}{2}E\varepsilon^2 + \frac{1}{2}C\mathbf{g} \cdot \mathbf{g}, \tag{7.17}$$

where $W(\mathbf{F})$ refers to the energy function of matrix material. In the present study, we adopt the Mooney-Rivlin strain energy potential for the characterization of hyperelastic matrix materials (see, also, [105]-[106]):

$$W(\mathbf{F}) = \frac{\mu}{2}(I_1 - 3) + \frac{\kappa}{2}(I_2 - 3), \tag{7.18}$$

where I_1 and I_2 are the principal invariants of the deformation gradient tensor defined by

$$I_1 = tr(\mathbf{F}^T\mathbf{F}) \text{ and } I_2 = \frac{1}{2}[(tr(\mathbf{F}^T\mathbf{F}))^2 - tr((\mathbf{F}^T\mathbf{F})^2)]. \tag{7.19}$$

Now, we may write the energy function of matrix material, $W(\mathbf{F})$, in variational form as follows:

$$W_{\mathbf{F}} \cdot \dot{\mathbf{F}} = [\frac{\mu}{2}(I_1)_{\mathbf{F}} + \frac{\kappa}{2}(I_2)_{\mathbf{F}}] \cdot \dot{\mathbf{F}} = [\mu\mathbf{F} + \kappa\mathbf{F}\{(\mathbf{F} \cdot \mathbf{F})\mathbf{I} - \mathbf{F}^T\mathbf{F}\}] \cdot \dot{\mathbf{F}}, \tag{7.20}$$

where $(I_1)_{\mathbf{F}} = 2\mathbf{F}$ and $(I_2)_{\mathbf{F}} = 2\mathbf{F}(I_1\mathbf{I} - \mathbf{F}^T \cdot \mathbf{F})$.

236

Lastly, we evaluate the induced energy variation of the response function (Eq. (7.17)) as

$$\dot{W}(\mathbf{F}, \varepsilon, \mathbf{g}) = W(\mathbf{F})_{\mathbf{F}} \cdot \dot{\mathbf{F}} + W(\varepsilon)_{\varepsilon} \varepsilon_{\mathbf{F}} \cdot \dot{\mathbf{F}} + C\mathbf{g} \cdot \dot{\mathbf{g}}, \qquad (7.21)$$

which will be used in the derivation of Euler equilibrium equation and the associated boundary conditions.

7.1.2 Transformation to the randomly oriented fiber-matrix system

In the previous section, we derived the kinematic expressions of continuous unidirectional fibers embedded in a hyperelastic matrix material. In this section, we reformulate the obtained expressions into a randomly oriented fiber-matrix system. To proceed, we introduce the following energy potential based on Eq. (7.17)

$$W(\mathbf{F}, \varepsilon, \mathbf{g}) = (1 - \alpha) \left[\frac{\mu}{2}(I_1 - 3) + \frac{\kappa}{2}(I_2 - 3) \right] + \alpha \left[\frac{1}{2} E \varepsilon^2 + \frac{1}{2} C\mathbf{g} \cdot \mathbf{g} \right], \qquad (7.22)$$

where α is the energy fraction parameter pertaining to the fiber volume fraction of composites. In the case of composite materials reinforced with discontinuous fibers, the load is transmitted from the matrix to the fibers through the mechanisms of interfacial shear stress transfer [184]-[185]. It has been reported that the stress transfer has a strong dependence on the size of the fibers, which may be described by the shear lag theory [181]-[182]. When the aspect ratio of fiber is small, the strain along the axial direction of the fiber is minimized due to the weak stress transfer at the interface. The corresponding strain distribution along the fiber appears to be in dome shape (see, gray line in Fig. 7.2). As the aspect ratio of the fiber increases, the strain in the fiber builds up and becomes more uniform over the axial domain (see, red line in Fig. 7.2) resulting an enhanced reinforcing performance of fibers.

Based on the shear lag theory [186], we define the following expression of n_l, which is the ratio of fiber strain, $\varepsilon_{fiber}(x)$, to the matrix strain, ε_m. This strain ratio parameter, n_l allows us to accommodate the relation between the fiber strain and the aspect ratio.

$$n_l = \frac{\varepsilon_{fiber}(x)}{\varepsilon_m} = \left(1 - \frac{\cosh(\beta x)}{\cosh(\beta L)} \right), \qquad (7.23)$$

$$\beta = \sqrt{\frac{K}{E_g h}}. \qquad (7.24)$$
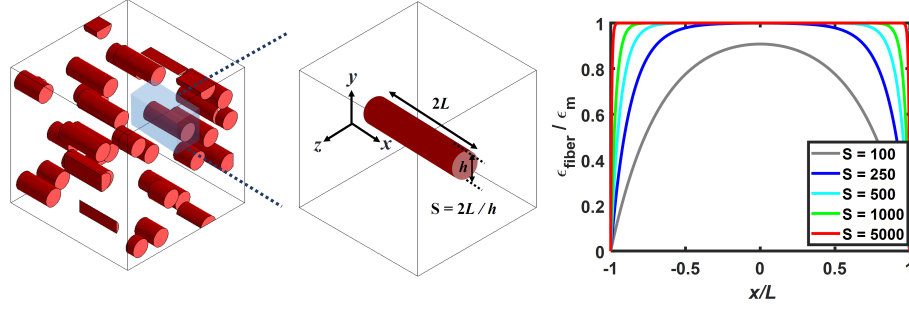
Figure 7.2: Schematics of short fiber-reinforced composites unit cell (left, middle) and axial strain distribution of a fiber (right).

In the above, K is the parameter pertaining to the stiffness of the interface which may be obtained through Molecular dynamics (MD) simulation (see, later section), L is the half-length of the fiber, h is the thickness of the fiber, and E_g is the Young's modulus of the fiber. By plotting $n_l = \frac{\varepsilon_{fiber}(x)}{\varepsilon_m}$ with respect to the nondimensional fiber length coordinate, x/L, we obtain the axial strain distribution of a fiber (see, for example, Fig. 7.2). Now, evaluating the integration of the parameter n_l over the length of the fiber, we obtain the shear lag parameter, also reported as fiber length distribution factor (see, also, [183]) as follows:

$$
\begin{aligned}
\varsigma &= \left[\frac{1}{2L} \int_{-L}^{L} \left(1 - \frac{\cosh(\beta x)}{\cosh(\beta L)} \right) dx \right] \\
&= \left(1 - \frac{\tanh(\beta L)}{\beta L} \right).
\end{aligned}
\tag{7.25}
$$

Hence, from Eq. (7.8), we find

$$
\begin{aligned}
W(\varepsilon) &= \frac{1}{2} E_g \left(\varsigma \varepsilon \right)^2 \\
&= \frac{1}{2} E_g \left(1 - \frac{\tanh(\beta L)}{\beta L} \right)^2 \varepsilon^2.
\end{aligned}
\tag{7.26}
$$

The substitution of Eq. (7.26) into Eq. (7.22) then yields

$$
\begin{aligned}
W(\mathbf{F}, \varepsilon, \mathbf{g}) &= (1-\alpha)[\frac{\mu}{2}(I_1 - 3) + \frac{\kappa}{2}(I_2 - 3)] + \alpha[\frac{1}{2}E_g \left(1 - \frac{\tanh(\beta L)}{\beta L} \right)^2 \varepsilon^2 \\
&\quad + \frac{1}{2} C \mathbf{g} \cdot \mathbf{g}].
\end{aligned}
\tag{7.27}
$$

Lastly, we introduce the following Krenchel orientation factor (see, [187]-[188]) to

238

transform the aligned short fibers into randomly oriented fibers

$$\eta_0 = \frac{8}{15} + \frac{8}{21} \langle P_2 \cos \theta \rangle + \frac{3}{35} \langle P_4 \cos \theta \rangle, \tag{7.28}$$

where $P_2 \cos \theta$ and $P_4 \cos \theta$ may be obtained from experimental measurements of the angular dependence of the polarized Raman scattering intensities (see, for example, [187]-[189]). For perfectly oriented (aligned) fibers, $P_2 \cos \theta = P_4 \cos \theta = 1$ while for randomly oriented fibers, $P_2 \cos \theta = P_4 \cos \theta = 0$. Hence, substituting Eq. (7.28) into (7.27), we find

$$\begin{aligned} W(\mathbf{F}, \varepsilon, \mathbf{g}) &= (1-\alpha)[\frac{\mu}{2}(I_1 - 3) + \frac{\kappa}{2}(I_2 - 3)] + \alpha[\frac{1}{2}\eta_0 E_g \left(1 - \frac{\tanh(\beta L)}{\beta L}\right)^2 \varepsilon^2 \\ &+ \frac{1}{2}C\mathbf{g} \cdot \mathbf{g}]. \end{aligned} \tag{7.29}$$

The Eq. (7.29) may be used to characterize the responses of a hyperelastic matrix material reinforced with randomly oriented nanofibers. The implementations of the proposed energy potential (Eq. (7.29)) and the associated derivations will be discussed in the following sections.

7.2 Equilibrium & Boundary conditions

The Euler equilibrium equations and the associated boundary conditions will be derived in this section within the framework of the virtual work statement and variational principles. To proceed, we evaluate the potential energy of the system as

$$E = \int_\Omega W(\mathbf{F}, \varepsilon, \mathbf{g}) \, dA. \tag{7.30}$$

Hence, the weak form of the equilibrium equation is obtained via the virtual work statement,

$$\dot{E} = P, \tag{7.31}$$

where P is the virtual power of the applied loads and the superposed dot denotes the variational derivative. In the above, the conservative loads are characterized by the existence of a potential L such that $P = \dot{L}$. Thus, the problem of determining equilibrium deformations is reduced to the problem of minimizing the potential energy, $E - L$. In the present problem, this furnishes

$$\dot{E} = \int_\Omega \dot{W}(\mathbf{F}, \varepsilon, \mathbf{g}) \, dA. \tag{7.32}$$

239

We note that volumetric changes in materials' deformations are, in general, energetically expensive processes and therefore are typically constrained in the constitutive modeling of engineering materials (see, also, [105]-[106]). This may be achieved by augmenting the condition of bulk incompressibility (i.e., $p(J-1)$) on the proposed energy potential (Eq. (7.29)) that

$$U(\mathbf{F}, \varepsilon, \mathbf{g}, p) = (1-\alpha)W(\mathbf{F}) + \alpha\eta_0\varsigma^2 W(\varepsilon) + \frac{1}{2}\alpha C\mathbf{g}\cdot\mathbf{g} - p(J-1) , \qquad (7.33)$$

where J is determinant of $\mathbf{F}$ and p is a constitutively indeterminate Lagrange multiplier field. In the above, $W(\mathbf{F})$ and $W(\varepsilon)$ can be found from Eqs. (7.18) and (7.8), respectively. Thus, Eq. (7.32) becomes

$$\dot{E} = \int_\Omega \dot{U}(\mathbf{F}, \varepsilon, \mathbf{g}, p)dA. \qquad (7.34)$$

In view of Eqs. (7.21) and (7.33), the associated energy variation yields

$$\dot{U} = (1-\alpha)W(\mathbf{F})_\mathbf{F}\cdot\dot{\mathbf{F}} + \alpha\eta_0\varsigma^2 W(\varepsilon)_\varepsilon\varepsilon_\mathbf{F}\cdot\dot{\mathbf{F}} + \alpha C\mathbf{g}\cdot\dot{\mathbf{g}} - p\dot{J}, \text{ and } \dot{J} = J_\mathbf{F}\mathbf{F}\cdot\dot{\mathbf{F}} = \mathbf{F}^*\cdot\dot{\mathbf{F}}. \qquad (7.35)$$

The substitution of Eqs. (7.16), (7.20) and (7.35) into Eq.(7.34) then furnishes

$$
\begin{aligned}
\dot{E} &= \int_\Omega [\{(1-\alpha)\mu\mathbf{F} + (1-\alpha)\kappa\mathbf{F}((\mathbf{F}\cdot\mathbf{F})\mathbf{I} - \mathbf{F}^T\mathbf{F}) + \alpha\eta_0\varsigma^2 W_\varepsilon\varepsilon_\mathbf{F} - p\mathbf{F}^*\}\cdot\dot{\mathbf{F}} \\
&\quad + \alpha(C\mathbf{g}\otimes\mathbf{D}\otimes\mathbf{D})\cdot\dot{\mathbf{G}}]dA, \qquad (7.36)
\end{aligned}
$$

or in components form,

$$
\begin{aligned}
\dot{E} &= \int_\Omega [\{(1-\alpha)\mu F_{iA} + (1-\alpha)\kappa F_{iB}(F_{jC}F_{jC}\delta_{AB} - F_{jA}F_{jB}) + \alpha\eta_0\varsigma^2 W_\varepsilon\varepsilon_{F_{iA}} \\
&\quad - pF_{iA}^*\}\dot{\chi}_{i,A} + \alpha C(g_i D_A D_B)\dot{\chi}_{i,AB}]dA, \qquad (7.37)
\end{aligned}
$$

where $\dot{F}_{iA} = \dot{\chi}_{i,A}$ and $\dot{G}_{iAB} = \dot{\chi}_{i,AB}$ are the variations of the first and second gradient of deformations. In the above, W_ε can be evaluated as $E\varepsilon$ and $\varepsilon_{F_{iA}}$ can be found in Eq. (7.7). We note here that, in the forthcoming derivations, we use the component forms of vectors and tensors (e.g., Eq. (7.37)) for the sake of clarity and and mathematical tractability.

Now, applying integration by part on the last term of Eq. (7.37), we find

$$\alpha C(g_i D_A D_B)\dot{\chi}_{i,AB} = \alpha C(g_i D_A D_B\dot{\chi}_{i,A})_{,B} - \alpha C(g_i D_A D_B)_{,B}\dot{\chi}_{i,A}. \qquad (7.38)$$

240

Substituting the above into Eq. (7.37) then yields

$$\dot{E} = \int_{\Omega} [\{(1-\alpha)\mu F_{iA} + (1-\alpha)\kappa F_{iB}(F_{jC}F_{jC}\delta_{AB} - F_{jA}F_{jB}) + \alpha\eta_0\varsigma^2 W_\varepsilon \varepsilon_{F_{iA}}$$
$$- pF_{iA}^*\}\dot{\chi}_{i,A} - \alpha C(g_i D_A D_B)_{,B}\dot{\chi}_{i,A} + \alpha C(g_i D_A D_B \dot{\chi}_{i,A})_{,B}] dA. \tag{7.39}$$

Applying Green–Stokes' theorem in the last term, we reduce Eq. (7.39) to

$$\dot{E} = \int_{\Omega} [(1-\alpha)\mu F_{iA} + (1-\alpha)\kappa F_{iB}(F_{jC}F_{jC}\delta_{AB} - F_{jA}F_{jB}) + \alpha\eta_0\varsigma^2 W_\varepsilon \varepsilon_{F_{iA}} - pF_{iA}^*$$
$$- \alpha C(g_i D_A D_B)_{,B}]\dot{\chi}_{i,A} dA + \int_{\partial\Omega} \alpha C(g_i D_A D_B \dot{\chi}_{i,A}) N_B dS, \tag{7.40}$$

where N_B is the rightward unit normal to $\partial\Omega$ in the sense of Green–Stokes' theorem. Eq. (7.40) may be rewrite as

$$\dot{E} = \int_{\Omega} P_{iA}\dot{\chi}_{i,A} dA + \int_{\partial\Omega} \alpha C(g_i D_A D_B \dot{\chi}_{i,A}) N_B dS, \tag{7.41}$$

where

$$P_{iA} = (1-\alpha)\mu F_{iA} + (1-\alpha)\kappa F_{iB}(F_{jC}F_{jC}\delta_{AB} - F_{jA}F_{jB}) - pF_{iA}^* - \alpha C(g_i D_A D_B)_{,B}$$
$$+ \alpha\eta_0\varsigma^2 \frac{E_g}{2}(F_{jC}F_{jD}D_C D_D - 1)F_{iB}D_B D_A, \tag{7.42}$$

is the formulation of the Piola type stress. Further, in the case of initially straight fibers (see, Eq. (7.11)), the above can be simplified to

$$P_{iA} = (1-\alpha)\mu F_{iA} + (1-\alpha)\kappa F_{iB}(F_{jC}F_{jC}\delta_{AB} - F_{jA}F_{jB}) - pF_{iA}^* - \alpha C g_{i,B} D_A D_B$$
$$+ \alpha\eta_0\varsigma^2 \frac{E_g}{2}(F_{jC}F_{jD}D_C D_D - 1)F_{iB}D_B D_A. \tag{7.43}$$

Hence, the Euler equilibrium equation satisfies

$$P_{iA,A} = 0 \text{ or } Div(\mathbf{P}) = 0, \text{ which holds in } \Omega. \tag{7.44}$$

In view of Eqs. (7.11)-(7.13) and (7.43), we obtain the following Euler Equilibrium equation as

$$0 = P_{iA,A} = (1-\alpha)\mu\chi_{i,AA} + (1-\alpha)\kappa(\chi_{i,AA}\chi_{j,C}\chi_{j,C} - \chi_{i,BA}\chi_{j,A}\chi_{j,B})$$
$$+ (1-\alpha)\kappa\chi_{i,B}(2\chi_{j,CB}\chi_{j,C} - \chi_{j,AA}\chi_{j,B} - \chi_{j,A}\chi_{j,BA}) - p_{,A}\varepsilon_{ij}\varepsilon_{AB}\chi_{j,B}$$
$$- \alpha C\chi_{i,ABCD}D_A D_B D_C D_D + \alpha\eta_0\varsigma^2 \frac{E_g}{2}(\chi_{j,C}\chi_{j,D}\chi_{i,B})_{,A}D_A D_B D_C D_D$$
$$- \alpha\eta_0\varsigma^2 \frac{E_g}{2}\chi_{i,BA}D_B D_A, \tag{7.45}$$

where $F_{iA} = \chi_{i,A} = \partial\chi_i/\partial X_A$, $g_{i,AB} = \chi_{i,ABCD}D_A D_B D_C D_D$, $F_{iA}^* = \varepsilon_{ij}\varepsilon_{AB}F_{jB}$, and ε_{ij} is the 2-D permutation; $\varepsilon_{12} = -\varepsilon_{21} = 1$, $\varepsilon_{11} = -\varepsilon_{22} = 0$. Eq. (7.45) together with the constraint of the bulk incompressibility,

$$\det \mathbf{F} = \chi_{1,1}\chi_{2,2} - \chi_{1,2}\chi_{2,1} = 1, \tag{7.46}$$

solve the unknown potentials of χ_1, χ_2, and p which describe the mechanical responses of the nanofiber reinforced hyperelastic composites material. The numerical solution of the above system of Partial Differential Equations (PDEs) (Eqs. (7.45)-(7.46)) may be accommodated via commercial packages (e.g., MATLAB, COMSOL etc.).

We now derive the expressions of the associated boundary conditions. For the stated purpose, we apply integration by part on Eq. (7.41) (i.e., $P_{iA}\dot{\chi}_{i,A} = (P_{iA}\dot{\chi}_i)_{,A} - (P_{iA})_{,A}\dot{\chi}_i$) and obtain

$$\dot{E} = \int_{\partial\Omega} P_{iA}\dot{\chi}_i N_A dS + \int_{\partial\Omega} \alpha C(g_i D_A D_B \dot{\chi}_{i,A}) N_B dS - \int_\Omega P_{iA,A}\dot{\chi}_i dA, \tag{7.47}$$

where the Green-Stokes' theorem is applied in the first term of the above, i.e.,

$$\int_\Omega (P_{iA}\dot{\chi}_i)_{,A} dA = \int_{\partial\Omega} P_{iA}\dot{\chi}_i N_A dS. \tag{7.48}$$

Since the Euler equation ($P_{iA,A} = 0$) holds in Ω, Eq. (7.47) reduces to

$$\dot{E} = \int_{\partial\Omega} P_{iA}\dot{\chi}_i N_A dS + \int_{\partial\Omega} \alpha C(g_i D_A D_B \dot{\chi}_{i,A}) N_B dS. \tag{7.49}$$

The decomposition of $\dot{\chi}_{i,A}$ now furnishes

$$\dot{\chi}_{i,A} = \frac{\partial\dot{\chi}_i}{\partial S}\frac{\partial S}{\partial X_A} + \frac{\partial\dot{\chi}_i}{\partial N}\frac{\partial N}{\partial X_A} = \dot{\chi}_i' T_A + \dot{\chi}_{i,N} N_A, \tag{7.50}$$

where $T_A = \partial S/\partial X_A$ and $N_A = \partial N/\partial X_A$ are respectively, the unit tangent and normal to the boundary $\partial\Omega$. Combining Eqs. (7.49)-(7.50), we obtain

$$\dot{E} = \int_{\partial\Omega} P_{iA}\dot{\chi}_i N_A dS + \int_{\partial\Omega} \alpha C g_i D_A D_B \left(\dot{\chi}_i' T_A N_B + \dot{\chi}_{i,N} N_A N_B\right) dS. \tag{7.51}$$

In addition, since

$$\alpha C g_i D_A D_B T_A N_B \dot{\chi}_i' = (\alpha C g_i D_A D_B T_A N_B \dot{\chi}_i)' - (\alpha C g_i D_A D_B T_A N_B)' \dot{\chi}_i, \tag{7.52}$$

Eq. (7.51) becomes

$$\dot{E} = \int_{\partial\Omega} [P_{iA}N_A - (\alpha C g_i D_A D_B T_A N_B)']\dot{\chi}_i dS + \int_{\partial\Omega} \alpha C g_i D_A D_B \dot{\chi}_{i,N} N_A N_B dS$$
$$+ \int_{\partial\Omega} (\alpha C g_i D_A D_B T_A N_B \dot{\chi}_i)' dS. \tag{7.53}$$

242

The above may be recast to yield the standard form:

$$\dot{E} = \int_{\partial\Omega} [P_{iA}N_A - (\alpha C g_i D_A T_A D_B N_B)']\dot{\chi}_i dS + \int_{\partial\Omega} \alpha C g_i D_A N_A D_B N_B \dot{\chi}_{i,N} dS$$
$$+ \sum \|\alpha C g_i D_A T_A D_B N_B \dot{\chi}_i\|, \tag{7.54}$$

where the double bar symbol refers to the jump across the discontinuities on the boundary $\partial\Omega$ (i.e., $\|*\| = (*)^+ - (*)^-$) and the sum denotes the collection of all discontinuities.

Lastly, it follows from Eq. (7.31) that the admissible mechanical powers take the following form

$$P = \int_{\partial w_t} t_i \dot{\chi}_i dS + \int_{\partial w} m_i \dot{\chi}_{i,N} dS + \sum f_i \dot{\chi}_i. \tag{7.55}$$

Thus, by comparing Eqs. (7.54) and (7.55), we conclude that

$$t_i = P_{iA}N_A - \frac{d}{dS}[\alpha C g_i D_A T_A D_B N_B],$$
$$m_i = \alpha C g_i D_A N_A D_B N_B,$$
$$f_i = \alpha C g_i D_A T_A D_B N_B, \tag{7.56}$$

where t_i, m_i, and f_i are the expressions of edge tractions, edge moments, and the corner forces, respectively. It is also noted here that the stress expression in Eq. (7.42) is a combination of the Piola-type stress $((1-\alpha)\mu F_{iA}+(1-\alpha)\kappa F_{iB}(F_{jC}F_{jC}\delta_{AB}-F_{jA}F_{jB})+\alpha\eta_0\varsigma^2 W_\varepsilon \varepsilon_{F_{iA}} - pF_{iA}^*)$ and double stress $(\alpha C(g_i D_A D_B)_{,B})$ such that the second gradient of the deformation term (i.e., $\alpha C(g_i D_A D_B)_{,B}$) may be interpreted as the energy conjugate to the admissible double force m_i when it is prescribed on the desired boundaries of the composite.

The solutions of the above system of PDEs may be determined by imposing the following boundary conditions (see, Fig. 7.3) and the corresponding results are discussed in the model implementation and discussion section.

$$t_1 = P_{11}, \; t_2 = P_{12} = 0 \text{ at } X_1 = a, -a \text{ and}$$
$$t_1 = P_{21} = 0, \; t_2 = P_{22} = 0 \text{ at } X_2 = b, -b. \tag{7.57}$$
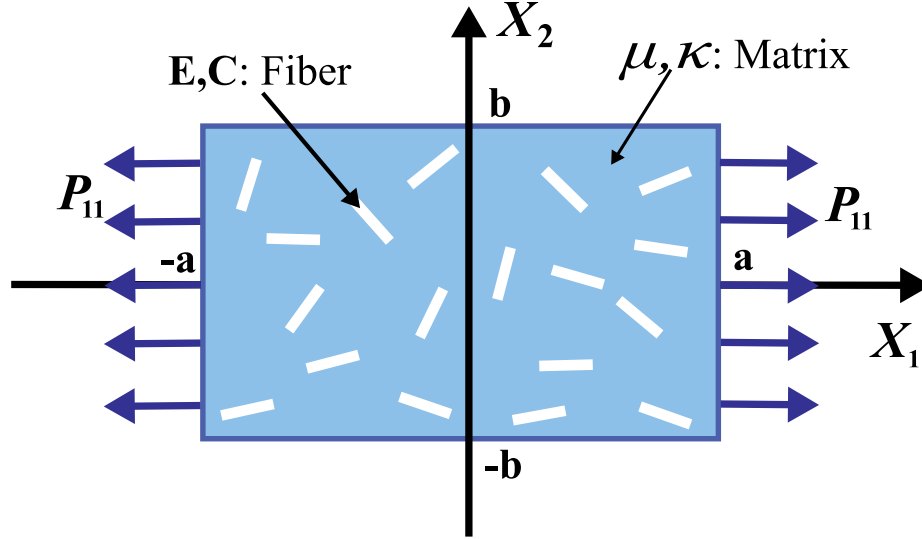
Figure 7.3: Schematic of the problem.

7.3 Model for damage mechanics of short/nano fiber-reinforced composite due to interfacial debondings

When nanofiber-reinforced composite experiences sufficiently high strain exceeding a certain threshold, the interfaces between the nanofibers and matrix material are damaged. It has been experimentally observed that when the strain is increased to a sufficiently high magnitude, the strain distribution along the interface of nanofiber and matrix material changes from a dome-shaped to an M-shaped distribution ([184] and [190]) (see, also, Fig. 7.10 (b) and 7.12 (b)). Other studies indicate that, especially for those with long fibers, multiple drops in the strain distributions are observed along the middle portion of the fiber interface [191]-[192]. In the present study, we confine our analysis to the cases of M-shaped axial strain distributions for the sake of increased visibility and mathematical tractability. The cases of multiple dropped strain distributions may readily be accommodated by modifying the proposed interface stiffness function. The strain drop along the interface is due to the debonding between the matrix and fiber, resulting in accumulated damages on the interface [184]. This further causes a reduction in the interface stiffness moduli, K. To accommodate such a reduction in K and, further, to assimilate the M-shaped axial strain distribution along the interface, we proposed the following non-uniform interface stiffness

potential

$$K_{eff} = K_0 - fun(\hat{\varepsilon})e^{-6.7\left(\frac{x}{L}\right)^2}, \tag{7.58}$$

where $fun(\hat{\varepsilon})$ is the damage characterizing function, pertaining to the reduction of interface stiffness which may be expressed as

$$fun(\hat{\varepsilon}) = a\Gamma\left(\hat{\varepsilon} - \hat{\varepsilon}_{cric}\right)\left(1 + \hat{\varepsilon}_{cric}\right)^b. \tag{7.59}$$

In the above, $\Gamma\left(\hat{\varepsilon} - \hat{\varepsilon}_{cric}\right)$ is referred to as the damage activation function which is switched from inactive mode to active mode when the critical value (in this case critical strain, $\hat{\varepsilon}_{cric}$) is exceeded. In the above, $\hat{\varepsilon}$ refers to the overall strain of the material, computed as the ratio of change in length of the composite to the initial length. The proposed interface damage function (Eqs. (7.58)-(7.59)) is inspired by the Weibull damage model [92], which has been successfully adopted to simulate the fiber damages in the composites [193]-[194]. The activation of the interface damage function is governed by the condition:

$$\Gamma(x) = \begin{cases} x \leq 0; \Gamma(x) = 0 \text{ (inactive mode)} \\ x > 0; \Gamma(x) = x \text{ (active mode)} \end{cases}. \tag{7.60}$$

Hence, when the overall strain of the composite ($\hat{\varepsilon}$) is below a critical threshold ($\hat{\varepsilon}_{cric}$), $\Gamma\left(\hat{\varepsilon} - \hat{\varepsilon}_{cric}\right)$ remains inactivated (the corresponding value of Γ is zero). Accordingly, there is no interfacial debonding present and we expect to obtain a dome-shaped distribution of strain at the interface. When $\hat{\varepsilon}$ exceeds $\hat{\varepsilon}_{cric}$, interfacial debonding process initiates (the corresponding value of Γ is non-zero) and, hence, M-shaped axial strain distribution is expected. The corresponding critical value of the threshold ($\hat{\varepsilon}_{cric}$) may be obtained via the proposed MD simulation presented in the later section. The parameter a and b in Eq. (7.59) dictates the rate of the debonding process and they depend on the types of nanofiber and matrix material. It has been found that, when the nanofibers are embedded in a stiffer matrix material (e.g., Polyethylene terephthalate (PET)), the damage progresses rapidly which corresponds to high a and b values. On the other hand, when the nanofibers are embedded in a soft matrix material (e.g., ecoflex, Polydimethylsiloxane (PDMS), etc.), the interfacial damage gradually takes place which may be assimilated by low a and b values.

Now, using K_{eff} we define the shear lag parameter as follows:

$$\beta_{eff} = \sqrt{\frac{K_{eff}}{E_g h}}, \tag{7.61}$$

$$n_l = \left(1 - \frac{\cosh\left(\beta_{eff}x\right)}{\cosh\left(\beta_{eff}L\right)}\right), \tag{7.62}$$

$$\varsigma = \left[\frac{1}{2L}\int_{-L}^{L}\left(1 - \frac{\cosh\left(\beta_{eff}x\right)}{\cosh\left(\beta_{eff}L\right)}\right)dx\right]. \tag{7.63}$$

A similar process as presented in Eqs. (7.26) - (7.29) may be followed in order to obtain the expression of the energy function

$$W(\mathbf{F}, \varepsilon, \mathbf{g}) = (1-\alpha)\left[\frac{\mu}{2}(I_1 - 3) + \frac{\kappa}{2}(I_2 - 3)\right] + \alpha\left[\frac{1}{2}\eta_0 E_g\varsigma^2\varepsilon^2 + \frac{1}{2}C\mathbf{g}\cdot\mathbf{g}\right]. \tag{7.64}$$

7.4 Model implementation and discussions

In this section, the implementation of the proposed model along with the MD simulation results are presented. We begin with the atomistic simulations for the micromechanical responses of the three distinct types of graphene-reinforced Polyethylene terephthalate (PET) nanocomposites with altered/defective interfaces. We then discuss the damage mechanics of the composite systems due to interfacial debonding of two distinct types of nanocomposites addressing both gradual and rapid debonding processes at the interfaces. Lastly, using the obtained model, we assimilate the deformation configurations of a highly stretchable elastomeric nanocomposite.

7.4.1 Atomistic molecular dynamics simulations

In order to apply the proposed model to predict the effective elastic properties of single-layer graphene/polymer nanocomposites with varying interfacial imperfection, the damage parameter K (interface stiffness), E_g, and h defined in Eqs. (7.23)-(7.24) and elastic properties of the matrix material were determined using the atomistic molecular dynamics simulation procedures presented in [195]. For the sake of completeness and coherence, the MD simulation procedures to obtain all the required parameters are summarized in this section. In general, the interface between defect-free graphene and typical engineering polymer is weak in nature, thus, a cohesive shear

lag model needs to be used to predict the damage-dependent properties of nanocomposites. As has been discussed in detail, structural defects formed in graphene alter not only the elasticity of graphene but also the interfacial damage parameters. Therefore, we considered pristine, hydroxylated, and Thrower-Stone-Wales (TSW) defected graphene embedded in Polyethylene terephthalate (PET) matrix to validate the performance of the proposed model.

Ethylene terephthalate (monomer)

Polyethylene terephthalate (10mer)

Graphene/PET Nanocomposites
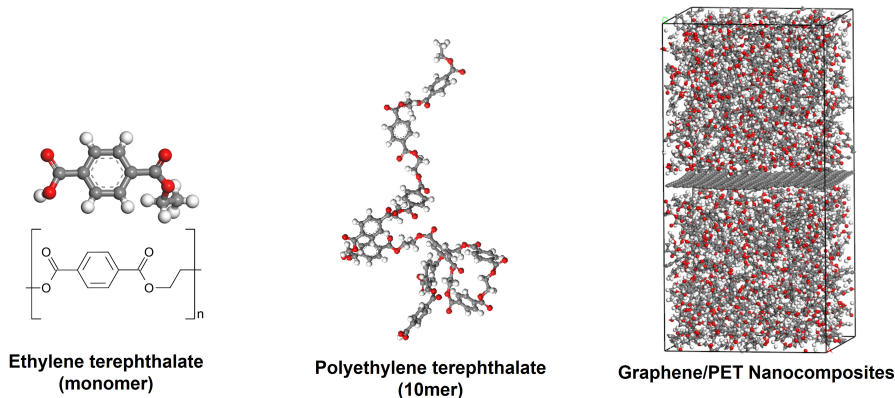
Figure 7.4: Molecular models of PET matrix, PET chain, and Graphene/PET nanocomposites [195].

To construct the molecular unit cell representing fully aligned nanocomposites, an amorphous PET matrix consisting of 16 PET chains polymerized with 10 ethylene terephthalate monomers and each defected graphene were constructed respectively. The dimension of pure PET matrix is approximately $32.73\mathring{A} \times 32.73\mathring{A} \times 32.73\mathring{A}$. Three single layer graphenes were modeled as reinforcement: pristine, 10 TSW defected and 10 hydroxilated graphene respectively. By laminating two PET matrices and one graphene as shown in Fig. 7.4, the transversely isotropic nanocomposites could be modeled. The thickness of graphene (h) is $3.4\mathring{A}$ which has been widely used for the equivalent continuum description of graphene [196]-[197]. The volume fraction of graphene in each nanocomposite is nearly 4.6%. To eliminate the finite size effect, all periodic boundary conditions was applied to the unit cell. All the molecular structures were equilibrated at $300K$ and $1atm$ before each production run to derive the elastic constants of graphene, PET matrix and nanocomposites. The dimension nanocomposites are approximately $33.97\mathring{A} \times 34.09\mathring{A} \times 68\mathring{A}$. The number of atoms considered in each molecular model is enough to derive thermodynamic properties of the

systems in equilibrating and predicting the mechanical properties of each structures with Virial theorem.

To draw the stress-strain curves of nanocomposites and to obtain elastic moduli, longitudinal tension and longitudinal shearing were applied to the unit cell with finite true strain rate of $0.0002/psec$. Within 2% of elastic strain, the longitudinal Young's modulus of nanocomposites was determined. In the same manner, the Young's modulus of pure PET was determined. The elastic modulus of graphene E_g was determined from the dynamic tensile simulation of each graphene at $300K$. To predict the tangential damage initiation at the interface, the shear stress in PET matrix according to the applied shear strain to the nanocomposites was determined. Fig. 7.11 shows the variation of shear stress in 10 hydroxylated graphene under the longitudinal shearing of nanocomposites unit cell. The overall variation of shear stress including a sudden drop down will be discussed in the later section.

The damage parameter K was determined from the mode II interfacial sliding simulation of the graphene-PET laminate model. For the sliding simulation, the nanocomposites unit cell shown in Fig. 7.11 was modified into a finite two-layer structure with a vacuum area below the graphene by eliminating the periodic boundary condition along the through-the-thickness direction of graphene. To draw the sliding distance-traction relationship, graphene was tangentially displaced with a velocity of $0.025\mathring{A}/4psec$ while the upper part of PET was frozen. Lastly, the slope of traction-displacement relationship within $2\mathring{A}$ of sliding displacement was determined as the damage parameter K.

All the interfacial parameters and properties of nanocomposites determined from MD simulations are arranged in Table-1 according to the type of structural defect in graphene, where E_L, G_L, and G_g are the longitudinal Young's modulus of the composite, shear modulus of the composite, and shear modulus of the graphene, respectively. To validate the performance of proposed model in predicting responses of nanocomposites with damaged interface, the data arranged in Table 7.1 were used in the proposed model and conventional Mori-Tanaka model to predict the longitudinal Young's modulus of nanocomposites at varying aspect ratios of graphene.

Table 7.1: Interfacial parameters and properties of nanocomposites determined from MD simulations.

Graphene/PET	$K[GPa/nm]$	$E_g[GPa]$	$G_g[GPa]$	$h[nm]$	$E_L[GPa]$	$G_L[GPa]$
Pristine	0.173	1023	397	0.34	49.03	0.07
Hydroxylated	3.03	956	386	0.34	45.47	0.77
TSW Decfected	0.931	335	156	0.34	23.36	0.76
PET	−	−	−	−	3.09	1.06

7.4.2 Micromechanics of PET-Graphene nanocomposite using MD integrated continuum model

In this section, we estimate the Young's modulus of PET-Graphene nanocomposite with respect to the varying aspect ratios of fibers by employing the proposed model. The required values of parameters (i.e., h, E_g, K, and $C = G_g$) in Eq. (7.29) are obtained from the MD simulation as summarized in the Table-1. The energy fraction, α is assumed to be equivalent to the fiber volume fraction, 4.6%. The Mooney-Rivlin parameters are chosen as $\mu = 1.026\, GPa$ and $\kappa = 0$, which produce the same response of the PET matrix with the modulus of $E_L = 3.09\, GPa$ (refer, Table-1). For the Krenchel orientation factor (η_0), we consider the case of perfectly aligned fibers with $P_2 \cos\theta = P_4 \cos\theta = 1$, and, hence obtain $\eta_0 = 1$ from Eq. (7.28).
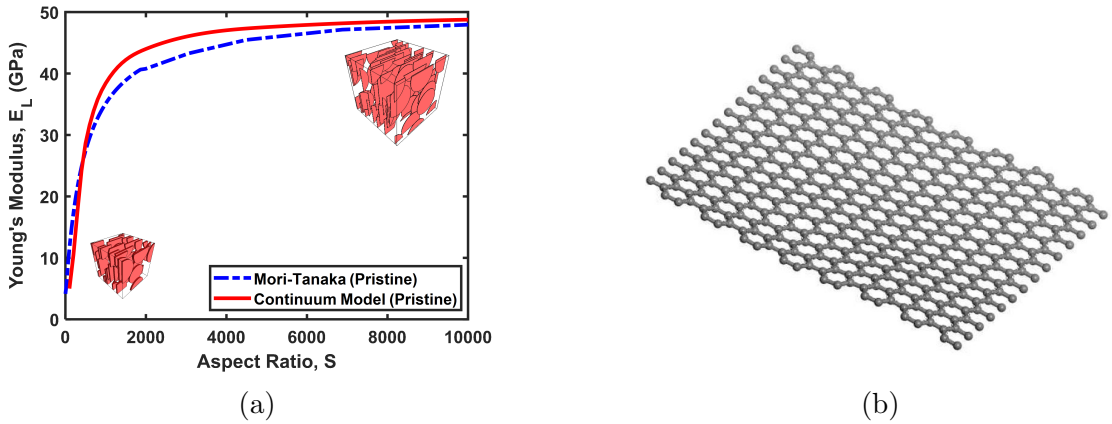
Figure 7.5: (a) Young's modulus VS aspect ratio plot for pristine graphene-reinforced PET case. (b) MD model of the pristine graphene sheet [195].

In our model, we consider different cases of nanofiber reinforcements by varying the aspect ratios of graphene sheets ($S = 2L/h$) between 10 to 10000. For each case, we solve our model using the finite element method with uniaxial tensile loading

249

(a)   (b)
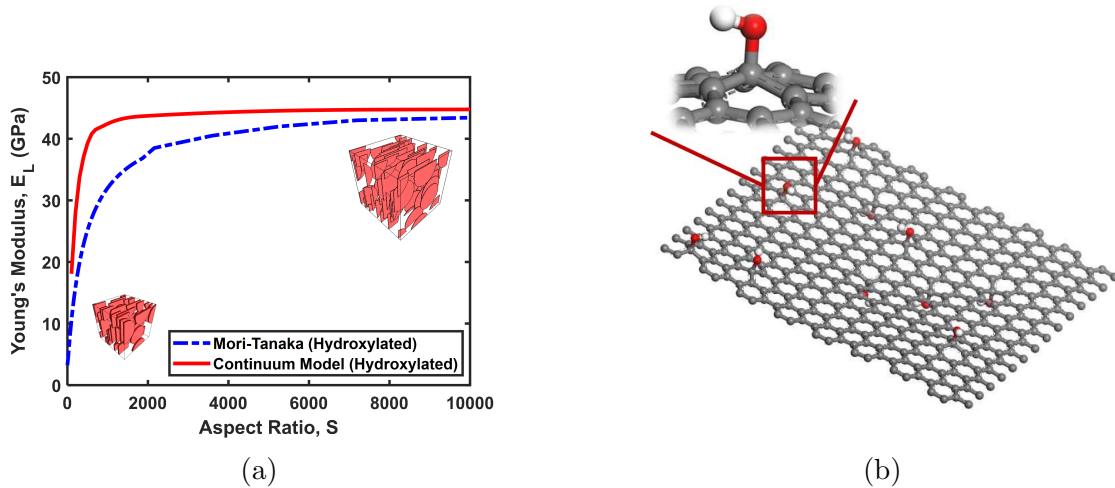
Figure 7.6: (a) Young's modulus VS aspect ratio plot for hydroxylated graphene-reinforced PET case. (b) MD model of the hydroxylated graphene sheet [195].

(as shown in Fig. 7.3), and stress-strain responses are obtained. From the stress-strain responses, we calculate the longitudinal Young's modulus (E_L) using the initial tangent modulus expression, $E_L = \left(\frac{d\sigma}{d\varepsilon}\right)_{\varepsilon=0}$. Hence, we obtain the Young's modulus of the composite with different aspect ratios of the graphene sheet. We repeat the same procedure for three different configurations of altered/defective graphene interfaces embedded in PET matrix. The obtained results from the proposed continuum model for the cases of pristine, hydroxylated, and TSW defected graphene embedded in PET matrix are presented through Figs. 7.5-7.7. The estimations using the modified Mori-Tanaka model (see, [195]) are also presented for the purpose of cross-examination. It is found that the longitudinal Young's modulus of nanocomposites determined from the proposed continuum model and Mori-Tanaka (M-T) model converge to nearly $49GPa$, $45GPa$, and $19GPa$ for the pristine, hydroxylated, and TSW defected cases, respectively. The converged values of the longitudinal Young's modulus agree fairly well with the MD simulation results shown in Table 7.1 ($E_L[GPa]$) for the cases of infinitely long graphene. Therefore, it is suggested that the proposed model may be used as an effective alternative in predicting the stiffness of PET composite, and perhaps similar kinds of materials, with altered/defective graphene interfaces.

Lastly, using Eqs. (7.23)-(7.24), we estimate the strain distributions along the graphene-PET interface with respect to the varying aspect ratios (Fig. 7.8). The
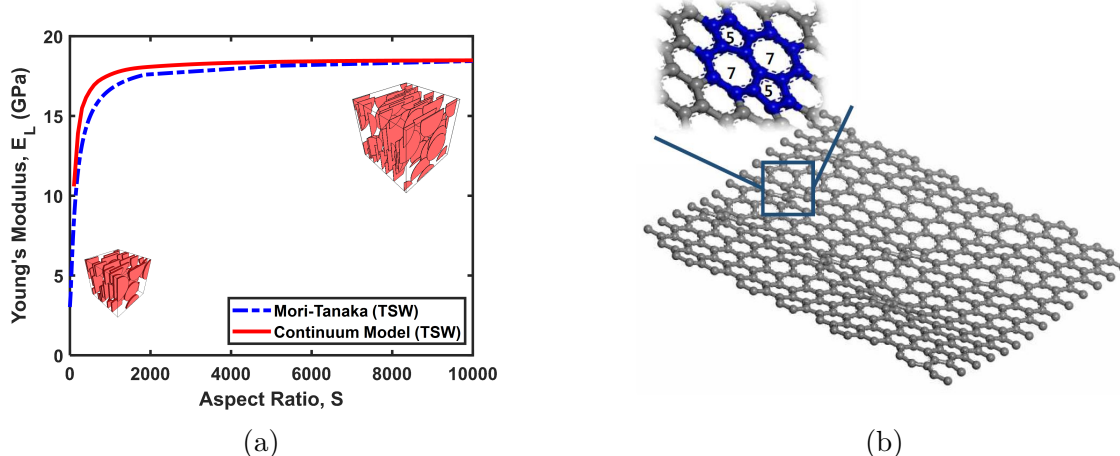
Figure 7.7: (a) Young's modulus VS aspect ratio plot for TSW defected graphene-reinforced PET case. (b) MD model of the TSW defected graphene sheet [195].

dome-shaped axial strain distribution is predicted when the aspect ratio is small enough. In this case, the ratio of fiber strain ($\varepsilon_{fiber}(x)$) to matrix strain (ε_m) is well below 1, which further suggests that strain transfer from fibers to matrix material is substantially limited. As the aspect ratio increases, the strain distributions become more uniform, especially in the midsection, and the corresponding $\frac{\varepsilon_{fiber}(x)}{\varepsilon_m}$ ratio converges to 1. The result indicates that a strong load transfer between the fiber and matrix is achieved and, hence the reinforcing effect of fibers is maximized.
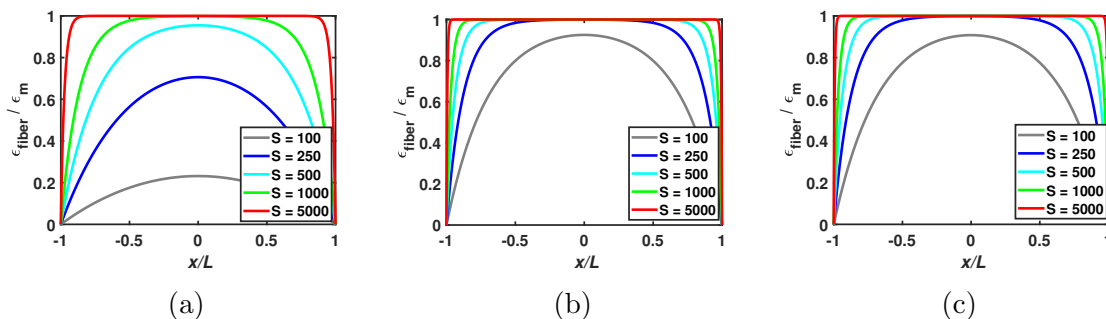
Figure 7.8: Strain distributions along the fiber with respect to varying aspect ratios; (a) pristine, (b) hydroxylated, (c) TSW defected graphene cases.

7.4.3 Prediction of damage mechanics of nanofiber composites due to interfacial debonding

In this section, the obtained model developed through Eqs. (7.58) - (7.64) is used to assimilate the damage mechanics of nanocomposites induced by the debonding process of fibers at the interface. Debonding at the interface is a type of damage typically observed in nanocomposites due to the weak nature of the interface between the relatively soft matrix material and stiff fibers (see, for example, [184] and [190]-[192]). To demonstrate the utility of the proposed model in assimilating the damage mechanics, we analyze two distinct cases. In the first case, we consider a soft matrix-based nanocomposite, where it is generally observed that the damage progression is gradual and may sustain relatively large strain during the damage phase. In the latter case, a relatively stiff matrix-based nanocomposite is considered, which generally undergoes rapid damage and breaks off within a very small strain range during the damage phase.

Gradual debonding of soft matrix-based nanocomposites

In this case, we consider nanocomposite made from cellulose nanofiber (CNF) / carbon nanotube (CNT) nano-network reinforced Polydimethylsiloxane (PDMS). Polydimethylsiloxane (PDMS) is a widely used polymer in various applications, including wearable/implantable devices and microfluidics, owing to its biocompatibility, optical transparency, and flexibility [198]-[199]. When CNF/CNT nano-networks are embedded in the PDMS, it produces a conductive-based material which is very useful in the manufacture of flexible electronic devices [200]. In [200], CNF/CNT film is prepared via mixing and vacuum filtration. The CNF/CNT film is then served as a template to develop nanocomposite via the immersion process. In the resulting composite, the CNF/CNT nano-networks provided both improved mechanical strength and electrical conductivity due to the nano-network structures and the continuous electronic transmittance pathways in the nanocomposite. From the experiment, it is found that the CNF/CNT film forms a rigid structure with tensile strength, Young's modulus, and a fracture strain of $61.7 MPa$, $5132 MPa$, and 1.1%, respectively. The volume fraction of CNF/CNT is found to be 76.3%. We use the Mooney-Rivlin model to characterize

the PDMS matrix material, the results are shown in Fig. 7.9. The values of all the parameters that are used in the proposed model (developed through Eqs. (7.58) - (7.64)) are summarized in Table 7.2.
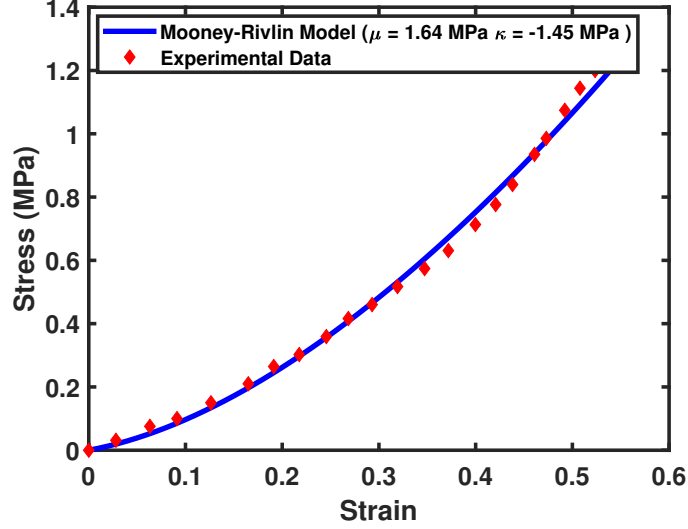
Figure 7.9: Mooney-Rivlin characterization of PDMS matrix [200].

Table 7.2: Interfacial parameters and properties of CNF/CNT nano-networks reinforced PDMS nanocomposite.

$\eta_0 E_g$ [MPa]	h [nm]	α	μ [MPa]	κ [MPa]	C [MPa]	K_0 [MPa/μm]	S	a	b	$\hat{\varepsilon}_{cric}$
5132	20	76.3%	1.64	-1.45	3888	8.00	500	1.56	2	1.2%

We solve the obtained model using the finite element method with uniaxial tensile load applied (as shown in Fig. 7.3) and the stress-strain responses are estimated from the solution. The results are then compared with the experimental data presented in [200], where a uniaxial tensile test was performed for the CNF/CNT nano-network reinforced PDMS nanocomposite sample using a universal material-testing machine at room temperature (see, Fig. 7.10 (a)). It is observed that the proposed model successfully predicts the nonlinear stress-strain (strain-softening) response of the nanocomposite with good accuracy (maximum error of 4.4%). As the strain of the material is increased beyond 1.2% (which is the critical strain value chosen for this case), the stiffness of the material is predicted to be progressively decreased with

the activation of the proposed damage function (see, Eqs. (7.59)-(7.60)). From the Eqs. (7.61)-(7.62), we also estimate the $\frac{\varepsilon_{fiber}(x)}{\varepsilon_m}$ distributions along the fiber (see, Fig. 7.10 (b)). Up until 1.2% strain of the composite, the distribution appears to be dome-shaped. Once the overall composite strain increases beyond 1.2%, the profile gradually changes from dome-shaped to M-shaped distributions indicating the initiation of debonding at the interface.
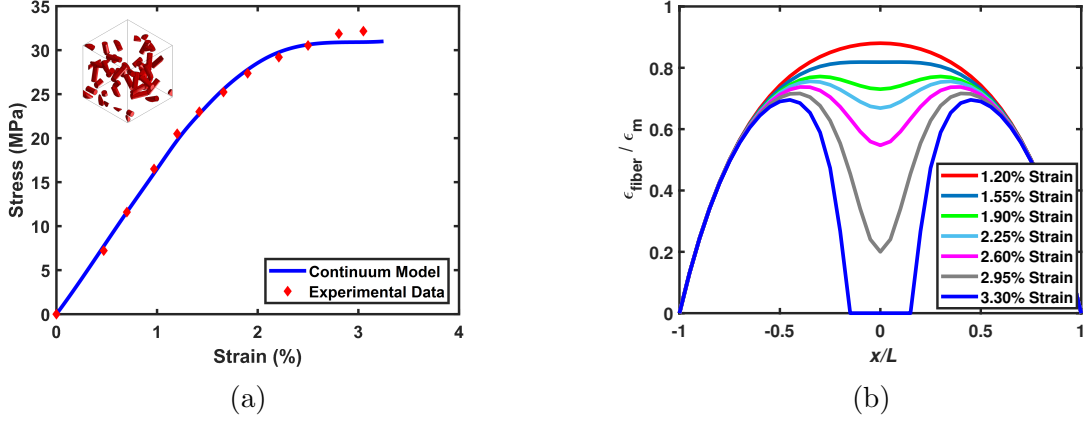
Figure 7.10: (a) Stress-strain plot of CNF/CNT nano-network reinforced PDMS composite [200]. (b) Strain distribution along the fiber with respect to varying strain levels of the composite.

Rapid debonding of stiff matrix-based nanocomposites

To demonstrate the performance of the proposed model in predicting the rapid debonding damages, we consider the case of the PET matrix material reinforced with hydroxylated graphene. The values of the interfacial parameters and properties of the nanocomposite are obtained from the proposed MD simulation which is summarized in Table-1. The critical strain value ($\hat{\varepsilon}_{cric}$) at which the debonding is initiated at the interface is predicted through the assimilation of tangential damage initiation process. For this purpose, the shear stress in graphene-reinforced PET nanocomposite is determined from the MD simulation. In Fig. 7.11 (a), the shear stress with respect to longitudinal shear strain (γ_{xy}) is presented for the case of hydorxylated graphene-reinforced PET composite. It is observed from Fig. 7.11 (a) that the stress drops sharply in the strain range between $0.07 - 0.08$, which indicates possible tangential damage initiation at the interface. From the obtained value of γ_{xy}, we then estimate

the critical normal strain ($\hat{\varepsilon}_{cric}$) using the following relation;

$$\hat{\varepsilon}_{cric} = \frac{\gamma_{xy}\beta L}{4\tanh{(\beta L)}}.$$ (7.65)
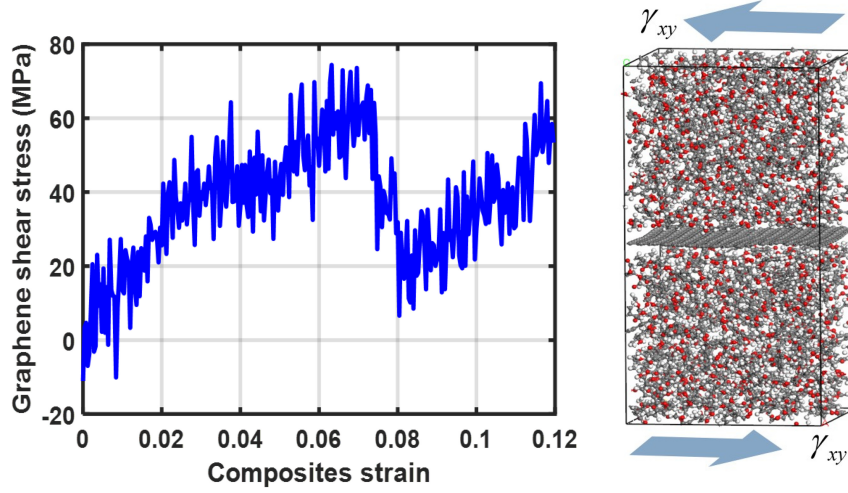
Figure 7.11: Graphene shear stress VS composites applied strain under longitudinal. Shear of nanocomposite (left). Nanocomposites under longitudinal shearing (MD simulation) (right) [195].

To compare the results from the continuum model with the experimental data, we consider the experiment performed in [201], where graphene-reinforced PET composite is tested under uniaxial tensile loading. The volume fraction of graphene in the composite sample is found to be 5%, thus $\alpha = 5$ is used in the continuum model. For the Krenchel orientation factor (η_0), we chose randomly oriented fibers with $P_2\cos\theta = P_4\cos\theta = 0$, and we get $\eta_0 = \frac{8}{15}$. The aspect ratio is found to be, $S = 500$. After conversion, we obtained $\hat{\varepsilon}_{cric} = 2.3\%$ by using Eq. (7.65). In the Eq. (7.59), we used $a = 5.77$, $b = 7$, and $\hat{\varepsilon}_{cric} = 2.3\%$. The obtained model is then solved using the custom-built finite element procedure and the corresponding results are summarized in Fig. 7.12. The stress-strain results in Fig. 7.12 (a) indicate that the proposed model successfully predicts the rapid damage progression of the composite with good accuracy (the maximum error is 2.5%). More precisely, as the strain of the material is increased beyond 2.3% (which is the critical strain value), the stiffness of the material is predicted to be rapidly decreased with the activation of the proposed damage function (see, Eqs. (7.59)-(7.60)). Fig. 7.12 (b) illustrates the changes in the strain

distributions along the fiber as the overall strain of the composite is increased. Up until 2.3% strain, the distribution appears to be dome-shaped. As the overall composite strain exceeds 2.3%, the profile changes from dome-shaped to M-shaped distribution which further indicates the initiation of debonding process at the interface.
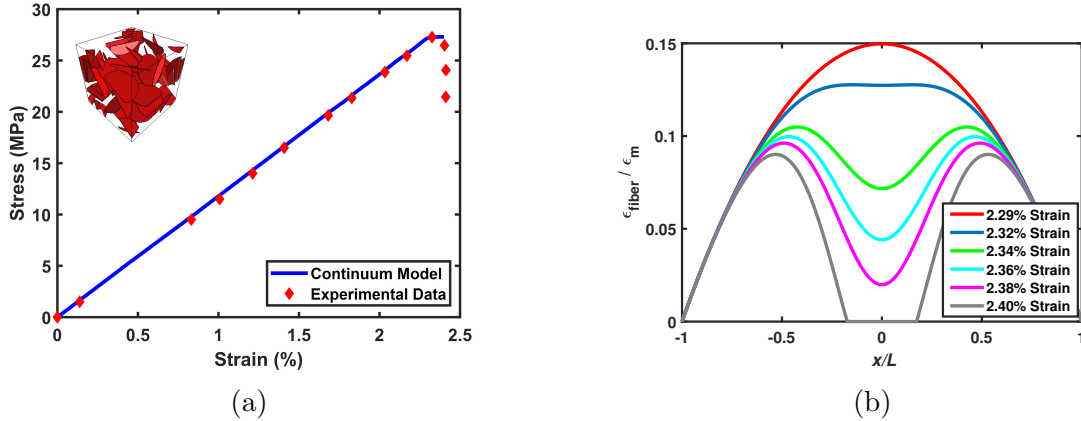
Figure 7.12: (a) Stress-strain plot of graphene-reinforced PET composite [201]. (b) Strain distributions along the fiber with respect to varying strain levels of the composite.

7.4.4 Deformation analysis of Hyperelastic nanocomposite

In this section, we examine the performance of the proposed model in assimilating large deformation of an elastomeric nanocomposite. For the demonstration purpose, the experimental results of multi-walled carbon nanotubes (MWCNTs) reinforced Ecoflex-0030 elastomeric nanocomposite is chosen from the work of [29] because of its ability to withstand an exceptionally large strain (up to 10 times to its initial dimension). Due to its highly flexible characteristics, Ecoflex matrix-based nanocomposite may be used in many applications involving flexible electronic devices, wearable sensors, and soft robotics ([29]-[30],[34], and [202]). The nanocomposite sample is made from multi-walled carbon nanotubes (MWCNTs) embedded in the highly stretchable elastomeric matrix, Ecoflex-0030. The sample is tested under uniaxial tensile loading (see, further details in [29]). We characterize the responses of Ecoflex-0030 matrix using the Mooney-Rivlin model with the configuration parameters of $\mu = 0.01 MPa$ and $\kappa = 0.002 MPa$, respectively (see, Fig. 7.13). The values of all the parameters that are used in the proposed model are summarized in the Table 7.3. The stress-strain

responses obtained from the proposed model and the experimental work of [29] are presented in Fig. 7.14. The result indicates that the proposed model closely assimilates the non-linear (strain-stiffening) responses of the nanocomposite with maximum prediction error of 3.5%.
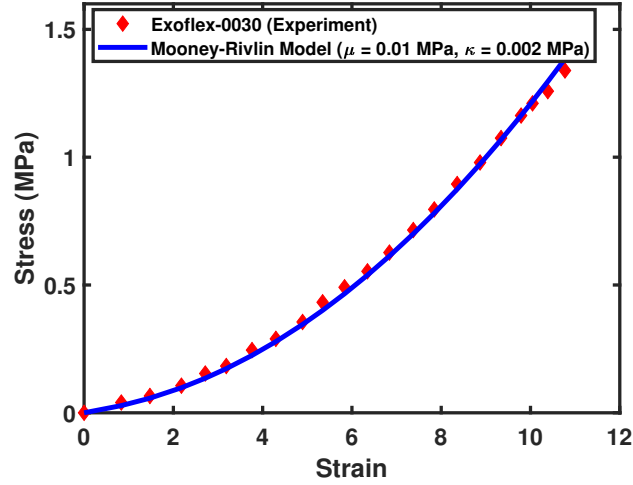
Figure 7.13: Stress-strain characterization of Ecoflex-0030 matrix using Mooney-Rivlin Model.

Table 7.3: Properties of MWCNTs/Ecoflex-0030 nanocomposite.

$E_g[GPa]$	$h[nm]$	$K_0[MPa/nm]$	S	$\mu[MPa]$	$\kappa[MPa]$	α	$C[GPa]$	η_0
900	65	0.65	460	0.01	0.002	1%	361	$\frac{8}{15}$

In Fig. 7.15, the deformation contours of the nanocomposite are presented at different stretch levels (up to 10 times) and the corresponding deformation contours are calculated as the norms of displacement fields, i.e., $\sqrt{\chi_1^2 + \chi_2^2}$. It is observed that the deformation profiles closely resemble the deformation of a hyperelastic material under tension. Especially, the change in the lateral dimension along the length of the material follows a smooth parabolic curve that is typically observed in the hyperelastic material under uniaxial tensile loading ([125],[180], and [35]). The existence of second gradient term allows the proposed model to capture the smooth and nonlinear deformation profile by regularizing any discontinuities that arise from the classical first gradient model, the similar phenomena is also discussed in [203].

Lastly, the corresponding shear strain distributions are computed through the de-
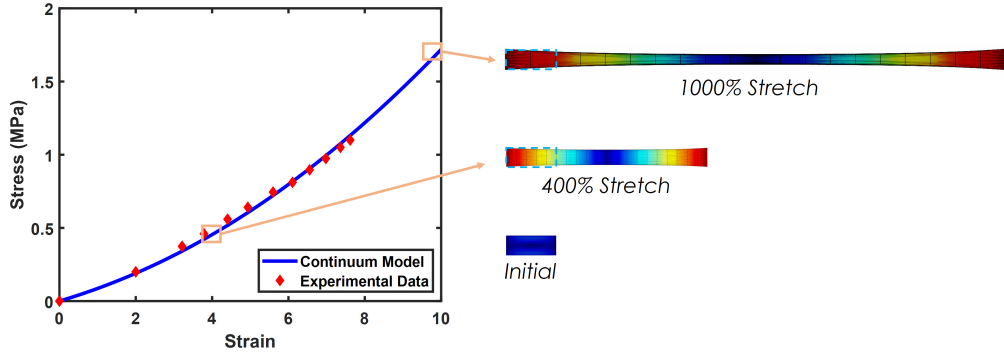
Figure 7.14: Stress-strain curves (left) and deformed configurations at different stretches (right) for MWCNTs reinforced Ecoflex-0030 composite [29].

formation maps of χ_1 and χ_2 by using the relations: $\gamma_{xy} = \alpha + \beta$, where $\tan^{-1}\left(\frac{\chi_{2,1}}{1+\chi_{1,1}}\right) = \alpha$, $\tan^{-1}\left(\frac{\chi_{1,2}}{1+\chi_{2,2}}\right) = \beta$ and the results are presented in Fig. 7.16. It is apparent from Fig. 7.16 that the proposed model produces smooth and continuous shear strain fields throughout the entire domain of interest, unlike those obtained from the classical (first-order) continuum theory, where the corresponding shear strain fields experience significant discontinuities (see, for example, [85], [87], and [112]). In Fig. 7.16, three
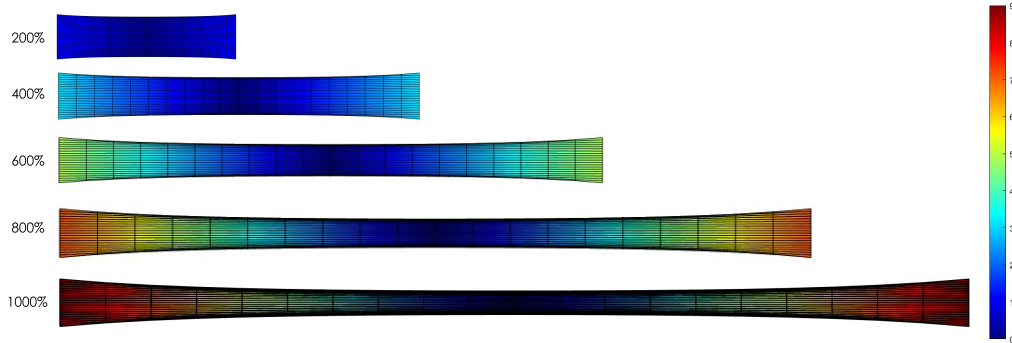
Figure 7.15: Deformation contours of MWCNTs/Ecoflex-0030 nanocomposite at different stretches.

distinct shear angle zones may be clearly visible. The dark blue regions close to the left and right edges of the domain represent low shear angle regions. The dark red area near the center of the domain represents high shear angle region. Whereas, the areas in between low and high shear regions represent transition regions, where the shear angle changes smoothly transitioning from low to high shear. In Fig. 7.16, three internal parameters (i.e., l_m, γ_m, θ) are defined to quantify the changes within

258

the shear angle fields at different stretch levels. It may be observed that as the stretch increases, the length of the high shear zone, l_m (where l_0 is the undeformed length of the material) and maximum shear angle value, γ_m both increase. Whereas, the tip angle, θ of the high shear zone decreases with increasing stretch.
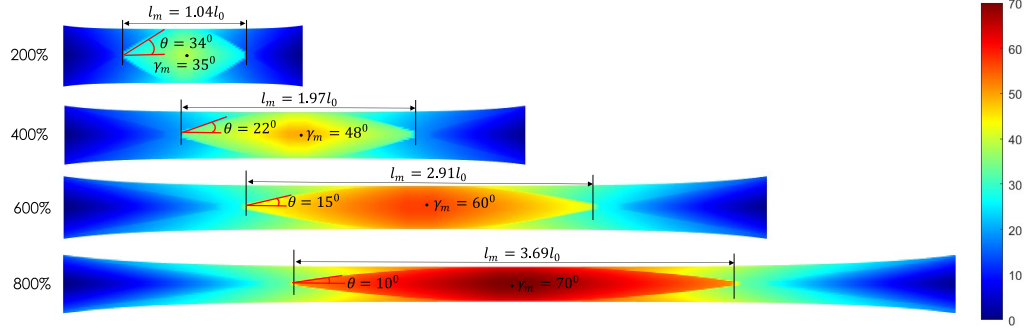
Figure 7.16: Shear strain contours of MWCNTs/Ecoflex-0030 nanocomposite at different stretches.

7.5 Finite element analysis of the 4th order coupled PDE:

The system of PDEs in Eq. (7.45) are 4th order coupled differential equations. The case of such less regular PDE system deserves delicate mathematical treatment and is of particular practical interest. Therefore, it may not be trivial to report the associated FEA procedure. After performing the Einstein summation and applying $\mathbf{D} = \mathbf{E}_1$ (i.e., $D_1 = 1$, $D_2 = 0$), Eq. (7.45) may be rearranged into the following form:

$$
\begin{aligned}
0 = {} & (1-\alpha)\mu(Q + \chi_{1,22}) + (1-\alpha)\kappa(Q + E_{,2})(CC + EE + DD + FF) \\
& -(1-\alpha)\kappa(Q + C_{,2} + E_{,1} + E_{,2})(CC + CE + EC + EE + DD \\
& +DF + FD + FF) + (1-\alpha)\kappa(C + E)(2QC + 2E_{,1}E + 2C_{,2}C \\
& +2E_{,2}E - QC - QE - E_{,2}C - E_{,2}E - CQ - CE_{,1} \\
& -EC_{,2} - EE_{,2} + 2RD + 2F_{,1}F + 2D_{,2}D + 2F_{,2}F - RD \\
& -RF - F_{,2}D - F_{,2}F - DR - DF_{,1} - FD_{,2} - FF_{,2}) \\
& +\alpha\eta_0\varsigma^2\frac{E_g}{2}(CC\chi_{1,1} + DD\chi_{1,1})_{,1} - \alpha\eta_0\varsigma^2\frac{E_g}{2}Q \\
& -A_0\chi_{2,2} + B_0\chi_{2,1} - \alpha cQ_{,11},
\end{aligned}
$$

259

$$
\begin{aligned}
0 = \ & (1-\alpha)\mu(R + \chi_{2,22}) + (1-\alpha)\kappa(R + F_{,2})(CC + EE + DD + FF) \\
& -(1-\alpha)\kappa(R + D_{,2} + F_{,1} + F_{,2})(CC + CE + EC + EE + DD \\
& +DF + FD + FF) + (1-\alpha)\kappa(D + F)(2QC + 2E_{,1}E + 2C_{,2}C \\
& +2E_{,2}E - QC - QE - E_{,2}C - E_{,2}E - CQ - CE_{,1} \\
& -EC_{,2} - EE_{,2} + 2RD + 2F_{,1}F + 2D_{,2}D + 2F_{,2}F - RD \\
& -RF - F_{,2}D - F_{,2}F - DR - DF_{,1} - FD_{,2} - FF_{,2}) \\
& +\alpha\eta_0\varsigma^2\frac{E_g}{2}(CC\chi_{2,1} + DD\chi_{2,1})_{,1} - \alpha\eta_0\varsigma^2\frac{E_g}{2}R \\
& +A_0\chi_{1,2} - B_0\chi_{1,1} - \alpha c R_{,11},
\end{aligned}
$$

$$
\begin{aligned}
0 &= Q - \chi_{1,11}, \\
0 &= R - \chi_{2,11}, \\
0 &= C - \chi_{1,1}, \\
0 &= D - \chi_{2,1}, \\
0 &= E - \chi_{1,2}, \\
0 &= F - \chi_{2,2}, \\
0 &= A - (1-\alpha)\mu(Q + \chi_{1,22}) - \alpha c Q_{,11}, \\
0 &= B - (1-\alpha)\mu(R + \chi_{2,22}) - \alpha c R_{,11}, \quad\quad (7.66)
\end{aligned}
$$

where $Q = \chi_{1,11}$, $R = \chi_{2,11}$, $C = \chi_{1,1}$, $D = \chi_{2,1}, E = \chi_{1,2}$, and $F = \chi_{2,2}$. Hence, the differential equations are transformed from the three coupled equations of the 4th order to ten coupled equations of the 2nd order. Especially, the non-linear terms in the above equations (e.g., $A\chi_{2,2}, B\chi_{2,1}$ etc...) may be systematically treated via the Picard iterative procedure and/or Newton method;

$$
\begin{aligned}
-A^{initial}\chi_{2,2}^{initial} + B^{initial}\chi_{2,1}^{initial} &\implies -A_0\chi_{2,2}^0 + B_0\chi_{2,1}^0 \\
A^{initial}\chi_{1,2}^{initial} - B^{initial}\chi_{1,1}^{initial} &\implies A_0\chi_{1,2}^0 - B_0\chi_{1,1}^0, \quad\quad (7.67)
\end{aligned}
$$

where the estimated values of A, B continue to be updated based on their previous estimations (e.g., A_1 and B_1 are refreshed by their previous estimations of A_o and B_o) as iteration progresses and similarly for the rest of non-linear terms.

Also, the weight forms of Eq. (7.66) can be found as

$$
\begin{aligned}
0 = \int_\Omega & w_1\{(1-\alpha)\mu(Q+\chi_{1,22}) + (1-\alpha)\kappa(Q+E_{,2})(CC+EE+DD+FF) \\
& -(1-\alpha)\kappa(Q+C_{,2}+E_{,1}+E_{,2})(CC+CE+EC+EE+DD+DF+FD \\
& +FF) + (1-\alpha)\kappa(C+E)(2QC+2E_{,1}E+2C_{,2}C+2E_{,2}E-QC-QE \\
& -E_{,2}C - E_{,2}E - CQ - CE_{,1} - EC_{,2} - EE_{,2} + 2RD + 2F_{,1}F + 2D_{,2}D \\
& +2F_{,2}F - RD - RF - F_{,2}D - F_{,2}F - DR - DF_{,1} - FD_{,2} - FF_{,2}) \\
& +\alpha\eta_0\varsigma^2\frac{E_g}{2}(CC\chi_{1,1}+DD\chi_{1,1})_{,1} - \alpha\eta_0\varsigma^2\frac{E_g}{2}Q - A_0\chi_{2,2} + B_0\chi_{2,1} \\
& -\alpha c Q_{,11}\}d\Omega,
\end{aligned}
$$

$$
\begin{aligned}
0 = \int_\Omega & w_2\{(1-\alpha)\mu(R+\chi_{2,22}) + (1-\alpha)\kappa(R+F_{,2})(CC+EE+DD+FF) \\
& -(1-\alpha)\kappa(R+D_{,2}+F_{,1}+F_{,2})(CC+CE+EC+EE+DD+DF+FD \\
& +FF) + (1-\alpha)\kappa(D+F)(2QC+2E_{,1}E+2C_{,2}C+2E_{,2}E-QC-QE \\
& -E_{,2}C - E_{,2}E - CQ - CE_{,1} - EC_{,2} - EE_{,2} + 2RD + 2F_{,1}F + 2D_{,2}D \\
& +2F_{,2}F - RD - RF - F_{,2}D - F_{,2}F - DR - DF_{,1} - FD_{,2} - FF_{,2}) \\
& +\alpha\eta_0\varsigma^2\frac{E_g}{2}(CC\chi_{2,1}+DD\chi_{2,1})_{,1} - \alpha\eta_0\varsigma^2\frac{E_g}{2}R + A_0\chi_{1,2} - B_0\chi_{1,1} \\
& -\alpha c R_{,11}\}d\Omega,
\end{aligned}
$$

$$
\begin{aligned}
0 &= \int_\Omega w_3(Q - \chi_{1,11})d\Omega, \\
0 &= \int_\Omega w_4(R - \chi_{2,11})d\Omega, \\
0 &= \int_\Omega w_5(C - \chi_{1,1})d\Omega, \\
0 &= \int_\Omega w_6(D - \chi_{2,1})d\Omega, \\
0 &= \int_\Omega w_7(E - \chi_{1,2})d\Omega, \\
0 &= \int_\Omega w_8(F - \chi_{2,2})d\Omega, \\
0 &= \int_\Omega w_9(A - (1-\alpha)\mu(Q+\chi_{1,22}) - \alpha c Q_{,11})d\Omega, \\
0 &= \int_\Omega w_{10}(B - (1-\alpha)\mu(R+\chi_{2,22}) - \alpha c R_{,11})d\Omega. \tag{7.68}
\end{aligned}
$$

261

Thus, we apply integration by part and the Green-Stokes' theorem, (e.g., $\mu \int_{\Omega^e} w_1 \chi_{1,22} d\Omega =$ $-\mu \int_{\Omega^e} w_{1,2} \chi_{1,2} d\Omega + \mu \int_{\partial\Gamma} w_1 \chi_{1,2} N d\Gamma$) and thereby obtain the following weak forms of Eq. (7.68):

$$
\begin{aligned}
0 = \int_\Omega \{ & (1-\alpha)\mu w_1 Q - (1-\alpha)\mu w_{1,2}\chi_{1,2} + (1-\alpha)\kappa w_1(Q + E_{,2})(CC + EE \\
& + DD + FF) - (1-\alpha)\kappa w_1(Q + C_{,2} + E_{,1} + E_{,2})(CC + CE + EC + EE \\
& + DD + DF + FD + FF) + (1-\alpha)\kappa w_1(C + E)(2QC + 2E_{,1}E + 2C_{,2}C \\
& + 2E_{,2}E - QC - QE - E_{,2}C - E_{,2}E - CQ - CE_{,1} - EC_{,2} - EE_{,2} + 2RD \\
& + 2F_{,1}F + 2D_{,2}D + 2F_{,2}F - RD - RF - F_{,2}D - F_{,2}F - DR - DF_{,1} \\
& - FD_{,2} - FF_{,2}) + \alpha\eta_0\varsigma^2 \frac{E_g}{2} w_1(CC\chi_{1,1} + DD\chi_{1,1})_{,1} - \alpha\eta_0\varsigma^2 w_1 \frac{E_g}{2}Q \\
& - A_0 w_1\chi_{2,2} + B_0 w_1\chi_{2,1} + \alpha c w_{1,1}Q_{,1}\}d\Omega - c\alpha \int_{\partial\Gamma} w_1 Q_{,1} N d\Gamma \\
& + (1-\alpha)\mu \int_{\partial\Gamma} w_1 \chi_{1,2} N d\Gamma,
\end{aligned}
$$

$$
\begin{aligned}
0 = \int_\Omega \{ & (1-\alpha)w_2\mu R - (1-\alpha)w_{2,2}\mu\chi_{2,2} + (1-\alpha)\kappa w_2(R + F_{,2})(CC + EE \\
& + DD + FF) - (1-\alpha)\kappa w_2(R + D_{,2} + F_{,1} + F_{,2})(CC + CE + EC + EE \\
& + DD + DF + FD + FF) + (1-\alpha)\kappa w_2(D + F)(2QC + 2E_{,1}E + 2C_{,2}C \\
& + 2E_{,2}E - QC - QE - E_{,2}C - E_{,2}E - CQ - CE_{,1} - EC_{,2} - EE_{,2} + 2RD \\
& + 2F_{,1}F + 2D_{,2}D + 2F_{,2}F - RD - RF - F_{,2}D - F_{,2}F - DR - DF_{,1} \\
& - FD_{,2} - FF_{,2}) + \alpha\eta_0\varsigma^2 \frac{E_g}{2} w_2(CC\chi_{2,1} + DD\chi_{2,1})_{,1} - \alpha\eta_0\varsigma^2 w_2 \frac{E_g}{2}R \\
& + A_0 w_2\chi_{1,2} - B_0 w_2\chi_{1,1} + \alpha c w_{2,1}R_{,1}\}d\Omega - \alpha c \int_{\partial\Gamma} w_2 R_{,1} N d\Gamma \\
& + (1-\alpha)\mu \int_{\partial\Gamma} w_2 \chi_{2,2} N d\Gamma,
\end{aligned}
$$

$$0 = \int_\Omega (w_3 Q + w_{3,1}\chi_{1,1})d\Omega - \int_{\partial\Gamma} w_3\chi_{1,1}Nd\Gamma,$$

$$0 = \int_\Omega (w_4 R + w_{4,1}\chi_{2,1})d\Omega - \int_{\partial\Gamma} w_{4,1}\chi_{2,1}Nd\Gamma,$$

$$0 = \int_\Omega (w_5 C - w_5\chi_{1,1})d\Omega,$$

$$0 = \int_\Omega w_6(D - \chi_{2,1})d\Omega,$$

$$0 = \int_\Omega w_7(E - \chi_{1,2})d\Omega,$$

$$0 = \int_\Omega w_8(F - \chi_{2,2})d\Omega,$$

$$0 = \int_\Omega (w_9 A - (1-\alpha)\mu w_9 Q + (1-\alpha)\mu w_{9,2}\chi_{1,2} + \alpha c w_{9,1}Q_{,1})d\Omega$$
$$- \int_{\partial\Gamma} (1-\alpha)\mu w_9\chi_{1,2}Nd\Gamma - \int_{\partial\Gamma} \alpha c w_9 Q_{,1}Nd\Gamma,$$

$$0 = \int_\Omega (w_{10} B - (1-\alpha)\mu w_{10} R + (1-\alpha)\mu w_{10,2}\chi_{2,2} + \alpha c w_{10,1}R_{,1})d\Omega$$
$$- \int_{\partial\Gamma} (1-\alpha)\mu w_{10}\chi_{2,2}Nd\Gamma - \int_{\partial\Gamma} \alpha c w_{10}R_{,1}Nd\Gamma, \tag{7.69}$$

where Ω, $\partial\Gamma$, and N are respectively, the domain of interest, the associated boundary, and the rightward unit normal to the boundary $\partial\Gamma$ in the sense of the Green-Stokes' theorem. The unknown potentials of χ_1, χ_2, Q, R, C, D, E, F, A, and B may be expressed in the form of Lagrangian polynomial that

$$(*) = \sum_{j=1}^{n=4} [(*)_j \Psi_j(x, y)]. \tag{7.70}$$

Accordingly, the test function w is found to be

$$w_m = \sum_{i=1}^{n=4} w_m^i \Psi_i(x, y); \ \ i = 1, 2, 3, 4, \ \text{and} \ m = 1, 2, 3, 4, \dots.10, \tag{7.71}$$

where w_i is the weight of the test function and $\Psi_i(x, y)$ are the associated shape functions; $\Psi_1 = \frac{(x-2)(y-1)}{2}$, $\Psi_2 = \frac{x(y-1)}{-2}$, $\Psi_3 = \frac{xy}{2}$, and $\Psi_4 = \frac{y(x-2)}{-2}$. Invoking Eq. (7.70), the Eq. (7.69) can be recast in terms of Lagrangian polynomial representation as

$$
\begin{aligned}
0 \;=\; & \sum_{i,j=1}^{n=4} \int_{\Omega^e} \{ (1-\alpha)\mu\Psi_i\Psi_j Q_j - (1-\alpha)\mu\Psi_{i,2}\Psi_{j,2}\chi_{1j} + (1-\alpha)\kappa(\Psi_i\Psi_j Q_j + \Psi_{i,2}\Psi_{j,2}E_j) \\
& (CC + EE + DD + FF) - (1-\alpha)\kappa(\Psi_i\Psi_j Q + \Psi_i\Psi_{j,2}C_j + \Psi_i\Psi_{j,1}E_j + \Psi_i\Psi_{j,2}E_j) \\
& (CC + CE + EC + EE + DD + DF + FD + FF) + (1-\alpha)\kappa(C + E)(2\Psi_i\Psi_j QC_j \\
& + 2\Psi_i\Psi_{j,1}E_j E + 2\Psi_i\Psi_{j,2}C_j C + 2\Psi_i\Psi_{j,2}E_j E - \Psi_i\Psi_j QC - \Psi_i\Psi_j QE - \Psi_i\Psi_{j,2}E_j C \\
& - \Psi_i\Psi_{j,2}E_j E - \Psi_i\Psi_j CQ - \Psi_i\Psi_{j,1}CE_j - \Psi_i\Psi_{j,2}EC_j - \Psi_i\Psi_{j,2}EE_j + 2\Psi_i\Psi_j RD \\
& + 2\Psi_i\Psi_{j,1}F_j F + 2\Psi_i\Psi_{j,2}D_j D + 2\Psi_i\Psi_{j,2}F_j F - \Psi_i\Psi_j RD - \Psi_i\Psi_j RF - \Psi_i\Psi_{j,2}F_j D \\
& - \Psi_i\Psi_{j,2}F_j F - \Psi_i\Psi_j DR - \Psi_i\Psi_{j,1}DF_j - \Psi_i\Psi_{j,2}FD_j - \Psi_i\Psi_{j,2}FF_j) \\
& + \alpha\eta_0\varsigma^2\frac{E_g}{2}(2\Psi_i\Psi_{j,1}QC\chi_{1,1} + \Psi_i\Psi_{j,1}CCQ_{,1} + 2\Psi_i\Psi_{j,1}RD\chi_{1,1} + \Psi_i\Psi_{j,1}DDQ_{,1}) \\
& - \alpha\eta_0\varsigma^2\Psi_i\Psi_j\frac{E_g}{2}Q - A_0\Psi_i\Psi_{j,2}\chi_{2j} + B_0\Psi_i\Psi_{j,1}\chi_{2j} + \alpha c\Psi_{i,1}\Psi_{j,1}Q_j\} d\Omega \\
& + \sum_{i=1}^{n=4} \{ (1-\alpha)\mu \int_{\partial\Gamma_e} w_i\chi_{1,2}Nd\Gamma - \alpha c \int_{\partial\Gamma^e} w_i Q_{,1}Nd\Gamma \},
\end{aligned}
$$

$$
\begin{aligned}
0 \;=\; & \sum_{i,j=1}^{n=4} \int_{\Omega^e} \{ (1-\alpha)\mu\Psi_i\Psi_j R_j - (1-\alpha)\mu\Psi_{i,2}\Psi_{j,2}\chi_{2j} + (1-\alpha)\mu(\Psi_i\Psi_j R_j + \Psi_{i,2}\Psi_{j,2}F_j) \\
& (CC + EE + DD + FF) - (1-\alpha)\mu(\Psi_i\Psi_j R + \Psi_i\Psi_{j,2}D_j + \Psi_i\Psi_{j,1}F_j + \Psi_i\Psi_{j,2}F_j) \\
& (CC + CE + EC + EE + DD + DF + FD + FF) + (1-\alpha)\mu w_2(D + F)(2\Psi_i\Psi_j QC_j \\
& + 2\Psi_i\Psi_{j,1}E_j E + 2\Psi_i\Psi_{j,2}C_j C + 2\Psi_i\Psi_{j,2}E_j E - \Psi_i\Psi_j QC - \Psi_i\Psi_j QE - \Psi_i\Psi_{j,2}E_j C \\
& - \Psi_i\Psi_{j,2}E_j E - \Psi_i\Psi_j CQ - \Psi_i\Psi_{j,1}CE_j - \Psi_i\Psi_{j,2}EC_j - \Psi_i\Psi_{j,2}EE_j + 2\Psi_i\Psi_j RD \\
& + 2\Psi_i\Psi_{j,1}F_j F + 2\Psi_i\Psi_{j,2}D_j D + 2\Psi_i\Psi_{j,2}F_j F - \Psi_i\Psi_j RD - \Psi_i\Psi_j RF - \Psi_i\Psi_{j,2}F_j D \\
& - \Psi_i\Psi_{j,2}F_j F - \Psi_i\Psi_j DR - \Psi_i\Psi_{j,1}DF_j - \Psi_i\Psi_{j,2}FD_j - \Psi_i\Psi_{j,2}FF_j) \\
& + \alpha\eta_0\varsigma^2\frac{E_g}{2}(2\Psi_i\Psi_{j,1}QC\chi_{1,1} + \Psi_i\Psi_{j,1}CCQ_{,1} + 2\Psi_i\Psi_{j,1}RD\chi_{2,1} + \Psi_i\Psi_{j,1}DDR_{,1}) \\
& - \alpha\eta_0\varsigma^2\Psi_i\Psi_j\frac{E_g}{2}R + A_0\Psi_i\Psi_{j,2}\chi_{1j} - B_0\Psi_i\Psi_{j,1}\chi_{1j} + \alpha c\Psi_{i,1}\Psi_{j,1}R_j\} d\Omega \\
& + \sum_{i=1}^{n=4} \{ (1-\alpha)\mu \int_{\partial\Gamma^e} w_i\chi_{2,2}Nd\Gamma - \alpha c \int_{\partial\Gamma^e} w_i R_{,1}Nd\Gamma \},
\end{aligned}
$$

264

$$0 = \sum_{i,j=1}^{n=4}\{\int_{\Omega^e}(\Psi_i\Psi_j)d\Omega\}Q_j + \sum_{i,j=1}^{n=4}\{\int_{\Omega^e}\Psi_{i,1}\Psi_{j,1})d\Omega\}\chi_{1j} - \sum_{i=1}^{n=4}\int_{\partial\Gamma^e}(\Psi_i\chi_{1,1})Nd\Gamma,$$

$$0 = \sum_{i,j=1}^{n=4}\int_{\Omega^e}(w_4 R + w_{4,1}\chi_{2,1})d\Omega - \sum_{i=1}^{n=4}\int_{\partial\Gamma^e}w_{4,1}\chi_{2,1}Nd\Gamma,$$

$$0 = \sum_{i,j=1}^{n=4}\{\int_{\Omega^e}(\Psi_i\Psi_j)d\Omega\}R_j + \sum_{i,j=1}^{n=4}\{\int_{\Omega^e}\Psi_{i,1}\Psi_{j,1})d\Omega\}\chi_{2j} - \sum_{i=1}^{n=4}\int_{\partial\Gamma^e}(\Psi_i\chi_{2,1})Nd\Gamma,$$

$$0 = \sum_{i,j=1}^{n=4}\{\int_{\Omega^e}(\Psi_i\Psi_j)d\Omega\}C_j - \sum_{i,j=1}^{n=4}\{\int_{\Omega^e}(\Psi_i\Psi_{j,1})d\Omega\}\chi_{1j},$$

$$0 = \sum_{i,j=1}^{n=4}\{\int_{\Omega^e}(\Psi_i\Psi_j)d\Omega\}D_j - \sum_{i,j=1}^{n=4}\{\int_{\Omega^e}(\Psi_i\Psi_{j,1})d\Omega\}\chi_{2j},$$

$$0 = \sum_{i,j=1}^{n=4}\{\int_{\Omega^e}(\Psi_i\Psi_j)d\Omega\}E_j - \sum_{i,j=1}^{n=4}\{\int_{\Omega^e}(\Psi_i\Psi_{j,2})d\Omega\}\chi_{1j},$$

$$0 = \sum_{i,j=1}^{n=4}\{\int_{\Omega^e}(\Psi_i\Psi_j)d\Omega\}F_j - \sum_{i,j=1}^{n=4}\{\int_{\Omega^e}(\Psi_i\Psi_{j,2})d\Omega\}\chi_{2j},$$

$$0 = \sum_{i,j=1}^{n=4}\{\int_{\Omega^e}(\Psi_i\Psi_j)d\Omega\}A_j + \sum_{i,j=1}^{n=4}\{\int_{\Omega^e}(-(1-\alpha)\mu\Psi_i\Psi_j + \alpha c\Psi_{i,1}\Psi_{j,1})d\Omega\}Q_j$$

$$+ \sum_{i,j=1}^{n=4}\{\int_{\Omega^e}(1-\alpha)(\mu\Psi_{i,2}\Psi_{j,2})d\Omega\}\chi_{1j} - \sum_{i=1}^{n=4}\{\int_{\partial\Gamma^e}(1-\alpha)(\mu\Psi_i\chi_{1,2})Nd\Gamma$$

$$- \int_{\partial\Gamma^e}(\alpha c\Psi_i Q_{,1})Nd\Gamma\},$$

$$0 = \sum_{i,j=1}^{n=4}\{\int_{\Omega^e}(\Psi_i\Psi_j)d\Omega\}B_j + \sum_{i,j=1}^{n=4}\int_{\Omega^e}\{-(1-\alpha)\mu\Psi_i\Psi_j + \alpha c\Psi_{i,1}\Psi_{j,1}\}d\Omega R_j$$

$$+ \sum_{i,j=1}^{n=4}\{\int_{\Omega^e}(1-\alpha)(\mu\Psi_{i,2}\Psi_{j,2})d\Omega\}\chi_{2j} - \sum_{i=1}^{n=4}\{\int_{\partial\Gamma^e}(1-\alpha)(\mu\Psi_i\chi_{2,2})Nd\Gamma$$

$$- \int_{\partial\Gamma^e}(\alpha c\Psi_i R_{,1})Nd\Gamma\}. \tag{7.72}$$

Now, for the local stiffness matrices and forcing vectors for each element, we find

$$\begin{bmatrix} K_{11}^{11} & K_{12}^{11} & K_{13}^{11} & K_{14}^{11} \\ K_{21}^{11} & K_{22}^{11} & K_{23}^{11} & K_{24}^{11} \\ K_{31}^{11} & K_{32}^{11} & K_{33}^{11} & K_{34}^{11} \\ K_{41}^{11} & K_{42}^{11} & K_{43}^{11} & K_{44}^{11} \end{bmatrix}_{Local} \begin{bmatrix} \chi_1^1 \\ \chi_1^2 \\ \chi_1^3 \\ \chi_1^4 \end{bmatrix}_{Local} = \begin{bmatrix} F_1^1 \\ F_2^1 \\ F_3^1 \\ F_4^1 \end{bmatrix}_{Local}, \tag{7.73}$$

where

$$[K_{ij}^{11}] = \int_{\Omega^e}\{-(1-\alpha)\mu\Psi_{i,2}\Psi_{j,2}\}d\Omega, \tag{7.74}$$

265

and

$$\{F_i^1\} = -\mu \int_{\partial\Gamma^e} w_i \chi_{1,2} N d\Gamma + c \int_{\partial\Gamma^e} w_i Q_{,1} N d\Gamma. \qquad (7.75)$$

Thus, the unknown potentials (i.e., χ_1, χ_2, Q, R, C, D, E, F, A, and B) can be expressed as

$$Q_i = \{\chi_1^i\}_{,11}, \ R_i = \{\chi_2^i\}_{,11}, \ \text{etc...}, \qquad (7.76)$$

and similarly for the rest of unknowns.

Consequently, we obtain the following systems of equations (in the Global form) for each individual element as

$$
\begin{bmatrix}
[K^{11}] & [K^{12}] & \cdot & \cdot & \cdot & \cdot & \cdot & [K^{19}] & [K^{110}] \\
[K^{21}] & [K^{22}] & \cdot & \cdot & \cdot & \cdot & \cdot & [K^{29}] & [K^{210}] \\
[K^{31}] & [K^{32}] & \cdot & \cdot & \cdot & \cdot & \cdot & [K^{39}] & [K^{310}] \\
[K^{41}] & [K^{42}] & \cdot & \cdot & \cdot & \cdot & \cdot & [K^{49}] & [K^{410}] \\
[K^{51}] & [K^{52}] & \cdot & \cdot & \cdot & \cdot & \cdot & [K^{59}] & [K^{510}] \\
[K^{61}] & [K^{62}] & \cdot & \cdot & \cdot & \cdot & \cdot & [K^{69}] & [K^{610}] \\
[K^{71}] & [K^{72}] & \cdot & \cdot & \cdot & \cdot & \cdot & [K^{79}] & [K^{710}] \\
[K^{81}] & [K^{82}] & \cdot & \cdot & \cdot & \cdot & \cdot & [K^{89}] & [K^{810}] \\
[K^{91}] & [K^{92}] & \cdot & \cdot & \cdot & \cdot & \cdot & [K^{99}] & [K^{910}] \\
[K^{101}] & [K^{102}] & \cdot & \cdot & \cdot & \cdot & \cdot & [K^{109}] & [K^{1010}]
\end{bmatrix}
\begin{bmatrix}
\chi_1^i \\ \chi_2^i \\ Q_i \\ R_i \\ C_i \\ D_i \\ E_i \\ F_i \\ A_i \\ B_i
\end{bmatrix}
=
\begin{bmatrix}
\{F_1\} \\ \{F_2\} \\ \{F_3\} \\ \{F_4\} \\ \{F_5\} \\ \{F_6\} \\ \{F_7\} \\ \{F_8\} \\ \{F_9\} \\ \{F_{10}\}
\end{bmatrix}
. \qquad (7.77)
$$

In the simulation, we employed the following convergence criteria

$$|A_{n+1} - A_n| = e_1 \le \varepsilon, \ |B_{n+1} - B_n| = e_2 \le \varepsilon, \ \text{where } \varepsilon = \text{maximum error} = 10^{-10},$$

which demonstrates fast (quadratic) convergence within just 5 iterations using FEniCS nonlinear solver (see, 7.4).

Table 7.4: Maximum numerical errors with respect to the number of iterations.

Number of iteration	Mximum error
1	2.623e+01
2	8.035e-02
3	1.226-04
4	1.295e-08
5	3.888e-15

7.6   Denouement

In this chapter, a multiscale continuum model for the mechanics of hyperelastic nanocomposites reinforced with randomly oriented fibers is presented in finite plane

elastostatics. This includes the refinement of a set of strain energy potential of fibers in light of the shear lag theory and the orientation model of Krenchel. The kinematics of embedded fibers, including bending and extension responses, are formulated via the first and second gradient of continuum deformations and subsequently incorporated into the model describing the mechanical responses of the fiber-matrix system. The non-linear (strain-stiffening) responses of matrix material are characterized by using the Mooney-Rivlin strain energy potential. Within the framework of variational principles and a virtual work statement, the Euler equilibrium equation and the associated boundary conditions are derived. The resulting equations are in the form of the systems of coupled nonlinear PDEs from which a set of numerical solutions describing the hyperelastic responses of the elastomeric nanocomposites are obtained via the custom-built FEA procedure. Atomistic molecular dynamics (MD) simulation is also performed to obtain micromechanical properties of fiber composites which are then integrated into the proposed multiscale continuum model.

Throughout the cross-examination with the existing experimental results and MD simulations, we show that the presented model successfully estimates the stiffness of the graphene fiber reinforced composite with respect to varying fiber's aspect ratio. The obtained model demonstrates equivalent (and/or better) predictions performance over the conventional mean-field micromechanical predictive model (Mori-Tanaka) and hence, may serve as an alternative to the Mori-Tanaka model. Further, we extend the obtained model by proposing a non-uniform interface stiffness parameter (inspired by the Weibull damage model) to assimilate the damage mechanics of nanofiber-reinforced elastomeric composites induced by interfacial debonding. It is found that the results from the generalized model closely assimilate both the gradual and rapid debonding processes of a certain type of soft/stiff matrix-based nanocomposite. Lastly, we consider the hyperextension of MWCNTs/Ecoflex elastomeric nanocomposite material. The results demonstrate that the proposed model predicts non-linear stress-strain response (strain-stiffening) of the composite with reasonable accuracy and produces smooth and continuous shear strain distributions throughout the domain of interest.

Chapter 8

Conclusion and Future works

8.1 Conclusion

In this thesis, we have presented a generalized higher-order gradient-based continuum model for the fiber-reinforced hyperelastic composite material. In each chapter of this thesis, we have step-by-step refined the model ultimately leading to a generalized continuum model that can incorporate multiple features including, higher-order gradient continua, precise characterization of fiber reinforcement, pseudoelasticity, damage mechanics, and multi-scale capability. All these combinedly make the presented model uniquely versatile in the modeling and design of hyperelastic composites. The roadmap of this research work is presented below briefly.

We start with a third-order gradient composite model where Neo-Hookean type hyperelastic matrix material is reinforced by unidirectional fibers having resistance in flexure (see, chapter 2). The results from the presented model convey some understanding of the effects of higher-gradient terms on the solution fields. It is observed that the higher gradient model is able to produce smooth and dilatational shear angle distribution. Also, the third gradient term affects the changes in the curvature of fibers. Next, we refine the energy density function by incorporating the fiber extension potential term along with bending resistance and considering the Mooney-Rivlin potential for the hyperelastic matrix material (see, chapter 3). The obtained results demonstrate that the model is able to capture large deformation under uniaxial loading and provide reasonably accurate predictions of the deformation profiles. After that, we further generalize the energy density function by incorporating bi-directional fibers having different orientations (i.e., 45 and 90-degree orientations),

different types of nonlinear extension potential (i.e., polynomial and exponential), and torsional resistance (see, chapter 4 and 5). The results from the generalized model demonstrate excellent correspondence to the experimental results in capturing the deformations and mechanical responses under different loading conditions including uniaxial tension, and out-of-plane deformations. To incorporate pseudoelasticity, the model is then further extended by introducing damage parameters and damage functions inspired by Ogden Roxburgh's model and Weibull's fiber damage model (see, chapter 6). It is demonstrated that the obtained model can successfully predict the Mullins effects in biological soft tissues and strain softening due to fiber breakage. Furthermore, we have augmented our model to accommodate the size, orientation effects, and volume fraction of the reinforcing fibers by introducing the shear-lag, Krenchel orientation, and energy fraction parameters, respectively (see, chapter 7). This adaptation allows the model to predict the responses of nanofiber-reinforced hyperelastic composites having different micromechanical characterizations. Also, It allows the multi-scale capability of the model by incorporating the effects of some micro/nanoscale properties (e.g., interface stiffness, volume fraction, fiber aspect ratio, etc...). Again, we propose a non-uniform interface stiffness parameter to incorporate the damage mechanics of nanofiber-reinforced elastomeric composites due to interfacial debonding. The resulting model closely assimilates both the gradual and rapid debonding processes of a certain type of soft/stiff matrix-based nanocomposite.

This generalization of the presented model leads to the following conclusion:

- The higher gradient term has strong effects on the shear angle fields. By increasing the order of the continuum model, it is possible to produce a more smooth and dilatational shear angle distribution.

- The higher-order gradient model allows us to accurately capture the local microstructural changes in the continua.

- The presented model is able to predict very large deformation, i.e., extension up to 10 times the initial length of the domain.

- The presented model is able to accommodate different types of fiber reinforcement including, unidirectional continuous fibers and bidirectional continuous

fibers having different orientations. Moreover, the model can also accommodate different types of fiber responses by utilizing multiple types of extension potential functions.

- By incorporating damage parameters, the presented model is able to capture Mullins effect and strain softening due to fiber breakage.

- The presented model is able to accommodate micro/nano structural characterizations of the short / nanofibers and capture the effects of these parameters on the mechanical responses of the composite.

- The presented model is able to capture the strain-softening effect of the composites induced by both gradual and rapid debonding processes.

8.2 Contributions of the proposed model to the scientific community

The generalized hyperelastic model for composite material presented in this thesis work can make valuable contributions to the scientific community. In this study, we have developed a higher-order gradient-based hyperelastic model that can accommodate the complete kinematic description of fiber reinforcement by incorporating the extension, bending, and torsional potentials of fiber reinforcement, which the existing classical models fail to accommodate. With the help of higher gradient theory, the presented model can also produce precise characterizations of microstructures, and prediction of large & nonlinear deformation. Furthermore, the presented model provides the means to predict the response of the composite material prior to its fabrication by only utilizing the properties of its constituents, which the existing classical models can not. Moreover, the proposed model can likewise accommodate the size effect of fiber reinforcement, pseudoelastic response, and damage mechanics of the composite. This level of versatility is unprecedented in the existing literature in terms of the modeling of hyperelastic composites. All these capabilities make our model very useful in the design and analysis of hyperelastic composites, which may help to extend our knowledge regarding the mechanics of these materials.

8.3   Future Works

We already mentioned in the introduction section that hyperelastic composite materials have great potential in various engineering applications involving biomedical applications, shape-morphing structures, soft robotics, and wearable devices. The proposed model may be deemed useful in the design of such engineering devices and structures made up of hyperelastic composite materials. Moreover, the proposed model may be useful in analyzing complex biocomposites like chitin with helical fiber arrangement or other types of similar composites with complex fiber arrangements.

The present work opens the gate to new possibilities for further research into the hyperelastic composite based on multiscale modeling approach. The proposed model may be further investigated along with molecular dynamics simulation to have a better understanding of the damage mechanics induced by the deboning process at the interface of matrix and fiber, which may allow us to further refine our model by utilizing micro or nanomechanics-based damage characterizing function. Furthermore, using the presented model alongside molecular dynamics simulation it might be also possible to have a better understating of pseudoelastic behavior like the Mullins effect, where we may relate the associated parameters with micromechanical characteristics of the fibers.

The model at hand can pave the way for further research related to damage mechanics and the pseudoelastic studies of hyperelastic composite. Till now, the proposed model can accommodate up to only a few cycles of pseudoelastic loading-unloading. It may be possible to further extend the model so that it can capture the pseudoelastic behavior under a large number of cycles. The present work may be further extended to analyze the problems related to fracture mechanics and crack propagation, especially from soft composite materials. For this purpose, it is necessary to further investigate the non-recoverable portion of the energy density function and come up with a suitable governing equation for the damage variable that is able to capture the damage progression in fiber-reinforced soft materials. Finally, the viscoelastic materials may also be analyzed in a similar mathematical framework with custom-built fiber potential functions.

References

[1] *Hyperelastic materials*, 2022. [Online]. Available: `https://www.simscale.com/docs/simulation-setup/materials/hyperelastic-materials/`.

[2] N. Dishovsky and M. Mihaylov, *Elastomer-Based Composite Materials*. Taylor and Francis Group, 2018.

[3] D. Myung, W. Koh, J. Ko, *et al.*, "Biomimetic strain hardening in interpenetrating polymer network hydrogels," *Polymer*, vol. 48, pp. 5376–5387, 2007.

[4] R. E. Shadwick, "Mechanical design in arteries," *Journal of Experimental Biology*, vol. 202, no. 23, pp. 3305–3313, 1999.

[5] M. Vatankhah-Varnosfaderani, W. Daniel, M. Everhart, *et al.*, "Mimicking biological stress-strain behaviour with synthetic elastomers," *Nature*, vol. 549, no. 7673, pp. 497–501, 2017.

[6] Y. Fung, *Biomechanics*. Springer, 1993.

[7] D. Zhalmuratova, T. La, K. Yu, *et al.*, "Mimicking 'j-shaped' and anisotropic stress-strain behavior of human and porcine aorta by fabric-reinforced elastomer composites," *ACS Applied Materials & Interfaces*, vol. 11, no. 36, pp. 33 323–33 335, 2019.

[8] C. Thill, J. Etches, I. Bond, K. Potter, and P. Weaver, "Morphing skins," *The Aeronautical Journal*, vol. 112, no. 1129, pp. 117–139, 2008.

[9] E. Cholleti, J. Stringer, M. Assadian, V. Battmann, C. Bowen, and K. Aw, "Highly stretchable capacitive sensor with printed carbon black electrodes on barium titanate elastomer composite," *Sensors*, vol. 19, no. 42, 2019.

[10] A. Bannych, S. Katz, Z. Karkay, and N. Lachman, "Preserving softness and elastic recovery in silicone-based stretchable electrodes using carbon nanotubes," *Polymers*, vol. 12, no. 6, p. 1345, 2020.

[11] H. Shao, J. Li, N. Chen, G. Shao, J. Jiang, and Y. Yang, "Experimental study on bi-axial mechanical properties of warp-knitted meshes with and without initial notches," *Materials*, vol. 11, no. 10, pp. 1999–2012, 2018.

[12] S. Bouillaguet, A. Schütt, P. Alander, *et al.*, "Hydrothermal and mechanical stresses degrade fiber/matrix interfacial bond strength in dental fiber-reinforced composites," *Journal of biomedical materials research. Part B, Applied biomaterials*, vol. 76, no. 1, pp. 98–105, 2006.

[13] L. Bailly, M. Toungara, L. Orgéas, E. Bertrand, V. Deplano, and C. Geindreau, "In-plane mechanics of soft architectured fibre-reinforced silicone rubber membranes," *Journal of the mechanical behavior of biomedical materials*, vol. 40, pp. 339–353, 2014.

[14] K. Leong, S. Ramakrishna, Z. Huang, and B. G.A., "The potential of knitting for engineering composites. a review," *Composites. Part A, Applied science and manufacturing*, vol. 31, no. 3, pp. 197–220, 2000.

[15] M. Maurer, B. Röhrnbauer, A. Feola, J. Deprest, and E. Mazza, "Prosthetic meshes for repair of hernia and pelvic organ prolapse: Comparison of biomechanical properties," *Materials*, vol. 8, no. 5, pp. 2794–2808, 2015.

[16] R. Martinez, J. L. Branch, C. R. Fish, *et al.*, "Robotic tentacles with three-dimensional mobility based on flexible elastomers," *Advanced materials*, vol. 25, no. 2, pp. 205–212, 2013.

[17] Y. Fung, "Structure and stress-strain relationship of soft tissues," *American Zoologist*, vol. 24, pp. 13–22, 1984.

[18] K. Zhang, S. Kong, Y. Li, M. Lu, and D. Kong, "Soft elastomeric composite materials with skin-inspired mechanical properties for stretchable electronic circuit," *Lab on a Chip*, vol. 19, pp. 2709–2717, 2019.

[19] S. Kuthe, A. Schlothauer, S. Bodkhe, C. Hulme, and P. Ermanni, "3d printed mechanically representative aortic model made of gelatin fiber reinforced silicone composite," *Materials Letters*, vol. 320, p. 132 396, 2022.

[20] L. Dorfmann and R. W. Ogden, "Nonlinear mechanics of soft fibrous materials," *International Centre for Mechanical Sciences (CISM)*, vol. 559, 2015.

[21] J. Eaton, *Lepidopteran Anatomy*. Wiley-Interscience, 1988.

[22] H. Nüesch, "The morphology of the thorax of telea polyphemus (lepidoptera). i. skeleton and muscles," *Journal of Morphology*, vol. 93, no. 3, 1953.

[23] M. S. Tu and T. L. Daniel, "Cardiac-like behavior of an insect flight muscle," *Journal of Experimental Biology*, vol. 207, no. 14, 2004.

[24] N. T. George, S. Sponberg, and T. L. Daniel, "Temperature gradients drive mechanical energy gradients in the flight muscle of manduca sexta," *Journal of Experimental Biology*, vol. 215, no. 3, 2012.

[25] N. T. George, T. C. Irving, C. D. Williams, and T. L. Daniel, "The cross-bridge spring: Can cool muscles store elastic energy?" *Science*, vol. 340, no. 6137, 2013.

[26] H. L. Granzier and T. C. Irving, "Passive tension in cardiac muscle: Contribution of collagen, titin, microtubules, and intermediate filaments," *Biophysical Journal*, vol. 68, no. 3, 1995.

[27] R. Horowits, "Passive force generation and titin isoforms in mammalian skeletal muscle," *Biophysical Journal*, vol. 61, no. 2, 1992.

[28] A. Dorfmann, B. A. Trimmer, and W. A. Woods, "A constitutive model for muscle properties in a soft-bodied arthropod," *Journal of the Royal Society Interface*, vol. 4, no. 13, 2007.

[29] H. Mai, R. Mutlu, C. Tawk, G. Alici, and V. Sencadas, "Ultra-stretchable mwcnt–ecoflex piezoresistive sensors for human motion detection applications," *Composites Science and Technology*, vol. 173, pp. 118–124, 2019.

[30] J. Gu, D. Kwon, J. Ahn, and I. Park, "Wearable strain sensors using light transmittance change of carbon nanotube-embedded elastomers with microcracks," *ACS Applied Materials & Interfaces*, vol. 12, no. 9, pp. 10 908–10 917, 2020.

[31] P. Zhang, Y. Chen, Y. Li, Y. Zhang, J. Zhang, and L. Huang, "A flexible strain sensor based on the porous structure of a carbon black/carbon nanotube conducting network for human motion detection," *Sensors*, vol. 20, no. 4, p. 1154, 2020.

[32] G. Yang, G. Pang, Z. Pang, Y. Gu, M. Mantysalo, and H. Yang, "Noninvasive flexible and stretchable wearable sensors with nano-based enhancement for chronic disease care," *IEEE Reviews in Biomedical Engineering*, vol. 12, pp. 34–71, 2019.

[33] Y. Zhang, X. Zhu, Y. Liu, *et al.*, "Ultra-stretchable monofilament flexible sensor with low hysteresis and linearity based on mwcnts/ecoflex composite materials," *Macromolecular Materials and Engineering*, vol. 306, no. 8, p. 2 100 113, 2021.

[34] H. Souri, H. Banerjee, A. Jusufi, *et al.*, "Wearable and stretchable strain sensors: Materials, sensing mechanisms, and applications," *Advanced Intelligent Systems*, vol. 2, no. 8, p. 2 000 039, 2020.

[35] S. Tadakaluru, W. Thongsuwan, and P. Singjai, "Stretchable and flexible high-strain sensors made using carbon nanotubes and graphite films on natural rubber," *Sensors*, vol. 14, no. 1, pp. 868–876, 2014.

[36] G. Liu, Y. Chen, M. Gong, *et al.*, "Enhanced dielectric performance of pdms-based three-phase percolative nanocomposite films incorporating a high dielectric constant ceramic and conductive multi-walled carbon nanotubes," *Journal of Materials Chemistry C*, vol. 6, no. 40, 2018.

[37] P. Feng, M. Zhong, and W. Zhao, "Stretchable multifunctional dielectric nanocomposites based on polydimethylsiloxane mixed with metal nanoparticles," *Materials Research Express*, vol. 7, no. 1, 2019.

[38] *Why do we need soft robotics?* May 2019. [Online]. Available: `https://comm unity.robotshop.com/blog/show/why-do-we-need-soft-robotics`.

[39] N. Sholl, A. Moss, M. Krieg, and K. Mohseni, "Controlling the deformation space of soft membranes using fiber reinforcement," *The International Journal of Robotics Research*, vol. 40, no. 1, pp. 178–196, 2021.

[40] V. Cacucciolo, F. Renda, E. Poccia, C. Laschi, and M. Cianchetti, "Modelling the nonlinear response of fibre-reinforced bending fluidic actuators," *Smart Materials and Structures*, vol. 25, no. 10, p. 105 020, 2016.

[41] T. Wang, L. Ge, and G. Gu, "Programmable design of soft pneu-net actuators with oblique chambers can generate coupled bending and twisting motions," *Sensors and Actuators A: Physical*, vol. 271, pp. 131–138, 2018.

[42] L. Wiggins, M. Stubbs, C. Johnston, H. Robertshaw, C. Reinholtz, and D. Inman, "A design and analysis of a morphing hyper-elliptic cambered span (hecs) wing," *American Institute of Aeronautics and Astronautics*, 2004.

[43] *Defining the future*, 2007. [Online]. Available: `https://www.lockheedmartin.com/en-us/who-we-are/business-areas/aeronautics/skunkworks.html`.

[44] *Focused innovation*, 2007. [Online]. Available: `https://www.nextgenaero.com`.

[45] M. Kikuta, "Mechanical properties of candidate materials for morphing wings," Ph.D. dissertation, Department of Mechanical Engineering, Virginia Polytechnic Institute and State University, 2003.

[46] S. Kota, J. Hetrick, and R. Osborn, "Adaptive structures: Moving into the mainstream," *Aerospace America*, vol. 44, no. 9, pp. 16–18, 2006.

[47] P. Weiss, "Ahead of the curve: Novel morphing wing may reduce aircraft's fuel use," *Science News*, pp. 406–407, 2006.

[48] *Flexibly engineering the "impossible"*, 2007. [Online]. Available: `https://www.flxsys.com`.

[49] M. J. Devereux and D. Tyler, "Pneumatic artificial muscles," Ph.D. dissertation, Department of Aerospace Engineering, University of Bristol, 2006.

[50] M. Philen, Y. Shan, C. Bakis, K. Wang, and C. Rahn, "Variable stiffness adaptive structures utilizing hydraulically pressurized flexible matrix composites with valve control," *47th AIAA/ASCE/AHS/ASC Structures, Structural Dynamics and Materials Conference*, 2006.

[51] Y. Shan and C. Bakis, "Flexible matrix composite actuators," *20th Annual Technical Conference of Amercian Society for Composites*, 2005.

[52] Y. Wei, Q. Fang, Z. Jin, and X. Feng, "Research progress on constitutive model of filled rubber," *Polymer Bulletin*, vol. 5, no. 2, pp. 15–21, 2014.

[53] H. Hong He, Q. Zhang, Y. Zhang, J. Chen, L. Zhang, and F. Li, "A comparative study of 85 hyperelastic constitutive models for both unfilled rubber and highly filled rubber nanocomposite material," *Nano Materials Science*, vol. 4, no. 2, pp. 64–82, 2022.

[54] L. D. Landau and E. M. Lifshitz, *Nonlinear Solid Mechanics. A Continuum Approach for Engineering.* John Wiley & Sons, 2001.

[55] L. Treloar, "The elasticity of a network of long-chain molecules," *Transactions of the Faraday Society*, vol. 39, pp. 241–246, 1943.

[56] M. Mooney, "A theory of large elastic deformation," *Journal of Applied Physics*, vol. 11, no. 9, pp. 582–592, 1940.

[57] A. Isihara, N. Hashitsume, and M. Tatibana, "Statistical theory of rubber-like elasticity," *The Journal of Chemical Physics*, vol. 19, no. 12, pp. 1508–1512, 1951.

[58] V. Biderman, *Calculation of Rubber Parts*. Rascheti na Prochnost, 1958.

[59] A. James, A. Green, and G. Simpson, "Strain energy functions of rubber. i. characterization of gum vulcanizates," *Polymer Science*, vol. 19, no. 7, 1975.

[60] M. Bahreman and H. Darijani, "New polynomial strain energy function; application to rubbery circular cylinders under finite extension and torsion," *Journal of Applied Polymer Science*, vol. 132, no. 13, pp. 1–14, 2015.

[61] K. Valanis and R. Landel, "The strain-energy function of a hyperelastic material in terms of the extension ratios," *Journal of Applied Physics*, vol. 38, no. 7, pp. 2997–3002, 1967.

[62] T. Beda and Y. Chevalier, "Hybrid continuum model for large elastic deformation of rubber," *Journal of Applied Physics*, vol. 94, no. 4, pp. 2701–2706, 2003.

[63] H. Bechir, L. Chevalier, M. Chaouche, and K. Boufala, "Hyperelastic constitutive model for rubber-like materials based on the first seth strain measures invariant," *Journal of Applied Physics*, vol. 25, no. 1, pp. 110–124, 2006.

[64] R. Sacco, G. Guidoboni, and A. Mauri, "A comprehensive physically based approach to modeling in bioengineering and life sciences," in A. M. R. Sacco G. Guidoboni, Ed. Academic Press, 2019, ch. Chapter 11 - Constitutive Relations for Solids.

[65] *Mooney–rivlin solid*, Jan. 2023. [Online]. Available: `https://en.wikipedia.org/wiki/Mooney%E2%80%93Rivlin_solid`.

[66] *Ogden hyperelastic model*, May 2022. [Online]. Available: `https://en.wikipedia.org/wiki/Ogden_hyperelastic_model`.

[67] *Polynomial hyperelastic model*, May 2022. [Online]. Available: `https://en.wikipedia.org/wiki/Polynomial_hyperelastic_model`.

[68] *Hyperelastic material*, Jan. 2023. [Online]. Available: `https://en.wikipedia.org/wiki/Hyperelastic_material`.

[69] W. Kuhn, "Über die gestalt fadenförmiger moleküle in lösungen," *Kolloid-Zeitschrift*, vol. 68, no. 1, pp. 2–15, 1934.

[70] P. Flory, "Etwork structure and the elastic properties of vulcanized rubber," *Chemical Reviews*, vol. 35, no. 1, pp. 51–75, 1944.

[71] E. Arruda and M. Boyce, "A three-dimensional constitutive model for the large stretch behavior of rubber elastic materials," *Journal of the Mechanics and Physics of*, vol. 41, no. 2, pp. 389–412, 1993.

[72] L. Treloar and G. Riding, "A non-gaussian theory for rubber in biaxial strain. i. mechanical properties," *Proceedings of the Royal Society A*, vol. 369, no. 1737, pp. 261–280, 1979.

[73] P. Wu and E. Giessen, "On improved 3-d non-gaussian network models for rubber elasticity," *Mechanics Research Communications*, vol. 19, no. 5, pp. 427–433, 1992.

[74] A. Zuniga and M. Beatty, "Constitutive equations for amended non-gaussian network models of rubber elasticity," *International Journal of Engineering Science*, vol. 40, no. 20, pp. 2265–2294, 2002.

[75] H. Bechir, L. Chevalier, and M. Idjeri, "A three-dimensional network model for rubber elasticity: The effect of local entanglements constraints," *International Journal of Engineering Science*, vol. 48, no. 3, pp. 265–274, 2010.

[76] *Arruda–boyce model*, Aug. 2022. [Online]. Available: `https://en.wikipedia.org/wiki/Arruda%E2%80%93Boyce_model`.

[77] *Neo-hookean solid*, Oct. 2022. [Online]. Available: `https://en.wikipedia.org/wiki/Neo-Hookean_solid`.

[78] *Gent hyperelastic model*, May 2022. [Online]. Available: `https://en.wikipedia.org/wiki/Gent_hyperelastic_model`.

[79] *Hyperelastic material behavior*. [Online]. Available: `https://classes.engineering.wustl.edu/2009/spring/mase5513/abaqus/docs/v6.6/`.

[80] M. T. Duong, N. H. Nguyen, and M. Staat, "Physical response of hyperelastic models for composite materials and soft tissues," *Asia Pacific Journal on Computational Engineering*, vol. 2, no. 3, 2015.

[81] N. Nguyen, M. Duong, T. N. Tran, O. Grottke, R. Tolba, and M. Staat, "Influence of a freeze–thaw decomposition on the stress–stretch curves of capsules of porcine abdominal organs," *Journal of Biomechanics*, vol. 45, no. 14, pp. 2382–2386, 2012.

[82] M. Duong, N. Nguyen, T. N. Tran, R. Tolba, and M. Staat, "Influence of refrigerated storage on tensile mechanical properties of porcine liver and spleen," *International Biomechanics*, vol. 2, no. 1, pp. 79–88, 2015.

[83] J. Humphrey and F. Yin, "On constitutive relations and finite deformations of passive cardiac tissue: I. a pseudostrain-energy function," *International Journal of Engineering Science*, vol. 109, no. 4, pp. 298–304, 1987.

[84] M. M. Zeidi, "Gradient elasticity modelling and analysis for the mechanics of unidirectional and bidirectional fiber reinforced composites," Ph.D. dissertation, University of Alberta, 2018.

[85] F. dell'Isola, A. Della Corte, L. Greco, and A. Luongo, "Plane bias extension test for a continuum with two inextensible families of fibers: A variational treatment with lagrange multipliers and a perturbation solution," *International Journal of Solids and Structures*, vol. 81, pp. 1–12, 2016.

[86] M. Zeidi and C. Kim, "Gradient elasticity theory for fiber composites with fibers resistant to extension and flexure," *International Journal of Engineering Science*, vol. 131, pp. 80–99, 2018.

[87] C. I. Kim and S. Islam, "Mechanics of third-gradient continua reinforced with fibers resistant to flexure in finite plane elastostatics," *Continuum Mechanics and Thermodynamics*, vol. 32, pp. 1595–1617, 2020.

[88] C. I. Kim and S. Ehsan, "Linear theory for the mechanics of third-gradient continua reinforced with fibers resistance to flexure," *Mathematics and Mechanics of Solids*, vol. 25, no. 4, pp. 937–960, 2019.

[89] R. S. Rivlin, "Iutam symposium on anisotropy, inhomogeneity and nonlinearity in solid mechanics," in D. Parker and A. England, Eds. Dordrecht: Kluwer Academic Publishers, 1995, ch. Constitutive equations for a fiber-reinforced lamina.

[90] D. J. Steigmann, "Theory of elastic solids reinforced with fibers resistant to extension, flexure and twist," *International Journal of Non-Linear Mechanics*, vol. 47, pp. 743–742, 2012.

[91] R. W. Ogden and D. G. Roxburgh, "A pseudo-elastic model for the mullins effect in filled rubber," *Proceedings of the Royal Society A: Mathematical, Physical and Engineering Sciences*, vol. 455, no. 1988, 1999.

[92] W. Weibull, "A statistical distribution function of wide applicability," *Journal of Applied Mechanics*, vol. 18, no. 3, pp. 293–297, 1951.

[93] A. Spencer and K. Soldatos, "Finite deformations of fibre-reinforced elastic solids with fibre bending stiffness," *International Journal of Non-Linear Mechanics*, vol. 42, pp. 355–368, 2007.

[94] E. Fried and M. Gurtin, "Gradient nanoscale polycrystalline elasticity: Intergrain interactions and triple-junction conditions," *Journal of the Mechanics and Physics of Solids*, vol. 57, pp. 1749–1779, 2009.

[95] M. Zeidi and C. Kim, "Mechanics of fiber composites with fibers resistant to extension and flexure," *Mathematics and Mechanics of Solids*, vol. 24, no. 1, pp. 3–17, 2017.

[96] M. Zeidi and C. Kim, "Finite plane deformations of elastic solids reinforced with fibers resistant to flexure: Complete solution," *Archive of Applied Mechanics*, 2017.

[97] F. Dell'Isola and D. Steigmann, "A two-dimensional gradient-elasticity theory for woven fabrics," *Journal of Elasticity*, vol. 118, no. 1, pp. 113–125, 2015.

[98] R. Mindlin and H. Tiersten, "Effects of couple-stresses in linear elasticity," *Archive for Rational Mechanics and Analysis*, vol. 11, pp. 415–448, 1962.

[99] F. Dell'Isola, P. Seppecher, and A. Madeo, "How contact interactions may depend on the shape of cauchy cuts in nth gradient continua: Approach "a la d'alembert"," *Zeitschrift für Angewandte Mathematik und Physik*, vol. 63, pp. 1119–1141, 2012.

[100] F. Dell'Isola, A. D. Corte, and I. Giorgio, "Higher-gradient continua: The legacy of piola, mindlin, sedov and toupin and some future research perspectives," *Mathematics and Mechanics of Solids*, vol. 22, no. 4, pp. 852–872, 2016.

[101] P. Germain, "The method of virtual power in continuum mechanics, part 2: Microstructure," *SIAM Journal on Applied Mathematics*, vol. 25, pp. 556–575, 1973.

[102] F. Dell'Isola and P. Seppecher, "The relationship between edge contact forces, double forces and interstitial working allowed by the principl of virtual power," *Comptes rendus de l'Académie des sciences. Série IIb, Mécanique, physique, astronomie*, p. 7, 1995.

[103] H. Askes, S. A., and L. Sluys, "A classification of higher-order strain-gradient models – linear analysis," *Archive of Applied Mechanics*, vol. 72, pp. 171–188, 2002.

[104] A. J.J., S. P., and F. Dell'Isola, "Truss modular beams with deformation energy depending on higher displacement gradients," *Archive of Applied Mechanics*, vol. 8, no. 1, pp. 51–73, 2003.

[105] D. J. Steigmann, *Finite Elasticity Theory*. Oxford University Press, 2017.

[106] R. Ogden, *Non-Linear Elastic Deformations*. Wiley, 1984.

[107] R. Toupin, "Theories of elasticity with couple stress," *Archive for Rational Mechanics and Analysis*, vol. 38, no. 8, pp. 634–640, 1971.

[108] W. Koiter, "Couple-stresses in the theory of elasticity," *Proceedings of the Koninklijke Nederlandse Akademie van Wetenschappen, Series B*, vol. 67, pp. 17–44, 1964.

[109] A. Javili, F. dell'Isola, and P. Steinmann, "Geometrically nonlinear higher-gradient elasticity with energetic boundaries," *Journal of the Mechanics and Physics of Solids*, vol. 61, no. 12, pp. 2381–2401, 2013.

[110] M. Zeidi and C. Kim, "Mechanics of an elastic solid reinforced with bidirectional fiber in finite plane elastostatics: Complete analysis," *Continuum Mechanics and Thermodynamics*, vol. 30, no. 3, pp. 573–592, 2018.

[111] F. Dell'Isola, I. Giorgio, M. Pawlikowski, and N. L. Rizzi, "Large deformations of planar extensible beams and pantographic lattices: Heuristic homogenization, experimental and numerical examples of equilibrium," *Proceedings of the Royal Society A*, vol. 472, no. 2185, 2016.

[112] F. Dell'Isola, M. Cuomo, L. Greco, and A. Della Corte, "Bias extension test for pantographic sheets: Numerical simulations based on second gradient shear energies," *Journal of Engineering Mathematics*, vol. 103, no. 1, pp. 127–157, 2017.

[113] D. Steigmann and F. Dell'Isola, "Mechanical response of fabric sheets to three-dimensional bending, twisting, and stretching," *Acta Mechanica Sinica*, vol. 31, no. 3, pp. 373–382, 2015.

[114] D. J. Steigmann, "Invariants of the stretch tensors and their application to finite elasticity theory," *Mathematics and mechanics of solids*, vol. 7, no. 4, pp. 393–404, 2002.

[115] M. Zeidi and C. Kim, "Mechanics of fiber composites with fibers resistant to extension and flexure," *Non-Linear Mechanics*, vol. 24, no. 1, pp. 3–17, 2017.

[116] L. Mihai and A. Goriely, "How to characterize a nonlinear elastic material? a review on nonlinear constitutive parameters in isotropic finite elasticity," *Proceedings of the Royal Society A*, vol. 473, 2017.

[117] G. Holzapfel, T. Gasser, and R. Ogden, "A new constitutive framework for arterial wall mechanics and a comparative study of material models," *Journal of Elasticity*, vol. 61, pp. 1–48, 2000.

[118] B. Yan, J. Huang, L. Han, *et al.*, "Duplicating dynamic strain-stiffening behavior and nanomechanics of biological tissues in a synthetic self-healing flexible network hydrogel," *ACS Nano*, vol. 11, pp. 11 074–11 081, 2017.

[119] H. A. K. Hayashi, *Data book on mechanical properties of living cells, tissues, and organs.* Springer, 1996.

[120] C. I. Kim, "Strain-gradient elasticity theory for the mechanics of fiber composites subjected to finite plane deformations: Comprehensive analysis," *Multiscale Science and Engineering*, vol. 1, no. 2, pp. 150–160, 2019.

[121] A. J. M. Spencer, *Deformations of Fibre-reinforced Materials.* Oxford University Press, 1972.

[122] A. J. M. Spencer and K. P. Soldatos, "Finite deformations of fibre-reinforced elastic solids with fibre bending stiffness," *International Journal of Non-Linear Mechanics*, vol. 42, pp. 355–368, 2007.

[123] G. A. Holzapfel and R. W. Ogden, *Mechanics of Biological Tissue.* Springer, 2006.

[124] Y. Ma, X. Feng, J. Rogers, Y. Huang, and Y. Zhang, "Design and application of 'jshaped' stress-strain behavior in stretchable electronics: A review," *Lab on a chip*, vol. 17, no. 1, pp. 1689–1704, 2017.

[125] S. Islam, D. Zhalmuratova, H. Chung, and C. I. Kim, "A model for hyperelastic materials reinforced with fibers resistance to extension and flexure," *International Journal of Solids and Structures*, vol. 193-194, pp. 418–433, 2020.

[126] J. E. Q. Quinsaat, I. Burda, R. Kramer, *et al.*, "Conductive silicone elastomers electrodes processable by screen printing," *Scientific Reports*, vol. 9, no. 1, pp. 1–11, 2019.

[127] L. Yang, S. L. Phua, C. L. Toh, *et al.*, "Polydopamine-coated graphene as multifunctional nanofillers in polyurethane," *RSC Advances*, vol. 3, no. 18, p. 6377, 2013.

[128] J. C. Yeo, J. Yu, Z. M. Koh, Z. Wang, and C. T. Lim, "Wearable tactile sensor based on flexible microfluidics," *Lab on a Chip*, vol. 16, no. 17, pp. 3244–3250, 2016.

[129] Y. Elsayed, A. Vincensi, C. Lekakou, *et al.*, "Finite element analysis and design optimization of a pneumatically actuating silicone module for robotic surgery applications," *Soft Robotics*, vol. 1, no. 4, pp. 255–262, 2014.

[130] J. L. Sparks, N. A. Vavalle, K. E. Kasting, *et al.*, "Use of silicone materials to simulate tissue biomechanics as related to deep tissue injury," *Advances in Skin & Wound Care*, vol. 28, no. 2, pp. 59–68, 2015.

[131] L. D. Landau and E. M. Lifshitz, *Theory of Elasticity (3rd ed.)* Pergamon Press, 1986.

[132] S. S. Antman, *Nonlinear Problems of Elasticity.* Springer, 2005.

[133] E. Reissner, "A further note on finite-strain force and moment stress elasticity," *Zeitschrift fur angewandte Mathematik und Physik*, vol. 38, pp. 665–673, 1987.

[134] A. R. Trivedi and C. R. Siviour, "A simple rate-temperature dependent hyperelastic model applied to neoprene rubber," *Journal of Dynamic Behavior of Materials*, vol. 6, no. 3, pp. 336–347, 2020.

[135] Y. Bai, C. Liu, G. Huang, W. Li, and S. Feng, "A hyper-viscoelastic constitutive model for polyurea under uniaxial compressive loading," *Polymers*, vol. 8, no. 4, p. 133, 2016.

[136] C. Siviour and J. Jordan, "High strain rate mechanics of polymers: A review," *Journal of Dynamic Behavior of Materials*, vol. 2, no. 1, pp. 15–32, 2016.

[137] B. Zheng, X. Gao, M. Li, *et al.*, "Formability and failure mechanisms of woven cf/peek composite sheet in solid-state thermoforming," *Polymers*, vol. 11, no. 6, p. 966, 2019.

[138] N. Fazita, K. Jayaraman, and D. Bhattacharyya, "Formability analysis of bamboo fabric reinforced poly (lactic) acid composites," *Materials*, vol. 9, no. 7, p. 539, 2016.

[139] B. Zheng, H. Wang, Z. Huang, Y. Zhang, H. Zhou, and L. D., "Experimental investigation and constitutive modeling of the deformation behavior of poly-ether-ether-ketone at elevated temperatures," *Polymer Testing*, vol. 63, pp. 349–359, 2017.

[140] M. Dworak, R. A., M. J., and S. Blazewicz, "Dynamic mechanical properties of carbon fibre-reinforced peek composites in simulated body-fluid," *Composite Structures*, vol. 161, pp. 428–434, 2017.

[141] N. Boudeau, D. Liksonov, T. Barriere, L. Maslovc, and J. C. Gelin, "Composite based on polyetheretherketone reinforced with carbon fibres, an alternative to conventional materials for femoral implant: Manufacturing process and resulting structural behaviour," *Materials & Design*, vol. 40, pp. 148–156, 2012.

[142] U. K. Vaidya and K. K. Chawla, "Processing of fibre reinforced thermoplastic composites. international materials reviews," *International Materials Reviews*, vol. 53, no. 4, pp. 185–218, 2013.

[143] A. P. Morales, A. Güemes, A. Fernandez-Lopez, V. C. Valero, and S. D. L. R. Llano, "Bamboo-polylactic acid (pla) composite material for structural applications," *Materials*, vol. 10, no. 11, p. 1286, 2017.

[144] N. Abilash and M. Sivapragash, "Optimizing the delamination failure in bamboo fiber reinforced polyester composite," *Journal of King Saud University - Engineering Sciences*, vol. 28, no. 1, pp. 92–102, 2016.

[145] H. Takuda, T. Enami, K. Kubota, and T. Hatta, "The formability of a thin sheet of mg-8.5li-1zn alloy," *Journal of Materials Processing Technology*, vol. 101, no. 3, pp. 281–286, 2000.

[146] T. Deng, W. Zhang, W. Jiang, *et al.*, "A hybrid lamination model for simulation of woven fabric reinforced thermoplastic composites solid-state thermo-stamping," *Materials & Design*, vol. 200, p. 109 419, 2021.

[147] S. Biswas, Q. Ahsan, A. Cenna, M. Hasan, and A. Hassan, "Physical and mechanical properties of jute, bamboo and coir natural fiber," *Fibers and Polymers*, vol. 14, pp. 1762–1767, 2013.

[148] X. Wei, H. Zhou, F. Chen, and G. Wang, "Bending flexibility of moso bamboo (phyllostachys edulis) with functionally graded structure," *Materials*, vol. 12, no. 12, 2018.

[149] S. Mirkhalaf and M. Fagerström, "The mechanical behavior of polylactic acid (pla) films: Fabrication, experiments and modelling," *Mechanics of Time-Dependent Materials*, vol. 25, pp. 119–131, 2019.

[150] J. Bai, D. Chen, J. Xiong, and R. Shenoi, "Folding analysis for thin-walled deployable composite boom," *Acta Astronautica*, vol. 159, pp. 622–636, 2019.

[151] H. Huanga, F. Guan, L. Pan, and Y. Xu., "Design and deploying study of a new petal-type deployable solid surface antenna," *Acta Astronautica*, vol. 148, pp. 99–110, 2018.

[152] Z. Chu, Z. Deng, X. Qi, and B. Li, "Modeling and analysis of a large deployable antenna structure," *Acta Astronautica*, vol. 95, pp. 51–60, 2014.

[153] J. Block, M. Straubel, and M. Wiedemann, "Ultralight deployable booms for solar sails and other large gossamer structures in space," *Acta Astronautica*, vol. 68, pp. 7–8, 2011.

[154] M. Pankow and C. White., "Design and testing of bi-stable booms for space applications," *20th International Conference on Composite Materials*, vol. 3405, no. 4, 2015.

[155] S. Wang, M. Schenk, S. Jiang, and A. Viquerat, "Blossoming analysis of composite deployable booms," *Thin-Walled Structures*, vol. 157, 2020.

[156] H. Y. C. Mallikarachchi, "Thin-walled composite deployable booms with tape-spring hinges," Ph.D. dissertation, University of Cambridge, 2011.

[157] C. Lüders, "Nonlinear-elastic orthotropic material modeling of an epoxy-based polymer for predicting the material behavior of transversely loaded fiber-reinforced composites," *Journal of Composites Science*, vol. 4, no. 2, 2020.

[158] I. Giorgio, F. Dell'Isola, and D. Steigmann, "Edge effects in hypar nets.," *Comptes Rendus Mécanique*, vol. 347, pp. 114–123, 2019.

[159] F. Carpi, G. Frediani, S. Turco, and D. D. Rossi, "Bioinspired tunable lens with muscle-like electroactive elastomers," *Advanced Functional Materials*, vol. 21, pp. 4152–4158, 2011.

[160] G. Holzapfel, "Handbook of materials behavior models," in J. Lemaitre, Ed. New York: Academic Press, 2001, ch. Biomechanics of soft tissue.

[161] F. Verzar, "International review of connective tissue research, volume 2," in D. A. Hall, Ed. New York: Academic Press, 1964, ch. Aging of the collagen fiber.

[162] P. Brinckmann, W. Frobin, and G. Leivseth, *Musculoskeletal Biomechanics*. Thieme, 2002.

[163] S. Nesbitt, W. Scott, J. Macione, and S. Kotha, "Collagen fibrils in skin orient in the direction of applied uniaxial load in proportion to stress while exhibiting differential strains around hair follicles," *Materials*, vol. 8, no. 4, pp. 1841–1857, 2015.

[164] F. Silver, J. Freeman, and D. Devore, "Viscoelastic properties of human skin and processed dermis," *Skin Research and Technology*, vol. 7, pp. 18–23, 2001.

[165] S. Hirabayashi and M. Iwamoto, "Finite element analysis of biological soft tissue surrounded by a deformable membrane that controls transmembrane flow," *Theoretical Biology and Medical Modelling*, vol. 15, no. 1, 2018.

[166] L. Horny, E. Gultova, H. Chlup, *et al.*, "Mullins effect in an aorta and limiting extensibility evolution," *Proceedings of the Royal Society A: Mathematical, Physical and Engineering Sciences*, vol. 6, no. 21, 2010.

[167] J. Jancar, J. F. Douglas, F. W. Starr, *et al.*, "Current issues in research on structure-property relationships in polymer nanocomposites," *Polymer*, vol. 51, no. 15, 2010.

[168] ABAQUS, "Analysis user's manual, version 6.14," *SIMULIA Inc.*, 2014.

[169] E. J. Barbero, *Finite element analysis of composite materials using abaqus*. CRC Press, 2013.

[170] O. Gültekin, S. P. Hager, H. Dal, and G. A. Holzapfel, "Computational modeling of progressive damage and rupture in fibrous biological tissues: Application to aortic dissection," *Biomechanics and Modeling in Mechanobiology*, vol. 18, no. 6, 2019.

[171] G. A. Holzapfel, T. C. Gasser, and M. Stadler, "A structural model for the viscoelastic behavior of arterial walls: Continuum formulation and finite element analysis," *European Journal of Mechanics, A-Solids*, vol. 21, no. 3, 2001.

[172] H. Gong, W. Ma, S. Chen, G. Wang, R. Khairallah, and T. Irving, "Localization of the elastic proteins in the flight muscle of manduca sexta," *International Journal of Molecular Sciences*, vol. 21, no. 15, 2020.

[173] H. L. Granzier and S. Labeit, "The giant protein titin: A major player in myocardial mechanics, signaling, and disease," *Circulation Research*, vol. 94, no. 3, 2004.

[174] L. Tskhovrebova and J. Trinick, "Role of titin in vertebrate striated muscle," *Philosophical Transactions of the Royal Society B: Biological Sciences*, vol. 357, no. 1418, 2002.

[175] L. Tskhovrebova and J. Trinick, "Titin: Properties and family relationships," *Nature Reviews Molecular Cell Biology*, vol. 4, no. 9, 2003.

[176] L. Tskhovrebova, J. Trinick, J. A. Sleep, and R. M. Simmons, "Elasticity and unfolding of single molecules of the giant muscle protein titin," *Nature*, vol. 387, no. 6630, 1997.

[177] C. Ziegler, "Titin-related proteins in invertebrate muscles.," *Comparative Biochemistry and Physiology - Part A: Physiology*, vol. 109, no. 4, 1994.

[178] *Neo-hookean solid*, 2023. [Online]. Available: https://www.joelsartore.com/ins015-00031/.

[179] O. Orki, A. Ayali, O. Shai, and U. Ben-Hanan, "Modeling of caterpillar crawl using novel tensegrity structures," *Bioinspiration and Biomimetics*, vol. 7, no. 4, 2012.

[180] S. Islam, S. E. S. Bolouri, and C. I. Kim, "Mechanics of hyperelastic composites reinforced with nonlinear elastic fibrous materials in finite plane elastostatics," *International Journal of Engineering Science*, vol. 165, p. 103 491, 2021.

[181] C. T. Lu, A. Weerasinghe, D. Maroudas, and A. Ramasubramaniam, "A comparison of the elastic properties of graphene- and fullerene-reinforced polymer composites: The role of filler morphology and size," *Scientific Reports*, vol. 6, p. 31 735, 2016.

[182] H. L. Cox, "The elasticity and strength of paper and other fibrous materials," *British Journal of Applied Physics*, vol. 3, no. 3, p. 72, 1952.

[183] N. G. Andre and Z. A. M. Ishak, "Predicting the tensile modulus of randomly oriented nonwoven kenaf/epoxy composites," *Procedia Chemistry*, vol. 19, pp. 419–425, 2016.

[184] L. Gong, I. A. Kinloch, R. J. Young, I. Riaz, R. Jalil, and K. S. Novoselov, "Interfacial stress transfer in a graphene monolayer nanocomposite," *Advanced Materials*, vol. 22, no. 24, pp. 2694–2697, 2010.

[185] T. Yu, Z. Ni, C. Du, Y. You, Y. Wang, and Z. Shen, "Raman mapping investigation of graphene on transparent flexible substrate: The strain effect," *The Journal of Physical Chemistry C*, vol. 112, no. 33, pp. 12 602–12 605, 2008.

[186] G. Guo and Y. Zhu, "Cohesive-shear-lag modeling of interfacial stress transfer between a monolayer graphene and a polymer substrate," *Journal of Applied Mechanics*, vol. 82, no. 3, p. 031 005, 2015.

[187] Z. Li, R. J. Young, N. R. Wilson, I. A. Kinloch, C. Vallés, and Z. Li, "Effect of the orientation of graphene-based nanoplatelets upon the young's modulus of nanocomposites," *Journal of Applied Mechanics*, vol. 82, no. 3, p. 031 005, 2015.

[188] H. Krenchel, *Fibre reinforcement; theoretical and practical investigations of the elasticity and strength of fibre-reinforced materials*. Akademisk Forlag, 1964.

[189] F. M. Blighe, K. Young, J. J. Vilatela, *et al.*, "The effect of nanotube content and orientation on the mechanical properties of polymer-nanotube composite fibers: Separating intrinsic reinforcement from orientational effects," *Advanced Functional Materials*, vol. 21, no. 2, pp. 364–371, 2011.

[190] Z. Yang, D. Wang, Z. Lu, and W. Hu, "Atomistic simulation on the plastic deformation and fracture of bio-inspired graphene/ni nanocomposites," *Applied Physics Letters*, vol. 109, no. 19, p. 191 909, 2016.

[191] G. Wang, L. Liu, and Z. Zhang, "Interface mechanics in carbon nanomaterials-based nanocomposites," *Composites Part A: Applied Science and Manufacturing*, vol. 141, p. 106 212, 2021.

[192] R. J. Young, "Structural integrity and durability of advanced composites: Innovative modelling methods and intelligent design," in Elsevier International Publishing, 2015, ch. Composite micromechanics: From carbon fibres to graphene.

[193] F. Islam, S. Joannes, A. Bunsell, and L. Laiarinandrasana, "Adaptation of weibull analysis to represent strength behaviour of brittle fibres," *International Conference on Composite Materials*, pp. 1916–1921, 2019.

[194] A. Hanif, Y. Kim, and C. Park, "Numerical validation of two-parameter weibull model for assessing failure fatigue lives of laminated cementitious composites-comparative assessment of modeling approaches," *Materials*, vol. 12, no. 1, p. 110, 2018.

[195] D. Shin, I. Jeon, and S. Yang, "Multiscale modeling assessment of the interfacial properties and critical aspect ratio of structurally defected graphene in polymer nanocomposites for defect engineering," *European Journal of Mechanics - A/Solids*, vol. 96, p. 104 728, 2022.

[196] Y. R. Jang, K. Y. Kim, and K. H. Yoo, "Accurate measurement of thickness of large-area graphene layers by neutron reflectometry," *Journal of Materials Science*, vol. 51, no. 22, pp. 10 059–10 065, 2016.

[197] N. Margaryan, N. Kokanyan, and E. Kokanyan, "Low-temperature synthesis and characteristics of fractal graphene layers," *Journal of Saudi Chemical Society*, vol. 23, no. 1, pp. 13–20, 2019.

[198] J. Osicka, M. Mrlik, M. Ilcikova, *et al.*, "Reversible actuation ability upon light stimulation of the smart systems with controllably grafted graphene oxide with poly (glycidyl methacrylate) and pdms elastomer: Effect of compatibility and graphene oxide reduction on the photo-actuation performance," *Polymers*, vol. 10, no. 8, p. 832, 2018.

[199] J. González-Rivera, R. Iglio, G. Barillaro, C. Duce, and M. R. Tiné, "Structural and thermoanalytical characterization of 3d porous pdms foam materials: The effect of impurities derived from a sugar templating process," *Polymers*, vol. 8, no. 6, p. 616, 2018.

[200] C. Chen, X. Bu, Q. Feng, and D. Li, "Cellulose nanofiber/carbon nanotube conductive nano-network as a reinforcement template for polydimethylsiloxane nanocomposite," *Polymers*, vol. 10, no. 9, p. 1000, 2018.

[201] B. A. Alshammari, M. Hossain, A. M. Alenad, A. G. Alharbi, and B. M. AlOtaibi, "Experimental and theoretical analysis of mechanical properties of graphite/polyethylene terephthalate nanocomposites," *Polymers*, vol. 14, no. 9, p. 1718, 2022.

[202] J. S. Noh, "Conductive elastomers for stretchable electronics, sensors and energy harvesters," *Polymers*, vol. 8, no. 4, p. 123, 2016.

[203] M. Cuomo, F. dell'Isola, L. Greco, and N. L. Rizzi, "First versus second gradient energies for planar sheets with two families of inextensible fibres: Investigation on deformation boundary layers, discontinuities and geometrical instabilities," *Composites Part B: Engineering*, pp. 1–16, 2016.